NGU REPORT 2015.063

Coop Phase 2 Crustal Onshore-Offshore Project.

GEOLOGY FOR SOCIETY

SINCE 1858

GEOLOGICAL SURVEY OF NORWAY

- NGU -

NGU REPORT
2015.063

Coop Phase 2 Crustal Onshore-Offshore Project

NORGES GEOLOGISKE UNDERSØKELSE
- NGU -

REPORT

Geological Survey of Norway
P.O.Box 6315 Sluppen
NO-7491 TRONDHEIM
Tel.: 47 73 90 40 00

Report no.: 2015.063

ISSN: 0800-3416 (print)
ISSN: 2387-3515 (online)

Grading: Open

Title:
Coop Phase 2 Crustal Onshore-Offshore Project

Authors: Odleiv Olesen, Vikas Barnawal, Marco Brönner, Einar Dalsegg, Marie-Andrée Dumais, Jomar Gellein, Laurent Gernigon, Tom Heldal, Bjørn Eskil Larsen, Torleif Lauritsen, Ole Lutro, Yuriy Maystrenko, Aziz Nasuti, David Roberts, Håkon Rueslåtten, Jan Steinar Rønning, Trond Slagstad, Arne Solli, Alexandros Stampolidis

Clients: BayernGas, Centrica, ConocoPhillips, Dea, Det norske, DONG, Eni, E.On, GdF Suez, Lundin, Maersk, NGU, Noreco, Oljedirektoratet, Repsol, Statoil, Suncor, Total, VNG and Wintershall.

County:
Møre & Romsdal, Sør-Trøndelag, Nord-Trøndelag

Commune:

Map-sheet name (M=1:250.000) Ulsteinvik, Ålesund, Kristiansund, Trondheim, Namsos, Vega

Map-sheet no. and -name (M=1:50.000)

Deposit name and grid-reference:

Number of pages: 410 **Price (NOK):**
Map enclosures:

Fieldwork carried out:
2010-2015

Date of report:
7.12.2015

Project no.:
336600

Person responsible:

Summary: The Crustal Onshore-Offshore Project (Coop) is an integrated mapping and research project established to study the onshore-offshore relationships in the northeastern North Sea and Mid Norway. The Coop Phase 2 Report summarises the results from the Mid Norway and Møre Margin-Haltenbanken region. New aeromagnetic, radiometric and petrophysical data have been acquired. All new data were compiled with the Coop Phase 1 data from western Norway and the North Sea. Information on mainland basement structures, deep weathering and heat production has been extrapolated to the offshore region. The newly identified Folda-Rørvik-Brønnøysund shear zone appears to represent an old and major continental, strike-slip feature along the coast of central Norway. This shear zone probably influenced the offshore prolongation of the Kollstraumen and Høybakken detachments. We conclude that the Norwegian strandflat is an exhumed weathered and peneplaned surface of Late Triassic to Early Jurassic age that has been modified and levelled during Pleistocene erosion. This surface was preserved beneath Late Jurassic and Cretaceous strata until the Neogene. Support for this conclusion comes from the AMAGER mapping and the occurrence of a relatively flat and gently westward-dipping top of basement beneath the Jurassic sedimentary rocks close to the coastline. The heat generation of the mainland basement rocks has been calculated from the chemical analyses of the U, Th and K contents in c. 2600 bedrock samples and airborne radiometric measurements along the coast of western and central Norway. The heat generation varies with one order of magnitude. The Precambrian granitic gneisses in Nord-Trøndelag show the highest heat production within the Coop2 study area. An area of increased radiogenic heat production also dominates the central part of the offshore area through the Cretaceous and Cenozoic stratigraphic intervals and implies a possible inheritance from the transport of eroded clastic material from the same erosional area. 2D/3D crustal models of the Mid Norway mainland and offshore have been established from gravity, magnetic, seismic, well log and bedrock mapping data. The Frøya High is interpreted as a Precambrian granitic complex quite similar to the magnetic Transcandinavian Igneous Belt (TIB) granitoids observed in Sweden and Norway. Similar high-density lower-crustal bodies in the central/outer Møre Basin, are most likely related to the pre-breakup heterogeneities in the lower continental crust. Our model lends no support for an extensive serpentinisation of the mantle where the preserved continental crust is relatively thick. By attributing thermal properties (e.g., radiogenic heat production and thermal conductivity) to the individual basement bodies we have calculated the heat flow from the basement into the sedimentary basins. The observed and modelled heat flow is strongly controlled by the lithology and structures in the crust. Plans for Coop Phase 3 are summarised at the end of the report.

Keywords: Geofysikk (Geophysics)	Kontinentalsokkel (Continental shelf)	Tolkning (Interpretation)
Berggrunnsgeologi (Bedrock geology)	Magnetometri (Magnetometry)	Varmestrøm (Heat flow)
Petrofysikk (Petrophysics)	Gravimetri (Gravimetry)	Fagrapport (Scientific report)

CONTENTS

1. INTRODUCTION

The Crustal Onshore-Offshore Project (Coop) was initiated by the Geological Survey of Norway (NGU) in 2010 to study the onshore-offshore relationships along the coast of western Norway. The integrated mapping and research project was originally financed by NGU, Oljedirektoratet (NPD) and the petroleum companies BayernGas, ConocoPhillips, Det norske, Lundin, Noreco, Statoil, Total and Wintershall, with the goal especially to improve our knowledge of onshore-offshore tectonic links, deep weathering and heat flow along the coast of western Norway. Phase 1 of the project was reported in January 2013 (Olesen et al. 2013b), December 2013 (Maystrenko 2013) and June 2014 (Maystrenko 2014). Data compilations, 3D models, reports and Powerpoint presentations can be downloaded from the ftp2.ngu.no site. Usernames and passwords to the seven FTP accounts have been distributed to the partners. The content depends on the data access of the different companies. The energy and petroleum companies BKK, Eni, E.ON, GdF Suez, Maersk, Repsol, RWE-Dea and VNG joined the project in 2011 and 2012 as late participants and the project was extended to a Phase 2 including the Møre margin, the Møre-Trøndelag Fault Complex and the Haltenbanken area. The total Coop area includes at the present stage the Viking and Central grabens and the Froan, Møre, Stord, Egersund and Norwegian-Danish basins. The petroleum companies DONG, Centrica and Suncor joined the Coop project in 2014. Coop Phase 1 and 2 together have at the moment a total of 20 external sponsors. Centrica and Suncor joined at the same time a follow-up project (Coop Phase 3) to study the Frøya High, the Slørebotn Sub-Basin and the Sogn Graben in more detail. The present report documents the status from Phase 2. Reprocessing of radiometric data and an updated bedrock map from the Coop1 area are also included. Phase 3 of the project is registered as a separate project at NGU and is financed by Centrica, DONG, E.On, GdF Suez, Lundin, Repsol, Statoil, Suncor, VNG, NPD and NGU. The project will be finished by the end of 2017.

The Coop1 & 2 projects include acquisition of five new airborne surveys acquired in the years 2010-2013, in addition to new gravity and heat-flow data. The aeromagnetic surveys (CNAS-10 and STAS-13) have a profile spacing of 1 km while the combined aeromagnetic and radiometric surveys along the coast of western and Mid Norway (BESTAS-10, SAS-11 and TRAS-13) have a line spacing of 250 m. NGU has in Phase 2 compiled both new surveys (TRAS-12 and STAS-13) and Phase 1 data in addition to other existing aeromagnetic surveys on the mainland and offshore to provide a comprehensive and state-of-the-art aeromagnetic grid of Mid Norway (Nasuti 2013, Olesen et al. 2013b). New petrophysical data such as magnetic properties, density and the K, U and Th contents from spectrometer measurements on outcrops have been acquired in order to facilitate the interpretation of the new surveys.

By attributing thermal properties (e.g., radiogenic heat production and thermal conductivity) to the individual basement bodies from potential field modelling, it is possible to calculate the heat flow from the basement into the sedimentary basins. Understanding heat-flow variation in sedimentary basins is of vital importance for the success of petroleum exploration campaigns. Temperature is critical for both source rock maturation and the diagenesis and quality of reservoir rocks. Petroleum reservoirs occur mainly within the 'Golden Zone' (60-

120°C) (Bjørkum et al. 1998). The depth to this temperature interval depends to a large degree on the basement heat production which contributes approximately 50% of the heat-flow values offshore Norway (Ritter et al. 2004). The heat production within the crystalline basement depends on the content of the radioactive elements K, U and Th. The contents of these elements show a wide variation within the crystalline basement of mainland Norway. We therefore need to upgrade our knowledge of the basement rock composition below the Norwegian continental shelf. The products of the Coop projects include a basement characterization as well as full 3D crustal and thermal models. Relatively felsic rocks such as the Precambrian gneisses and granites generate more heat than the intermediate-mafic rocks within the Caledonian nappes and high-grade metamorphic and igneous units. Assuming a constant heat production from the continental crust in basin modelling studies offshore Norway will therefore lead to considerable errors in the calculation of the temperature regime in sedimentary basins. Analysis of offshore and onshore well data is a fundamental step to obtaining a detailed input for heat flow and thermal gradients.

By this day near 1% of discovered petroleum fields in the world are solely or partly attributed to weathered, fractured and altered basement rocks of different consolidation age. Recent petroleum discoveries on the Utsira High have demonstrated that deeply weathered basement rocks constitute a viable petroleum reservoir on the Norwegian continental shelf. Information on deep weathering of basement rocks on the mainland can be extrapolated from the mainland to the offshore region. Aeromagnetic and gravity data provide continuous coverage of the mainland and offshore areas and act as a bridge between areas traditionally investigated by two different methods: field bedrock mapping and seismic interpretation. High-resolution aeromagnetic surveys are particularly useful for detailed mapping of basement lithology and basement depth, igneous bodies, sand channels, salt diapirs, fault systems and deep weathering. The onshore-offshore geophysical interpretations are also constrained by age-dating and petrophysical analysis of basement core samples obtained from offshore exploration wells (Appendices C and D in Olesen et al. 2013b).

The Coop studies have aimed at compiling lithogeochemical information on basement rocks along the coast of western and central Norway with emphasis on characterising the U, Th and K contents. Geophysical information such as seismic, aeromagnetic and gravity data, together with well penetrations of basement, provides a basis for extending this information below the offshore sedimentary basins. Seismic velocity and seismic-reflection patterns from offshore basement rocks help in distinguishing between Caledonian nappe complexes and more massive Precambrian granites and gneisses. Hence, an updated version of the Slagstad et al. (2009) and Slagstad & Lauritsen (2013) basement-related heat-production maps has been produced (Chapter 6 of the present report).

An additional element of relevance to the heat flow in sedimentary basins is the structural relief of the basement; basement highs most likely act as focusing points for fluids that are being driven out from the overlying sediments. The basement highs will also most likely focus the heat flow since the thermal conductivity in basement rocks is usually higher than in sedimentary seccessions. An element of the project has therefore been to map the basement structure and to combine this with the mapped distribution of rock-types. Temperatures from bottom-hole measurements and drill-stem tests (DST) from selected wells have been used to calibrate the crustal and temperature model.

2. COMPILATION OF AEROMAGNETIC DATA

Aziz Nasuti, Odleiv Olesen, Vikas Barnawal & Marie-Andrée Dumais

2.1 Merger of the COOP grids

Following the Coop Phase 1 project we have assembled a new magnetic compilation for the Coop Phase 2 project area. In this compilation the newly acquired aeromagnetic data from two fixed-wing surveys, TRAS-12 and STAS-13, have been compiled together with some of the existing, onshore, high-resolution helicopter magnetic data (Figure 2.1). It should be noted that only those helicopter data which have good quality and are also located adjacent to the new surveys have been merged with fixed-wing data. The line spacing for helicopter surveys in onshore and near-shore areas is less than for fixed-wing surveys. Therefore, the resolution of helicopter surveys is higher than for fixed-wing surveys. In order to fill the gaps between the newly acquired high-resolution data we have used vintage NGU aeromagnetic data.

For merging, we used the Geosoft software module Grid-knitting (Geosoft 2010a) which allows the merging of multiple grids in a selected order, depending on the quality and resolution of the various surveys (Table 2.1). However, in order to have a full control on the merging process, grids have been merged one by one. The processing steps and a detailed description of the methods were presented in earlier NGU reports (Nasuti et al. 2012; Olesen et al. 2013b).

The grid-merge of data with different quality can locally decrease the resolution of high-quality datasets (in particular in the overlapping areas). For local interpretation and modelling, we consequently recommend using the original grids for a local study. Data from onshore and near-shore areas have been gridded with 50 × 50 m cell size to maintain the details of the high-resolution surveys (Figure 2.2). The offshore data are gridded with 250 × 250 cell size (Figure 2.3). The offshore data are subsequently merged with the onshore data. The grid cell sizes area compromise for preserving the quality and detail of the acquired data.

The complete compilation grid can be provided only to the partners that also purchased the TGS UHAM-09 magnetic dataset, which was used for this compilation. For other sponsors, we have substituted the modern grid with the vintage NGU 74/45 survey.

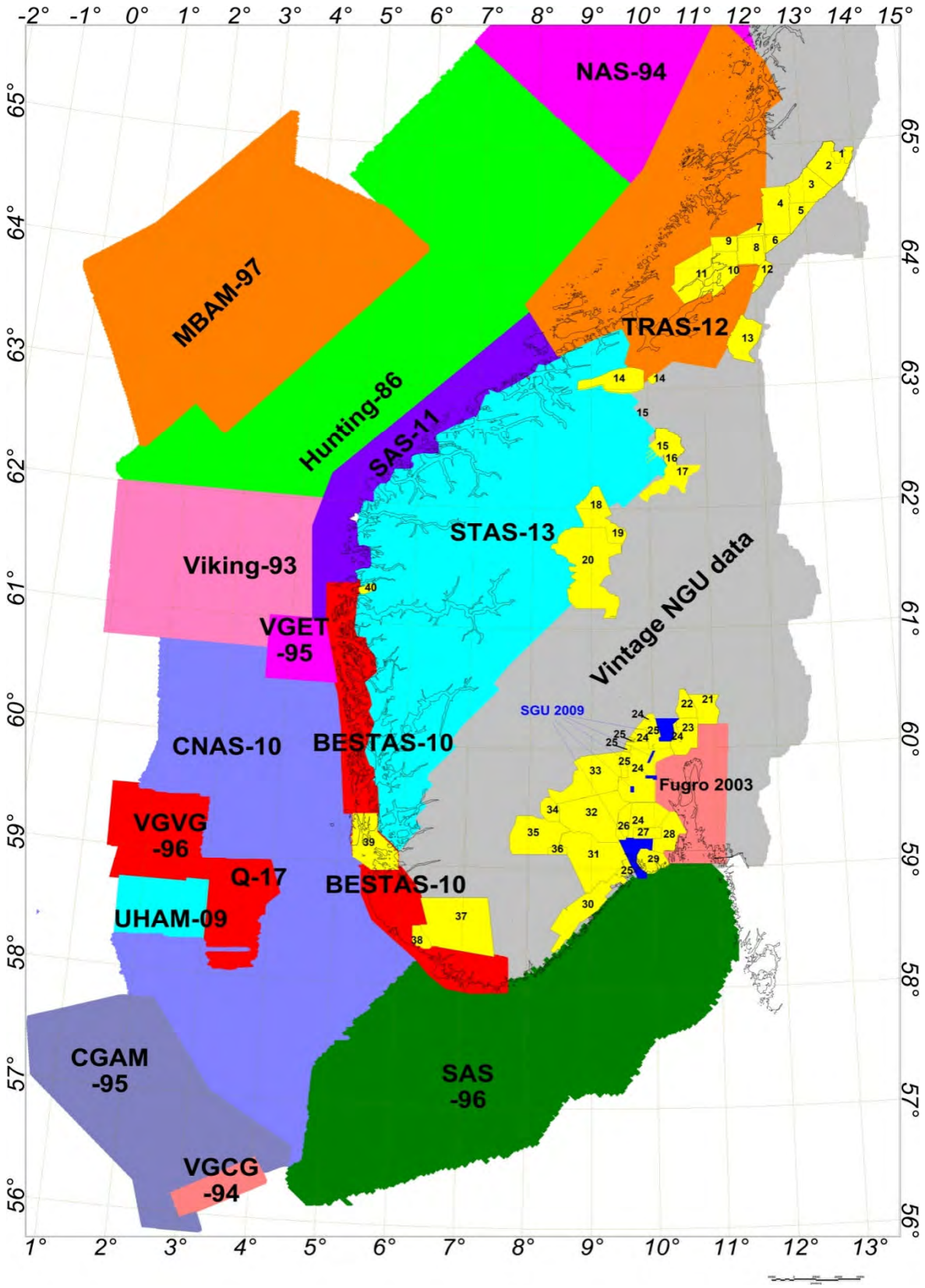

Figure 2.1. Magnetic surveys. Outlines of the various magnetic surveys that have been compiled for the Coop phase 2 project. The solid black line represents the outline of Coop Phase 1. Helicopter surveys are shown with yellow polygons and the numbers depict different surveys. See Table 2.1 for the details.

Table 2.1. Aeromagnetic surveys that have been used for the magnetic compilation.

Year	Area	Operator, Reference	Survey name	Sensor elevation m	Line spacing km	Length km
1986	Trøndelag Platform	Hunting, TGS	Hunting-86	200	2	57.000
1993	N. Viking Graben	Skilbrei & Kihle 1995	Viking-93	150	0.5-2	28.000
1994	Nordland Ridge-Helgeland	Olesen & Smethurst 1995	NAS-94	150	2	38.580
1994	Vøring Basin	Amarok/TGS, 22	VGVB-94	140	1-3	31.800
1994	S. Viking Graben	Amarok/TGS, 24	VGVG-94	160	0.2	44.800
1994	Central Graben, North Sea	TGS 1994	VGCG-94	-	0.6-0.8	11,904
1995	Central Graben, North Sea	TGS 1995	CGAM-95	-	2.5-7.5	17,327
1995	East Troll, North Sea	TGS 1995	VGET-95	-	0.2-0.6	21,866
1996	Quadrant 17, North Sea	TGS 1996	Q17		0.45-1.2	21,347
1996	Skagerrak	NGU, Olesen et al. 2004	SAS-96	150	2	42.000
1997	Møre Basin	Amarok/TGS, 26	MBAM-97	220	1-2	46.600
2003	Oslo region	Fugro 2003	Fugro 2003	60 &100	0.25-0.5	
2009	Utsira high, North Sea	TGS 2009	UHAM-09			
2009	Skien, Kongsberg, Hokksund, Vikersund, Hønefoss1	SGU 2009	SPAS-09	60	0.2	
2010	Central North Sea	Nasuti et al., 2012	CNAS-10	115	1	82.000
2010	Bergen-Stavanger Region	FUGRO, 2010	BESTAS-10			
2011	Stad region (western coast of Norway)	Novatem 2012	SAS-11	60	0.25	
2012	Trøndelag Region Airborne Survey	Novatem 2014	TRAS-12	60	0.25	170.418
2013	Stavanger-Trondheim Aeromagnetic Survey	E.ON 2014	STAS-13	200 drape	1	75.115

Helicopter data

Year	Area	Operator, Reference	Survey name	Sensor elevation m	Line spacing km	Length km	Number on the map Figure 1
1985	Nord-Trøndelag	Skilbrei 1994	Røyrvik, Jomafjell 85				1
1988	Nord-Trøndelag	Rønning et al. 1990	Harran	60	0.25	4.000	2
1993-1994	Nord-Trøndelag	Rønning 1995a	Røyrvik, Grong, Namsskogan, Lierne	60	0.1, 0.2, 0.4	14.200	3
1990	Nord-Trøndelag	Rønning 1991	Grong, Snåsa, Lierne	60	0.2	1.700	5
1992	Nord-Trøndelag	Rønning 1992a	Snåsa	60	0.2	910	6
1992	Nord-Trøndelag	Rønning 1992b	Overhalla	60	0.2	780	7
1992	Nord-Trøndelag	Rønning 1992c	Steinkjer, Snåsa	60	0.2	3.640	8
1986-88	Nord Trøndelag	Mogaard et al. 1989	Steinkjer; Namdalseid; Verran	60	0.2	3.350	9
1991	Nord Trøndelag	Rønning 1995b	Stiklestad 91	60	0.2	1.600	10
1992	Nord Trøndelag	Rønning 1995c	Verran, Mosvik, Leksvik, Inderøy, Rissa, Åfjord	60	0.2	6.250	11

1992	Nord Trøndelag	Skilbrei 1994	Steinkjer, Verdal	60	0.1	1.780	12
1991	Nord Trøndelag	Mogaard & Blokkum 1993	Meråker	60	0.2	4.100	13
1981	Sør-Trøndelag	Kilty & Dvorrak 1982	Løkken 1982	50	-	4.415	14
1983	Sør-Trøndelag	Håbrekke 1983	Rennebu og Oppdal	60	0.2	3.100	15
2004	Hedmark	Mogaard 2004	Røros	60	0.15	3.750	16
1982	Hedmark	Håbrekke 1982	Alvdal , Tynset	60	0.2	2.2	17
1979	Oppland	Håbrekke 1980	Dombås - Vågå - Sjoa	60	0.5	2.200	18
1979	Oppland	Håbrekke 1980	Dombås - Vågå - Sjoa	60	0.5	2.200	19
2011	Oppland	Baranwal et al. 2011					20
2000	Akershus, Oppland	Beard and Mogaard, 2001	Hurdal	60	0.2	2.780	21
1997	Oslo	Beard 1998	Gran	80	0.2	20.20	22
1997-1999	Oslo	Beard 1998 Beard & Rønning1997	Oppkuven	80	0.2	3.260	23
2008-2011	Telemark, Vestfold, Buskerud	Baranwal et al. 2013	Kongsberg Nord & Sør Krøderen, Sokna and Hønefoss 2	75	0.2	13.985	24
2005-2006	Telemark, Buskerud	Mogaard 2006	Bamble Sigdal & Ramsdal Ertelien	60	0.1	3.250	25
1999	Telemark, Buskerud	Mogard & Beard 2000	Nordagutu	60	0.2	1.925	26
1981	Telemark, Vestfold	Håbrekke 1982	Siljan	60	0.2	1.500	27
2000	Vestfold	Mogaard 2001	Sandefjord	60	0.2	3.450	28
1997-1998	Telemark, Vestfold	Mogaard 1998 Beard 1999	Larvik	60 & 80	0.1-0.2	3.684	29
2006	Telemark		Bamle 2006	60	0.1		30
2014	Telemark and Aust -Agder	Stampolidis & Ofstad 2014	Skien and Arendal	50	0.2	10.350	31
2013	Telemark	Stampolidis et al. 2013	Skien	80	0.2	9.960	32
2013-2014	Telemark	Rodionov et al. 2014	Notodden	60	0.2	9.700	33
2012	Telemark	Baranwal et al. 2012	Kviteseid, Seljord og Tokke	65	0.05-0.1	3.514	34
2015	Telemark	Stampolidis & Ofstad 2015	Kviteseid, Nissedal, Fyresdal and Dalen	55	0.2	7.340	35
2012	Telemark	Rønning et al. 2012	Nissedal	60	0.2	2.174	36
2013-2014	Vest-Agder and Rogaland	Ofstad 2015	Kvinesdal, Sirdal, Soknedal, Lund, Bjerkreim, Audnedal	55	0.2	14.600	37
1995	Rogaland	Rønning 1995d	Sokndal	60	0.1	2.400	38
2006	Rogaland	Bystrøm 2006	ROGAS	100	0.25		39
1994	Sogn og Fjordane	Rønning & Mogaard 1995	Dale	60	0.1	1.065	40

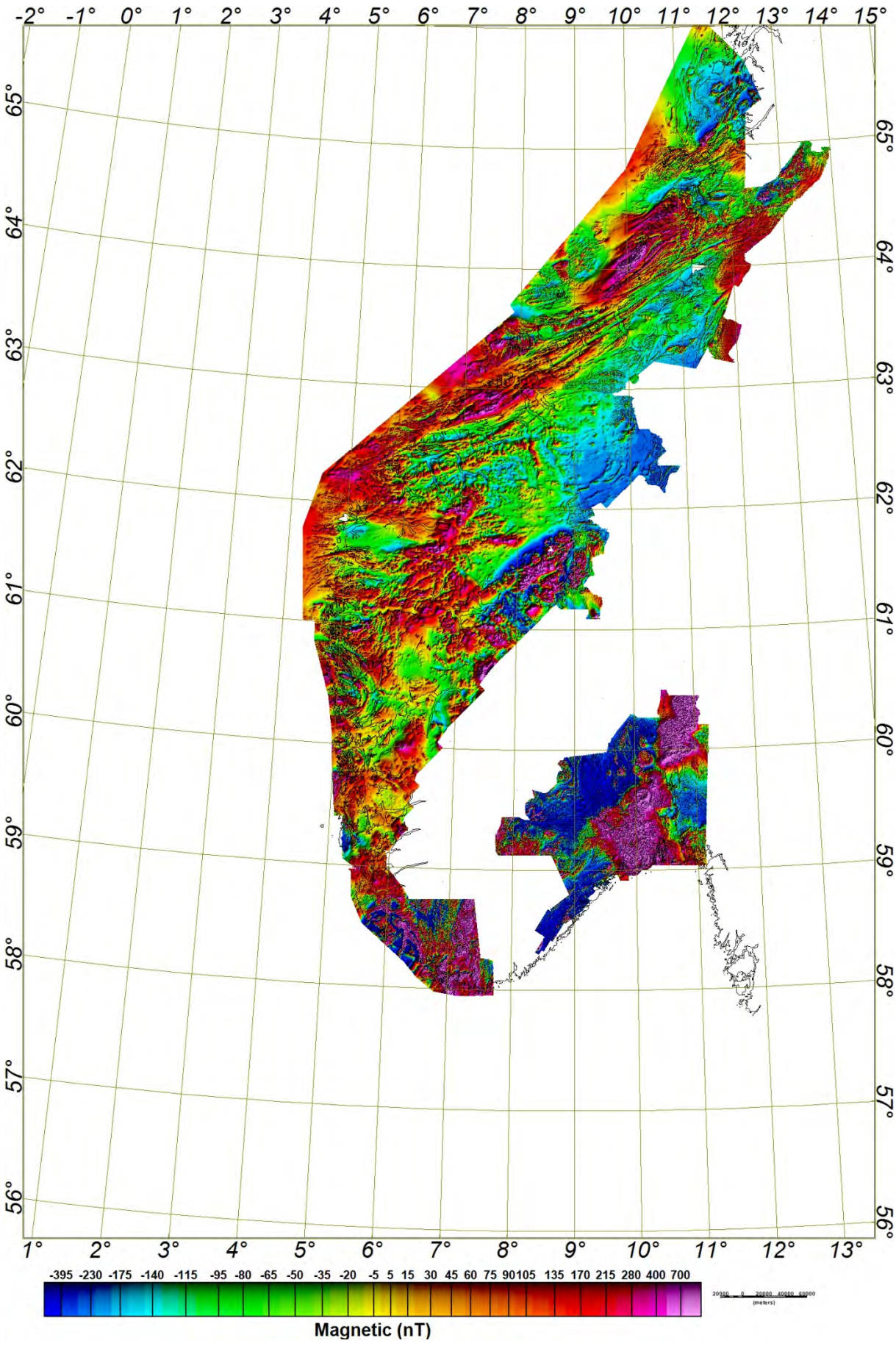

Figure 2.2. Total magnetic field referred to IGRF for onshore and near-shore areas.

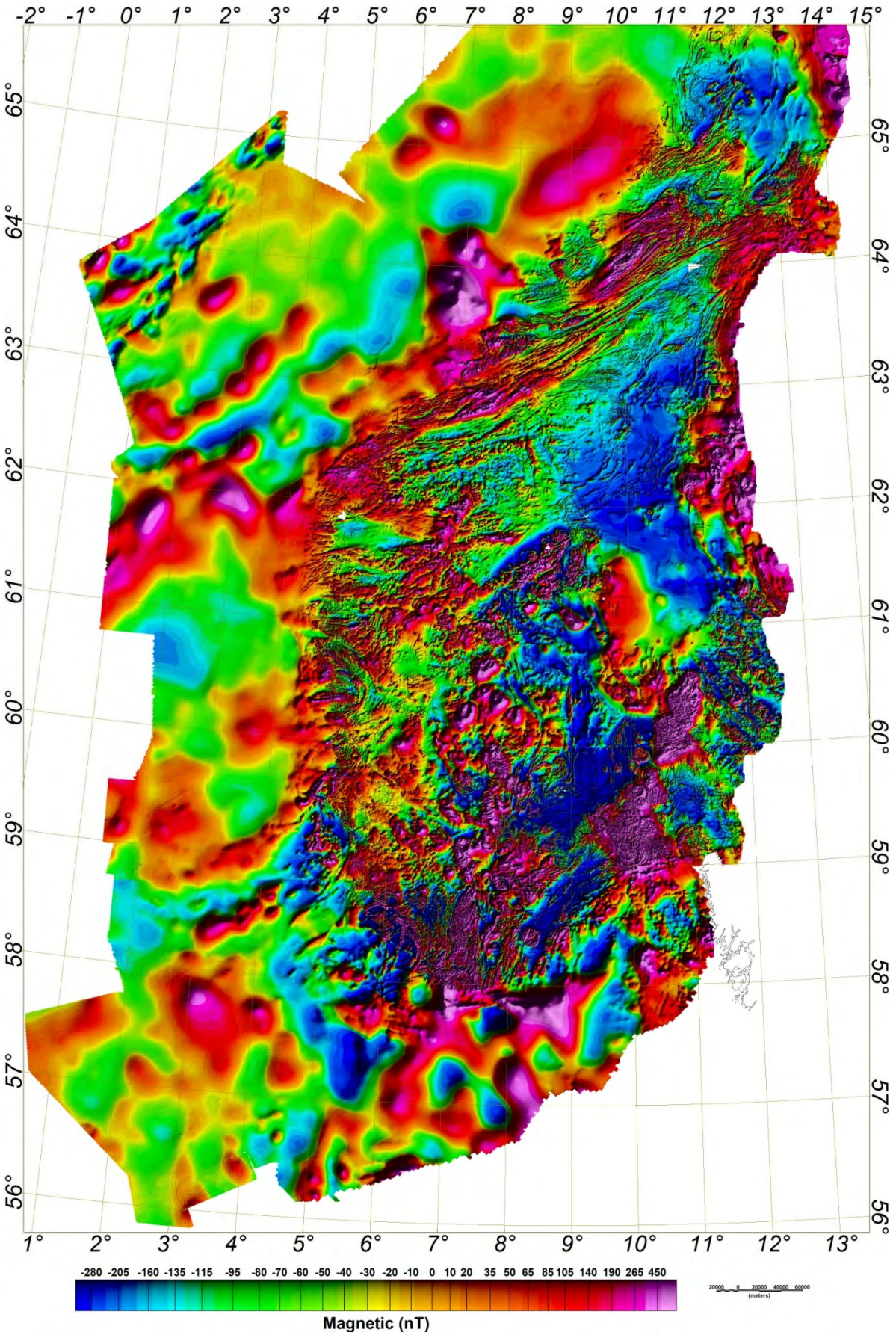

Figure 2.3. Total magnetic field referred to IGRF for the Coop Phase 2 Project.

2.2 Comparison with the previous compilation

In comparison with the previous compilation presented in the Coop Phase 1 report (Nasuti et al. 2012, 2013, Olesen et al. 2013b), the new compilation includes the most recent surveys, TRAS-12, STAS-13, in addition to the high-resolution heliborne datasets. The new data reveal a significant improvement in data quality and resolution (Figures 2.2 & 2.3). The acquisition of the new data during the last five years also aimed at closing the gap between offshore and onshore observations to allow a combined interpretation and correlation of the onshore geology to the offshore regions in the western coastal areas of Norway. A number of additional linear features, which can be linked to structures observed onshore, could be followed into the offshore regions and thus permitted a better onshore-offshore correlation and provided a better basis for the interpretation of particular features. For example, the STAS-13 survey is compared with old datasets from NGU (64-76) (Olesen et al. 2010) in Figure 2.4. The new database shows not only much more details but also a significant improvement in terms of noise and artefacts (Figure 2.5). The improvements are most noticeable when data are filtered for anomaly enhancements (discussed later in this chapter).

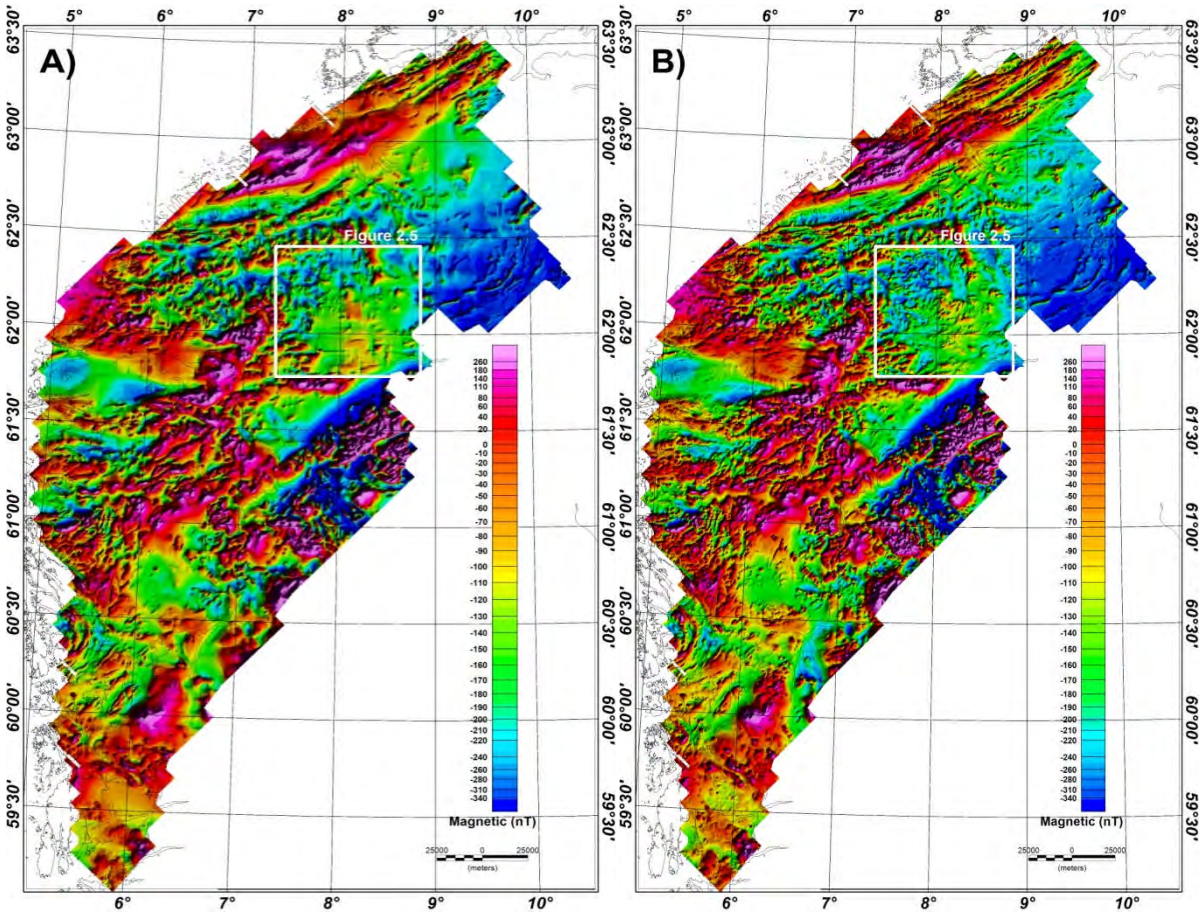

Figure 2.4. Comparison of vintage and new datasets; (A) old NGU dataset, (B) new STAS-13 Survey. See Figure 2.1 and Table 2.1 for the location and details of the survey.

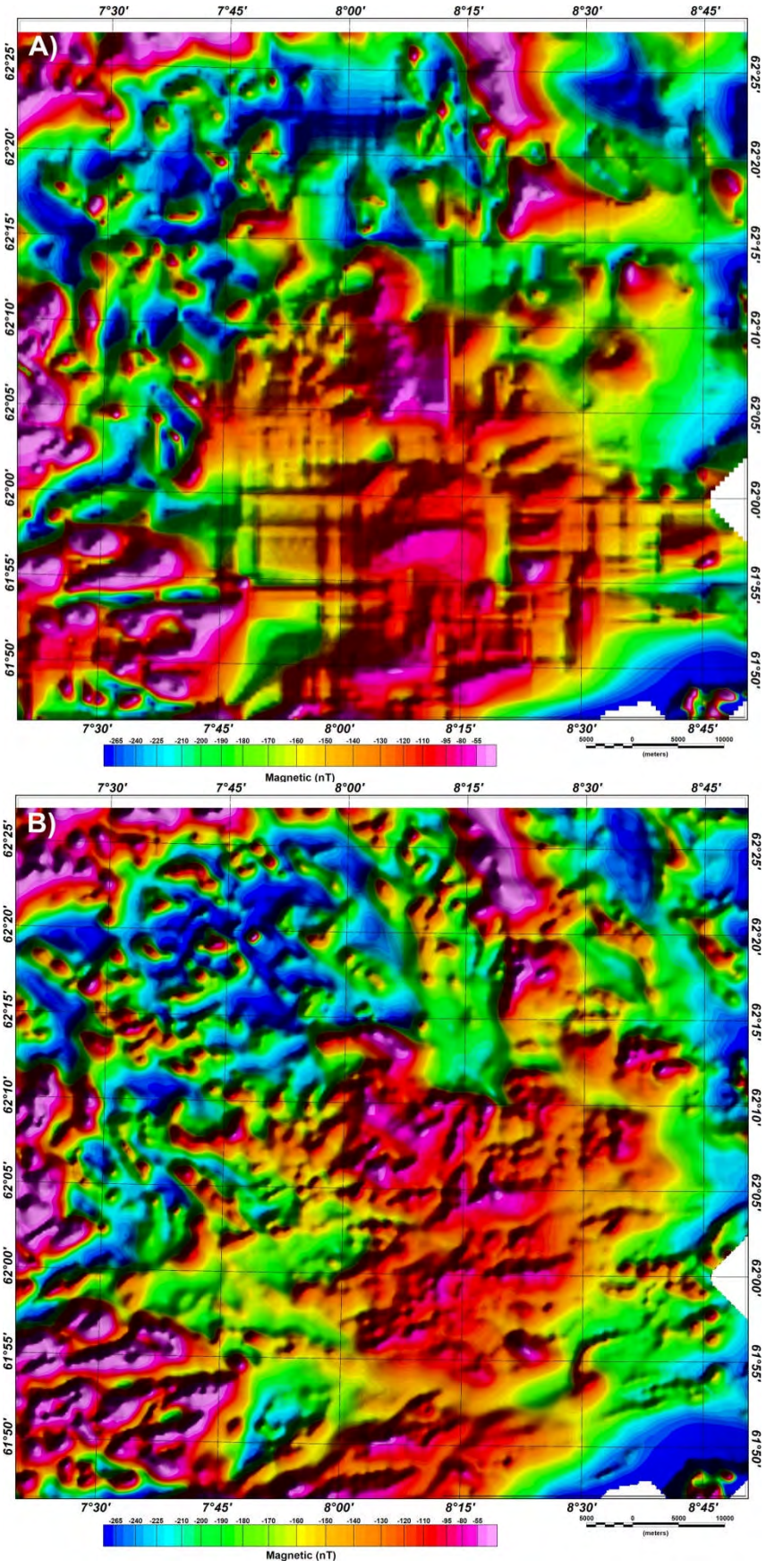

Figure 2.5. Comparison of NGU vintage data with the new STAS-13 survey. (A) NGU vintage data. (B) STAS-13 aeromagnetic survey. See Figure 4.2 for the location of the area.

2.3 Data enhancement

In order to detect the main geological structures and trends the aeromagnetic data are filtered as a qualitative aspect of interpretation. Horizontal gradient, analytical signal and the tilt-derivative method are utilised to enhance magnetic anomalies associated with faults and other structural discontinuities.

The total horizontal gradient (THG) method is considered as one of the simplest approaches to estimate the contact locations (e.g. faults). The method is the one less susceptible to noise in the data, because it requires only the two, first-order, horizontal derivatives of the magnetic field. If *T* (*x*, *y*) is the magnetic field and the horizontal derivatives of the field are (*∂T / ∂x and ∂T / ∂y)*, then the horizontal gradient *HG* (*x*, *y*) is given by:

$$THG = \sqrt{(\frac{\partial T}{\partial x})^2 + (\frac{\partial T}{\partial y})^2}$$

The derived horizontal gradient map is shown in Figure 2.6 and its shaded relief version is depicted in Figure 2.7.

The analytic signal, although commonly less continuous than the horizontal gradient, can, however, generate a maximum directly over discrete bodies as well as along their edges. The width of a maximum, or ridge, is an indicator of the depth to the contact, as long as the signal arising from a single contact can be resolved. The analytical signal is formed through a combination of horizontal and vertical gradients of a magnetic anomaly (Blakely 1996).

$$AS = \sqrt{(\frac{\partial T}{\partial x})^2 + (\frac{\partial T}{\partial y})^2 + (\frac{\partial T}{\partial \mathrm{z}})^2}$$

The analytical signal maps in colour are shown in Figure 2.8.

We also used the tilt-derivative method (TDR) in order to enhance the edges of sources. The tilt derivative is the angle between the total horizontal derivative (x and y directions) and the first vertical derivative and is defined by Miller and Singh (1994) as:

$$TDR = tan^{-1}(\frac{\frac{\partial T}{\partial z}}{\sqrt{(\frac{\partial T}{\partial x})^2 + (\frac{\partial T}{\partial y})^2}})$$

where *T* (*x*, *y*) is the magnetic field and the horizontal derivatives of the field are (*∂T / ∂x and ∂T / ∂y)* and the vertical derivative is *∂T / ∂z.* Tilt angle responses vary between positive values over the source, zero over or near the edge, and negative values outside the body (Cooper & Cowan 2006). The results are depicted in Figure 2.9.

The filtered data show a significant difference between the recently acquired and the vintage NGU data. Also, it is clear that the helicopter data have more resolution and show considerable detail. Artifacts are visible in the old NGU data in a window pattern. An example is shown in Figure 2.7 & Figure 2.10, where the artifacts are the result of gridding of a dataset based on hand-drawn contours.

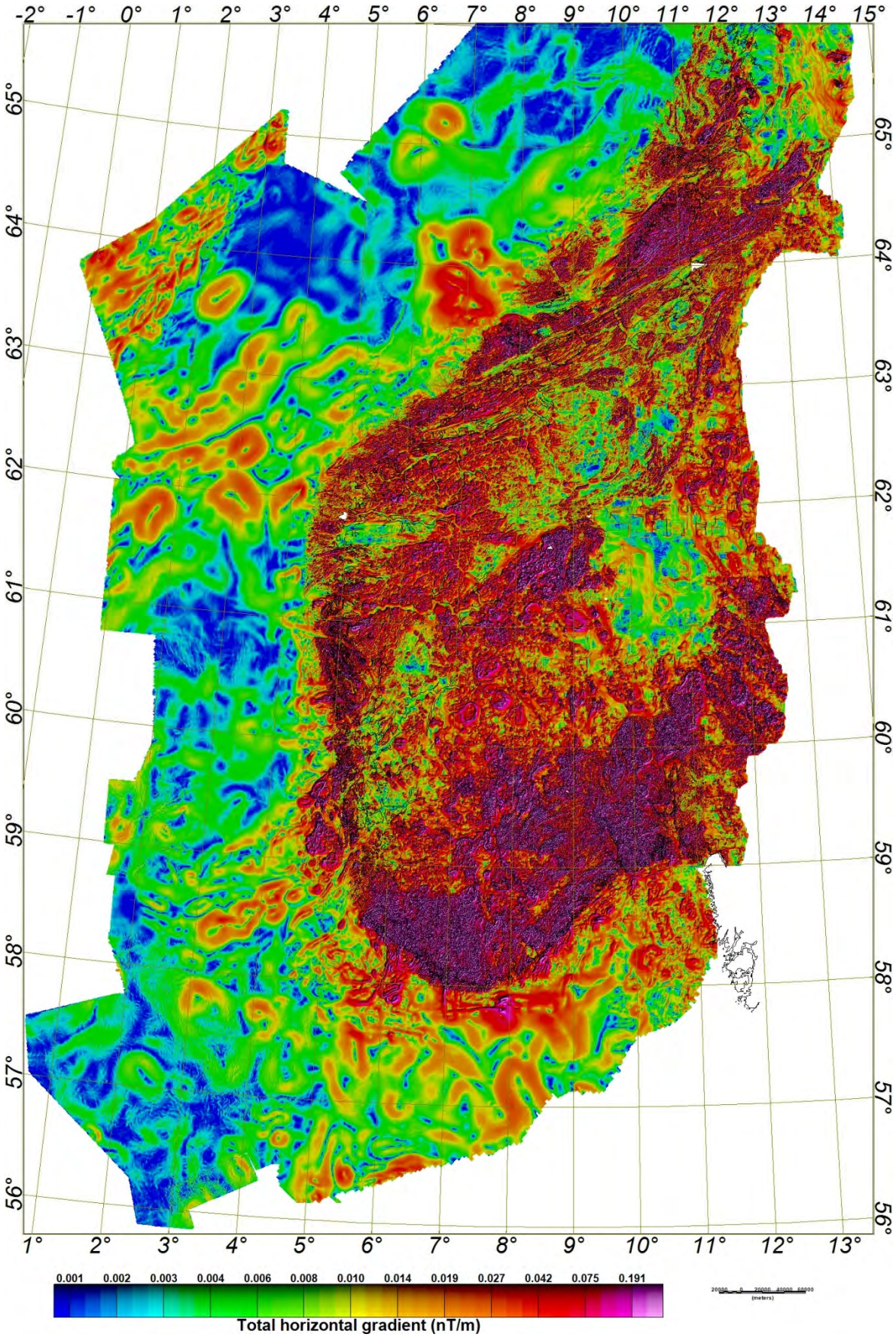

Figure 2.6. Total horizontal gradient map of the aeromagnetic data.

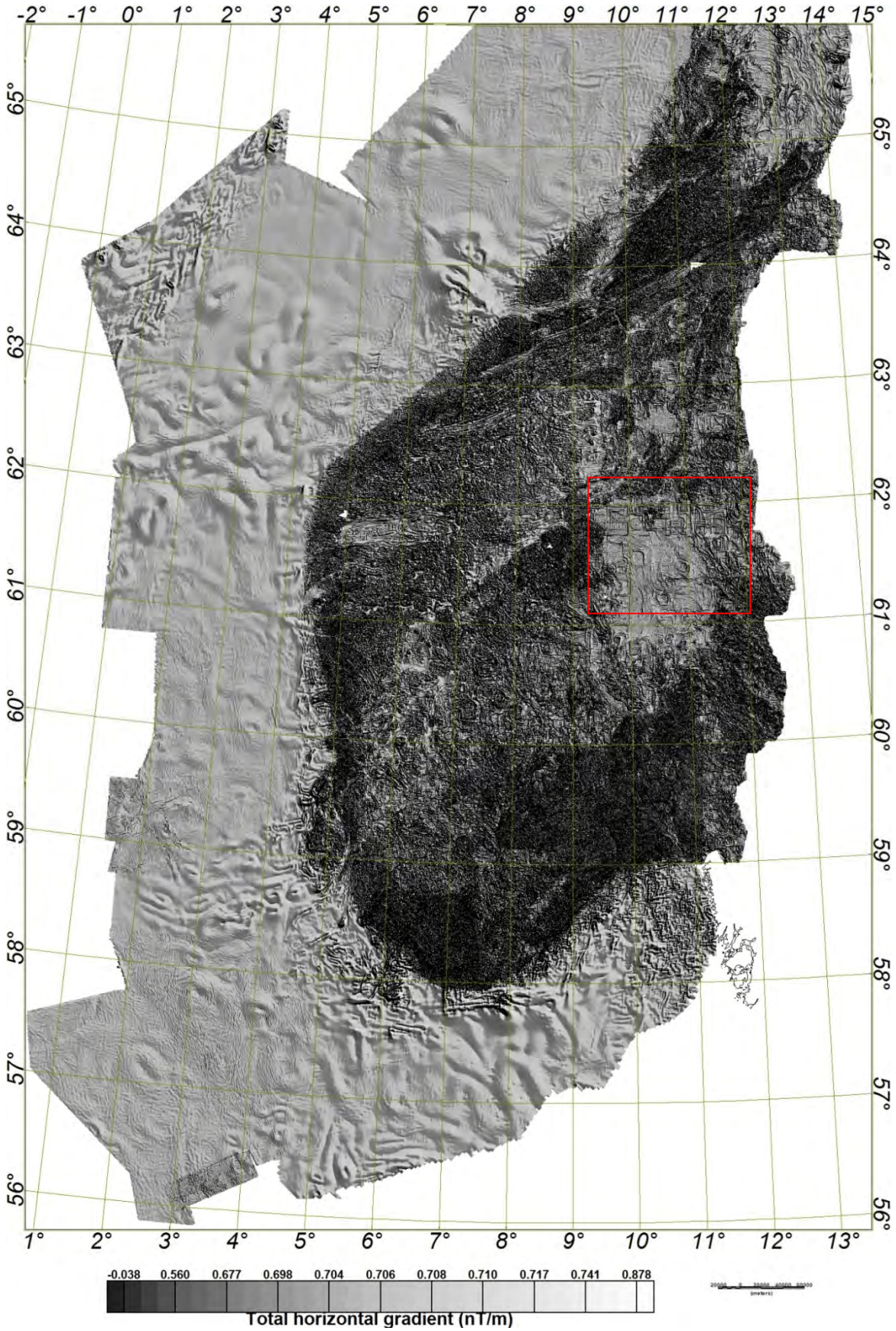

Figure 2.7. Grey tone shaded relief map of the total horizontal gradient of the magnetic data. The window pattern artefact from the vintage data is outlined by a red box.

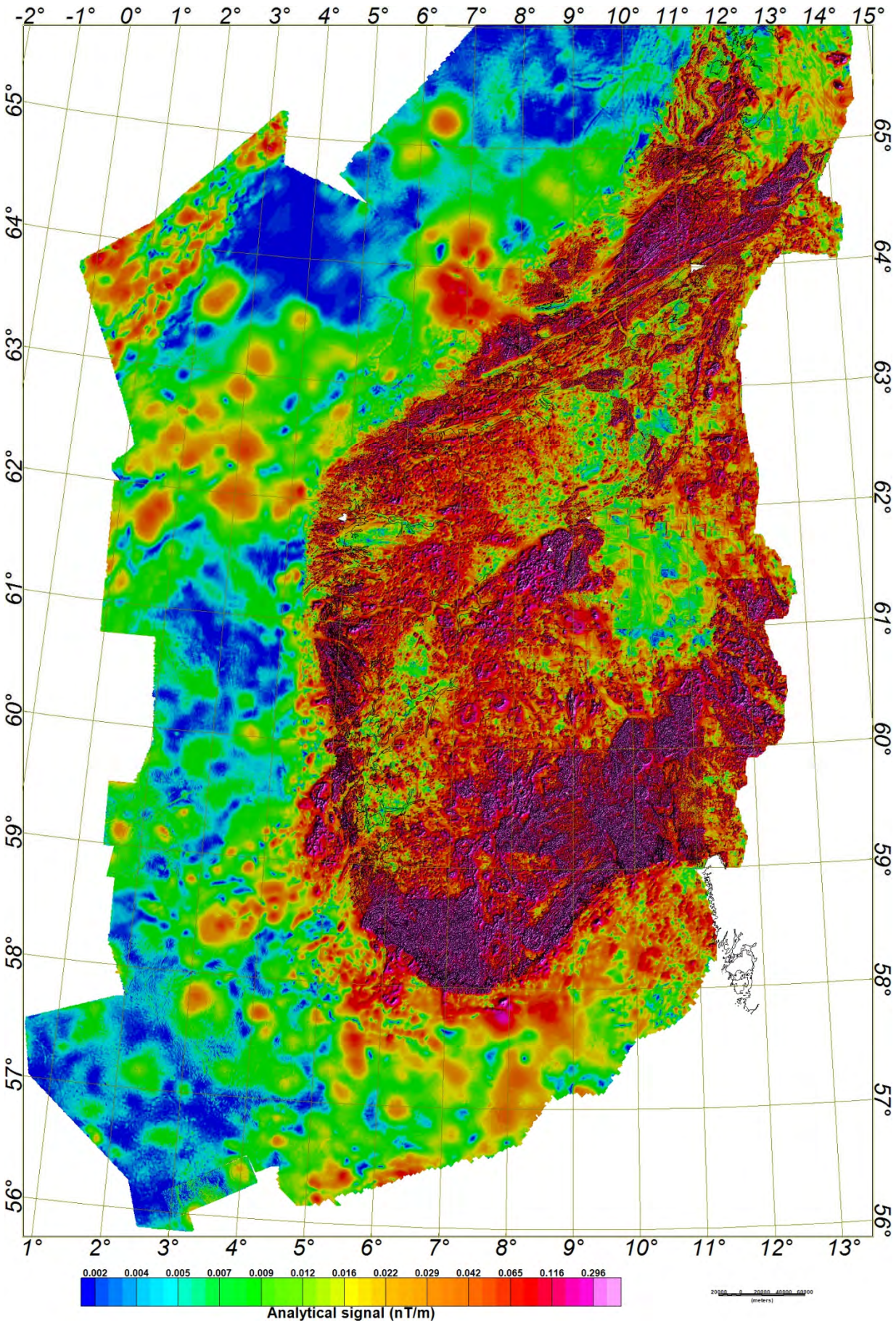

Figure 2.8. Analytical signal map of the aeromagnetic surveys in the study area.

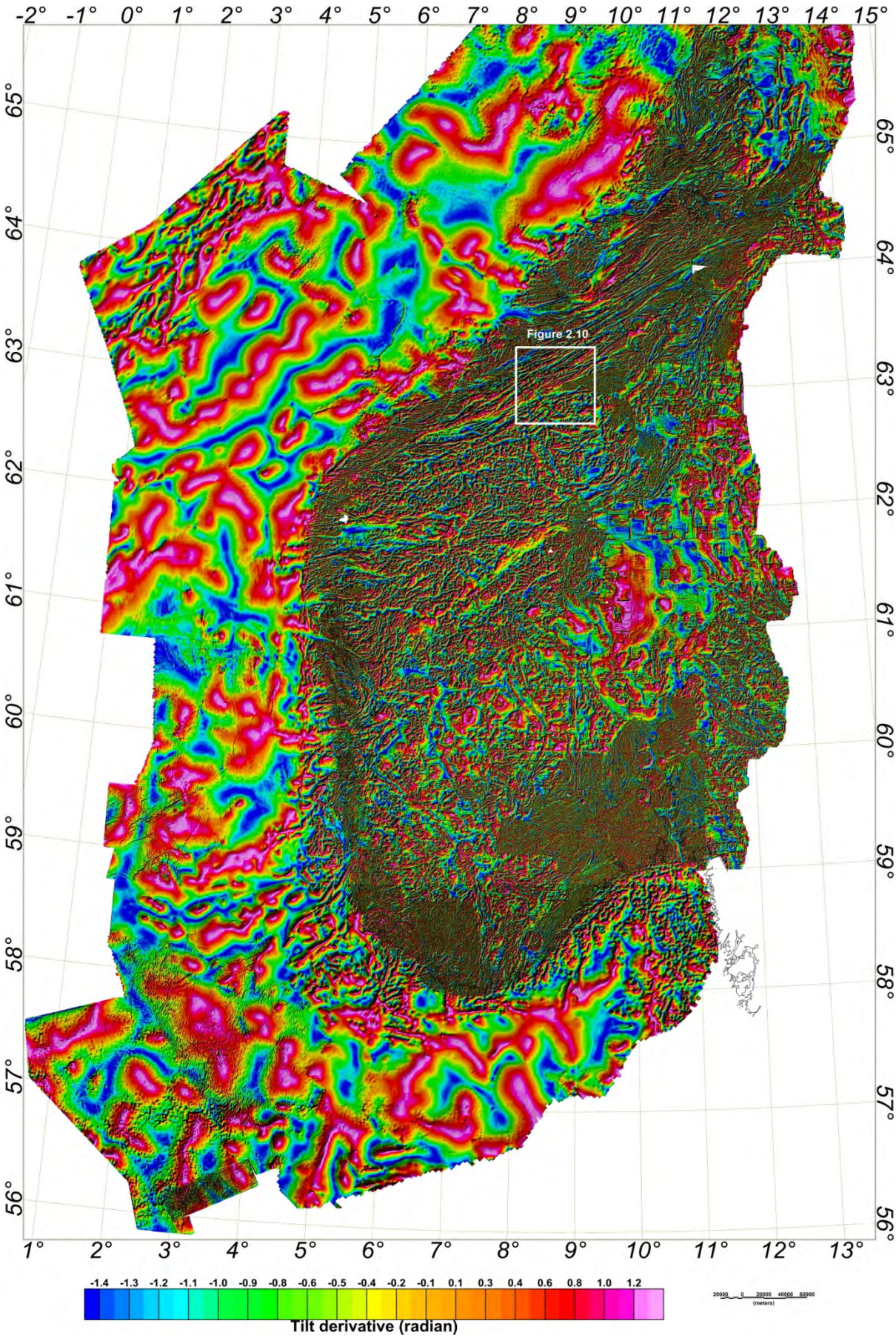

Figure 2.9. Tilt-derivative map of the aeromagnetic surveys in the study area.

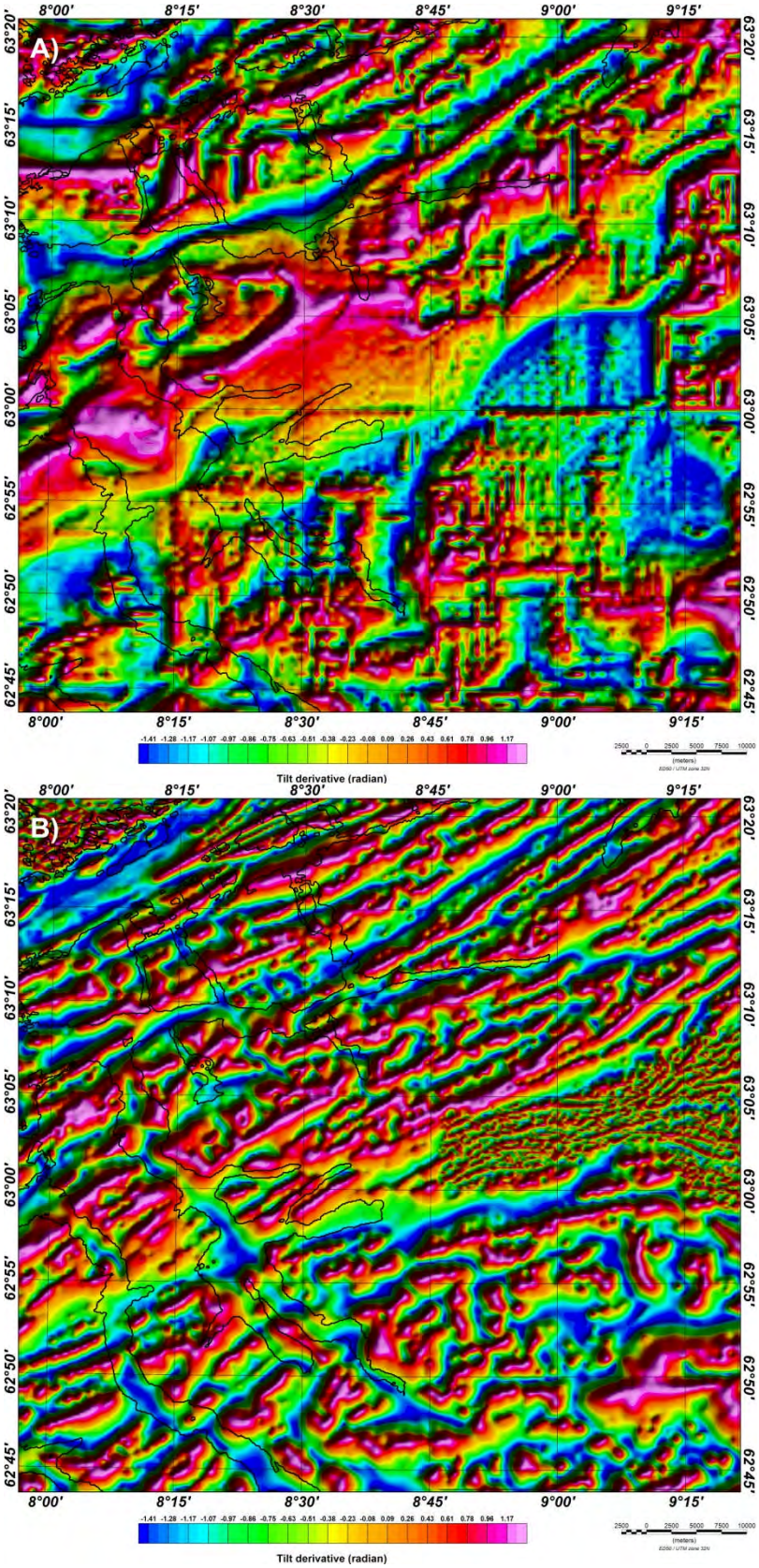

Figure 2.10. Comparison of the NGU vintage data with the new Coop survey. (A) Tilt-derivative map of the NGU vintage data. (B) Tilt-derivative map of the new aeromagnetic compilation. See Figure 2.9 for the location of the area. The window pattern artefact is seen on the old NGU data.

3. CORRECTION AND COMPILATION OF AIRBORNE RADIOMETRIC DATA

Marie-Andrée Dumais, Jomar Gellein, Torleif Lauritsen & Alexandros Stampolidis

There are many naturally existing radioactive elements. However, only three have isotopes that emit gamma radiation of sufficient intensity to be measured by airborne gamma ray spectrometry. The three major sources of gamma radiation are K-40, daughter products in the ^{238}U decay series and daughter products in the ^{232}Th series.

The multi-channel gamma spectrometry data used in the present study were acquired from fixed-wing and helicopter surveys (1986-2014). Figure 3.1 shows their locations.

In addition to the Coop1 project, we included the surveys Kvinesdal/Sirdal 2014 and TRAS-2012. The newly acquired data were also merged with data previously acquired by NGU in Nord-Trøndelag between 1986 and 1993. For these data, only count rates were available. Thus, concentrations were calculated using the overlap with TRAS-12 survey. Acquisition details are presented in Table 3.1.

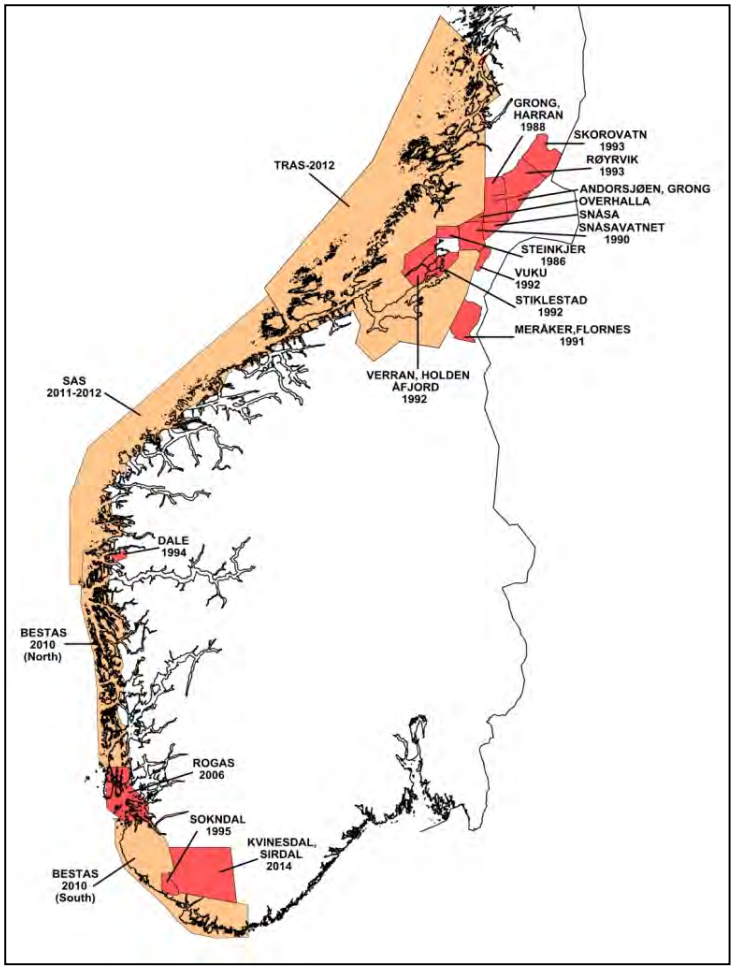

Figure 3.1. Airborne gamma ray spectrometry surveys within the Coop2 project.

Table 3.1. Acquisition details, radiometric data.

Survey	Year	Contractor	Platform	*Flying height (m)*	Line spacing (m)	cps/ppm
Steinkjer	1986	NGU	Helicopter	60	200	cps
Grong, Harran	1988	NGU	Helicopter	60	250	cps
Andorsjøen, Grong, Snåsavatnet (Snåsa, Overhalla)	1990	NGU	Helicopter	60	200	cps
Meråker, Flornes	1991	NGU	Helicopter	60	200	cps
Stiklestad	1991	NGU	Helicopter	60	200	cps
Verran, Holden, Åfjord	1992	NGU	Helicopter	60	200	cps
Vuku	1992	NGU	Helicopter	60	100	cps
Røyrvik, Skorovatn	1993/94	NGU	Helicopter	60	100/200	cps
Dale	1994	NGU	Helicopter	60	100	cps
Sokndal	1995	NGU	Helicopter	60	100	cps
ROGAS	2006	SGU	Fixed-wing	60-100	250	ppm/%
BESTAS	2010	FUGRO	Fixed-wing	60	250	ppm/%
SAS	2011/12	Novatem	Fixed-wing	60	250	ppm/%
Trøndelag Region Airborne Survey (TRAS)	2012-14	Novatem	Fixed-wing	60	250	ppm/%
Kvinesdal, Sirdal	2014	NGU	Helicopter	60	200	ppm/%

3.1 Correction and Compilation Western Norway

Data from two fixed-wing surveys (ROGAS, 2006; BESTAS North and BESTAS South, 2010) and a helicopter borne survey (KVINESDAL and SIRDAL, 2014) were used in this compilation (see Table 3.1 for acquisition details). Significant level differences between them were observed, see for example Thorium map of Figure 3.2.

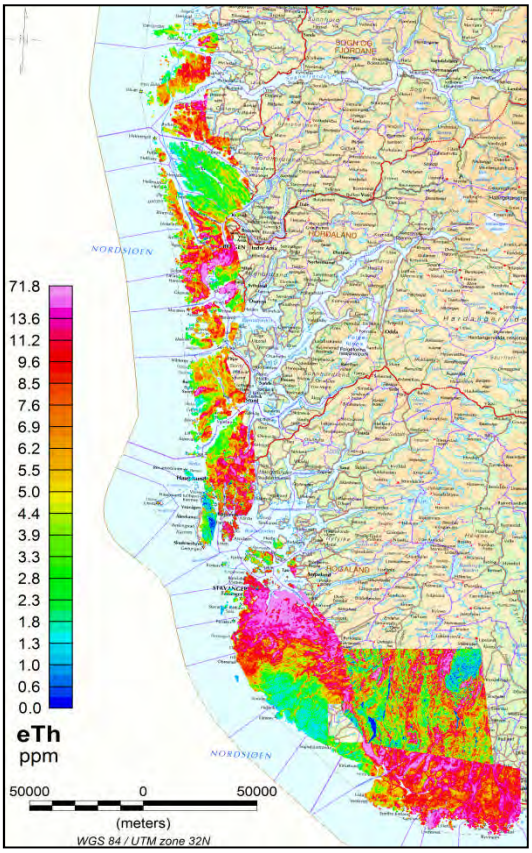

Figure 3.2. Thorium map compilation of Western Norway (ppm).

These surveys partially overlap. The anomaly patterns of individual surveys at overlapping regions were very similar, but on the other hand their estimated concentrations had different scale ranges (see the example in Figures 3.3 & 3.4).

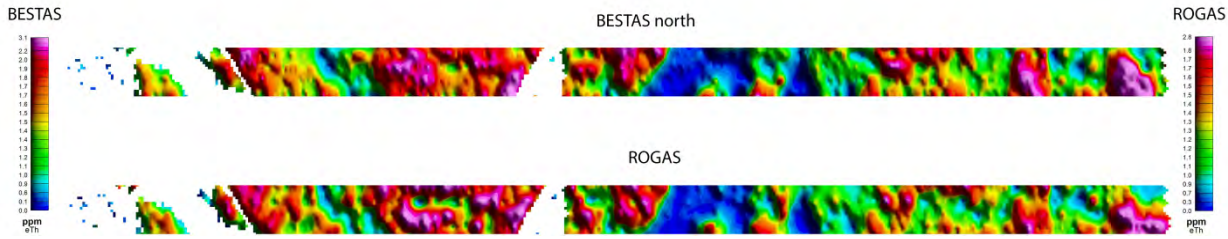

Figure 3.3. Thorium concentration on overlapping area between Bestas north and ROGAS (ppm).

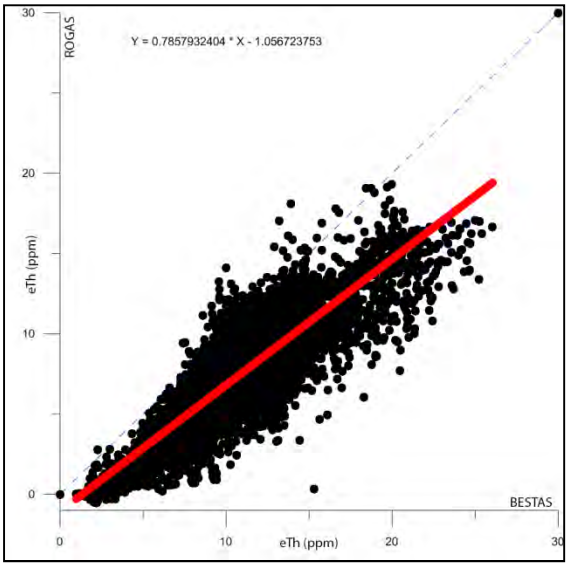

Figure 3.4. Scatter diagram for Thorium concentration on overlapping area between Bestas north and ROGAS (ppm).

We concluded that a possible source for these levelling differences may be the processing sequence applied to each survey. The datasets from ROGAS (SGU) and Kvinesdal, Sirdal (NGU) were processed following the standard processing procedures recommended by IAEE (1991) according to their reports. The BESTAS dataset had been processed slightly different, it was filtered prior to standard processing (IAEE, 1991) using the NASVD spectral method for removing random noise from the raw spectrum.

The noise reduction filtering is not a necessary step in the processing sequence, thus in order to homogenize the datasets of all three surveys, we reprocessed the raw spectra from the BESTAS survey. We used the same calibration parameters as described in the BESTAS report. Furthermore, we split Kvinesdal, Sirdal dataset into three sub-datasets based on their acquisition period, to correct the level differences observed within this survey. The raw spectra sub-datasets were re-processed and then knitted to give homogeneous grids. The ROGAS data were not re-processed because we only had access to final processed grids. The level differences between individual grids were significantly reduced on the re-processed grids. Figure 3.5 shows the Potassium map before and after re-processing.

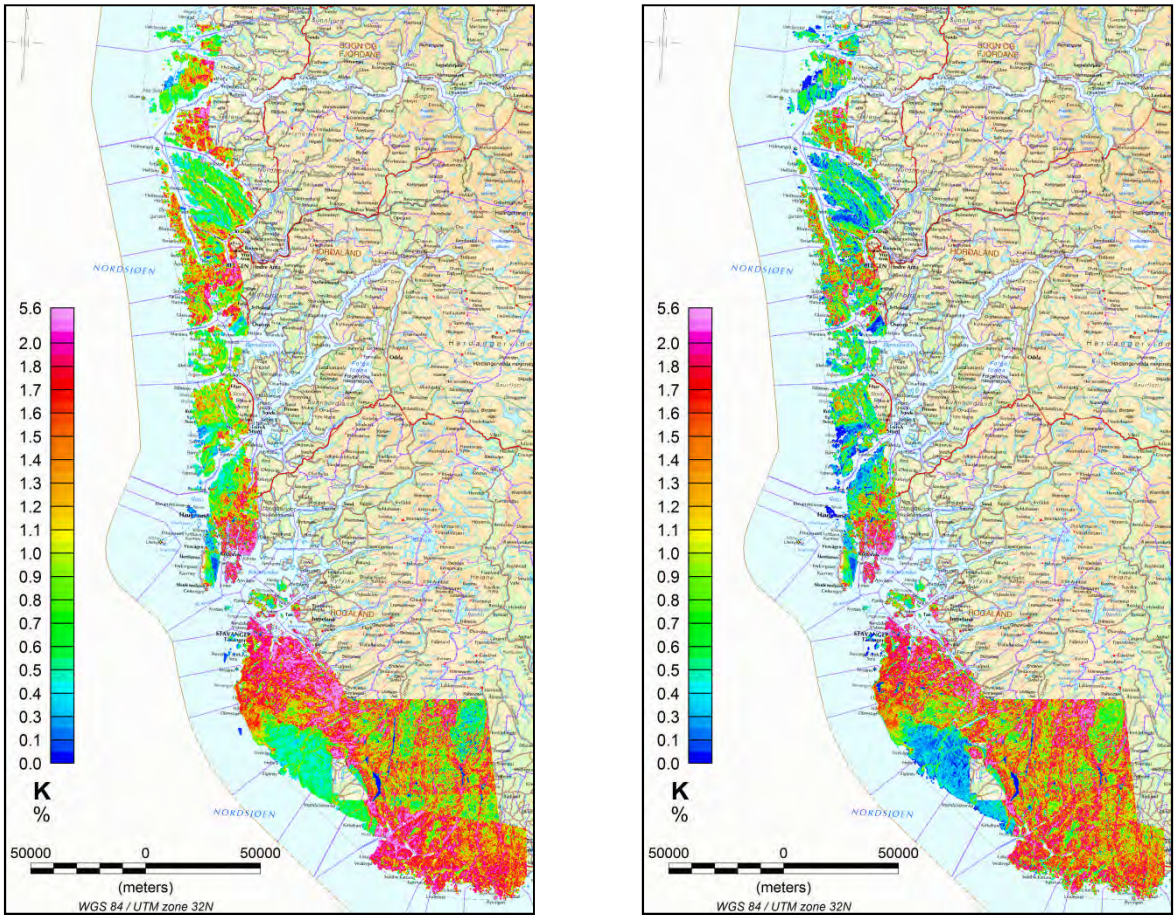

Figure 3.5. Potassium concentration map before and after re-processing (%).

Normally, the count rates in the K, U, and Th windows will be converted to apparent radioelement concentrations, K %, eU ppm and eTh ppm. For the older surveys at Sokndal (1995) and Dale (1994) this was not done. These two datasets occur simply with count rates in the K, U and Th windows. However, both NGU surveys partially overlap the FUGRO survey from 2010, and have thus enabled the making of scatter diagrams and calculations of regression equations.

In Figures 3.6, 3.7 and 3.8 we present the scatter diagrams for the relationships between the Dale94 survey and the Coop1 compilation with regard to uranium, thorium and potassium. Similar scatter diagrams for the Sokndal and Coop1 compilation were also produced.

The regression equations are then used to convert count rates to radioelement concentrations in the two helicopter surveys. For the Dale94 survey the regression equations are:

Uranium (ppm) = 0.29883 + (Uranium (cps) * 0.1)
Thorium (ppm) = 0.25301 + (Thorium (cps) * 0.032447)
Potassium (%) = 0.22961 + (Potassium (cps) * 0.0055444

The regression equations for the Sokndal95 survey are:

Uranium (ppm) = 0.41304 + (Uranium (cps) * 0.060141)
Thorium (ppm) = 0.63201 + (Thorium (cps) * 0.1853)
Potassium (%) = 0.045205 + (Potassium (cps) * 0.0086457)

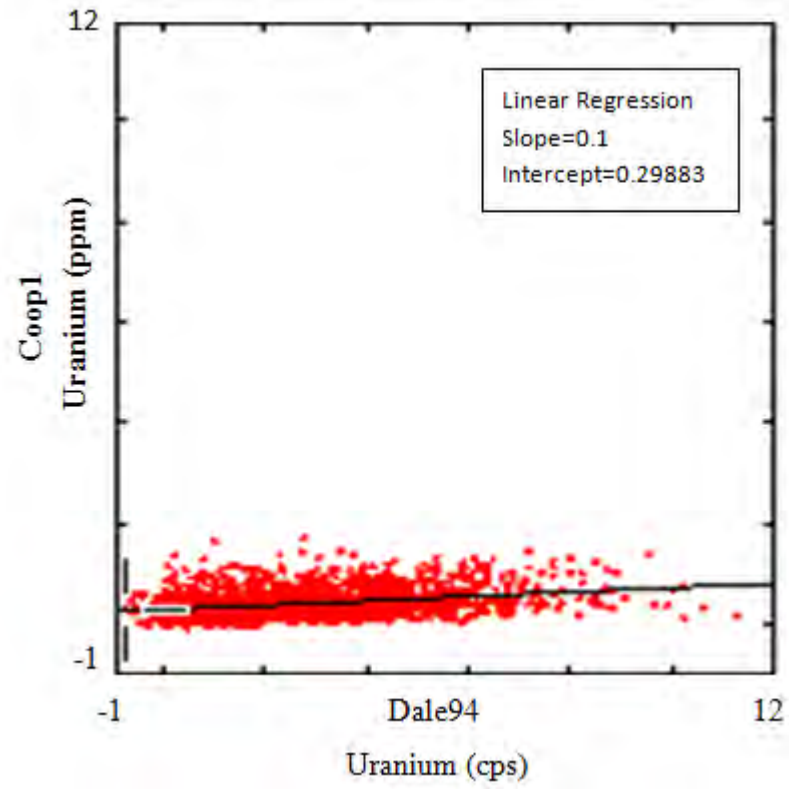

*Figure 3.6 Scatter diagram for uranium in Coop1 (ppm) vs. DALE (cps). The regression equation is Y=0.29883+(X*0.1).*

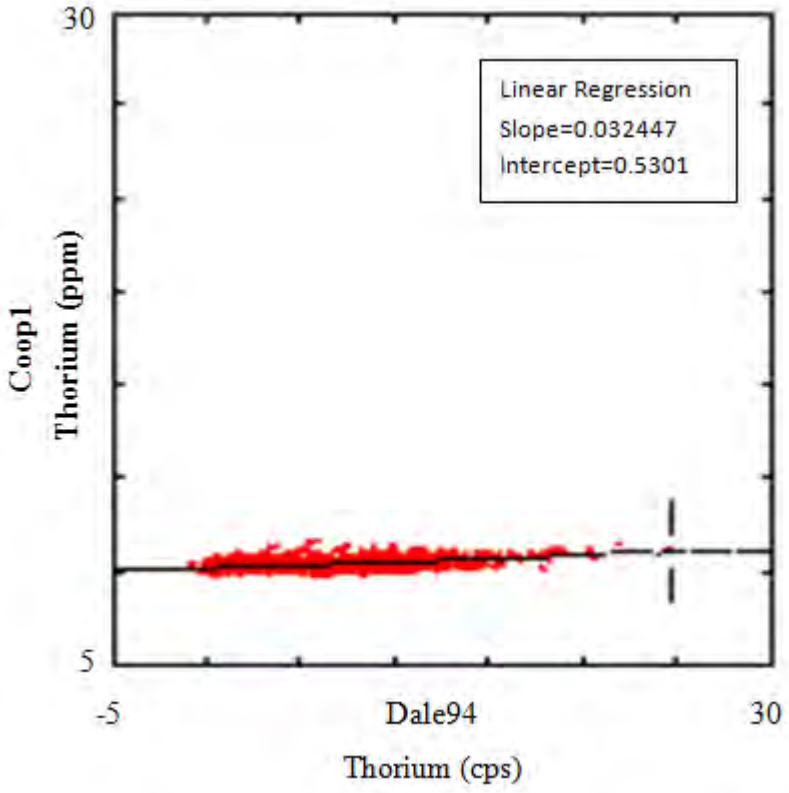

*Figure 3.7. Scatter diagram for thorium in Coop1 (ppm) vs. DALE (cps). The regression equation is Y=0.5301+(X*0.032447).*

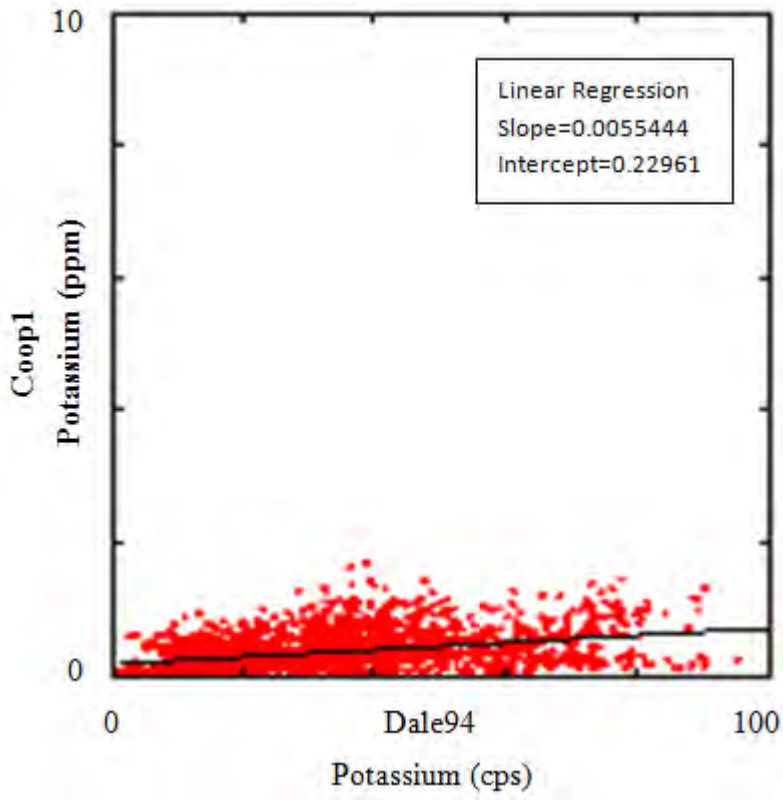

*Figure 3.8. Scatter diagram for potassium in Coop1 (ppm) vs. DALE (cps). The regression equation is Y=0.22961+(X*0.0055444).*

3.2 Correction and Compilation Mid Norway

All the projects of interest for this compilation are listed in Table 3.1 with their reference number from NGU's DRAGON database, location and year of acquisition. They are also presented in the map below. All data were previously processed and assumed corrected for dead-time, stripping ratio, attenuation, background and standard temperature and pressure (STP) height corrections (IAEA 1991). For all these projects, only the count rates were available. Between June 2012 and March 2014, Novatem, a Canadian airborne geophysics company, carried out an airborne geophysics survey in the Trøndelag region (Trøndelag Region Airborne Survey (TRAS-12) for NGU. The radiometric data are presented in this section.

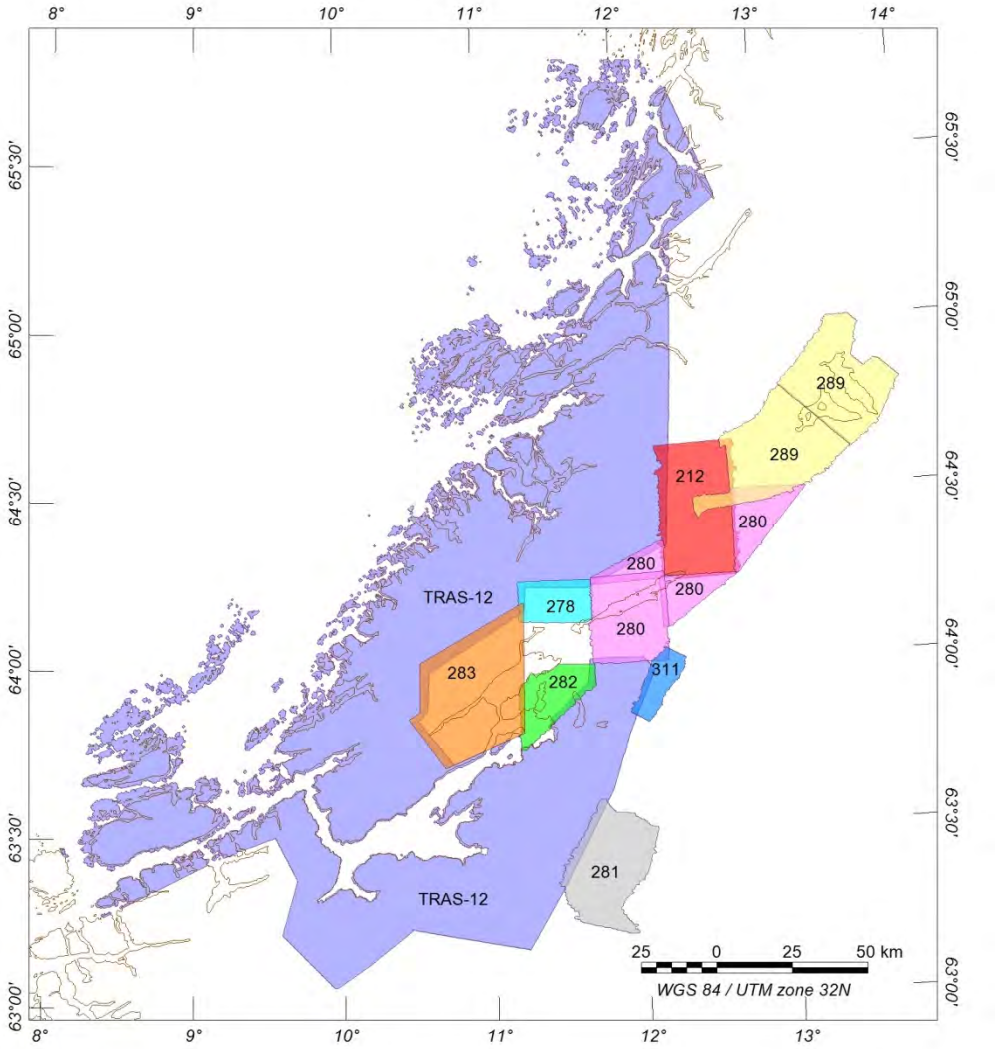

Figure 3.9. Survey area map.

All these projects are heli-borne using NGU equipment except TRAS-12 which was acquired by an external company *Novatem* with an aircraft equipped with similar equipment.

All these projects have been acquired with various survey parameters as listed below, Table 3.2.

Table 3.2. Survey parameters. Downward-looking detectors are considered only.

DRAGON # / Name	Aircraft	Altitude (m)	Radiometric instrument	# crystals	Volume (L)
212	Helicopter - *Aerospatiale Ecureuil SA 350 B1*	60	*Geometrics GR-800*	4	16.8
278	Helicopter - *Aerospatiale Ecureuil SA 350 B1*	60	*Geometrics GR-800*	4	16.8
280	Helicopter - *Aerospatiale Ecureuil SA 350 B1*	60	*Geometrics GR-800*	4	16.8
281	Helicopter - *Aerospatiale Ecureuil SA 350 B1*	60	*Geometrics GR-800*	4	16.8
282	Helicopter - *Aerospatiale Ecureuil SA 350 B1*	60	*Geometrics GR-800*	4	16.8
283	Helicopter - *Aerospatiale Ecureuil SA 350 B1*	60	*Geometrics GR-800*	4	16.8
289	Helicopter - *Aerospatiale Ecureuil SA 350 B1*	60	*Geometrics GR-800 / Exploranium GR820 (1994)*	4	16.8
311	Helicopter - *Aerospatiale Ecureuil SA 350 B1*	60	*Geometrics GR-800*	4	16.8
TRAS12	Piper Navajo PA-31	60	*Radiation Solutions RSX-5*	8	33.4

3.3 Reprocessing method

Several datasets, mainly uranium counts, needed to be reprocessed prior to concentration calculation and merging. The filtering and editing required is described below.

3.4 212 - Grong, Harran - 1988

The original uranium data displayed a horizontal noise trend near the top of the grid (Rønning, 1990). Hence, a micro-levelling was required to enhance the data. A decorrugation cutoff wavelength of 4000 m and a Naudy filter of 500 m were used (Figure 3.9).

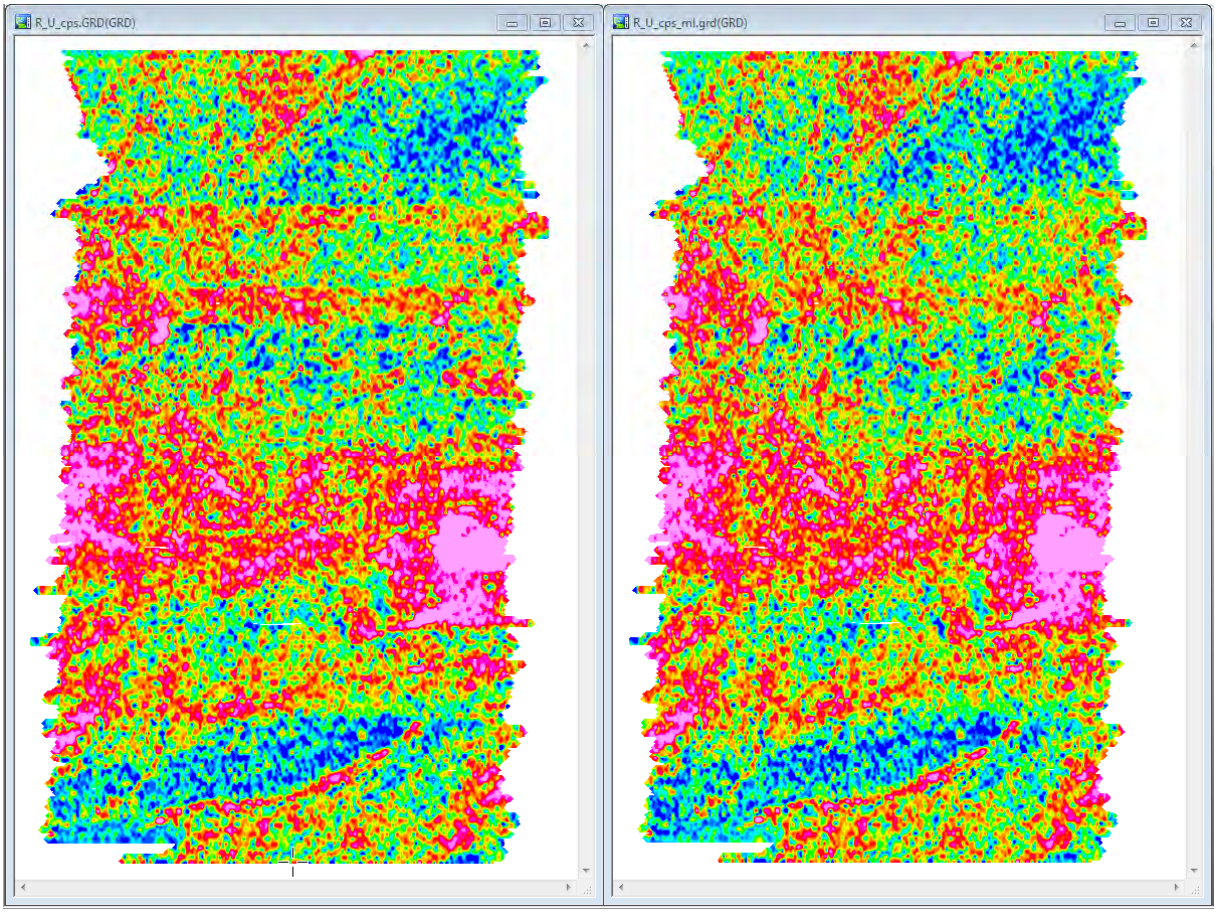

Figure 3.9. 212 - Grong, Harran - Uranium count.

3.5 278 - Steinkjer - 1986

The original uranium data displayed horizontal noise trends at the bottom of the grid (Mogaard, 1989). Hence, a micro-levelling was required to enhance the data. A decorrugation cutoff wavelength of 3000 m and a Naudy filter of 400 m were used (Figure 3.10)

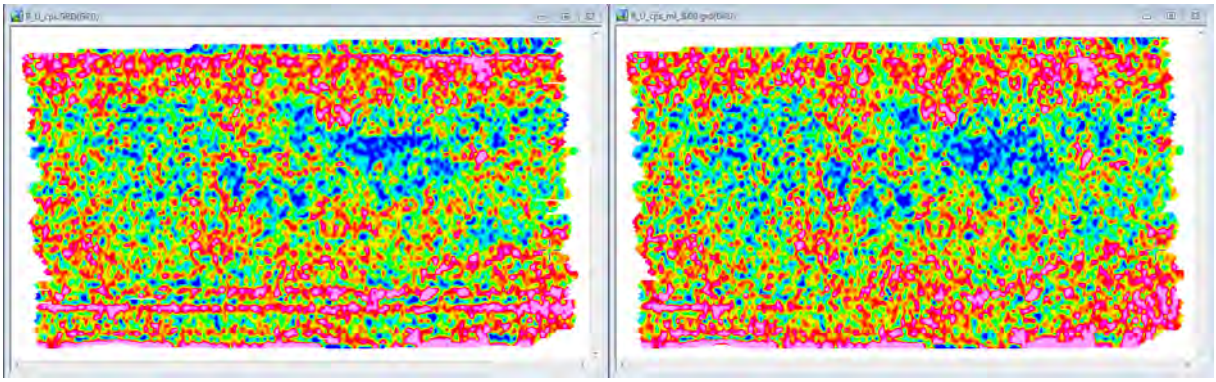

Figure 3.10 278 - Steinkjer - Uranium count.

3.6 280 - Andorsjøen, Grong, Snåsavatnet - 1990

This area consists of 4 sub-areas: Andorsjøen, Snåsa, Snåsavatnet and Overhalla (Rønning 1991, 1992a, 1992b & 1992c). Of these four datasets, only the Snåsa and Snåsavatnet uranium grids displayed noisy trends. For both grids, a light micro-levelling was applied to

enhance the quality of the data with a decorrugation cutoff wavelength of 3000 m and a Naudy filter of 400 m (Figure 3.11 and Figure 3.12).

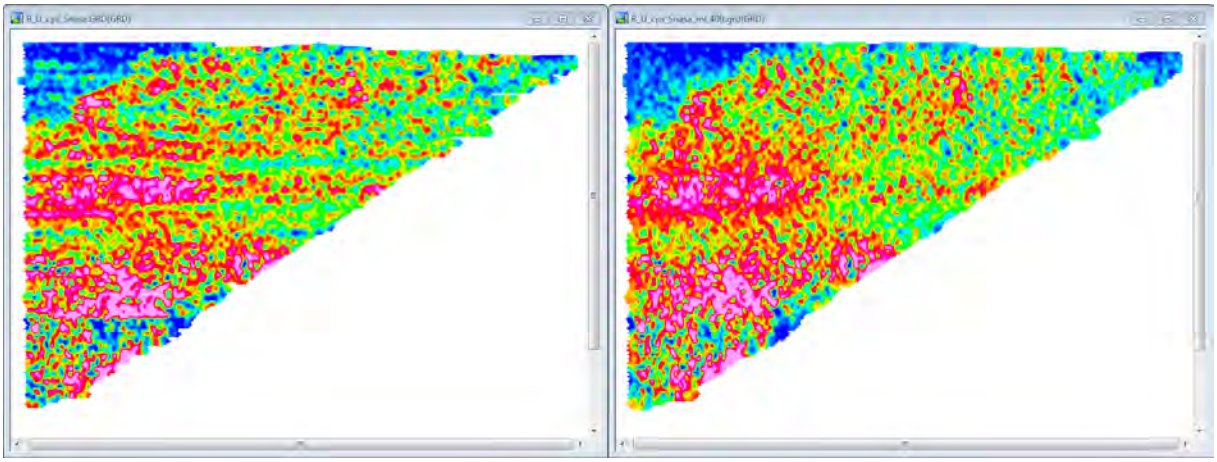

Figure 3.11. 280 - Snåsa - Uranium count.

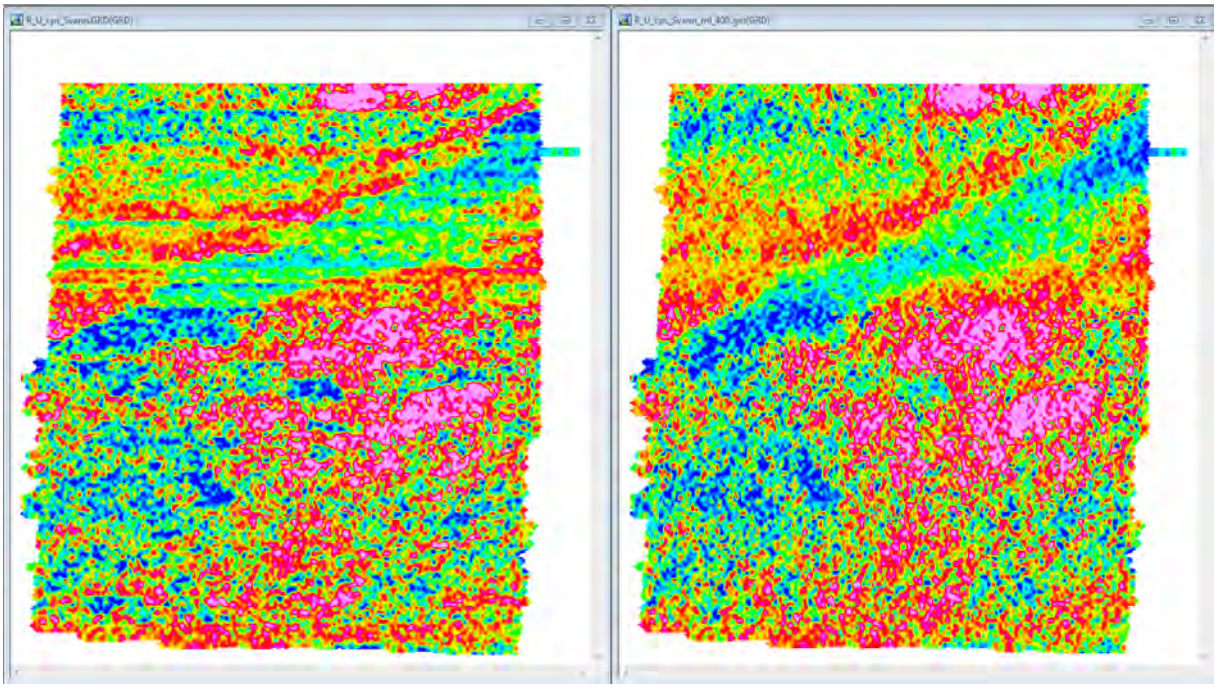

Figure 3.12. 280 - Snåsavatnet - Uranium count.

3.7 281 - Meråker - 1991

The original uranium data displayed several horizontal noise trends (Mogaard, 1993). Hence, a micro-levelling was required to enhance the data. A decorrugation cutoff wavelength of 8000 m and a Naudy filter of 1000 m were used (Figure 3.13).

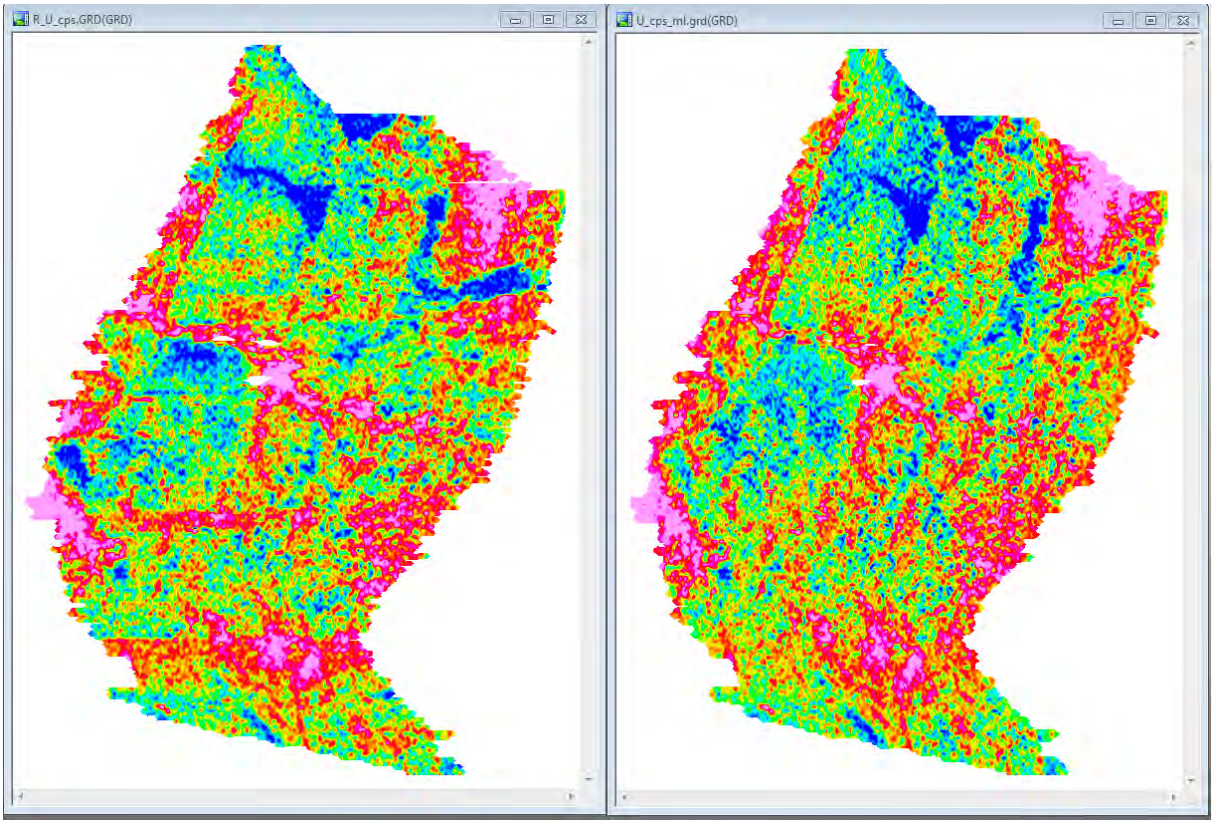

Figure 3.13. 281 - Meråker - Uranium count.

3.8 282 - Stiklestad - 1991

The original uranium data displayed a horizontal noise trend near the top of the grid (Rønning, 1995a). Hence, a micro-levelling was required to enhance the data. A decorrugation cutoff wavelength of 4000 m and a Naudy filter of 1000 m were used (Figure 3.14).

There is also a stripe at the bottom of the grid. Since this part of the data is above water and disregarded during the merging process, no action was taken to minimise this noise.

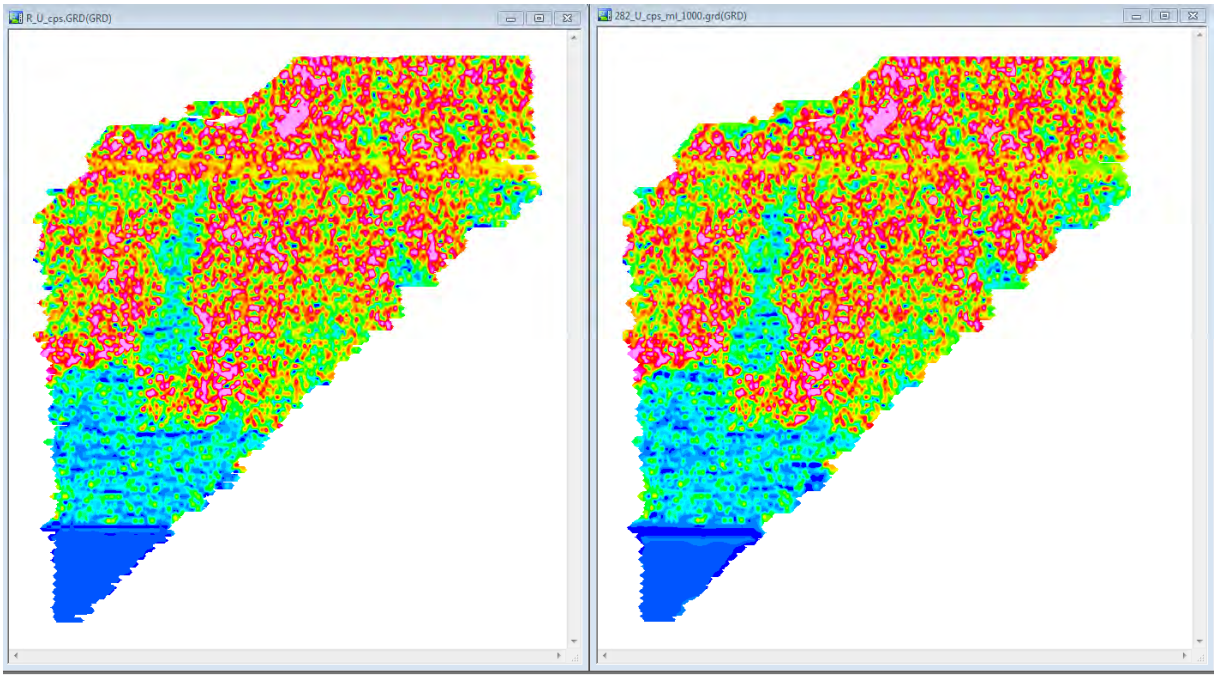

Figure 3.14. 282 - Stiklestad - Uranium count.

3.9 283 - Verran, Holden, Åfjord - 1992

This dataset was flown in 1992 above several water bodies (Rønning, 1995c). On the potassium and thorium grids, a light micro-levelling was applied using a decorrugation cutoff wavelength of 800 m and a Naudy filter of 1000 m (Figure 3.15 and Figure 3.14).

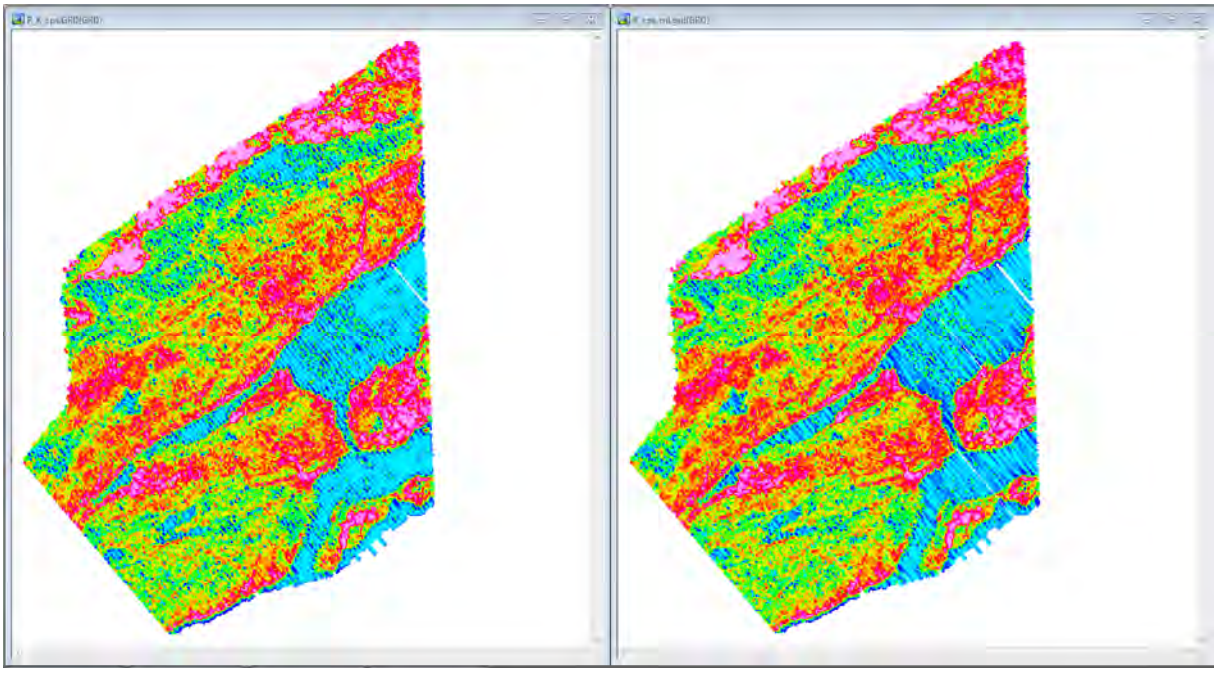

Figure 3.15. 283 - Verran, Holden, Åfjord - Potassium count.

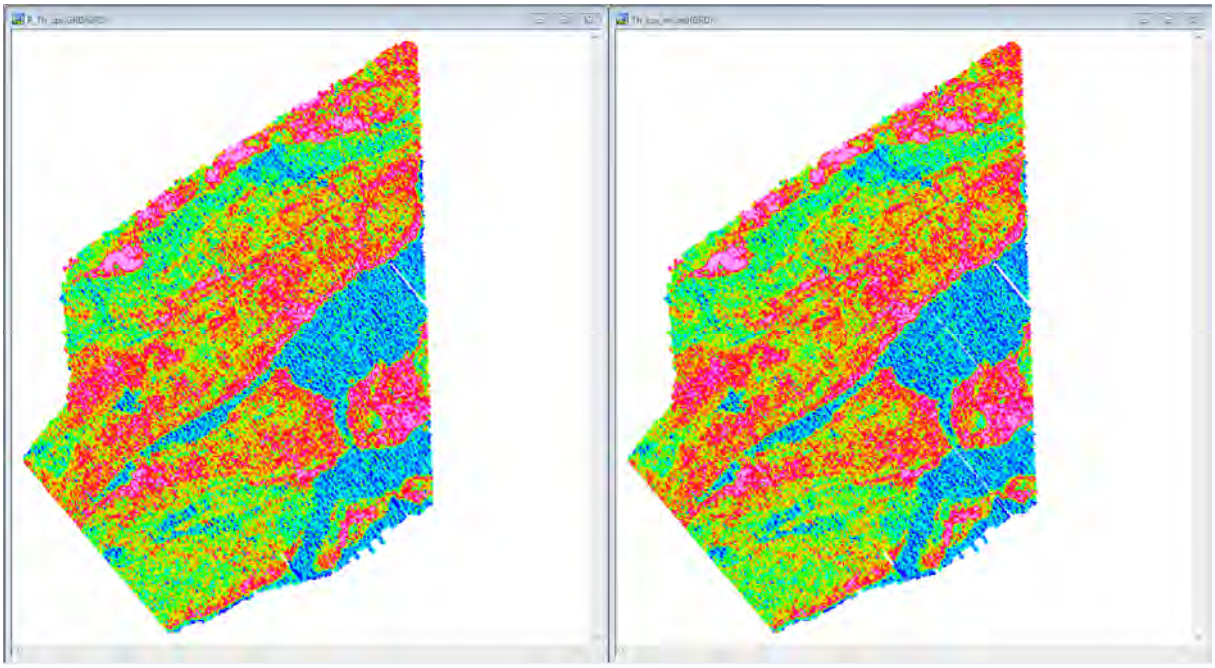

Figure 3.16. 283 - Verran, Holden, Åfjord - Thorium count.

The original uranium data displayed a linear noise trend along the lines (Rønning, 1995c). In this dataset, the noise level in some areas is as high as the uranium signature itself. It is also noted that the background on land and on water are very similar. To reflect a consistent background and improve the levelling, lines were initially manually levelled (Table 3.3).

Table 3.3. 283 - Uranium manual correction.

Line	Uranium adjustment (cps)
670 680 690	-12
750 760 770 780 790 791	-8
All others	0

Following the coarse adjustment, a micro-levelling was applied to the data, a decorrugation cutoff wavelength of 10,000 m and a Naudy filter of 1000 m (Figure 3.17).

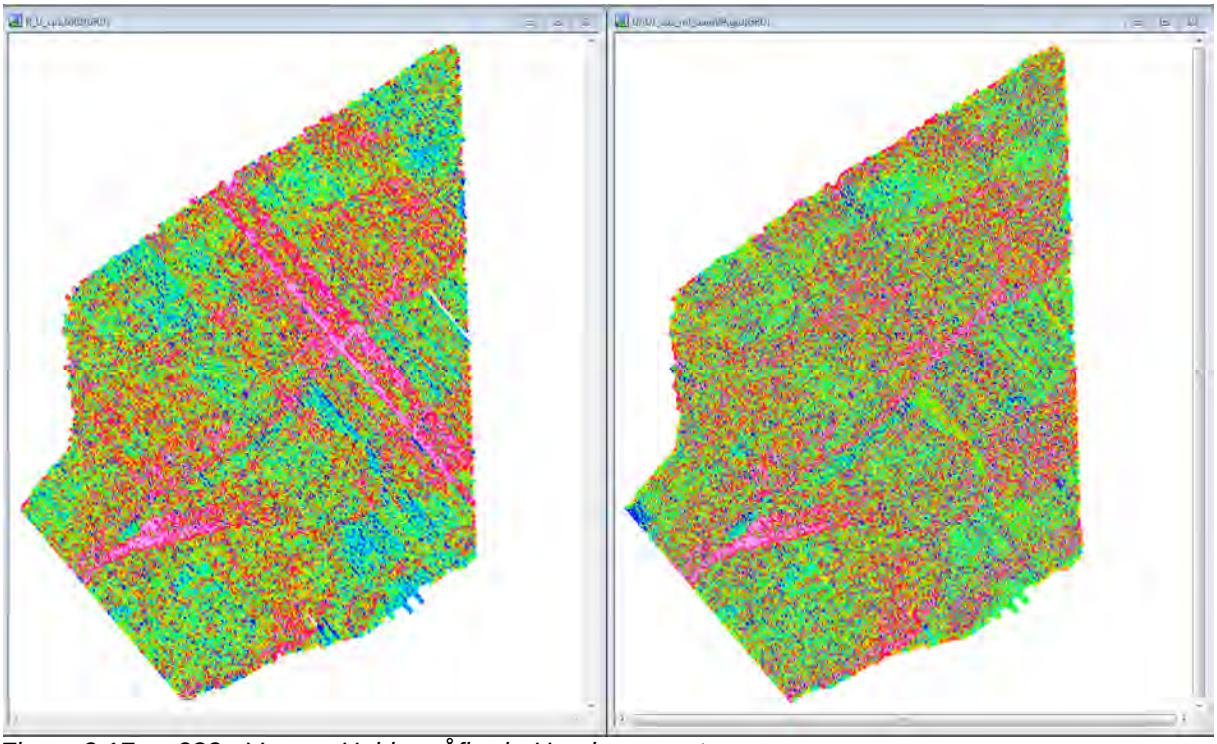

Figure 3.17 283 - Verran, Holden, Åfjord - Uranium count.

3.10 289 - Skorovatn - 1993

The Røyrvik and Skorovatn areas were flown over two summer seasons. A slight mis-fit appears between several lines for all element count grids (Rønning, 1995b). A micro-levelling was performed on all grids to enhance the final data. A decorrugation cutoff wavelength of 800 m was used for the micro-levelling of potassium (Figure 3.18) and thorium (Figure 3.19) and 10,000 m for uranium (Figure 3.20). A Naudy filter of 1000 m was used for all elements.

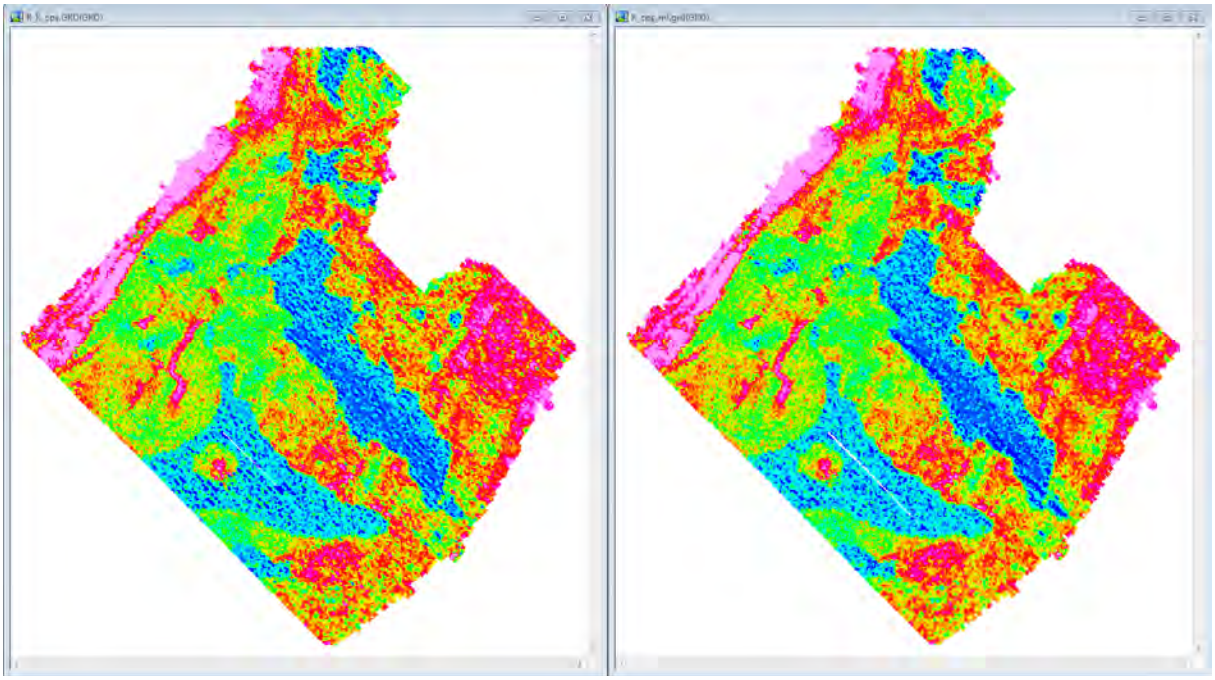

Figure 3.18. 289 - Røyrvik, Limingen area - Potassium count.

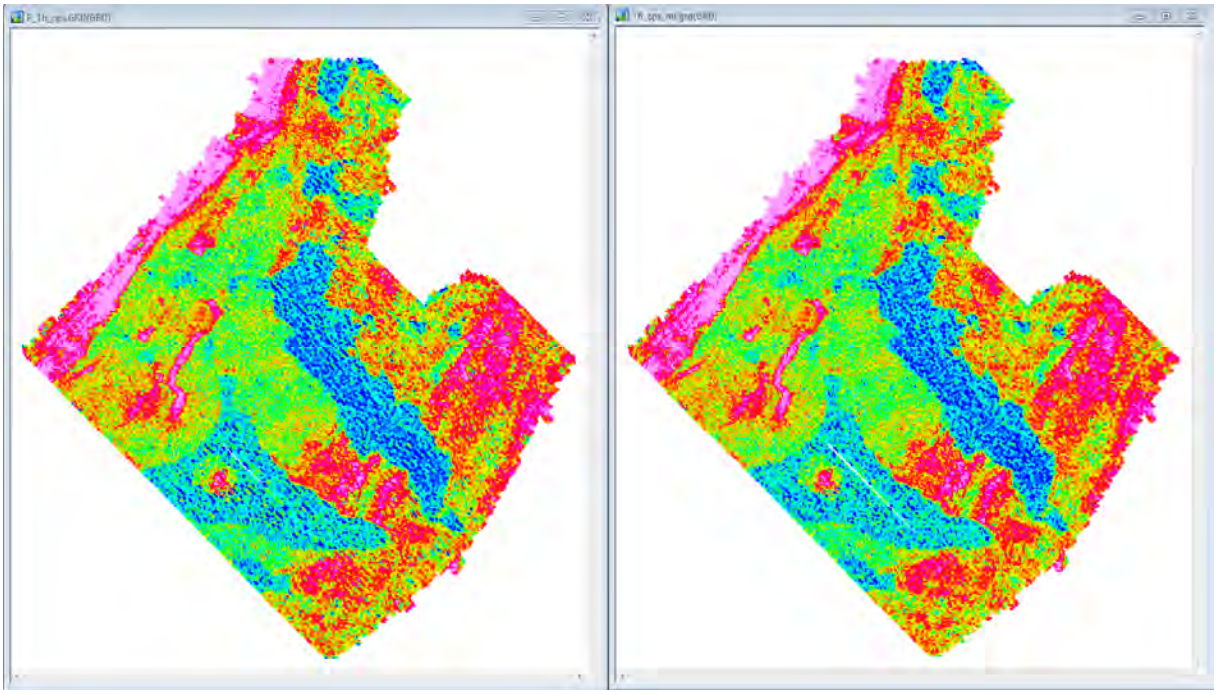

Figure 3.19. 289 - Røyrvik, Limingen area - Thorium count.

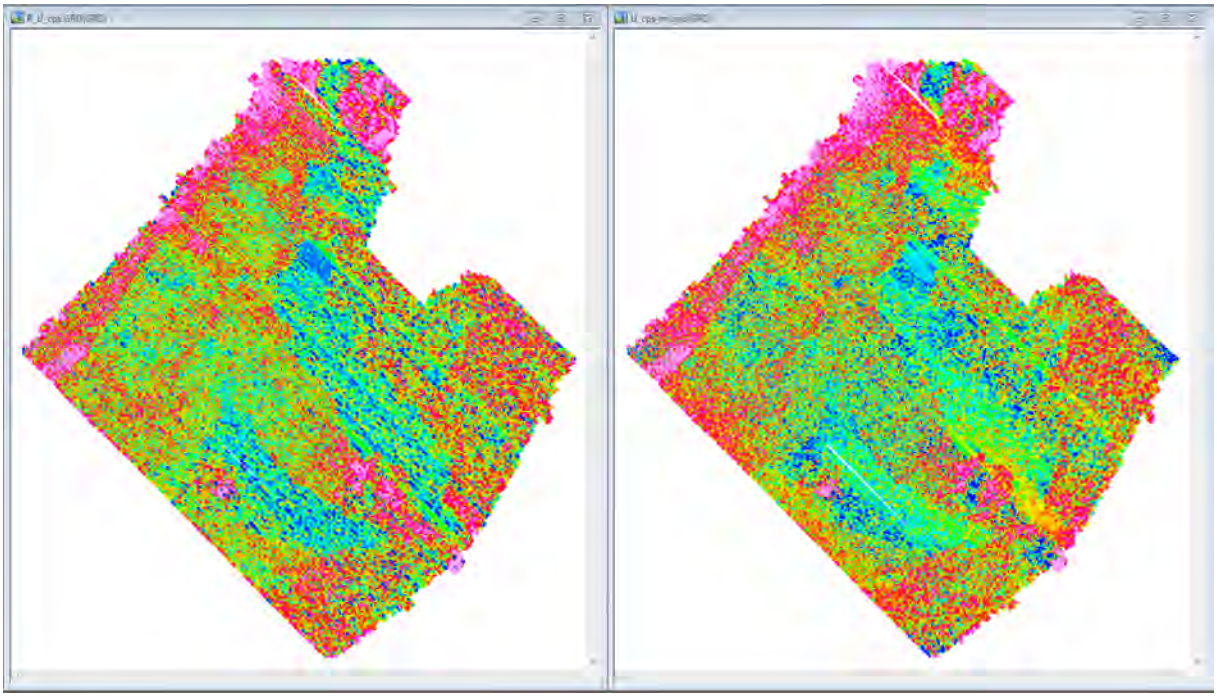

Figure 3.20. 289 - Røyrvik, Limingen area - Uranium count.

3.11 289-2 - Skorovatn - 1993

This dataset shows faint stripes in the northernmost corner and at the southwestern tip of the uranium grid (Rønning, 1995b). This area was flown with two line directions of 0° and 135°. Two micro-levelling processes with a decorrugation cutoff wavelength of 400 m and a Naudy filter of 500 m were applied to the data for each line direction (Figure 3.21).

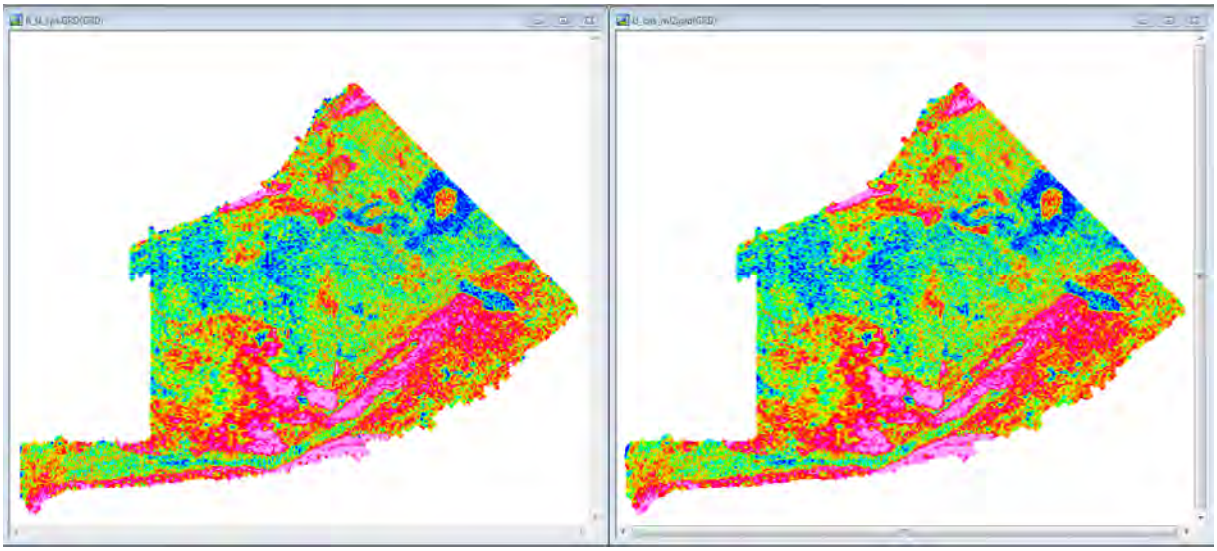

Figure 3.21 289-2 - Skorovatn - Uranium count.

3.12 311 - Vuku - 1992

Faint linear noisy trends are seen on all element count grids for the Vuku area (Skilbrei, 1993). A micro-levelling was performed on all grids to enhance the final data. A decorrugation cutoff wavelength of 800 m was used for the micro-levelling of potassium (Figure 3.22) and thorium (Figure 3.23) and 9,000 m for uranium (Figure 3.24). A Naudy filter of 500 m was used for all elements.

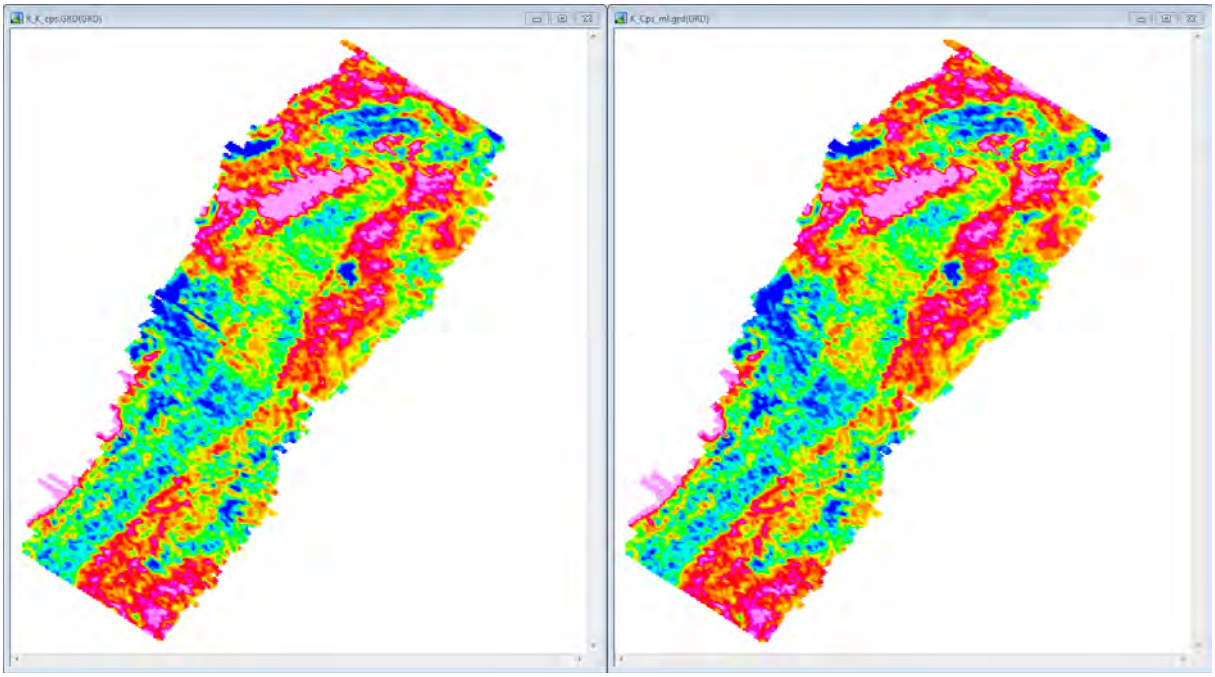

Figure 3.22. 311 - Vuku - Potassium count.

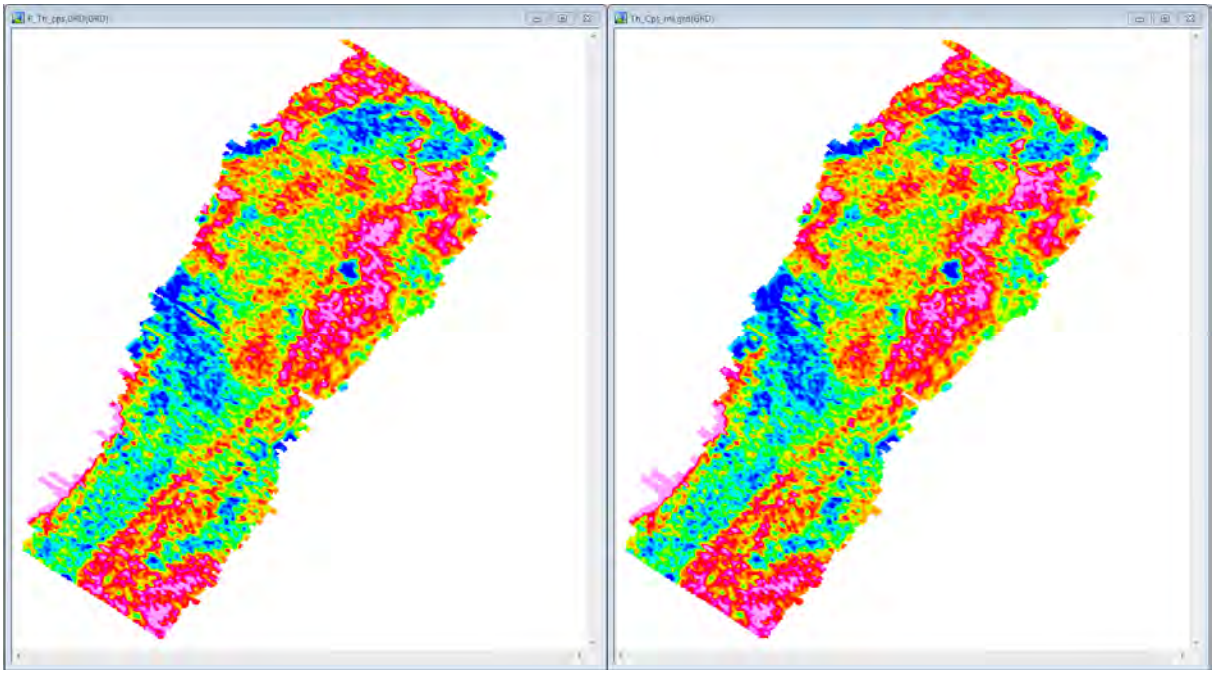

Figure 3.23. 311 - Vuku - Thorium count.

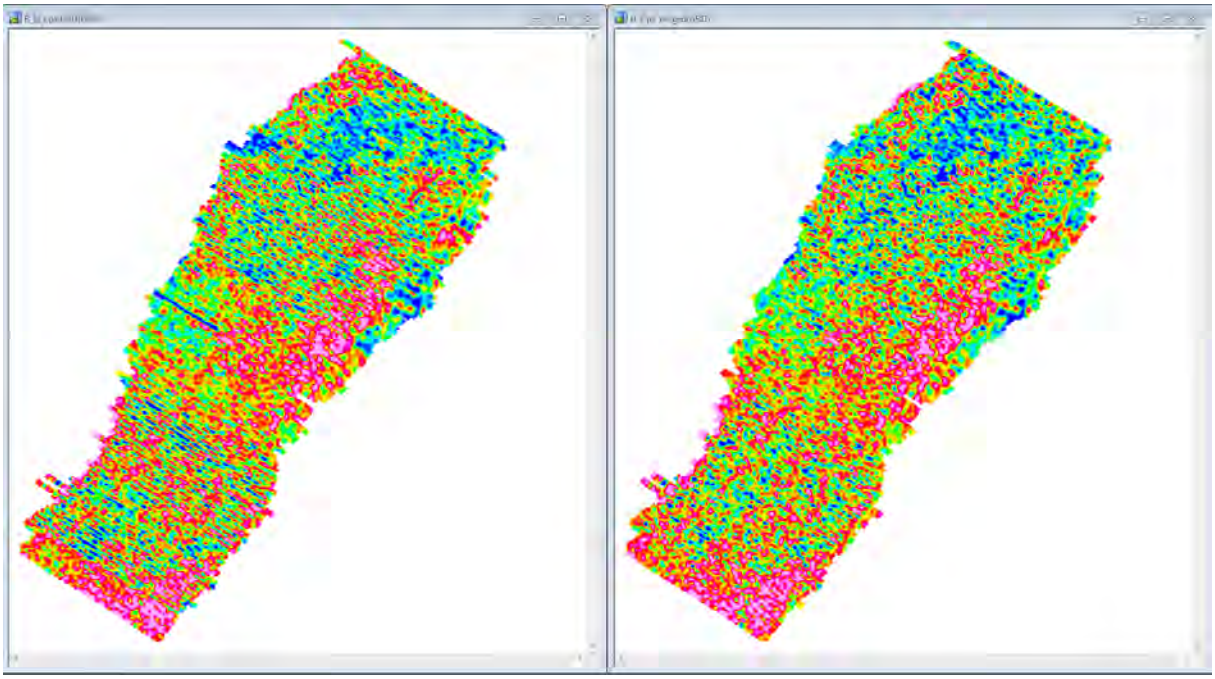

Figure 3.24. 311 - Vuku - Uranium count.

3.13 Calculation of concentrations

For data analysis and comparison, the count rates were adjusted to the relevant ground concentrations. Normally, the ground concentrations of the radio-elements are calculated using the so-called sensitivity coefficients obtained from a calibration test (IAEA 1991). By using a calibrated portable spectrometer and recording airborne data of few passes on one and the same line, the sensitivity coefficients are measured.

$$C_e = \frac{n_e}{S_e}$$

The *concentration C* of a given *element e* (Th, K or U) is proportional to the *sensitivity coefficient S* and to the *count rate n* corrected for dead-time, stripping ratio, background and attenuation.

In this case, data are sometimes 30 years old with very little information on their acquisition. To obtain the concentrations from these data, a concentration reference must be used. As most datasets overlapped with TRAS-12 radiometric grids, they were used as a reference to calculate the concentration. As seen above, a linear correlation exists between the count values and the concentration values. For the overlap area, all points are plotted in a graph from which the linear regression is calculated.

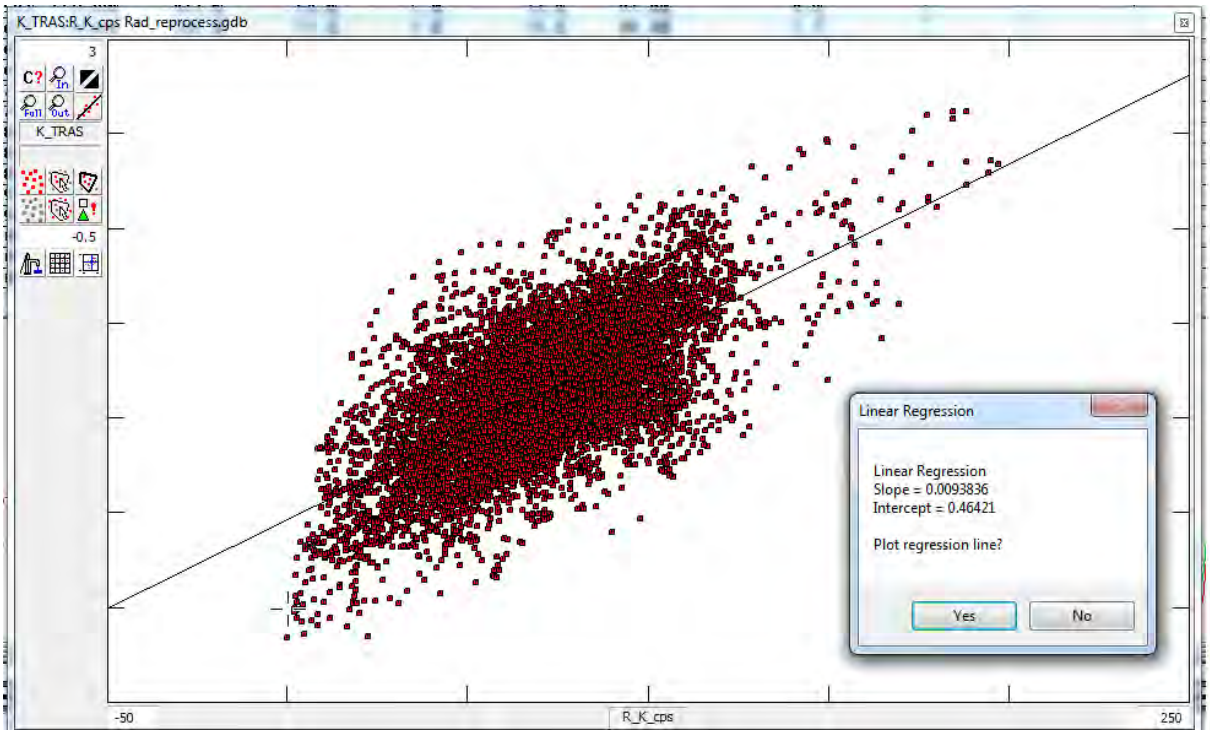

Figure 3.25. Linear regression used for concentration calculation.

The Figure above shows an example of a linear regression in an overlapped area between projects TRAS-12 (Concentration) and survey #278 (Counts per second). In this case, the thorium linear regression is calculated. The slope and intercept calculated by the Geosoft module are later used for the concentration estimation of survey #278:

$$C_{278} = an_{278} + b$$

In this example, C is the concentration for the thorium data of survey #278, n is the count rate for the thorium data of survey #278 and a and b are the slope and intercept, respectively, as calculated from the linear regression.

The slope and intercept are shown in Table 4 below for each grid:

Table 3.4. Linear regression results.

Project	Element	Slope	Intercept
212	**K**	0.016088	-0.03505
	Th	0.28615	0.31834
	U	0.13862	-0.54648
278	**K**	0.0093836	0.46421
	Th	0.13744	3.0114
	U	0.018252	1.2436
280	**K**	0.022737	-0.15329
	Th	0.31508	0.11509
	U	0.19758	-0.23834
281	**K**	0.013217	-0.17765
	Th	0.23012	0.36864
	U	0.082348	-0.29926
282	**K**	0.011441	0.18269
	Th	0.17279	1.5011
	U	0.10181	0.82783
283	**K**	0.011119	0.28934
	Th	0.18127	2.2695
	U	0.020547	1.0229
289	**K**	0.010085	0.1116
	Th	0.18664	1.6519
	U	0.0229	1.0061
311	**K**	0.014107	-0.25731
	Th	0.16476	0.89409
	U	0.04473	0.53630

The uranium concentration calculation proved to be a problem for several of the datasets. The count rate level was often within the noise of the instrument. The very low values of the concentration level calculated in TRAS-12 and the low level of the count rates of NGU surveys made the regression calculation uncertain. As can be seen for potassium and thorium, the coefficients for the uranium regression should have a similar magnitude. This is expected as the same system with the same crystal volume was used for all acquisitions. Several attempts were made and the best fitted grid was produced using the coefficient from survey #280.

3.14 Grid knitting

Grids are merged together using the Geosoft Oasis Montaj tool called Grid Knitting. In the process, a slight shift is introduced to match the grids. Shifts have been calculated as:

$Shift = E_{comp} - E_{XXX}$, E is the element grid, comp the compilation and XXX the project number

The average shift within any one grid is recorded in Table 3.5.

Table 3.5. Grid knitting shifts.

Project Code	Project Name	Year	Shift Potassium (%K)	Shift Thorium (ppm)	Shift Uranium (ppm)
212	Grong, Harran	1988	-0.0002	-0.0107	-0.0220
278	Steinkjer	1986	-0.0053	-0.0203	0.0342
280	Andorsjøen Grong Snåsavatnet Snåsa, Overhalla	1990	-0.0286	-0.1402	0.0201
			-0.0042	0.0018	0.0148
			0.0030	0.0308	0.0142
			-0.0008	0.0205	-0.0098
281	Meråker, Flornes	1991	0.0015	0.0102	-0.0035
282	Stiklestad	1991	0.0083	0.0322	0.1132
283	Verran, Holden, Åfjord	1992	-0.0003	-0.0023	-0.0036
289	Skorovatn Røyrvik	1993/94	0.0010	0.0006	-0.0001
			0.0170	0.0651	-0.0648
311	Vuku	1992	0.0153	0.0446	0.0051
TRAS-12	Trøndelag Region Airborne Survey (TRAS)	2012-14	0.0003	0.0011	-0.0035

The shifts of the various grids after the knitting process are much lower than the resolution of the data itself. The final grid is also very consistent.

3.15 Radiometrics maps

All the grids (K, U and Th) were knitted together for each element with a grid cell size of 50 m. The maps are presented below.

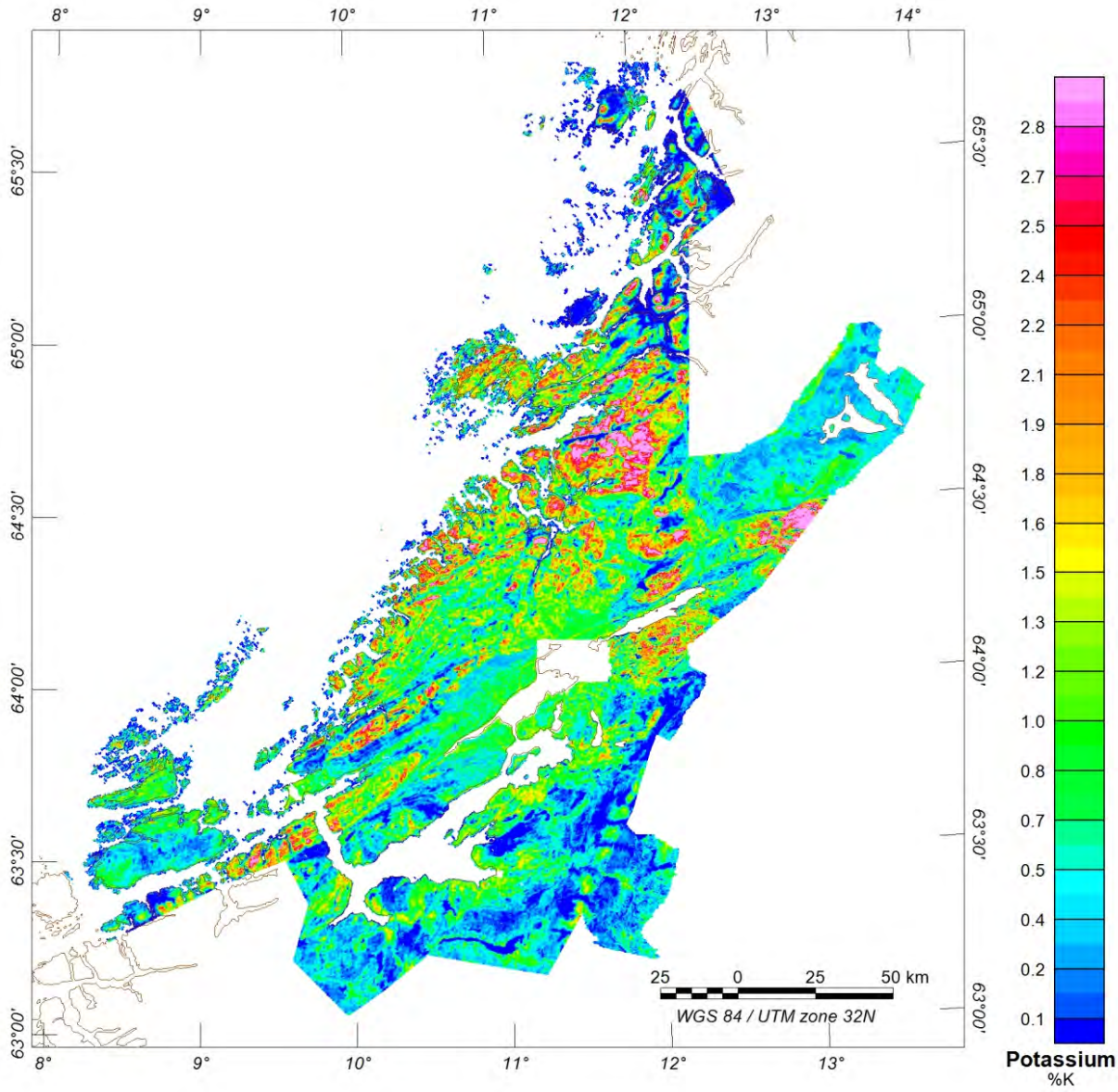

Figure 3.26. Potassium map of the Trøndelag area (%K).

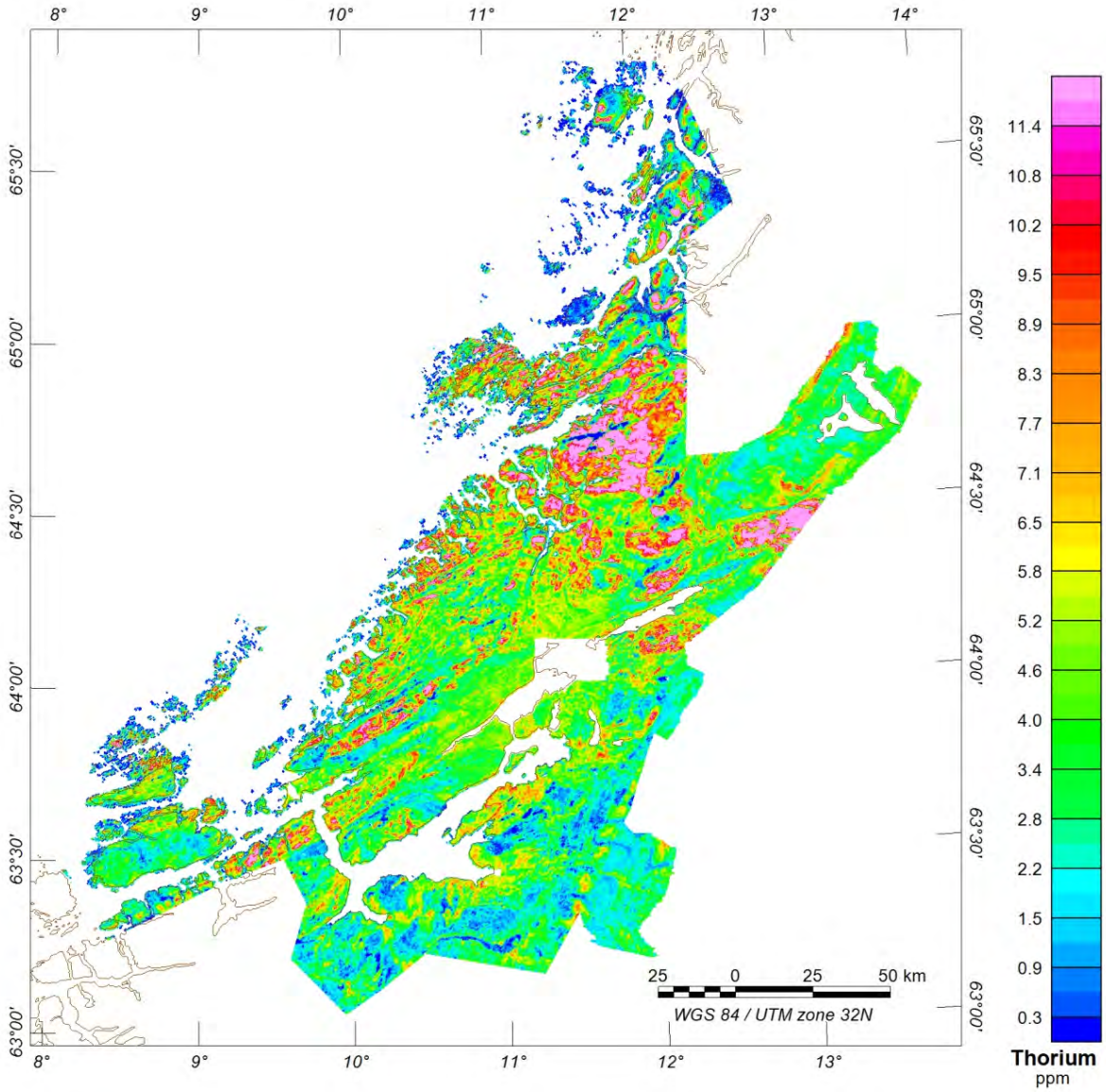

Figure 3.27. Thorium map of the Trøndelag area (ppm).

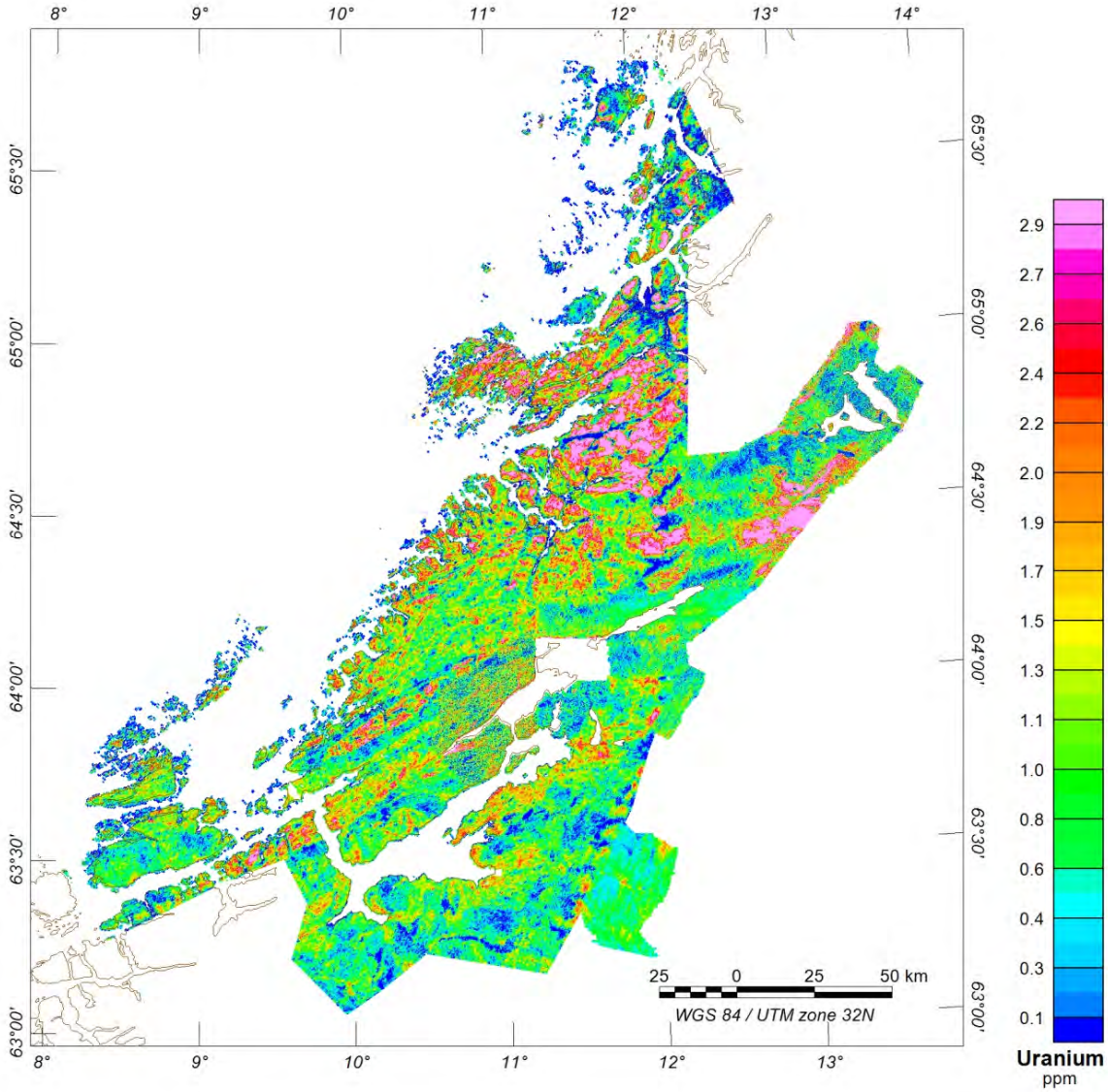

Figure 3.28. Uranium map of the Trøndelag area (ppm).

3.16 Conclusions

We were able to improve the quality of all radiometric datasets flown between 1986 and 1994 by manual adjustments and micro-levelling techniques. The main difficulty was the very low counts per second acquired especially for the uranium data. The reprocessed grids were very consistent from one to another and the merging step did not create any major artefacts. The resulting maps (%K, eTh and eU) are available in UTM zone 32N projection at WGS-84 datum.The uranium, thorium and potassium data from each survey were gridded with a grid cell size of 50 x 50 metres. The six surveys were then knitted together with respect to each radioactive element. The results of this combination are presented in Figure 3.29.

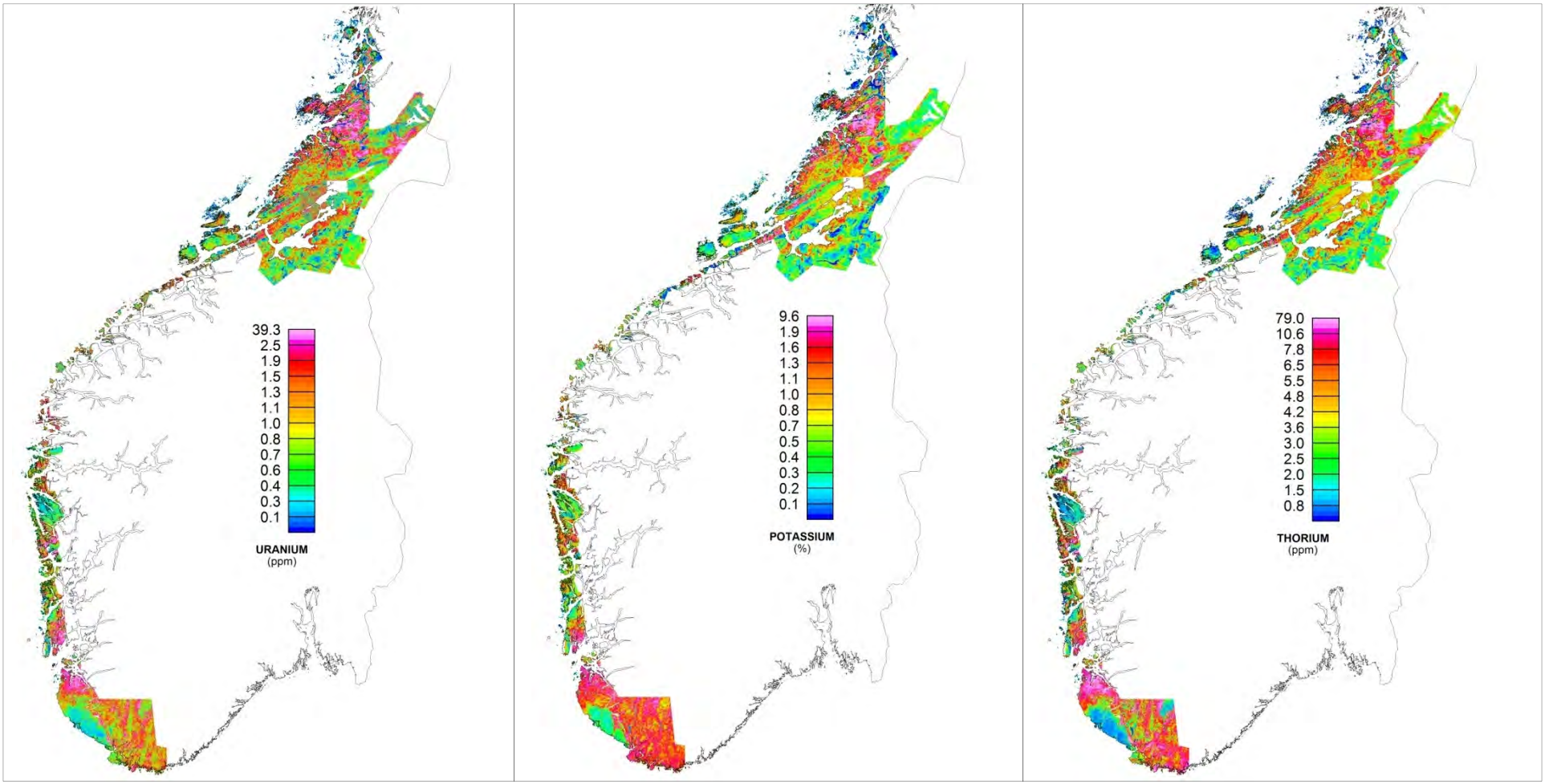

Figure 3.29. The results of the radiometric measurements: apparent radioelement concentrations of uranium (ppm), thorium (ppm) and potassium (%).

4. COMPILATION OF GEOLOGICAL MAPS

Ole Lutro, Arne Solli & Tom Heldal

The bedrock map of the Coop2 area covers in a broad sense the coastal region from Stad to Røyrvik. It is compiled from several sources. The southern part is mainly based on the 1:250.000 map sheets Ulsteinvik (Tveten et al. 1998), Ålesund (Lutro et al. 1998) and Kristiansund (Askvik & Rokoengen 1985). The northern part derives from Digitalt berggrunnskart over Nord-Trøndelag og Fosen (Solli 1995) and the 1:250.000 map sheet Trondheim (Wolff 1976). Both the Coop magnetic map and the bathymetric shaded relief map, including the OLEX data set, have been used to interpret the bedrock geology on the shelf area.

In the current compilation, the Coop1 and Coop2 maps have been merged into one data set. To make a seamless map of these different maps, the feature hovedbergart/MainRockType that includes 107 rock-types has been used. Note that there are some recent changes/updates in the Coop1-part. The Sirdal Igneous Belt has been included in the map. The Utsira Complex has been outlined using the geophysical data.

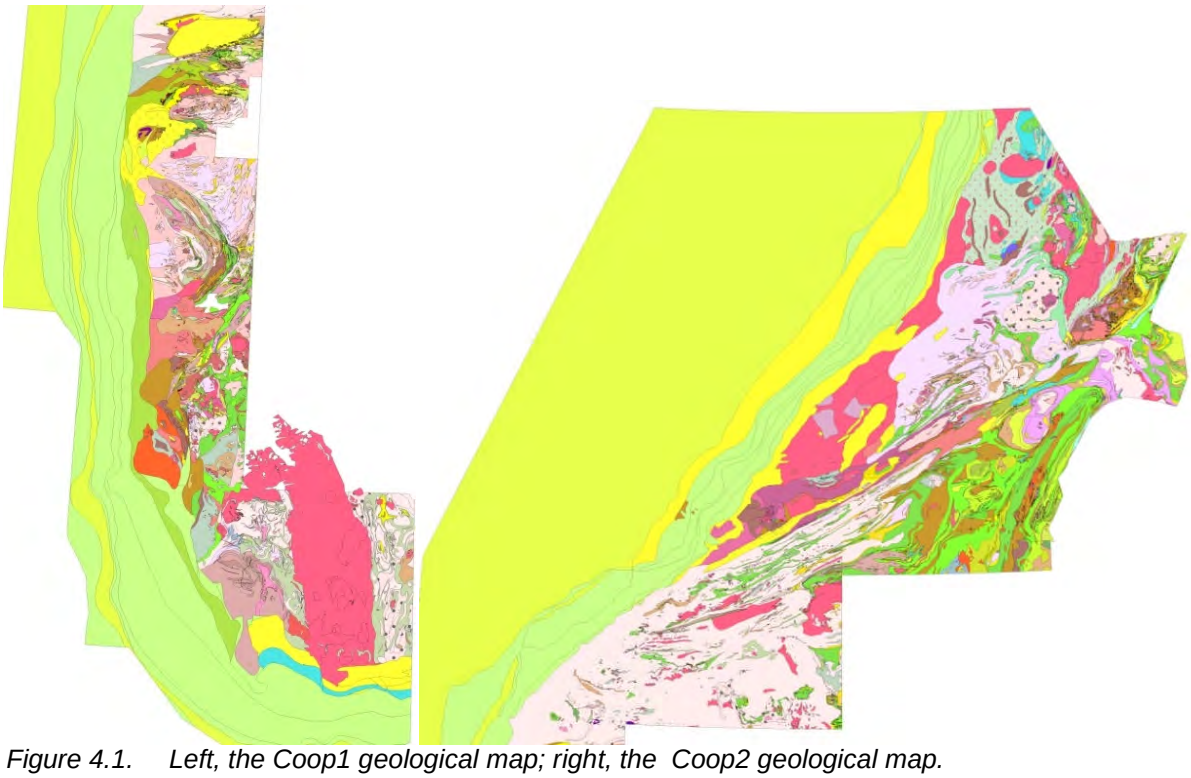

Figure 4.1. Left, the Coop1 geological map; right, the Coop2 geological map.

4.1 Geology

The area is mainly made up of a basement of Proterozoic gneisses and granites overlain by nappes thrust during the Caledonian Orogeny. The Caledonian nappes contain both Lower Palaeozoic sedimentary and volcanic rocks and Precambrian gneisses. At a late stage of the orogeny, Devonian sandstones and conglomerates were deposited on top of the thrust sheets. The Devonian rocks are closely related to a late extensional phase which led to the formation of several gently-dipping detachment zones.

4.2 Precambrian basement

The basement rocks are present in two areas. (1) In the Western Gneiss Region of the north western part of Western Norway and (2) the Fosen Peninsula in Trøndelag. The Western Gneiss Region (WGR) is composed of Mesoproterozoic gneisses and migmatites, mainly of intrusive origin. These rocks were formed both during the Gothian (1700-1500 Ma) and the Sveconorwegian orogeny (1200-900 Ma). On the map some granite bodies are shown as separate units. Most probably these represent less altered and deformed parts of larger bodies that have been mapped together with the surrounding gneisses.

Figure 4.2. Left, migmatitic gneis form the WGR; right, deformed granite from Otrøya.

Gabbros occur widespread in the WGR and are in many places garnet-bearing. Eclogites are common, mostly as smaller bodies within the gneisses, although larger bodies are found, i.e. at Ulsteinvik. The formation of the eclogites is assigned to the subduction of Baltica underneath Laurentia during the Scandian collisional phase of Caledonian orogeny.

Sillimanite-bearing rocks are found in the WGR; these are interpreted as altered supracrustal rocks. The sillimanite occur both as nodules and more evenly scattered in the rock.

In Trollheimen and south of Moldefjorden a quartzite layer, in some places with a basal conglomerate, is present sandwiched between basement rocks, indicating that basement rocks occur at two different structural levels in the area, one thrust on top of the other (Robinson et al. 2014).This relation is easily seen when the quartzite is present, and difficult or impossible to asses when the quartzite is absent. There is, however, a difference between the two basement units as the lower one does not contain eclogite and garnetiferous gabbros (Robinson et al. 2014). On top of the upper basement is another autochthonous sandstone/conglomerate layer in the Åmotsdal Formation.

The basement area north of Trondheimsfjorden has mainly the same rock units as in the WGR, consisting mainly of strongly foliated migmatitic gneisses of granitic/granodioritic composition. Braathen et al. (2002) denoted this area the Central Norway basement window, and from the new Coop-interpretation the area appears to occur as a Precambrian window surrounded by the Trondheim Nappe Complex in the east and the Helgeland Nappe Complex in the offshore areas. The deepest part of this basement is exposed in the coastal Roan area where rocks of high-pressure granulitic grade and eclogite are described (Möller et al. 1988).The area has a strong positive magnetic signature.

North of the Grong-Olden culmination the magnetic signature in the basement is less prominent , but on the other hand the rocks have a strong radiometric signal. The main rock type here is a granitic augen gneiss. Only a few age determinations exist from this area, indicating that the basement in this northern part of the Central Norway basement window has an age of about 2100-1800 Ma. This is in contrast to the areas farther south and in the WGR where the ages are in the time span 1680-1500 Ma, see e.g., Bingen & Solli (2009).

Precambrian rocks also occur in the Tømmerås window NE of the inner part of Trondheimsfjorden, and in the Grong-Olden culmination that separates the Caledonides in the Trøndelag area from the Caledonides in the Nordland area. These rocks have generally been assigned to the Lower Allochthon (the Olden and Formofoss Nappes, see e.g., Roberts 1997). However, it remains an open question whether or not the entire Central Norway basement window and "the upper basement" of the WGR are part of the Lower Allochthon, see e.g., Robinson et al. (2014), Figure 4.1, and discussion therein.

4.3 Caledonian nappes

The nappes present in the area are, from the bottom to top, the Risberget Nappe, Sætra Nappe and the Blåhø Nappe belonging to the Middle Allocthon, the Trondheim Nappe Complex of the Upper Allochthon, and the Helgeland Nappe Complex of the Uppermost Allochthon.

The Risberget Nappe consists mainly of granitic augen gneiss with feldspar augens that may be up to 10 cm long. The augen gneisses are dated to 1650-1642 and 1190-1180 Ma. Included in the Risberget Nappe are also anorthositic rocks and some ultramafic rocks that are typically found in Tafjord. The Risberget nappe is not present north of Trondheims-fjorden.

Figure 4.3. Left, Risberget augen gneiss, locality in Drivdalen, south of Oppdal; right, Ultramafic rocks and anorthosite from Tafjord.

The Sætra Nappe consists of meta-arkose and dolerite dykes. The Neoproterozoic sandstones were deposited at the Baltica margin during the break-up of Rodinia, and they are intruded by dolerite dykes related to the break-up. This succession is hundreds of meter thick in the Trollheimen area, whereas in the WGR a structurally highly attenuated unit might be only a few metres thick. North of Trondheimsfjorden sandstones intruded by mafic dykes

are wrapping around the Precambrian Tømmerås window in the Leksdal Nappe (Roberts 1997) and they can be correlated with the Sætra Nappe.

Figure 4.4. Meta-arkose from the Sætra Nappe, intruded by a eclogitised dolerite dyke.

4.4 Blåhø Nappe

The Blåhø Nappe consists mainly of garnet mica-schist and amphibolites and some marbles and ultramafic rocks. This nappe has previously been considered part of the Upper Allochthon, but has recently been assigned to the Middle Allochton as the rocks probably originated on the Baltica margin (Gee et al. 2013).

Figure 4.5. Garnet mica-schist in the Blåhø Nappe, left from Ekna, right from Otrøya

Within the WGR garnet mica-schist, amphibolite, marble, and meta-arkose occur in zones that are mainly oriented in a NNE-SSW direction. These have generally been interpreted as Caledonian Nappes and correlated with nappes found in Central Norway, for the most part the Blåhø Nappe. In the Molde area, a nappe tectonostratigraphy similar to that in the

Trollheimen/Trondheim area is present, whereas in other areas only one or some of the nappes are present.

North of Trondheimsfjorden Blåhø Nappe equivalents, with the local name Skjøtingen Nappe, see e.g., Roberts (1997), occur as rather thin slivers down-folded into the Central Norway basement window. This unit is also present as a rather thin rim of rocks beneath the Trondheim and Helgeland Nappe Complexes. The Skjøtingen Nappe also occurs in the Lierne area where it forms a continuation of the Seve Nappe in Sweden. The nappe is dominated by mica schist, amphibolite and some marble and generally shows a low magnetic signal in contrast to the basement.

4.5 Trondheim Nappe Complex

This nappe complex has a wide distribution in the inner part of Trøndelag but is not represented in the coastal and offshore districts except in the Smøla and Hitra area. A comprehensive description of the nappe complex is given in Gee et al. (1985) and Wolff (1979).

The Gula Nappe constitutes the central part of the nappe comlex. This nappe is dominated of mica schist, partly containing kyanite, and staurolite typical of amphibolite facies metamorphism. The nappe also contains amphibolites interpreted as volcanic rocks.

The Gula Nappe is flanked by the Støren Nappe to the west and the Meråker Nappe to the east. These nappes consist of the same types of rocks, they are commonly correlated and are generally interpreted to be situated on top of the Gula Nappe. Both nappes are in are in greenschist facies, in contrast to the high-grade metamorphism in the Gula Nappe. The oldest parts of the Støren and Meråker Nappe are greenstone units where ophiolite fragments locally appear (e.g., Vassfjellet, Løkken). These are of late Cambrian to early Ordovician age and have a weak positive magnetic signature (Grenne et al. 1980, Slagstad et al. 2013). In the Fosen area the Støren Nappe consists mainly of intermediate to felsic intrusive rocks.

The main part of the Støren and Meråker nappes is composed of sedimentary rocks that originated in a volcanic arc environment, including greywacke, sandstone, schist/slate and some limestone. The common interpretation is that the sediments occur as synclines between the greenstone belts, and a classic stratigraphy has been developed. Numerous fossils show that the age of the sediments is Early to Mid/Late Ordovician. The fossils are in places of Laurentian affinity, indicating formation close to the Laurentian margin (Bruton & Bockelie 1980, 1982).

The nappe complex is intruded by a wide variety of intrusive rocks ranging in composition from gabbro to trondhjemite. One of the largest intrusions is the Smøla-Hitra Batholith. New geophysical data indicate that this batholith might continue to the mainland at Fosen where dioritic and granitic rocks earlier interpreted as Precambrian have been shown to be Ordovician in age (Tucker et al. 2004).

The Trondheim Nappe Complex has an equivalent north of the Grong-Olden Culmination in the Gjersvik, Orklump and Bjørkvatnet Nappes (Roberts 1997).

In the Western Gneiss Complex the Støren Nappe is mainly composed of fine-grained amphibolites with associated gabbro and diorite.

4.6 Helgeland Nappe Complex

The Helgeland Nappe Complex belongs to the Uppermost Allochthon of the Caledonides of Norway. It extends from Grong in the south and occupies most of the Nordland County south of Mosjøen. The new Coop data also indicates that it occupies the offshore areas outside Trøndelag possibly as far south as Hitra and Frøya. The Helgeland Nappe Complex is regarded as the most exotic of the nappes in this region and originated on the eastern margin of Laurentia. Roberts et al. (2007) have given a general description of the Uppermost Allochthon. A more detailed description of the Helgeland Nappe Complex in the coastal areas is found in Barnes et al. (2007) and McArthur et al. (2013).

The nappe complex consists of a wide variety of sedimentary and intrusive rocks. The sedimentary rocks are dominated by mica schist, marble and calc-silicate rocks, and generally these represent the low magnetic areas on the map. There are also some sandstones and conglomerates.

The most prominent positive magnetic anomalies appear to be connected to greenstones and ophiolite fragments where Leka is the most prominent member. The ophiolites appear to be located in the lower part of the nappe sequence and occur in a strongly folded pattern (Figure 4.6).

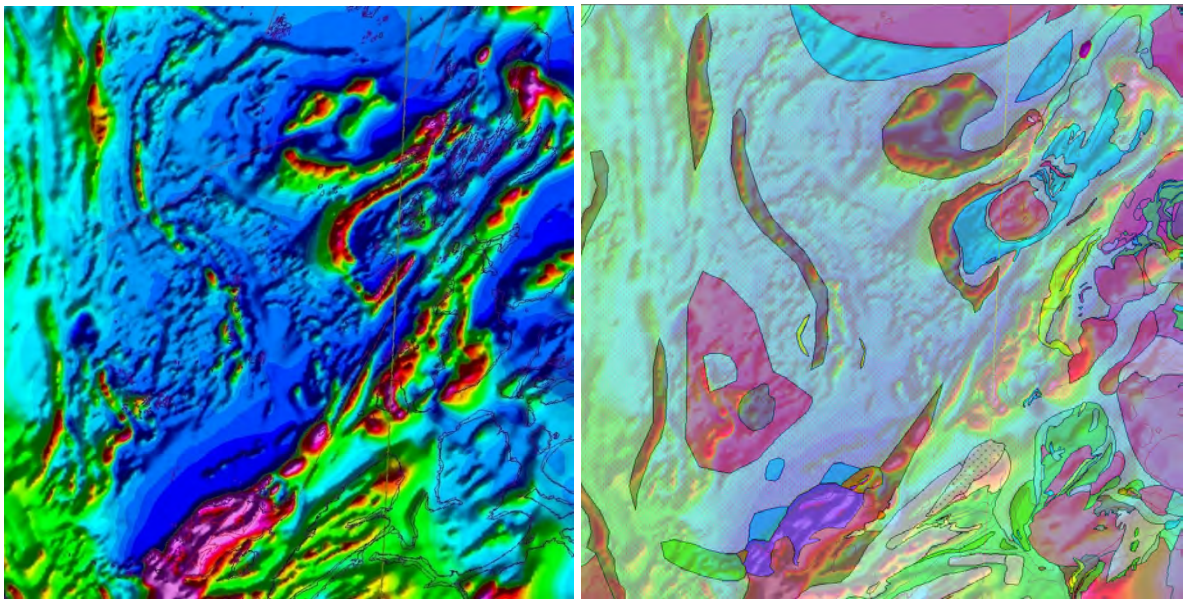

Figure 4.6. Left, positive magnetic anomalies interpreted to be associated with the ophiolites in coastal Helgeland; right, the interpreted geological map based on the magnetic anomalies. Leka in the bottom part of the figures.

A large part of the distribution of the ophiolite complex are interpreted from the anomalies on the sea floor, and only a small part of the sequence is exposed on small islands.

A major part of the Helgeland Nappe Complex consists of granitoid intrusions. There are a few gabbroic bodies, but the majority of the intrusions are felsic to intermediate rocks of calc-alkaline to alkali-calcic composition. Age determinations have shown that there is an older group of rocks ranging in age from about 480 to 465 Ma. These rocks seem to have intruded during a regional phase of high-grade metamorphism and migmatization. A younger group of rocks emplaced in the period c. 450-425 Ma occur more like regular plutons emplaced in the mid to upper crust in a continental arc setting (Barnes et al. 2011).

Many of the intrusive bodies have a low magnetic signature like e.g., the Vega intrusive complex. In the offshore areas it can therefore be difficult to differentiate between supracrustal and intrusive rocks. However, the metasedimentary rocks mostly have a layered signature on the bathymetry whereas the intrusive rocks have an irregular pattern, and this difference have been used when interpreting the geology.

4.7 Devonian deposits

The Devonian deposits are mainly sandstone and conglomerates. They are present on mainland Fosen, on the southeastern coast of Hitra/Smøla and nearby islands, and on small islands outside Fosen and in Frohavet, i.e.Vingleia light house. It also is found to occupy most of Trondheimsleia, the ship lane between Smøla/Hitra, and the mainland. On Fosen the Devonian rocks rests directly on top of the Høystakken detachment.

Figure 4.7. Devonian conglomerate from Ørlandet.

4.8 Extensional features

In general, extension of the complex Caledonian (Scandian) nappe pile started in the Early Devonian. Several studies from central Norway have documented the late- to post-orogenic evolution of the most important onshore structural elements (e.g., Braathen et al. 2000, 2002, Nordgulen et al. 2002, Osmundsen et al. 2003, 2006, Roberts et al. 2005, Robinson et al. 2013, and references therein). In the Early- to Mid Devonian exhumation of the Central Norway basement window took place during top-NE shearing along the northern part of the Kollstraumen detachment, top-SW movement along the Høybakken detachment (Kendrick et al. 2003) in southwestern Fosen, combined with sinistral shear along the Møre-Trøndelag Fault Complex. Further to the north, the top-WSW Nesna shear zone coincide with the lower boundary of the Helgeland Nappe Complex. Notably, folding along axes parallel to the ENE-WSW elongation direction overlapped in time with development of extensional detachments, showing that shortening normal to the extension direction took place at this stage. In the WGR, south of the Møre-Trøndelag Fault Complex, extensional structures are less obvious. However, Tucker et al. (2004) and Robinson et al. (2013) have shown that the somewhat older Agdenes detachment, separating the Upper Allochthon from subjacent Precambrian basement rock units, has regional importance in the northwestern parts of the WGR.

5. COMPILATION OF PETROPHYSICAL DATA

Torleif Lauritsen & Jomar Gellein

Approximately 47,000 rock samples from the whole of Norway, collected during geological mapping and geophysical studies, have been measured with respect to density, susceptibility and remanence (Torsvik & Olesen 1988). The data are stored in NGUs petrophysical database (Olesen et al. 1993). Figure 5.1 a displays the geographical distribution of a selection of these petrophysical samples on the mainland of southern Norway.

We have produced maps of susceptibility and density by calculating the average values within each geological unit present in the geological map (Sigmond 1996) (Figure 5.1b).

Non-representative samples (e.g., sulphide mineralisations, hydrothermal alterations, mylonites, dolerite and eclogite) were removed from the dataset before map production. We then selected points within each polygon on the bedrock map. An average of these points was attributed to each polygon. The applied colour scale for the susceptibility map is logarithmic in order to depict the several magnitude-wide distributions for each rock unit.

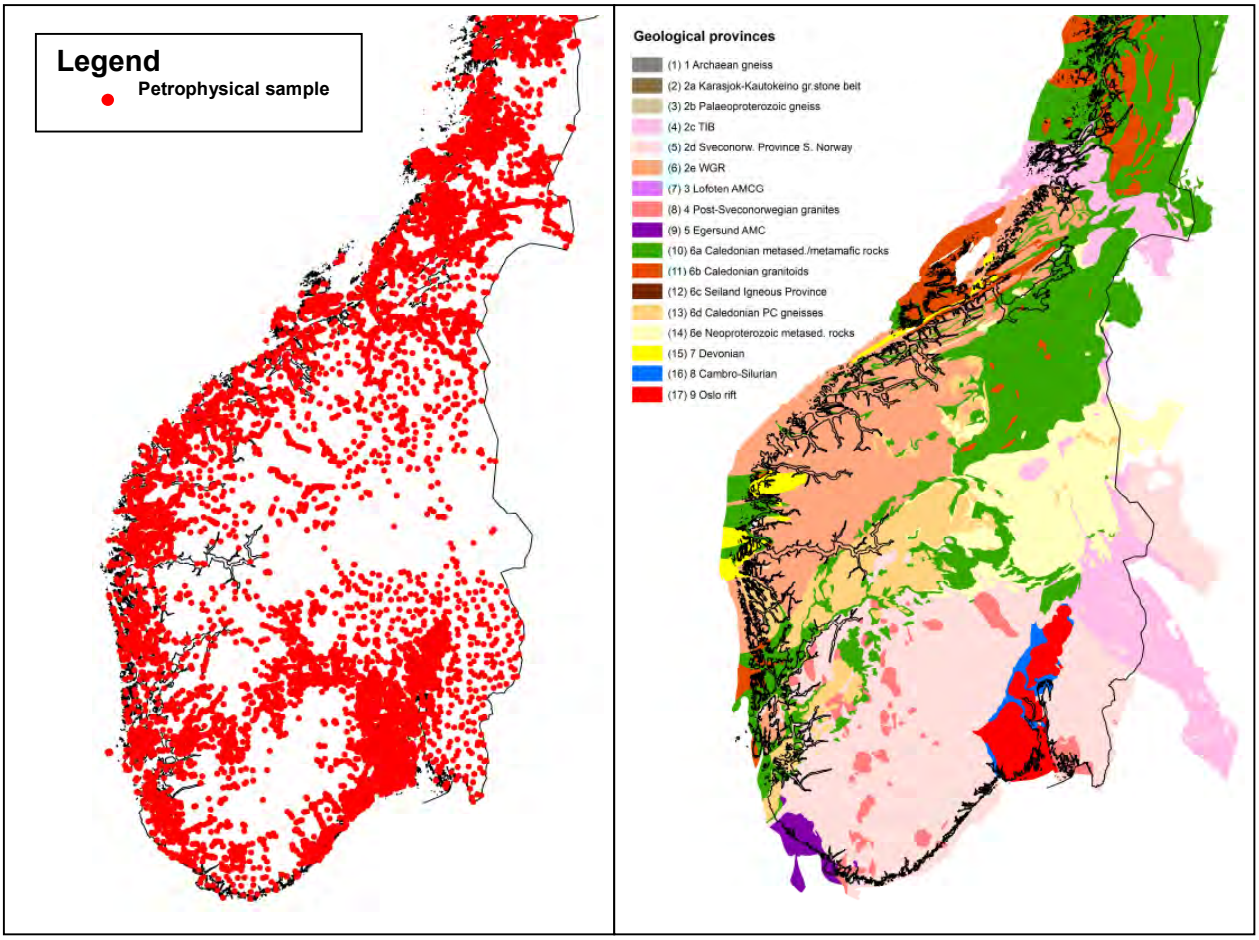

Figure 5.1 a) Geographical distribution of the petrophysical samples on the south Norwegian mainland. b) Simplified bedrock map of southern Norway (Sigmond 1996); legend as in Figure 6.1a.

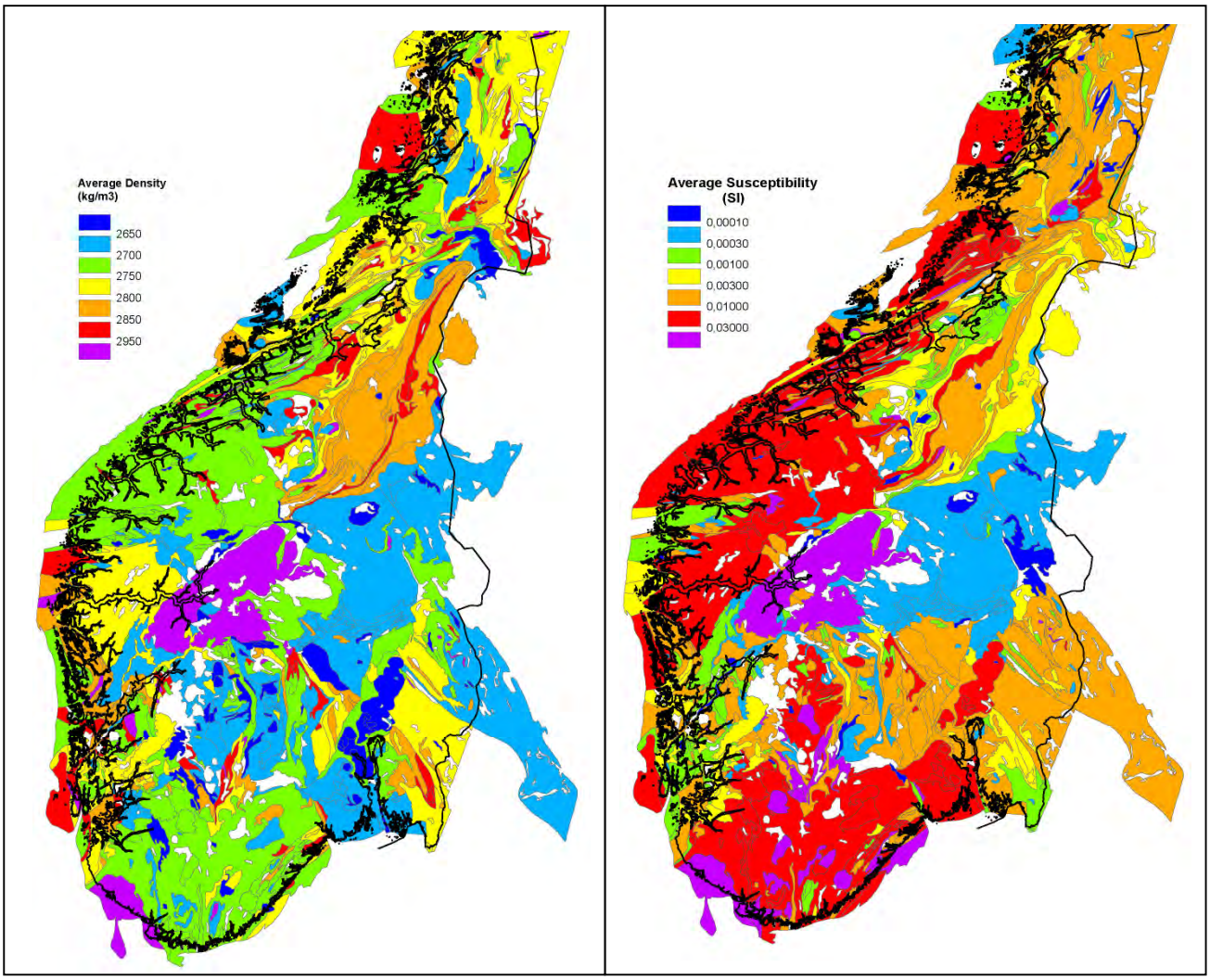

Figure 5.2 a) and b). Average density and average susceptibility of surface bedrock samples within each geological unit on the bedrock map of southern Norway (Sigmond 1996). Average density in kg/m^3 and average susceptibility in SI units. The applied colour scale for the susceptibility data is logarithmic in order to depict the wide distribution of the mean values.

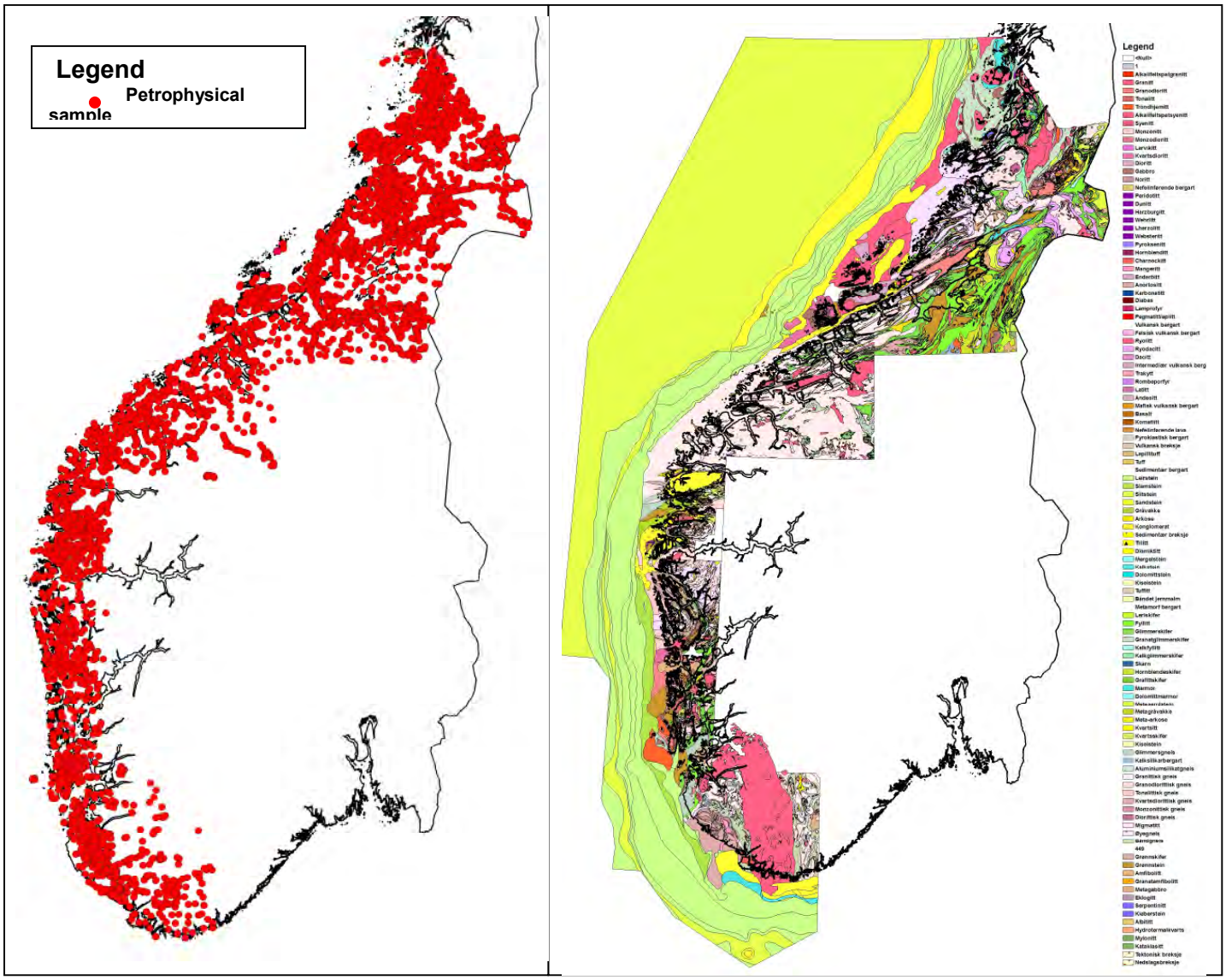

Figure 5.3 a). A selection of petrophysical bedrock samples situated within the outline of the detailed bedrock map. A total of 12,671 surface bedrock samples have been measured in this area. b) Coop2 project bedrock map (Lutro et al. 2015, Chapter 4 in the present report).

The samples have an even and dense geographical distribution within the area of this project (Figure 5.3 a). Thus, the level of detail in the bedrock map defines the resolution of the density and average susceptibility maps. We have therefore decided to combine these samples in a more detailed geological map (Figure 5.3 b).

Figure 5.4 presents the average density (a) and average susceptibility (b) of bedrock samples within each geological unit on the Coop2 project bedrock map (Lutro et al. 2015, Chapter 4 in the present report).

The average density map shows the highest values (> 2950 kg/m^3) in the mafic extrusive rocks (greenstones) of the Sunnfjord area, and relatively high values (> 2850 kg/m^3) in the monzonites, migmatites and anorthosites of the Lindås Nappe and the metabasalts and amphibolites of the Hardangerfjord Nappe (both nappes are located in the Bergen Arc). High values (2850 - 2950 kg/m^3) are also recorded in the migmatites and amphibolites of the Boknafjord Nappe. The granitic gneisses of the Øygard complex (to the west of the Bergen Arc) are visible as a low-density area (< 2650 kg/m^3), similar to the banded gneisses of the

Mandal area. Furthermore, the gneisses north-northeast of Fensfjord appear to have lower densities (2650-2700 kg/m^3) than the surrounding bedrock units.

Granites and gneisses of the Farsund-Mandal area and the anorthosites of the Egersund area show higher magnetisation (susceptibility > 0.01 SI) than the surrounding bedrock, but also the Western Gneiss Region has relatively high values (0.003-0.03 SI).

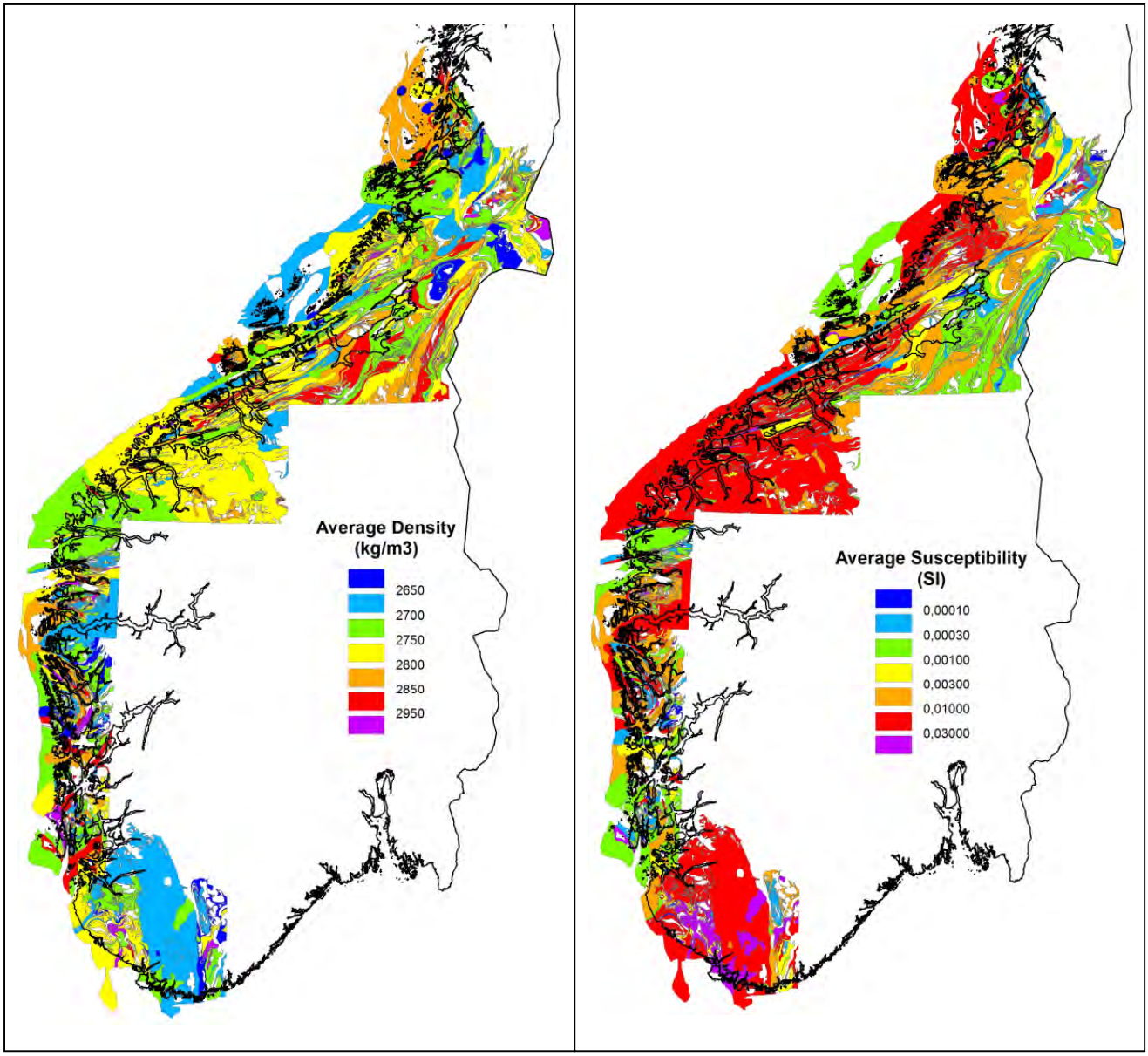

Figure 5.4 a) and b). Average density and average susceptibility of bedrock samples within each geological unit of the Coop2 project bedrock map (Lutro et al. 2015, Chapter 4). Average density in kg/m^3 and average susceptibility in SI units. The applied colour scale for the susceptibility data is logarithmic in order to depict the wide distribution of the mean values.

6. HEAT-PRODUCTION CALCULATIONS

Torleif Lauritsen & Trond Slagstad

6.1 Introduction

Internal radiogenic heat production is a major factor determining the thermal structure of continental crust (e.g., Turcotte & Schubert 1982), and variation in internal heat production may have important implications for temperature-dependent crustal processes such as metamorphism, magmatism and deformation (Bea et al. 2003, Andreoli et al. 2006, Sandiford & McLaren 2006). Regional investigations of heat production at the surface, coupled with heat-flow data that provide information about heat production at depth in the crust (e.g., Jaupart & Mareschal 2003), are necessary for understanding the present-day thermal structure of the crust, which in turn may be used to reconstruct the thermal structure of the crust prior to, during and after past tectonic events (Ranalli & Murphy 1987, Karlstrom & Williams 1998).

This part of the Coop Phase 2 report presents the results of radiogenic heat-production calculations based on measurements of U, Th and K on rock samples, as well as airborne radiometric measurements. These data are integral in understanding the thermal and geological structure of the continent-ocean transition of the Norwegian continental margin. The first part of this section deals with heat-production data from chemical analyses of rock samples whilst the second part deals with heat-production data from airborne gamma ray measurements.

6.2 Sources of heat-production data

The chemical data used to calculate heat production were obtained by XRF (K) and LA–ICP–MS (U, Th). Flem et al. (2005) described the procedures for LA–ICP–MS analysis in detail. For the majority of the samples, densities have been determined using Archimedes' principle by weighing the samples in air and immersed in water, or, if geometrically simple samples are available (e.g., drillcores), by weighing the samples and dividing by the calculated volume. For samples where the original authors reported densities, these densities have been used. If density data are unavailable, density was estimated based on lithology.

Table 6.1. Sources of heat-production data.

Source	n	Analytical method
LITO-project	2755	XRF, LA–ICP–MS
Other NGU data	1538	XRF, LA–ICP–MS

6.3 Heat-production calculations

More than 98% of present-day heat production is the result of the decay series ^{238}U and ^{232}Th and the single-step decay of ^{40}K. The isotope ^{235}U has a significantly shorter half-life than ^{238}U (c. 0.7 billion years and 4.5 billion years, respectively) and is now reduced to 0.7% of the total naturally occurring uranium. Other, short-lived radioactive isotopes may have

made significant thermal contributions in early stages of the Earth's history, but they are not detected now. Other long-lived radioactive isotopes also exist, but their decay rates are so slow that they have never made any significant contribution to the Earth's heat (e.g., ^{87}Rb with a half-life of c. 49 billion years and ^{147}Sm with a half-life of c. 106 billion years). The heat-production rate of a rock can thus be calculated based on the rock's K, U and Th concentrations and density (Rybach 1988), as shown in Equation 6.1. C_U and C_{Th} represent U and Th concentrations in ppm, respectively, C_K represents K concentration in wt.%, and δ is density.

$$A = \delta * (9.52C_U + 2.56C_{Th} + 3.48C_K) * 10^{-5} \qquad (6.1)$$

6.4 Heat production of Norwegian bedrock

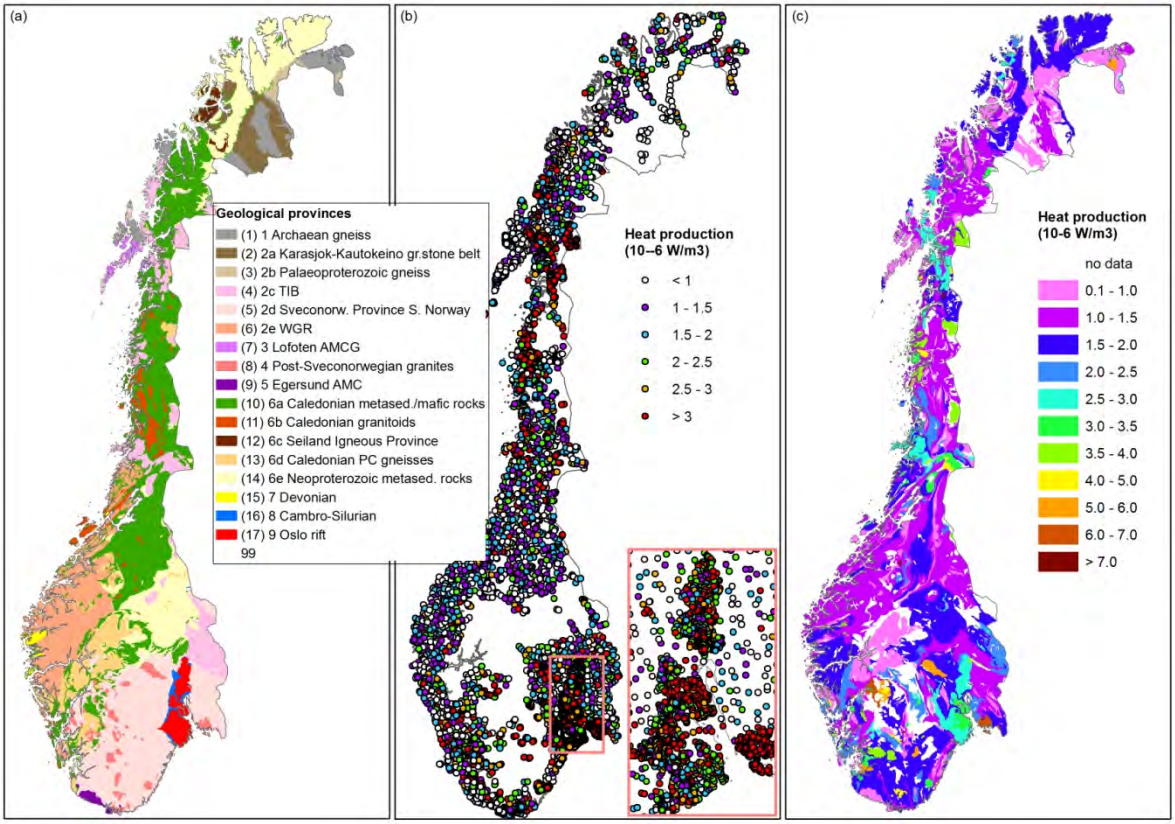

Figure 6.1 (a) Simplified geological map, modified after Sigmond (1996). (b) Heat-production data. (c) Average heat-production rates for geological units where data are available.

A number of factors, of which lithology, tectonic setting, tectonometamorphic history and age are the most obvious, may influence the heat production of a geological unit or province. The work presented here is part of a larger effort to enhance our understanding of the geological and thermal structure of the continental margin of Norway (and the Baltic Shield). This means that heat-production values must be assigned to geological units onshore that can be correlated offshore onto the continental margin using seismic or potential field data. With these objectives in mind, Slagstad (2008) presented and discussed the then available heat-production data with reference to specific geological provinces, subdivided based on lithology, tectonic setting, tectonometamorphic history and age. The subdivision includes nine major and several minor provinces, ranging in age from Archaean to Permian. Table

6.2 and Figure 6.1 present a summary of geological and heat-production information currently available. The table and figure are updated from that presented by Slagstad (2008), and include additional data acquired in this project. For a detailed discussion of the various geological provinces and the heat-production data, see Slagstad (2008). Figure 6.2 presents a more detailed view of the area covered in the Coop2 projects.

Figure 6.2. Heat production in the Coop2 project area.

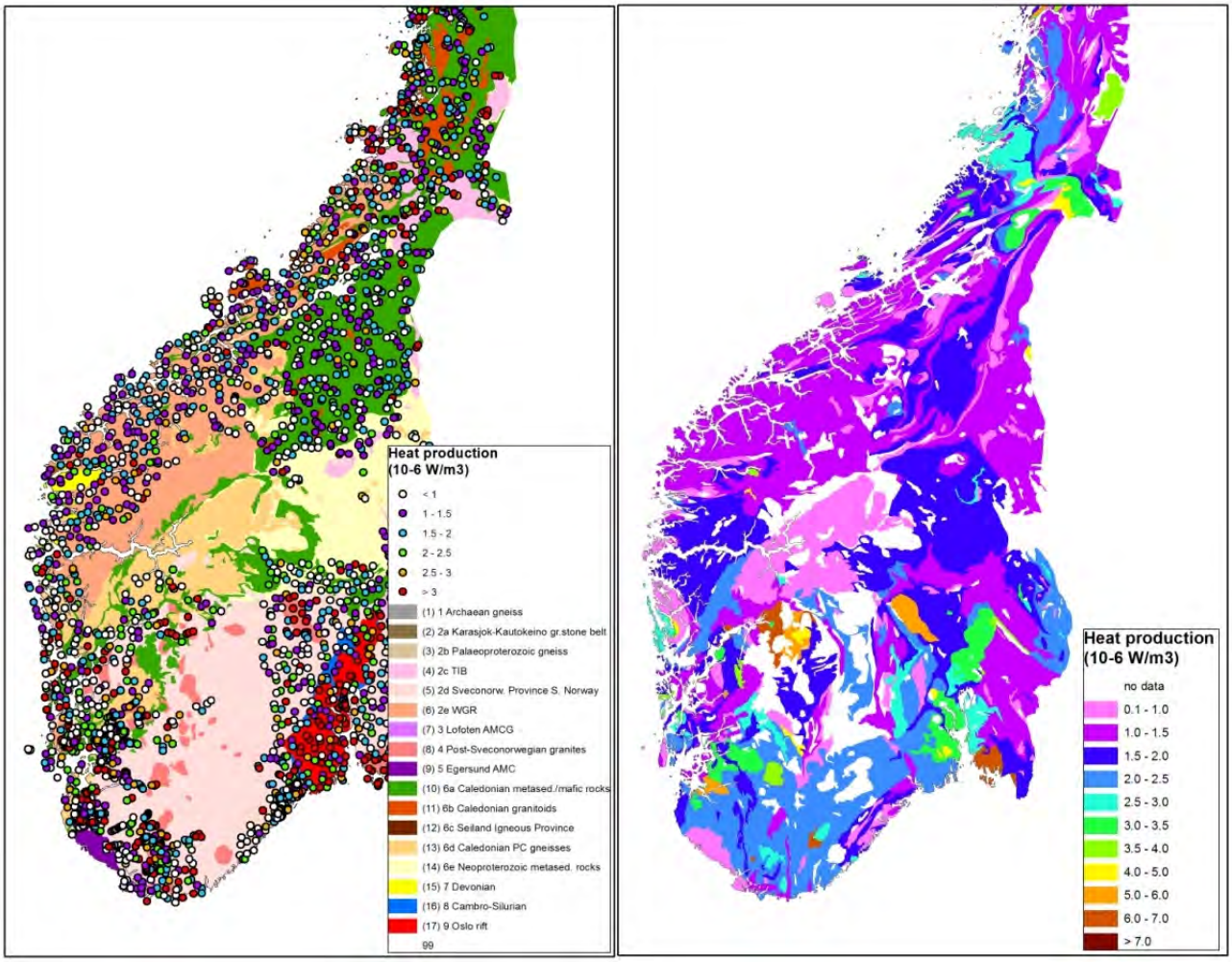

Table 6.2. Simplified geological history and heat-production rates of geological provinces in Norway. See text for details and references.

	Geological province	n	Age (Ma)	Lithology	Tectonic setting	Tectonometamorphic history	Heat production rate (μW m^{-3})	
							Area wtd. mean[1]	Median ±1σ
1	Archaean gneisses	176	3000–2500	Dominantly tonalitic to granitic gneisses		Palaeoproferozoic (c. 2.0–1.8 Ga) amphibolite- to granulite-facies metamorphism.	1.06	0.99 ± 1.44
2	Proterozoic gneissic rocks							
2a	Karasjok-Kautokeino greenstone belts, NE Norway	63	2100-2000	Tholeiitic metabasalts, amphibolites and interlayered metasedimentary rocks	Continental rifting and oceanic subduction	Metamorphosed under greenschist- to amphibolite-facies conditions during obduction onto the Karelian craton at c. 1.9 Ga.	0.58	0.41 ± 0.44
2b	Palaeoproterozoic gneisses	38	2000–1900	Garnet-quartz-feldspar paragneiss and hypersthene-plagioclase orthogneiss	Deposition in continental back-arc basin	High-grade metamorphism during continent-continent collision at c. 1900 Ma	0.89	1.27 ± 1.30
2c	Transscandinavian Igneous Belt (TIB)	686	1810–1770	Alkali-calcic to calc-alkaline quartz monzonites to granites	Active continental margin, back-arc extension	Deformation and metamorphism at c. 1.46–1.42 and 1.0 Ga in SW Sweden. Variable Caledonian effects in NW Norway at c. 420 Ma.	2.65	2.50 ± 2.01
2d	Sveconorwegian Province, S Norway	1138	1500–1000	Tholeiitic to calc-alkaline, intermediate to felsic, metavolcanic and plutonic suites	Active continental margin and continental back-arc.	Local crustal reworking at 1.26–1.16 Ga. Continent-continent collision and associated medium- to high-grade metamorphism at c. 1.0 Ga. Very low-grade Caledonian metamorphism at c. 400 Ma in western areas.	1.91	1.47 ± 1.60
2e	Western Gneiss Region, W Norway	444	1750–1000	Dominantly tonalitic to granitic gneisses	Active continental margin	Sveconorwegian and Caledonian high-grade metamorphism at c. 1000 and 400 Ma, respectively.	1.51	1.46 ± 1.34
3	Lofoten anorthosite-mangerite-charnockite-granite (AMCG) complex	137	1800–1790	Mangerite, smaller volumes of gabbro, anorthosite, charnockite and granite	Related to TIB 1 magmatism	Crystallised under low-P granulite-facies conditions. No significant later metamorphic events.	0.49	0.44 ± 0.48
4	Post-Sveconorwegian granites, S Norway	505	930–920	Dominantly granite, locally grading to diorite	Extensional, post-tectonic magmatism	Generally no significant metamorphic overprinting.	3.92	2.84 ± 2.78
5	Egersund anorthosite-mangerite-charnockite (AMC) complex	62	930	Massive anorthosite, lesser volumes of leuconorite, mangerite and charnockite	Extensional, post-tectonic magmatism	Very low-grade Caledonian metamorphism at c. 400 Ma.	0.72	0.64 ± 1.94

	Geological province	n	Age (Ma)	Lithology	Tectonic setting	Tectonometamorphic history	Heat production rate (μW m^{-3})	
							Area wtd. mean[1]	Median ±1σ
6	Caledonian thrust-sheets							
6a	Late Proterozoic to Palaeozoic metasedimentary and metamafic rocks	965	500–450	Metagreywacke, phyllite, mica schist, lesser volumes of marble and greenstone.	Passive margin sequences. Greenstones formed in oceanic arc / back-arc.	Low- to high-grade metamorphism during the Caledonian orogeny at c. 450–400 Ma.	1.46	1.36 ± 1.30
6b	Caledonian intrusive rocks	183	480–430	Dominantly calc-alkaline diorite, tonalite, granodiorite and granite. Minor trondhjemitic intrusions.	Active continental margin.	Variable overprinting during the Caledonian orogeny at c. 430–410 Ma.	1.83	1.72 ± 1.80
6c	Seiland igneous province	15	570–560	Gabbro, lesser volumes of ultramafic and alkaline rocks, and intermediate granitoid rocks.	Intracontinental rift.	Variable overprinting during the Caledonian orogeny at c. 420 Ma.	1.25	0.88 ± 0.95
6d	Precambrian gneissic rocks	113	1690–950	Syenitic to monzonitic gneisses, anorthosite-mangerite-charnockite-granite suites	Active continental margin. AMCG suite formed in intraplate setting (?)	Late Sveconorwegian, high-grade metamorphism at c. 930 Ma. Variable, but locally high-grade metamorphism at c. 450 Ma.	1.30	1.23 ± 1.94
6e	Neoproterozoic metasedimentary rocks	268	1000–500	Quartzitic to arkosic sandstone, mica schist, pelite and volumetrically subordinate carbonate	Continental shelf	Variable high- to low-grade Scandian and pre-Scandian metamorphism in Finnmark. Low-grade overprinting in Lillehammer during the Scandian phase at c. 430-400 Ma.	1.58	1.47 ± 0.90
7	Devonian sedimentary rocks	21	400–390	Fluvial sandstones, conglomerate, breccia	Post-orogenic extension	No metamorphic overprinting.	1.10	1.12 ± 0.47
8	Cambro–Silurian sedimentary rocks	39	540–420	Marine shales, carbonates, sandstones	Epicontinental basin, later foreland basin	Low-grade metamorphism and deformation during the Caledonian orogeny at c. 420 Ma; local contact metamorphism during formation of Oslo rift at c. 300–280 Ma.	1.90	1.66 ± 1.37
9	Oslo Rift	1052	300–280	Tholeiitic basalts, monzonite, syenite and granite	Intracontinental rift.	No metamorphic overprinting.	2.91	2.53 ± 1.66

[1]The area-weighted heat production of a geological province is calculated by first calculating the average heat production of all polygons on Sigmond's (1996) map from which heat-production data are available. The average value for each polygon is then multiplied by the area of the polygon and divided by the total area of all polygons belonging to a particular geological province, giving the area-weighted heat production.

6.5 Airborne gamma ray spectrometry

In addition to the laboratory measurements, we have applied the airborne gamma ray spectrometer measurements in order to calculate the heat production from the different rock units exposed at the surface. We have, in this case, also calculated heat generation rates (A in $\mu W/m^3$) using Rybach's formula (6.1) (Rybach 1988).

While gamma rays in the energy range used for the mapping of natural sources of radiation can penetrate several hundred metres of air, they are completely impeded by about 30-50 cm of rock or soil. This has several implications for the mapping of natural sources of radiation.

The airborne gamma ray spectrometry method is thus a surface mapping method, because most of the gamma rays emanating from the Earth's surface originate in the top 30 cm of the surface. This means that the interpretation of these data requires an understanding of surface processes such as weathering, and the relationship between surface materials and bedrock geology.

The flight altitude above ground level is an important operational variable, because gamma rays are attenuated by air, and corrections must be made for variations in flight altitude. As a general rule, spectrometric data obtained at an altitude greater than 250 m will be of little value. Thus, data from a flight altitude greater than 250 m have been masked out.

Finally, we corrected the heat generation map for the effect of the sedimentary cover and lakes. Lakes and the Quaternary sediments act as a blanket, absorbing gamma particles generated in the rocks that they overlie. In order to obtain a reliable heat generation map of the bedrock, we carefully checked the locations where the bedrock is exposed and filtered out the other areas where it is covered by sediments and lakes.

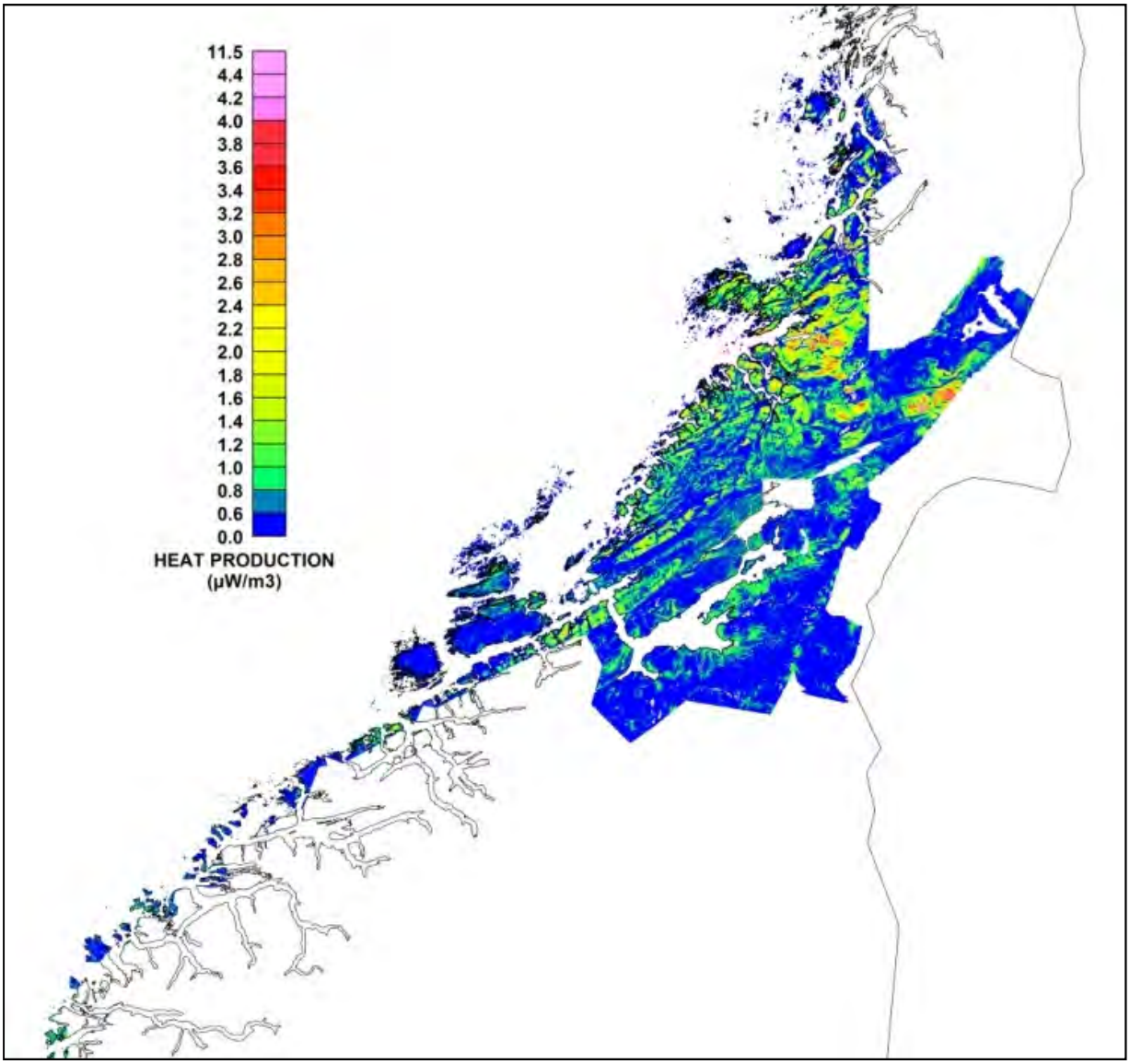

Figure 6.3 a). Heat-generation values calculated from airborne multi-channel gamma spectrometry surveys. Note that the results are not corrected for the attenuation effect of the lakes and the Quaternary sediments, and a flight altitude over 250 m.

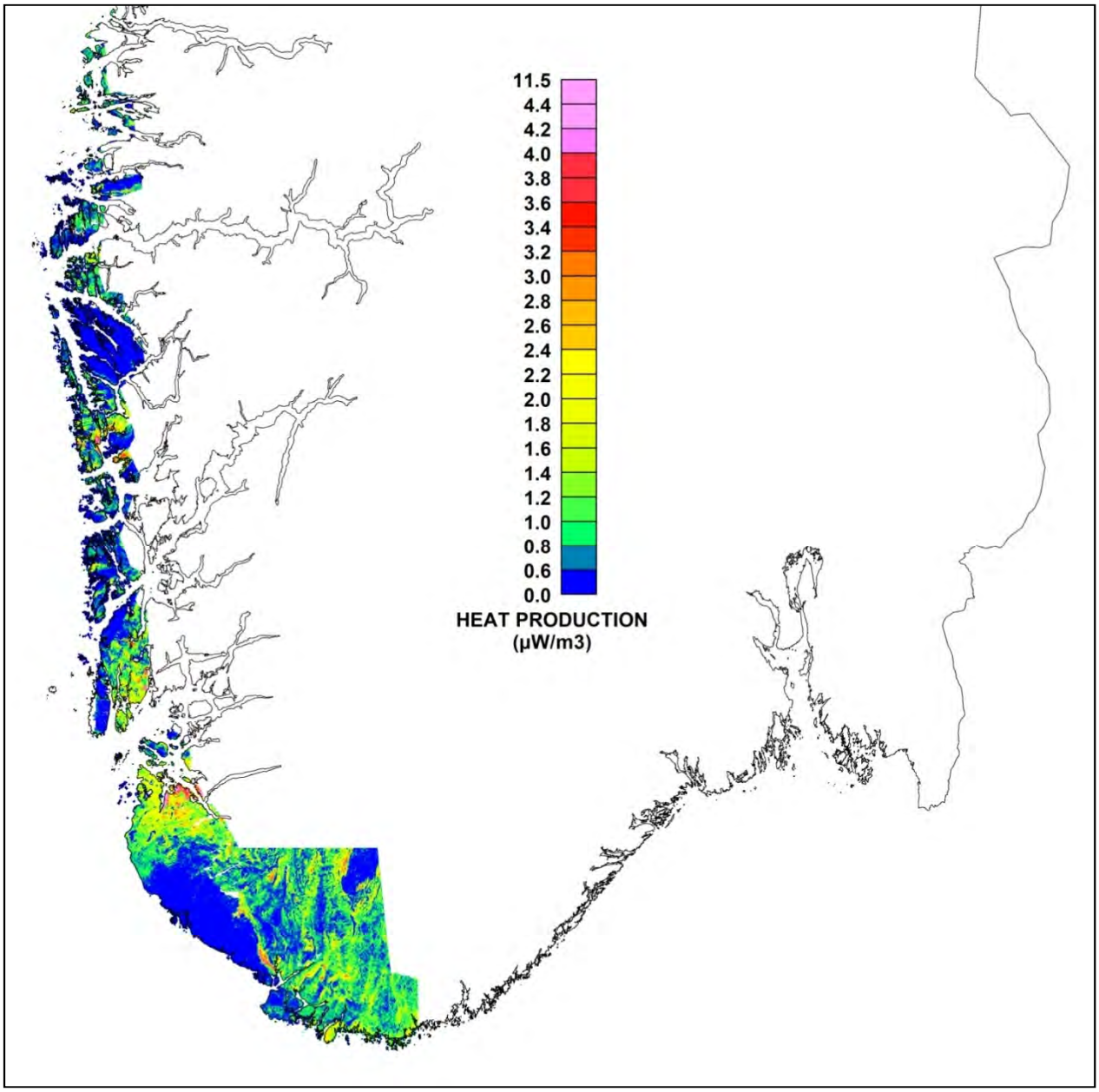

Figure 6.3 b). Heat-generation values calculated from airborne multi-channel gamma spectrometry surveys. Note that the results are not corrected for the attenuation effect of the lakes and the Quaternary sediments, and a flight altitude over 250 m.

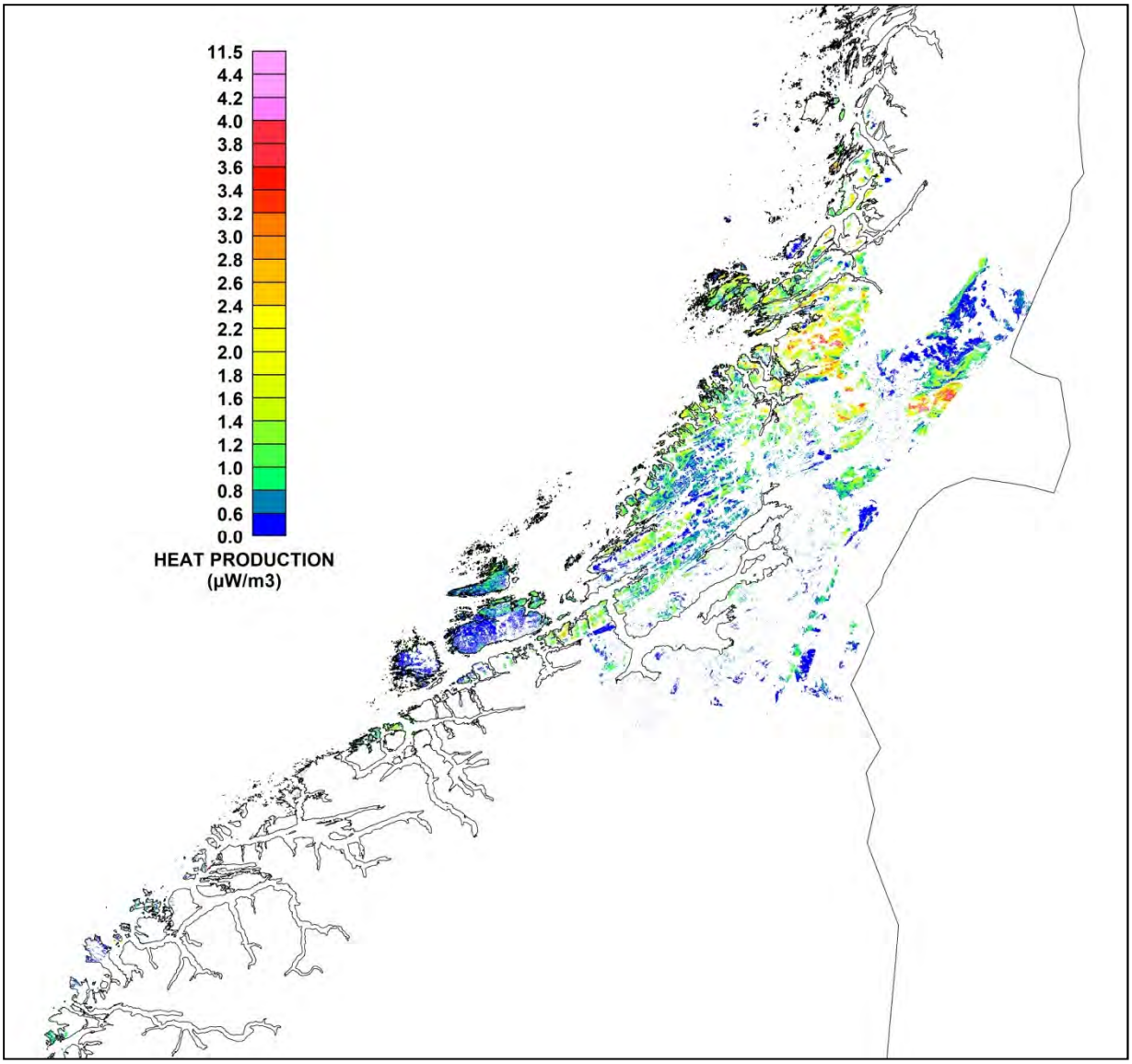

Figure 6.3 c). Heat-generation values calculated from airborne multi-channel gamma spectrometry surveys. The results are corrected for the attenuation effect of the lakes and the Quaternary sediments, and a flight altitude over 250 m.

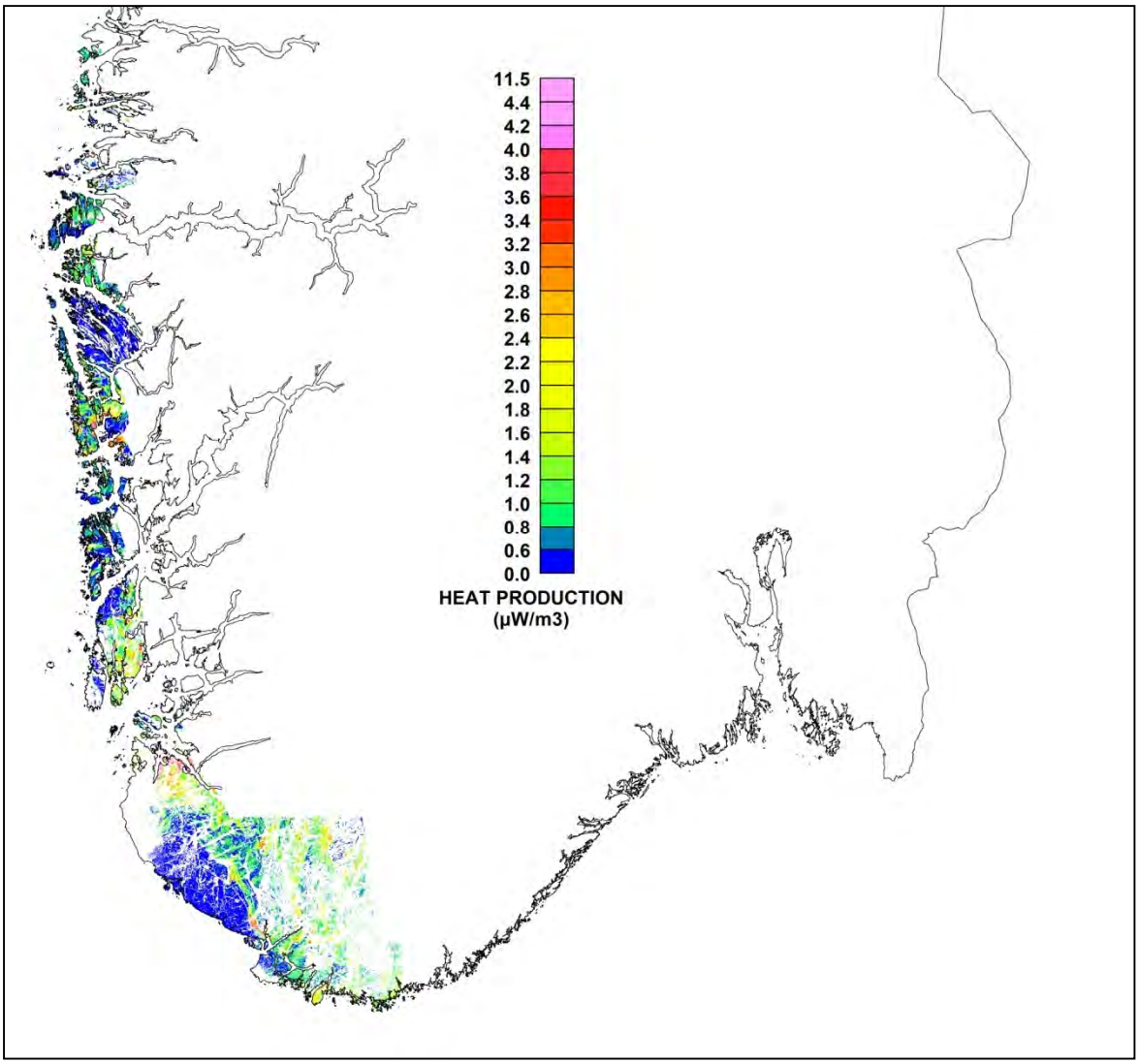

Figure 6.3 d). Heat-generation values calculated from airborne multi-channel gamma spectrometry surveys. The results are corrected for the attenuation effect of the lakes and the Quaternary sediments, and a flight altitude over 250 m.

The final corrected heat-production grid (Figures 6.3c,d) was then converted to a raster (in Arcmap). A raster is a digital image composed of rows and columns, where each element is assigned one value. The raster values were then converted to a point-shape file. We then joined these points to the detailed bedrock map polygons. Each polygon was given an average value of the points that fell within it. By this process we thus produced an average heat-production map.

Normally, the rock density (ρ) is assumed to be equal to 2700 kg/m^3 (Equation 6.1). Having produced an average density map (Chapter 5, Figure 5.4a), we then had the possibility of joining this map to the average heat-production map, and thus multiplying the average heat-generation values by a correction factor based on the real average density values within each bedrock unit. Where we had no petrophysical samples the correction factor was set to 1. The final average heat-generation map is shown in Figures 6.4a and b.

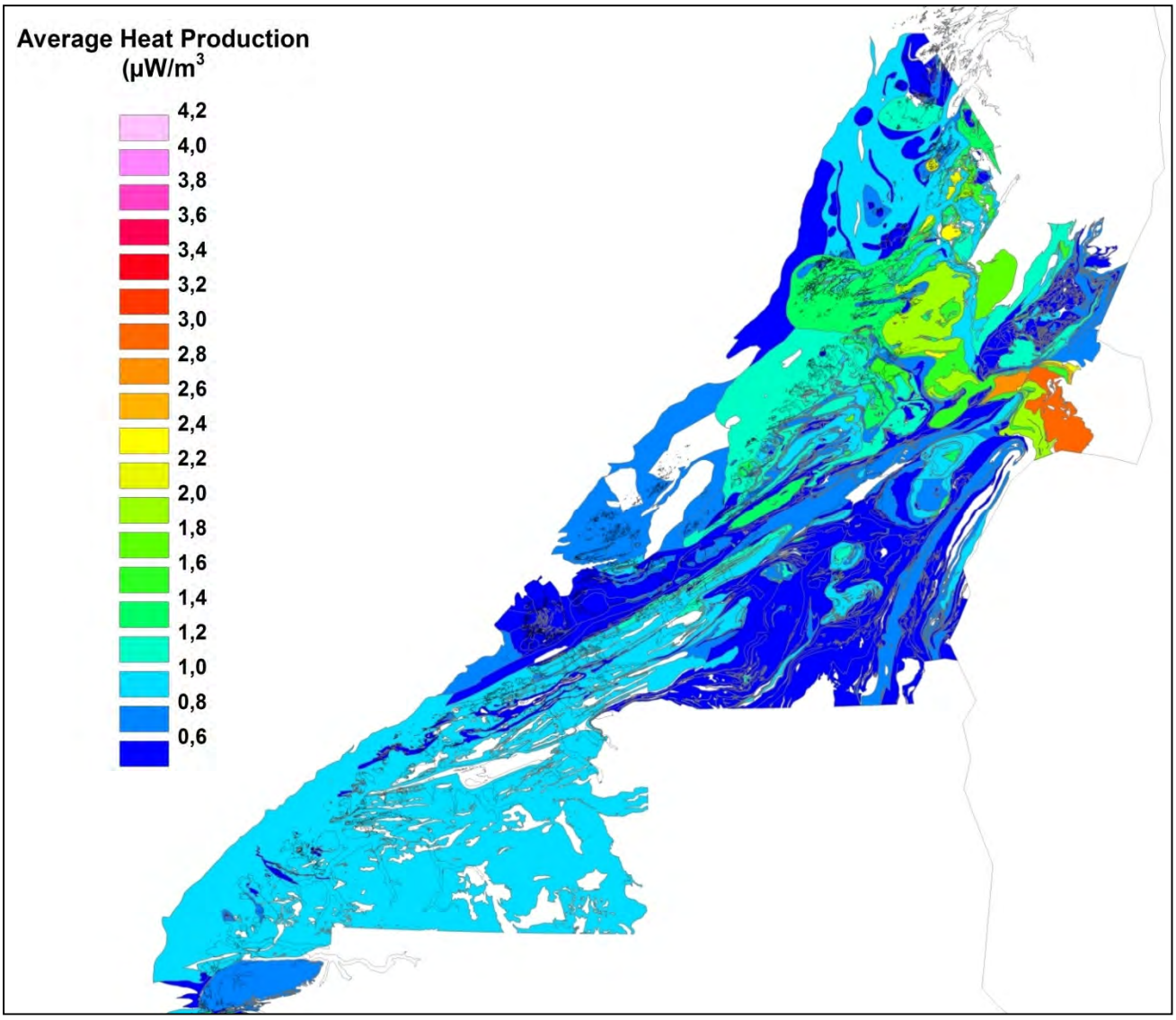

Figure 6.4 a). Average heat-generation map of the northern Coop region as derived from airborne gamma spectrometry surveys and corrected for the attenuation effect of sedimentary overburden and lakes, and masked for a flight altitude higher than 250 m.

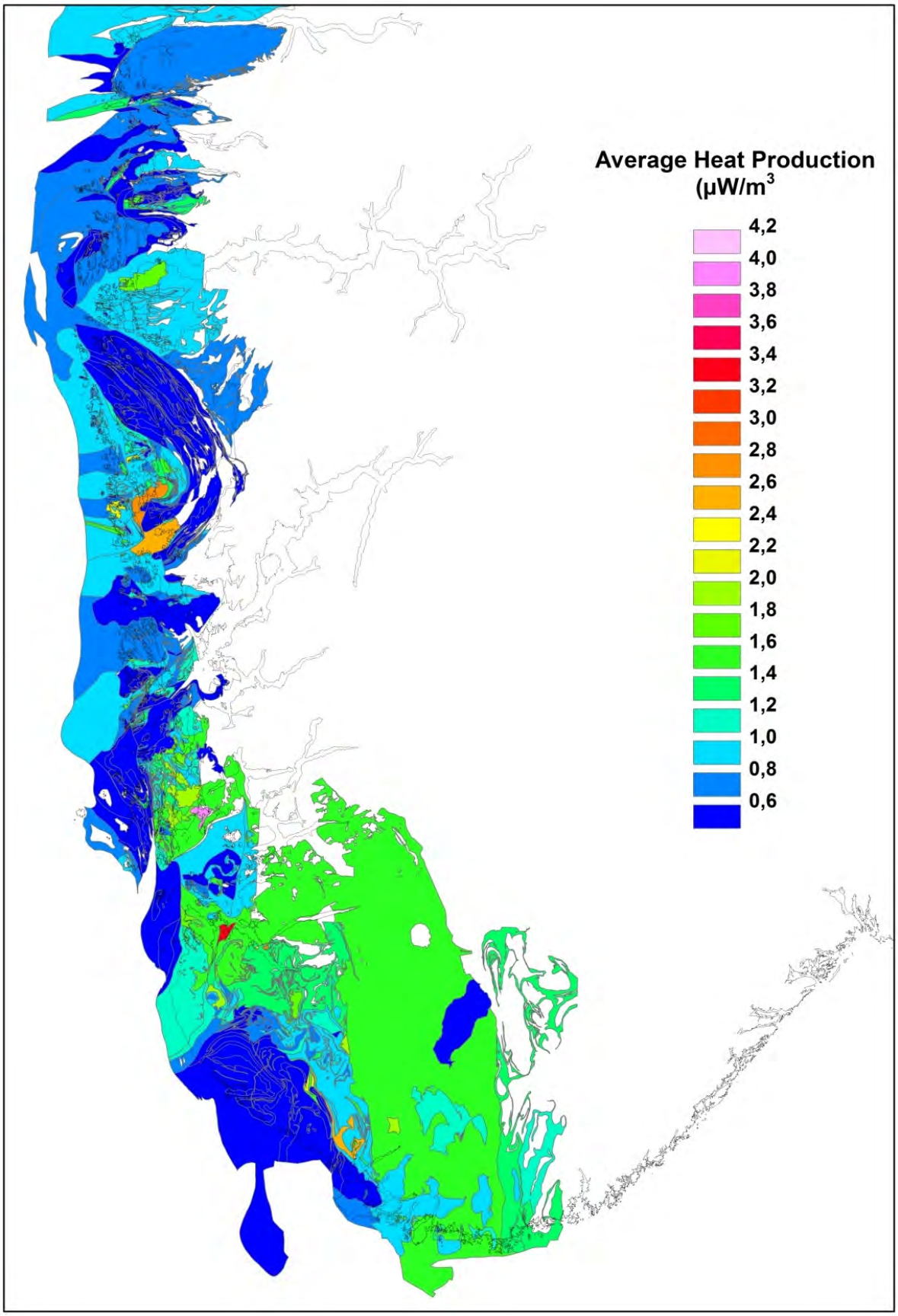

Figure 6.4 b). Average heat-generation map of the southern Coop region as derived from airborne gamma spectrometry surveys and corrected for the attenuation effect of sedimentary overburden and lakes, and masked for a flight altitude higher than 250 m.

The most evident areas of heat-producing bedrock are the Korsnes granite (2.4-2.6 μW/m^3) and the granitic gneisses from Fyllingsdalen to Sotra (2.6-2.8 μW/m^3), commonly referred to as the Løvstakken granite. We have recorded even higher values in the granites across Hervikfjorden (3.8-4.0 μW/m^3) and in the granodiorites around Riskafjorden (3.2-3.4 μW/m^3) east of Hillevåg. Also, the granitic gneisses around Flekkefjord stand out with 2.4-2.6 μW/m^3. The extensive porphyric granites/granodiorites of Vest-Agder display values of 1.4-1.6 μW/m^3.

In the northern part of the Coop project area (north of Snåsavatn) the most prominent areas are the granitic gneisses in the Olden Nappe (2.6-3.0 μW/m^3), and the augen gneisses/-migmatites/granites/rhyodacites in the Formofoss Nappe Complex (1.4-2.2 μW/m^3). The granites and augen gneisses within the Helgeland Nappe Complex stand out with (1.7-2.4 μW/m^3). In the northwestern gneiss region the granitic gneisses and augen gneisses have values of 1.8-2.0 μW/m^3.

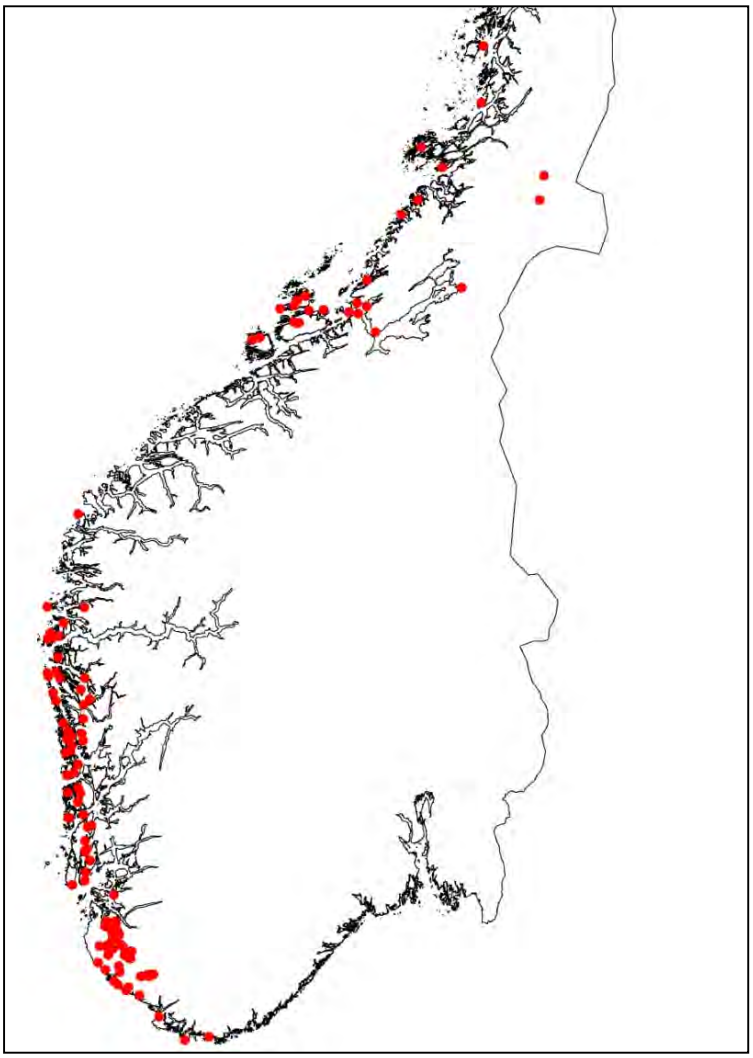

Beyond these areas the major part of the Coop project area is characterised by very low heat-production values (< 1.4 μW/m^3).

We have compared the heat-production values calculated from the chemical analyses of LITO-project samples with those calculated from the airborne gamma ray spectrometer surveying. This was done by merging the airborne heat-generation grid into the database of heat-generation from the chemical analyses (Oasis Montaj). This gives us a dual heat generation dataset for any mutual pair of coordinates (Figure 6.5).

A scatter diagram in Figure 6.6 shows the regression equation between the two datasets: Y = 0.4944 + 0.30677*X.

Figure 6.5. Chemically analysed LITO-project samples that have mutual coordinates with airborne gamma spectrometer measurements.

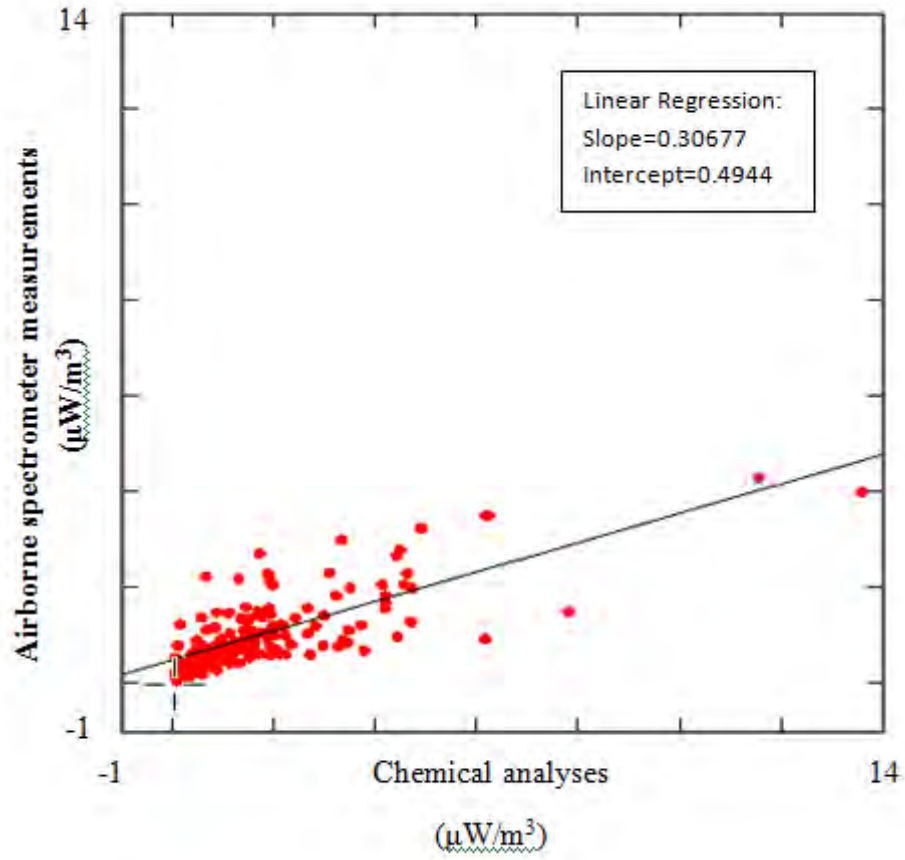

Figure 6.6. Scatter diagram: heat production from chemical analyses of mutual LITO-project samples vs heat production from airborne gamma ray spectrometer surveying.

We find a reasonably good agreement between heat-generation values calculated from the airborne gamma ray spectrometer surveying and those calculated from the chemical analyses (Figure 6.7). Because the aircraft moves forward during the accumulation time, the area of ground sampled is elongated. A rule of thumb indicates that 60-70% of the counts originate in a rectangle with a width of twice the flying altitude, and a length of twice the flying altitude plus the distance travelled during accumulation. For a typical fixed-wing survey, at an altitude of 60 m, a speed of 225 km/h and accumulation time 0.5 s, the area represented by each sample is about 120 m x 150 m. Thus, airborne surveys normally result in lower heat-generation values, because they average contributions from a variety of radioactive sources.

Another reason why airborne surveys may record lower heat generation values is the ground moisture. Waterlogged surfaces reduce the amount of radiation emanating from the ground. Areas of recent heavy rain should therefore be avoided during surveying.

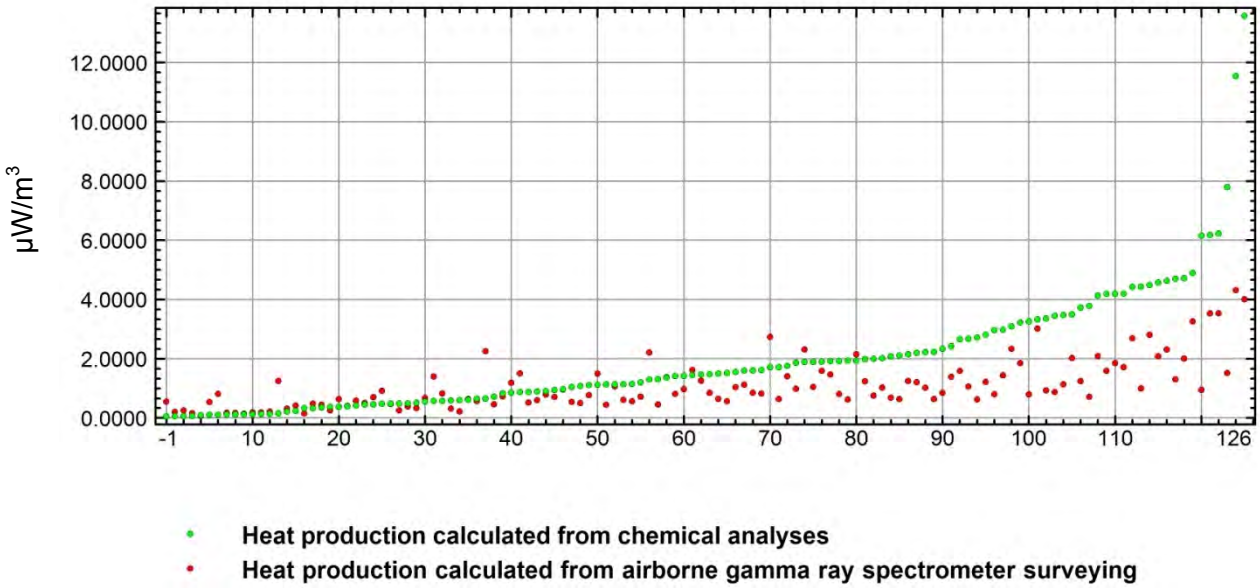

Figure 6.7. Comparison of heat-production calculated from chemical analyses and airborne gamma ray spectrometer surveying. The chemical values are presented in an ascending sequence.

Another way of showing the relationship between the two datasets is by illustrating their ratio (Figure 6.8).

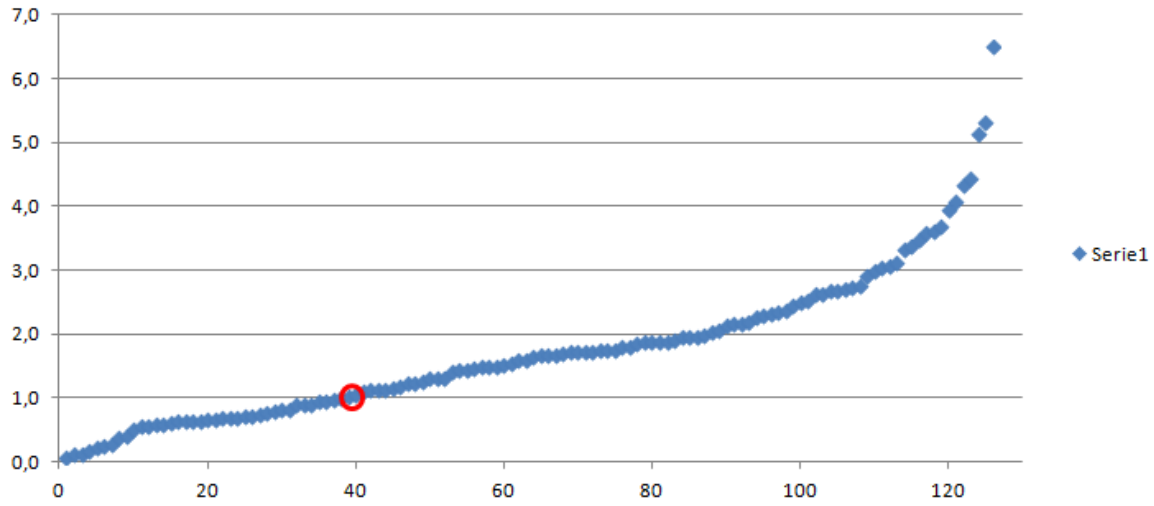

Figure 6.8. Calculated heat production ratio of chemical analyses to airborne surveying. A total of 85 samples are included in the analysis. The red circle represents a 1:1 ratio.

The ratio shows the relationship between the calculated heat productions from chemical analyses and those derived by congruent airborne gamma ray spectrometer surveying, using a total of 126 samples. The highest ratio of chemical analyses to airborne surveying is 6.5 to 1. Furthermore, this figure shows that c. 38 ratios, i.e. c. 30 %, are less than 1. This means that 30 % of the LITO-project samples have a heat generation calculated from chemical analyses that is smaller than the ones calculated from airborne measurements. This number may indicate that 30% of LITO-project samples were collected from rock types that are not

representative of the average or main bedrock type, i.e., from lenses of an uncommon bedrock or from dykes that have only minor contents of heat-producing radioactive elements. Another reason for this mismatch might be that some of the airborne values could have been influenced by Quarternary deposits with higher than average radio-activities.

As in the case of the airborne gamma ray spectrometry study, we used the concentrations of uranium, thorium and potassium derived from portable gamma spectrometry measurements in the Bergen area, and calculated heat-generation values according to Equation 6.1. Figure 6.9 shows the portable spectrometry measurements that have mutual coordinates with the airborne gamma spectrometer measurements.

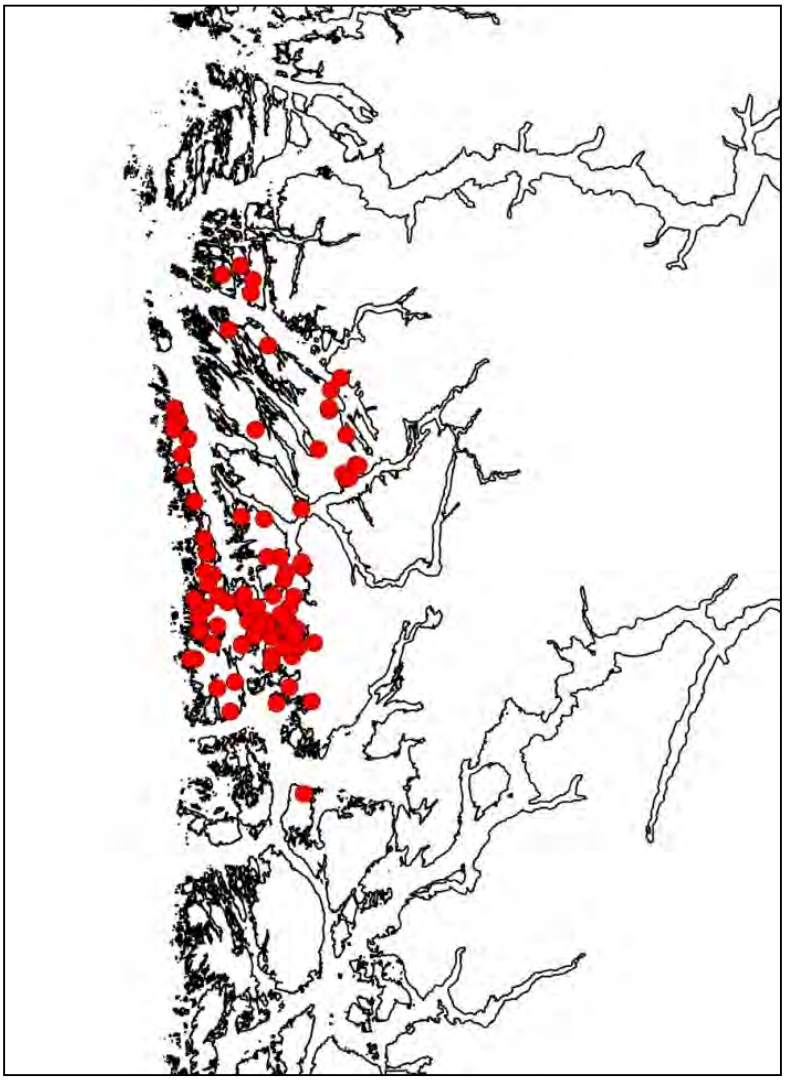

Figure 6.9. Portable spectrometer measurements that have mutual coordinates with the airborne gamma spectrometer measurements in the Bergen area.

A scatter diagram in figure 6.10 shows the regression equation between the two datasets:
Y = 0.71872 + 0.22676*X.

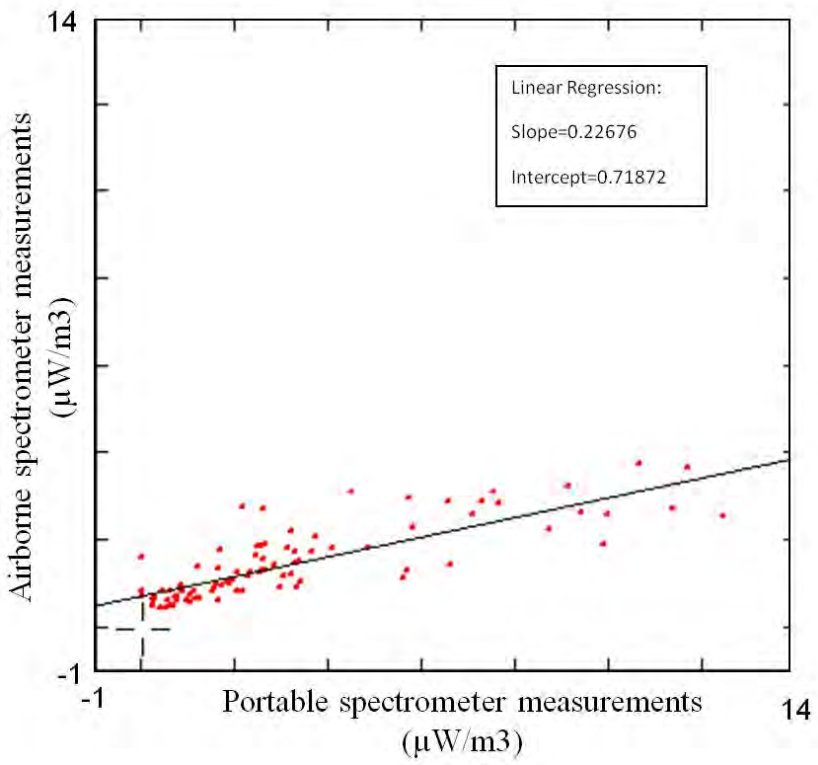

Figure 6.10. Scatter diagram: heat production from portable spectrometer ground measurements vs heat production from airborne gamma ray spectrometer surveying.

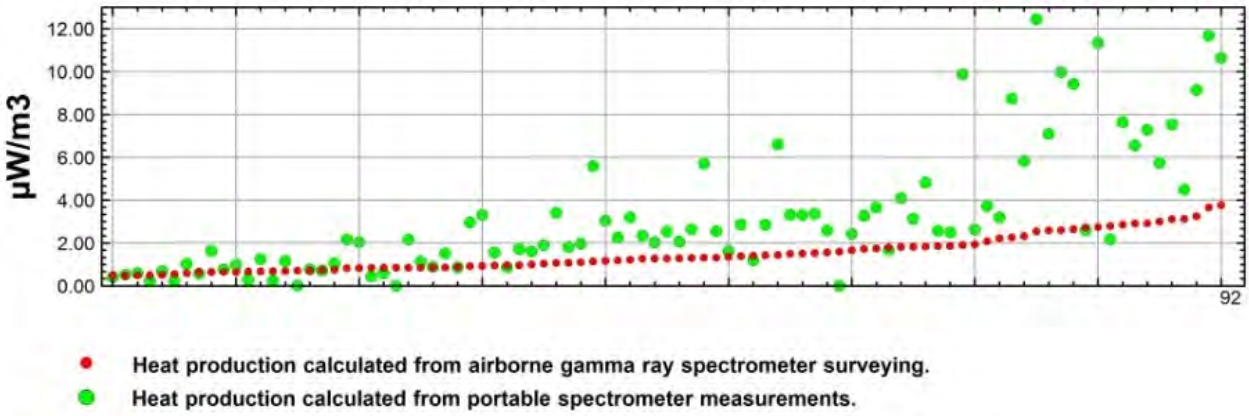

Figure 6.11. Comparison of heat production calculated from portable spectrometer measurements and airborne gamma ray spectrometer surveying. The heat production values calculated from the airborne measurements are presented in an ascending sequence.

As for the chemical measurements, we find a reasonably good agreement between heat-generation values calculated from airborne gamma spectrometer surveying and those calculated from portable spectrometer measurements (Figure 6.11). Nevertheless, the portable spectrometer values show a considerable spread as compared with the airborne values. This can be a consequence of the actual number of portable spectrometer readings; the more readings that are taken, the more accurate will be the calculated ground concentration.

However, with respect to ground surveys, airborne surveys result in lower heat generation, because they average the contributions from various radioactive sources. This is typical for bedrock units with high radioactivity but limited surface exposure.

Figure 6.12 shows the calculated heat production ratio of the portable spectrometry to the airborne surveying.

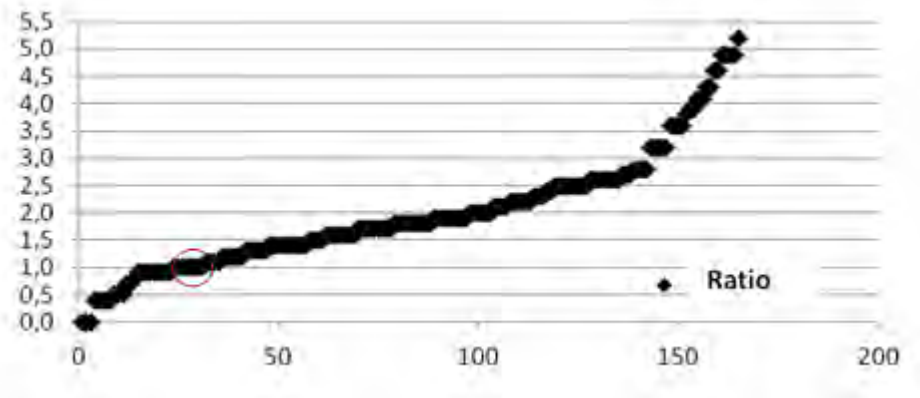

Figure 6.12. Calculated heat production ratio of the portable spectrometry to the airborne surveying. The red circle represents a 1:1 ratio.

7. DEEPLY WEATHERED BASEMENT ALONG THE NORWEGIAN COAST AND IMPLICATIONS FOR THE STRANDFLAT

Marco Brönner, Odleiv Olesen, Einar Dalsegg, Bjørn Eskil Larsen & Jan Steinar Rønning

7.1 Introduction

Scandinavia was exposed to several glaciations that eroded and removed almost entirely the overlying sedimentary successions. The preglacial landscape is consequently masked by glacial erosion but still reflects the impact of deep weathering. The numerous sounds and islands along the Norwegian coast could therefore to a large extent be conditioned by exhumation and erosion of weathered basement.

The Norwegian strandflat is also suggested to be an old landscape, formed during periods of intensive weathering and subsequently eroded due to changing sea-levels and ice and wave abrasion.

7.2 Bathymetry map and interpretation of the strandflat

The AMAGER method (AeroMAgnetic and GEomorphological Relations, Olesen et al. 2007a) was successfully applied onshore Norway to indicate weakness zones such as fractured basement and remains of deep weathering. The method is based on the not necessarily but for Norway common observation that deeply weathered basement shows a noticeably reduced magnetisation of the parent material (Figures 7.1 & 7.3) and is moreover easily erodible. Relative magnetic lows correlating with topographic depressions in eroded and exposed basement landscapes are therefore likely to indicate the location and distribution of deep weathering. The method requires high-quality aeromagnetic data and digital elevation grids to achieve reliable results. The grid cell size must be 100 x 100 m or preferentially 50 x 50 m. Furthermore, detailed geological maps and a profound knowledge of the geology are useful to delineate areas with Quaternary overburden.

The AMAGER study carried out within the frame of the Coop1 Project identified from the high-resolution magnetic compilation quite a few linear magnetic lows that did not correlate with lows in the existing topography data. It was noticeable that these features were mainly concentrated in areas with very little morphological variation along the coast where topography was low and the strandflat was particularly distinct. It is also likely that the accuracy of the digital elevation grid (DEM) for these areas was not sufficient. Furthermore, a large amount of quite recent and good quality bathymetry data with 50 m resolution became available during the time of this project, where the marine extension of the strandflat is resolved and the imprint of the basement surface can be recognised. We have previously discussed that the AMAGER method is limited to onshore areas, where the basement morphology is not concealed by overlying sediments. For large parts of the marine strandflat, however, the sedimentary cover is apparently very thin and the basement morphology is still reflected in the seafloor. Therefore, we compiled a high-resolution onshore-offshore DEM grid using the latest available bathymetry-topography data.

For onshore Norway, in 2013 the Norwegian Mapping Authority (Kartverket) published a new DEM with a higher accuracy and 10 m resolution. For the offshore part along the Norwegian

coast and the fjords we gained access to 50 m resolution bathymetry data from the Mareano project (www.mareano.no), FFI and reprocessed bathymetry data from Olex (www.olex.no). Shallow-water data near the shorelines were provided by the Norwegian Mapping Authority and have varying resolution and accuracy.

The data were compiled in a common database and quality-controlled. For the gridding of the data, a minimum curvature algorithm was applied with 50 x 50 m resolution.

Table 7.1. Overview of resolution and location of bathymetry and topography data used for the compilation.

	Resolution	Area
Mareano bathymetry data	50 m	Northern Norway
Olex bathymetry data	50 m	Central and southwestern Norway
FFI bathymetry data	50 m	Southwestern Norway
Shallow water data from Norwegian Mapping Authority	various	Coastal areas offshore Norway
Norway topography from Norwegian Mapping Authority	10 m	Onshore Norway

The resulting grid is the first onshore-offshore DEM grid at such high resolution, which was compiled for the area of southern and Mid Norway. In particular for the strandflat, this grid is an important achievement since for the first time the marine and mainland strandflat can be displayed and investigated together over such a large area.

The term 'strandflat' was introduced by Reusch already in 1894 and describes a landform along and off the Norwegian coast of noticeably flat terrain onshore and shallow water in between cliffs and islets offshore (Reusch 1894). The origin of the strandflat has been controversially discussed (e.g., Nansen 1922, Holtedahl 1929, Holtedahl 1959, Olesen et al. 2013a). Today, marine and glacial erosion during repeated glacial and interglacial periods are commonly proposed as the main mechanism which had formed this landscape (Klemsdal 1982, Holtedahl 1998, Sulebak 2007). Olesen et al. (2013a) argued that the present strandflat is actually an old weathering surface, which was exposed due to the Plio-Pleistocene uplift and the easy erosion of the deeply weathered bedrock. Thermal modelling for southwestern Norway indicates a Permo-Triassic exhumation along the coast and a close surface position of the basement since Mid Jurassic time before it was reburied during the Cretaceous (Ksienzyk et al. 2014). This could point to the Triassic to Early Jurassic period with significant weathering and saprolite production along the Norwegian coast, which would be in accordance with observations made in southern Sweden and Denmark (Fredin et al. 2014). Active tectonic faulting associated with rifting phases during this time (Brekke 2000) and the position of Baltica at lower latitude with warmer and partly humid climate (Torsvik & Cocks 2005) are beneficial conditions to promote high rates of weathering. The subsequent burial of the regolith in the Cretaceous shielded it from erosion during the Paleogene and the opening of the North Atlantic until the Plio-Pleistocene. During the ice ages the sedimentary strata and the major part of the saprolite along the coast were removed and the strandflat as an old weathering front was duly exposed as described above.

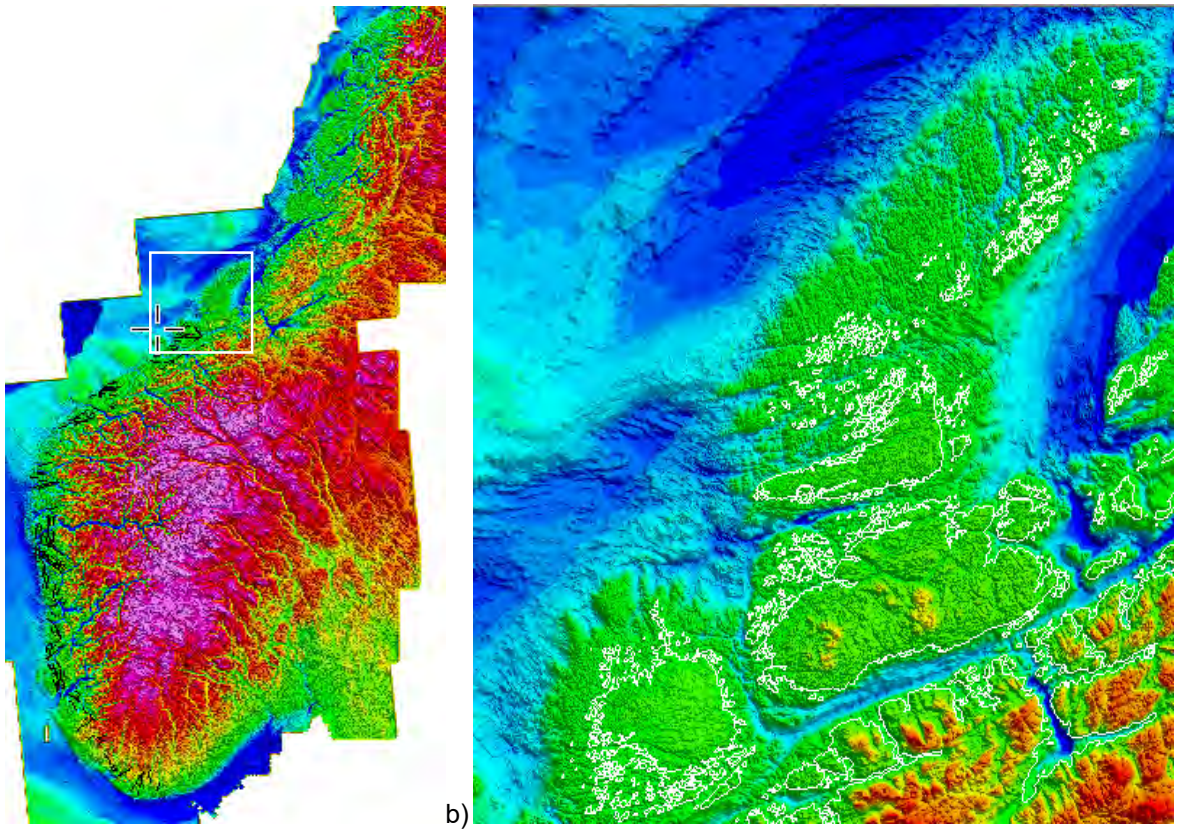

Figure 7.1. *a) New compilation of high-resolution bathymetry and topography for southern and central Norway. The new compilation reveals basement features offshore along the Norwegian coast. b) Example from Mid Norway, the islands of Smøla, Frøya and Hitra.*

Holtedahl (1998) defined characteristic features for the strandflat based on *"present quantitative material available, and modern knowledge of different aspects of Cenozoic geology"* and mapped it accordingly along the Norwegian coast.

The new DEM compilation, however, provides a more detailed picture of the bathymetry along the coast and reveals quite a few areas where basement structures can be observed on the seafloor which were not previously interpreted as part of the strandflat. These areas were consequently exposed to uplift and significant erosion which, to our understanding per definition, is considered as strandflat. Mapping of these areas reveals that the marine strandflat is significantly larger than has been proposed earlier (Figure 7.2).

The noticeable imprint of basement structures for the observed marine strandflat makes the AMAGER applicable to shallow-marine areas as well, and can provide additional structural information on the distribution of weakness zones and possible remains of deep weathering along the Norwegian coast.

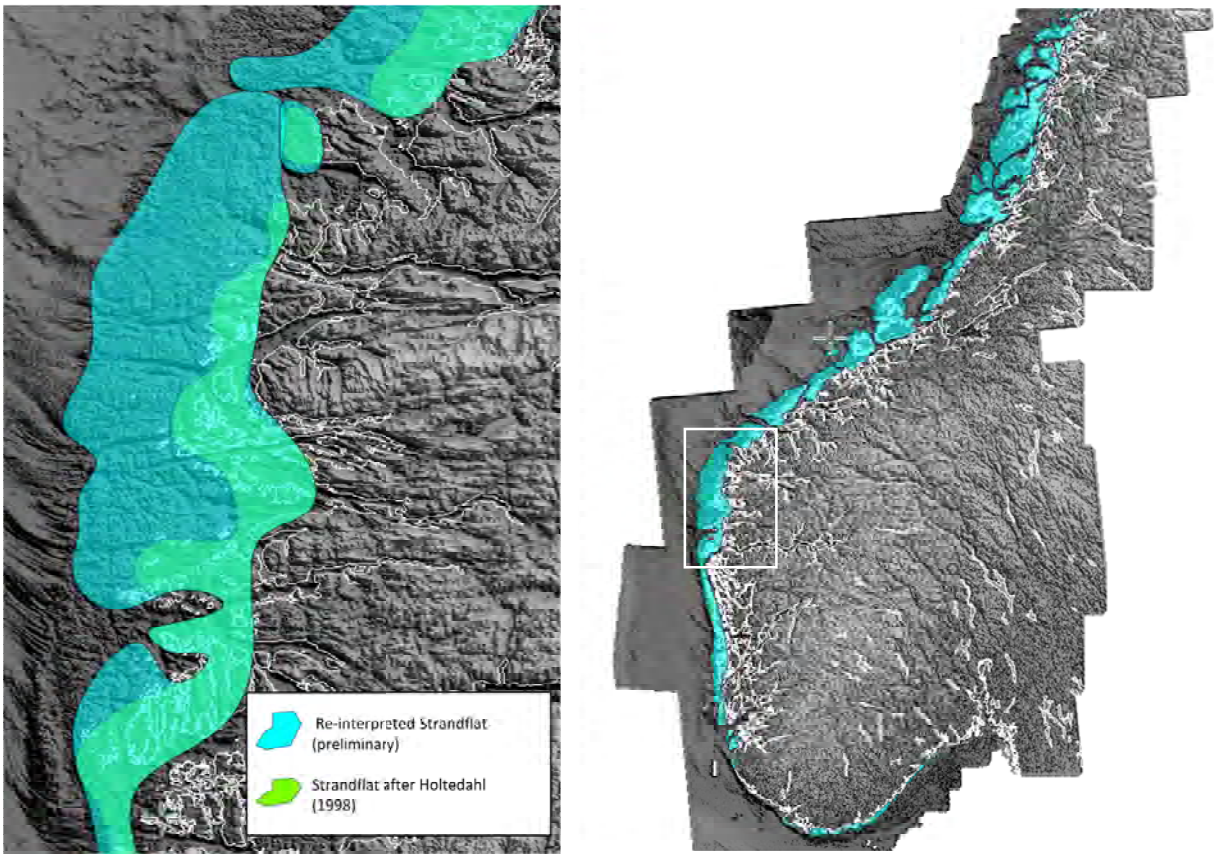

Figure 7.2. The new topography-bathymetry compilation reveals basement features along the Norwegian coast with high resolution. The strandflat was consequently reinterpreted and appears to be locally much wider than previously construed.

7.3 Mapping of deep weathering onshore Norway and its offshore extensions

The AMAGER technique was applied to 1 km high-pass filtered data of both the aeromagnetic and the topography-bathymetry grid (Figure 7.3). The large size of the area and the different basement structures, with partly significant changes in amplitude and orientation of the magnetisation, made it very difficult to find a common correlation function which could give reliable results.

The reliability was estimated from a comparison of the calculated solution and known deep-weathering sites (e.g., on Lista and Karmøy) and fine-tuned if necessary. Locations with deeply weathered bedrock and low-resistivity zones on geoelectric profiles (Appendix A) were also used as a quality control. The correlation functions, which are considered to be most reliable but do not produce too many solutions, were a correlation between a topographic depression of 5 m or more and a magnetic low of 5 nT or more, which could be observed over a distance of more than 1 km in areas with either normal or no magnetic remanence. Another correlation with possible deep weathering was used, which was most sensitive in areas with very little topography or low-magnetic bedrock. We correlated between a topographic depression of 2 m or more and a magnetic low of 2 nT or more. This correlation of course generated a much higher number of solutions, which we consider as *possible* locations for deep weathering or weakness zones. Model calculations by Olesen et al. (2007a) showed that similar low-magnetic zones in the outer Oslofjord area are not only related to terrain-effects but also to low-magnetic material extending to a depth of up to 300 m in the bedrock.

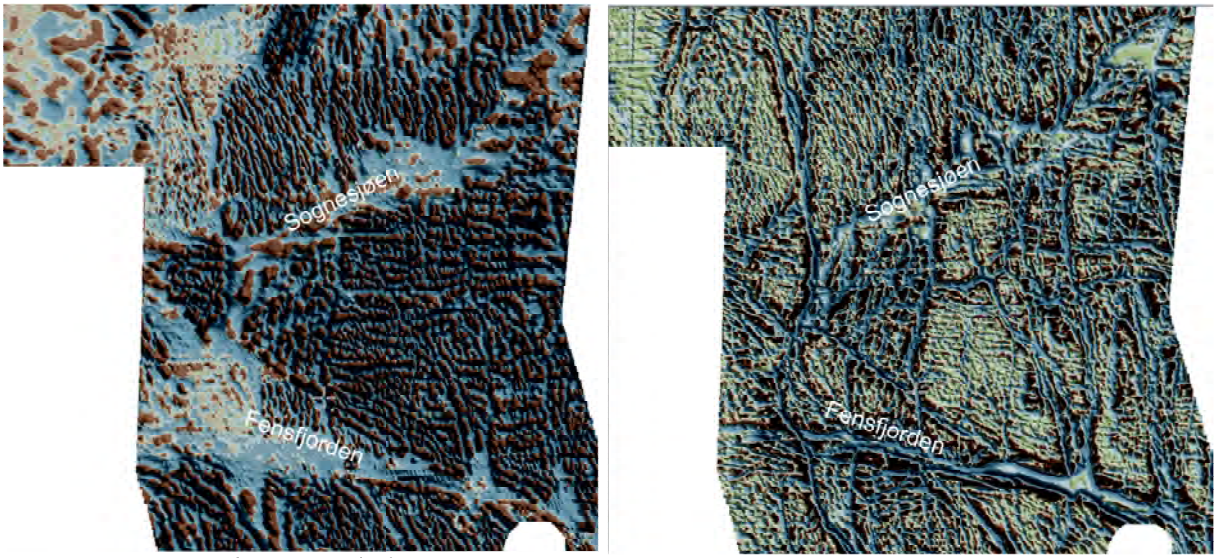

Figure 7.3. a) Example of high-pass filtered (1 km) magnetic data from the BESTAS-10 and CNAS-10 surveys (Nordhordland-outer Sognefjord area). b) High-pass filtered (1 km) topographic grid, clipped to the onshore area of the BESTAS-10 data. The cell size for both grids is 50 x 50 m. The AMAGER method (Olesen et al. 2007a) is partly based on a correlation between the two grids.

From the density of solutions, an obvious correlation with the basement magnetisation is observed. Low-magnetic gneiss regions show very sparse or no solutions, whilst high-magnetic norites and mangerites have a high density of solutions. However, to compensate – at least partly – for this effect we applied an Automatic Gain Control filter (AGC) to increase the number of low magnetic anomalies in gneiss regions.

7.4 Deep weathering and tectonics

Tectonics and the accompanying development of fractures and faults in bedrock have an important impact on the development of deep weathering and the rates of progress in weathering profiles. Weathering starts as a physical breakdown of the bedrock and subsequently there is a chemical alteration of minerals starts due to the circulation of acidic pore fluids which over time propagates downwards in the system of fractures and joints (Figure 7.4).

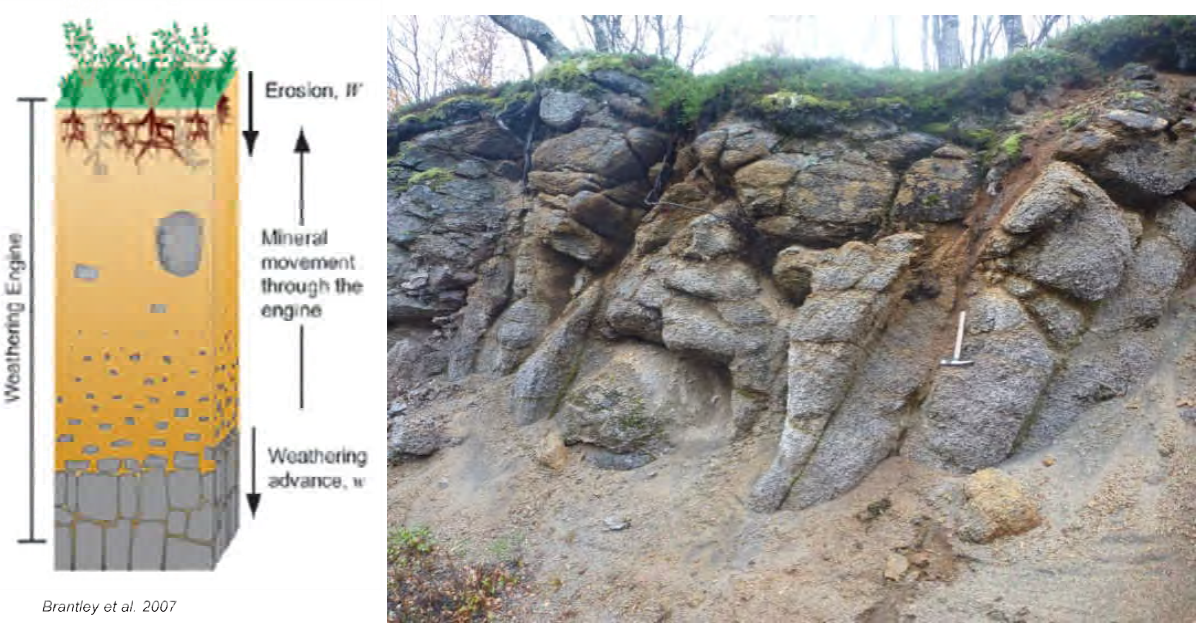

Figure 7.4. *a) Concept of a regolith profile (after Brantley et al. 2007). The development of weathering is fracture-controlled, where fluids penetrate into the bedrock and physically break down and chemically dissolve the bedrock structure. b) Example of a deeply weathered quartz-monzonite from the Eiavatnet area in Sørfold, northern Norway, where core-stones and saprolite have developed along and perpendicular to a fault system (UTM coord. 533380-7506253 zone 33, WGS84 datum).*

It is still not entirely understood what kinds of factors control the actual processes of weathering. However, it is commonly accepted that increasing the thickness of the regolith slows down the weathering processes (Gilbert 1877, Dietrich et al. 1995, Riebe et al. 2003). Consequently, an active tectonic system with vertical movements and high denudation rates is an important factor and facilitates the process of weathering.

The development of the Norwegian margin is directly related to the rift- and post-rift tectonics ascribed to the opening of the North Atlantic. Various rifting phases since the Devonian have controlled uplift and erosion. However, an example from western Norway shows a very good correlation of the fault pattern offshore with detected weakness zones and possible remains of deep weathering onshore and on the strandflat (Figure 7.5). The offshore faults were mapped from the base Cretaceous seismic interpretation and we can speculate whether the offshore faults are from Late Jurassic-Early Cretaceous times or an even older reactivated fault system inherited from the basement. However, the correlation confirms the close coupling between these two domains and shows how much the basement along the coast is affected and fractured. This physical disintegration increases the likelihood that weathering was taking place continuously with variable weathering rates and different impacts on the geomorphology due to erosion phases, where the regolith and the sedimentary strata were repeatedly and at least partly removed. Ksienzyk et al. (2014) discussed briefly the different landscape development models for Norway (Lidmar-Bergström et al. 2000, Nielsen et al. 2009, Johannessen 2012, Redfield & Osmundsen 2013) and suggested for southwestern Norway a very dynamic fault tectonic controlled evolution of the landscape. Based on our results, which are described later in this chapter, we agree with this suggestion and note its validity for all the coastal areas from southwestern to Mid Norway, where we see indications for repeated deep weathering and recognise a significant impact of this phenomenon during several phases of erosion and shaping of the landscape. There are differences though as to

how distinctive the development of the strandflat actually is, and we suggest that its progress is the visible expression of how much the geomorphology is controlled by active tectonics with phases of uplift, weathering and erosion.

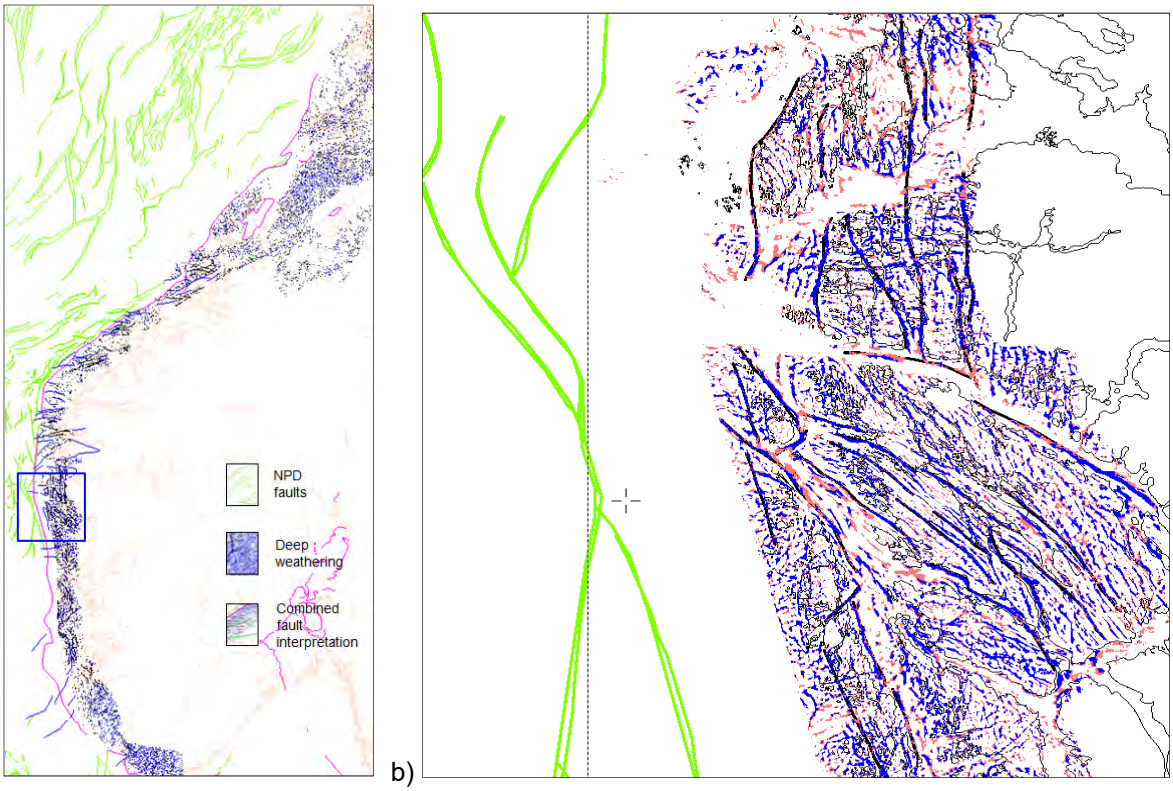

Figure 7.5. *a) Correlation between observed faults and detected weakness zones along the coast of western Norway using the AMAGER method with base Cretaceous faults offshore interpreted from seismic (source: NPD). b) Subset of the regional map from the Nordhordland - outer Sognefjord area depicted by the blue frame in a).*

7.5 Deep weathering interpretation

We applied the AMAGER method as described by Olesen et al. (2007a) and Brönner et al. (2013) in the Coop 1 report (Chapter 11.2) to the Coop 2 aeromagnetic compilation and the new high-resolution topography-bathymetry compilation. The results (Figure 7.6) show a multiplicity of solutions along the coast and for the Trondheimsfjorden-Selbu area in Mid Norway. However, as discussed above such a correlation for such a large area always contains a generalisation which might lead to over-interpretation or loss of details. To test some of the areas and the likely existence of deep weathering, NGU carried out a series of resistivity profiles (see also Coop1 Report, Brönner et al. 2013, Olesen et al. 2013b). This methodology has successfully been applied before (Brönner et al. 2012a, Olesen et al. 2012, 2013a,b) to map fractures, joints and weathered basement. The technique, briefly described in Appendix A, measures the electric resistivity in the subsurface where in general fresh bedrock shows high resistivity and sedimentary rocks and fractured or weathered bedrock have of lower resistivity. The methodology is applicable for imaging the subsurface down to a depth of c. 100 m. In the following we will present four of these areas and discuss the results.

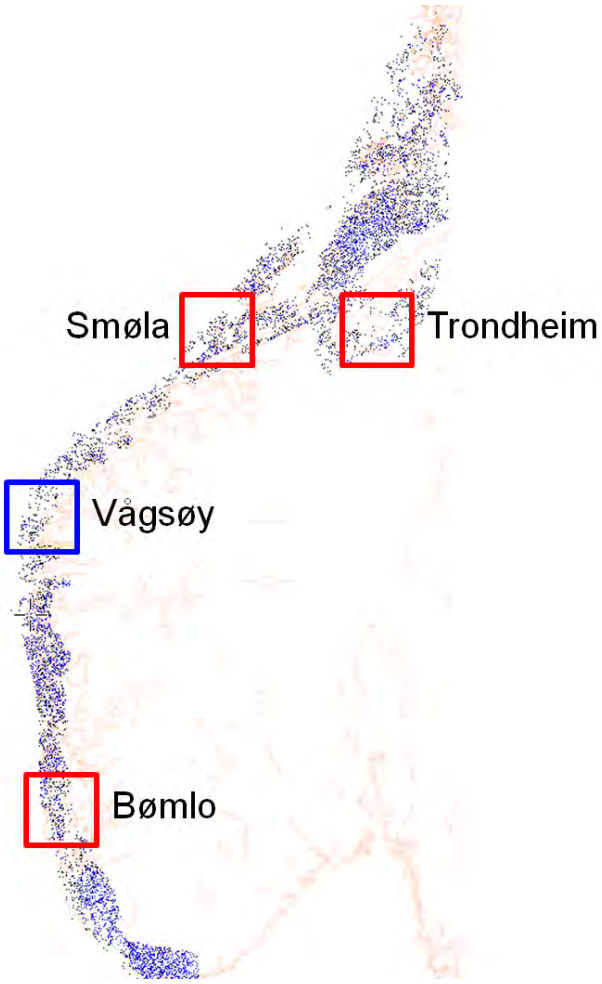

Figure 7.6. AMAGER solutions along southern and Mid Norway. Four areas at Smøla, Vågsøy, Bømlo and Trondheim will be discussed in more detail. The resistivity profiles from the Vågsøy area (depicted by the blue frame) were also reported in the TWIN Project (Olesen et al. 2012).

7.5.1 Smøla

The island of Smøla is situated in Mid Norway, southwest of Hitra and Frøya, and represents a part of the Mid Norwegian strandflat. The island's topography is fairly low-lying with an average altitude of c. 30 m and the highest point at 63 m above sea level. The outcropping basement shows mostly linear structures with ENE-WSW to E-W trends, but faults with a N-S orientation are also observed which are parallel with the orientation of bedrock features mapped in the eastern part of the island (Figure 7.7a). Due to the very small variation in topography, the results from the AMAGER technique were comparatively few and mainly considered as 'possible deep weathering' (Figure 7.7b).

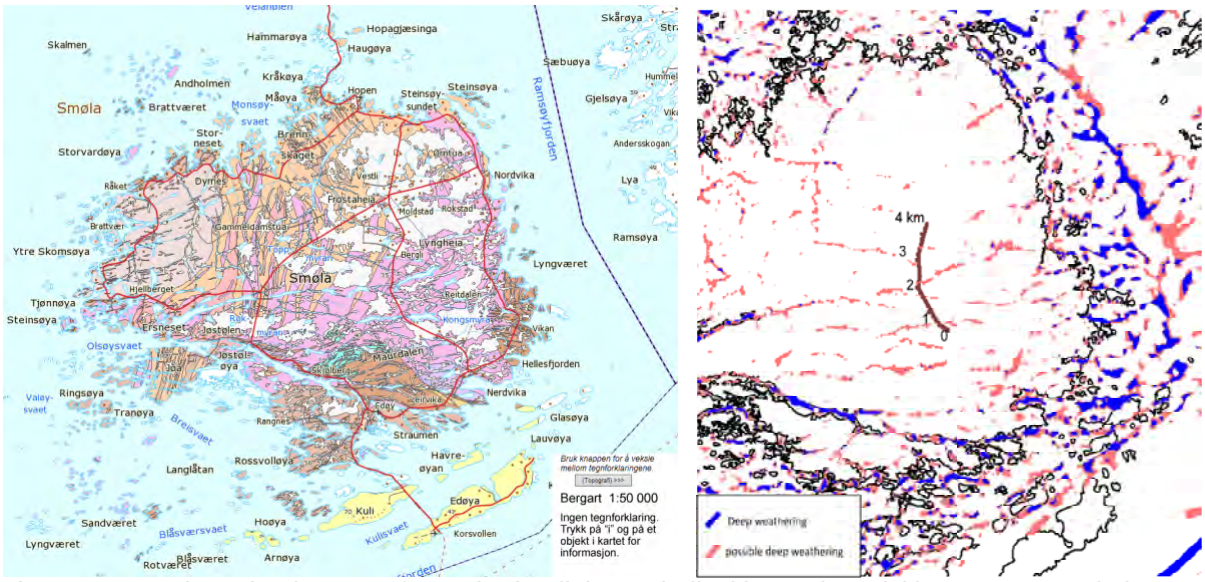

Figure 7.7. a) Bedrock map of Smøla (Fediuk & Siedlecki 1977) and b) AMAGER solutions. A resistivity profile was measured in the centre of the island.

However, a resistivity profile was placed approximately in the centre of the island and oriented almost N-S across some ENE-WSW-striking topographical depression lineaments. These topographic features could be detected in the magnetic data and consequently also gave solutions from the AMAGER study. The resistivity profiling (Figure 7.8) detected varying resistivity for the basement, which could indicate significant fracturing. The land surface is locally undulating with small basement depressions of tens of metres in depth, which is fairly characteristic for a weathering surface. The depressions show a low-resistivity infilling of possibly unconsolidated Quaternary sediments or deep weathering remnants, or both. Where the AMAGER study provided solutions, the profile indicates deep fracture zones. Especially the ones at the southern end of the profile (0.3 km) and in the central part (2.1 km) are dominant features. The fracture at 0.3 km can be correlated with a topographic lineament striking NW-SE and can be followed in the offshore part of the strandflat (Figure 7.9). The central fault is of even larger dimension and cross-cuts the island and also continues in the marine part of the strandflat. The fault at 2.9 km, however, is very weak in the AMAGER study, which is most likely due to its rather small expression in the topography. The topographic imprint of this fault is larger to the west of the profile and the lineament can be followed offshore, where it apparently merges with the NW-SE-striking fault observed at 0.3 km along the profile.

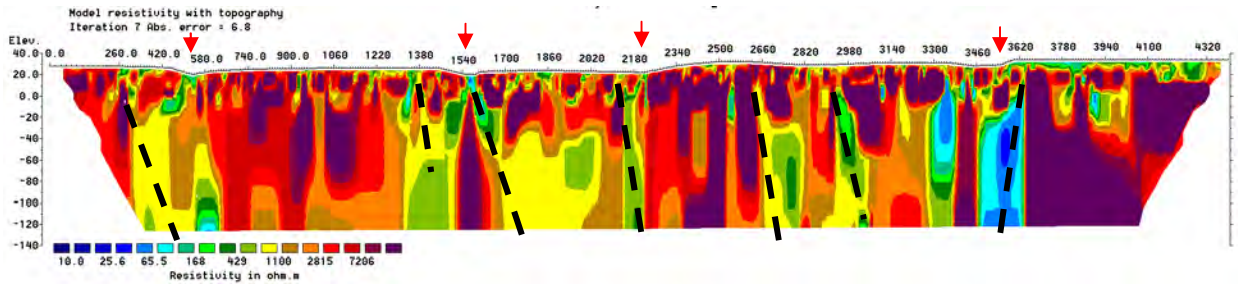

Figure 7.8. Resistivity profile in the centre of Smøla (vert. exaggeration 4x). The top basement surface is quite undulating and pits with a low-resistivity infill are noticeable. Different weakness zones are indicating possible fractured and/or weathered basement. Previous studies by Rønning et al. (2014) have shown that fracture zones with a lower resistivity than 500 Ωm are indicative of clay-bearing zones. The red arrows depict the AMAGER interpretations from Figure 7.7b.

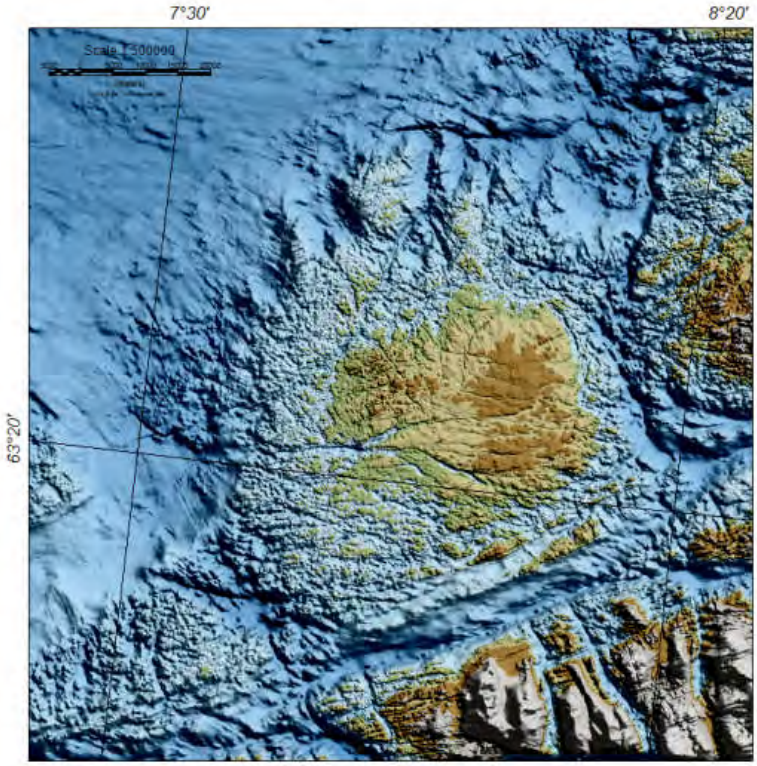

Figure 7.9. DEM map for Smøla shows the island's flat terrain and the surrounding strandflat with noticeable imprints of basement features. Quite a few structural elements extend into the offshore domain.

7.5.2 Vågsøy

The Vågsøy area is noticeably embossed by the erosion and flattening of the landscape due to glacial abrasion (Figure 7.10a and Larsen & Longva 1979). It was extensively described in the TWIN project (Olesen et al. 2012) since a deeply weathered gabbro on Vågsøy and weathered granitic gneiss at Stad had already been studied by Larsen & Longva (1979) and Roaldset et al. (1982). Two resistivity profiles on Vågsøy were acquired within the frame of the TWIN project (Brönner et al. 2012a, Olesen et al. 2012), indicating several weakness zones (Figures 7.11 & 7.12). The pronounced weakness zone in Profile 1 is interpreted as the continuation of the weathered gabbro. Profile 2, however, shows fracture zones with varying dips but they are not particularly prominent. The weathered gabbro does not seem to occur on this profile. This is also confirmed by the AMAGER solution (Figure 7.10b), where we obtain a pronounced solution on Profile 1, whilst for Profile 2 there are no solutions at all. The solution for Profile 1 however, does not coincide with the position of the weakness zone from the resistivity profiling.

a) 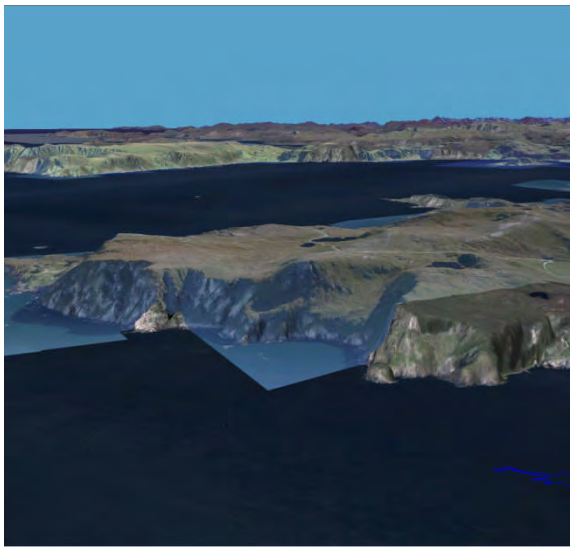 b) 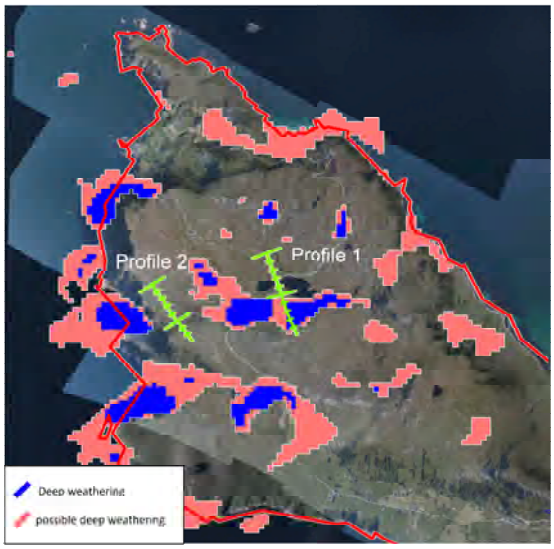

Figure 7.10. a)Perspective view of the landscape of the Vågsøy area looking to the SE (from Norgei3D.no). The area is a noticeably flat terrain separated from the marine strandflat by a steep coastal relief. b) The AMAGER technique applied to Vågsøy indicates weakness zones mostly trending E-W. A prominent solution occurs on resistivity Profile 1 which can be interpreted as the outcropping weathered gabbro. No AMAGER solutions were detected along Profile 2.

Different from the strandflat in Mid and West Norway, the coastal area at Vågsøy protrudes c. 60-100 m above sea-level with a possible paleosurface on top and a steep cliff-like coastal relief. This area can represent a transition phase from the Mesozoic paleo-surface to a Quaternary strandflat. Holtendahl (1959) described the strandflat in this area as more or less total absent but from the DEM grid we can identify basement features up to c. 17 km offshore Vågsøy.

The basement features seen up to c. 10 km off the coast of Vågsøy are mostly N-S oriented and parallel to the platform edge (Figure 7.13a). The bathymetrical depressions are obviously tectonically related to extensional faults associated with the opening of the North Atlantic. E-W lineaments are also observed and can be correlated with the AMAGER solutions onshore Vågsøy and possibly with the observed weathered gabbro. Farther offshore the pattern in the basement becomes more irregular. Approximately N-S-striking lineaments cross-cut E-W striking lineaments, which might indicate a more complex and varying stress pattern for the outer platform, possibly related to the Møre-Trøndelag Fault Complex which might to some extent control the NE-SW striking shearing at that level. The isostatic, relaxation-related, late Scandian collapse of the Caledonian mountains resulted in gently W-dipping detachments and must be mentioned here as well as they indicate an even older fault system. Furthermore, the ice movement is considered to have been predominantly towards the west (Figure 7.13b), which consequently is likely to have generated plough marks and abrasion features in this direction (Sejrup et al. 1996, 2003).

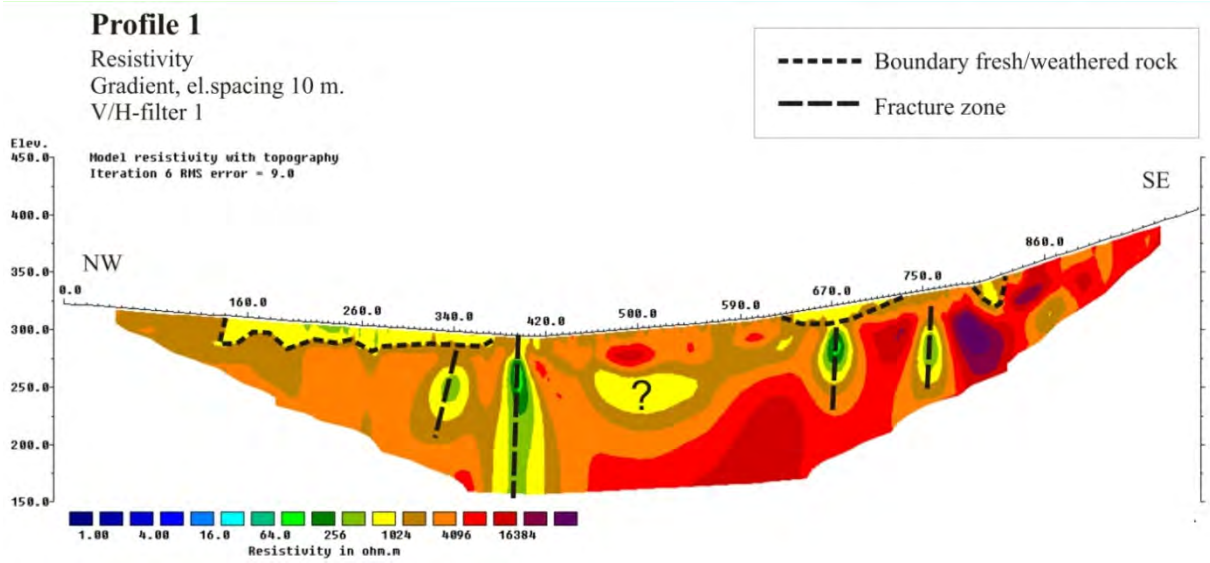

Figure 7.11. Resistivity Profile 1 on Vågsøy showing a pronounced low-resistivity zone at c. 410 m along the profile. This zone may represent the prolongation of the weathered gabbro, observed at the surface nearby. Other less developed weakness zones are observed under the 10-25 m thick overburden.

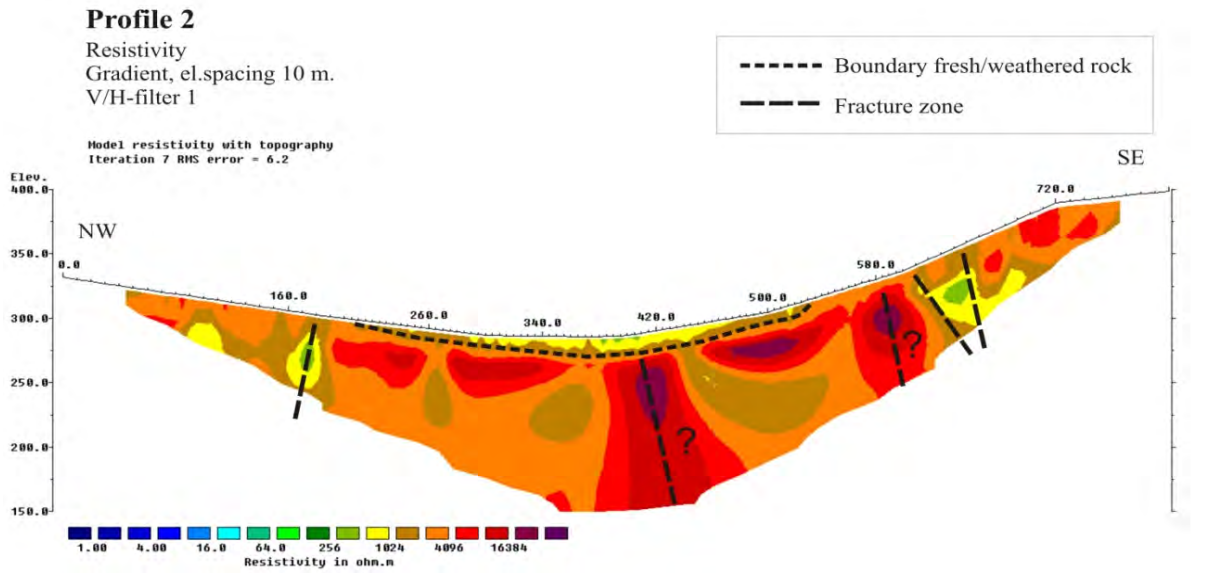

Figure 7.12. Resistivity Profile 2 on Vågsøy shows different zones indicating fractures and faults. However, these zones appear less developed and their origin remains unclear. The low resistivity at c. 400 m along the profile may indicate groundwater draining down a fracture zone along the steep western cliff of Vågsøy.

The noticeably flat surface of Vågsøy could indicate an old paleosurface. The strandflat off the coast is rather narrow compared to the adjacent Mid Norway area and the coast is steep. Assuming that the present topography/bathymetry represents the same weathering front, developed during different phases of weathering possibly since the Palaeozoic, the present strandflat area must have been significantly easier to modify and regolith production was consequently higher. From the Måløy Terrace farther off the coast, fractured and weathered basement is indicated in two exploration wells (NPD web-pages, well reports 35/9-2, 36/1-2). Episodes of uplift are reported from western Norway since the Devonian (Ksienzyk et al. 2014) and in Mid Norway in Early Paleozoic and Triassic-Jurassic times (Grønlie et al. 1994). Extension induced polyphase normal faulting and basin development occurred before and during break-up. Rapid basin development and subsequent sedimentation would have

reduced erosion and preserved possible weathering remains, which fits very well with shows of deep weathering in exploration wells from the Måløy Terrace.

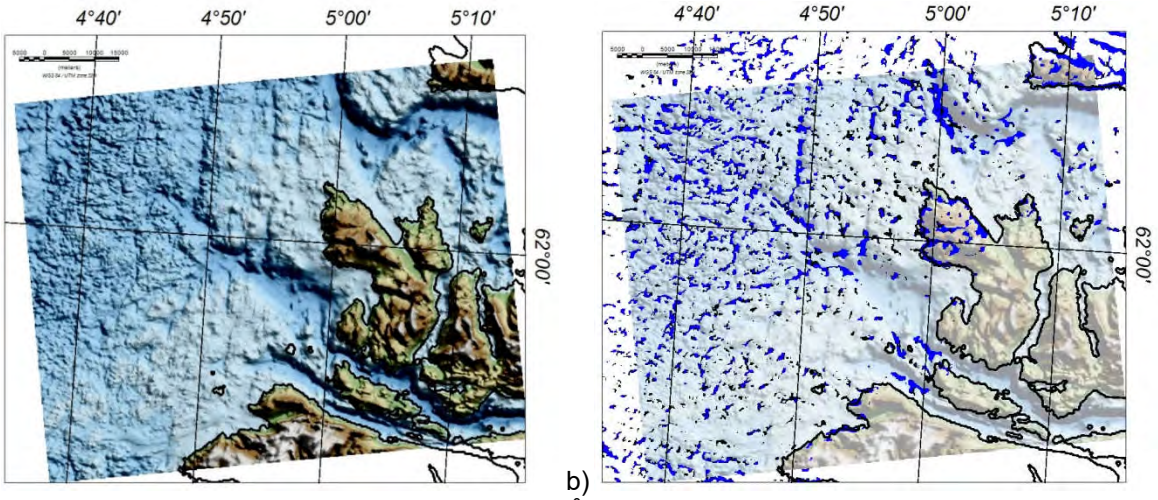

a) b)

Figure 7.13. a) Bathymetry-topography map for Vågsøy and the strandflat area and b) with AMAGER solutions. Weakness zones are predominantly N-S oriented out to c. 10 km on the strandflat. Farther offshore the pattern becomes more complex with cross-cutting lineaments trending E-W.

7.5.3 Bømlo

The Bømlo area represents a rather narrow part of the Norwegian strandflat (Figure 7.14a). The basement geology is complex and is characterised by different lithologies within the Upper Allochthon. Slagstad et al. (2011) describes a correlation between the age, petrology and tectonisation of the granites of Sunnhordaland and the granites drilled at the Utsira High offshore, which indicate that Bømlo is a good analogue for the Utsira basement high where hydrocarbons have been observed in weathered basement rocks.

The weathering products observed on Bømlo are of the grussy clay-poor type and thus similar to what is observed at the other locations in western Norway. However, one location is worth mentioning since it shows a detailed teeth-like structure (Figure 7.15), which was described by Lidmar-Bergström et al. (1999) in a regional scale model. Although this site is of much smaller scale and the weathering products have apparently been completely removed and replaced by soil, it remains a good example of how weathering evolves in fractures and joints and how physical and chemical weathering widens the weakness zones as the weathering propagates downwards.

The AMAGER technique was applied to the area which had been covered by the new high-resolution aeromagentic data, but which unfortunately did not cover the entire strandflat for the Bømlo area. The CNAS-10 aeromagentic survey to the west was flown with a larger line spacing of 1000 m and does not have sufficient resolution. The observed weakness zones from AMAGER are mainly NNW-SSE oriented (Figure 7.16b) and thus sub-parallel to the shelf, likely related to offshore extension and the opening of the North Atlantic. This is also confirmed by the resistivity profile (Figure 7.17b), which shows significant and almost vertical weakness zones at 0.7 km and 1 km. The bedrock contacts show a NE-SW trend, which can also be observed in southern Bømlo but does not continue farther east on Stord (Figure 7.16a). The contacts between different basement rocks are most likely but not necessarily weakness zones and could favour weathering or fracturing. The example from Bømlo again underlines the importance of the tectonic factor for the development of weathering.

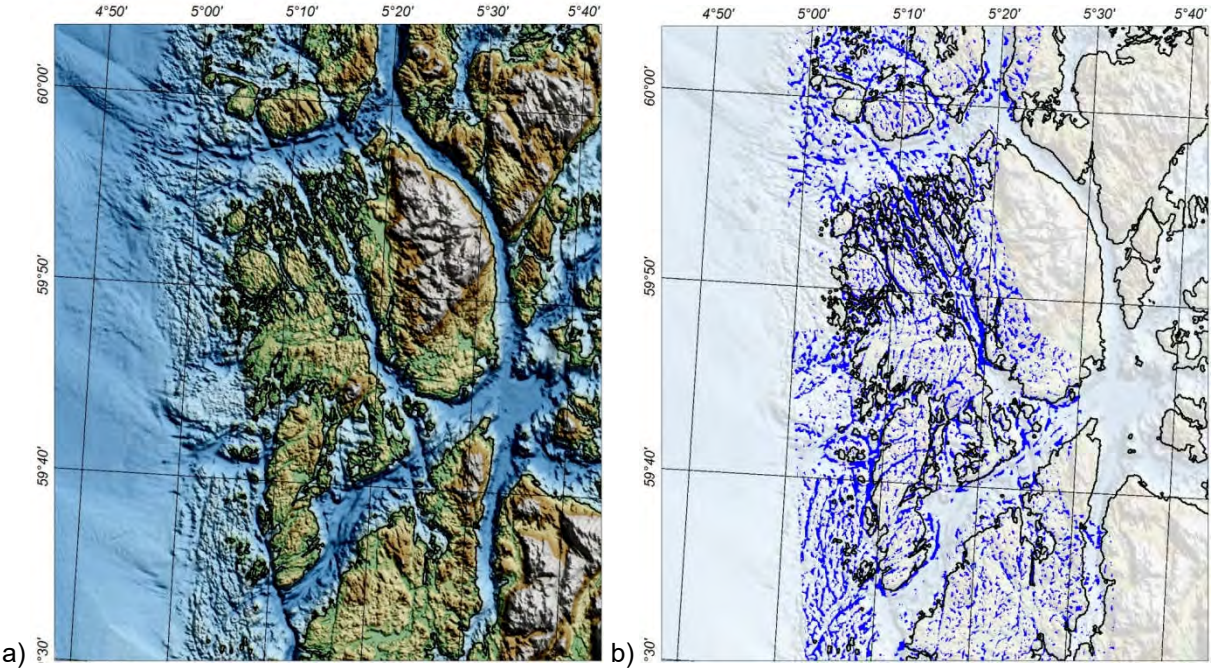

Figure 7.14. a)Bathymetry-topography map for Bømlo and the strandflat area. b) Bathymetry-topography map with superimposed AMAGER solutions. Weakness zones are predominantly NNW-SSE oriented out to c. 7 km on the strandflat.

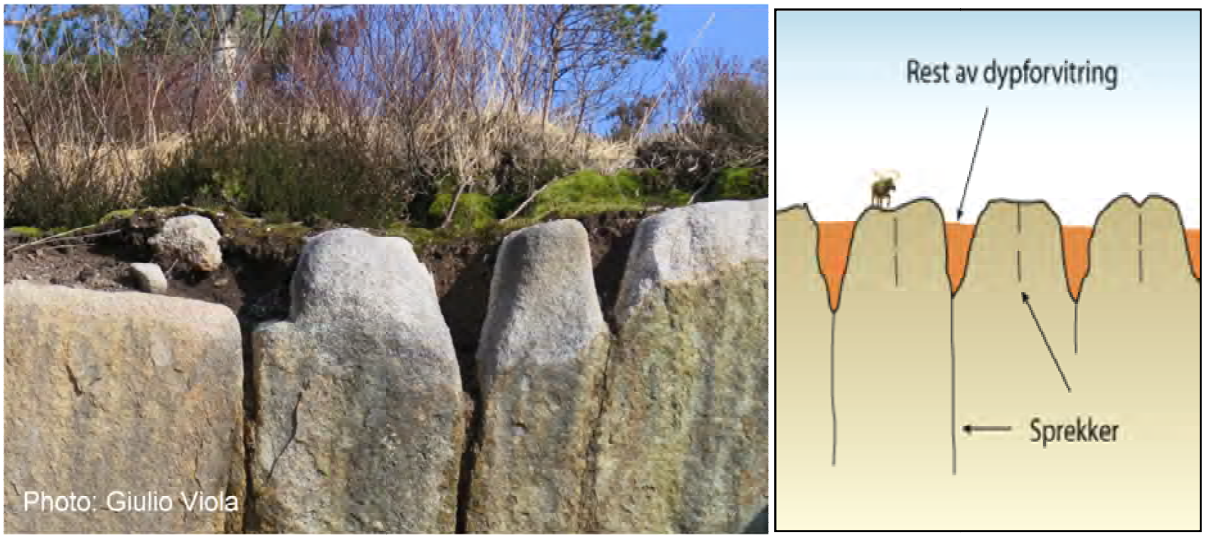

Figure 7.15. Teeth-like structures on Bømlo as described by Lidmar-Bergström et al. (1999). The joints between the teeth are filled with soil, all weathering remains having been eroded.

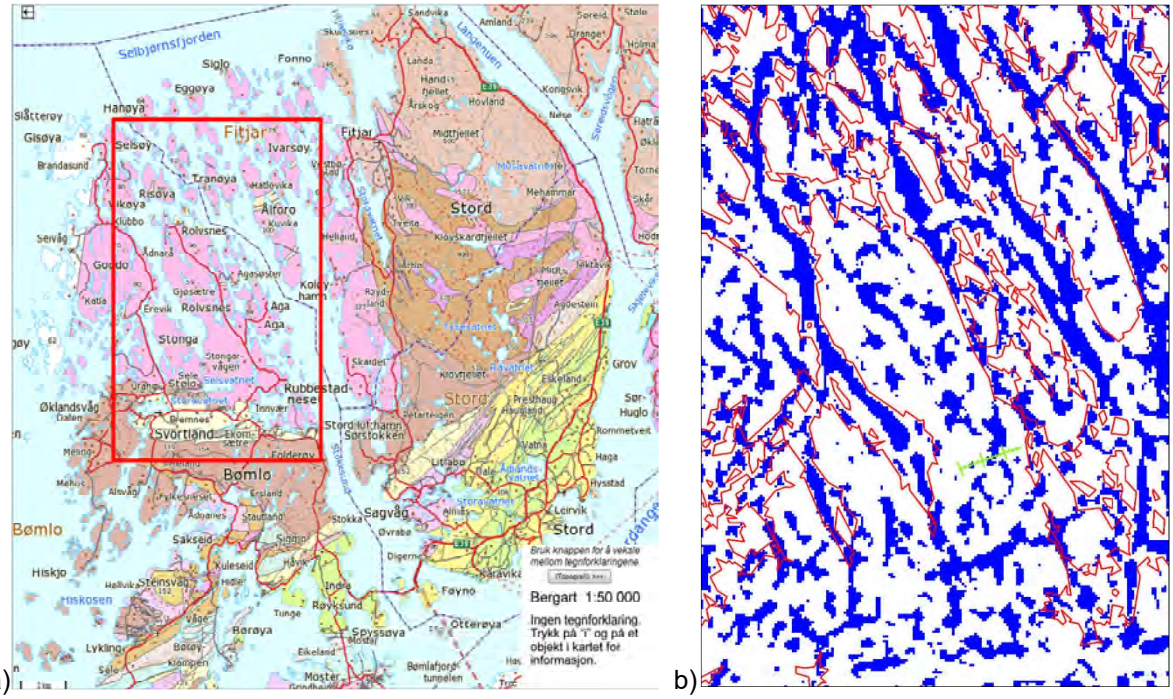

a) b)

Figure 7.16. a) Bedrock map showing an E-W orientation of the bedrock units. b) The AMAGER solutions for Bømlo are mostly oriented along NNW-SSE-striking lineaments. Weakness zones on the resistivity profile (shown in green) are also indicated by the AMAGER method.

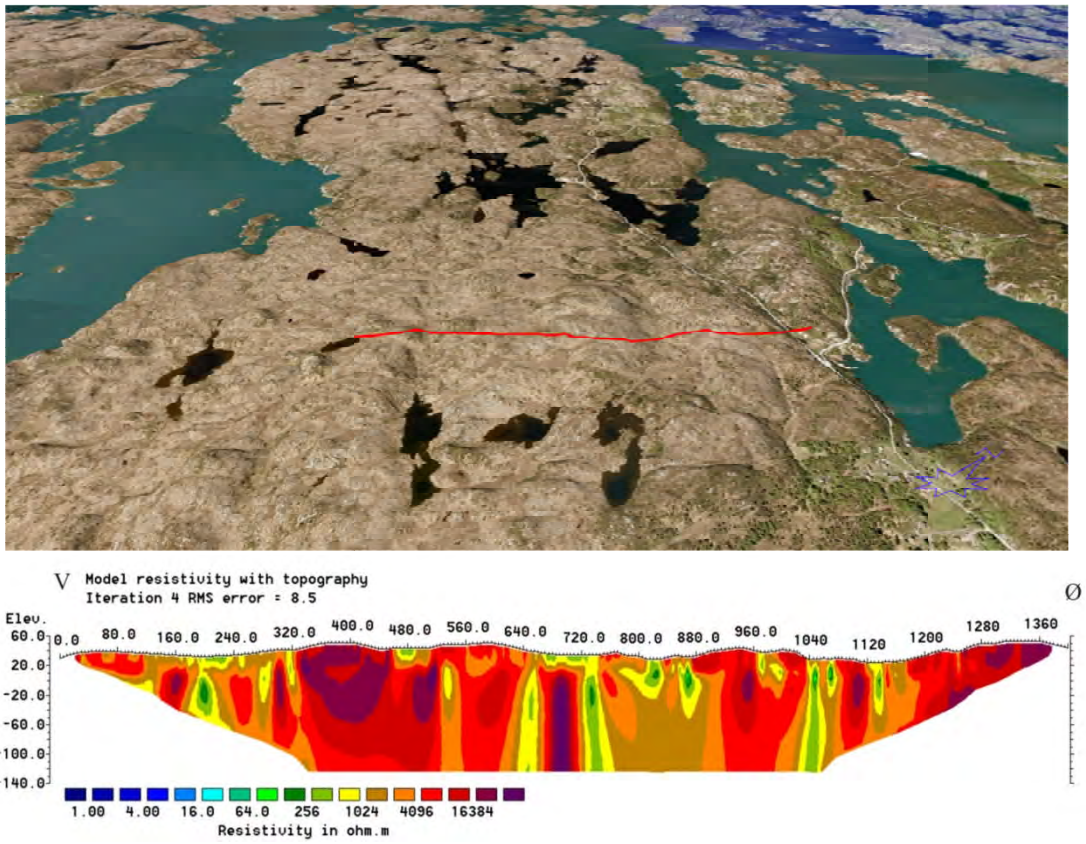

a)

b)

Figure 7.17. a) Draped aerial photographs on topography data (www.norgei3d.no) from the island of Bømlo with the position of the resistivity profile. b) Resistivity profile with interpreted weakness zones. The electrode spacing is 10 m and the applied V/H filter is 1.

7.5.4 Estenstadmarka, Trondheim

Three distinct fault-controlled valleys occur in the Estenstadmarka area located 6-8 km to the southeast of the centre of Trondheim. The locations of the E-W-trending Styggdalen, Ramdalen and Ratåsdalen faults are shown in Figures 7.18 and 7.19. The valleys are up to 70 m deep and 150 m wide and crosscut a plateau located at an altitude of 370-400 m above sea level. Some of the paths through these valleys have been widened by the use of an excavator during the last few years to facilitate tracks for ski skating. The excavations have exposed several deep weathering zones (Figure 7.20). The distances between these valleys vary from 1000 m to 1600 m. The Styggdalen joint valley extends across the whole of the Estenstad-marka plateau while the Ramdalen and Ratåsen valleys indent from either side into the plateau but are quite shallow in the middle (c. 20 m). This is consistent with Styggdalen having the lowest electrical resistivity and most likely the most pervasive weathering (Figure 7.21).

The weathered greenstone in Estenstadmarka is generally fine-grained with a high content of clay minerals. This is quite different from the grus-weathering observed in the intermediate and felsic magmatic rocks in the Vestfold and Lofoten-Vesterålen areas (Olesen et al. 2007a, 2013a). The clay mineralogy and grain size are described in more detail in the next chapter of the present report (Rueslåtten 2015). Both rounded and angular core stones with dimensions of up to two metres can be seen in the outcrops in Styggdalen and Ramdalen. A westward extension of the Styggdalen fracture zone can be found in the Leirsjøen area in Bymarka where clay-bearing fractures have been observed (H. Bunkholt, pers. comm. 2015). The lowest degree of weathering is observed in the third joint valley (Ratåsdalen). This can be observed in the resistivity profile as well as in the exposures in the Lia open pit (Figures 7.21c & 8.7). Several 5-15 cm-wide clay zones can be observed where the Ratåsen joint valley is exposed within the open pit (Figure 8.7). The location of the samples described in the next chapter of the present report by Rueslåtten (2015) is shown in Figure 7.21b.

The AMAGER method does not reveal the deep weathering of the joint valleys in Estenstad-marka due to the low susceptibility of the greenstones.

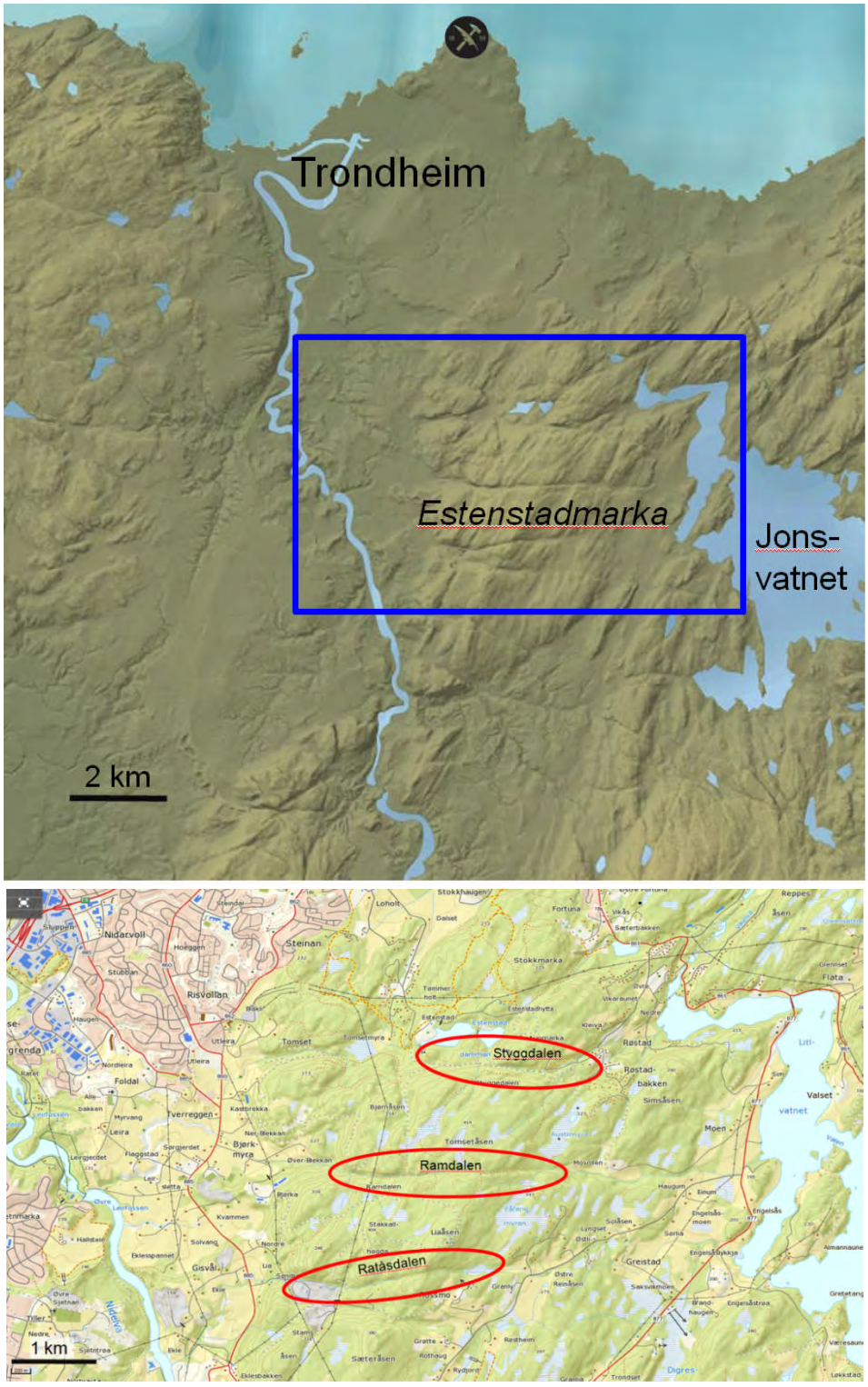

Figure 7.18. a) Digital terrain data from the Trondheim area showing the three E-W trending joint valleys in Estenstadmarka (data from the Norwegian Mapping Authority, Kartverket). b) Detailed topography map of the Estenstadmarka area. The three joint valleys (Styggdalen, Ramdalen and Ratåsdalen) are depicted by the three red ovals (from www.norgeskart.no). The valleys are up to 70 m deep and 150 m wide.

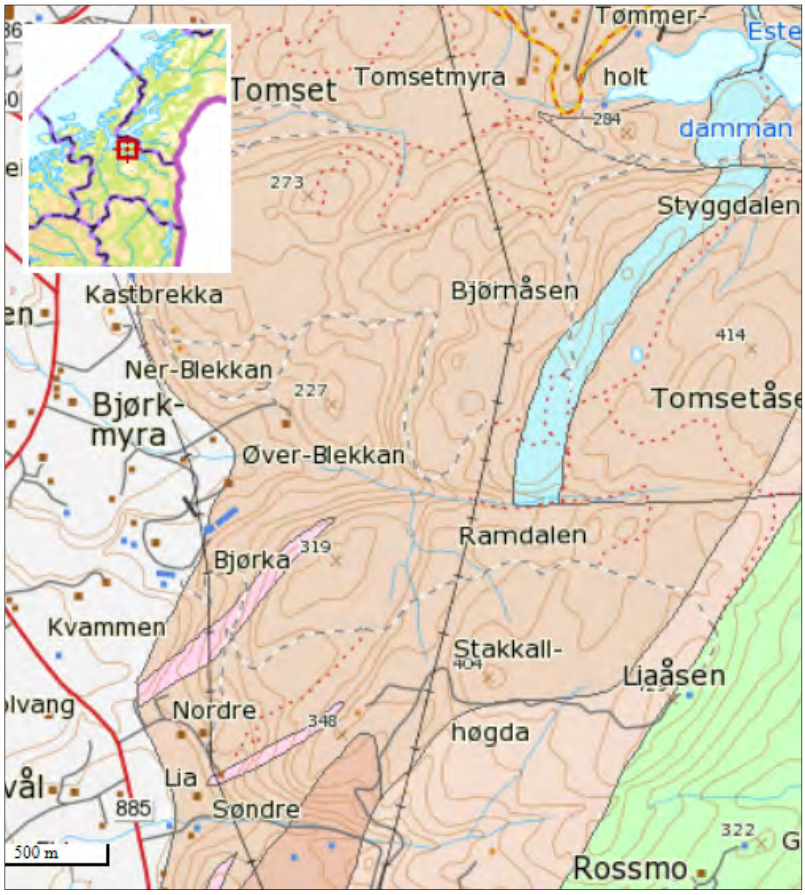

Figure 7.19. E-W trending fault zones in Styggdalen, Ramdalen and Ratåsdalen (Lia) from the 1:50.000 map sheet Trondheim (Solli et al. 2003). Brown and blue colours show greenstones and marbles, respectively.

a)

b)

Figure 7.20. Weathered and fresh greenstone in a) Styggdalen and b) Ramdalen. The weathering is exposed due to widening of the paths by use of an excavator. The weathering location in Styggdalen is located close to the bottom of the valley while the Ramdalen location is located at the escarpment of the valley, i.e. immediately below the Liaåsen plateau at an altitude of 370-400 m above sea level. The clay minerals and geochemistry of the fresh greenstone and the weathering from these locations are described in the next chapter of the present report (Chapter 8, Rueslåtten 2015).

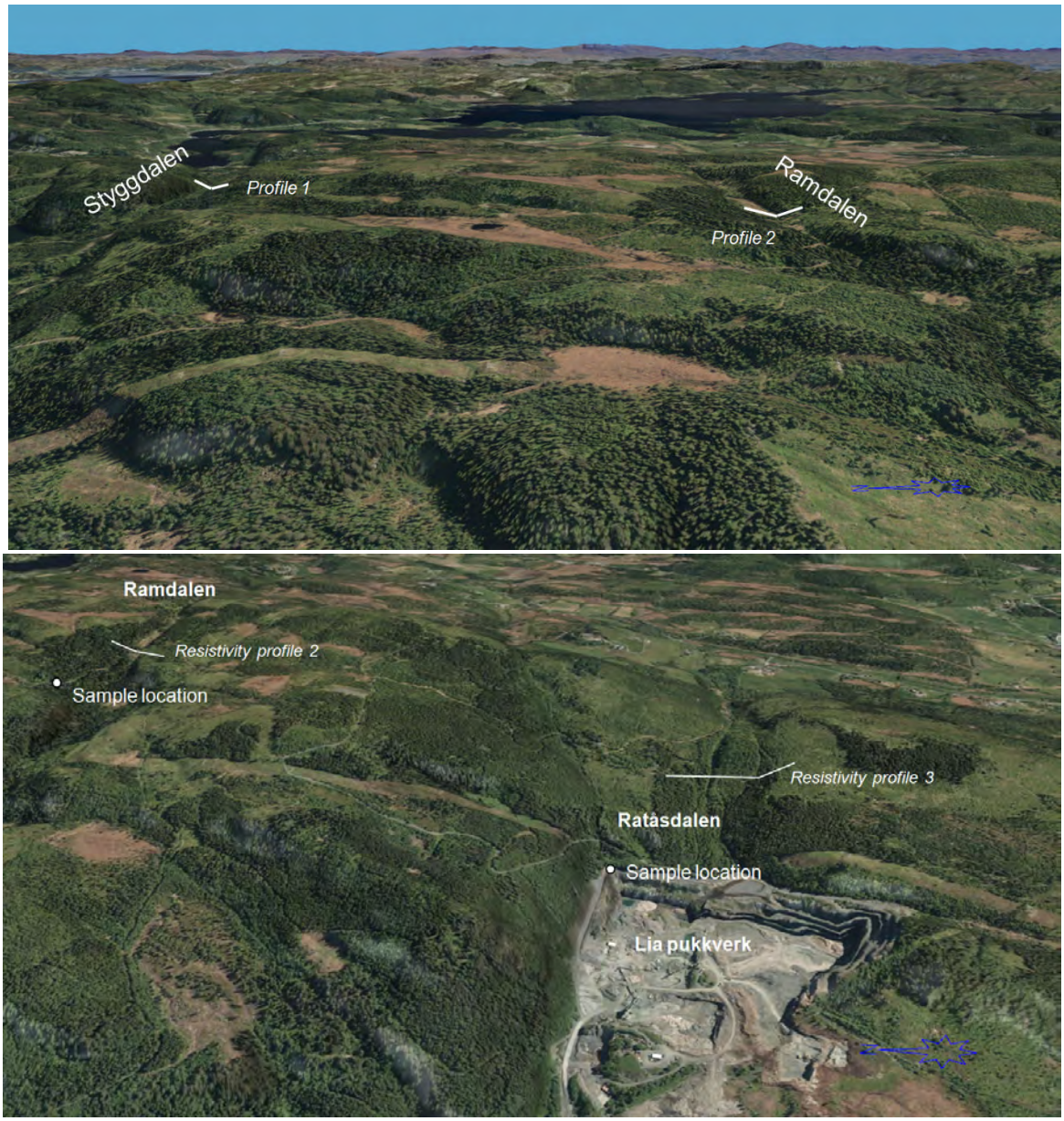

Figure 7.21. 3D perspective diagrams looking to the east at a) the northern and b) the southern Estenstadmarka areas. The joint valleys Styggdalen and Ramdalen are shown in a) while Ramdalen and Ratåsdalen can be seen in b). The relatively flat plateau between the valleys is also well illustrated. The locations of the three resistivity profiles (Figure 7.22) are also indicated.

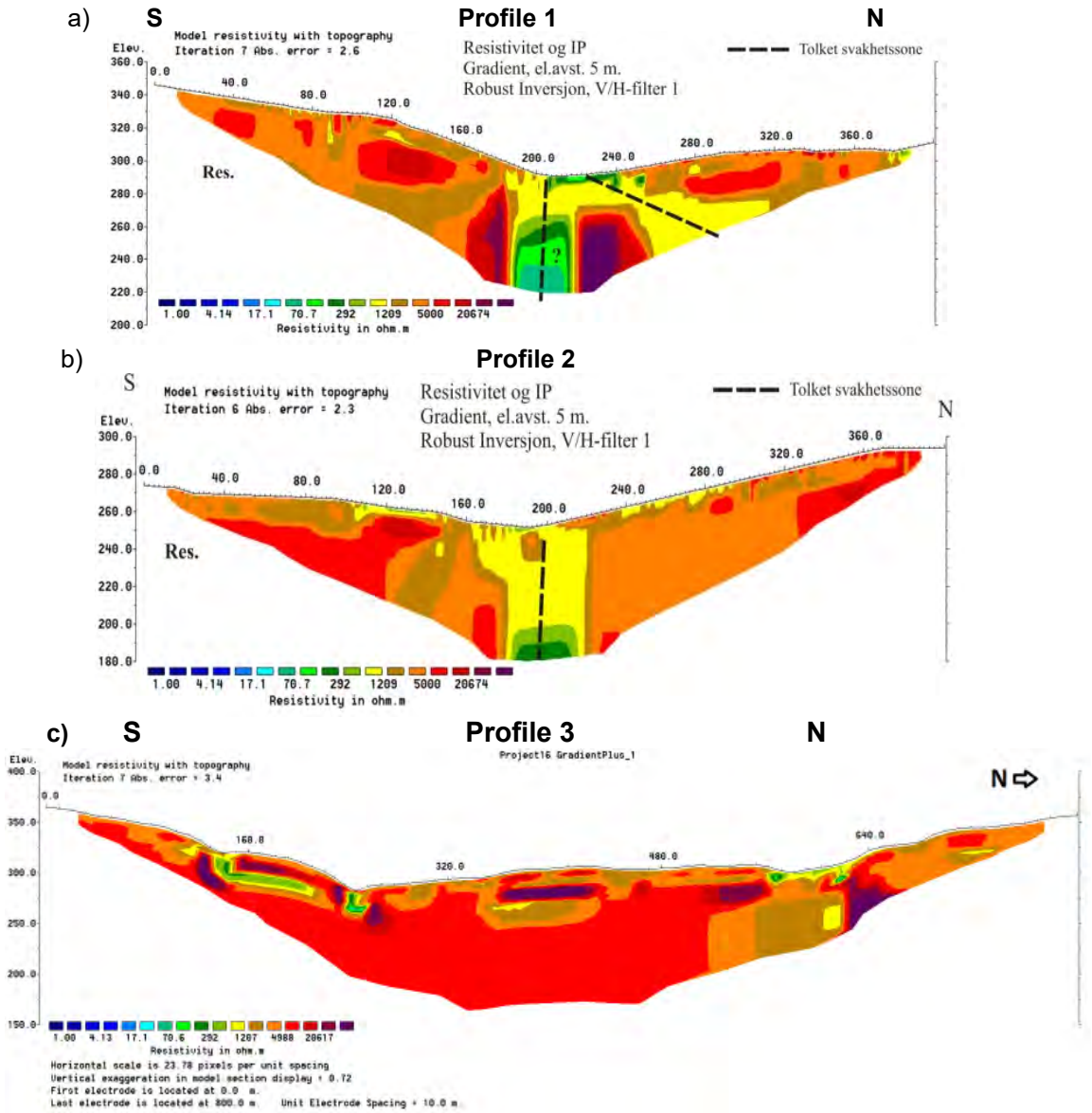

Figure 7.22. Resistivity profiles 1-3 across the three joint valleys in Estenstadmarka: a) Styggdalen, b) Ramdalen, c) Ratåsdalen. The electrode spacing for profiles 1 and 2 is 5 m while Profile 3 has a electrode spacing of 10 m. The low resistivity in the central part of Profile 1 indicates a high clay content while the fracture zones along Profile 3 have a higher resistivity and consequently a lower content of clay. The uppermost bedrock along Profile 2 has an intermediate resistivity indicating weathering along the paleo-surface at the Liaåsen plateau between the fault valleys.

7.6 Discussion

This study of the strandflat with the presented examples consistently indicates the large impact of tectonic events during the opening of the North Atlantic on the Norwegian margin and links them directly to the morphology of the coastal landscape. Fracturing, uplift and erosion are the controlling factors for the development of basement weathering. With the exception of hydrothermal weathering, climate conditions and denudation rates, mineralogy and petrology define the weathering rates.

As suggested earlier (Olesen et al. 2013a), the strandflat area has been exposed to deep weathering, repeatedly eroded and covered with sedimentary rocks during various phases of uplift and transgression (Figure 7.23).

We want to extend the model in relation to the development of the Norwegian margin and suggest multiple phases of weathering, which are related to major rifting episodes along the Norwegian margin. Based on the observation described in this study, it appears likely that already with the onset of the continental rifting in Late Palaeocene, the increased fracturing of the upper crust significantly stimulated deep weathering. The continuing crustal extension formed basins and basement highs, and uplift and subsidence mainly controlled the weathering but also whether or not the saprolite was buried and preserved underneath the sedimentary strata. Depending on the erosion and denudation, areas in high position consequently experienced a 'renewal' of the weathering, whereas saprolite was buried in sedimentary basins. We can relate this idea to the development of the present strandflat and the uplift of adjacent areas. The repeated weathering phases in the uplifted areas yielded a more developed levelling of the landscape, and the strandflat is consequently an old weathering front which can extend back even to Late Palaeozoic times.

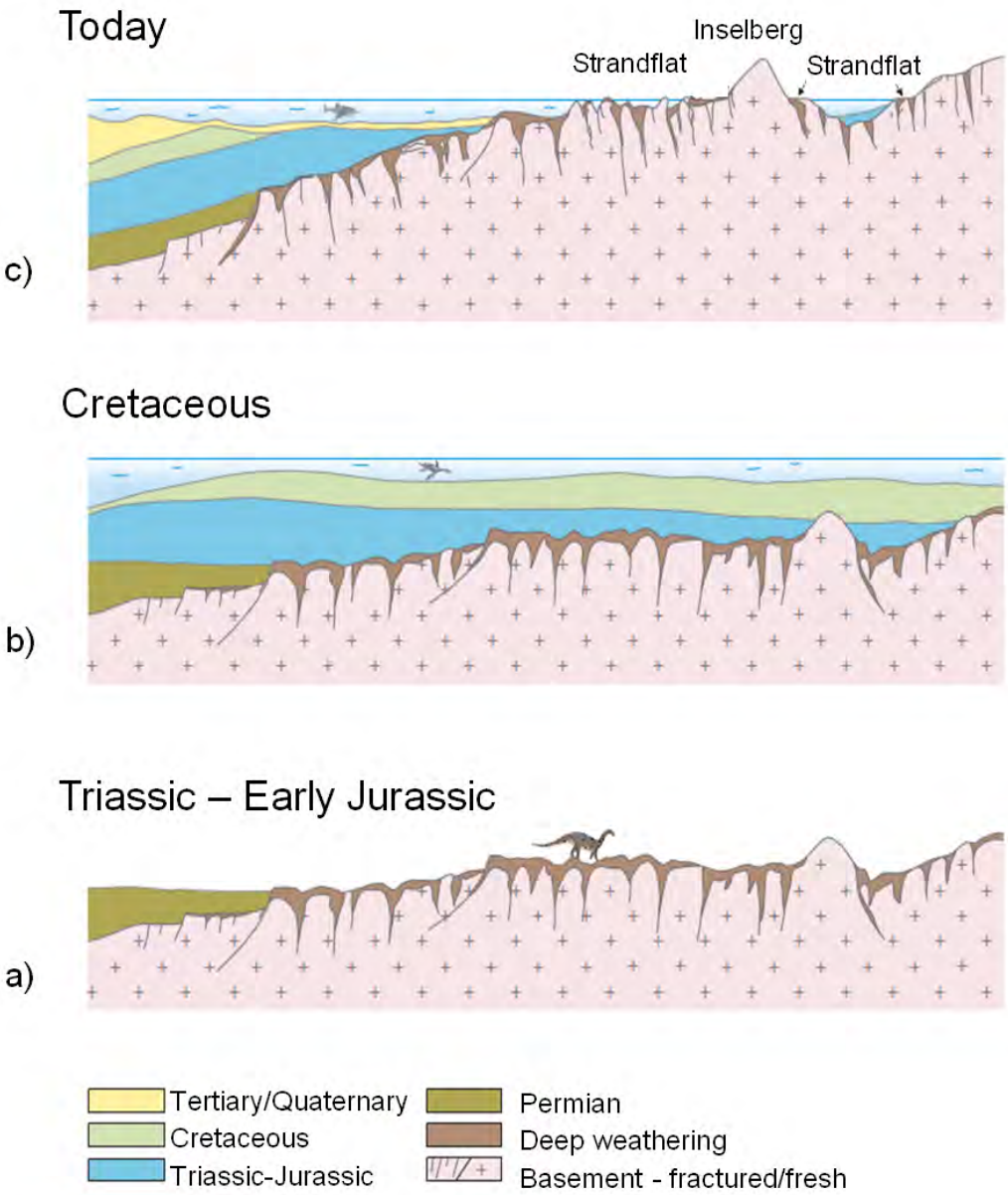

Figure 7.23. Conceptual model for strandflat development along the Nordland coast from the Triassic to the present day. a) Triassic–Jurassic subtropical weathering (etching) across the entire palaeosurface with deeper penetration into pre-existing fracture zones. Subsequent block-faulting in the Late Jurassic. b) Preservation of chemical weathering below shales and carbonate rocks deposited during the Late Jurassic to Cretaceous transgression. c) Uplift and erosion during the Neogene. The bulk of the chemical weathering was removed leaving an immature etch-surface landscape with joints and faults as valleys, sounds and fjords. Some of the valleys have been excavated by the glaciers to form fjords. Remnants of the old weathering surface are left as strandflats, often occurring as rims of low land around islands and peninsulas. The clay zones containing smectite and kaolinite were preserved at depth along the fracture zones (modified after Lidmar-Bergström 1995, Olesen et al. 2013a, Olesen 2014). The described locations observed at Bømlo, Vågsøy, Smøla and Trondheim represent different weathering surfaces at different altitudes above sea level. Trondheim and Vågsøy are the highest and correspond most likely to the Mesozoic palaeosurface whereas Smøla and Bømlo are lower and more characteristic for the younger strandflat.

The saprolite we observe in Norway is mostly the clay-poor grussy type and several authors related this type of weathering to relatively young Plio-Pleistocene ages, but not older than Tertiary (e.g., Migon & Lidmar Bergström 2002, Lidmar-Bergström et al. 1999), and have argued for warm and humid climate conditions during e.g., the Eocene. So far, there are only

a few dates on saprolite in Norway but K/Ar dating of saprolite from the Ramså Basin revealed Carboniferous ages (Sturt et al. 1979), which confirm the existence of very old weathering with the Middle Jurassic strata on top, providing proof of a minimum age of this weathering. Other saprolite dating results (Fredin et al. 2013, Olesen et al. 2013a and references therein) have yielded mainly Mesozoic ages with Triassic as the predominant period.

However, we cannot rule out the one or the other, but want to point out that our observations support a link to major tectonic rifting episodes. As a first-order concept to explain the mostly grussy type of weathering observed in Norway, which shows a rather low degree of chemical weathering and alteration to clay minerals, we can argue that the present remains reflect the deepest part in the weathering zone (Brönner et al. 2012a,b, Olesen et al. 2012, 2013a). The upper part of the regolith was eroded and mostly removed during the ice ages. The weathering engine gradually extends downwards along fractures and faults in the basement, where the deepest part is the least chemically altered weathering product. The weathering rates and types vary depending on the external conditions, and the weathering process might even halt temporarily and recommence at a later stage. An analogue for this concept is found in Ukraine, where the grussy weathering is overlain by thick packages of clay-rich weathering products, which are locally observed underneath Palaeozoic (?) sedimentary rocks. Although Ukraine and Fennoscandia were parts of the same shield, Ukraine was not exposed to glacial erosion and therefore more representative remnants of the paleo-saprolite are preserved there. In Norway, however, the upper, clay rich part of the regolith is apparently eroded.

Ukraine can therefore be considered as an analogue for the development of the landscape of Fennoscandia until at least the Late Mesozoic. However, there are obviously differences between these two examples since Ukraine, placed in the centre of the craton, has been in a quite stable position over time, whereas Fennoscandia has experienced several continental collisions and breakups since the Proterozoic. Significant phases with uplift and erosion, subsidence and transgression make it difficult to explain the present weathering remains by such a simple model. We would therefore like to suggest a variation of the proposed concept and introduce an element of continental drift of Fennoscandia with variations in the type of weathering over time. As already mentioned, Ukraine is part of the same shield and has of course experienced the same continental drift, which resulted in overprinting of weathering, as in Australia, but perhaps not as extreme as observed there since Australia has remained at, or is still moving into latitudes more beneficial for weathering.

In Fennoscandia and especially in the coastal areas of Norway, we can assume significant rates of erosion through time and repeated denudation of the basement in a large part of the area, in particular since the onset of continental rifting in the Devonian. At that time, Norway was at the equator with tropical, humid and warm climate conditions. Weathering rates were high and in particular the chemical alteration of rocks with high rates of clay production was probably quite advanced. Whilst the continent Baltica-Laurentia was moving northwards (Torsvik & Cocks 2005), the rifting continued and the landscape was repeatedly reorganised due to uplift and erosion, and large parts of the clay-rich saprolite were removed, locally down to the unweathered basement. During the Mesozoic, Baltica-Laurentia had more sub-tropical climatic conditions which resulted in a more arid, clay-poor type of weathering of the

basement and overprinting of older weathering remnants. Repeated transgression and a significantly higher sedimentation rate protected large parts of the saprolite and these are the remains we can observe today, most likely overprinted several times during periods of warm and humid climate in the Cenozoic.

This refinement of our conceptual model is compliant with the observations we have so far and it would also explain the occurrence of clay-rich weathering remains at some locations like Ivö in southern Sweden (Lidmar-Bergström 1989) and in Scotland (Krabbendam & Bradwell 2014), which could consequently but not necessarily be of a significantly older age or have been exposed to severe overprinting.

However, at the present time this concept is still speculative and needs to be substantiated by further dating of saprolites in Norway and from the Norwegian shelf.

8. MINERALOGICAL AND GEOCHEMICAL STUDIES OF DEEP BASEMENT WEATHERING IN NORWAY

Håkon Gunnar Rueslåtten

8.1 Introduction

The present chapter summarises the work done on 20 rock samples from 12 different localities, comprising both 'fresh' and weathered rock material. The work is a part of the COOP project on deep basement weathering.

8.2 Materials and methods

The complete sample list with their respective UTM coordinates is given in Table 8.1, and a map showing sample localities is given in Figure 8.1.

Table 8.1. Complete sample list, with numbers, sample ID's, geographical coordinates, and short description.

Serial no.	NGU Sample no.	Sample ID	UTM-coordinates EUREF89 (WGS 84)			Sample description:
			Zone	East (m)	North (m)	Rock type
1	108501	1201A	33	533380	7506253	Quartz monzonite, Eiavatnet
2	108502	1201B	33	533380	7506253	Weathered quartz monzonite, Eiavatnet
3	108503	1202A	33	499168	7442026	Pyroxenite, Karbøl, Misvær
4	108504	1202B	33	499168	7442026	Weathered pyroxenite, Karbøl, Misvær
5	108505	1203A	33	426331	7390791	Granitic gneiss, Amundvatnet
6	108506	1203B	33	426331	7390791	Weathered granitic gneiss, Amundvatnet
7	108507	1204A	32	573753	7028483	Greenstone, Liaåsen
8	108508	1204B	32	573753	7028483	Weathered greenstone, Liaåsen
9	108509	1205A	32	573757	7028483	Greenstone, Liaåsen
10	108510	1205B	32	573757	7028483	Weathered greenstone, Liaåsen
11	108511	1206A	32	574613	7029698	Greenstone, Styggdalen
12	108512	1206B	32	574613	7029698	Weathered greenstone, Styggdalen
13	108513	1207A	32	443934	6707696	Gneiss, Ustaoset
14	108514	1207B	32	443934	6707696	Weathered gneiss, Ustaoset
15	108515	1208A	32	623502	6748212	Alum Shale, Heggvin, Hamar; well depth 69-72 m
16	108516	1208B	32	623502	6748212	Weathered Alum Shale, Heggvin, Hamar; well depth 21-24 m
17	108517	1209	32	294648	6695267	Weathered granite, Fyllingsdalen, drill cuttings; 495.27-495.40 m depth
18	108518	1210	32	294648	6695267	Weathered granite, Fyllingsdalen, drill cuttings; 514.27-514.44 m depth
20	108520	1501A	32	573070	7027155	Greenstone, Lia Pukkverk
21	108521	1501B	32	573070	7027155	Weathered greenstone, Lia Pukkverk

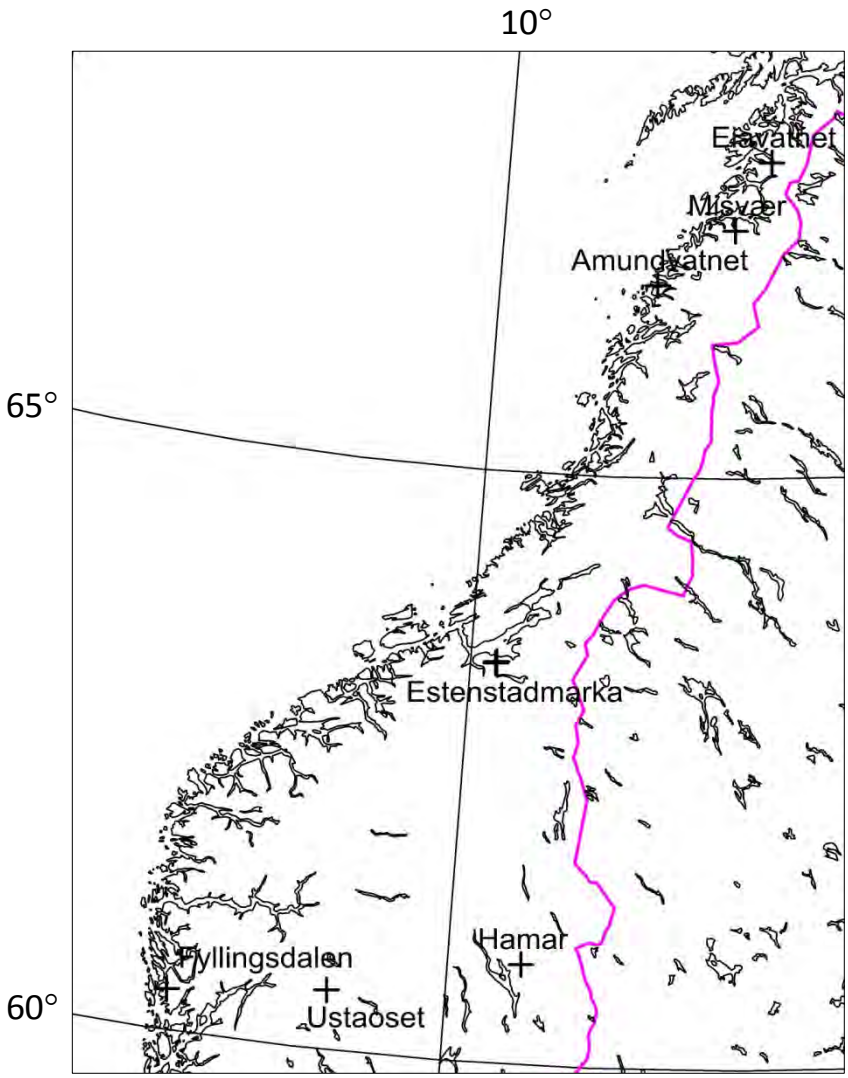

Figure 8.1. A simplified map showing sample localities.

Pictures from some of the localities

Pictures from some of the key localities are given below, to illustrate the degree of weathering in the outcrop zone.

Figure 8.2. Eiavatnet locality, showing the deeply weathered quartz monzonite; sample numbers 108501 and -02.

Figure 8.3. Misvær locality, showing the deeply weathered pyroxenite; sample numbers 108503 and -04.

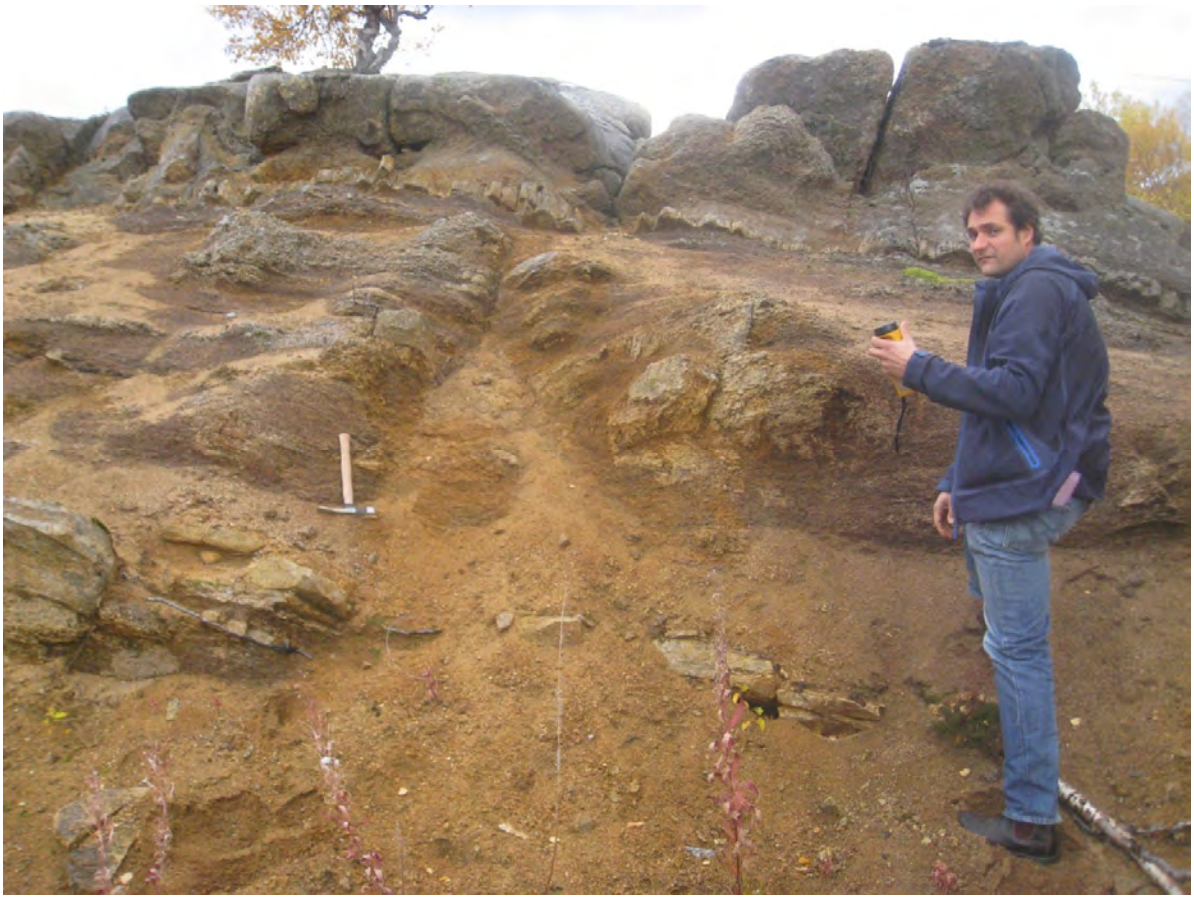

Figure 8.4. Amundvatnet locality, showing the deeply weathered granitic gneiss, sample numbers 108505 and -06.

Figure 8.5. Ustaoset locality, showing the deeply weathered gneiss; sample numbers 108513 and -14.

Figure 8.6. Deep weathering in greenstone at the Styggdalen locality; sample numbers 108511 and -12.

Figure 8.7. Deep weathering in greenstone at the Lia Pukkverk locality; sample numbers 108520 and -21.

Figure 8.8. Fyllingsdalen locality; deep weathering of granitic rock; sample numbers 108517 and -18.

Preparation of samples
All preparation and analytical work has been done by NGU personnel at NGU's laboratories and according to NGU's standard procedures.

The non-weathered (fresh rock) samples were crushed and micronised to pass the 63 micron sieve, prior to preparation of specimens for XRD (dry powder) and XRF analysis (tablets).

The weathered samples were dispersed in water - mechanically and in an ultra-sonic bath - before wet sieving through the sieves 8 mm, 2 mm and 63 micron, followed by drying and weighing.

The <63 micron fractions (from the weathered samples) were split into four parts:

1. XRD analysis of <63 micron fraction: dry sample to determine the mineral composition.
2. XRD of fine fraction: separate out the <6 micron fraction by sedimentation in water. The fraction <6 micron is analysed on XRD in both dry and glycolated state (to identify smectite minerals).
3. XRF analyses:
    - XRF of main elements: the dry sample <63 micron is ignited at 1000 degree C, before mixing it 1:7 with lithium-tetraborate, prior to melting a pill in a platinum crucible for XRF analysis. This includes also analysis of a number of trace elements.
    - XRF analysis of trace elements. Same sample material as above pressed to dry powder pills. Six of the samples had too little material for these analyses (see below).
4. Grain size distribution of <63 micron fraction: Coulter Counter analyses.

Step 1 and 3 was also carried out for the non-weathered rock samples. The main part of the work reported here includes an interpretation and quantitative estimation based on X-ray diffractograms of the samples, provided by NGU. The XRD analyses were conducted by Jasmin Schoenenberger, NGU.

8.3 Grain-size distributions

Weathering processes
Meteoric water is initially percolating through soil profiles where acid humic substances are mixing into the pore water. These humic substances are efficient complexing agents for mineral components that are dissolved by the percolating water; e.g., base cations (Ca, Mg, Na, and K), iron, and aluminum. Minerals that are particularly vulnerable to such chemical weathering are carbonates, iron-bearing minerals (e.g., amphiboles, biotite and chlorite) and feldspars.

The weathering is commonly initiated along fractures and fissures in the rock, where the percolating meteoric water has access to large rock surfaces. These rock surfaces are commonly composed of a number of mineral types, and the water is seeking into micro-pores along the boundaries between minerals, and particularly those that are vulnerable to dissolution in oxygenated acid water. Thus, this weathering is causing disintegration of the

parent rock, a process referred to as arenisation. A weathering attack on, e.g., coarse-grained granite may cause disintegration of the rock into sandy/gravelly material without producing significant amounts of clay (Braga et al. 2002).

Continued chemical weathering may eventually cause complete dissolution of the feldspars, while the quartz crystals are left more or less intact. The sizes of the quartz crystals will then contribute to give a characteristic grain-size distribution of the weathered rock material. The dissolved components (from feldspars, etc.) will commonly crystallise as clay minerals; e.g., smectite and/or kaolinite. However, this is highly dependent on the climate at the site. The newly formed clay minerals are commonly finer than 6 micron, and contribute to an increased fine fraction of the weathered material. The grain-size analyses of the weathered material are focused on identifying such features.

The grain size distribution of the material larger than 63 micron is given in Table 8.2, both by weight and weight-%.

Table 8.2. Weight (g) and weight-% of fractions >63 micron of weathered rocks.

NGU	Rock types	Fraction >8mm	Fraction 8mm - 2mm	Fraction 2mm - 0.063mm	Fraction >8mm	Fraction 8mm - 2mm	Fraction 2mm - 0.063mm
Sample #.		(g)	(g)	(g)	(wt%)	(wt%)	(wt%)
108502	Monzonite	15,69	92,89	378,47	3,2	19,1	77,7
108504	Pyroxenite	2,68	13,67	152,01	1,6	8,1	90,3
108506	Granitic gneiss	1,31	93,58	242,78	0,4	27,7	71,9
108508	Greenstone	18,43	49,73	287,52	5,2	14	80,8
108510	Greenstone	9,22	121,31	179,22	3	39,2	57,9
108512	Greenstone	79,18	77,53	188,03	23	22,5	54,5
108514	Gneiss	0,67	1,66	96,26	0,7	1,7	97,6
108516	Alum shale	3,36	0,80	26,08	11,1	2,6	86,2
108517	Granitic gneiss	180,85	32,91	23,04	76,4	13,9	9,7
108518	Granitic gneiss	244,62	98,06	49,82	62,3	25	12,7
108521	Greenstone	96,87	115,22	137,22	27,7	33	39,3

An illustration of the grain-size distribution (in weight-%) as bar graphs is shown in Figure 8.9. A guide to the sample numbers is given in the diagram.

The samples numbered 1, 2 and 3 on the x-axis are developed from granitic, monzonitic and pyroxenite rocks, respectively, and are characterised by large sand fractions (fraction 0.063mm-2mm). The sand fractions are either single mineral grains (reflecting the dominating crystal size of the parent rocks) or sand-sized rock fragments.

The two samples with X-axis numbers 9 and 10 represent weathered granitic rocks, sampled in drillcore material from Fyllingsdalen. Here, the fraction >8mm dominates, indicating a lesser degree of penetrating weathering.

The four greenstone samples have X-axis numbers 4, 5, 6 and 11 in this bar diagram. They have large sand fractions, but the most weathered sample, no.11, also has a large coarser fractions. These rock samples are shales that are disintegrating, and the particles larger than 63 micron are mainly rock fragments rather than single mineral grains.

The weathered gneiss from Ustaoset (no. 7) and the Alum Shale from Hamar (no. 8) are both dominated by their sand fractions. In this case, the Alum Shale particles are mainly rock fragments, while the Ustaoset sample may have single mineral grains as a significant part of the sand fraction (mainly quartz and feldspar).

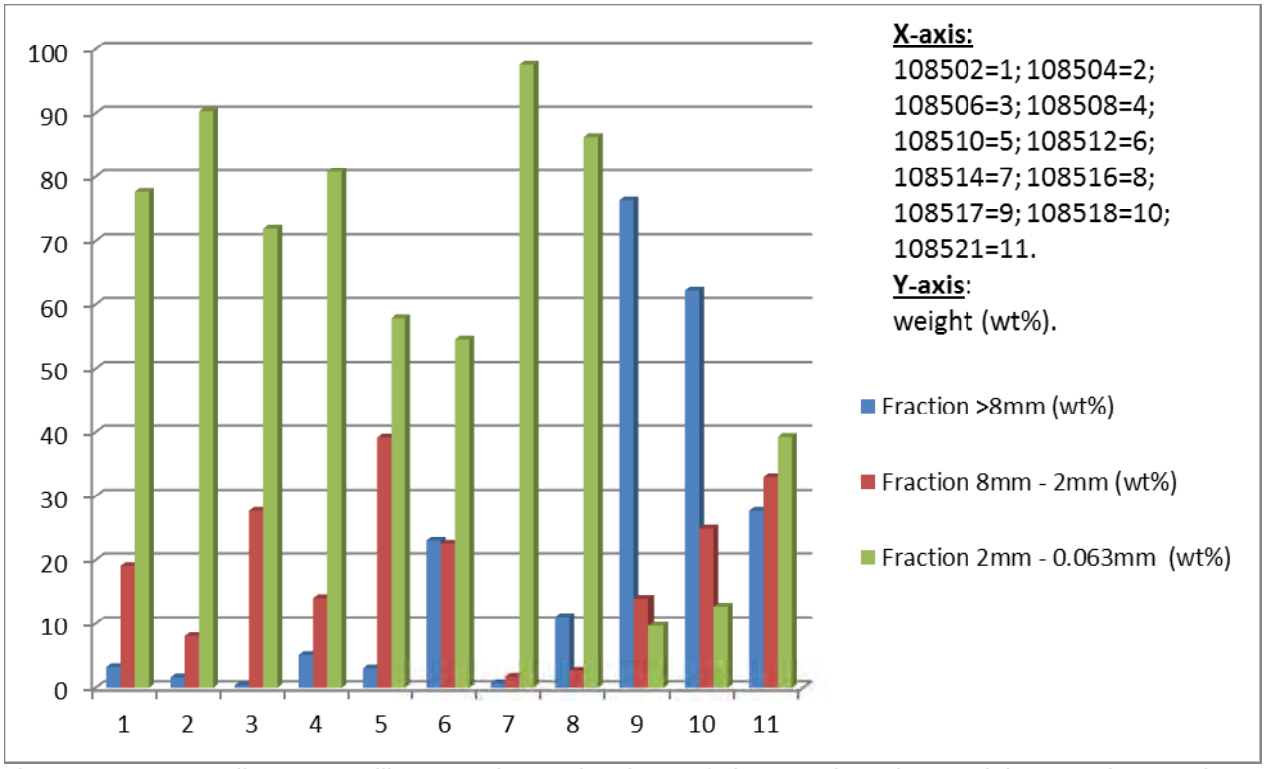

Figure 8.9. Bar diagram to illustrate the grain sizes of the weathered material >63 micron. The samples are numbered along the x-axis, and a guide to the associated sample numbers is given in the diagram.

8.3.1 Grain size distribution of <63 micron fractions

The Coulter Counter technology is used to obtain the grain-size distribution of the <63 micron fractions. The method is based on laser-diffraction. Laser light is refracted at different angles depending on the size of the particles, and the refracted beams are registered by several detectors. The angles of the received beams are a function of the particle sizes, and the intensity of the signal is related to the number of particles. The grain sizes are determined by their volumes (as spherical grains). The results are illustrated in Figures 8.10 and 8.11. Figure 8.10 gives the cumulative grain-size distribution of the <63 micron fractions for all weathered samples except the four greenstone samples. They are shown in Figure 8.11.

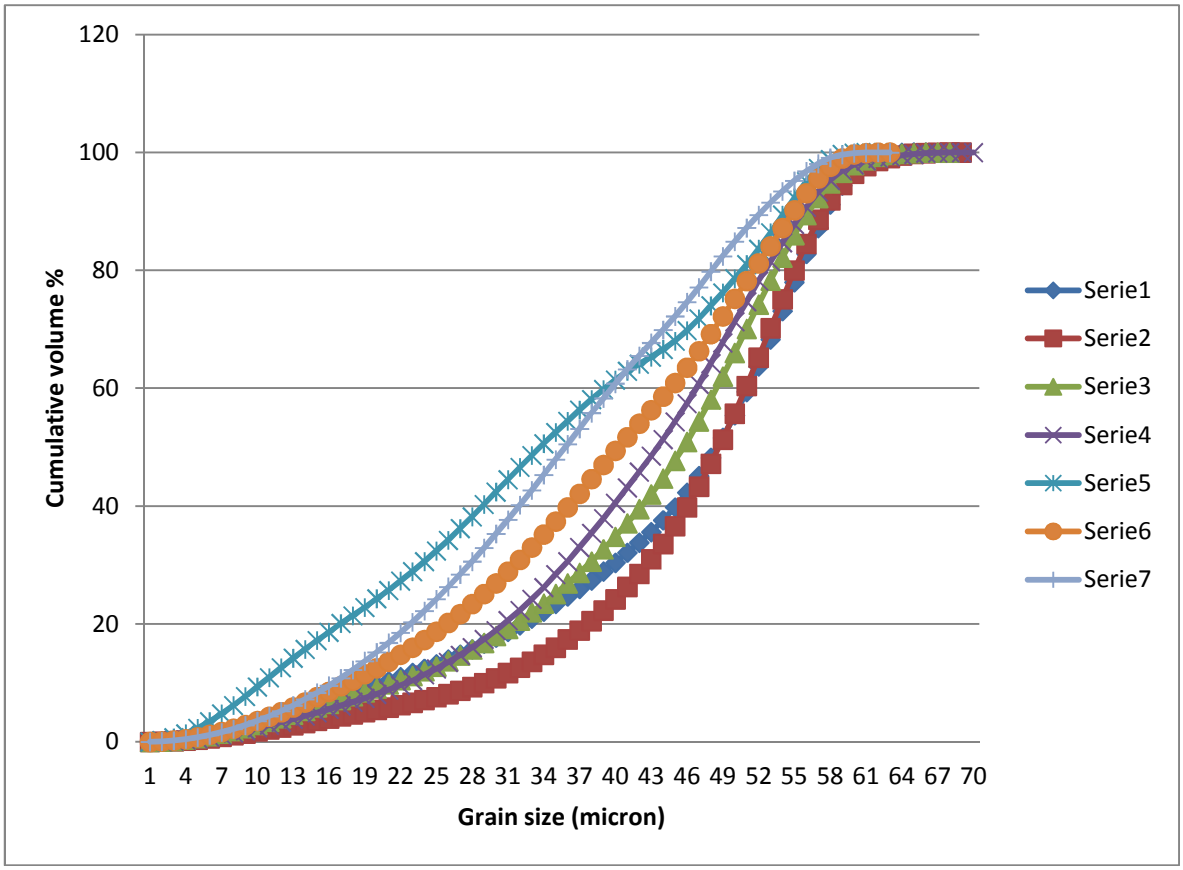

Figure 8.10. Grain-size distribution of fractions <63 micron for all weathered samples, except the four samples from the greenstone belt in Trondheim (see Figure 8.11). Coulter Counter analysis, giving cumulative volume-% of the particles of the samples <63 micron. The sample numbers and associated serial numbers (given in the diagram) are: Series 1: 108502 (monzonite); Series 2: 108504 (pyroxenite); Series 3: 108506 (granitic gneiss); Serie 4: 108514 (gneiss); Series 5: 108516 (alum shale); Series 6: 108517 (granitic gneiss); Series 7: 108518 (granitic gneiss).

A large spread in grain size distributions is seen in Figure 8.10; the extremes being in Series 2: Sample 108504 (weathered pyroxenite, Misvær) with least fines, and Series 5: Sample 108516 (weathered Alum Shale) containing most fines.

Series 4 and 5; i.e., samples 108514 and 108516, are also characterised by high contents of fines. These two samples are the weathered gneiss from Ustaoset, and the weathered Alum Shale from Hamar, respectively.

The two last samples 108517 and 108518 (Series 6 and 7) are the granitic core samples from Fyllingsdalen near Bergen. They also contain abundant fine material.

Cumulative volume-% (Y-axis) versus grain sizes in micron (X-axis) for the four weathered greenstone samples is shown in Figure 8.11. Sample 108521 (Series 4) is the one with the highest content of fines in the medium silt fraction (Series 11 in Figure 8.11). This sample is also the one with the highest content of smectite, which is a proxy for a high degree of weathering. The remaining three greenstone samples are rather similar with respect to grain-size distribution.

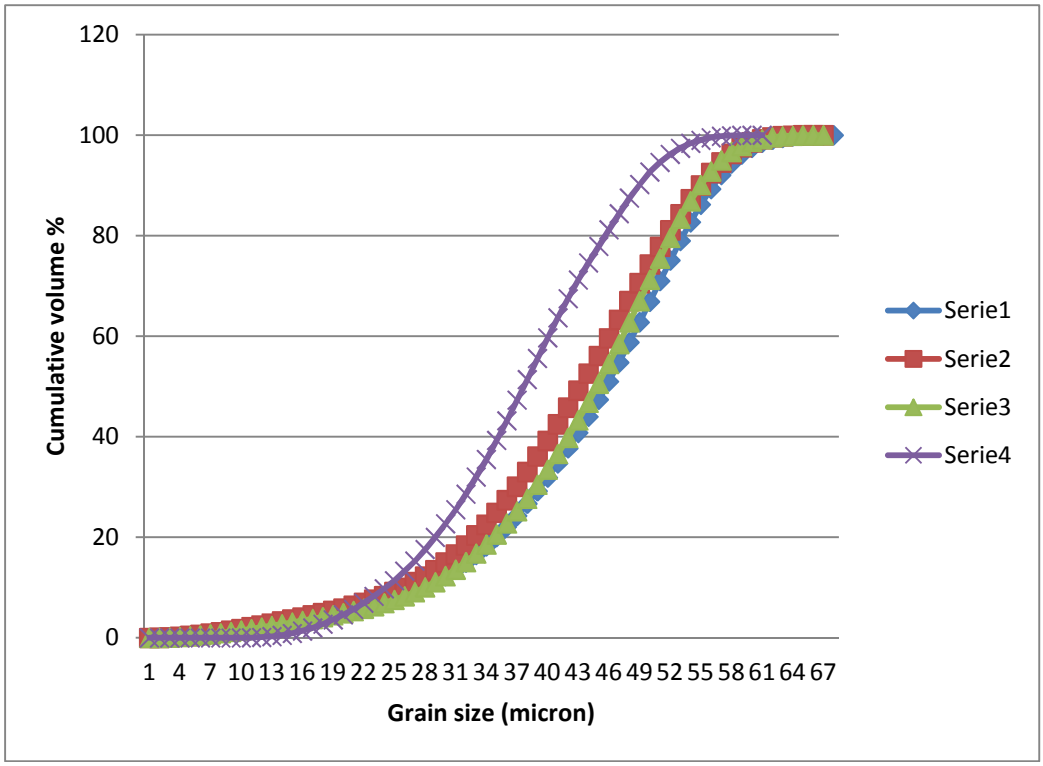

Figure 8.11. Cumulative grain-size distribution of the <63 micron fraction of the weathered samples from the greenstone belt in Trondheim. The sample numbers and associated serial numbers (given in the diagram) are: Series 1: sample 108508 (Liaåsen), Series 2: sample 108510 (Liaåsen), Series 3: sample 108512 (Styggdalen), Series 4: sample 108621 (Lia Pukkverk).

8.4 Mineralogy

8.4.1 X-ray diffraction analysis

When atomic planes of a mineral in a powder sample attain an appropriate angle towards the incoming X-ray beam, they will diffract the X-rays according to Bragg's Law:

$$n\lambda = 2d \sin\theta$$

where

λ = wavelength of the X-rays (Å)
d = spacing in the crystal lattice (Å)
θ = angle of diffraction (°)
n = integral number (1, 2, 3 ...)

Each mineral type has characteristic reflections on the X-ray diffractogram and can therefore be identified. The samples were scanned in the range (2θ) 2° to 68°. The radiation applied is monochromatic CuK_{α}.

The mineralogical composition was determined by the interpretation of characteristic reflections on the X-ray diffractograms. The quantification of each mineral type was based on the product of the peak height (multiplied by width at half height) and multiplied by a weighting factor (based on empirical investigations of weighed standard samples) for the following minerals and reflections:

Quartz: 4.26 Å · 1.0 K-feldspar: 3.24 Å · 0.5 Plagioclase: 3.19 Å · 0.5 Chlorite: 4.7 Å · 2.1 or 7 Å · 0.7 Kaolinite: [7 Å - (4.7 Å · 3)] · 0.7 Mica: 10 Å · 1.0 Illite: 10 Å · 1.4 Mixed layer clay minerals: 10 to 14 Å · 0.55 Smectite: (14 Å - 4.7Å) · 0.35 Calcite: 3.04 Å · 0.25 OpalCT: 4.1 Å · 0.15	Siderite: 2.79 Å · 0.25 Dolomite/ankerite: 2.89 Å · 0.2 Pyrite: 2.71 Å · 0.7 Clinoptilolite: 8.92 Å · 0.5 Talc: 9.33 Å · 0.15 Hornblende/Actinolite: 8.5Å · 0.5 Pyrophyllite: 9.1Å · 1.0 Pyroxene: 3.17Å/2.99Å · 1.0 Anatase: 3.5Å · 0.15 Apatite: 2.81Å · 0.5 Jarosite: 5.1 Å · 0.5

The quantification of mineralogy from XRD is associated with significant uncertainty, and the estimates must be regarded as semi-quantitative only.

8.5 Mineralogy from XRD

The qualitative and quantitative investigations of the X-ray diffractograms are summarised in Tables 8.3, 8.4 and 8.5. In these three tables, only the last four digits of the sample numbers are given. Each sample number should have '10' prior to these four digits; e.g. 8501=108501. It is of interest to identify the type of mica and illite; i.e. whether they are trioctahedral (e.g. biotite) or dioctahedral (e.g. muscovite). The ratio between their 10Å and 5Å reflections gives an indication of their crystal structure. Muscovite has a characteristic 10Å/5Å ratio of ~2, while biotite has a ratio of ~10 or more. These ratios are given in the tables. A more detailed discussion of each sample set is presented in the next paragraphs.

Table 8.3. Mineral composition of the non-weathered rock samples; bulk analyses XRD. Only the last four digits of the sample numbers are given in the table; i.e. 8501=108501. The phyllosilicates are marked yellow. The ratio 10Å/5Å = ratio of the 10Å and 5Å reflections of mica/illite (marked orange). Abbr.:tr=traces.

'Fresh Rock'	8501	8503	8505	8507	8509	8511	8513	8515	8520
Quartz	17	1	39	2	3	tr	26	27	2
K-feldspar	19	2	19	1	1	1	35	1	tr
Plagioclase	28	5	26	18	28	14	4	4	4
Amphibole	6	14	14	21	20	16	-	-	12
Pyroxene	-	1	-	-	-	-	-	-	-
Chlorite	-	-	-	55	37	22	-	-	73
Mica/Illite	30	70	1	-	3	39	31	41	2
Pyrophyllite	-	3	-	<0,5	3	2	-	-	4
Vermiculite	-	-	-	-	-	2	-	-	-
Pyrite	-	3	-	3	4	3	-	17	-
Magnetite	-	-	-	-	-	-	-	-	-
Carbonate	-	-	-	-	1	1	-	10	2
OpalCT	-	-	-	-	-				1
Anatase	-	-	<0.5	tr	-	-	4	-	-
Apatite	-	1	-	-	-	-	-	-	-
10Å/5Å	21	100	18	-	2.5	16	12	4	2

Table 8.4. **Mineral composition of the weathered rock samples; fraction <63 micron. The ratio 10Å/5Å = ratio of the 10Å and 5Å reflections of mica/illite. Only the last four digits of the sample numbers are given in the table; i.e. 8502=108502. The phyllosilicates are marked yellow, while the 10Å/5Å ratios of mica and illite are marked orange. The mineral called 'Mixed Layer" refers to a 10Å/14Å mineral of the type illite/vermiculite. Abbr.: tr=traces, *=vermiculite + smectite, #= chlorite + kaolinite.**

Weathered <63 micron	8502	8504	8506	8508	8510	8512	8514	8516	8517	8518	8521
Quartz	12	3	4	1	1	2	1	20	11	27	tr
K-feldspar	8	3	3	tr	tr	1	6	3	2	10	<0.5
Plagioclase	18	8	11	tr	4	7	-	-	6	14	<0.5
Amphibole	11	9	3	8	1	10	-	-	-	-	12
Chlorite	4	-	2	45	29	60	3	-	4#	1	68
Mica/Illite	14	3	10	1	tr	tr	10	56	64	30	1
Vermiculite	30	11	64	27	57	14*	74	-	4*	4*	16*
Mixed Layer	-	60	2	16	7	4	-	tr	1	9	-
Gibbsite	-	-	-	-	-	-	tr	-	-	tr	-
Pyrite	-	-	-	2	-	1	2	14	3	1	-
Jarosite	-	-	-	-	-	-	1	4	-	-	-
Gypsum	-	-	-	-	-	-	-	2	-	-	-
Goethite	-	-	-	-	-	-	3	-	-	-	-
OpalCT	3	1	1	-	1	1	-	-	5	4	-
Apatite	-	3	-	-	-	-	-	-	-	-	-
Carbonates	-	-	-	-	-	-	-	1	-	-	-
10Å/5Å	20	6	10	-	-	-	7	4	80	17	2

Table 8.5. Mineral composition of the weathered rock samples; fraction <6 micron in glycolated state. The ratio 10Å/5Å = ratio of the 10Å and 5Å reflections of illite. Only the last four digits of the sample numbers are given in the table; i.e. 8502=108502. The phyllosilicates are marked yellow, while the 10Å/5Å ratios of mica and illite are marked orange. Abbr.: tr=traces, Mixed Layer=10Å/14Å mixed layered mineral (illite/vermiculite).

Weathered <6micron. Ethylene Glycol	8502	8504	8506	8508	8510	8512	8514	8516	8517	8518	8521
Quartz	8	3	6	3	tr	1	13	3	2	18	1
K-feldspar	16	5	6	tr	tr	2	14	tr	2	5	-
Plagioclase	23	4	1	3	5	5	3	1	3	1	tr
Amphibole	-	14	-	4	-	-	-	-	-	-	3
Chlorite	7	4	14	82	83	83	2	4	11	7	81
Kaolinite	-	-	tr	-	-	-	-	-	6	-	-
Illite	33	11	35	4	4	2	28	90	67	32	1
Mixed Layer	-	54	-	4	8	5	-	-	-	tr	-
Smectite	-	-	-	-	-	2	-	-	9	36	14
Vermiculite	10	5	37	-	-	-	21	-	-	-	-
Gibbsite	-	-	-	-	-	-	5	-	-	-	-
OpalCT	3	-	1	-	-	-	tr	-	-	1	-
Pyrite	-	-	-	-	-	-	-	2	-	-	-
Goethite	-	-	-	-	-	-	5	-	-	-	-
Jarosite	-	-	-	-	-	-	3	-	-	-	-
10Å/5Å	3	2	4	-	-	-	3	2	7	4	-

8.6 Discussion of each pair of samples

A comparison of non-weathered and weathered rock samples from each sampling locality is given below. Phyllosilicates that are formed in the weathering zones are smectite, vermiculite and mixed-layered minerals (illite/vermiculite). These minerals are referred to as 'new-formed' phyllosilicates, and this is because only smectite is really authigenic; i.e. crystallised in the formation water of the weathering zone, while vermiculite and the illite/vermiculite mixed-layered mineral may have formed by degradation of biotite and chlorite.

Sample 108501 and 108502; Quartz-monzonite, Eiavatnet:

Table 8.6 and Figure 8.12 show the mineral composition of the non-weathered rock (108501) and the fractions <63 and <6 micron from the weathered zone (108512).

Table 8.6. Mineral composition of samples 108501 (non-weathered rock) and 108502 (weathered zone), where the fractions <63 micron and <6 micron are analysed. Abb.: ML= 10Å/14Å mixed layered minerals. Ratio 10Å/5Å = ratio between the 10Å and 5Å reflections of illite and mica.

Sample 108501 and 108502 <63 micron and <6 micron			
Minerals	Fresh	Weathered <63 micron	Weathered <6 micron
Quartz	17	12	8
K-feldspar	19	8	16
Plagioclase	28	18	23
Amphibole	6	11	0
Chlorite	0	4	7
Mica/Illite	30	14	33
Vermiculite	0	30	10
OpalCT	0	3	3
10Å/5Å	21	20	3

Composition of the fresh rock:

The rock is composed dominantly of quartz, two feldspars, mica and some amphibole (hornblende/actinolite). The high ratio between the mica reflections 10Å/5Å (~21) indicates a trioctahedral structure; e.g., biotite.

Composition of the fraction <63 micron; weathered zone:

The fraction <63 micron also contains abundant quartz and feldspars, but a large increase in phyllosilicates (marked yellow) and amphibole is seen. The new minerals identified here are vermiculite and opalCT. The high 10Å/5Å ratio for mica indicates that biotite is also present here.

Composition of the fraction <6 micron; weathered zone:

This fraction has similar contents of quartz and feldspars as the <63 micron fraction, but more phyllosilicates, and no amphibole and opalCT.

Comments:

- It is well known that biotite easily loses potassium by the leaching of meteoric water. This process causes an alteration of biotite to hydro-mica (alternating layers of biotite and vermiculite), and further to vermiculite (Coleman & Leroux 1963). Therefore, the vermiculite observed in the weathering zone is considered to be a weathering product of biotite. This process goes on also in boreal and arctic climates.
- The 10Å/5Å ratio for mica and illite is reduced from 20 to 3 in the fine fraction (<6 micron) of the weathered zone; indicating a more dominant content of dioctahedral illite. A typical 10Å/5Å ratio for muscovite is ~2. This indicates that most of the biotite in the fine fraction is altered to vermiculite, and that this fraction is enriched in dioctahedral illite; i.e. from sericite and muscovite in the parent rock.

- An increased content of chlorite in the <6 micron fraction is interpreted as an effect of the general trend of increasing contents of phyllosilicates in the finer grain-size fractions.
- An XRD reflection at 4.05Å in the fraction <63 micron indicates the presence of opalCT. It is suggested that this opalCT is a product of excess silica, released during dissolution of minerals (e.g., feldspars) in the weathering zone. OpalCT and amphibole are not seen in the fine fraction, indicating that small particles of these minerals are dissolving in the pore water.

An illustration of the mineral distribution for the three samples is given in Figure 8.12.

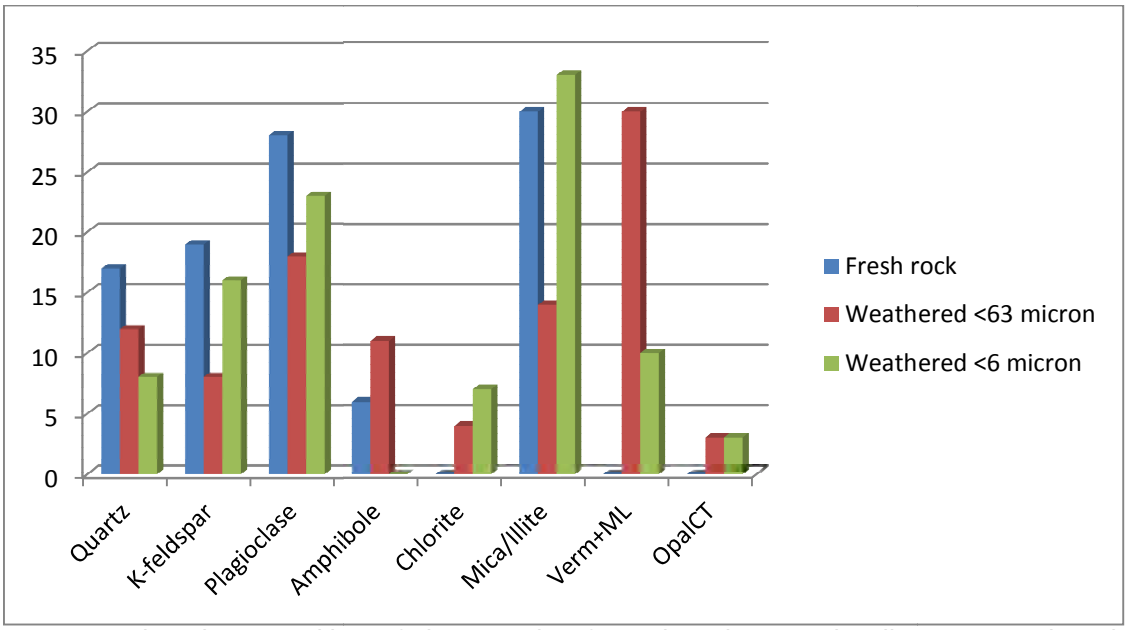

Figure 8.12. Mineral composition of the samples from the Eiavatnet locality; non-weathered rock (108501) and two fractions from the weathered zone; <63 micron and <6 micron (108502). The reduction in feldspar content and the increase in phyllosilicates in the weathering zone are illustrated. Amphibole and opalCT are not found in the fine fraction.

Sample 108503 and 108504; Pyroxenite, Karbøl, Misvær:

Table 8.7 and Figure 8.13 show the mineral composition for fresh rock (108503) and the fractions <63 and <6 micron from the weathered zone (108504).

Table 8.7. Mineral composition of samples 108503 (non-weathered rock) and 108504 (weathered rock), where the fractions <63 micron and <6 micron are analysed. Abb.: ML= 10Å/14Å mixed layered minerals. Ratio 10Å/5Å = ratio between the 10Å and 5Å reflections of illite and mica.

Sample 108503 and 108504, Pyroxenite, Karbøl, Misvær			
Minerals	Fresh rock	Weathered <63 micron	Weathered <6 micron
Quartz	1	3	3
K-feldspar	2	3	5
Plagioclase	5	8	4
Amphibole+Pyroxene	14+1	9+0	14+0
Chlorite	0	0	4
Mica/Illite+Pyrophyllite	70+3	3	11
Vermiculite+ML	0	11+60	5+54
Pyrite	3	0	0
OpalCT	0	1	0
Apatite	1	0	0
10Å/5Å	100	6	2

Composition of the fresh rock:

The rock is composed dominantly of mica and amphibole. The remaining minerals identified are feldspars and quartz, some pyrophyllite and small amounts of pyroxene and apatite. The exceptionally high ratio between the mica reflections 10Å/5Å (100) indicates a trioctahedral crystal structure. However, the ratio is much higher than what is commonly found for biotite (~10).

Composition of the fraction <63 micron; weathered zone:

The fraction <63 micron also contains mainly phyllosilicates (marked yellow), but here it is vermiculite and a 12Å mixed-layered mineral (ML) that dominate. The ML is interpreted to be illite/vermiculite. The 10Å/5Å ratio for mica indicates less biotite here. The remaining minerals are amphibole, feldspars and quartz; similar to the fresh rock. A new mineral identified is opalCT.

Composition of the fraction <6 micron; weathered zone:

The fine fraction has similar contents of quartz, feldspars and amphibole as the <63 micron fraction, but more phyllosilicates, and no opalCT.

Comments:

- It is well known that biotite easily loses potassium by the leaching of meteoric water. This process causes an alteration of biotite; initially to hydro-mica (alternating layers of biotite and vermiculite), and finally to vermiculite (Coleman & Leroux 1963). Therefore, the vermiculite observed in the weathering zone is considered to be a weathering product of biotite. This process goes on also in boreal and arctic climates.
- The 10Å/5Å ratio for mica and illite is reduced to 2 in the fine fraction (<6 micron) of the weathered zone; indicating mainly dioctahedral illite. This indicates that most of the

biotite in the fine fraction is altered to vermiculite, and that this fraction is enriched in dioctahedral illite; i.e. from sericite and muscovite in the parent rock.

- An XRD reflection at 4.05Å in the fraction <63 micron indicates the presence of opalCT. It is suggested that this opalCT is a product of excess silica, released during dissolution of minerals (e.g., feldspars) in the weathering zone. OpalCT is not seen in the fine fraction.

An illustration of the mineral distribution for the three samples is given in Figure 8.13.

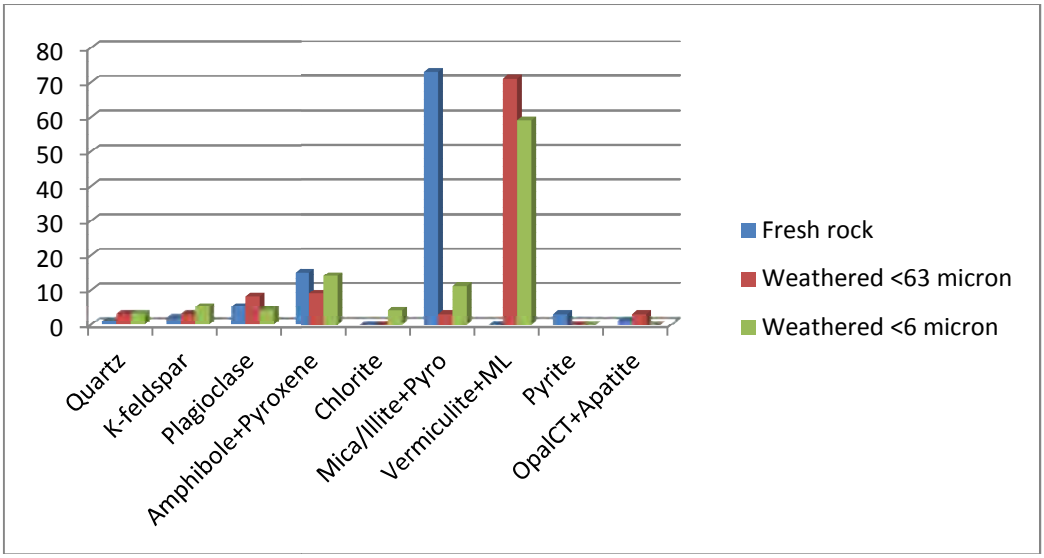

Figure 8.13. Mineral composition of the samples from Karbøl, Misvær: non-weathered rock (108503) and two fractions from the weathered zone; <63 micron and <6 micron (108504). A strong reduction in the content of mica is observed in the weathered samples, while new formed vermiculite and illite/vermiculite mixed-layered mineral is dominant here. OpalCT is only found in the <63 micron fraction of the weathered zone.

Sample 108505 og 108506, Granitic gneiss, Amundvatnet:

Table 8.8 and Figure 8.14 give the mineral composition of non-weathered rock (108505) and the fractions <63 and <6 micron from the weathered zone (108506).

Table 8.8. Mineral composition of samples 108505 (non-weathered rock) and 108506 (weathered rock), where the fractions <63 micron and <6 micron are analysed. Abb.: ML= 10Å/14Å mixed layered minerals. Ratio 10Å/5Å = ratio between the 10Å and 5Å reflections of illite and mica.

Sample 108505 and 108506, Granitic Gneiss, Amundvatnet			
Minerals	Fresh rock	Weathered <63 micron	Weathered <6 micron
Quartz	39	4	6
K-feldspar	19	3	6
Plagioclase	26	11	1
Amphibole	14	3	0
Chlorite	0	2	14
Mica/Illite	1	10	35
Vermiculite+ML	0	64+2	37+0
OpalCT+Pyrite	0	1+0	1+0
10Å/5Å	-	10	4

Composition of the fresh rock:
The rock is composed mainly of quartz feldspars and amphibole. Only 1% of mica is identified.

Composition of the fraction <63 micron; weathered zone:
The fraction <63 micron contains dominantly phyllosilicates (marked yellow), and the main mineral is vermiculite. A 12Å mixed-layered mineral (ML) is also identified. This ML is interpreted to be illite/vermiculite. The 10Å/5Å ratio for mica indicates biotite. The remaining minerals are feldspars, quartz and amphibole. OpalCT is also identified.

Composition of the fraction <6 micron; weathered zone:
The fine fraction is composed mainly of phyllosilicates, but also some feldspars and quartz. No amphibole and opalCT is found here. A 10Å/5Å ratio of 2.5 indicates a dioctahedral illite; i.e. a muscovite like structure.

Comments:

- The 'fresh rock' shows a composition representative of granitic gneiss. The weathered material, however, is very different from the 'fresh rock', by its dominating content of phyllosilicates. This difference may be explained (at least partly) by grain sizes, in that quartz and feldspars in the fresh rock have crystal sizes bigger than 63 micron. Still, the weathered zone is very different by its content of biotite, chlorite and abundant vermiculite. The 14Å X-ray reflection for this vermiculite is very sharp, indicating a well crystalline mineral. Because of the significant content of biotite in the <63 micron fraction, it is suggested that the vermiculite is a weathering product of biotite (like the previous sample).
- The <6 micron fraction has an even higher content of phyllosilicates than the <63 micron fraction. The 10Å/5Å ratio for mica and illite is reduced to 2.5 in the fine fraction (<6 micron) of the weathered zone; indicating mainly dioctahedral illite. This indicates that most of the biotite in the fine fraction is altered to vermiculite, or dissolved, and that this fraction is enriched in dioctahedral illite; i.e. from sericite and muscovite in the parent rock.
- An XRD reflection at 4.05Å in the fraction <63 micron indicates the presence of opalCT. It is suggested that this opalCT is a product of excess silica, released during dissolution of minerals (e.g., feldspars) in the weathering zone. OpalCT is not seen in the fine fraction.
- It is suggested that the weathering zone is a micaceous zone in the gneiss that is more permeable to the percolation of meteoric water. This has caused the weathering phenomena observed.
- The micaceous composition of the zone may be the result of previous hydrothermal activity.

An illustration of the mineral distribution for the three samples is given in Figure 8.14.

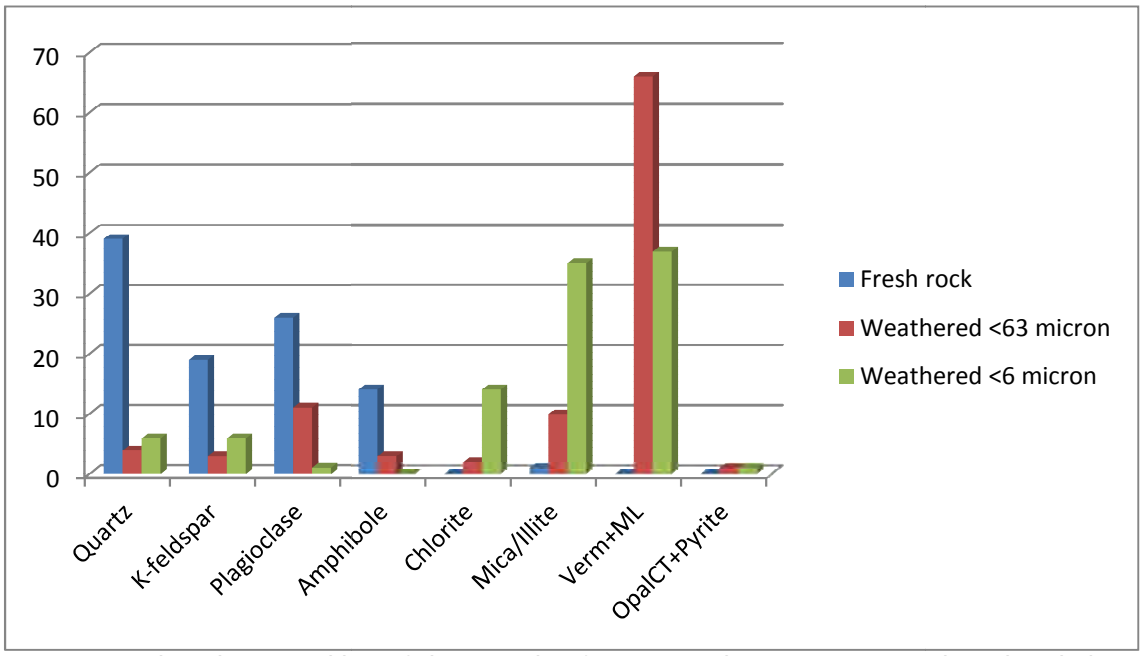

Figure 8.13. Mineral composition of the samples from Amundvatnet: non-weathered rock (108505) and two fractions from the weathered zone; <63 micron and <6 micron (108506). A strong reduction in the content of feldspars and quartz is observed in the weathered samples, while vermiculite and illite is increasing. No smectite is identified; only vermiculite ("Verm") and an illite/vermiculite mixed layered mineral. OpalCT and pyrite are only found in the weathered zone.

Sample 108507 and 108508, Greenstone, Liaåsen:

Table 8.9 and Figure 8.14 give the mineral composition of the non-weathered rock (108507) and the fractions <63 and <6 micron from the weathered zone (108508).

Table 8.9. Mineral composition of samples 108507 (non-weathered rock) and 108508 (weathered rock), where the fractions <63 micron and <6 micron are analysed. Abb.: ML= 10Å/14Å mixed layered minerals.

Sample 108507 and 108508, Greenstone, Liaåsen			
Minerals	Fresh rock	Weathered <63 micron	Weathered <6 micron
Quartz	2	1	3
K-feldspar	1	0	tr
Plagioclase	18	0	3
Amphibole	21	8	4
Chlorite	55	46	82
Mica/Illite	0	1	4
Vermiculite+ML	0	27+17	0+4
Pyrite	3	0	0

Composition of the fresh rock:

The rock is composed of chlorite, amphibole, feldspars and quartz. No mica is detected.

Composition of the fraction <63 micron; weathered zone:

The fraction <63 micron contains dominantly phyllosilicates (marked yellow), and the main minerals are chlorite, vermiculite and an illite/vermiculite mixed-layered mineral (ML). The remaining minerals are amphibole and small amounts of quartz and mica/illite.

Composition of the fraction <6 micron; weathered zone:

The fine fraction is also composed mainly of phyllosilicates (90%), chlorite and illite/vermiculite ML. Some amphibole, feldspars, quartz and anatase are also detected. No smectite is observed in the glycolated sample.

Comments:

- The 'fresh rock' shows a composition representative of greenstone.
- The weathered material <63 micron, however, is very different from the 'fresh rock', by its dominating content of phyllosilicates. The chlorite content is nearly the same as in the fresh rock, but in addition it contains abundant vermiculite and illite/vermiculite ML. The 14Å X-ray reflection for vermiculite is very sharp, indicating a well crystalline mineral with relatively large particle sizes (unlike, e.g., smectite).
- The precursor of vermiculite is frequently biotite, but no biotite is identified, either in the fresh rock or in the <63 micron fraction of the weathered rock. It is possible that biotite has been present in the weathering zone at an earlier stage. Another possibility is that the vermiculite is a degradation product of chlorite, but that is also pure speculation.
- The <6 micron fraction has an even higher content of phyllosilicates than the <63 micron fraction: some 80% chlorite and 8% illite/vermiculite ML.
- A minorl content of anatase in the fine fraction may be remnants of titanium oxide from dissolved minerals (Malm et al. 1984).

An illustration of the mineral distribution for the three samples is given in Figure 8.14.

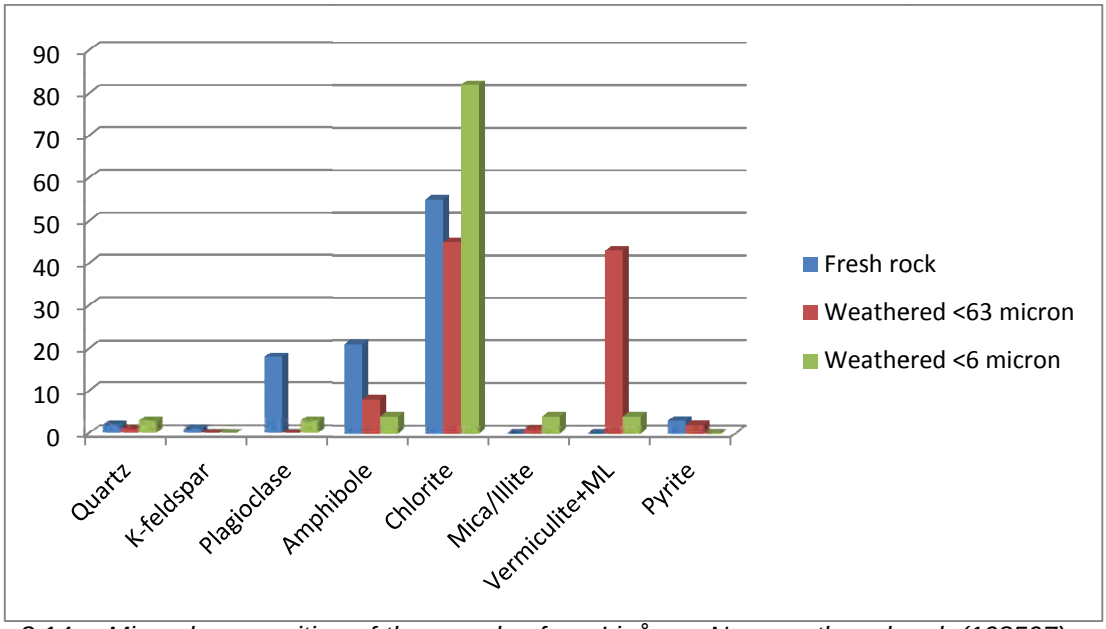

Figure 8.14. Mineral composition of the samples from Liaåsen. Non-weathered rock (108507) and two fractions from the weathered zone; <63 micron and <6 micron (108508). A strong reduction in the content of plagioclase and amphibole is observed in the weathered samples, while vermiculite and illite/vermiculite ML are increasing. Small amounts of anatase is found in the <6 micron fraction.

Sample 108509 and 108510, Greenstone, Liaåsen:

Table 8.10 and Figure 8.15 give the mineral composition of non-weathered rock (108509) and the fractions <63 and <6 micron from the weathered zone (108510).

Table 8.10. Mineral composition of samples 108509 (non-weathered rock) and 108510 (weathered rock), where the fractions <63 micron and <6 micron are analysed. Abb.: ML= 10Å/14Å mixed layered minerals. Pyroph=pyrophyllite, ML= 10Å/14Å mixed layered minerals. 10Å/5Å = ratio between the 10Å and 5Å XRD reflections of illite and mica.

Sample 108509 and 108510, Greenstone, Liaåsen			
Minerals	Fresh rock	Weathered <63 micron	Weathered <6 micron
Quartz	3	1	0
K-feldspar	1	0	0
Plagioclase	28	4	5
Amphibole	20	1	0
Chlorite	37	29	83
Mica/Illite+Pyroph	3+3	0	4
Vermiculite+ML	0	57+7	0+8
Pyrite+Ankerite	4+1	0	0
OpalCT	-	1	1
10Å/5Å	2,5	-	-

Composition of the fresh rock:

The rock is composed of chlorite, amphibole, feldspars and quartz. No mica is detected.

Composition of the fraction <63 micron; weathered zone:

The fraction <63 micron contains dominantly phyllosilicates (marked yellow), and the main minerals are chlorite, vermiculite and an illite/vermiculite mixed-layered mineral (ML). The remaining minerals are small amounts of amphibole, quartz and plagioclase.

Composition of the fraction <6 micron; weathered zone:

The fine fraction is also composed mainly of phyllosilicates; chlorite, illite and illite/vermiculite ML. Some plagioclase is also detected, but no smectite.

An illustration of the mineral distribution for the three samples is given in Figure 8.16.

Comments:

- The 'fresh rock' shows a composition very representative of greenstone.
- The weathered material <63 micron, however, is very different from the 'fresh rock', by its dominating content of phyllosilicates. The chlorite content is nearly the same as in the fresh rock, but in addition it contains an abundance of vermiculite and illite/vermiculite ML. The 14Å X-ray reflection for vermiculite is very sharp, indicating a well crystalline mineral with relatively large particle sizes (unlike, e.g., smectite).
- The precursor of vermiculite is frequently biotite, but no biotite is identified, either in the fresh rock or in the <63 micron fraction of the weathered rock. It is possible that biotite

has been present in the weathering zone at an earlier stage. Another possibility is that the vermiculite is a degradation product of chlorite, but that is also pure speculation.

- The <6 micron fraction has an even higher content of phyllosilicates than the <63 micron fraction: some 80% chlorite and 8% illite/vermiculite ML. No smectite is identified.
- Small amounts of feldspars in the fraction <6 micron may be a result of abrasion of the weathered feldspar particles during the dispersion and wet sieving.
- The small contents of pyrite and carbonate in the fresh rock are absent in the weathered samples.

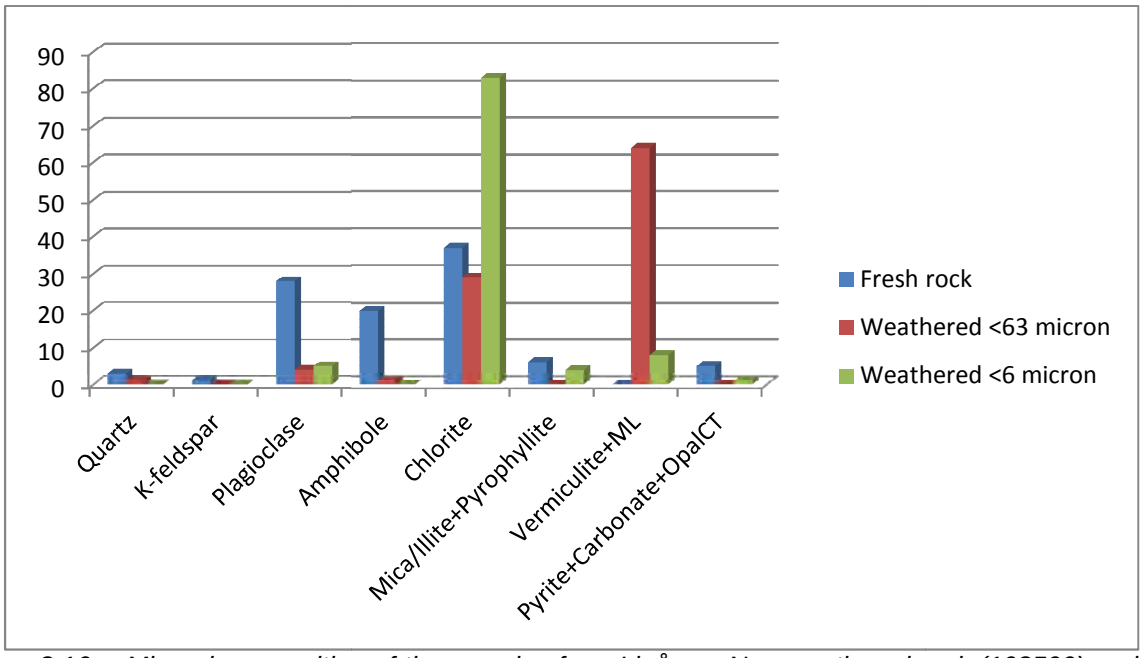

Figure 8.16. Mineral composition of the samples from Liaåsen. Non-weathered rock (108509) and two fractions from the weathered zone; <63 micron and <6 micron (108510). A strong reduction in the content of plagioclase and amphibole is observed in the weathered samples, while vermiculite and an illite/vermiculite mixed layered mineral are increasing. Pyrite and carbonate are absent in the weathered samples.

Sample108511 and 108512, Greenstone, Styggdalen:

Table 8.11 and Figure 8.17 give the mineral composition of non-weathered rock (108511) and the fractions <63 and <6 micron from the weathered zone (108512).

Table 8.11. Mineral composition of samples 108511 (non-weathered rock) and 108512 (weathered rock), where the fractions <63 micron and <6 micron are analysed. Abb.: Verm= vermiculite, ML= 10Å/14Å mixed layered mineral, 10Å/5Å = ratio between the 10Å and 5Å XRD reflections of illite and mica.

Sample 108511 and 108512, Greenstone, Styggdalen			
Minerals	Fresh rock	Weathered <63 micron	Weathered <6 micron
Quartz	0	2	1
K-feldspar	1	1	2
Plagioclase	14	7	5
Amphibole	16	10	0
Chlorite	22	60	83
Mica/Illite+Pyrophyllite	39+2	tr	2
Smectite/Vermiculite+ML	2+0	14+4	2+5
Pyrite+Carbonates	3+1	1+0	0
OpalCT	0	1	0
10Å/5Å	15,8	-	-

Composition of the fresh rock:
The rock is composed of chlorite, amphibole and feldspars (mainly plagioclase). No mica or quartz is detected.

Composition of the fraction <63 micron; weathered zone:
The fraction <63 micron contains dominantly phyllosilicates (marked yellow), and the main minerals are chlorite, vermiculite and an illite/vermiculite mixed-layered mineral (ML) (or smectite; see below). The remaining minerals are amphibole, opalCT, quartz and small amounts of feldspars and pyrite.

Composition of the fraction <6 micron; weathered zone:
The fine fraction is also composed mainly of phyllosilicates; chlorite, illite, smectite and illite/vermiculite ML. Some feldspars and quartz are also detected.

An illustration of the mineral distribution for the three samples is given in Figure 8.17.

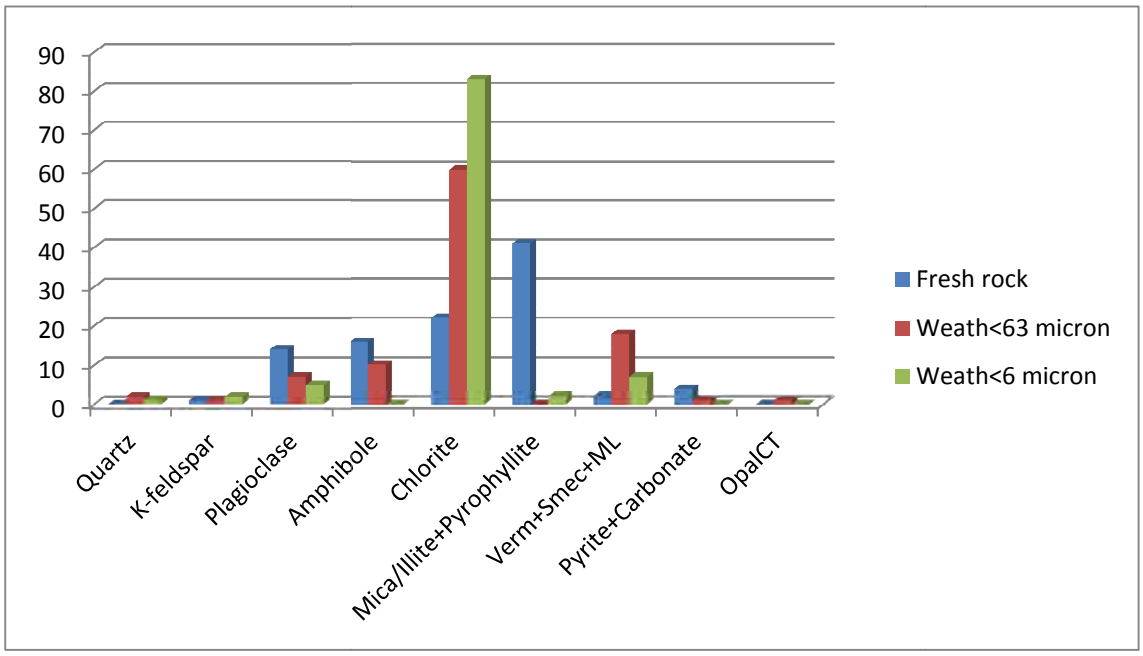

Figure 8.17. Non-weathered rock (108511) and two fractions from the weathered zone; <63 micron and <6 micron (108512). A strong reduction in mica/illite is observed in the weathered samples, while chlorite, vermiculite +smectite and illite/vermiculite ML are increasing. OpalCT is found in the <63 micron fraction of the weathered zone, but is not found in the fine fraction. Abb.: Verm= vermiculite; Smec=smectite; ML= mixed layered mineral (illite/vermiculite).

Comments:

- The 'fresh rock' shows a composition representative of greenstone, with the exception of having high contents of mica/illite. Generally, the greenstones have only small amounts of mica, but locally a significant content of sericite is observed (pers. comm. Tor Grenne, 2015).
- The weathered material <63 micron, however, is different from the 'fresh rock' by having no mica/illite, but the chlorite content is nearly twice that of the fresh rock. There are also significant contents of vermiculite and ML. The 14Å X-ray reflection for vermiculite is very sharp, indicating a well crystalline mineral with relatively large particle sizes (unlike e.g., smectite).
- The precursor of vermiculite is frequently biotite, but here no biotite is identified, neither in the fresh rock, nor in the <63 micron fraction of the weathered rock. Another possibility is that vermiculite is a degradation product of chlorite. The presence of opalCT in this fraction is suggested to be a product from the dissolution of silicate minerals (e.g., plagioclase and amphibole) in the weathering zone.
- The <6 micron fraction has an even higher content of phyllosilicates than the <63 micron fraction: some 80% chlorite, 8% illite/vermiculite ML and 2% smectite.
- Small amounts of feldspars in the fraction <6 micron may result from abrasion of weathered feldspar particles during dispersion and wet sieving.
- The opalCT and small contents of pyrite and carbonate in the fresh rock are absent in the weathered sample.

Sample 108513 and 14; Ustaoset:

Table 8.12 and Figure 8.18 give the mineral composition of non-weathered rock (108513) and the fractions <63 and <6 micron from the weathered zone (108514). The samples were collected at the surface.

Table 8.12. Mineral composition of samples 108513 (non-weathered rock) and 108514 (weathered rock), where the fractions <63 micron and <6 micron are analysed. Abb.: 10Å/5Å = ratio between the 10Å and 5Å XRD reflections of illite and mica.

Samples 108513 ('fresh rock') and 108514 (weathered); Ustaoset.			
Minerals	Fresh rock	Weathered <63 micron	Weathered <6 micron
Quartz	26	1	13
K-feldspar	35	6	14
Plagioclase	4	0	3
Chlorite	0	3	2
Mica/Illite	31	10	28
Vermiculite	0	74	21
Gibbsite	0	tr	5
Pyrite	0	2	0
Goethite	0	3	5
Jarosite	0	1	3
Anatase	4	0	6
OpalCT	0	tr	tr
10Å/5Å	12	7	3

Composition of the fresh rock:

The rock is a Precambrian gneiss, composed mainly of quartz, feldspars (mainly K-feldspar) and mica (biotite?). Some anatase is also detected.

Composition of the fraction <63 micron; weathered zone:

The fraction <63 micron contains dominantly phyllosilicates (marked yellow), and the main minerals are vermiculite, illite and chlorite. The remaining minerals are K-feldspar, pyrite, goethite and small amounts of quartz and jarosite.

Composition of the fraction <6 micron; weathered zone:

The fine fraction is also composed mainly of phyllosilicates; illite, vermiculite and chlorite. The remaining minerals are feldspars, quartz, anatase, gibbsite and goethite.

An illustration of the mineral distribution for the three samples is given in Figure 8.18.

Comments:

- The 'fresh rock' shows a syenitic composition and with high contents of mica. The high 10Å/5Å ratio on XRD indicates that the mica is biotite (Table 5.10).
- The weathered material <63 micron is different from the 'fresh rock' by having high contents of a 14Å mineral, interpreted to be vermiculite. The second XRD scan of the fine fraction in the glycolated state verified that the 14Å reflection represents

vermiculite; i.e., no swelling with glycol. Based on this fact, it is expected that the 14Å mineral in the <63 micron fraction is also vermiculite.

- A strong reduction in feldspars and quartz is seen in the <63 micron fraction. This is partly explained by bigger crystal sizes of these minerals, but dissolution is also an important factor.

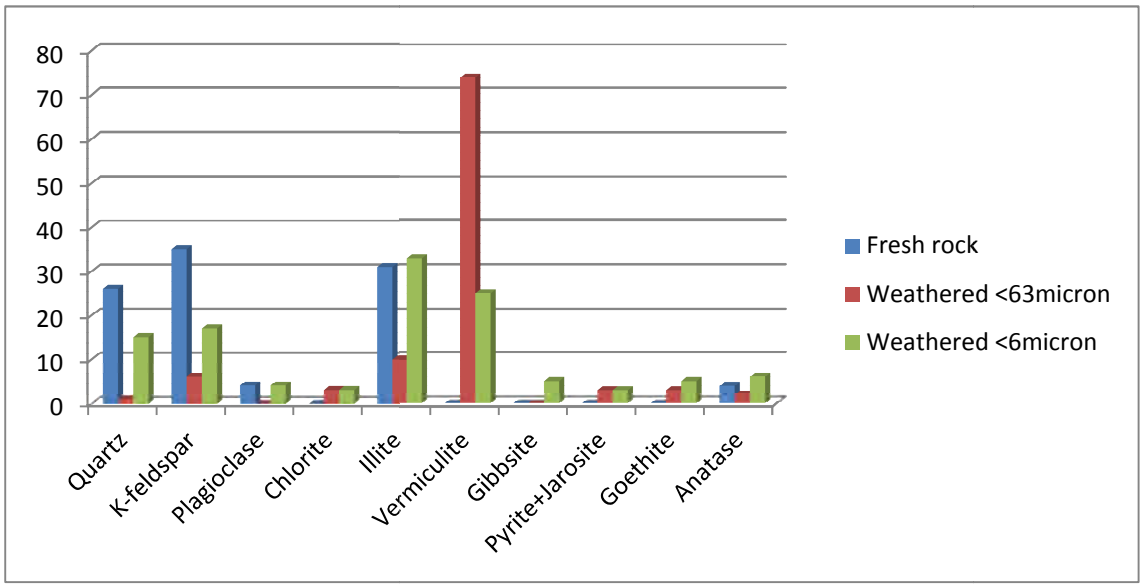

Figure 8.18 Mineral composition of the weathering zone at Uggen, Ustaoset: Fresh rock (108513) and the fractions <63 micron and <6 micron from the weathering zone (108514). The figure illustrates the reduction in quartz and feldspars in the weathered zone and the formation of vermiculite, gibbsite, jarosite and goethite.

- A 'new' mineral not seen in the fresh rock is chlorite. Chlorite may have formed from weathered biotite.
- The fine fraction (<6 micron) has a 10Å/5Å ratio of 3 for the mica/illite; i.e., much lower than the 7 of the <63 micron fraction, indicating a dioctahedral crystal structure of the illite in the fine fraction. This may be explained by two processes: 1) biotite is more vulnerable to weathering, by initially losing potassium and transforming into vermiculite. By further weathering, this trioctahedral vermiculite may dissolve completely. 2) Primary sericite (dioctahedral) in the feldspars will contribute to the fine fraction upon dissolution of the feldspars.

Sample 108515 and 108516, Alum shale, Heggvin, Hamar:

These samples are from a well drilled through Ordovician black shales at the waste disposal site Heggvin, run by Hamar municipality. The non-weathered rock (108515) is core material sampled from 69-72 m depth; and the weathered sample is core material collected from 21-24 m depth (108516). The fractions <63 and <6 micron from the weathered zone are analysed. Table 8.13 and Figure 8.19 give the mineral compositions.

Table 8.13. Mineral composition of samples 108515 (non-weathered rock) and 108516 (weathered rock), where the fractions <63 micron and <6 micron are analysed. Abb.: 10Å/5Å = ratio between the 10Å and 5Å XRD reflections of illite and mica.

Sample 108515 and 108516, Alum Shale, Hamar.			
Mineral	Fresh rock	Weathered <63 micron	Weathered <6 micron
Quartz	27	20	3
K-feldspar	1	3	0
Plagioclase	4	0	1
Chlorite	0	0	4
Illite	41	56	90
Pyrite+Jarosite+gypsum	17+0+0	14+4+2	2+0+0
Carbonates	10	1	0
10Å/5Å	4	4	2

Composition of the fresh rock:

The rock is Ordovician black shale, composed mainly of illite, quartz, pyrite and carbonates, and small amounts of feldspars.

Composition of the fraction <63 micron; weathered zone:

The fraction <63 micron contains dominantly illite. The remaining minerals are quartz, pyrite, jarosite, gypsum and some feldspar and carbonates.

Composition of the fraction <6 micron; weathered zone:

The fine fraction is also composed mainly of illite and chlorite. The remaining minerals are some pyrite, quartz and plagioclase.

An illustration of the mineral distribution for the three samples is given in Figure 8.19.

Comments:

- The 'fresh rock' shows a typical composition of Ordovician black shale in the Hamar region, with high contents of mica/illite, pyrite and carbonates (calcite and ankerite). The relatively low 10Å/5Å ratio on XRD indicates that the mica/illite is mainly dioctahedral.
- The weathered material <63 micron is similar to the 'fresh rock' by having high contents of illite, and with the same 10Å/5Å ratio, and only small amounts of carbonates and no plagioclase. The presence of jarosite and traces of gypsum in this sample demonstrates the weathering and oxidation of pyrite. It also indicates an acidic environment that dissolves carbonates and plagioclase.
- The fine fraction (<6 micron) contains 94% phyllosilicates; illite and chlorite, and small amounts of quartz and plagioclase. The 10Å/5Å ratio of illite is down to 2, indicating a dioctahedral illite. This means that either the trioctahedral illite is dissolved in the fine fraction or it is transformed into chlorite. The presence of chlorite is unexpected due to the supposedly acidic environment.

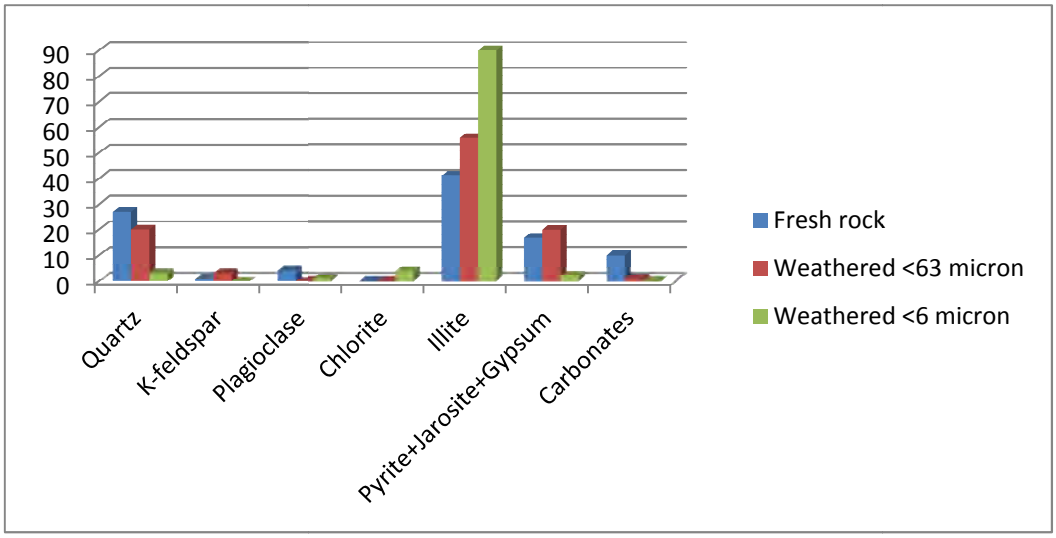

Figure 8.19. Mineral composition of Alum Shale at Heggvin, Hamar. The samples are core material from a newly drilled well. 'Fresh rock' sampled at 69-72 m depth (108515), and the fractions <63 micron and <6 micron from a 'weathering zone' at 21-24 m depth in the borehole (108516). The figure illustrates the reduction in quartz and feldspars and the increase in illite in the weathered zone. Jarosite and gypsum are formed from dissolved and oxidised pyrite. No carbonates are seen in the fine fraction of the weathered zone. The occurrence of chlorite in the weathered zone is difficult to explain in view of the supposedly acidic environment, but it may have formed from weathered biotite.

Sample 108517, Granite, Fyllingsdalen:

The sample is from a well drilled in Precambrian granitic rocks in Fyllingsdalen, Bergen. The material is collected from core material at a depth of 495.27-495.40 m. The sample is dispersed in water and wet sieved to obtain the fractions 4-0.063 mm and <0.063 mm. The fraction <6 micron is obtained by sedimentation in water. The mineral composition is given in Table 8.14 and Figure 8.19.

Table 8.14. Mineral composition of weathered rock; sample 108517, where the fractions <63 micron and <6 micron are analysed. Abb.: 10Å/5Å=ratio between the 10Å and 5Å XRD reflections of illite and mica.

Sample 108517, Weathered Granite, Fyllingsdalen. Core samples.		
Minerals	Weathered <63 micron	Weathered <6 micron
Quartz	11	2
K-feldspar	2	2
Plagioclase	6	3
Chlorite	2	11
Illite	64	67
Smectite	4	9
Mixed Layered	1	-
Kaolinite	2	6
OpalCT	5	0
Pyrite	3	0
10Å/5Å	80	7

Composition of the fraction <63 micron; weathered zone:
The fraction <63 micron contains dominantly mica/illite, some chlorite, smectite (or vermiculite) and kaolinite (marked yellow). The remaining minerals are quartz, feldspars, opalCT and pyrite.

Composition of the fraction <6 micron; weathered zone:
The fine fraction is also composed mainly of illite, smectite, kaolinite and chlorite. The remaining minerals are some quartz and feldspars.

An illustration of the mineral distribution for the three samples is given in Figure 8.20.

Comments:

- The high contents of mica/illite are mainly a grain size effect because quartz and feldspar crystals in the rock are generally larger than 63 micron. The high 10Å/5Å ratio on XRD indicates that this mica/illite is mainly trioctahedral; e.g., biotite.
- The <63 micron fraction has also a significant content of opalCT and pyrite, in addition to some quartz and feldspars. The OpalCT has been formed from silica from dissolved minerals and gives a hint of the degree of weathering. Pyrite indicates a reduced environment, where pyrite is stable. That is not unusual this far below the groundwater table (several hundred metres).
- The fine fraction (<6 micron) has 94% phyllosilicates; illite, smectite, kaolinite and chlorite. The 10Å/5Å ratio has come down to 7, indicating that this fraction is richer in dioctahedral illite. It is cautiously suggested that the chlorite is a transformation from biotite. Smectite is crystallised from dissolved minerals; e.g., feldspars.

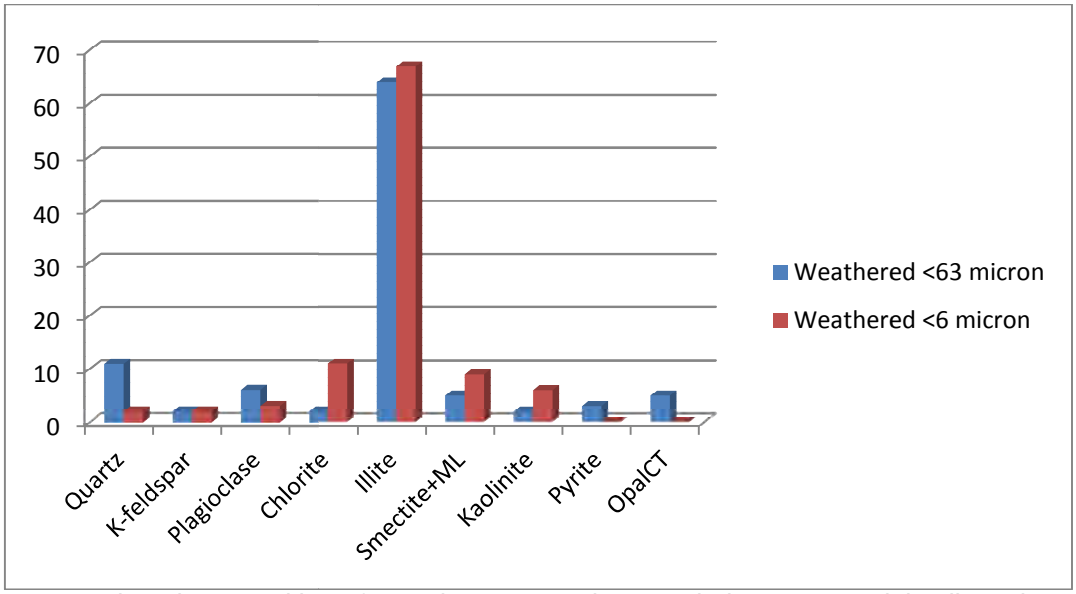

Figure 8.20. Mineral composition of sample 108517. The sample is core material collected at 495.27-495.40 m depth in a well drilled in granitic rocks. Illite is the main mineral in the <63 micron fraction of this weathered zone. More interesting, however, is the presence of smectite and kaolinite. The fine fraction (<6 micron) has even higher contents of phyllosilicates, mainly illite, chlorite, smectite and kaolinite.

Sample 108518, Granite, Fyllingsdalen:

The sample is from a well drilled in Precambrian granitic rocks in Fyllingsdalen, Bergen. The material is collected from core material at a depth of 514.27-514.44 m. The sample is dispersed in water and wet sieved to obtain the fractions 4-0.063 mm and <0.063 mm. The fraction <6 micron is obtained by sedimentation in water. The mineral composition is given in Table 8.15 and Figure 8.21.

Table 8.15. Mineral composition of weathered rock; sample 108518, where the fractions <63 micron and <6 micron are analysed. Abb.: ML= 10Å/14Å mixed layered mineral, 10Å/5Å=ratio between the 10Å and 5Å XRD reflections of illite and mica.

Sample 108518, Weathered Granite, Fyllingsdalen. Core sample.		
Minerals	Weathered <63 micron	Weathered <6 micron
Quartz	27	18
K-feldspar	10	5
Plagioclase	14	1
Chlorite	1	7
Illite	30	32
Smectite	4	36
Mixed Layered	9	0
OpalCT	4	1
Pyrite	1	0
10Å/5Å	17	4

Composition of the fraction <63 micron; weathered zone:

The fraction <63 micron of sample 108518 has a more 'granitic' composition compared to the previous sample, 108517. Quartz and feldspars constitute more than half of the material. The phyllosilicates are mica/illite, smectite, vermiculite, a 10Å/14Å mixed-layered mineral (ML) and some chlorite. The ML may be illite/vermiculite. OpalCT and pyrite are also seen in this sample. The relatively high 10Å/5Å ratio (17) indicates that the mica/illite is trioctahedral; e.g., biotite.

Composition of the fraction <6 micron; weathered zone:

The fine fraction is also composed mainly of illite, smectite and chlorite. The remaining minerals are some quartz and feldspars. Here, the 10Å/5Å ratio is down to 4, indicating a more dioctahedral illite.

An illustration of the mineral distribution for the two samples is given in Figure 8.21.

Comments:

- The higher contents of feldspars may be due to abrasion of mechanically weakened feldspar due to weathering. The high contents of mica/illite are mainly a grain size effect because quartz and feldspar crystals in the rock are generally larger than 63 micron. The high 10Å/5Å ratio on XRD indicates a trioctahedral mica/illite; e.g., biotite.

- The <63 micron fraction contains both vermiculite and smectite. The vermiculite is suggested to be degraded biotite; leached for potassium. A significant content of opalCT and pyrite is also seen, which is suggested to have formed from silica released during mineral dissolution. Pyrite indicates a reduced environment, where pyrite is stable. That is not unusual this far below the groundwater table (several hundred metres).
- The fine fraction (<6 micron) has 90% phyllosilicates; smectite, illite and chlorite. The 10Å/5Å ratio has come down to 4, indicating that this fraction is richer in dioctahedral illite. It is cautiously suggested that the chlorite is a transformation from biotite. Smectite is crystallised from dissolved minerals; e.g., feldspars. No kaolinite is seen.
- 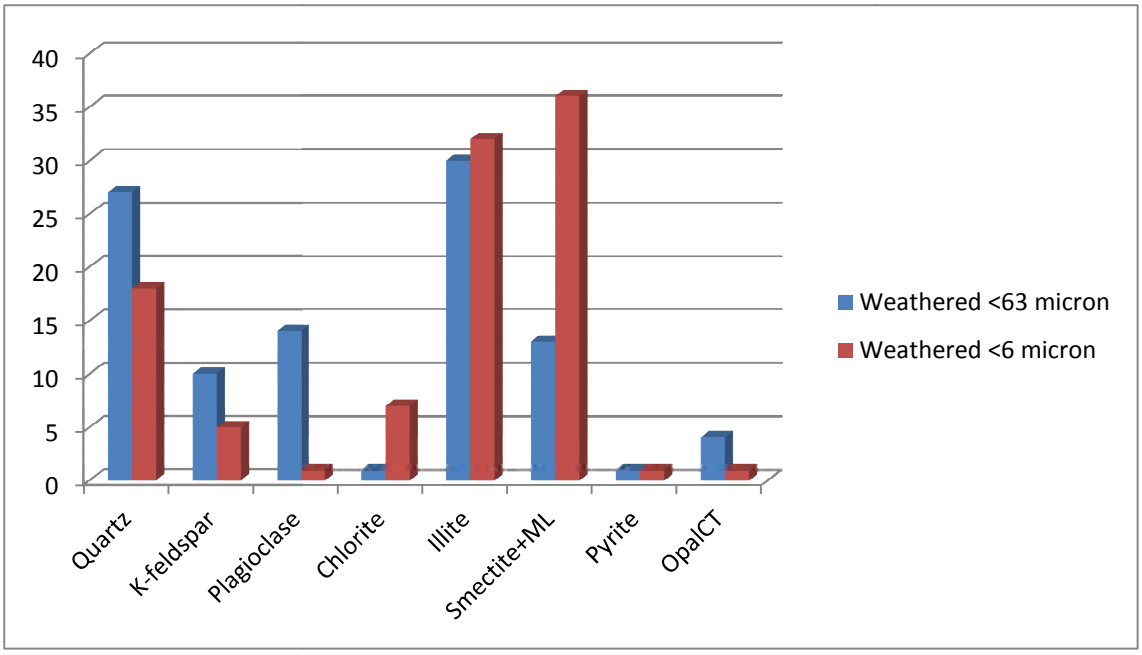

Figure 8.21. Mineral composition of sample 108518. The sample is the <63 micron fraction of core material collected at 514.27-514.44m m depth in a well drilled in granitic rocks. The main mineral in this weathered zone is illite. The fine fraction (<6 micron) is even richer in phyllosilicates, mainly illite, but also chlorite and smectite. No kaolinite is detected in this sample.

Samples 108520 and 108521, Greenstone, Lia Pukkverk, Trondheim:

Table 8.16 and Figure 8.22 give the mineral composition of non-weathered rock (108520) and the fractions <63 and <6 micron from the weathered zone (108521).

Table 8.16. Mineral composition of samples 108520 (non-weathered) and 108521 (weathered). Abb.: 10Å/5Å = ratio between the 10Å and 5Å XRD reflections of illite and mica.

Sample 108520 and 108521, Greenstone, Lia Pukkverk			
Minerals	Fresh rock	Weathered <63 micron	Weathered <6 micron
Quartz	2	0	1
K-feldspar	0	0	0
Plagioclase	4	0	0
Amphibole	12	12	3
Chlorite	73	68	81
Illite+Pyrophyllite	2+4	1+0	1+0
Smectite	0	16	14
Ankerite+OpalCT	2+1	0	0
10Å/5Å	2	2	

Composition of the fresh rock:
The rock is composed mainly of chlorite and amphibole. Additional minerals are plagioclase, quartz, mica/illite, pyrophyllite, carbonates and opalCT.

Composition of the fraction <63 micron; weathered zone:
The fraction <63 micron contains dominantly phyllosilicates (marked yellow), and the main minerals are chlorite and vermiculite. The remaining minerals are amphibole and small amounts of mica/illite.

Composition of the fraction <6 micron; weathered zone:
The fine fraction is also composed mainly of phyllosilicates (95%); chlorite and some illite. In addition there is some amphibole and quartz.

An illustration of the mineral distribution for the three samples is given in Figure 8.22.

Comments:

- The 'fresh rock' shows a typical greenstone composition. The low 10Å/5Å ratio indicates dioctahedral illite.
- The weathered material <63 micron is different mainly due to its content of smectite, and lacking feldspar and quartz.
- The <6 micron fraction has an even higher content of chlorite than the <63 micron fraction, and abundant smectite. OpalCT and carbonates have not been found in the fine fraction.

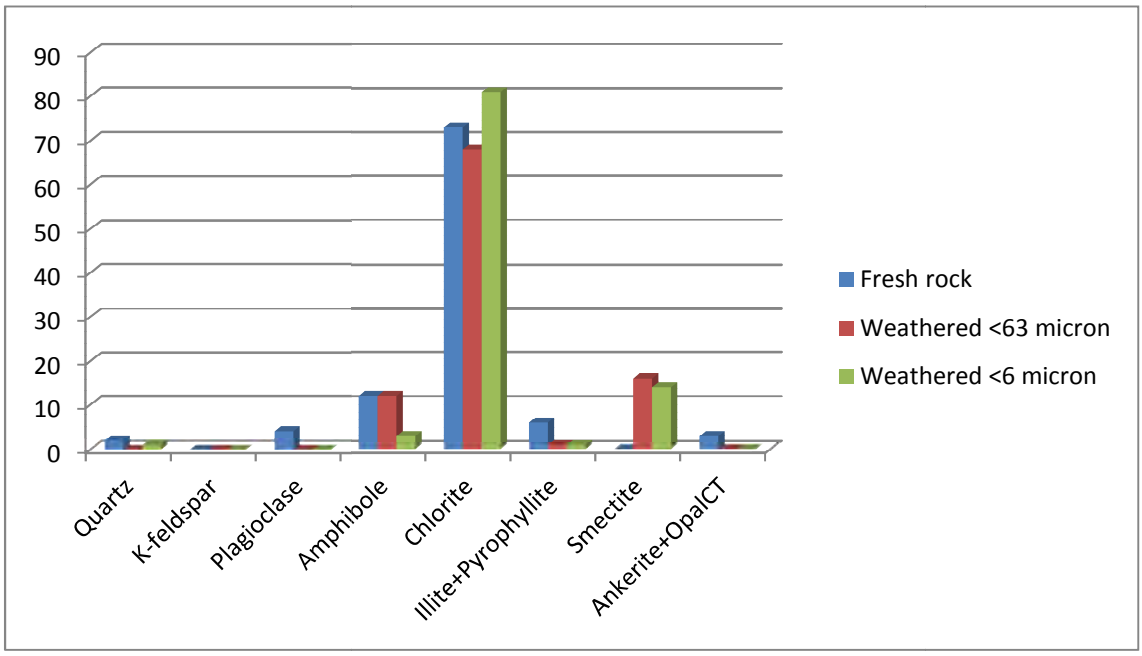

Figure 8.22. Mineral composition of sample 108520 and 108521 from Lia Pukkverk. The figure illustrates the increase of chlorite in the weathering zone. Smectite is identified in the <6 micron fraction, and is expected to be present in the <63 micron fraction, too.

8.6.1 Comparison of the four greenstone samples

Four of the sampling sites are in the greenstone belt of the Trondheim area; part of a Late Cambrian-Early Ordovician ophiolite. The composition of the samples is shown in the sections above. Here, the four samples, both fresh and weathered, are compared.

Fresh rock samples:

The composition of the non-weathered rocks are shown in Figure 8.23. The main minerals in all four samples are chlorite, plagioclase and amphibole. The main difference between the samples is that the sample Styggdalen 108511 has nearly 40% mica/illite, whereas the other three samples have small/negligible amounts.

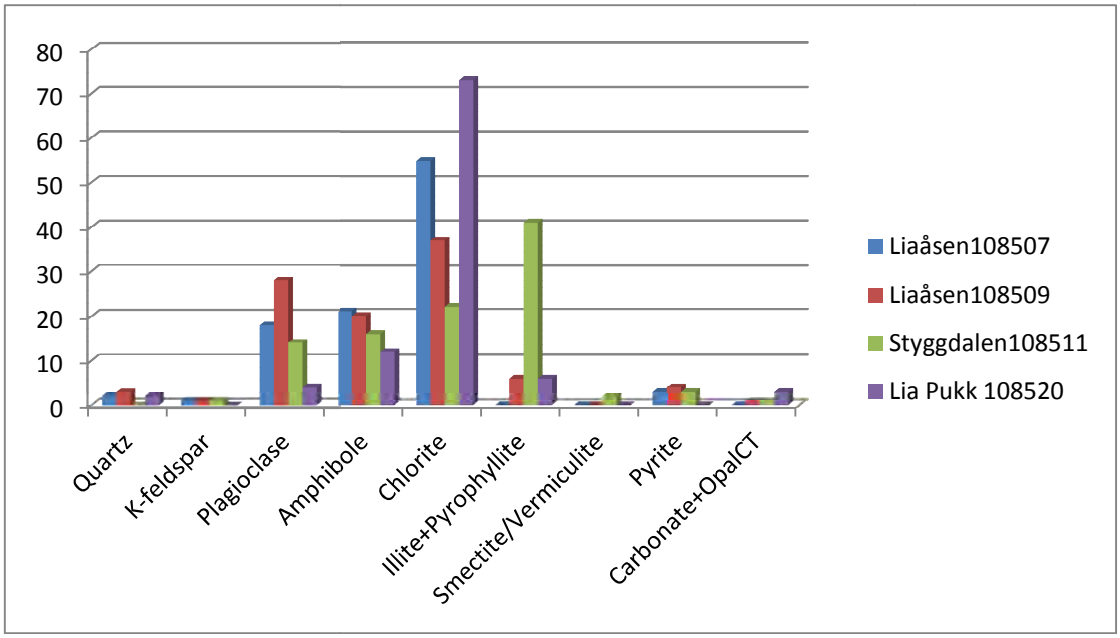

Figure 8.23. Mineral composition of the four non-weathered greenstone samples from the ophiolite in the Trondheim area. Generally, they have similar mineralogy, with chlorite, plagioclase and amphibole as the most abundant minerals. However, one of the samples, Styggdalen 108511, also has abundant mica/illite, whereas the other three samples, 108520, 108607 and 108509, have low contents of these minerals.

Fraction <63 micron from the weathered zones:

The composition of the <63 micron fractions of the weathered rocks are shown in Figure 8.24. All of the samples have an increased content of phyllosilicates compared to the non-weathered samples. It is also seen that the two samples from Liaåsen (108507 and 108509) have much less vermiculite and the illite/vermiculite mixed-layered mineral compared to the other two samples.

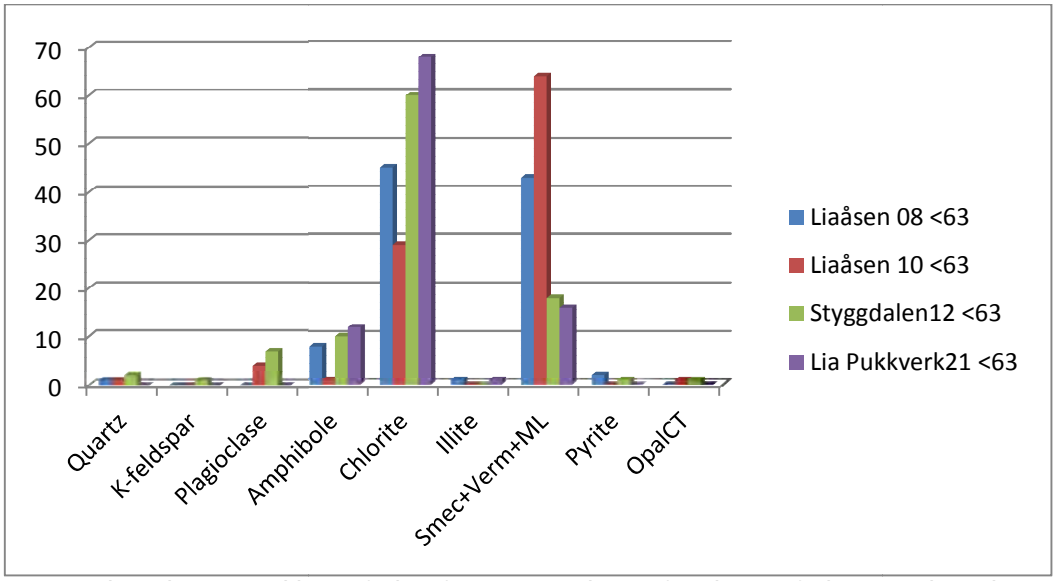

Figure 8.24. Mineral composition of the four <63 micron fractions of the weathered greenstone samples. All four samples have increased their contents of phyllosilicates compared to the non-weathered ones. The most important minerals are chlorite, vermiculite and illite/vermiculite mixed-layered mineral (ML). However, the samples Styggdalen (108512) and Lia Pukkverk (108521) have significant contents of smectite. Sample 108512 also contains a significant amount of opalCT, not seen in the non-weathered rock.

Fraction <6 micron from the weathered zones:

The compositions of the <6 micron fractions of the weathered rocks are shown in Figure 8.25. All of the samples have an increased content of phyllosilicates compared to the <63 micron fraction. The four samples are also very similar in composition, and chlorite is by far the most important mineral. Smectite is identified in the samples from Lia Pukkverk (21) and Styggdalen (12), and sample 21 is the more weathered of these two.

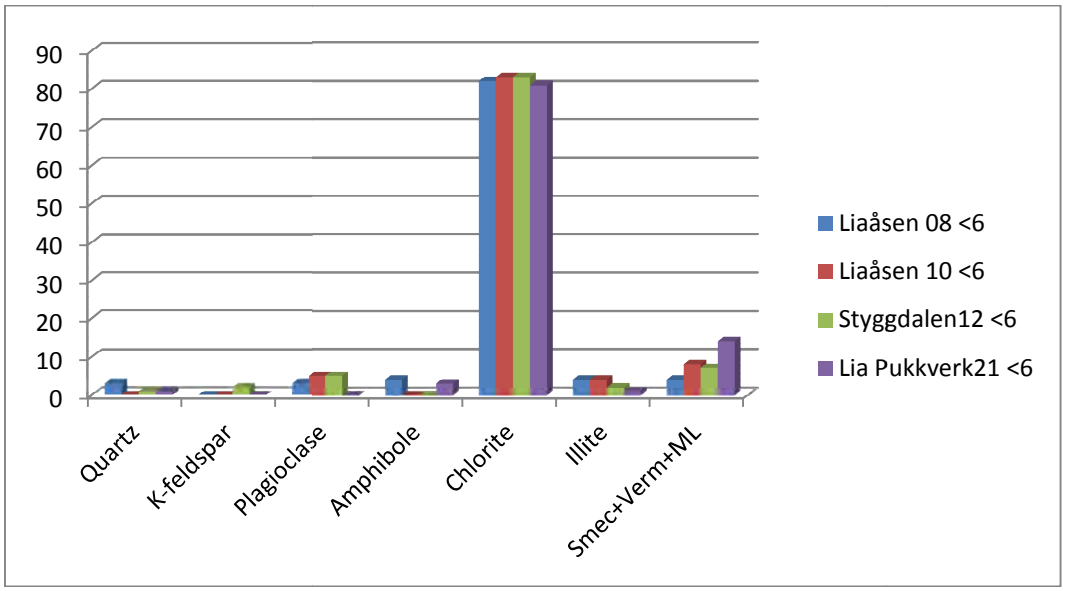

Figure 8.25. Mineral composition of the fraction <6 micron from the four weathered samples. Generally, they have similar mineralogy, with chlorite being the most abundant mineral. Two of the samples (108512 and 108521) also contain smectite, and three of the samples contain the illite/vermiculite mixed-layered mineral.

8.7 Geochemistry from XRF

The preparation of the samples prior to XRF analysis is explained above in section 8.2, and the results of the main element analyses are given in Table 8.17 and some trace elements in Table 8.18. The chemistry of the samples is serving two main purposes:

- Evaluate the weathering phenomena, with respect to leaching and mineral changes.
- Evaluate the XRD data, with respect both to mineral identification and to quantification.

The approach taken to make these evaluations is by cross-plotting XRD and XRF data. The first plot is to study the covariation of two important parameters from the XRF analyses; iron content and ignition loss, Figure 8.26.

Table 8.17. XRF analysis of main elements of fresh rock and fractions <63 micron of weathered samples, based on melted pills with lithium-tetraborate.

Sample id.	SiO_2	$Al2O_3$	$Fe2O_3$	TiO2	MgO	CaO	Na_2O	K2O	MnO	P_2O_5	Ignition loss	Sum
*	[%]	[%]	[%]	[%]	[%]	[%]	[%]	[%]	[%]	[%]	[%]	[%]
108501	68,2	14,7	3,70	0,335	0,113	1,27	4,12	5,89	0,081	0,050	0,185	98,7
108502	49,4	13,2	13,0	1,77	0,331	3,81	3,20	3,65	0,518	0,720	6,74	96,4
108503	46,3	11,2	10,6	1,03	11,4	8,14	1,55	4,56	0,183	1,07	1,63	97,6
108504	40,4	12,1	15,7	2,40	6,34	4,91	2,50	2,57	0,319	1,45	9,19	97,9
108505	74,2	11,8	2,95	0,347	0,060	0,529	3,45	5,10	0,085	0,028	0,180	98,7
108506	39,0	11,4	23,0	2,02	0,868	2,11	2,42	2,23	0,667	0,356	13,8	97,8
108507	49,9	15,8	11,2	0,828	7,91	4,95	4,47	0,164	0,171	0,075	3,30	98,8
108508	36,6	13,0	20,6	0,866	8,99	5,14	0,69	0,699	0,476	0,120	11,2	98,3
108509	53,9	16,1	7,85	0,893	6,69	4,31	5,55	0,474	0,098	0,109	2,60	98,5
108510	36,0	15,3	19,0	1,12	8,95	2,73	1,78	0,809	0,450	0,181	12,5	98,8
108511	47,1	15,9	9,81	1,15	6,80	8,05	4,19	1,48	0,149	0,063	3,89	98,7
108512	47,5	15,4	11,4	1,32	9,72	3,76	3,64	0,628	0,260	0,081	5,36	99,1
108513	61,7	17,5	1,76	0,506	0,975	0,432	0,76	12,1	0,060	0,099	2,27	98,2
108514	41,8	17,9	11,9	1,24	4,64	1,27	0,30	6,59	0,296	0,441	11,6	98,0
108515	42,6	11,2	10,5	0,611	1,22	8,41	0,23	3,13	0,091	0,132	14,7	92,9
108516	43,8	16,5	8,67	0,924	1,24	1,36	0,22	4,65	0,030	0,177	20,5	98,1
108517	50,6	16,2	10,7	0,970	2,06	2,02	2,47	3,07	0,121	0,628	8,41	97,2
108518	57,7	17,5	5,44	0,611	1,71	1,78	1,53	3,21	0,055	0,256	8,46	98,3
108520	42,0	15,5	11,7	0,759	12,0	8,95	1,52	0,283	0,126	0,073	5,41	98,3
108521	37,4	13,8	13,3	0,632	18,8	4,58	0,49	0,431	0,179	0,047	9,29	99,0

Table 8.18. XRF analysis of trace elements of fresh rock and fractions <63 micron of weathered samples, based on melted pills with lithium-tetraborate.

BaO	Cr_2O_3	CuO	NiO	PbO	SrO	ZnO	V2O5	ZrO_2	SO_3
[%]	[%]	[%]	[%]	[%]	[%]	[%]	[%]	[%]	[%]
0,053	<0.02	<0.01	<0.01	<0.01	<0.04	0,017	<0.02	0,080	<0.1
<0.025	<0.02	0,015	<0.01	<0.01	<0.04	0,042	0,022	0,447	<0.1
0,303	0,078	<0.01	0,023	<0.01	0,180	0,016	0,053	0,040	<0.1
0,315	<0.02	0,023	<0.01	<0.01	0,083	0,029	0,081	0,070	<0.1
<0.025	<0.02	<0.01	<0.01	<0.01	<0.04	0,010	<0.02	0,094	<0.1
<0.025	<0.02	<0.01	<0.01	<0.01	<0.04	0,065	0,021	0,110	<0.1
<0.025	0,065	<0.01	0,024	<0.01	<0.04	0,013	0,044	<0.02	<0.1
<0.025	0,068	<0.01	0,025	<0.01	<0.04	0,034	0,048	<0.02	<0.1
<0.025	0,040	<0.01	0,013	<0.01	<0.04	<0.01	0,051	<0.02	<0.1
<0.025	0,072	0,031	0,022	<0.01	<0.04	0,017	0,080	<0.02	<0.1
<0.025	0,046	<0.01	0,013	<0.01	<0.04	<0.01	0,053	<0.02	<0.1
<0.025	0,052	0,030	0,019	<0.01	<0.04	0,013	0,056	<0.02	<0.1
0,338	<0.02	<0.01	<0.01	<0.01	<0.04	<0.01	<0.02	0,039	<0.1
0,206	<0.02	<0.01	<0.01	0,019	<0.04	0,026	0,039	0,056	<0.1
0,107	<0.02	0,022	0,016	<0.01	<0.04	0,018	0,067	<0.02	5,15
0,182	0,021	0,028	0,037	<0.01	<0.04	0,014	0,148	<0.02	0,49
<0.025	<0.02	<0.01	<0.01	<0.01	<0.04	0,025	<0.02	0,059	0,59
<0.025	<0.02	0,010	<0.01	<0.01	<0.04	0,023	<0.02	0,042	0,29
<0.025	<0.02	0,563	<0.01	<0.01	<0.04	<0.01	<0.02	<0.02	<0.1
<0.025	0,086	<0.01	0,029	<0.01	<0.04	<0.01	0,054	<0.02	<0.1
<0.025	0,241	0,021	0,090	<0.01	<0.04	0,013	0,036	<0.02	<0.1

The good covariation of these two parameters is caused mainly by the fact that the weathered material is represented only by their <63 micron fractions, whereas the fresh rocks are prepared as bulk samples. This means that the fresh rocks contain more coarse crystalline material, e.g., quartz and feldspars, while the <63 micron fractions are enriched in phyllosilicates, with higher ignition losses and also higher iron contents. Since every second sample (odd numbers) from sample 108501 through to 108516 is of non-weathered rocks, they have lower ignition losses compared to the weathered ones (even numbers). Exceptions are samples 108517 and -18, which are both of weathered material. Samples -20 and -21 are greenstone samples from Lia Pukkverk, where number -20 is fresh rock and -21 is the weathered one.

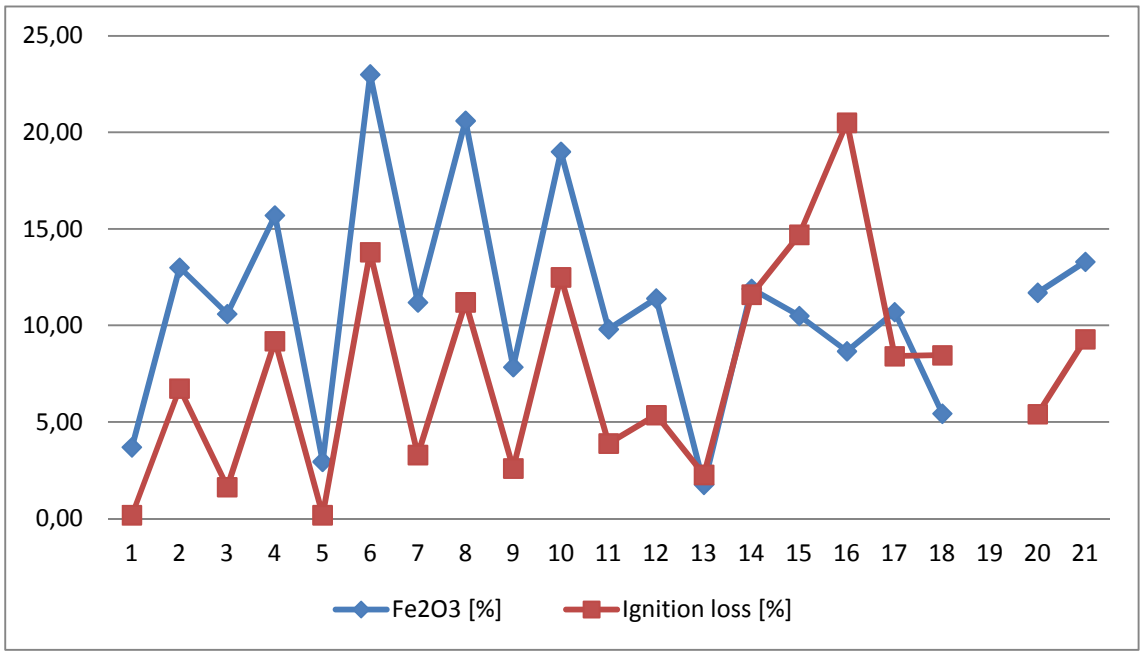

Figure 8.26. XRF data in weight-% from Table 8.17. A covariation plot for Ignition loss (weight %) versus iron content (Fe_2O_3 weight%) for the entire sample sets. The numbers along the x-axis corresponds to the last two integers of the sample numbers. Every second sample (odd numbers) from sample 108501 through to 108515 is of fresh rocks, and they are characterised by having lower ignition losses and iron contents compared to the corresponding weathered ones (even numbers). This is caused by the fact that phyllosilicates and iron-bearing minerals are more abundant in the fraction <63 micron than in the corresponding bulk fresh rock samples. Consequently, the <63 fractions have higher ignition losses and higher iron contents than the corresponding fresh rock samples. Samples 108517 and -18 are both of weathered material <63 micron. Samples 108520 and -21 are greenstone samples, where number -20 is the fresh rock and -21 the weathered one.

Leaching of base cations ($CaO + Na_2O + K_2O$) may be used as a proxy for weathering, because it may indicate dissolution of feldspars.

As seen on the previous figure (Figure 8.27), ignition loss is a proxy for the enrichment of (partly new-formed) phyllosilicates (e.g., smectite, vermiculite and mixed-layer minerals) in the weathered zone, and is, thus, also an indication of weathering. A cross-plot of Ignition loss versus base cations is shown in Figure 8.27. A clear trend is seen of increasing ignition loss with decreasing base cations.

The two samples of Alum Shale (108515 and 108516) are falling above the trend, due to their high contents of phyllosilicates, carbonates, and also some jarosite (in the weathered sample -16).

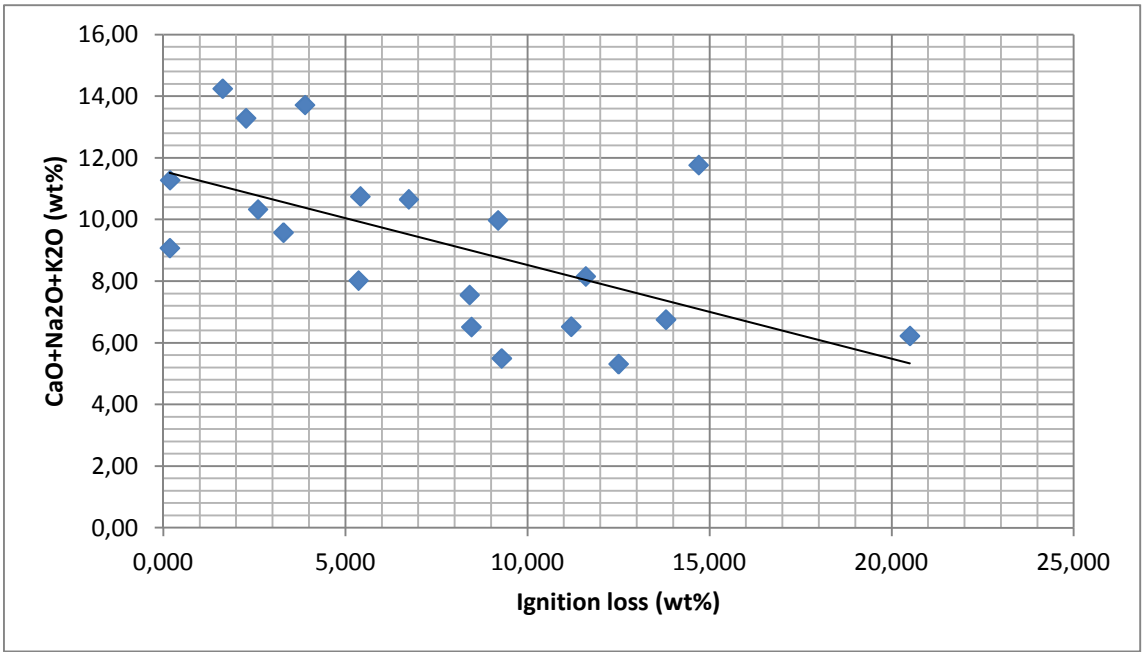

Figure 8.27. XRF data in weight%. Ignition loss is plotted versus the sum CaO + Na_2O + K_2O for all of the samples 108601 through to 108521. A clear trend is seen, with increasing ignition loss at decreasing contents of base cations. The two samples above the trend are the Alum Shale samples, 108515 and 108516, with carbonates and high contents of phyllosilicates.

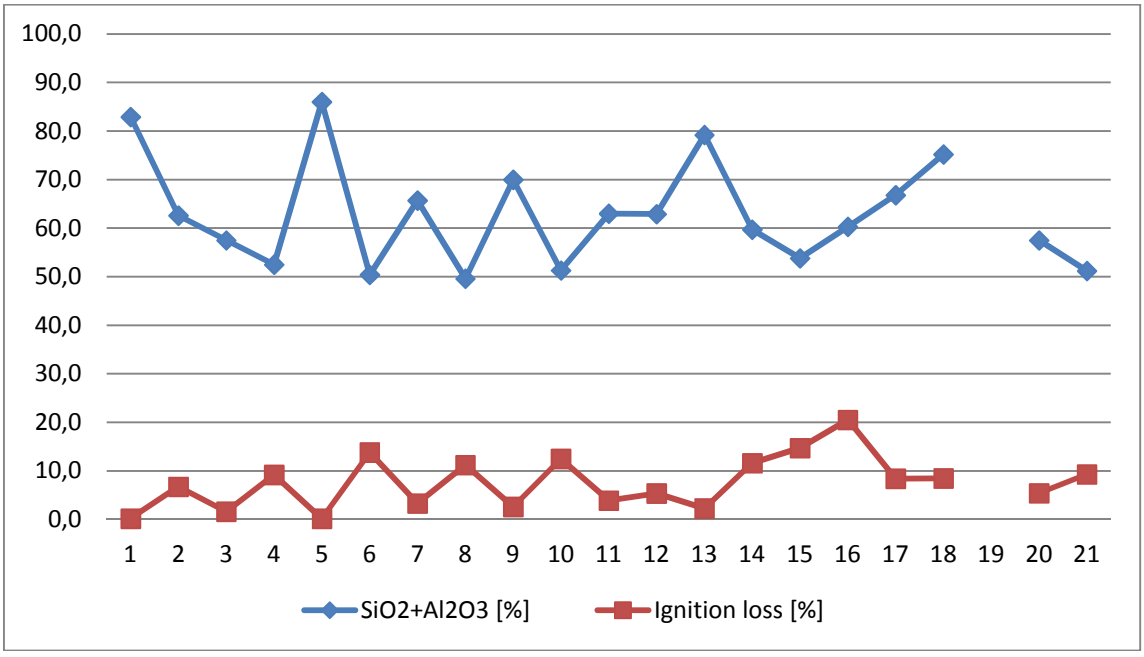

Figure 8.28. XRF data in weight%. Variation of SiO2 + Al_2O_3 and Ignition loss, for all samples 108601 through to 108521. The numbers along the x-axis correspond to the last integers in the sample numbers. SiO_2 + Al_2O_3 is seen to be much higher for the fresh rocks (odd numbers) compared to their respective weathered ones (even numbers, except samples 108517 and 108521 that are also weathered samples). The ignition loss shows higher values for the weathered samples (also demonstrated in Figure 8.26).

Figures 8.26 and 8.27 indicate that ignition loss is a proxy for increased weathering. This is mainly due to three factors:

- Increased contents of phyllosilicates in the fraction <63 micron due to sieving off the larger tectosilicate grains (quartz, feldspars and rock fragments).
- Weathered samples are enriched in phyllosilicates; both due to dissolution of other minerals.
- The formation of new clay minerals; e.g., smectite.

8.7.1 Correlation between XRF and XRD data

Quantification of mineralogy from XRD alone is associated with significant uncertainty. It is therefore of interest to study and compare the main components from the two datasets; XRD and XRF.

Figure 8.29 shows a cross-plot of quartz + feldspars (XRD data) versus SiO_2 + Al_2O_3 (XRF data). Even though SiO_2 + Al_2O_3 are main elements also in the phyllosilicates, a good correlation is seen, particularly for the samples with high values of quartz + feldspars. This indicates that the interpretation of the XRD data is acceptable.

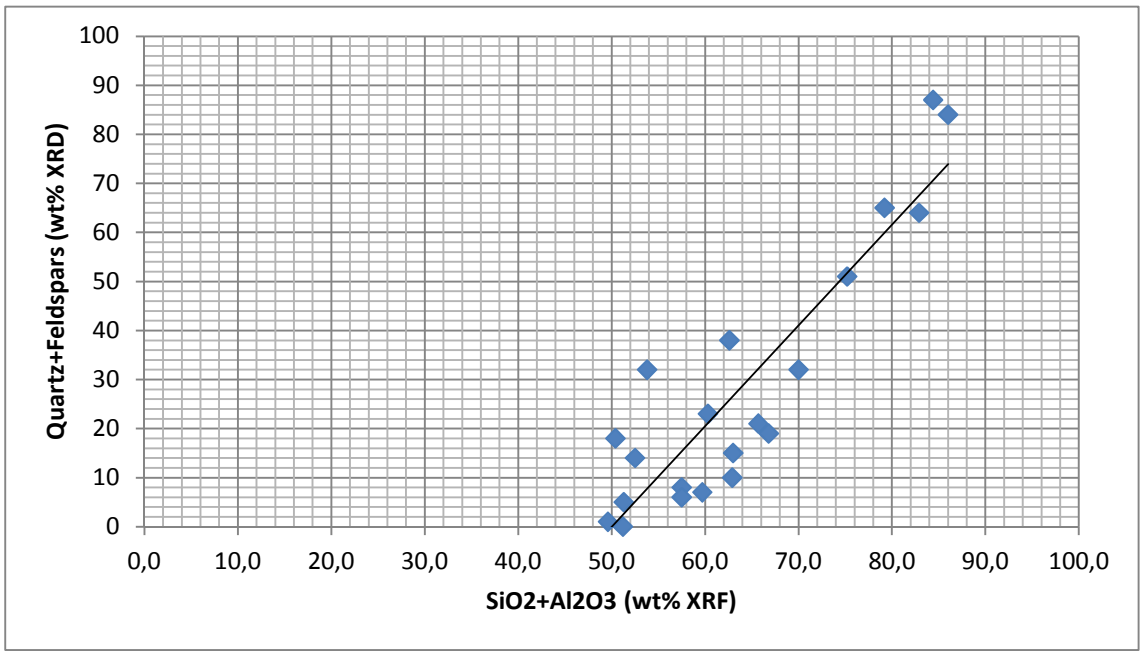

Figure 8.29. SiO_2 + Al_2O_3 from chemical analysis (Table 6.1) plotted versus content of quartz and feldspars for all of the samples 108601 through to 108521. Quartz and feldspars are abundant minerals in many of the samples and, thus, a good correlation with the chemical data indicates an acceptable quantification of the XRD data. The statistical correlation line is included in the figure.

A cross-plot with sum phyllosilicates versus Fe_2O_3 + MgO is shown in Figure 8.30. A good trend is seen, which is mainly an effect of the fact that most of the samples contain ferromagnesian phyllosilicates; e.g., chlorite and biotite.

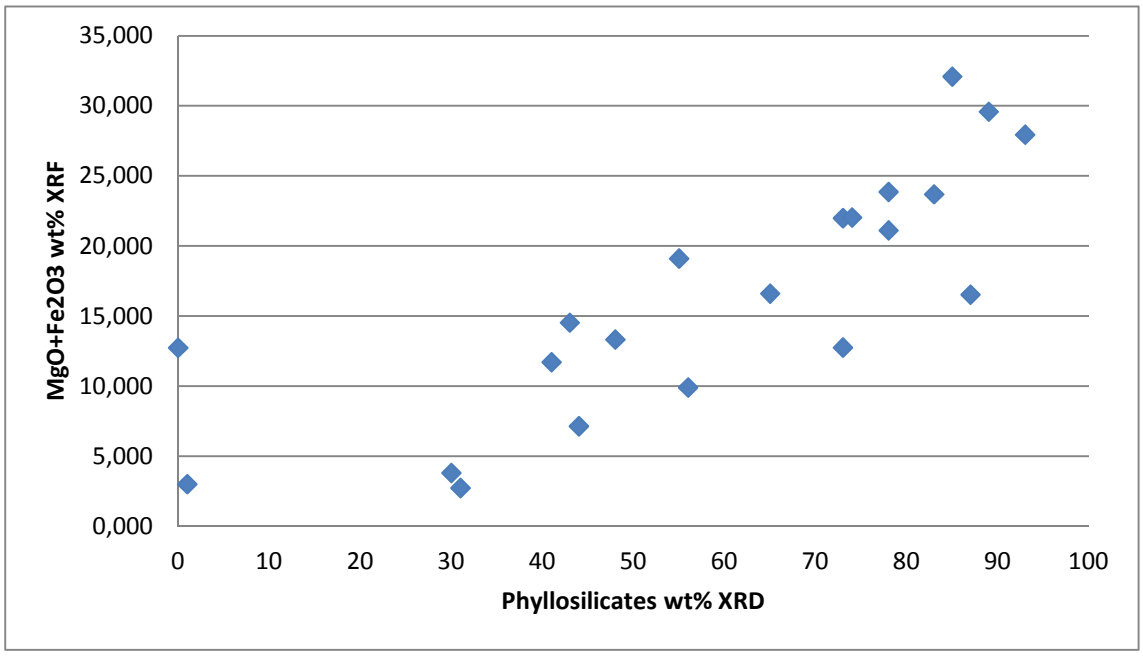

Figure 8.30. *MgO + Fe_2O_3 from chemical analysis (Table 8.17) plotted versus content of phyllosilicates for all samples 108601 through to 108521. MgO + Fe_2O_3 increase with increasing contents of phyllosilicates. Sample 108519 falls outside the trend, with 12.7% Fe_2O_3 and no phyllosilicates.*

Phyllosilicates have higher ignition losses due to their content of OH-groups in the crystal lattice. 'New-formed' phyllosilicates in the weathering profiles; e.g., smectite, vermiculite and mixed-layered minerals (mainly illite/vermiculite) are therefore characterised by high ignition losses. The phyllosilicates in most of the samples are also associated with iron (shown in Figure 8.30). This relationship is demonstrated in Figure 8.31 where the co-variation between ignition loss, iron (Fe_2O_3), and the sum of the three phyllosilicates smectite + vermiculite + mixed-layered minerals is illustrated.

A particularly good co-variation is seen for the samples 108601 through to 108514. The two samples 108515 and 108516 are Alum Shale, containing abundant illite, carbonates and pyrite, and the weathered sample also contains jarosite (oxidation product from pyrite + potassium from etched illite). Samples 108517 and 108518 are weathered samples (<63 micron fraction), and samples 108520 (fresh rock) and 108521 (weathered rock) are the two greenstone samples from Lia Pukkverk.

The four weathered greenstone samples are 108508, -10, -12, and -21, and it is a bit strange that the two most weathered of them, namely -12 and -21, are the ones with the lowest contents of 'new-formed' phyllosilicates. However, the new-formed mineral in these samples is smectite, which indicates a profound chemical weathering in a warm/temperate and humid climate. The 'new-formed' minerals in the other two samples are vermiculite and the illite/vermiculite mixed-layered mineral, which is probably degraded biotite and possibly also with some chlorite.

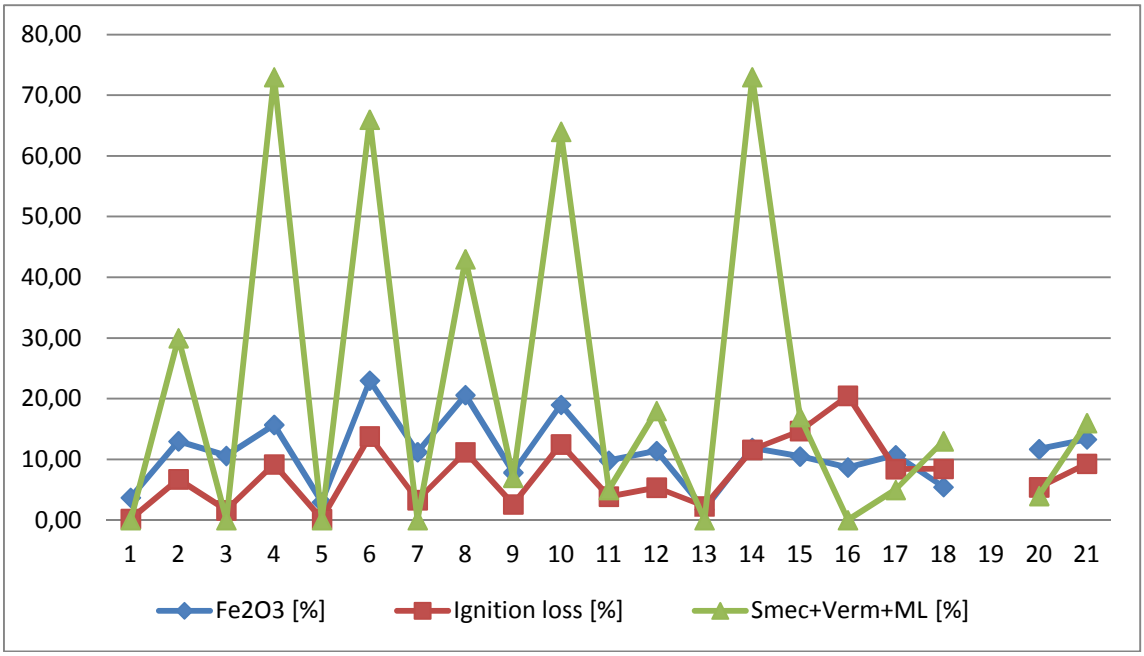

Figure 8.31. Variations in ignition loss for the entire sample sets, 108601 through to 108521 (data in Tables 8.3, 8.4 and 8.17). The numbers along the x-axis correspond to the last integers in the sample numbers. The samples 108601 through to 108516 with odd numbers are fresh rocks (bulk sample), except sample 108520 which is non-weathered. The samples with even numbers plus samples 108517 and 108521 are the weathered ones (<63 micron).

The chemical analyses show that the weathered samples are lower in SiO_2 and Al_2O_3 compared to the fresh (bulk) rock samples. This is illustrated in Figure 8.32, where the sum of 'new-formed' phyllosilicates (smectite + vermiculite + mixed-layered minerals)(from Tables 8.3 and 8.4) is plotted together with SiO_2+Al_2O_3 (from Table 8.17). Higher values of these phyllosilicates are correlated with lower values of SiO_2 + Al_2O_3 and indicate dissolution and leaching of aluminosilicate minerals in the weathering profiles. This trend is particularly clear for the samples 108501 to 108514.

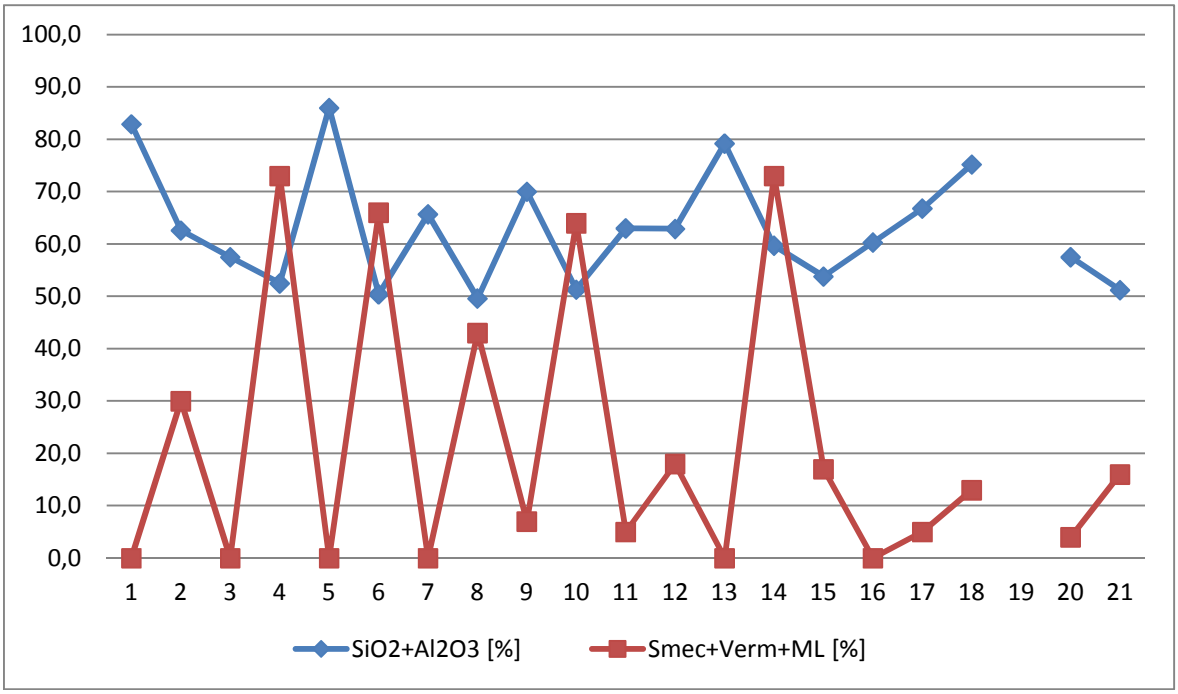

Figure 8.32. Variations in 'new-formed' phyllosilicates plotted together with the contents of SiO_2+Al_2O_3 of the entire sample sets, 108601 through to 108521 (data in Table 8.3, 8.4 and 8.17). The numbers along the x-axis correspond to the last integers in the sample numbers. The samples 108601 through to 108516 with odd numbers plus 108520 are fresh rocks (bulk sample) and the samples with even numbers plus samples 108517 and 108521 are the weathered ones (<63 micron).

8.8 Trace element analysis from XRF

Trace element analyses are carried out based on pressed pills of dry material, and the results are given in Tables 8.19 through to 8.22. Unfortunately, six of the samples had too little sample material to produce pills. These samples are coloured yellow in the tables. Several elements are below the detection limit in the analysis; e.g., silver (Ag) and cadmium (Cd) (in Table 8.19), antimony (Sb) (in Table 8.20) and tungsten (W) (in Table 8.21). Several other elements are detected only in some of the samples; e.g., arsenic (As) (in Table 8.19) and molybdenum (Mo) (in Table 8.20).

Table 8.19. XRF analysis of trace elements; fresh and weathered rock samples <63 micron. Six samples (marked yellow) were not analysed due to lack of sample material.

Sample id.	Ag	As	Ba	Cd	Ce	Co	Cr	Cu	Ga	La
	[mg/kg]	[mg/kg]	[mg/kg]	[mg/kg]	[mg/kg]	[mg/kg]	[mg/kg]	[mg/kg]	[mg/kg]	[mg/kg]
108501	<10	<10	581	<10	533	<4	<5	<5	25,0	291
108502										
108503	<10	<10	2400	<10	256	43,3	488	19,3	14,1	110
108504	<10	<10	2340	<10	1450	84,9	144	201	25,0	656
108505	<10	<10	48	<10	356	<4	<5	<5	22,5	178
108506	<10	<10	56	<10	4160	7,2	22,0	84,1	51,1	1050
108507	<10	<10	<10	<10	74	51,7	416	28,8	11,0	<15
108508	<10	<10	<10	<10	51	107	480	79,1	14,0	26
108509	<10	11	<10	<10	65	33,7	262	37,1	13,6	<15
108510										
108511	<10	<10	<10	<10	85	41,8	288	45,2	13,5	<15
108512	<10	<10	<10	<10	79	56,3	347	170	13,8	<15
108513	<10	<10	2970	<10	100	<4	7,1	11,0	14,2	59
108514										
108515	<10	62	946	<10	85	26,8	87,5	126	17,3	46
108516										
108517										
108518										
108520	<10	<10	<10	<10	54	54,0	566	64,0	14,2	<15
108521	<10	<10	<10	<10	45	97,0	1640	163	12,9	<15

Table 8.20. XRF analysis of trace elements; fresh and weathered rock samples <63 micron. Six samples (marked yellow) were not analysed due to lack of sample material.

Sample id.	Mo	Nb	Nd	Ni	Pb	Rb	Sb	Sc	Sn
	[mg/kg]	[mg/kg]	[mg/kg]	[mg/kg]	[mg/kg]	[mg/kg]	[mg/kg]	[mg/kg]	[mg/kg]
108501	<3	29,7	148	6,5	43,4	218	<15	<5	<5
108502									
108503	<3	13,3	103	171	19,8	144	<15	23,2	<5
108504	<3	40,2	350	68,1	40,5	112	<15	17,3	9,3
108505	<3	29,4	99	6,1	13,1	148	<15	<5	<5
108506	13,5	89,7	333	18,9	41,2	472	<15	9,1	7,5
108507	<3	2,3	<10	184	<5	<5	<15	31,2	<5
108508	<3	4,1	12	205	10,6	36,6	<15	30,7	<5
108509	<3	2,1	<10	111	<5	<5	<15	33,5	<5
108510									
108511	<3	<2	<10	105	<5	17,6	<15	33,0	<5
108512	<3	3,6	<10	140	<5	9,0	<15	31,5	<5
108513	<3	13,2	35	10,6	44,5	300	<15	<5	<5
108514									
108515	85,2	<2	38	118	26,1	89,1	<15	15,9	<5
108516									
108517									
108518									
108519	14,6	<2	<10	9,9	<5	5,9	<15	<5	<5
108520	<3	<2	<10	233	<5	<5	<15	34,2	<5
108521	<3	2,1	<10	691	<5	<5	<15	24,4	<5

Table 8.21. XRF analysis of trace elements; fresh and weathered rock samples <63 micron. Six samples (marked yellow) were not analysed due to lack of sample material.

Sample id.	Sr [mg/kg]	Th [mg/kg]	U [mg/kg]	V [mg/kg]	W [mg/kg]	Y [mg/kg]	Yb [mg/kg]	Zn [mg/kg]	Zr [mg/kg]	Cl [%]
108501	96,6	40,7	10,5	<5	<5	63,6	<5	127	524	0,021
108502										
108503	1450	18,2	<5	192	<5	43,5	<5	128	331	<0.02
108504	688	82,2	12,7	389	<5	150	<5	252	508	<0.02
108505	19,2	11,2	<5	6,2	<5	46,8	<5	78,3	651	<0.02
108506	55,1	99,4	13,7	45,4	<5	184	15,4	591	784	0,054
108507	89,1	<3	<5	223	<5	17,2	<5	113	40,9	<0.02
108508	112	<3	<5	281	<5	20,4	<5	291	56,7	0,021
108509	84,5	<3	<5	278	<5	26,7	<5	75,0	45,3	<0.02
108510										
108511	147	<3	<5	228	<5	24,2	<5	65,7	66,2	<0.02
108512	69,6	<3	<5	270	<5	22,4	<5	110	93,1	<0.02
108513	133	11,4	6,3	31,0	<5	84,9	<5	38,2	326	<0.02
108514										
108515	169	16,0	41,3	469	<5	50,5	<5	132	106	<0.02
108516										
108517										
108518										
108520	58,8	<3	<5	256	<5	20,3	<5	80,1	43,1	<0.02
108521	21,6	<3	<5	227	<5	16,2	<5	109	42,3	<0.02

Table 8.22. XRF analysis of trace elements; fresh and weathered rock samples <63 micron. Six samples (marked yellow) were not analysed due to lack of sample material.

Prøve id.	F [%]	S [%]	Br [mg/kg]	Cs [mg/kg]	Ge [mg/kg]	Hf [mg/kg]	Sm [mg/kg]	Ta [mg/kg]
108501	<0.2	<0.1	0	13	<2	14,7	27	<5
108502								
108503	<0.2	<0.1	0	16	2,1	8,4	20	<5
108504	<0.2	<0.1	9,44	31	<2	15,1	64	7,2
108505	<0.2	<0.1	0,01	<10	<2	16,6	18	<5
108506	<0.2	<0.1	21,5	94	3,5	22,9	51	<5
108507	<0.2	<0.1	0	<10	<2	<5	<10	<5
108508	<0.2	<0.1	25,8	<10	<2	<5	<10	<5
108509	<0.2	<0.1	0	<10	<2	<5	<10	<5
108510								
108511	<0.2	<0.1	0	<10	<2	<5	<10	<5
108512	<0.2	<0.1	3,32	<10	<2	<5	<10	<5
108513	<0.2	<0.1	0,83	<10	<2	8,7	<10	<5
108514								
108515	<0.2	3,02	0	<10	<2	<5	<10	<5
108516								
108517								
108518								
108520	<0.2	<0.1	0	<10	<2	<5	<10	<5
108521	<0.2	<0.1	0	<10	<2	<5	<10	<5

8.8.1 Trace Element Distributions

The main purpose of analysing trace elements is to study their behaviour in the weathering profiles; i.e., their leaching or accumulation. The investigation is hampered by the fact that trace elements were not analysed for six of the twenty samples due to lack of sample material. However, several trace elements were analysed together with the main elements, based on the melted sample pills. These analyses are including all samples and are shown in Table 8.18 and seem to correlate very well with the trace element analyses based on pressed powder pills; see Figure 8.33. A nearly one-to-one correlation is observed, which defends the use of trace element analyses from both datasets.

Many of the trace elements analysed are giving values below the detection limit and, consequently, only those that are detected in the majority of the samples are commented on in the following paragraph.

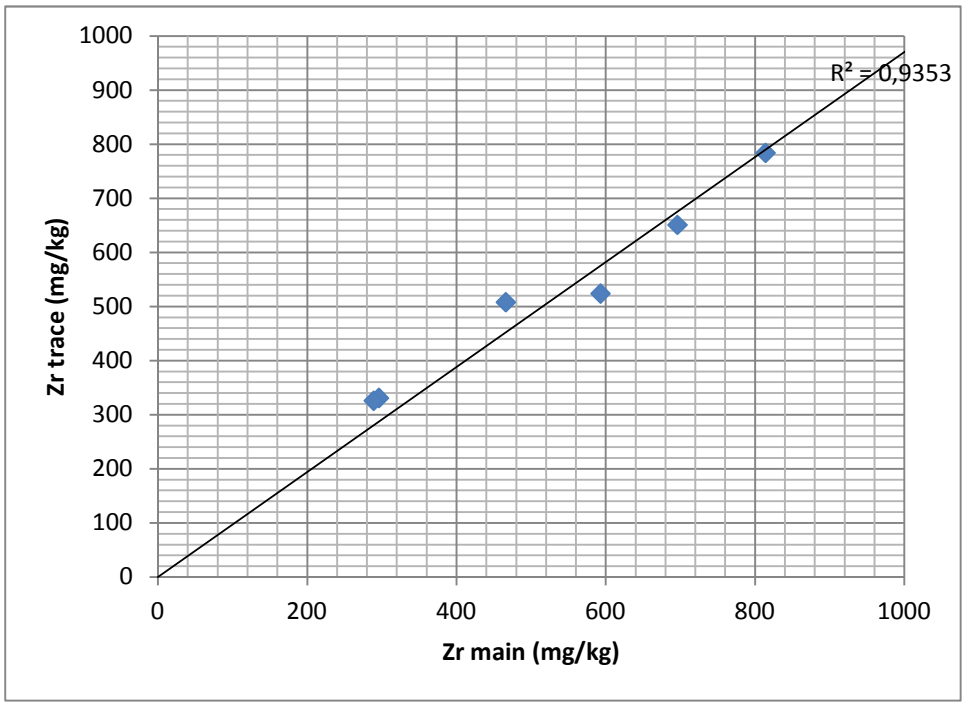

Figure 8.33. Cross-plot of Zr (zirconium) content from trace element analyses based on pressed pills (Y-axis), versus ZrO_2 analyses based on melted pills recalculated to elemental weight (in mg/kg)(X-axis).

8.8.2 Trace elements analysed with the main elements

The trace elements analysed together with the main elements are given in Tables 8.19.8.22. Some of the analyses are below the detection limits. The detection limits are marked in Tables 8.18 and 8.19 through to 8.22, as '<value' for each element.

The dark, iron-bearing minerals (e.g., biotite, chlorite and amphibole) and metal sulphides are commonly the first to be attacked in a weathering situation with percolating oxidised water, and the metals are mobilised in the acidic sulphate-containing water. All of these minerals are associated with a large number of trace elements.

Zirconium is also commonly found as small (micron-sized) zircon crystals in iron-bearing minerals. Zircon is very resistant to weathering, and when the iron-bearing mineral dissolves in a weathering process, zircon particles tend to accumulate. Therefore, the enrichment of zircon has been used as a proxy for the degree of weathering. However, a weathered zone that initially was enriched with iron-bearing minerals will also lead to increased values of Zr. Consequently, it may be difficult to interpret the results of chemical Zr analysis, without looking at the behavior of several other elements.

Thus, the behaviour of the transition metals, e.g., copper (Cu), nickel (Ni), zinc (Zn), vanadium (V) and chromium (Cr) in the weathering profiles is of interest. These metals are commonly mobilised at low pH; e.g., Zn is mobilised at pH below 5.5 and immobilised as hydroxide at pH between 5.5 and 10.5. Cu is immobilised as hydroxide above pH 8.

Since zirconium and the transition metals have very different behaviours in a weathering situation, the distributions of four of them; Cu (copper), Ni (nickel), V (vanadium) and Zn (zinc) are plotted together with Zr (zirconium) (as oxides) in Figure 8.34. These data are taken from Table 8.18, because those analyses include all samples.

The content of Zr is higher for some of the weathered samples and has increased more than six times for sample 108502 (compared to the fresh sample 108501). However, the accumulation of this element depends of course, on the content of Zr in the non-weathered rock, and the samples 108507 through to 108521 show very low Zr values.

It is well known that transition elements like Cu, Ni, V and Zn can substitute for Fe in iron-bearing minerals, and these elements increase when iron-bearing minerals are concentrated in the <63 micron fraction of the weathered samples. However, when such iron-bearing minerals dissolve in the weathering process, the transition metals may be leached out or be accumulated, depending on the pH conditions. In weathering zones where chlorite is stable (like in the sampled greenstone localities), the pH is usually close to 8, because the brucite layers of chlorite are stable above pH 7.8. At such pH levels, these transition elements tend to be immobilised as hydroxides.

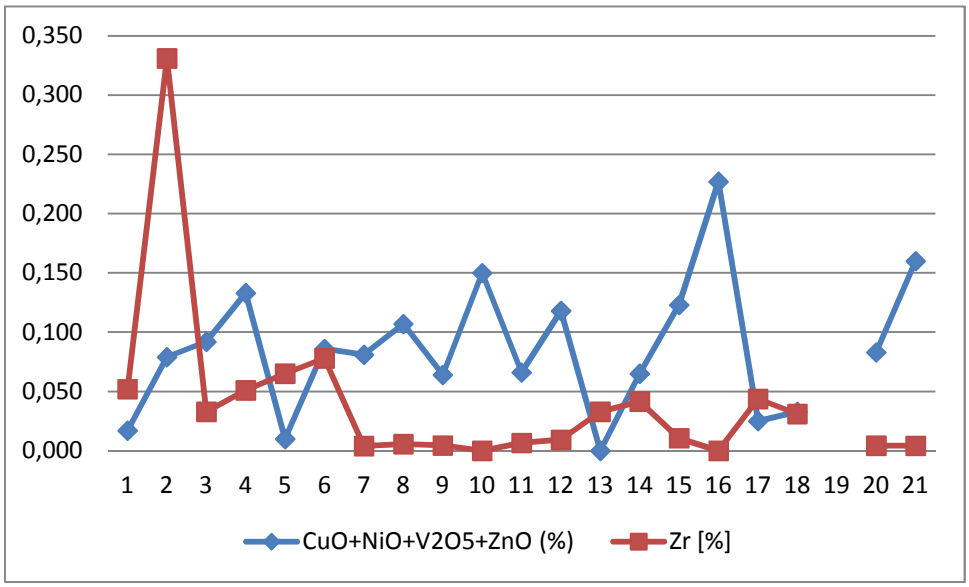

Figure 8.34. Distribution of the transition elements Cu, Ni, V and Zn versus Zr (as oxides) in the sample set from Table 8.18 and 8.19 through to 8.22. The detection limit is set to zero. The numbers along the x-axis correspond to the last integers in the sample numbers. The transition elements show positive anomalies in most of the weathered samples, but the behaviour of Zr is more difficult to interpret. Sample 108502 has the highest value of ZrO_2, with 0.33 weight%.

By comparing the distribution of Zr and transition elements, it is cautiously suggested that the positive anomalies of these elements are caused both by accumulation of iron-bearing minerals and in sufficiently high pH regimes to immobilise the transition metals.

The transition elements Cr and Ni seem to follow each other closely, also in the weathered samples. This is illustrated (with data from Table 8.18) in Figure 8.35. The two data points above the trend belong to the Alum shale samples; 108515 and -16.These two samples have a special composition of transition elements due to their abundance of sulphides (pyrite).

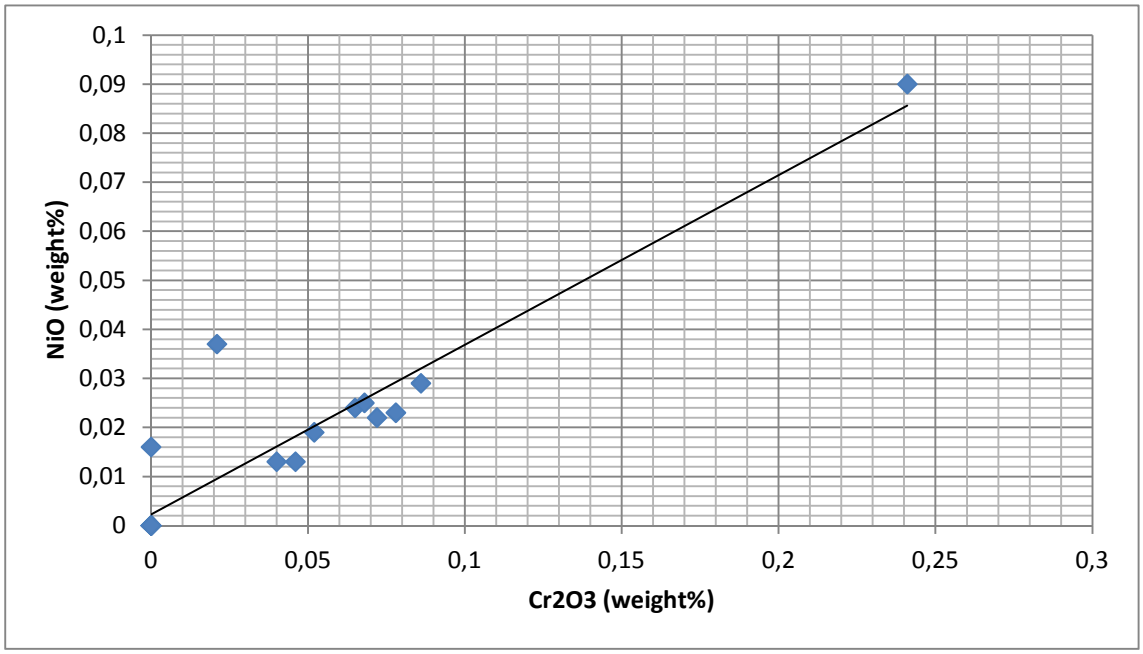

Figure 8.35. Cross-plot of Cr_2O_3 versus NiO (from Table 8.17). No data were avaialble for six samples in the trace element analysis. The transition elements Cr and Ni follow each other in both fresh and weathered samples. The detection limit is set to zero.

The correlation between Cr and the other transition elements, e.g., Cu, Ni, Vand Zn is not equally clear for the various samples. This is illustrated in Figure 8.36, which shows the distribution of Cr and the sum of the other transition metals for the entire sample sets.

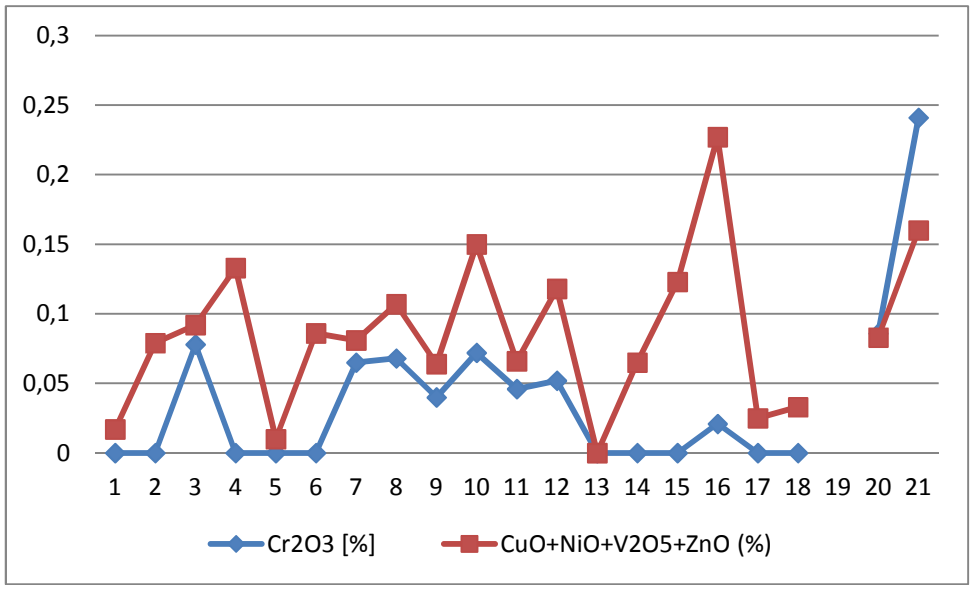

Figure 8.36. Co-variation of Cr_2O_3 versus the sum of transition elements CuO+NiO+V_2O_5+ZnO (from Table 8.18). The detection limit is set to zero.

Cr (chromium) and V (vanadium) have similar geochemical behavior, and they are substituting for iron in octahedral positions in trioctahedral minerals. They may also substitute for aluminum in dioctahedral phyllosilicates; e.g., muscovite (Deer et al. 1966). However, the content of each element in the rocks prior to weathering is also determining the level of accumulation.

8.8.3 Rare Earth Elements

The 'rare earth elements' include the elements with atomic numbers 57 through 71, commonly referred to as the lanthanide series. Named in order: lanthanum (La), cerium (Ce), praseodymium (Pr), neodymium (Nd), promethium (Pm), samarium (Sm), europium (Eu), gadolinium (Gd), terbium (Tb), dysprosium (Dy), holmium (Ho), erbium (Er), thulium (Tm), ytterbium (Yb) and lutetium (Lu). In addition, the elements yttrium (Y, atomic no. 39) and scandium (Sc, atomic no. 21) are sometimes included in the group of rare earth elements.

The lanthanides are known to fractionate and partly accumulate in weathering profiles, depending on their basicity, which follows their atomic weight. However, the types and amount of lanthanides in the parent rocks is, of course, determining what is found in the weathered zones. Ce (cerium) (the second lightest lanthanide) is known to give strong positive anomalies in weathering profiles. However, humic acids in the soils are known to stabilise soluble Ce3+ and prevent its precipitation. Thus, it is less likely to find positive Ce anomalies in the upper part of soil profiles, where the concentrations of humic acids are high (in areas with vegetation).

The distributions of Ce, Ga (gallium) and La (lanthanum) are seen in Figure 8.37. Sample 108504 shows a seven times increase in Ce compared to the non-weathered rock, while sample 108506 shows ten times increase. Negligible changes are seen for the other samples (Figure 8.37).

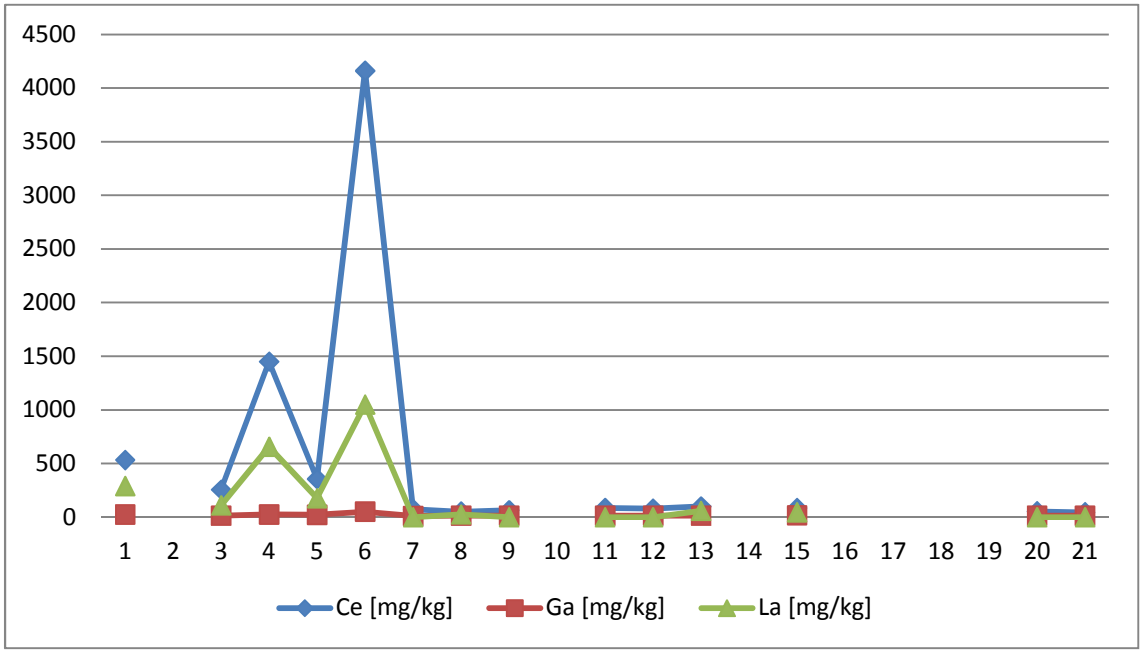

Figure 8.37. Distribution of Ce, Ga and La in the sample set; from Table 8.19. The detection limit is set to zero. The numbers along the x-axis correspond to the last integers in the sample numbers. La and Ce show strong positive anomalies in the weathering profiles 108504and 108506. Ga shows similar trends, but with much lower values; Figure 8.38.

Another interesting element is Ga (gallium) which is found to accumulate together with aluminum minerals in lateritic soil profiles. Commercial quantities of Ga are therefore extracted from bauxite. Figure 8.38 is a cross-plot of Ga versus La (lanthanum). The correlation is rather good, both for weathered and fresh rocks, indicating a geochemical coexistence between these two elements in the weathering profiles.

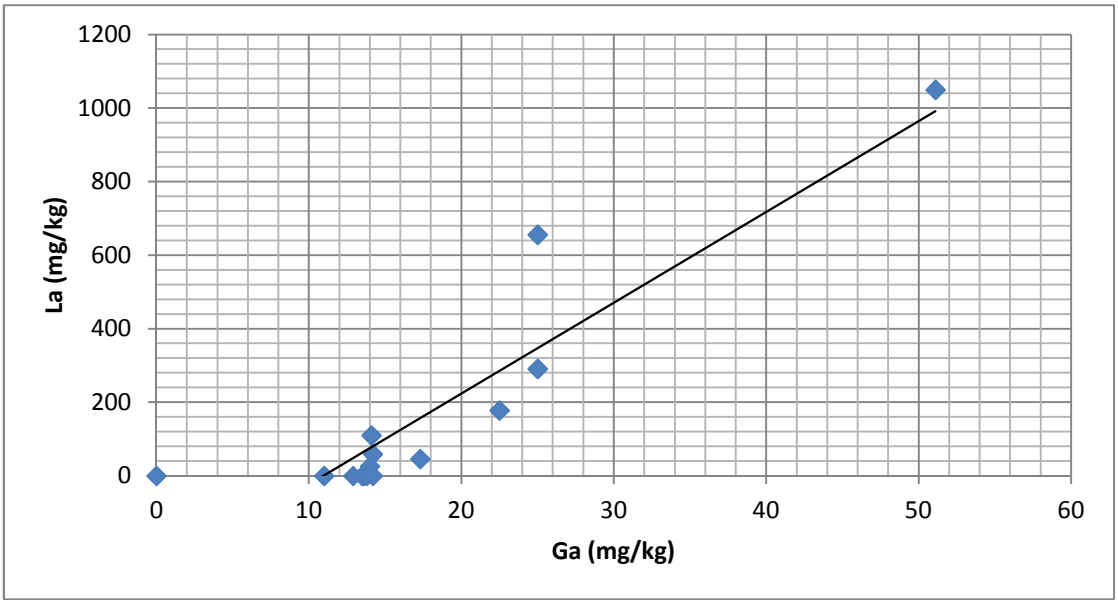

Figure 8.38. A cross-plot of Ga versus La seems to correlate, both for weathered and for non-weathered rocks, indicating that these two elements follow each other in the weathering process. The detection limit is set to zero.

Mn-oxides are known to co-precipitate light-weight lanthanides, while ferromanganese soils are found to be depleted in Y compared to the lanthanides (Vodyanitskii 2012). If the strong positive anomalies of La (lanthanum) are due to co-precipitation with manganese oxides, a depletion of Y should be expected according to this hypothesis. This is studied in Figure 8.39, where the lightest lanthanide, La, is plotted together with Y (yttrium) and Th (thorium). A rather good co-variation is seen, with increased values for all three elements in two of the weathering profiles; samples 108504 and 108506. No particular depletion of Y is seen that can explain any effect of Mn-oxides on the positive anomalies of lanthanides in the weathering profiles.

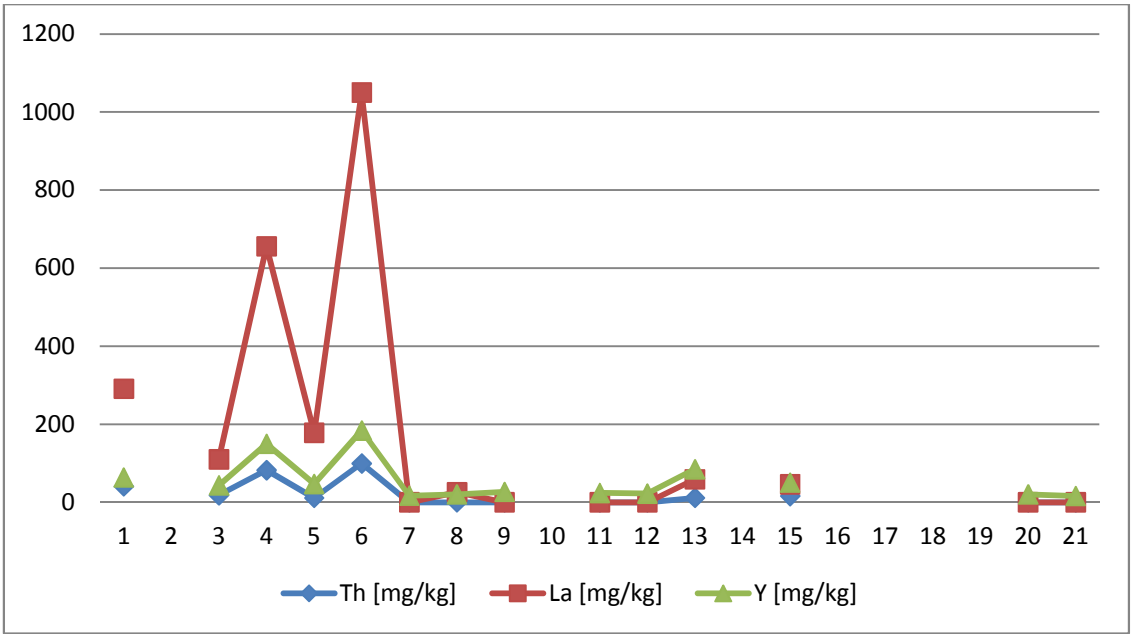

Figure 8.39. Distribution of Th, La and Y in the sample set. The detection limit is set to zero. The numbers along the x-axis correspond to the last integers in the sample numbers. A co-variation is observed for all three elements, and strong positive anomalies in two of the weathered samples, namely 108504 and 108506 compared to the fresh rocks.

Another of the light lanthanides, Nd (neodymium) is plotted together with Nb (niobium) and Sc (scandium) in Figure 8.40. Like La, it shows strong positive anomalies for the two weathered samples 108504 and 108506. Nb is showing similar trends, but the contents of these elements are much lower. Sc is not showing any particular trend.

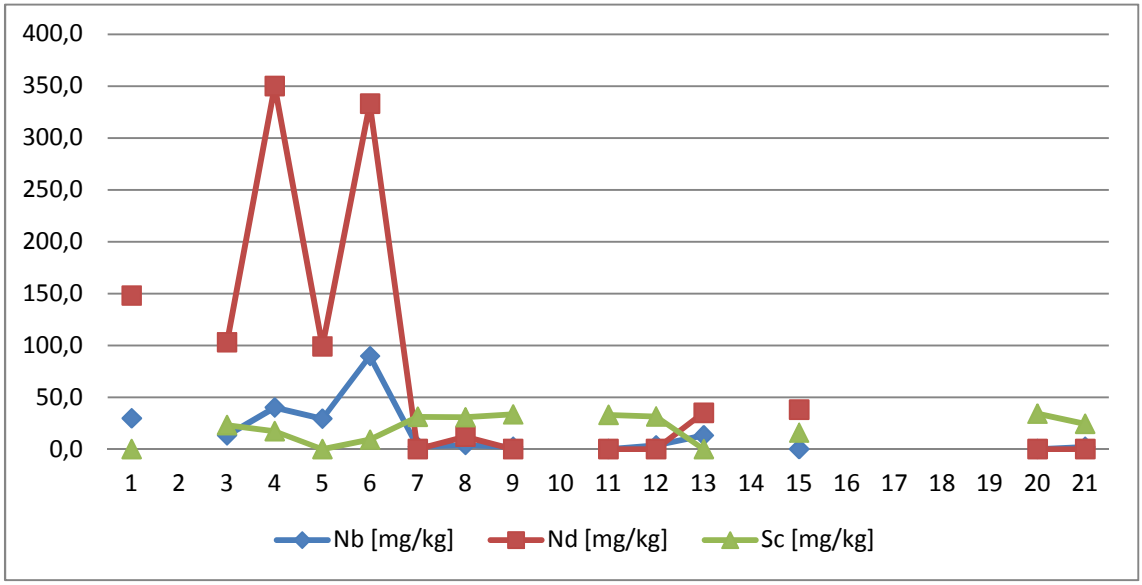

Figure 8.40. Distribution of Nb, Nd and Sc in the sample set. The detection limit is set to zero. The numbers along the x-axis correspond to the last integers in the sample numbers. A co-variation and accumulation of Nd and Nb is seen in the weathered samples 108504 and 108506 (compared to the fresh rocks). Sc is not showing any particular trend, and the values are low.

8.8.4 Trace elements in the greenstone samples

The four greenstone samples and their associated weathered material are studied separately for their trace element distributions. The main minerals in these rocks are trioctahedral; e.g., chlorite. Since Cr and Ni commonly substitute for Fe and Mg in these minerals, it is of interest to see if Cr and Ni can be associated directly with chlorite. Here, Mg is used as a proxy for chloriteand the sum of NiO and Cr2O3 is cross-plotted versus MgO in Figure 8.41. A rather good correlation is seen, supporting the suggestion that Ni and Cr are associated with chlorite in the greenstone formations.

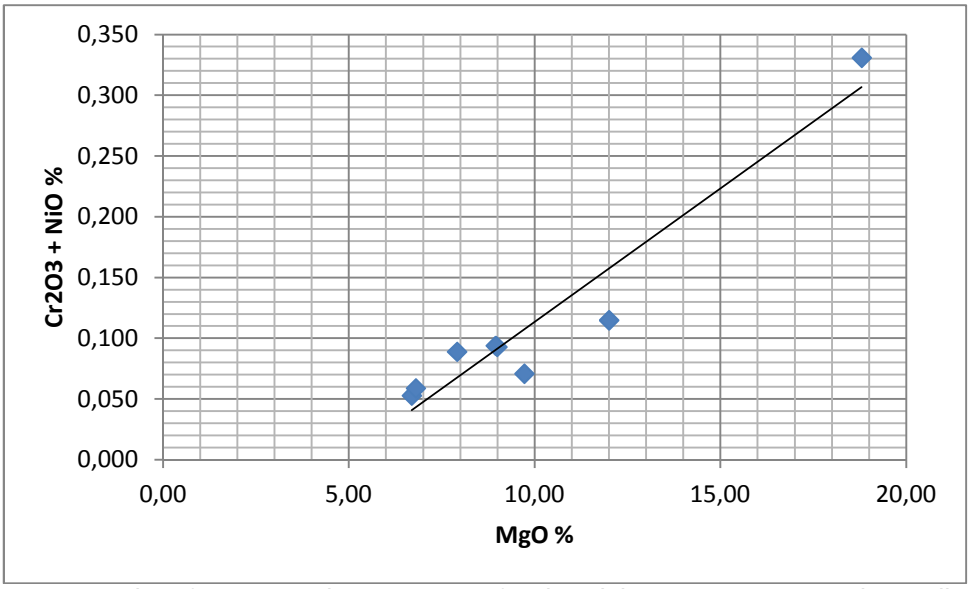

Figure 8.41. Cross-plot of Cr_2O_3 + NiO versus Mg for the eight greenstone samples. A linear trend is observed, indicating that these elements are associated with chlorite, the main mineral in the greenstones.

8.9 QUATERNARY WEATHERING VERSUS DEEP WEATHERING

8.9.1 Quaternary weathering and erosion

The Quaternary period is characterised by repeated glaciations in Scandinavia, separated by shorter periods with warmer climates. It is assumed that most of the regolith in Norway was eroded and transported out on to the Norwegian shelf during the Quaternary. Thus, it is expected that only saprolites protected from glacial and fluvial erosion remain on land; e.g., saprolites protected by younger rocks or preserved in deep faults and fractures. Weathering profiles developed in glacial and fluvial deposits during the periods with warmer climates were also, in general, eroded during the following glaciation.

Today, we find weathering profiles developed in glacial and fluvial deposits from the last glaciation. This is illustrated in Figure 8.42, with a podzol-profile developed in a thin glacial till deposit, covering a deeply weathered greenstone (Styggdalen, Trondheim).

Figure 8.42. Deeply weathered greenstone (in Styggdalen, Trondheim) covered by a thin layer of glacial till, where a podzol profile has developed during the last ten thousand years. The podzol weathering has had only a negligible effect on the weathered greenstone.

The podzol weathering is characterised by leaching processes, where acidic (pH~4) meteoric water percolates through the soil. The bleached layer is due to dissolution and removal of iron-bearing minerals. The brownish layer underneath is the zone where iron- and aluminum-complexes are precipitating. These complexes, with humic and fulvic acids, account for the brownish colour of this horizon.

No new minerals are formed in these environments, except for 'degraded' primary minerals. The pH is too low and the leaching too continuous for new minerals to crystallise. Examples of such “degraded' minerals are vermiculite and 'smectite' developed by leaching of potassium from biotite and muscovite, respectively. This 'smectite' (in the bleached layer only) is therefore not a proper smectite, but a swelling 'degraded' muscovite (or dioctahedral illite) (Rueslåtten & Jørgensen 1977).

8.9.2 General about saprolites

The present project is focused on studying deeply weathered bedrock in Norway. Weathered rocks are commonly referred to as saprolites ('rotten rocks'); defined by soft and clay-rich decomposed rocks remaining in their original place. The formation of saprolites is associated with humid, tropical to subtropical climates on the continental landmasses between latitudes 35°N and 35°S. Saprolites are formed in igneous, metamorphic or sedimentary rocks and their

stages of development can be characterised according to the degree of preservation of structures and textures from the fresh parent rocks (Bates & Jackson 1987).

This definition states that the formation of saprolites is governed by geochemical reactions. After Devonian time, land plants and microbial activity caused the development of soil profiles in the upper part, while the formation of saprolites takes place below this zone. The relief of the terrain must be moderate in order to prevent erosion of the weathering products, but allow for the removal of dissolved components from the chemical weathering. These conditions are preferably met during periods of tectonic stability.

More intense weathering results in a continuous transition from saprolite to laterite, and saprolites may have a cover of laterite. The term 'regolith' includes the loose layer of weathered rocks that rest upon the bedrock.

A special type of saprolite formation is 'arenization'. This process is characterised by a disintegration of the parent rock, producing a sandy material with a low clay content. A study of arenisation profiles in Portugal was published by Braga et al. (2002). They studied arenisation of granitoid rocks, and samples from depths below 10 m were characterised by having sand fractions of 27 to 53 weight-% and less than 7 weight-% clay (<2 micron). The mineral composition of the clay fraction consisted dominantly of kaolinite and gibbsite, with subordinate illite, chlorite, vermiculite and an illite/vermiculite mixed-layered mineral. The loss of potassium varies from 38.5% to 45.5%.

A study of pre-Quaternary deep weathering in Scandinavia concluded that thick kaolinitic saprolites were formed there in the period 200 to 66 million years ago and medium-thick immature saprolites 5 million years ago, and that these regoliths vary in thickness from a few metres to more than 150 m, depending on the age of the land surface and the parameters mentioned above (Oberhardt 2013). The weathered profiles investigated in our study, show large differences between the fresh rocks and their corresponding weathered material, with respect to both mineralogy and geochemistry. However, much of these differences can be explained by the fact that the fresh rocks are analysed as bulk (micronised powder), whereas the weathered samples are represented by their <63 micron fraction after wet sieving. For the gneissic and granitic rocks, this means that the <63 micron fraction contains less quartz and feldspars and more phyllosilicates compared to the bulk fresh rock. These effects are much less pronounced for the greenstone samples, and also for the Alum shale, because they have fewer coarse grains in the matrix of the fresh rock. A discussion of the various weathering localities is given below.

8.10 Discussion

8.10.1 Samples 108501 through to 108506

These samples represent quartz-monzonite, pyroxeniteand granitic gneiss. None of these samples contains clay minerals typical for saprolites (i.e., kaolinite, gibbsite and smectite). The identified clay minerals are vermiculite, illite/vermiculite mixed-layered mineral and small amounts of chlorite (sample -02 and -06). However, significant reductions in feldspars and dark

minerals in the weathered samples and also strong positive anomalies for the lanthanide elements suggest a pervasive chemical weathering. The reduction in the potassium content of the weathered samples (<63 micron) 108502, 108504 and 108506 compared to the fresh rocks is 38.0, 43.6 and 56.3 %, respectively. This is similar to the observations of Braga et al. (2002) (variations between 38.5 and 45.5%) and indicates an arenisation process for the three weathering profiles. Also, the sandy weathering material with low clay contents (Figure 8.4) indicates an arenisation process to describe these formations. Braga et al. (2002) interpret the arenisation profiles to be a result of weathering under the then prevailing temperate climate. For Norway, this is pointing towards a pre-Quaternary formation. Unfortunately, trace elements were not analysed for sample 108502 due to the low contents of sample material.

8.10.2 Samples 108513 and -14

Sample 108513 and -14 are from the Precambrian gneiss area at Ustaoset. The weathered zone is exposed on the surface of a glaciated area, surrounded by a glacial landscape with till deposits. No till is deposited upon the weathered zone. The weathering material is sandy, with low clay content, indicating an arenisation process in a warmer climate than today. This sample contains abundant vermiculite and also some gibbsite. Vermiculite is commonly found to be a weathering product of biotite; a weathering process that goes on also under the present climatic conditions. The presence of gibbsite, however, indicates that it is a product of lateritic weathering in a warm and humid climate. Such climatic conditions have not prevailed since the Tertiary. Lateritic weathering conditions are also indicated by the high loss of potassium; 45.5% compared to the fresh rock. Unfortunately, the weathered sample 108514 has no trace element analysis, due to insufficient sample material. However, some trace elements (mainly transition elements) were analysed together with the main elements.

8.10.3 Samples 108517 and -18

Samples 108517 and -18 are both weathered granitic core material from wells drilled in Fyllingsdalen. These weathered samples contain smectite, and Sample -17 also contains small amounts of kaolinite, indicating that both samples -17 and -18 were chemically weathered under warmer conditions than today (at more than 400 metres depth). This deep weathering may also have been affected by hydrothermal activity. For this reason, it is difficult to be conclusive regarding the climatic conditions.

Unfortunately, none of these two weathered samples (-17and -18) has trace element analyses, due to insufficient sample material. However, some trace elements (mainly transition elements) were analysed together with the main elements.

8.10.4 The greenstone samples; 108507 through to 108512 and 108520 and -21

The four investigated weathering zones in greenstones of the Mid-Norwegian ophiolite belt show significant variations with respect to the compositions of the non-weathered rocks, thus demonstrating the heterogeneity of the greenstone formations, particularly with respect to their contents of plagioclase, chlorite, amphibole and illite/mica (Figure 8.25). Good correlations are

seen between the XRD and XRF data, illustrated by a cross-plot between the sum of phyllosilicates (XRD data) versus $MgO+Fe_2O_3$ (XRF data) in Figure 8.42

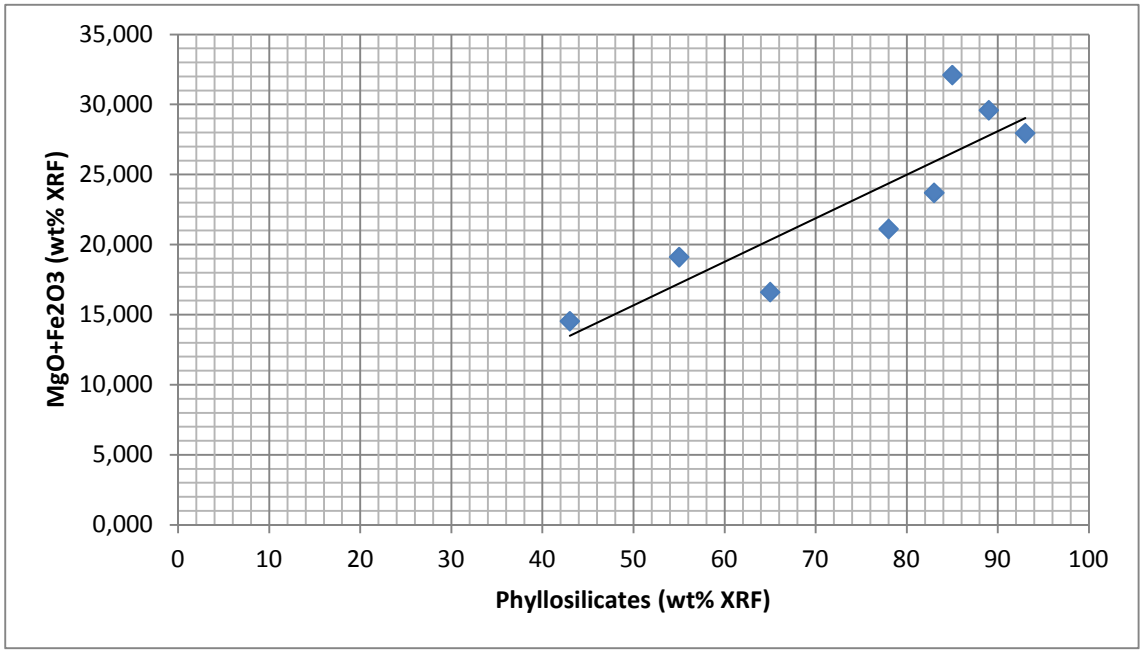

Figure 8.42. MgO+Fe2O3 from chemical analyses (Table 8.17) plotted versus the content of phyllosilicates (XRD data) for the greenstone samples. A clear trend is seen with increasing content of phyllosilicates at an increasing content of $MgO+Fe_2O_3$. The statistical correlation line is included in the figure.

The trend on the cross-plot shows that $MgO+Fe_2O_3$ is increasing with increasing contents of phyllosilicates, and three of the four weathered samples give the highest values. This trend illustrates that the phyllosilicates in these rocks are dominantly trioctahedral, even though the most weathered sample (108521 Lia Pukkverk) contains significant amounts of smectite. Smectite is commonly found to be dioctahedral, but the high contents of Fe and Mg in these samples indicate that this smectite may be trioctahedral; e.g., saponite. SEM analysis may provide an answer to this question. If the smectite is trioctahedral (e.g., saponite) the source may be chlorite. In this case, the process may include leaching of brucite layers (iron- and magnesium hydroxide) from chlorite.

Since smectite is unstable in the acidic soil profiles developed after the last glaciation, it is cautiously suggested that the smectite was formed in a warmer climate; e.g., before Quarternary, and protected from erosion and chemical alteration in the deep fractures of the parent rock. Trace element analysis (e.g., lanthanides) shows no positive anomalies for the weathered greenstone samples. Some of the trace metals, like Cr and Ni, are associated with chlorite, and are following each other also in the weathered samples.

In the weathered material <63 micron, the following is observed:

- Plagioclase, amphibole, mica/illite and pyrophyllite are strongly reduced; partly because of chemical dissolution, but also due to sieving off the larger grains during sample preparation.

- In the fraction <6 micron, chlorite is the main mineral (around 80 weight %) for all four weathered samples; indicating that chlorite must have been in geochemical equilibrium with the pore water over longer periods of geological time.
- The vermiculite found in the fraction <63 micron of the weathering zones is not found (or only in trace amounts) in the <6 micron fractions. This is explained by the following:
    - Vermiculite is easily formed from biotite by leaching of potassium, and from chlorite by leaching of brucite layers. The low contents of mica/illite in the rocks indicate that vermiculite is formed mainly from chlorite.
    - The vermiculite particles (formed from chlorite and biotite) are commonly larger than 6 micron and, hence, they are not a significant part of the <6 micron fractions. It may also be that vermiculite particles finer than 6 micron are vulnerable to dissolution in the pore water of the weathering zones; or
    - that these small vermiculite particles are regenerated to chlorite.
- Two of the greenstone samples contain authigenic smectite in their fine fractions. This mineral is not stable in the upper soil profile under the present-day climatic conditions, and must have crystallised in the weathering zone during warmer climatic periods (Rueslåtten 1985).
- The presence of opalCT in some of the weathering zones may be the result of chemical dissolution of silicate minerals (e.g., amphibole and plagioclase), where excess silica is crystallised as opalCT. The presence of opalCT indicates that the temperature was never above c. 50 OC, because it will have re-crystallised to quartz at higher temperatures. OpalCT is not found in the <6 micron fractions, indicating that this mineral is unstable in the present pore water.

8.10.5 Sample 108515 and -16; the Alum Shale

These core samples were provided by R&P Geo Services AS, and are from two different depths in a well drilled through Ordovician black shales. The original composition of the weathered strata is not fully known, but the analysis indicates oxidation of pyrite and dissolution of carbonates, with the formation of jarosite and gypsum. Illite is enriched in the weathered sample. Unfortunately, no trace element data are available for the weathered sample (108516) due to insufficient sample material. These shales were previously investigated by NGU (Sæther et al. 2009), and the average of their XRF results matches with the results obtained here.

8.11 Conclusions

The studied weathering zones are developed in a wide variety of rock types. All of the weathered samples, even the greenstones, are characterised by being sandy and having low clay contents. This is typical for weathering processes at depth in regoliths, termed arenisation; commonly found in the Mediterranean climate zone (Braga et al. 2002).

Some of the weathered samples contain smectite and kaolinite, which hints at a formation in a warmer climate, e.g., the climate in the Tertiary. The accumulation of lanthanides (particularly

cerium, lanthanum and neodymium) in some of the weathering zones also strengthens the impression that the weathering occurred in a warm (sub-tropical) climate. One of the samples (108514 Ustaoset) contains small amounts of gibbsite, which hints at lateritic weathering in a warm climate.

The composition of the weathered samples is very different from the pre-Jurassic weathering profiles on Andøya, which show a pervasive weathering with almost complete dissolution of feldspars in the gneiss and the simultaneous authigenic formation of kaolinite (Brönner et al. 2015). Based on this, it is suggested that the samples investigated in the present report are from the deepest parts of a pre-Quarternary regolith, characterised by arenisation. The upper parts of the regoliths were eroded by repeated glaciations and fluvio-glacial processes during the Quaternary.

9. INHERITANCE AND BASEMENT TECTONICS OF CENTRAL NORWAY: EVOLUTION FROM ONSHORE TO DEEP OFFSHORE DOMAINS

Laurent Gernigon, Marco Brönner, Marie-Andrée Dumais, Aziz Nasuti, Odleiv Olesen, Arne Solli & David Roberts

9.1 Introduction

The role of lithospheric, crustal and basement inheritance has often been suggested to influence the tectonic evolution and complexity of the continental deformation zone within rifts and passive rifted margins (Misra & Mukherjee 2015, Manatschal et al. 2015, Frizon de Lamotte et al. 2015). Although the details of the dynamics are still debated, this impact seems to be particularly important if the inherited basement fabrics represent initial and/or major, inherited, crustal deformation zones (sutures, mega shear zones)(Vauchez et al. 1997, Bellahsen et al. 2006, Audet and Bürgmann 2011). The long-term architecture of inheritance is commonly involved to explain the observed along-strike changes of the rift architecture and segmentation of rifted margins that seem to correlate with changes in the onshore geology that are often highlighted by potential field data (Blaich et al. 2009, Behn & Lin 2000). Several natural examples have illustrated the influence of inherited fabrics in the early stages of rift development and segmentation (Theunissen et al. 1996, Morley et al. 1999, Smethurst 2000, Vetel et al. 2005, Bird et al. 2015). Under specific conditions, basement fabrics can control the location of the initial rift, the geometry of the faults within the rift and the location of transfer zones (Morley et al. 1999, Færseth et al. 1995).

In the Mid-Norwegian margin (Figure 9.1), both the volcanic and the rift system that led to final continental breakup clearly developed along the axis of the Caledonian fold belt that was initially 'squeezed' between the Precambrian cratonic shield of Baltica and Laurentia (e.g., Ziegler 1992, Gasser et al. 2014, Schiffer et al. 2015). The Scandinavian element of the system resulted from convergence and collision between Laurentia (e.g., Greenland and North America) and Baltica (e.g., Norway and Fennoscandia). The convergence produced both eastward directed thrusting on the Baltican margin and southwestward directed thrusting on the Laurentian margin. The Caledonian and remobilised older terranes have been subsequently affected by several phases of extension and rifting leading to continental breakup in Early Tertiary time (Skogseid et al. 2000, Tsikalas et al. 2012).

The nature of the basement observed onshore Norway is relatively well constrained thanks to many decades of geological and geophysical mapping. However, the sedimentary rocks in the basins towards the west partly conceal the basement complexes and structural grain and except for a few basement boreholes in the proximal part of the Norwegian shelf (Slagstad et al. 2008), our knowledge of the basement offshore Norway (Figure 9.2) is very limited and is reliant on integrated studies including seismic and potential field data. Mid-Norwegian onshore-offshore relationships and extrapolation of the main onshore structures (e.g., shear zones, detachments, major faults, etc..) are also important in evaluating the role of inherited structures during rifted margin formation (Skilbrei et al. 2002, Olesen et al. 2010). These basement fractures could have been reactivated episodically during, or after, deposition of the Late

Paelozoic and younger sedimentary successions. Such reactivations could have controlled and/or created structures and/or sedimentary facies that have since become potential oil and gas traps and reservoirs. Alternatively, the weathered/fractured basement itself could have become a potential reservoir rock (e.g., P´an 1982, Trice 2014). On the Mid Norwegian margin, Doré et al. (1997), Fichler et al. (1999, 2011) and Skilbrei et al. (2002) showed that basement structures, highlighted by potential field data, have had a profound influence on the development of the Mesozoic basins. Thus, the mapping and/or extrapolation of the basement structures and lithologies where the sedimentary section is thin or absent could be relevant for hydrocarbon exploration. Precisely how inheritance controls and/or affects the development of sedimentary basins from the proximal to the distal rifted domains still remains unclear and/or controversial. Top basement estimation and the nature and thickness of the crust appear fundamentally unconstrained and/or controversial over a large part of the Mid-Norwegian margin (e.g., Ebbing et al. 2006, Nirrengarten et al. 2014, Gernigon et al. 2015).

In this study, we particularly revisited the shallow and deep basement structures of the Møre margin and Jan Mayen corridor, defined as a peculiar, large-scale, crustal transfer system that divided the Mid-Norwegian margin rift system before breakup (Figure 9.2). The Jan Mayen corridor is an oblique segment of the Mid-Norwegian margin which has never been investigated in detail. Maystrenko & Scheck-Wenderoth (2009) modelled atypical crustal and upper mantle anomalies along this Jan Mayen corridor. Previous aeromagnetic surveys have also suggested some relationships between this crustal transfer system, the old Precambrian history (Fichler et al. 1999) and, indirectly, the segmentation of the adjacent oceanic domain not properly remapped with high-resolution aeromagnetic data (Gernigon et al. 2015). A common view is that oceanic transform faults and oceanic segmentation are also related to pre-existing crustal and basement structures (Lister et al. 1986, Cochran & Martinez 1988, Bellahen et al. 2013). Recent discussions have suggested, however, that inheritance (if still present) controls neither the location of breakup nor the onset of seafloor spreading (e.g., Manatschal et al. 2015). Thus, although there is general agreement that inheritance has an important control on the evolution of rift systems, the precise role and of basement inheritance within multiply extended domains requires also careful consideration.

In this study, both qualitative and quantitative investigation of new geophysical data has been carried out in order to document the structural architecture and tectonic development of the basement of central Norway from onshore to the deep offshore basins. We analysed recent multichannel seismic-reflection profiles provided by TGS-NOPEC (Figure 9.2) in combination with the more recent potential field data acquired and processed during the continent onshore-offshore project (Coop Phase 2) initiated by NGU in 2013. In this regard, the study provides deep insights into along-margin segmentation, as well as the role played by pre-existing basement structures in determining rift geometry, margin architecture and possibly the early spreading segmentation.

9.2 Datasets

9.2.1 Geological maps and onshore information

Onshore-offshore observation has been a critical point in this project. The onshore geological information used in the project considered several geological maps available at NGU in paper and/or digital versions. We particularly refer to Wolff (1979), Askvik & Rokoengen (1985), Solli (1995), Solli et al. (1997), Lutro et al. (1998) and Tveten et al. (1998) for specific references and details about the geological map units described and observed in central Norway at 1: 250 000 scale. For the regional map of Scandinavia and Norway and main geological units and nomenclature, we also refer to the 1: 2 million maps of Koistinen et al. (2001) and Solli and Nordgulen (2006). As part of the Coop Project, several of the geological maps covering the onshore-offshore transition have been revised, merged together and digitally updated (Lutro et al. 2015, this report). A large number of onshore density and susceptibility measurements has also been compiled (e.g., Olesen et al. 2010, Lauritsen et al. 2015, this report).

9.2.2 Seismic data

The offshore geophysical dataset relies on a large dataset of released and interpreted 2D seismic-reflection data extending from 63°N to 67°N and 2°E to 6°E. As part of the Coop Project, TGS provided access to the most recent CFI-MNR and MNR long-offset dataset of the Mid-Norwegian margin interpreted and modelled in the second part of this report. These lines have been processed by TGS with their proprietary Clari-Fi imaging technique used to achieve true broadband images of the continental margin. This method deals first with the ghost effect and then solved for the Earth´s attenuation, thus improving the resolution and quality of the data in depth, especially in volcanic margin settings (e.g., Hardwick et al. 2012).

9.2.3 Gravity data

Seismic-reflection profiles were jointly interpreted with different gravity datasets. Both DTU13 satellite-derived free-air gravity anomalies (Andersen et al. 2014) and ship-track data (for the gradients) were integrated to constrain the deep structures of the basins. The gravity data used in this study rely on gravity compilations previously described by Olesen et al. (2010). This compilation was based offshore on measurements of c. 59 000 km of various shipboard gravity measurements provided by the Norwegian Petroleum Directorate, diverse oil company seismic contractorsand the Norwegian Mapping Authority. The surveys have been levelled using the International Standardization Net 1971 (IGSN 71) and the Gravity Formula 1980 for normal gravity. The combined dataset has been levelled and interpolated to square cells of 1×1 km size using the minimum curvature method. However, comparison with the recent satellite dataset and modern shiptrack gravity data has revealed that the long-wavelength component of the vintage gravity in the deep offshore domain was locally inaccurate, with differences of up to 10-15 mGal compared to previous compilations (Haase & Ebbing 2013, Ebbing & Gellein 2013). The main discrepancies have been observed along the Møre margin and in the Jan Mayen corridor and these have significant implication in terms of accuracy estimation of the crustal thickness. Therefore, for potential field modelling, we considered the shiptrack data for the filtered gradient and the DTU13 long-wavelength component of the gravity signal.

9.2.4 Bathymetry

Bathymetric data used for the deep-water part of the map are based on the IBCAO3 compilation (Jakobsson et al. 2012). Onshore and near shore, higher resolution shiptrack bathymetry are derived from a new combination of multi-beam echosounder provided by Olex (http://www.olex.no/olexsoftware_e.html) reprocessed and merged with a previous NGU Mareano acquisition (http://www.mareano.no/) and older bathymetric profiles (e.g., Olesen et al. 2010; Brönner & Olesen 2015, this report). The final bathymetric grid used for the onshore-offshore interpretation project was 50 × 50 m.

9.2.5 New aeromagnetic data

The new aeromagnetic data acquired and processed during the Coop Project covers a large part of the onshore-offshore transition in the coastal areas of the Møre margin and Jan Mayen corridor. The surveys and different filtered versions (e.g., tilt-derivative vertical/horizontal derivatives) were used to better constrain the near-shore inheritance and basement history in the platform region. The Coop Phase 1 and Phase 2 projects include acquisition of five new airborne surveys acquired in the years 2010-2013 in addition to new gravity and heat-flow data. The aeromagnetic surveys (CNAS-10 and STAS-13) have a profile spacing of 1 km while the combined aeromagnetic datasets along the coast of western and central Norway (BESTAS-10, SAS-11 and TRAS-13) have a line spacing of 250 m. The Continental Shelf Geophysics Team at NGU has, in Phase 2, compiled both the new surveys (TRAS-12 and STAS-13) and Phase 1 data (CNAS-10, BESTAS-10 and SAS-11) in addition to other existing aeromagnetic surveys on the mainland and offshore in order to provide a comprehensive and state-of-the-art aeromagnetic grid of the Mid-Norwegian margin and its onshore-offshore transition (Olesen et al. 2010, Nasuti 2015 et al., this report).

9.3 Regional and geodynamic setting

9.3.1 Precambrian and Caledonian orogenies

The mainland adjacent to the Mid-Norwegian margin has been the site of a long and complex inherited basement history (Figures 9.1, 9.2 & 9.3). Onshore, the well-exposed Scandinavian Caledonides represent a segment of the Early Palaeozoic Caledonian-Appalachian orogenic system that resulted in the amalgamation of several continental masses (Gee et al. 2008). The Fennoscandian Shield (Figure 9.2) encompasses several crustal domains and terranes of Archaean, Proterozoic and Phanerozoic tectonothermal ages (Gee & Stephenson 2006). The Archaean craton extends across northern Finland and northern Sweden into northern Norway (Lahtinen et al. 2015). The Palaeoproterozoic crust of southern Finland, Sweden and northern Norway was formed by the accretion of large-scale terranes and magmatic arc complexes during the Svecofennian orogeny (2.1–1.8 Ga ago)(Bingen et al. 2005, Lahtinen et al. 2015). At the terminal stage of this old orogeny (1.86–1.65 Ga ago), granitoids of the Trans-Scandinavian Igneous Belt (TIB) were emplaced at the edge of the Svecofennian domain between Sweeden and Norway (Högdahl et al. 2004, Olesen et al. 2010). Suggested emplacement mechanisms vary from an extensional intra-continental setting (Korja et al. 1993) to a continent-scale eastward subduction zone situation (e.g., Åhäll & Larson 2000; Lahtinen et al. 2009). The latter interpretation has recently received more favour (e.g Pascal et al. 2007, Gradmann & Ebbing 2015).

The thrust-sheets and nappes of the Scandinavian Caledonides overlying the autochthonous crystalline rocks of the Fenoscandian Shield were initiated during the Early Ordovician but most were emplaced during Silurian to Early Devonian time (Roberts 2003, Gee et al. 2008) (Figiures 9.2 & 9.3). Some of the nappes were translated up to hundreds of kilometres from their original settings towards onto the foreland. A progressive increase in translation distance from the short-transported lower nappes to the highest nappe units has been recorded in central Norway. Coupled with the fact that Caledonian pressure estimates increase dramatically westwards, towards the collision zone (hinterland), a regional model of west-directed subduction of the Baltoscandian margin of Baltica beneath Laurentia has been proposed during the Silurian-Early Devonian Scandian phase of the Caledonian orogeny (Stephens & Gee 1985, Roberts & Stephens 2000, Andersen et al. 1991). A tectonostratigraphic subdivision of the Scandinavian Caledonides has been proposed and further described in the literature (Gee et al. 1985, Roberts & Gee 1985, Roberts 2003, Gee et al. 2008). This involves thrust-sheets originally sourced from the Neoproterozoic and proximal Baltoscandian continental margin (Lower and Middle Allochthons) to outboard nappes derived from the Early Palaeozoic Iapetus Ocean (Upper Allochthon). Far-travelled units of inferred Laurentian affinity form the Uppermost Allochthon (Roberts 2003). Subsequent rapid exhumation of the (ultra)high-pressure rocks in the western part of the Norwegian Caledonides has been explained in terms of post-orogenic 'collapse' and is commonly linked to the formation of Devonian basins in Early to Late Devonian time which involved the reactivation of old Caledonian thrusts (Andersen et al. 1991, Séranne 1992, Osmundsen et al. 2002, Roberts 2003, Fossen 2010). The basement structures and fabric at the present day is clearly highlighted by the magnetic fabrics (Figures 9.4 & 9.5).

9.3.2 Mid-Norwegian rifted margin structure and evolution

First-order margin segments

The overall structural framework of the sedimentary basins lying on top of this compound Precambrian-Caledonian substratum consists, at the present day, of NE-SE trending deep Cretaceous basins flanked by paleo-highs, terraces and shallow platforms (Blystad et al. 1995). Our study area (Figure 9.1) mostly considers the complex structural and crustal domain located between the Vøring and Møre margin segments of the Mid-Norwegian margin and their adjacent platform and terrace domains (Figure 9.2). The Vøring margin consists of various structural elements including, from NW to SE, the Vøring Marginal High, the Vøring Basin, the Halten Terrace and the Trøndelag Platform in the inner part of the margin (Blystad et al. 1995). To the south, the Møre Margin represents a thicker Cretaceous depocentre, but differs from the Vøring segment by the lack of a broad platform and terrace structurally equivalent to the Trøndelag Platform and Halten/Dønna terraces observed on the Vøring Margin. To the south, the transition between the Møre and the Vøring basins represents in this study a regional transfer zone that defines a dominantly N-S tectonic corridor, which represents a zone rather than a lineament as has often been suggested in the literature (e.g., The Jan Mayen Lineament). In the distal part of the Mid-Norwegian margin, the shallow Vøring and Møre marginal highs consist of anomalously thick, intruded and underplated crust covered by thick Early Eocene flood-basalts, characterised as SDRs (seaward dipping reflectors). The basalts

were emplaced along the continent-ocean transition zone during the onset of breakup between Norway and Greenland.

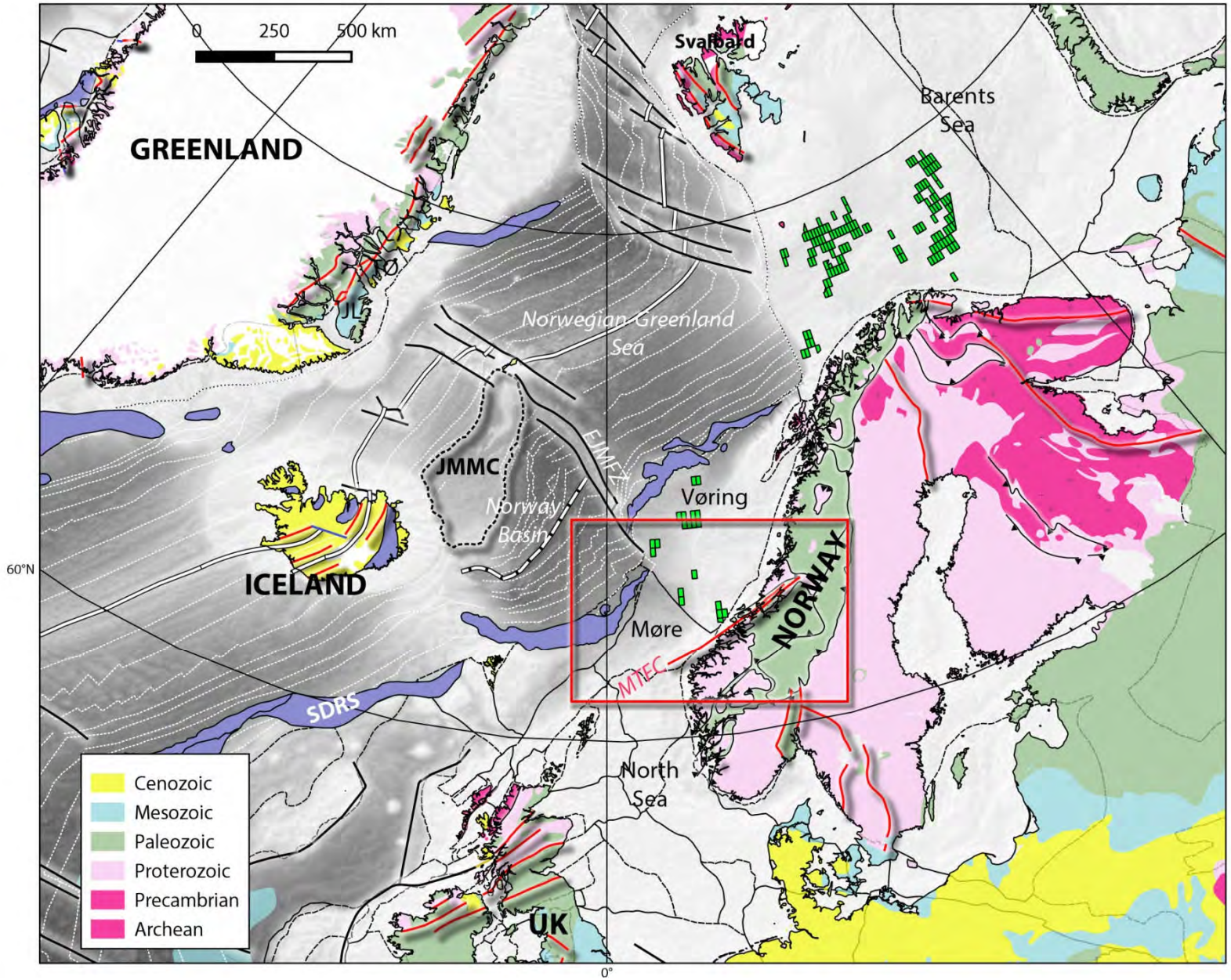

Figure 9.1. Regional setting and location of the main study area. The map also shows the nominated 23rd round licensing blocks (Green rectangles).

Shallow-water platform and terrace domains

The shallow water platform and the terrace domains offshore Norway (Figure 9.2) are probably the most constrained and dated structural domains of the Vøring Margin with more than 200 exploration/production wells and a super-abundance of 2D and 3D seismic data. Located in a prolongation of the Norwegian mainland, where Palaeozoic to Mesozoic rocks are locally exposed (Bøe & Skilbrei 1998), the Trøndelag Platform consists of thick Late Palaeozoic-Jurassic sedimentary rocks bounded by major detachment faults (Brekke & Riis 1987, Brekke 2000). To the east, the Halten Terrace is separated from the Trøndelag Platform by the Breimstein Fault Zone, and from the Møre Basin to the west by the Klakk Fault Complex. The Vingleia Fault Zone separates the Halten Terrace from the Frøya High to the south (Blystad et al. 1995, Elliot et al. 2012, Ehrlich & Gabrielsen 2004). Across most of the Trøndelag Platform, the Late Palaeozoic–Early Triassic (pre-salt) basin is 6-7 km thick and the Middle Triassic to Jurassic formations show a relatively uniform thickness (< 1.5 km) with a gradual thinning towards the souteastern border of the platform (Brekke 2000). The Jurassic series is overlapped by a thin, Cretaceous, condensed section reaching a maximum thickness of 1 km at the level of the Helgeland Basin, an isolated and intra-platform sag-basin genetically linked with the tectonic evolution of the Nordland Ridge. Farther south, the Froan Basin is bounded by the Vingleia and Bremstein fault complexes (Figure 9.2). This represents a long-lived reactivated half-graben situated at the eastern flank of the Frøya High, the most prominent structural and known basement high observed in the study area.

The Early Mesozoic evolution of the Mid-Norwegian margin has resulted in the development of both low-angle detachments and steeply-dipping fault structures influenced by inherited structure and/or salt tectonics (Withjack & Callaway 2000, Ehrlich & Gabrielsen 2004). The geometry and geological evolution of the pre-Middle Triassic basins have been described particularly by Müller et al. (2005) and Færseth et al. (2012). Færseth (2012) described the Late Permian-Early Triassic rift system as a series of 'en echelon' half-grabens controlled by a major east-dipping border fault extending from the Vestfjorden Basins to the Froan Basin. The structural style of the deep grabens may have involved the successive development of extensional detachments coupled or not with the shallow fault system which partly decoupled on the Triassic salt intervals (Withjack & Callaway 2000, Richardson et al. 2005). Overlying Upper Permian and Triassic strata in the half-grabens of the Froan Basin are regionally more extensive and were controlled by major normal faults which remained active during most of the Triassic.

To the west, the Halten Terrace marks the tectonic transition between the Trøndelag terrace and the deep Cretaceous basins. The terrace illustrates the large variety of structural styles (extensional forced folds, fault propagation folds, basement-involved and basement-detached normal faults and narrow grabens) symptomatic of stratified salt tectonics (Withjack & Callaway 2000, Richardson et al. 2005). Farther south, the eastern flank of the Møre Basin is characterised by a narrower and shallower platform which comprises a series of NE-SW-elongated basement highs (Gossa High, Ona High, Giske High and Manet Ridge) separating the Slørebotn Sub-Basin, the Magnus Trough and the Marulk Basin from the deep Møre Basin (Jongepier et al. 1996, Brekke 2000, Grunnaleite & Gabrielsen 1995). These NE-SW structures developed along the trend of the Møre-Trøndelag Fault Complex (MTFC). This regional and major fault complex has a clear topographic signature extending along the

proximal platform of the Møre margin and into the West Shetland Basin (e.g., Grønlie & Roberts 1989, Hurich et al. 1996, Doré et al. 1997). To the south, this inherited regional feature roughly delineates the transition between the northern North Sea and the Møre margin. The MTFC have a close relationship to other major and regional Caledonian shear zones such as the Highland Boundary Fault and Great Glen Fault (Doré et al. 1997, Watts et al. 2007).

Møre and Vøring Basin: regional sag basins

The principal feature of the Vøring and Møre basins (Figure 9.2, 9.6) that developed at the edge of the proximal platform domain is the huge thickness of Cretaceous sedimentary successions observed on seismic data (Brekke 2000, Lien et al. 2005). These basins are 125-150 km wide and the bases of these large 'sag' and flexural basins can locally reach depths of up to 8-9 km (Olafsson et al. 1992, Mjelde et al. 2005). At such depths older formations (if present) are so deeply buried that they are not seen as potential petroleum systems over much of the deepest depositional lows. The onlaps of the Lower Cretaceous sediments against the terraces and platform borders suggest that the entire unit has rapidly infilled the pre-existing rifted structures. This paleo-topography, highlighted by the base Cretaceous unconformity (BCU), is interpreted to be the result of either a limited Mid-Late Jurassic-earliest Cretaceous extensional rifting event (Færseth & Lien 2002) or alternatively a protracted Late Jurassic-Early-Mid Cretaceous rifting phase (Pascoe et al. 1998, Tsikalas et al. 2012, Henstra et al. 2015).

As part of the Vøring Basin, several sub-basins with synclinal appearances subdivide the large sag-basin (e.g., the Træna Basin and Någrind Syncline to the north and the Rås Basin and Vigrid Syncline to the south). Thick Cretaceous depocentres are usually observed in these synclinal sub-basins which are separated by the Utgard High, a major and central basement horst lying in the prolongation of the Lofoten Ridge outcropping farther north. Farther south, gravity data suggest that the Utgard High was progressively dislocated towards the Møre Basin and possibly linked with the deep crustal rafts expected at the level of the Slettringen, Grip and Vigra highs that developed in the so-called Jan Mayen corridor (Gernigon et al. 2015).

The Jan Mayen corridor: a crustal-scale transfer zone

The transition between the Møre and Vøring margin segments is not a clear and sharp tectonic boundary (e.g the Jan Mayen Lineament) (Figure 9.2, 9.6). The transition between the Møre and Vøring basins, mostly as reflected at the base Cretaceous unconformity level is interpreted rather as a broad crustal transfer system, 100 km wide (spatially and indirectly), and linked with the adjacent, segmented oceanic, Norway Basin (Gernigon et al. 2015). In the Jan Mayen corridor, the Cretaceous infill forms a broad and deep sedimentary sag basin which may extend to a depth of 10 km in its centre (Figure 9.6).

The atypical character of the Jan Mayen corridor is suggested by distinct gravity and magnetic domains (Figures 9.7 & 9.8). The corridor corresponds to a sudden change in the magnetic signature between the Møre Basin and the Vøring Basin. The Møre Basin is characterised by scattered round-shaped anomalies and a central NE-SW-elongated trend of positive magnetic anomalies. These anomalies have been modelled and explained by the presence of deep-seated, rotated, crustal (autochthonous) rafts consisting of highly-magnetic continental crust

(Gernigon et al. 2015). Alternative hypotheses have suggested the presence of Cretaceous seamounts (Lundin & Doré 1997). A quite distinct, low and regionally smoothed, magnetic amplitude dominates in most of the Jan Mayen corridor, except in the distal volcanic domain nearby the continent-ocean boundary at C24r. The Jan Mayen corridor also shows a contrasting regional gravity low between the Vøring and Møre basins. It strongly contrasts with the dominant gravity highs underlying the Fles, Klakk and Møre-Trøndelag fault complexes and the Frøya High. Oceanwards, the Jan Mayen corridor coincides with a specific oceanic spreading segment defined between the East Jan Mayen Fracture Zone and the Norway Basin pseudo-fault further documented by recent aeromagnetic data in the Norway Basin (Gernigon et al. 2015).

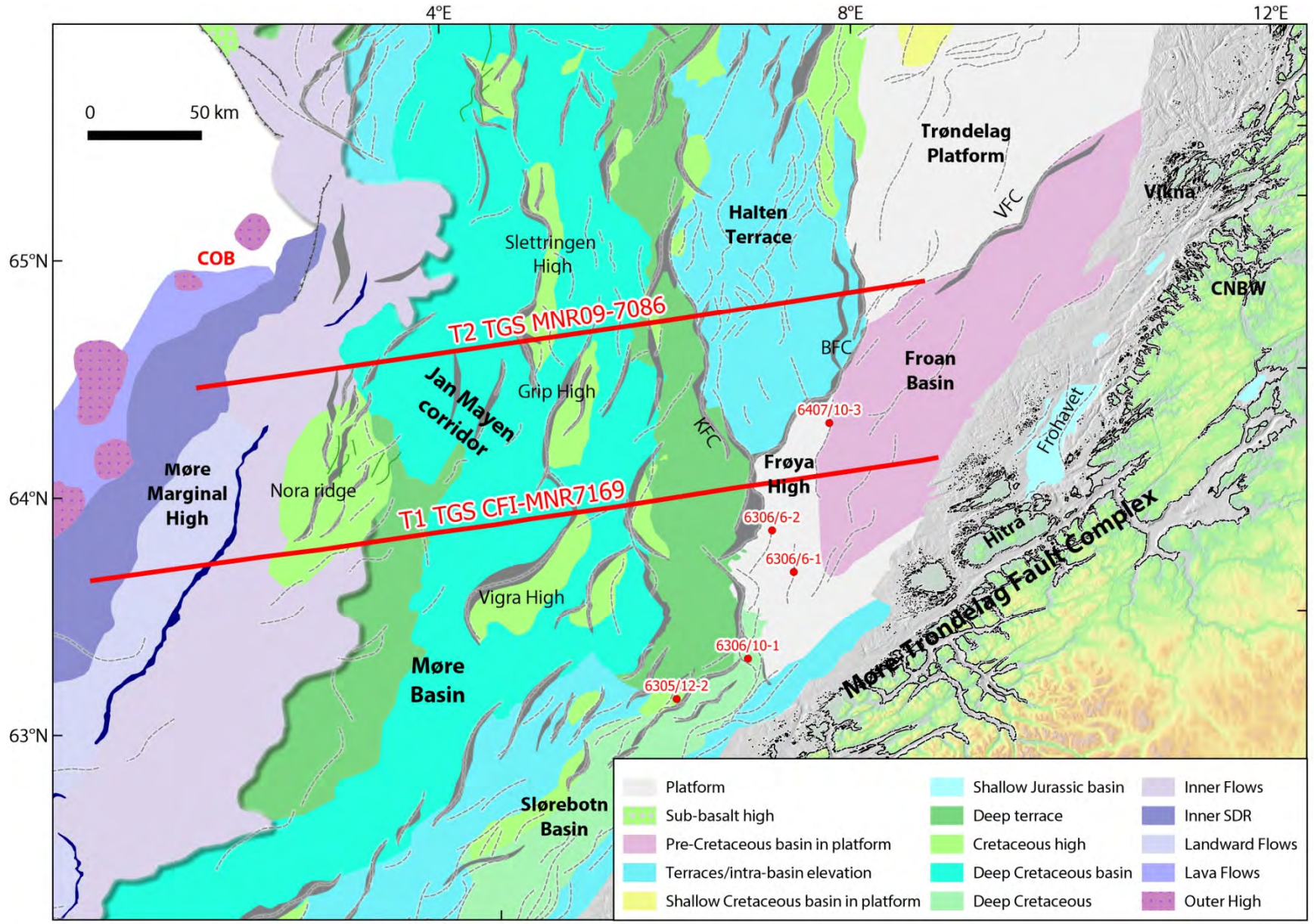

Figure 9.2. Outline of the main structural elements of the study area (modified after Sommaruga & Bøe 2002; Gernigon et al. 2003, 2015, Blystad et al. 1995, Berndt et al. 2001 and Abdelmalak et al. 2015). The map also shows the locations of the two transects modelled and discussed in the next sections. CNBW: Central Norway Basement Window. BFC: Bremstein Fault Complex; KFC: Klakk Fault Complex; VFC: Vingleia Fault Complex.

9.4 Basement inheritance and onshore-offshore relationships

The nature, age and structure of the basement rocks are largely unknown offshore Norway. Thanks to the new aeromagnetic data, we can correlate and extrapolate the magnetic pattern (Figures 9.3 & 9.4) with the basement units cropping out in closest vicinity to the sedimentary basins.

9.4.1 Onshore geology, near-shore basement and magnetic pattern

Our study area considers a large part of the Trondheim Region covered by the TRAS-13 survey. In the southeast of the study area lies the NE-plunging antiformal hinge of Trollheimen in the eastern part of the Western Gneiss Region (WGR) where Proterozoic basement is exposed (Figure 9.3). The NE-plunging Surnadal Synform separates Trollheimen from a highly deformed and metamorphosed region centred between Orkanger, Kristiansund and Molde. Together with the Central Norway Basement Window (CNBW), these regions show distinct, high-magnetic signatures correlating with a gravity high recognisable along the coastline (Figures 9.7 & 9.8). The high-magnetic anomalies coincide with highly deformed granite, diorite and migmatitic rocks deformed together with mafic rocks in the Proterozoic basement which is metamorphosed in upper amphibolite to eclogite facies (Solli & Nordgulen 2006). This highly deformed region, which also includes infolded rocks of the Caledonioan nappes, extends continuously in a NE-SW-trending belt highlighted by the magnetic TDR filter (Figures 9.4 & 9.5). Magnetisation of the crystalline basement is closely related to the metamorphic grade and the highest signature observed commonly coincides with granulitic rocks of intermediate to mafic composition. The magnetic pattern structurally matches with the prominent antiformal and synformal hinges, mostly NE-plunging, that are the result of a complex sequence of polyphase deformation of the pre-existing nappes (Grønlie & Roberts 1989). The northwestern part of study area is occupied mostly by rocks of the Støren Nappe of the Upper Allochthon, structurally overlain by the Helgeland Nappe Complex of the Uppermost Allochthon (Nordgulen et al. 2002) located at the margin of the new aeromagnetic survey.

The Middle Allochthon (Figure 9.3) is present around the margin of the old Precambrian basement gneiss windows and antiforms and generally consists of three units recently revised and discussed by Robinson et al. (2014). Low-grade sandstones (Offerdal Nappe) occur in the lowermost unit, with a mafic dyke intruded units above (Särv or Leksdal Nappe) and at the top of a succession of high-grade schists, gneisses, amphibolites and even ultramafic lens and eclogites (Seve nappes) with evidence of a pre-Scandian or very early Scandian metamorphism (Tucker et al. 2004, Gee et al. 2008, Robinson et al. 2014). Originally assigned to the Upper Allochthon, this Seve unit is now considered to be part of Middle Allochthon (Robinson et al. 2014) based on its original location along the Baltoscandian margin of Iapetus. In contrast, the Upper Allochthon rocks consist of diverse volcanosedimentary strata and ophiolites created within the Iapetus Ocean close to either the Laurentian or the Baltican margin (Hollocher et al. 2012, Gee et al. 2013, Robinson et al. 2014). Preserved remnants of the Seve nappes have been mapped on top of the CNBW (Solli et al. 1997) and coincide with the low, short-wavelength magnetic stripes observed above the Precambrian substratum.

The Upper Allochthon (Figure 9.3) occurs widely in the Trondheim Region (Gee et al. 1985, Solli 1995, Solli et al. 1997) and is represented by the Trondheim Nappe Complex, comprising

the Støren, Meråker and Gula nappes (Roberts & Stephens, 2000 and Robinson et al. 2014) all of which are part of the Köli nappes. The rocks of the Gula Nappe have been considered as an epicontinental assemblage of the outermost Baltoscandian continental margin, and to have been affected by locally high-grade metamorphism in pre- Scandian and/or early Scandian time (Roberts 2002). The Støren and Meråker nappes are considered to have an exotic origin from the Iapetus Ocean, based on the occurence of Late Cambrian- earliest Ordovician deformed ophiolites and volcanic-arc assemblage overlain unconformaly by Ordovician to Early Silurian basinal successions. Ordovician fossil affinities in the Støren Nappe in the Hølonda and Smøla area suggest a deposition of these starta proximal to Laurentia. In general, the Köli nappes show a large variety of sedimentary and volcanic rocks including greenstones, amphibolites and micaschists. The magnetic signal associated with these rocks shows a clear contrast compared to the high-magnetic anomalies observed at the level of the surrounding Precambrian basement gneiss regions. The Caledonian nappes of the Upper Allochthon unit have a dominantly low-magnetic regional signature (e.g., Skilbrei et al. 2002; Olesen et al. 2010). The Upper Allochthon unit also includes mafic to felsic plutonic rocks (500-430 Ma) showing generally low to moderate magnetic signatures.

The Uppermost Allochthon (Figure 9.3) (Solli & Nordgulen 2006; Gee et al. 2008) is located at the northern edge of the new TRAS-13 survey. The Kollstraumen detachment (KD, Figure 9.3) is also well expressed in the magnetic map and delimits this uppermost unit of the Caledonides east of the CNBW (e.g., Braathen et al. 2002). This detachment coincides with a clear magnetic contact feature observed (almost) at the same level. The rocks of the Uppermost Allochthon are diverse, but are interpreted to be part of Late Cambrian to Ordovician distal margin of Laurentia (Roberts 2003). In Nordland and Troms, the Köli Nappes are overlain by the Rödingsfjället and Helgeland nappe complexes (Nordgulen et al. 2002) which consist of either (1) high-grade commonly migmatitic Neoproterozoic through Ordovician metasedimentary rocks, for which protoliths include sandstones, graywackes, calcsilicate rocks and marble or (2) medium- to high-grade , non-migmatite metasedimentary rocks, which locally have depositional contacts on ophiolite fragments. Protoliths include mafic, carbonate and calc-silicate conglomerates; calc-silicate rocks and calcareous sandstone; and marble. Overall, the nappe sequences record deposition on a continental shelf and adjacent seafloor. The Helgeland Nappe Complex is interpreted to have origins along the Laurentian (east Greenland) margin of Iapetus (Stephens & Gee 1989, Yoshinobu et al. 2002, Roberts 2003, Barnes et al. 2012). There is evidence in southern Nordland for crust-derived Ordovician peraluminous intrusions at 477 to 466 Ma (Yoshinobu et al. 2002). Calc-alkaline intrusive rocks at 448 to 430 Ma are also present (Nordgulen et al. 2002). Recent age dating from different parts of the Uppermost Allochthon supports a Laurentian, or possibly even a microcontinental origin for the rocks (Yoshinobu et al. 2002). Robinson et al. (2014) have suggested that similar rocks could be exposed on the Frøya islands and the northern part of Hitra and could be part of the Helgeland Nappe Complex but Solli and Nordgulen (2006) still include them in the Upper Allochthon unit in their regional map. Relationships in the Upper Allochthon north of the Kollstraumen detachment are also controversial. Numerous units beneath the west-directed thrusts (part of the Taconian orogeny) currently assigned to the Uppermost Allochthon, hardly differ from rocks characterising the Upper Allochthon near Trondheim, and could simply have been part of the latter (Robinson et al. 2014). If this alternative interpretation is correct, then the Uppermost Allochthon rocks were tectonically emplaced westward over the highest nappes

of the Upper Allochthon before emplacement of the of Late Ordovician granitoid intrusions (Yoshinobu et al. 2002, Robinson et al. 2014). The rocks of the Uppermost Allochthon include mica-schist, migmatitic paragneisses and thick marble units and have been extensively intruded by Caledonian intrusions (granites, granodiorite, tonalite). Like the nappes of the Upper Allochthons, the rocks of the Uppermost Allochthon display similar low-magnetic signatures.

9.4.2 Structures, basement fabrics, detachments and magnetic lineaments

The Møre-Trøndelag Fault Complex (MTFC) represents a prominent NE–SW mega-fault that dominates the basement configuration and the magnetic pattern of coastal areas of central Norway (Figure 9.1)(Nasuti et al. 2012). This is supported by both gravity and the new magnetic data (Figures 9.4, 9.5 & 9.7). The MTFC is marked by a broad zone of elongated NE-SW anomalies (e.g., Fichler et al. 1999, Nasuti et al. 2012) which is much better highlighted now with the new high-resolution dataset. Onshore, the MTFC was active during the late Caledonian (Scandian) phase (c. 420-390 Ma), and developed as a sinistral strike-slip shear zone during the post-orogenic extensional collapse and backsliding of the nappes sheets (Grønlie & Roberts 1989, Séranne 1992, Fossen 2010). The Scandian development of the fault complex may have been preceded by a deeper Palaeoproterozoic weakness zone (Grønlie & Roberts 1989, Séranne 1992).

The new high-resolution aeromagnetic data have revealed the complexity of the MTFC system and basement fabrics (Figures 9.3 & 9.4). In the Trondheim Region and as far as the central Norwegian coastline, the aeromagnetic data signature suggests a structural pattern that involves lenses of unmylonitised protolith (metasediments, basement gneisses or igneous bodies) that are locally enveloped by up to kilometre-wide linear to arcuate shear zone (c.f Roberts 1986). Local magnetic geometries and structures are reminiscent of ductile boudinage, horses and duplexes that are commonly developed in thrust and transtensional tectonic regime (e.g., Vauchez et al. 1995, Corsini 1996). The Hitra-Snåsa Fault and the Verran Fault are the most prominent ENE-WSW megafractures showing the clearest set of magnetic lineaments recognised onshore between the Hitra-Smøla islands and the Grong area east of the CNBW. The Hitra-Snåsa Fault is at least 300 km long. These fault zones (and associated magnetic lineaments) have had a long and complex evolution, as seen by the presence of mylonites and superimposed cataclasites, breccias and fault gouge (Grønlie & Roberts 1989). The new aeromagnetic survey has been very useful for the delineation of lithologies and structures in the field, and in general there is a very good correlation between observed surface geology and the anomaly patterns. The new aeromagnetic survey data clearly highlight the main fault segments of the MTFC but also other subtle structural features. They locally have helped to extend or revise various known fractures. The MTFC is best expressed as composed of a series of major fault strands (e.g., Gabrielsen et al. 2002, Olsen et al. 2007). The main orientations of the magnetic lineaments within and south of the MTFC are dominantly ENE-WSW, NNE-SSW and E-W. Towards the northeast, the trends are ENE-WSW and NW-SE and there are subordinate E-W and N-S populations. This agrees with most of the previous onshore interpretations and lineament statistics based on aerial and/or Landsat imaging (Grønlie & Roberts 1989, Gabrielsen et al. 2002, Olsen et al. 2007). It also confirms that the high-resolution magnetic pattern observed in central Norway is strongly influenced by the pre-existing basement structural fabrics (e.g., fault, shear zone, fracture and foliations).

The NNE-SSW magnetic trends are also fitting locally with seismic faults observed close to the near-shore Mesozoic basins (e.g., Sommaruga & Bøe 2002).

Several low angle detachments associated with this major shear zone complex initiated as extensional structures that developed during the collapse and tectonic denudation of the orogen (Séranne 1992, Andersen 1998). This is exemplified by the steep MTFC that interacted with low-angle extensional detachment zones, both towards the southwest (Nordfjord-Sogn Detachment Zone; Norton 1987, Johnston et al. 2007, Fossen 2010) as well as northwards (Høybakken and Kollstraumen detachment zones; Séranne 1992; Braathen et al. 2000, 2002, Nordgulen et al. 2002, Osmundsen et al. 2002) (Figure 9.3). Southeast of the Høybakken detachment, field evidence indicates the presence of another detachment, named the Agdenes Detachment (Robinson et al. 2014), which also coincides with a visible magnetic contact. The proposed westward prolongation of the Devonian detachments towards the Trøndelag Platform and Froan Basin, as proposed by Skilbrei et al. (2002), Ebbing et al. (2006) and Olesen et al. (2010), do not appear so obvious in the light of the new data. The Høybakken and Kollstraumen detachments (Figure 9.3), for example, do not clearly cut the Froan Basin. They rather seem to be connected and/or merge with a prominent complex system of NNE-SSW faults and shear zones observed over large part of the coastal area, west of the CNBW and the Fosen Peninsula. The basin-bounding fault in Frohavet (Tarva Fault; Bøe et al. 2010) seems to be part of this large near-shore NNE-SSW fault complex but possibly shifted westward compared to the detachment prolongation suggested in this report. To the north, similar NNE-SSW minor faults are also sub-parallel to the Folda-Rørvik-Brønnøysund shear zone (Figure 9.3), named in this study and revealed by the new TRAS-12 survey. This prominent interpreted shear zone is particularly well expressed on the new magnetic data and extends from onshore Folda up to Leka and northeastwards to Brønnøysund. This regional brittle-ductile? megafault/shear zone complex is sub-parallel to the MTFC but appears disconnected from it and separated by the CNBW. Nonetheless, both the MTFC and the Folda-Rørvik-Brønnøysund shear zone (Figure 9.3) seem to have been part of the same large-scale (lithospheric) transcurrent and intraplate deformation belt that was active during the late Caledonian deformation stage. On the magnetic map, the new shear zone represents a clear set of magnetic lineations traceable for a distance of at least 150 km. These changes in magnetic signature appear to reflect metamorphic and possible metasomatic processes associated with the shear zone development. In between the Frohavet and Folda basins, south of Vikna, the magnetic pattern shows diverging NW-SE lineations linked with the Folda-Rørvik-Brønnøysund shear zone. The tectonic grains suggested by the magnetic data shows a progressive rotation of the inferred shear zones from NNE-SSW to NW-SE between Vikna and the Frohavet Basin. One such oblique NE-SW lineament, is clearly recognised on both the magnetic and the gravity maps. It also seems that the near-shore Jurassic basins developed and/or have been preserved in between these diverging NW-SE termination structures. We expect the result of the Coop 3 survey will confirm if this NW-SE trend joins up with the NNE-SSE Folda-Rørvik-Brønnøysund shear zone and also connects offshore with the Vingleia Fault Complex mapped at the western margin of the Froan Basin (Blystad et al. 1995). The NW-SE lineations are smaller and interpreted as strike-slip splays and/or ductile, diverging, termination features commonly observed at the end of major intracontinental strike-slip deformation belts (Storti et al. 2003, 2007). If this interpretation is correct, the geometry suggested by the new aeromagnetic data should imply, at some early stage, a right-lateral sense of shear. Shear

zones that merge and lie parallel to longer and continuous regional shear zones are common in ductile and transpressive regimes. Similar fabrics have been observed worldwide,(e.g., the Pernambuco shear zone in Brazil (Vauchez et al. 1995), the Bongolava-Ranotsara shear zone in Madagascar (Martelat et al. 2000) or the South Armorican Shear Zone in Bretagne (Augier et al. 2010). In these analogues, gneisses and/or granitoids display sub-vertical foliations bearing a well developed subhorizontal mineral stretching lineation and/or low-angle mylonitic fabrics. The progressive rotation and curvature of the shear system, as observed west of the CNBW Window and possibly north of Vikna, is not totally understood but could be related to the existence of continental-scale heterogeneities in the deformed lithosphere (e.g., Vauchez et al. 1995, Tomassi et al. 1995). The low-magnetic domain occuring between the CNBW and the Vingleia magnetic anomaly highs also suggests that the Folda-Rørvik-Brønnøysund shear zone developed preferentially either within the Caledonian nappes, or most likely at the edge of the Precambrian window cropping out onshore.

Farther south, the Palaeozoic volcanic and metasedimentary rocks on the island of Smøla north of the Hitra-Snåsa Fault represent the more distal basement outcrops of central Norway, just at the edge of the Froan Basin and Frøya High, offshore. The rocks on Smøla are typically of low metamorphic grade and contrast with the ultra high-pressure rocks of the Western Gneiss Region observed on the southeastern side of the Hitra-Snåsa Fault. On the island of Frøya, the basement includes granitic and granodioritic plutonic rocks (450-428 Ma) emplaced prior to the Scandian orogeny (Nordgulen et al. 1995). Such plutonic rocks are dominant on Smøla and Hitra where they form part of the Smøla-Hitra Batholith (Gautneb & Roberts 1989, Nordgulen et al. 1995). The granitoids observed on the Frøya and Froan archipelago are part of a large Batholith (Smøla-Hitra Batholith) which extends between the islands of Grip and Halten (Nordgulen et al. 1995). Between the islands of Frøya and Hitra, basement rocks have been observed during the Frøyfjorden tunnel construction (Sættem & Mørk 1996, Bøe et al. 2005). The sampled rocks included strongly weathered gneisses, granites and mafic rocks. Weathered breccias contains coal fragments and Mesozoic pollen in their matrix (Bøe et al. 2005).

On Hitra and Frøya (Figure 9.3), major magnetic lineaments show three main principal trends (Figures 9.3 & 9.4): ENE-WSW, NE-SW and NW-SE. In addition, N-S lineations are observed on Frøya and ENE-WSW trending lineaments have been recorded between the two islands. The magnetic data fit well with the foliations and contact zone of the dioritic intrusions. The different rock units mapped onshore also correlate well with the magnetic signal. On Hitra, the contacts between the granite, granodiorite, tonalite and diorite are quite clear and the gneiss and migmatite rocks show characteristic NE-SW magnetic trends. Between Hitra and Frøya and up to Halten islands to the north, the magnetic total field above the outcropping basement rocks shows a low-magnetic domain with negative values or amplitudes usually lower than 0-50 nT. This low-magnetic domain coincides well with the Caledonian nappes and granitoids that crop out in the archipelago. However, around Gjæsingen, there is a distinct magnetic domain with observed values higher than 50-100 nT is observed. This contrasts rather surprisingly with the two adjacent low domains. In general, the Ordovician to Early Silurian plutonic rocks usually show low to negative magnetic signatures. The high-magnetic signature around Gjæsingen looks quite similar to the magnetic high region observed to the east in the CNBW. The rocks sampled and dated in Gjæsingen are, however, related to the Caledonian

Smøla-Hitra Batholith (Nordgulen et al. 1995, Tucker et al. 2004). To explain the striking magnetic contrast, we propose that the Caledonian granitoids in this specific magnetic anomaly are probably thin and the underlying Precambrian basement quite shallow compared to rocks in the surrounding archipelagos. Unfortunately, we do not yet have any susceptibility-measurements for the rocks exposed on Gjæsingen.

At the edge of the Jan Mayen corridor, the Frøya High is one of the most prominent magnetic anomalies of the Norwegian shelf (Figures 9.2 & 9.7). It is also one of the few basement highs that has been drilled offshore Norway. The basement nature of the Frøya High, farther offshore has been shown by several exploration wells (6407/10-3, 6306/6-2, 6306/6-1 and 6306/10-1). IKU shallow well 6408/12-U-01 to the west has also penetrated crystalline rocks. Well 6407/10-3 shows fractured granitic basement on top of the Frøya High. Well 6306/10-1 has also drilled into quartz diorite (Slagstad et al. 2008, NPD fact pages). Retrograde quartz dioritic to monzonitic rocks have also been drilled in well 6305/12-2 on the western side of the Frøya High. The retrograde minerals recovered (sericitised feldspar, green hornblende, chlorite and epidote) show similarities to the Palaeozoic Smøla-Hitra Batholith described onshore (Mørk & Johnsen 2005). This crystalline basement is overlain by Middle Jurassic sediments (of the Garn formation) lying above a zone of red-brown paleosols (Jongepier et al. 1996) that may represent a weathered basement. Granitic basement underlying the Middle Jurassic sandstone has also been reached by IKU well 6408/12-U-01 in the northeastern part of the Froan Basin (Mørk & Johnsen 2005). This also shows significant weathering products including kaolinite. Farther south, crystalline basement revealing low-grade metamorphic greenstones, as recognised in the Caledonian nappes onshore, have been drilled below the Bathonian sediments recorded by well 6305/12-2 in the eastern flank of the outer Gossa High (Jongepier et al. 1996).

9.4.3 Devonian-Mesozoic coastal basins and reactivations

The existence of fault-controlled basins at the edge of the Møre Basin and Jan Mayen corridor illustrates a long reactivation history of the pre-existing Caledonian faults and shear zones that are now observed more clearly on the new aeromagnetic data. Onshore, the reactivation included brittle, oblique-slip, dextral strike-slip and normal fault episodes in Devonian, Permo-Triassic, post Mid-Jurassic and Cenozoic times (Grønlie & Roberts 1989, Gabrielsen et al. 1999, Redfield et al. 2005). Seismic and field evidence show that the MTFC, for example, was rejuvenated during the Late Palaeozoic and the Mesozoic periods (Bøe & Bjerklie 1989, Braathen et al. 2002, Redfield et al. 2005, Bøe et al. 2010). The regional NNE-SSW shear zone and fault complexes observed in the near-shore region have most likely been reactivated several times since the Caledonian orogeny. The timing of these events along the Folda-Rørvik-Brønnøysund shear zone is poorly constrained but could be similar to that of the complex MTFC history. This shear zone also coincides with a local and steep bathymetric escarpment suggesting quite recent activity.

At the top of the original Caledonian basement, moderately deformed and slightly metamorphosed conglomerates, sandstones, shales and rare limestones are locally preserved both onshore and offshore central Norway. The ‘Old Red Sandstone’ Devonian basins observed from Norway to Scotland and in surrounding coastal domains (Steel et al. 1985, Fossen 2010) are also known from the coastal region of Trøndelag. Remnants of the post-

orogenic basins exposed on Smøla, Edøya, Asenøya, Hitra and Ørlandet and over a large number of nearby small islands. These Early Devonian sedimentary rocks are similar to those observed in the major Devonian basins of western Norway (e.g., Hornelen, Håsteinen, Kvamshesten, and Solund) and also well expressed on the new Coop aeromagnetic dataset. The rocks on Hitra may be as old as Late Silurian (Bassett 1985). Early Devonian (Emsian) ages of 403-394 Ma in the Ørlandet region have been published by Tucker et al. (2004) but a younger age range of deposition at 386-371 Ma (Asenøya) is also recorded (Eide et al. 2005). Small Devonian basins have also been recognised along the steep faults of the MTFC and along reactivated Scandian low-angle detachments mapped onshore (e.g., the Høybakken detachment, Séranne 1992). The Devonian basin of Hitra rests on top of the magmatic basement rocks of the Støren Nappe exposed on the southern side of the island. However, the relationship with the rocks of the Helgeland Nappe Complex of northern Hitra, also proposed to lie above the extensional detachment remains unclear (Robinson et al. 2014). In the case of the basins near Ørlandet, detailed and earlier studies (Séranne 1992, Osmundsen et al. 2006) have shown that movement on the main detachment faults was west-southwestward, almost in the same direction as the slightly earlier and more ductile folds and dominant lineations that pervade the region and partly explain the magnetic fabrics (Figure 9.3, 9.4, 9.5). This classic tectonic model is in agreement with similar studies of other reactivated Devonian basins in Western Norway (Andersen 1993, Fossen 1992) and eastern Greenland (Hartz & Andresen 1995). All of the sedimentary strata that formed during the Late Caledonian collapse lie directly on the upper plate of the major extensional supradetachment faults that carried both the Devonian strata and their immediately underlying igneous-metamorphic substrate for many kilometres away from their original sites of deposition (Braathen et al. 2002, Fossen 2010, Vetti & Fossen 2012). During extension, rocks in the hangingwall of the detachments were affected mainly by low-grade metamorphism and semi-ductile to brittle deformation throughout, and characterised by faulting and associated basin formation (Sérannes 1992, Braathen et al. 2002). In view of the structural setting, the basement unroofing suggests that brittle faulting also prevailed in these units. A regional burial and subsidence then occurred, as recorded by low-grade metamorphism in several of the Devonian basins (Steel et al. 1985, Sturt & Braathen 2001). This metamorphic episode is considered to be of Late Devonian to Early Carboniferous age (Eide et al. 1997, 2005).

Preserved basins with Mesozoic rocks are also known to occur in the fjord and the coastal zone (Bøe & Skilbrei 1998, Sommaruga & Bøe 2002, Bøe et al. 2005)(Figure 9.3). NE-SW-oriented near-shore basins are identified in the Beitstadfjorden Basin (inner Trondheimsfjorden), in the Edøyfjorden Basin, around Griptarane near Kristiansund, and in the Frohavet Basin (Bøe 1991, Sommaruga & Bøe 2002, Bøe et al. 2010). These basins are often bounded by NE-SW trending fault associated with either the Verran or the Hitra Snåsa fault strands of the MTFC. The Frohavet Basin has a distinct magnetic pattern which partly blurs the underlying basement magnetic pattern (Figure 9.7). The border faults have local magnetic signatures but the main border faults of these basins do not always coincide with the main magnetic lineaments observed in the near-shore domain. South of Vikna smaller Jurassic basins have been identified (Sommaruga & Bøe 2002). The basin border faults are usually NNE-SSE trending but sub-parallel to the adjacent Folda-Rørvik-Brønnøysund shear zone (Figure 9.3).

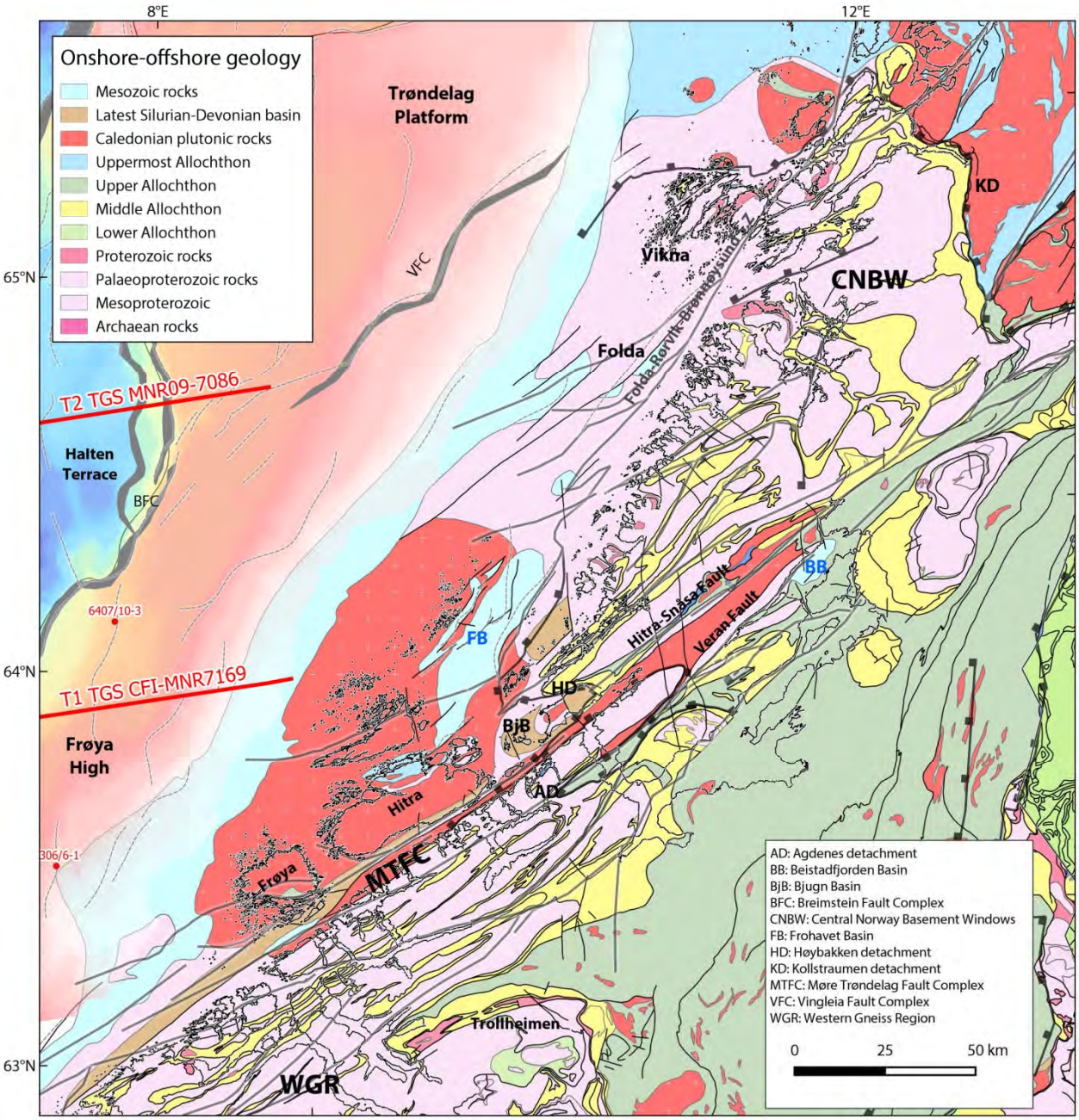

Figure 9.3. Onshore-offshore geology in the eastern area of the modelled transects. Geology map modified and updated after Koistinen et al. (2001) and Solli & Nordgulen (2006)

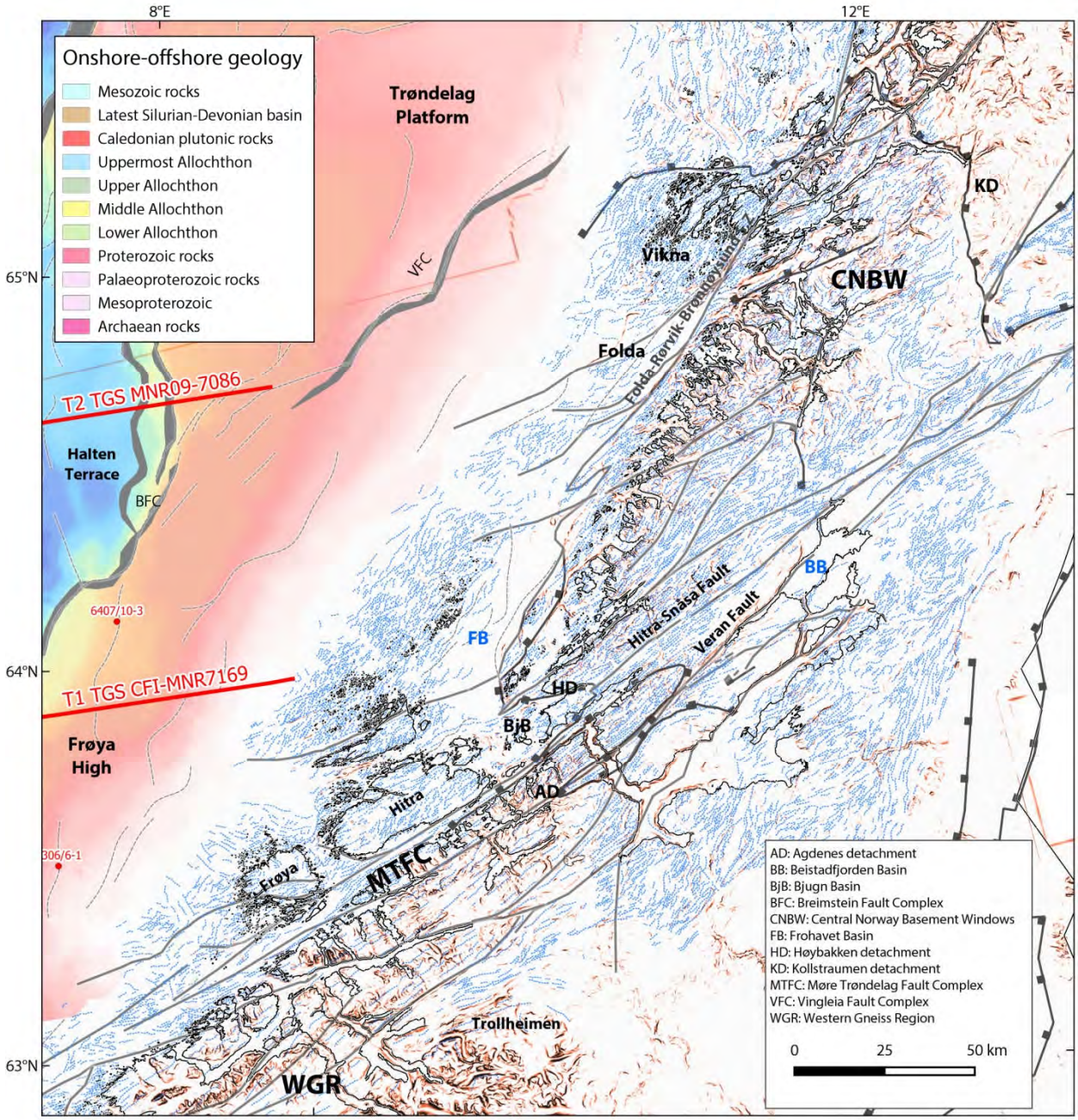

Figure 9.4. Onshore-offshore magnetic lineations based on the new TRAS-13 dataset. Background onshore is the slope filter of the topography (e.g., 50 × 50 m Coop elevation grid, Brönner et al. 2015). The outline of the base Cretaceous unconformity (BCU) isochron is shown in the offshore part.

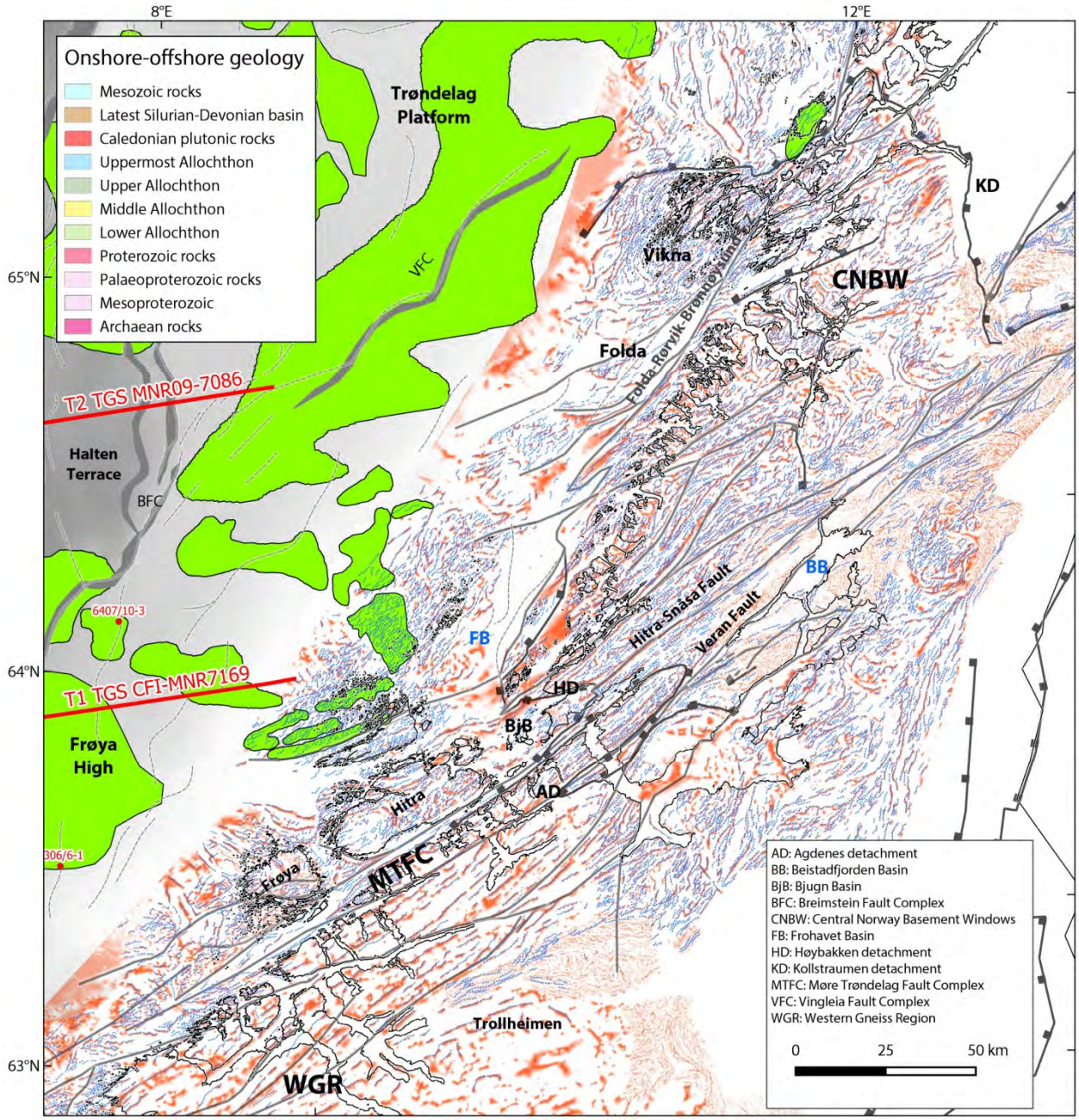

Figure 9.5. Onshore-offshore magnetic lineations and positive Tilt derivative anomalies based on the new Coop aeromagnetic compilation. The outline of the base Cretaceous unconformity (BCU) is shown (grey colors) in the offshore part together with the main magnetic anomalies offshore.

9.5 Potential field modelling across the Møre margin and adjacent Jan Mayen corridor

Potential field modelling is a powerful technique to estimate both basement depth and crustal thickness along selected seismic transects. It also helps to understand better the nature and properties of the crust expected underneath the adjacent sedimentary basins but more controversial due to the lack of direct access. During Coop 2, two crustal transects along the TGS sections CFI MNR-7169 and MNR09-7086 have been modelled across the Møre Basin and the Jan Mayen corridor in the prolongation of the near-shore domain (Figures 9.2 & 9.6). It illustrates the deep offshore prolongation of the basement structure and the overall crustal evolution of the margin from the coastal area to the distal volcanic margin and continent-ocean transition. The deep structural and basement insights of the Mid-Norwegian rifted system are usually poorly imaged due to local sill intrusions, poor migration and/or seismic wave attenuation. Combined with imaging interpretation ambiguities of the deepest extended terranes (see synthetic experiment from McDermott & Reston 2015), it is relatively difficult to estimate the amount of stretching and thinning directly from deep-seismic interpretation and classic structural restoration. Potential field modelling helps to understand not only the top basement estimation but the crustal thickness and derived crustal thinning ß factors.

9.5.1 Forward modelling approach

Foward gravity and magnetic modelling has been carried out using the commercial software GM-SYS (Northwest Geophysical Associates 2006) integrated within the Geosoft Oasis Montaj (Figures 9.9-9.12).

The forward modelling workflow is a step by step process:

- The interpretation and the depth conversion of each transect using the Petrel software. The transects have been subsequently compared with pre-existing NGU Moho and top basement compilations deduced from previous refraction datasets and similar potential field modelling carried out during the Coop Phase 1 (e.g., Nirrengarten et al. 2014, Gernigon et al. 2015). Our regional strategy was also to build a denser grid of 2D crustal transects in between the pre-existing refraction transects in order to first obtain a top basement grid estimation before further 3D modelling (see Maystrencko et al. 2015, this report). The velocity models used for the depth conversion consider regional velocity values derived locally from stack velocities and dynamically readjusted and extrapolated using calibrated and check-shot values derived directly from wells calibrations and synthetics when available (see Table 9.1 on page 213). The nature of and petrophysical information on the pre-Cretaceous and overlying sequences are mostly constrained in the platform area and speculative under the deep sag Cretaceous basins. Most of these wells are located on the Halten Terrace and adjacent platform areas (Figure 9.2) and tie principally the Triassic-Jurassic formations with a few wells reaching basement depth in the area of Frøya High. For the final model, the typical velocity ranges (and the colour code used for the formation layers) are summarised in Table 9.1 are 1.8-2.4 km/s, 3.0-3.2 km/s, 3.8-4.2 km/s, 3.2-5.0 km/s and 5.0-5.5 km/s for, respectively, the Tertiary, the Upper Cretaceous, Mid Cretaceous the Lower Cretaceous, and the Triassic-Jurassic and older formations. Deeper interval velocities and crustal units have been constrained with average velocities derived from the OBS modelling available in the literature (Mjelde et al. 2009, Raum 2000, Breivik et al. 2006, 2011, Kvarven et al. 2014). The OBS transects provide a first

indication of the depth to basement and Moho with an accuracy estimated from 1 km on average to a maximum of 2 km (Mjelde et al. 2009). Refraction data including vintage Expanded Spread Profiles (ESP) purchased between 1983 and 1986 in the framework of the old Elf Aquitaine Norge /University of Oslo REFRANORGE project (Vially & de Clarens 1986) have been considered in the proximal part of the margin. These vintage data were sorted, stacked to one single trace and then transformed from the distance-travel time (x-t) domain to the intercept time-ray parameter (tau-p) domain using the slant-stack procedure (Vially & de Clarens 1986). Our crust database was completed with similar sonobuoys and wide-angle refraction data as presented in detail in Eldholm & Mutter (1986), Planke et al. (1991) and Olafsson et al. (1992). Based on a first correlation with the initial depth model, the ESPs showed a good fit with the first 2D seismic depth model and consequently were used to constrain the crustal transect. More recent OBS modelling from Kvarven et al. (2014) also provided important crustal indications about the Moho, basement depths and crustal velocities from shallow water to the distal domains. The Magnus Rex experiment (Stratford & Thybo 2011, Maupin 2013) provided also indications about the deep crustal units onshore Norway/Fennoscandia.

- The definition of model polygons was then set with appropriate density and susceptibility values and their uncertainties (see Table 9.1 on page 2013). Densities have been deduced from well measurements where available. Others density values have been derived from the seismic velocities and calculated using conventional velocity versus density functions (Nafe & Drake 1957, Gardner et al. 1984, Christensen & Mooney 1995, Birch 1996). Onshore-offshore correlations have also been considered by extrapolating offshore the rock density and susceptibility measurements carried out onshore.

- The forward modelling was finally carried out and tested along the initial crustal sections. The forward modelling technique is based on the original and classic method of Talwani (1973) implemented in the GM-SYS software (Northwest Geophysical Associates 2006). This method computes the magnetic and gravity 2D response of irregular polygons with different susceptibility and density properties. The summation of the response from each polygon produces a signal, which is compared with the observed potential field signature. The free air gravity, the Gzz gravity gradient, the magnetic total field and the vertical gradient of the total magnetic field have been simultaneously modelled for each transect. The shape and properties of the polygons were modified/changed until we obtained the best fit for the anomalies and the best crustal and top basement/Moho depth estimation

9.5.2 Initial crustal parameters and properties

Density properties

The Moho represents a major density contrast in the lithosphere which influences the long wavelengths (>100 km) of the gravity field. A reference density value of 3275 kg/m³ was initially set for mantle rocks. The densities of the upper basement rocks vary from 2700 kg/m³ to 2800 kg/m³ and have been correlated locally with direct and/or extrapolated onshore basements measurements showing a similar range of density values in the Frøya-Hitra coastal area (Olesen et al. 2010). For the lower crust, an average crustal density of 2950 kg/m³ was chosen. These values are in the range of gneissic rocks to high-grade migmatites, gabbros and amphibolites. Middle crustal units are interpreted as quartzo-feldspathic rocks and have

been set with densities of 2830 to 2880 kg/m³. The densities agree with the velocities deduced from OBS modelling. Lower crustal bodies (LCBs) with higher velocities have been modelled with densities of 3050-3100 kg/m³. They have also been seismically recognised in the distal part of the margin (Mjelde et al. 2009, Raum et al. 2006, Kvarven et al. 2014) but also in the proximal part of the Møre margin (Kvarven et al. 2014) and beneath the Frøya High (Vially & de Clarens 1986). Overlying sediment densities vary with depth from 1900 to a maximum of 2700 kg/m³ in the deepest parts of the sedimentary basins.

Magnetic properties

Most of the sedimentary rocks have low magnetic susceptibility compared to igneous and volcanic rocks (Clark 1997, Mørk et al. 2002). Therefore, the effect of sedimentary rocks on the magnetic signal is considered to be negligible. The magnetic properties of the upper and middle crustal rocks likely explain most of the magnetic signal and the medium- to short-wavelength anomalies observed along the transects. To set the initial susceptibility model, we considered the nearby outcropping basement as an onshore analogue for the deep structures. As described before, the central Norway basement observed onshore is divided into two main groups showing contrasting magnetic properties: the Paleoproterozoic blocks and the Caledonian rocks. The old Precambrian rocks have, in general, a higher susceptibility (0.02-0.05 SI) compared to the overlying and younger Caledonian nappes (0.001-0.0015 SI) (e.g., Olesen et al. 2010). Close to the proto-breakup axis, volcanic rocks are observed at the western margins of the modelled transects. On average, the volcanic flows acquired a remanence around 5-10 A/m during their cooling; positive or negative as a function of the geomagnetic polarity (see ODP Hole 642 E measurements, Schönharting & Abrahamsen 1989). Except for these distal lava flows, the remanence contribution from the continental basement units and sedimentary rocks remains, however, largely unknown and was initially considered as zero. This is a limitation of the magnetic modelling. The magnitude of the IGRF field, the inclination and the declination used to calibrate the magnetic modelling represents the average IGRF values calculated along the four transects.

Werner deconvolution and magnetisation Vector Inversion modelling technique

The Werner deconvolution method (Werner 1955) was applied to the new magnetic dataset along the three seismic lines to support the 2D forward modelling (Figures 9.10-9.12). Early methods based on the Werner deconvolution method have been used by geophysicists since the 1950s and have been improved since that time. The robustness of the technique is such that no reduction to the pole is required and it works effectively with both induced and remnant magnetisations. Hartman et al. (1971) extended the original idea of Werner by considering the thin-dyke body as an approximation in resolving other kinds of magnetic anomalies. Hartman et al. (1971) showed for example that the Werner deconvolution can be extended by the fact that the horizontal gradient of the total field caused by the edge of a thick interface body is equivalent to the total field from the thin dyke. Ku & Sharp (1983) refined the method using a further refinement by the Maquardt non-linear least-square, best fitting approach which is also considered in our study. Werner deconvolution essentially searches for variations in slopes and curvatures and computes their approximate horizontal location, depth, susceptibility and dip. The shallow high-frequency anomalies tend to mask the interpretation of deeper anomalies rather than cause erroneous estimates. Werner (1955) already recognised that analysing magnetic anomalies could be complicated because of the interference from adjacent

anomalies and the effect of noise (e.g., diurnal variations, non-two-dimensionality and induced versus remnant magnetism). For this reason, the algorithm we used considers a quadratic form for the source/noise interference to determine the magnetisation properties of the causative bodies. To reduce the noise, we first applied an upward continuation filter to smooth the magnetic grid. If the deconvolution is successful in defining a magnetic source, then depth estimates should define either the edges of the causative body or the depth range of an interface or the upper boundary of an intrusion. This method has proved to be more successful than similar Euler deconvolution in our previous NGU studies and could be relevant when dealing with rift systems and first order basin analysis (e.g., Cochran & Karner 2007).

Magnetisation Vector Inversion modelling technique

The Magnetisation Vector Inversion modelling technique is a voxel based inversion algorithm (Ellis et al. 2012) which allows the magnetisation direction to vary within the model. It thus takes into account the combined effects of remanence, demagnetisation, anisotropy and induced magnetisation. The recovered model after inversion provided a Voxel representation of the rock magnetization at depth. This technique has been tested in the vicinity of the Frøya High. It allowed us to obtain an independent and inverted modelling result used for comparison, together with the forward modelling and Werner deconvolution modelling approaches (see Figures 10-9-9.13).

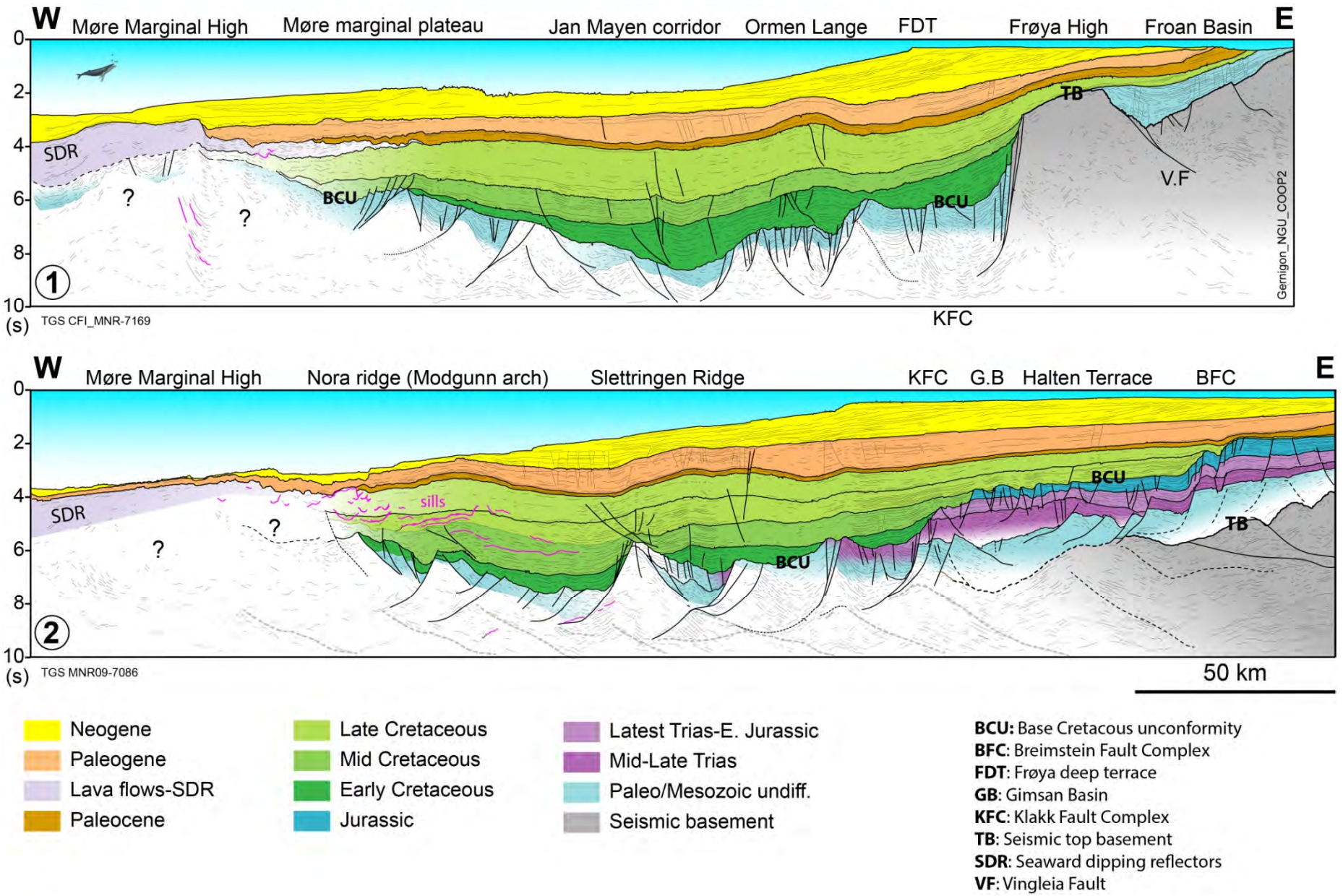

Figure 9.6. Interpretation of the two TGS seismic sections modelled along the Møre margin and the Jan Mayen corridor (see Figure 9.2 for lines location).

9.5.3 Modelling results

Transect 1 from Frøya High to the Møre Marginal High

Main structures

Transect 1 (T1) crosses the Jan Mayen corridor from approximately west to east (Figures 9.6 & 9.9). T1 has been modelled along the TGS seismic line CFI-MNR-7169. The transect extends from the Froan Basin to the Møre Marginal High. It crosses over the northern part of the Frøya High, extends in between the Vigra and Grip highs and covers a large part of the Outer Møre Basin, southwest of the Jan Mayen corridor. The eastern part of T1 is very close to the basement seismic subcrop near the islands of Hitra and Frøya previously described. The outcropping basement correlates well with a clear strong amplitude reflector that we can detect in most of the Froan Basin up to the Frøya High farther west from 500 ms to 3250 ms TWT. On top of this reflector, the Froan Basin represents a half-graben structure with Permo-Triassic to syn-rift Jurassic sediments (undifferentiated in the modelling). The half-graben is controlled by a major east-dipping fault located at the edge of the Frøya High, where a shallow top basement is observed, showing a smooth and gently westward-dipping reflector between 2000 and 3000 ms TWT. Along the transect T1, the Frøya High forms a 30 km-wide intra-basinal eroded horst at the eastern margin of the Møre sag-basin (e.g., Brekke 2000). To the west, the Frøya High is bounded by the eroded Klakk Fault Complex where the base Cretaceous unconformity (BCU) drops suddenly by around 4 km in the deep sag-basin. Between the Frøya High and the Ormen Lange area, a kind of deep terrace system (unofficially termed the Frøya terrace in the present report) has been interpreted. Normal faulting cut by the BCU is observed along a local major border fault, with several hundred metres of displacement which proves to be active up to Albo?-Aptian at the eastern edge of the Ormen Lange, but defined at a shallower level (well 6403/10-1). Along T1, seismic data shows seismic facies interpreted as pre-Cretaceous sediments (Permo-Triassic-Jurassic?) underneath the BCU.

At the level of the deep terrace to a maximum of 12 km along the Jan Mayen corridor, the BCU is relatively deep and estimated up to 7.5 s TWT in between the Vigra and Grip highs which are interpreted as crustal rafts (e.g., Gernigon et al. 2015). Closer to the Early Tertiary basaltic province, the TGS seismic line CFI-MNR-7169 shows that the BCU is rising up to a depth of 5 km near the Møre Marginal High. The new TGS seismic data show clear evidence of pre-BCU wedges in the outer part of the margin segments. They are tentatively interpreted as Permo-Triassic? to Jurassic in age, but the lack of drilling does not allow us to confirm this hypothesis. Nevertheless, we are confident that this seismic facies agrees with the presence of older and pre-sag and pre-Cretaceous sediments between the outer Møre Basin and the Jan Mayen corridor and close to the basaltic province (even below).

Correlation with gravity and magnetic data

Along T1, the gravity signal varies between a maximum of 40 mGal to a minimum of -60 mGal in the Jan Mayen corridor along the deepest BCU estimation (Figures 9.9 & 9.10). A second gravity high is observed in the outer part of the Møre Basin where the free-air gravity anomalies reach a maximum of 20 mGal along T1. Local gravity lows have been observed along the Froan Basin (<20 mGal) and at the level of the volcanic SDRs in the western part of T1.

The magnetic signal shows a clear contrast between the proximal platform domain and the deep basins. The Frøya High shows a prominent magnetic signature with a maximum close to 500 nT. West of the Frøya High the magnetic field is almost flat along the thick Cretaceous depocentre and close to 0 nT up to the volcanic traps where the lava flows have a clear magnetic signature. East of the Frøya High, a magnetic low is symptomatic of the Froan Basin.

Modelling results and deep structures

Underneath sediments, four crustal layers have been considered for the initial model (Figures 9.9 & 9.10) (see Table 9.1): The upper basement (grey colour) defined in the present study fits with the seismic Vp values > 6.0 ±0.2 km/s. It corresponds (in average) with an upper crustal unit showing densities of 2750 $kg.m^{-3}$ and an average magnetic susceptibility of 0.01 SI. Onshore, such properties mostly fit with the Caledonian nappes. Deeper, the middle crust unit (brown colour) shows a higher Vp velocity (6.3-6.6 km/s) and an average density of 2850 $kg.m^{-3}$. Usually, magnetic susceptibilities of the modelled middle crust unit have been considered higher than 0.01 SI and initially set to 0.02 SI on average. This roughly fits with the average properties of the Precambrian rocks sampled and measured onshore. We considered also a 'normal' lower continental crust with Vp velocities of 6.6-6.9 km/s and related densities of 2950 $kg.cm^{-3}$. High-density lower crustal bodies (pink and dark brown colours) are also assumed when Vp velocities are higher than 7.0 km/s. These lower crustal bodies (LCB) have densities higher than 3150 $kg.m^{-3}$. These lower crustal units have low magnetic susceptibilities (~0.005 SI), in agreement with previous potential modelling of the Mid-Norwegian margin (Ebbing et al. 2006, Reynisson et al. 2010).

Assuming the starting model, one of the major discrepancies was encountered at the level of the Frøya High. Accepting an upper crust susceptibility of 0.01 SI was not efficient enough to model the peculiar high and clear magnetic signature of the Frøya High. Both independent Werner and Magnetisation Vector Inversion solutions at that level suggests, however, that the Frøya High magnetic anomaly is restricted to the upper part of the continental crust. Werner cluster solutions show that the magnetic sources are focused between depths of 5 and 10 km with apparently a deeper and different set in the Froan Basin, farther east. Forward modelling and Magnetisation Vector Inversion suggests also that higher susceptibilities of 0.04 to 0.07 SI are necessary to explain the observed magnetic total field on top of this basement high. It contrasts with the low magnetic susceptibilities (0.01 SI) measured in rocks of the Caledonian nappes lying onshore close to the end of T1. These levels of susceptibilities are usually measured in Precambrian basement rocks and are in the range of average values commonly measured on old mafic granulites, andesites, diorites and /or metaperidotites (Clark 1997).

In the eastern part of T1, the depth of the Moho under the platform domain was tied with the old REFRANORGE ESPs (Figure 9.9). In the western part, T1 is constrained by more recent OBS data (Mjelde et al. 2009). Along the Jan Mayen corridor, only one ESP provides an indication about the top basement and Moho depths. In the proximal domain, a Moho is modelled at depths of 33-30 km, in agreement with the ESP data. Close to Hitra, the MAGNUS experiment (Stratford & Thybo 2011, Maupin 2013) suggests a consistent Moho depth at 35 km near the Norwegian coastline. Both our gravity modelling and the vintage ESP measurements in the platform area suggest that beneath the northern Frøya High and southern Froan Basin, up to 10 km of high-velocity (7.1-7.8 km/s)/high-density (3100 $kg.m^{-3}$)

lower crust (LCB) is lying underneath a large part of the platform. Similar proximal and continental LCBs have also been recognised farther south underneath the Slørebøtn sub-basin (Kvarven et al. 2014) and in the northern North Sea (Fichler et al. 2011). Surprisingly, the recent OBS modelling from Breivik et al. (2010) farther north shows that such a high-density LCB does not necessarily extend into the southern part of the Halten Terrace and in the northern part of the Froan Basin. This means that the Frøya High and the southern platform domain may have a different crustal configuration at the scale of the entire continental column.

To the west of the Frøya High, a clear and sharp necking zone can be detected. The modelled Moho is rising from 30 km to less than 25 underneath the adjacent and deep Frøya terrace. The shallowest Moho along T1 is observed at the level of the Jan Mayen corridor in the central part of the transect. The Moho is then deepening slightly to 21-22 km underneath the Møre Marginal High. At that level, Vp wave velocities of 7.1-7.5 km/s have also been recorded by refraction measurements (Olafson et al. 1992, Mjelde et al. 2009, Kvarven et al. 2014). We also considered a consistent high-density body at that level. Close to the continent-ocean transition, the high-velocity/high-density LCB is commonly interpreted as underplated mafic-ultramafic bodies emplaced during the continental breakup (Mjelde et al. 2009) but this model has been challenged. The Vp velocities ranging between 7.1 and 7.9 km/s in the western part of the T1 may indeed be related to underplating. However, the general absence of significant volcanogenetic features such as seaward-dipping reflectors, and the apparent low volume of landward lava flows, both suggest that a large part of the LCBs modelled might also be related to a pre-existing (and inherited) high-density lower crust similar in origin to those modelled underneath the platform domain to the west or observed in the adjacent outer Vøring Basin (Gernigon et al. 2003, Corfield et al. 2004, Ebbing et al. 2006).

The top magnetic basement estimation agrees with the depth of the seismic top basement in the Frøya High and Froan Basin areas. West of the Frøya High, the top magnetic basement was not clearly obvious on seismic, but our modelling proposes a top basement depth of 12-13 km in the deep Frøya terrace and at 15 km in the Jan Mayen corridor where the crust is particularly thin (e.g., 5 km) This area coincides with a local transfer fault zone inferred between the Vigra and Grip highs, and observed and mapped with seismic data at the BCU level. In the Møre marginal plateau, farther west, the top basement is shallower (15 to 9 km) in agreement with the OBS velocities modelled by Mjelde et al. (2009) and the ESP data (Olafsson et al. 1992). At that level the crust is thicker (> 10 km) and the crust preserved on top of the distal LCB is on average thicker than 5-6 km. Based on seismic observation and top basement estimations, 4 to 5 km of pre-Cretaceous sediments seem to be present underneath the BCU as detected in the Møre Marginal plateau. Both the density and the layered seismic facies of the distal wedge observed beneath the BCU suggest that pre-Cretaceous sedimentary rocks are likely to be present in the distal part of the Møre margin. Volcanic basins may also exist underneath the volcanic Inner and Landward Flows (e.g., Berndt et al.2001).

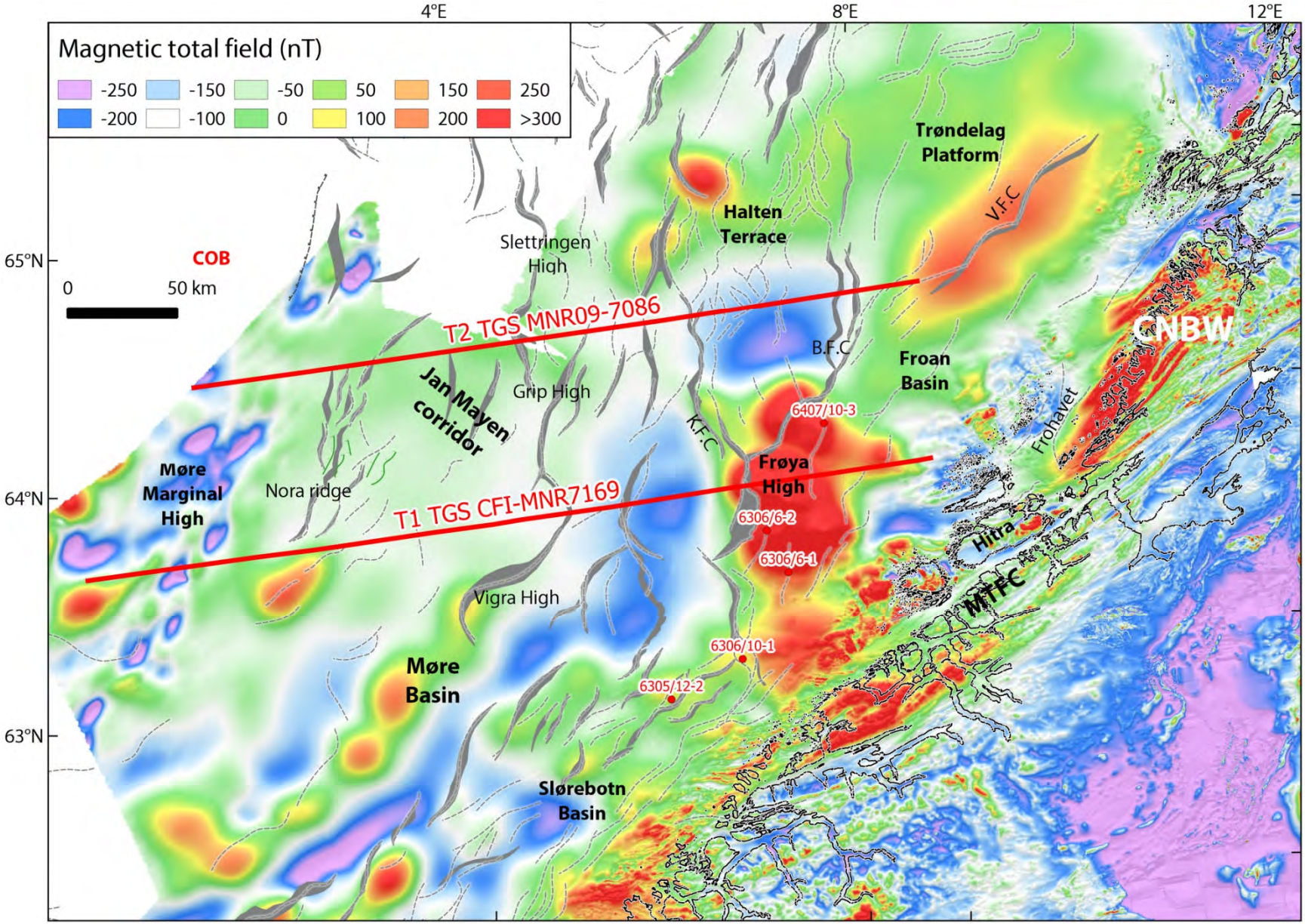

Figure 9.7. Magnetic total field and the location of the two transects modelled (after Nasuti et al. 2013, 2015, Chapter 2 in the present report). B.F.C.: Bremstein Fault Complex; K.F.C.: Klakk Fault Complex; V.F.C.: Vingleia Fault Complex.

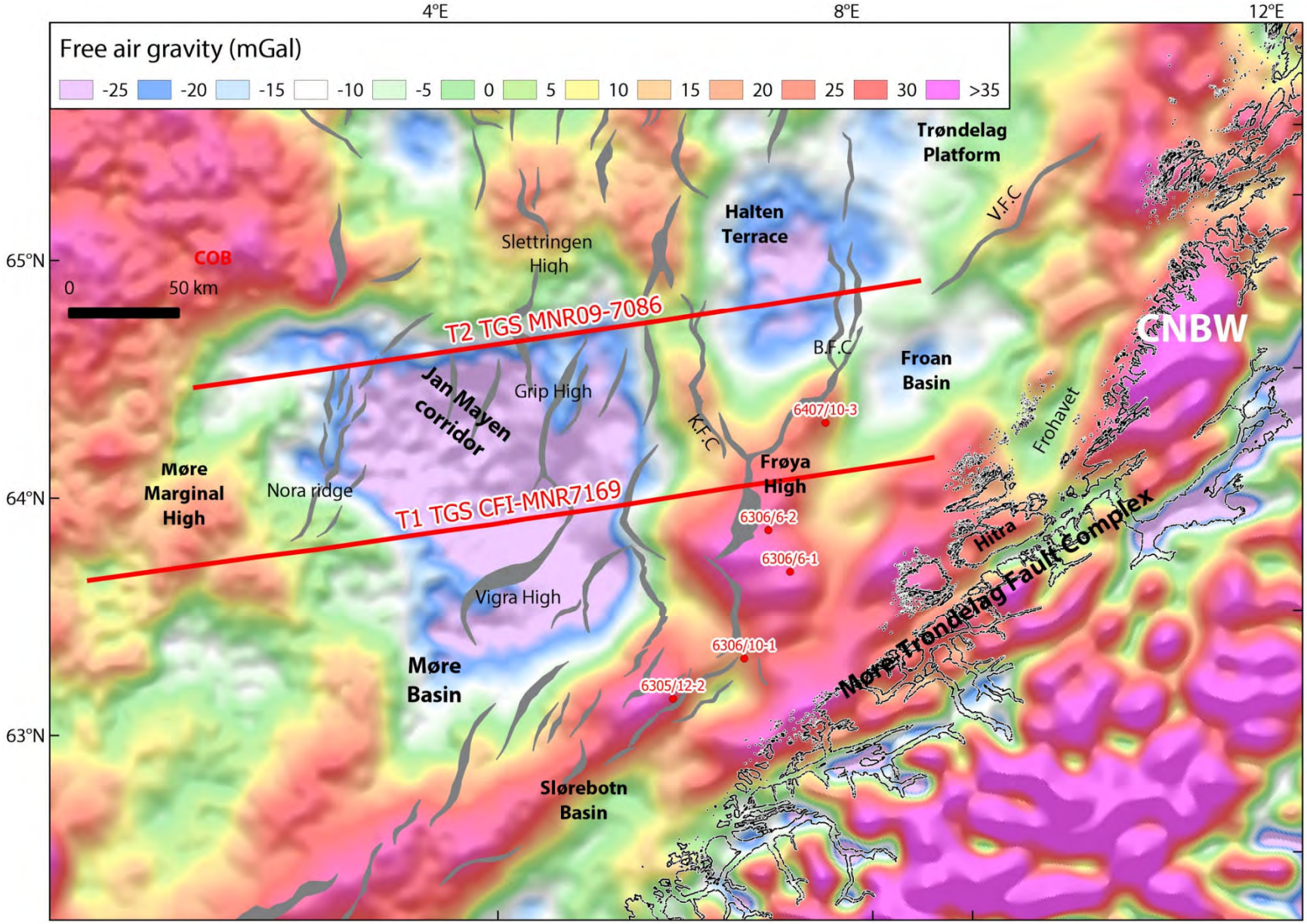

Figure 9.8. Location of the two transects modelled and Free Air gravity (DTU13) anomalies of the Møre margin and adjacent Jan Mayen corridor. B.F.C.: Bremstein Fault Complex; K.F.C.: Klakk Fault Complex; V.F.C.: Vingleia Fault Complex.

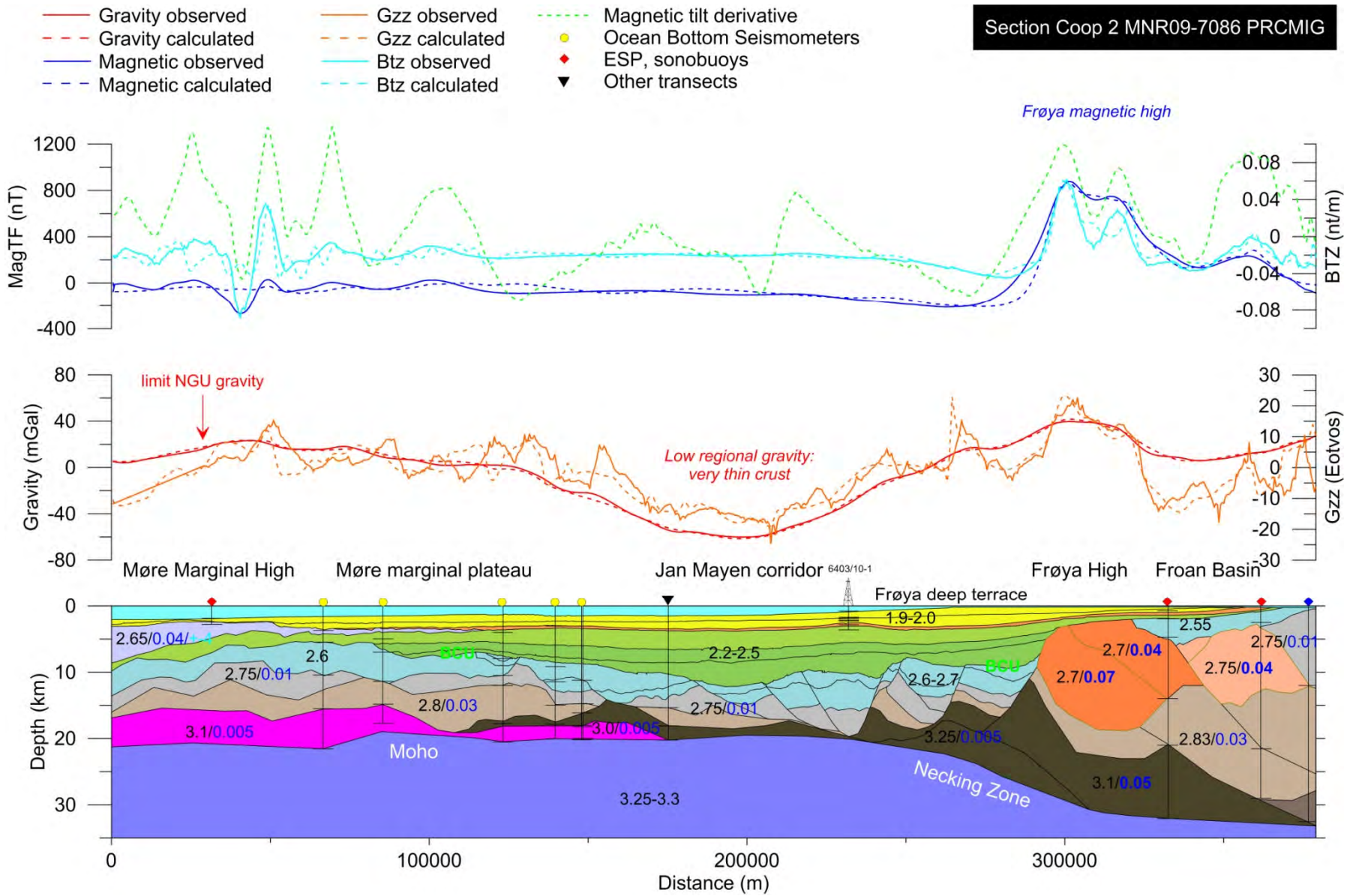

Figure 9.9. Forward modelling results along Transect 1. Each Polygon (see also Table 9.1 on page 213) is characterised by a density value in g.cm^{-3} (black numbers) and susceptibility in SI units (blue numbers). Gzz and Btz represent the vertical gradients of the gravity and magnetic fields, respectively.

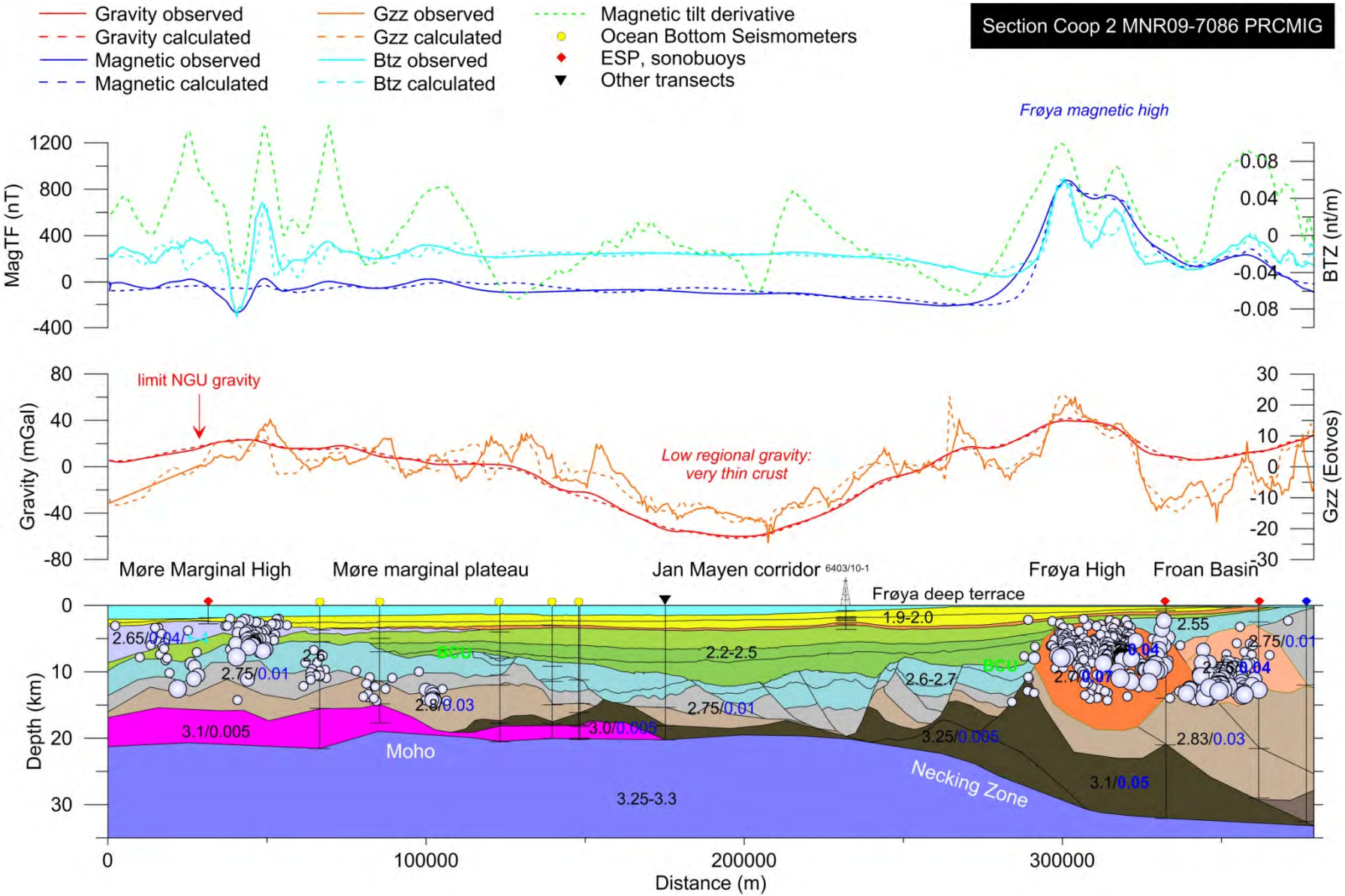

Figure 9.10. Forward modelling results along Transect 1 and Werner deconvolution solutions of the magnetic sources.

Transect 2 from Halten Terrace to the Møre Marginal High

Transect 2 (T2) illustrates the basinal and crustal structures from the southern part of the Trøndelag Platform to the outer Møre Basin (Figures 9.6 & 9.9-9.12). T2 has been modelled along the seismic line MNR09-7086 kindly provided by TGS. It covers the southern part of the Halten Terrace, the Gimsan Basin and the Jan Mayen corridor, including the Slettringen Ridge in the middle. To the west, the BCU can be observed south of the Nora ridge up to 5-6 s TW on the seismic line. To the east, the seismic section illustrates the Triassic-Jurassic platform and terrace system and shows a progressive deepening of the BCU towards the Jan Mayen corridor. The main regional block compartmentalisation, to the east, is characterised by the two major fault complexes and major sub-basin boundaries known in the area: 1) the Bremstein Fault Complex between the Trøndelag Platform and the Halten Terrace, and 2) the Klakk Fault Complex between the Halten Terrace and a deeper Mesozoic terrace (prolongation of the deep Frøya terrace ?) expected east of the Slettringen Ridge. Tectonic activity in the platform and adjacent terrace in the late-Mid Jurassic-Early Cretaceous has resulted in a clear fault development. The Triassic evaporitic layers (Ladinian-Carnian) functioned as local décollements, sub-dividing the decoupled complex into pre- and post-salt structural settings.

A deeper BCU at 7s TWT is observed east of the Nora Ridge (Figure 9.6). Even though numerous sill intrusions exist in this distal domain, a shallowing of the underlying pre-BCU sediments towards the basalt province and related SDRs can still be observed. On top of the interpreted BCU, the Cretaceous sag basin has developed between the Trøndelag Platform and the Møre Marginal High. A potential top (seismic) basement has been identified east of the Breimstein Fault Complex between 4000 and 6000 ms TWT. Intra-basement seismic features suggest a dominant set of east-dipping reactivated shear zones that probably control the pre-salt basin development and decoupled from the latest Triassic to Jurassic rotated fault system that mostly shows west-dipping faults. In the remaning parts of the section, the top basement location in depth remains speculative and is not clearly visible in the seismics.

Correlation with gravity and magnetic data

Along Transect T2, the gravity signal varies between 10 mGal at the western edge of the Halten Terrace (e.g., the Klakk Fault Complex) to a minimum value of -20 mGal observed in the Gimsan Basin area and in the distal part of the margin, west of the Grip High/Slettringen Ridge (Figure 9.11). The free air gravity signal is close to zero at both ends of Transect T2 (i.e. in the Møre Marginal High and in the Trøndelag Platform). The profile starts just at the western edge of the prominent NNE-SSW Vingleia-Vikna magnetic anomalies observed in the Trøndelag Platform. This magnetic anomaly looks similar to the magnetic high domain previously described in the Central Norway Basement Window on the Fosen Peninsula, onshore. The amplitude (100-200 nT), however, is lower compared to the Frøya High anomaly (>500 nT) where the basement is shallower. This magnetic anomaly coincides with a regional NNW-SSE gravity trend observed from Vikna to the northern Frøya High where well 6407/10-3 reaches the basement rocks. This gravity trend coincides with the transition zone in between the Froan Basin and the Halten Terrace. This linear gravity trend is similar to the elongated NNE-SSW gravity anomaly high observed south of the Frøya High and west of the Slørebotn Basin. It differs from the NW-SE gravity trends observed north of the Frøya High along the Klakk Fault Complex, modelled along T2. The gravity triple junction is the Frøya High gravity anomaly (Figure 9.8).

Modelling results and deep structures

The main crustal units have been initially set with similar properties to those of Transect 1 (see Table 9.1). In the plaftorm area, the Moho is at 27-28 km between the Trøndelag Platform and the eastern part of the Halten Terrace (Figure 9.11). Near the Klakk Fault Complex, the modelled Moho is progressively rising to less than 20 km and defines a clear necking zone. This necking zone looks smoother than the Frøya High necking zone described from approximately 100 km to the south. The Moho is deepening a bit under the Slettringen and Nora ridges but remains shallower than 21-22 km. Compared to the T1 modelling, no clear high-density lower crust (LCB) is observed in the platform and terrace domains. However, in the necking zone and underneath the Slettringen Ridge, small bodies with high densities (3100 $kg.m^{-3}$) are required to fit the observed gravity. Near the Klakk Fault Complex in the necking zone, the NW-SE gravity anomaly observed at that level represents the gravity response of such local LCBs also recognised beneath the Frøya High (Figure 9.8). To fit the magnetic signal at the edge of the Vingleia-Vikna magnetic anomaly, upper crustal rocks with magnetic susceptibilities of 0.05 SI are required to fit the observed magnetic total field (e.g., Figure 9.13). Fundamentally, this high-magnetic upper crust is similar to the upper crust modelled in the Frøya High area and a similar Precambrian age is proposed. However, the underlying lower crust looks different and it is not clear whether or not the two anomalies are genetically linked.

Top basement estimation in the eastern part of T2 shows a good correlation with the strong amplitude reflection observed and interpreted as seismic top basement along the seismic section MNR09-7086. East of the Vingleia Fault Complex, the magnetic basement is estimated to be between 5 and 10 km deep (Figure 9.11). West of the Vingleia Fault Complex, the basement is deepening gradually to more than 15 km at the level of the Gimsan Basin in the Halten Terrace. Here, 5 km of pre-salt sediments and/or low-magnetic Caledonian rocks are expected. This domain coincides with the magnetic low observed north of the Frøya High. Still unclear in this part of the margin, we think that Devonian to Permian basins might be present here as well. This is in agreement with the adjacent OBS modelling and top basement estimation (Breivik et al. 2011). Between the Klakk Fault Complex and the Slettringen Ridge, more than 5 km of sediment is proposed to exist between the BCU and the magnetic basement along T2. The MNR09-7086 seismic line shows clearly that pre-BCU wedges exist in this deep structural terrace. Similar sedimentary wedges are observed between the Grip High and the Slettringen Ridge (the section intersects the local transfer system and the intervening basin). However, due to our limited access to deep regional lines, it has not been possible for us to tie these wedges to any of the Jurassic and Triassic formations that are well known in the Halten Terrace. Similar pre-Cretaceous sediments are suggested in the area of the Nora ridge. Close to the basalt, we expect a top magnetic basement at 10 km with almost 5 km of preserved pre-Cretaceous sediments on top. Below the basalt, sediments are also expected in order to fit the gravity. These sub-basalt sediments are possibly Late Cretaceous-Paleocene in age. No shallow basement high and/or exhumed mantle is inferred close to or immediately berneath the Inner and Landward lava flows, as recently suggested in the literature (Péron-Pinvidic, 2013). The high densities involved (>2750-2950 $kg.m^{-3}$), assuming such a tectonic model would create a gravity high incompatible with the gravity anomalies observed in the distal domain. From a gravity point of view, this model has consequently been

ruled out. Near the Nora ridge, the preserved continental crust shows a thickness greater than 4-6 km on top of the LCB.

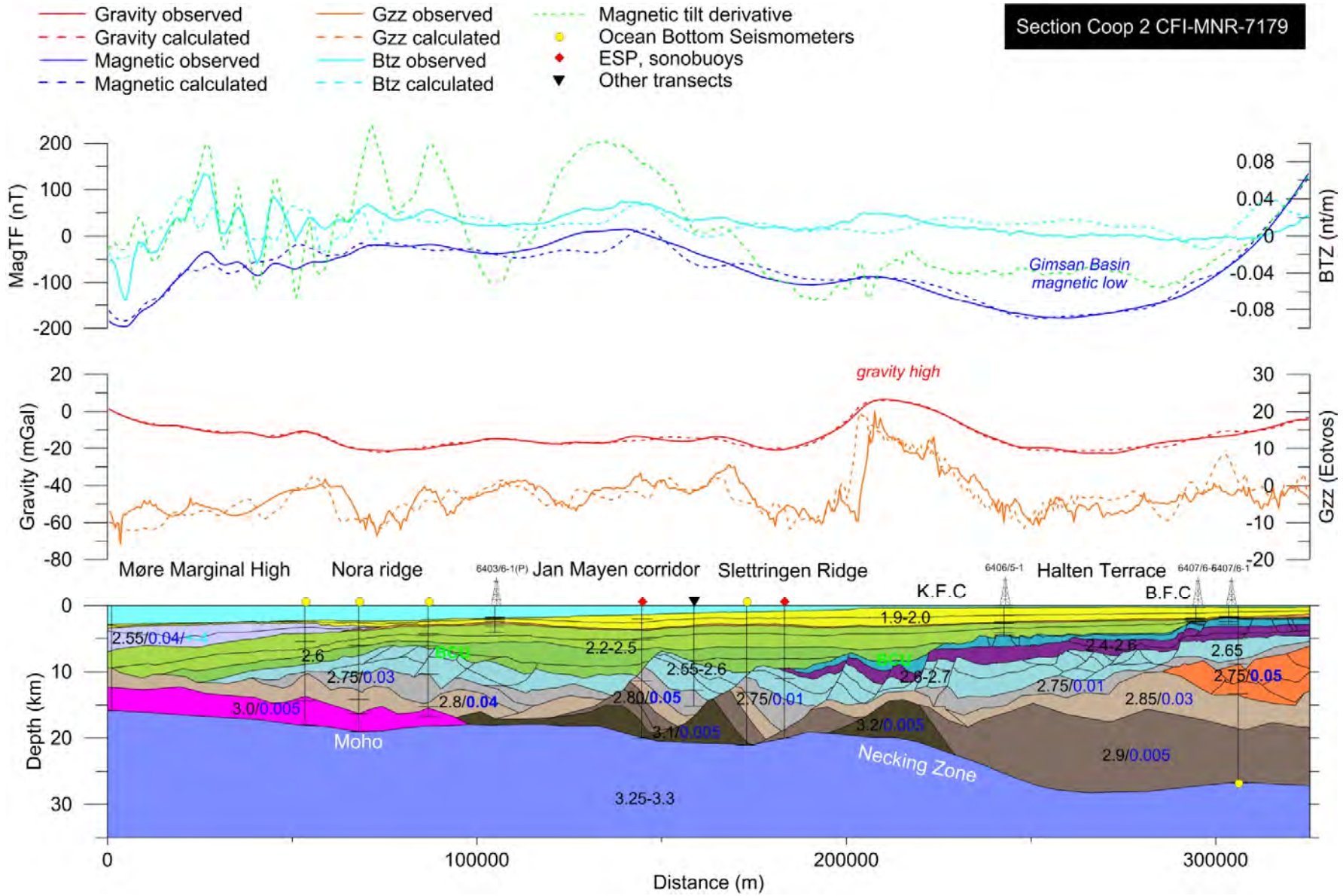

Figure 9.11. Forward modelling results along Transect 2- Each Polygon (see also Table 9.1) is characterised by a density value in g.cm^{-3} (black numbers) and susceptibility in SI units (blue numbers). Gzz and Btz represent the vertical gradients of the gravity and magnetic fields, respectively.

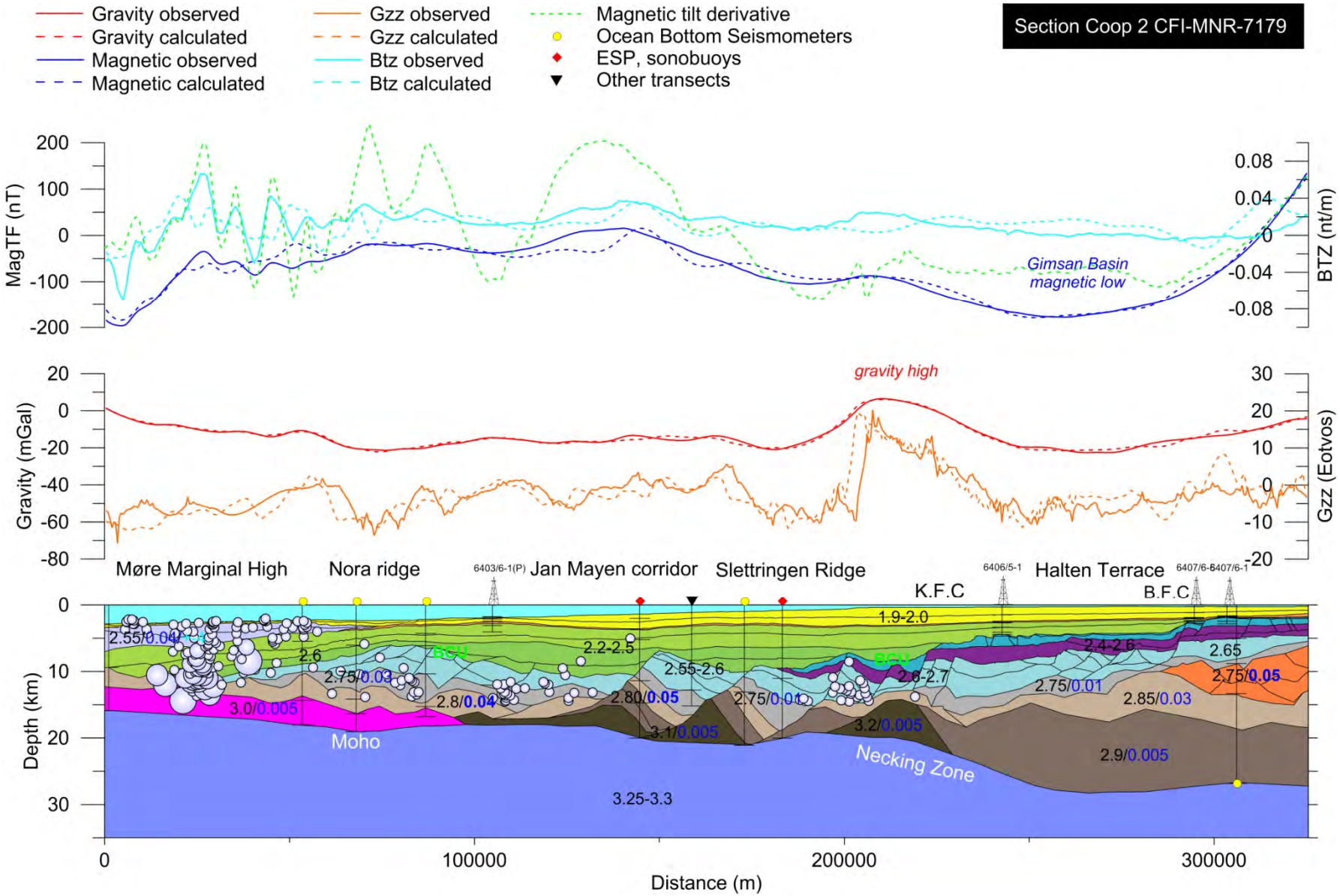

Figure 9.12. Forward modelling results along Transect 1 and Werner deconvolution solutions.

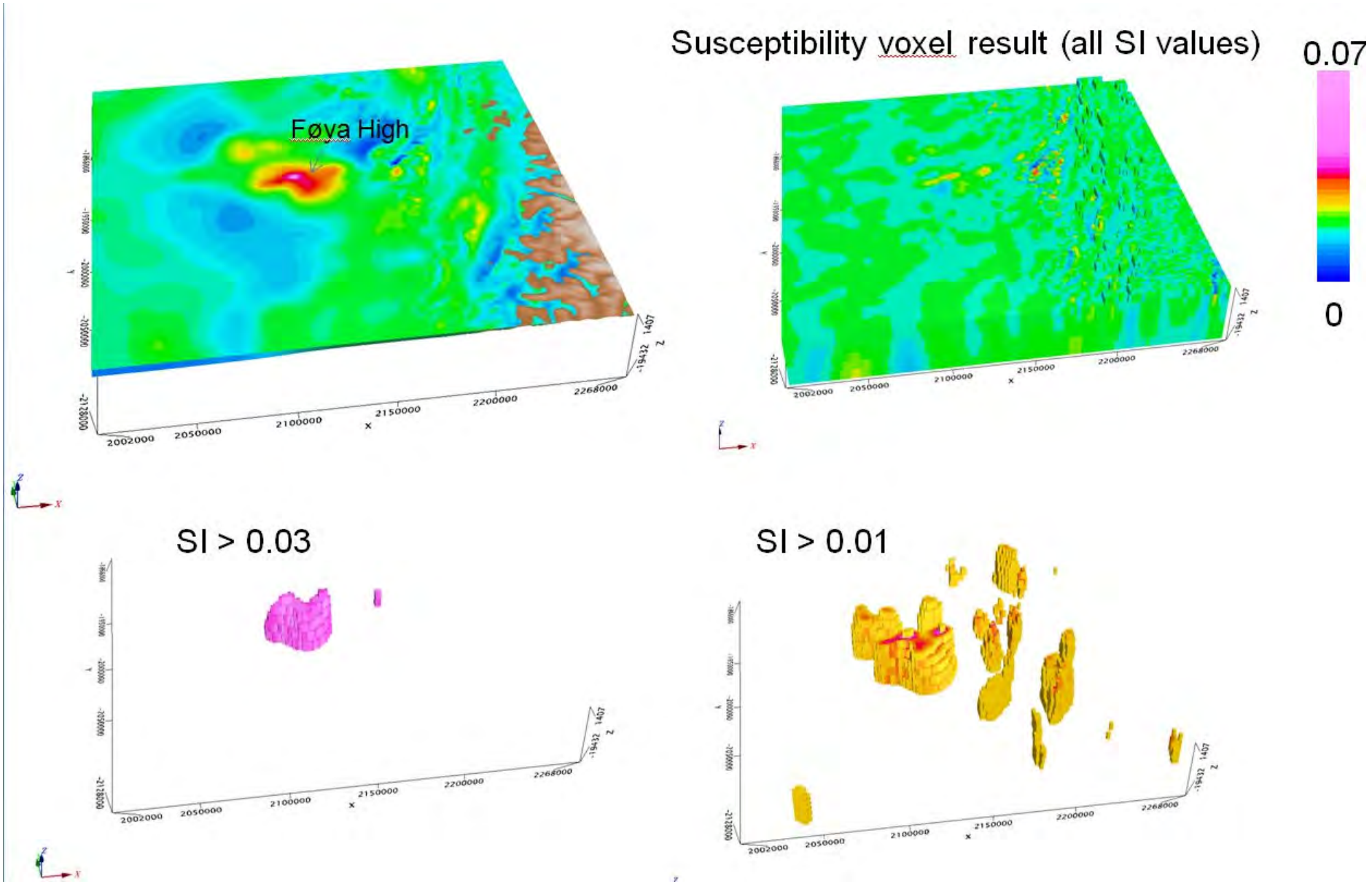

Figure 9.13. Result of the Magnetisation Vector Inversion modelling around the Frøya High.

9.6 Discussion and tectonic implications

9.6.1 Proximal LCB and Frøya High: magnetic dilemma and tectonic buffer

A number of refraction studies across the Møre rifted margin combined in our potential field modelling suggest the occurrence of high-density bodies (LCB) under the distal part of the Mid-Norwegian margin, but also in more central proximal positions along the margin (e.g., Olafsson et al. 1992, Mjelde et al. 2009, Kvarven et al. 2014, Nirrengarten et al. 2014). The significance of these continental LCBs is debatable but fundamental to really appreciating the nature of the lithospheric and crustal deformation involved before the breakup and subsequent spreading (see also Gernigon et al. 2015). The LCBs observed underneath the proximal platform domain and below the Frøya High most likely represent pre-existing and probably old, lower crustal, metamorphic rocks (e.g., Kvarven et al. 2014, Nirrengarten et al. 2014, Gernigon et al. 2015). The potential field modelling confirms that the continental lower crust required particularly high-density material in this proximal part of the margin (Figures 9.1). However, recent OBS data from Breivik et al. (2011) across the Vingleia-Vikna magnetic anomaly (Figure 9.7) suggest that such high Vp velocities/high-density LCB are not systematically present in the Mid Norwegian platform domain. Our modelling along T2 suggests that the lower crust is not always associated with any deeper LCB, north of the Frøya High. Nevertheless, we partly disagree with the suggested origin of the magnetic sources expected for the Vingleian-Vikna anomaly proposed by Breivik et al. (2011). Breivik et al. (2011) have suggested a lower crustal origin for the magnetic source but our modelling rather favours an upper crustal source as expected also in the Frøya High. This upper magnetic crust is located east of the Breimstein Fault Complex, possibly formed along the margin of this specific basement unit. Within this magnetic basement east-dipping fault/shear zones can be observed in the seismic. Between the Frøya High and the Vingleia-Vikna magnetic anomalies, we expect a major crustal contact which it is not necessarily the Høybakken detachment as suggested earlier by Skilbrei et al. (2002). The new magnetic data show that the proposed prolongation of the Høybakken detachment towards the Froan Basin and Halten Terrace is not particularly obvious (Figures 9.4 & 9.5). The main shear zone bifurcation associated with the Folda-Rørvik-Brønnøysund shear zone observed close to Folda, south of Vikna, may be an alternative candidate for such a deep-seated contact. The new Coop 3 aeromagnetic surveys and ongoing investigations should help us to solve this issue.

The Frøya High is the most significant offshore magnetic anomaly of the Mid-Norwegian margin (Figure 9.7). High magnetic susceptibilities are required in the upper crust in order to fit the large amplitudes observed at that level (Figures 9.9 & 9.13). Our modelling suggests that this peculiar magnetic and crustal feature of the Mid-Norwegian margin is probably and dominantly Precambrian in age. Our results are similar to the early model published by Skilbrei et al. (2002). However, we have obtained better seismic constraints from the CFI seismic line and our modelling suggests the presence of a thicker continental crust including a thick LCB under the Frøya High. Skilbrei et al. (2002) did not consider this high-density LCB but also agreed that the magnetic signature of the Frøya High should result from high-susceptibility rocks in the upper part of the crust. This magnetic upper crust unit modelled in our study consider magnetic susceptibilities greater than 0.05 SI and a relatively low to moderate density (2800 $kg.m^{-3}$) for the upper crust of the Frøya High. This magnetic upper crust has petrophysical properties

similar to the largely magnetic granites of the Trans-scandinavian Igneous Belt (TIB) occurring in SE Norway and western Sweden (Högdahl et al. 2004, Olesen et al. 2010).

The wells on top of the Frøya High recovered Palaeozoic rocks which are most likely part of the Caledonian nappes observed onshore (Slagstad et al. 2008). However, the rocks present in the Caledonian nappes usually show low-magnetic properties (<0.01-0.02 SI) as compiled and measured onshore. Susceptibilities higher than 0.02-0.05 SI are symptomatic of Precambrian rocks. To explain this magnetic dilemma, we suggest that the Frøya High may be characterised by small preserved klippes of Caledonian nappes on top of the Precambrian magnetic core. A close onshore analogue could be the CNBW (Figure 9.3), where thin low-magnetic nappes are preserved and infolded on top of the magnetic Paleoproterozoic substratum. The thin low-magnetic Caledonian units are so thin (<3 km) and spatially restricted to synforms that most of the regional magnetic signal remains strongly dominated by the magnetic Precambrian rocks (Figure 9.8).

The Frøya High also behaves as a possible rigid block reactivated and probably acting as a continental locking zone during the subsequent Late Palaeozoic and Mesozoic rift history. A tectonic contact between the Precambrian 'buffer' and the low-magnetic and intruded by plutons on Hitra and Frøya is most likely. Such an inherited contact may have been reactivated several times as a weakness zone, leading to the formation of the Froan Basin (Figure 9.2). The main border fault of the Froan Basin is dipping to the east and is quite similar to the inherited east-dipping faults and/or shear zones that are locally observed in the basement unit. The Froan Basin formed at the edge of the magnetic anomaly and subsequently developed during Permian-Triassic and Jurassic time and possibly even before (Devonian?).

At a deeper level, the Frøya High possibly influenced the style of the necking zone at a crustal scale. West of the Frøya High, a sharper Moho transition is observed between the platform domain and the Møre sag basin where the Moho thins from 30 km to less than 10 km. Analogue models (Sun et al. 2009) show that when stretched, pre-existing rigid blocks can behave as a structural high and its weak extension can cause its neighbouring areas to be thinned rapidly, leading to the formation of lateral deep sag basins. This may explain the sharp necking zone observed west of the Frøya High that developed at the edge of the LCB. A similar necking zone growing at the edge of a similar proximal LCB has been reported from the Angola margin of SW Africa at the edge of large, regional-scale sag basin similar to the Møre Basin in Norway (Contrucci et al. 2004, Moulin et al. 2010). This situation has been referred to a Type-II margin (Huismans & Beaumont 2014).

9.6.2 Distal configuration of the Møre margin and deep nature of the Jan Mayen corridor

The Jan Mayen corridor appears to have influenced the tectonic evolution and subsequent spreading history of the Vøring transform margin defined farther west at the edge of the Jan Mayen Fracture Zone, one of the major oceanic offset in the Norwegian-Greenland Sea (Figure 9.2). The atypical character of the Vøring transform margin and Jan Mayen corridor is particularly characterised by a lower amount of magmatic response compared to surrounding volcanic margin segments (Berndt et al. 2001). Gernigon et al.(2015) have earlier suggested that, in the trend of the Vøring transform margin, the Jan Mayen corridor is likely to represent a much older and long-lived tectonic and basin corridor and interpreted as a large regional

transfer system between the Møre and Vøring margin segments of the Mid-Norwegian margin. The Jan Mayen corridor is thought to represent a large crustal-scale accommodation zone during the stretching of the Mid-Norwegian margin and may have been controlled at depth by inherited NW-SE structure. Onshore Norway only minor NW-SE basement trends are observed in the Caledonian-related basement notably on the northwestern side of the MTFC. However, Strömberg (1976), Doré et al. (1997) and Fichler et al. (1999) have shown that a NW–SE set of Proterozoic lineaments does exist in the Fennoscandian Shield (e.g., Figure 9.1) which also influenced basement faulting and thrust imbrications during the Caledonian orogeny. Even if the prolongation of the Proterozoic lineaments from the shield to the Jan Mayen corridor is still unclear due to late Caledonian overprinting, the Jan Mayen corridor is possibly controlled at depth by similar pervasive NW-SE inherited structures.

The peculiar character of the Jan Mayen corridor is also observed along the continent-ocean transition, where a wide band between the Jan Mayen Fracture Zone and the Norway Basin pseudo-fault shows reduced magmatism and volcanism when compared with the bordering Møre and Vøring Marginal Highs (e.g., Berndt et al. 2001, Gernigon et al. 2015).

9.6.3 Superextension and ambiguity of magma-poor models?

Recently, there have been many studies suggesting the universal applicability of rifted margin models and concepts mostly developed on the Iberian and Newfoundland margins. In the Norwegian system, similar models and the presence of a zone of exhumed and denuded serpentinised mantle has also been suggested and promoted in the inner part of the (pre-breakup) rifted system (Osmundsen & Ebbing 2008, Reynisson et al. 2010, Lundin & Doré 2011, Rupke et al. 2013). Such large zones of exhumed and locally denuded mantle had already been recognised for a long time in the continent-ocean transition on the Newfoundland–Iberian margin. This has been thoroughly studied by different research groups and drilled by DSDP boreholes in key tectonic settings, resulting in a rather constrained crustal architecture model described in a plethora of scientific contributions (Reston et al. 1996, Lavier & Manatschal 2006, Sibuet et al. 2007, Ranero & Perez-Gussinye, 2010, Sutra & Manatschal 2012). Variations of this original conceptual model (as proposed by Boillot et al. 1989) have recently been proposed as a 'new paradigm' to explain the continental rupture and formation of the South Atlantic margin (Unternehr et al. 2010). Nonetheless, the applicability of the Iberian magma-poor model has been challenged and described as limited and questionable in the South Atlantic (Blaich et al. 2008, Mohriak & Leroy 2012, Clerc et al. 2015, Cowie et al. 2015). Nevertheless, similar concepts have been globally adopted based on the South and Central Atlantic margins to also explain the formation of the Møre margin (Péron-Pinvidic et al. 2013). The presence of a large zone of exhumed serpentinised mantle preceding breakup in the outer Møre margin has been suggested by Reynisson et al. (2010) and Péron-Pinvidic et al. (2013) and Rupke et al. (2013). Lundin and Doré (2011) have also suggested relationships between hyperextension (serpentinisation?) and the presence of compressive structures offshore Mid Norway.

We believe, however, that the geological environment and tectono-magmatic events recorded on the Møre margin and in the Jan Mayen corridor are radically different from the deep-water provinces of the Iberian and Newfoundland margins. First of all, it should be mentioned that the

inherited basement domain where the two rifted margins eventually evolved are fundamentally dissimilar. As described in previous paragraphs, the Mid-Norwegian volcanic rifted margin developed in regions of heterogeneous crust, where Early Palaeozoic orogenic belts have been 'squeezed' in between pre-existing Precambrian crust (Schiffer et al. 2015)(Figure 9.1). On the contrary, the Iberian and Newfoundland magma-poor margins typically developed in regions involving either uniformly old (Precambrian) crust or uniformly young (Palaeozoic) crust within the interiors of the orogenic belts (e.g., Bowling & Harry 2001, Chenin et al. 2015).

The dramatic amount of magma emplaced during the breakup and the thick syn-rift and post-rift sedimentary successions (Figure 9.6) observed on top of the thinned crust (>8-9 km) also represent major differences compared to the deep-water, sediment-starved, Iberian margin where the exhumed serpentinised mantle is almost in direct contact with the sea-water along the continent-ocean transition (Boillot et al. 1989, Whitmarsh et al. 2001). They usually occur adjacent to highly tilted rift blocks in a hyper-extended continental crust (less than 3-4 km thick) showing minor to moderate indications of pre-, syn- and post-rift volcanism (Whitmarsh et al. 2001, Brönner et al. 2011). This is a fundamentally different situation compared to the large volume of magma that were produced in the distal part of the Mid-Norwegian margin during the onset of breakup (e.g., Eldholm & Grue 1994, Berndt et al. 2001).

As earlier discussed in Gernigon et al. (2015), a zone of exhumed mantle in the Møre margin is not clearly obvious, nor formally identified. The size of the structure involved in the Møre Margin is also different and 2-3 times thicker and wider compared to the allochthonous blocks described from the Iberian margin (see 1 x 1 crustal scale comparison in Gernigon et al. 2015). Where clearly recognised (e.g., the Iberian margin), zones of exhumed continental and serpentinised mantle are commonly wider than 50 km, showing gradual and high Vp values >7 km/s with no abrupt Moho transitions (Minshull 2009). In that context, the distal part of the Møre margin and the nature of the LCB, is still controversial and the previous crustal studies of Reynisson et al. (2010) and Peron-Pinvidic et al. (2013) have already illustrated radically opposed and contradictory crustal models. The first has suggested the presence of a very thick continental ribbon at the outer Møre margin (15-20 km in thickness) while the second model has proposed a drastic thinning of the crust and the presence of a zone of exhumed continental mantle rising in the outer Møre Basin. The crustal modelling reported in the present study suggests that the thinned continental crust of the Møre margin and adjacent, oblique, Jan Mayen corridor still shows locally relatively thick continental terranes and preserved (pre-thinning) sediments. We estimate that the continental crust on top of the distal LCBs is locally too thick (> 5-8 km) to correlate with an underlying and hypothetical serpentinised body (Figures 9.9 & 9.11). The more recent Vp values of 7.2-7.3 km/s published by Kvarven et al. (2014) could be compatible velocities to those in layers of serpentinised mantle locally recognised in the North Atlantic (see review by Minschul 2009). Velocities of less than 7.6 km/s would require a much more drastic crustal thinning and a thickness of the overlying continental crust of less than 3-4 km (e.g., Nirrengarten et al. 2014, Gernigon et al. 2015). We also see on the new seismic that wedges of pre-Cretaceous sediment do exist in the distal parts of the Møre Basin. Our model looks similar to that of Reynisson et al. (2010) but we expect more thinning (almost twice as much) of the distal ribbon-block and less thinning under the Møre Basin (almost half). We suspect that this difference could be partly the result of the marine gravity compilation used by Reynisson et al. (2010) during their work. Our recent revaluation of this old NGU grid shows

locally 10-15 mGal of difference compared to the newest and corrected dataset (not available in 2011). A 10-15 mGal large difference is enough to explain the divergent thickening versus thinning interpretations when compared to our potential field modelling.

Local serpentinisation could eventually have occurred in the central part of the Møre Basin and Jan Mayen corridor, where the crust is locally much thinner but still thicker than 3-4 km (Figure 9.9). Seismic indications of symptomatic +7km/s velocities in the central parts of the Jan Mayen corridor will, however, be required to validate this hypothesis. The lack of LCB modelled in the inner part of the Møre sag basin (Kvarven et al. 2014) shows, conversely, that a very thin crust does not always and necessarily coincide with an underlying LCB usually symptomatic of mantle serpentinisation (Kvarven et al. 2014). A non-embrittlement of the whole crust and rapid sealing of already decoupled deep fault systems (and/or pre-existing, inherited low-angle detachments) may have prevented water from entering the inner part of the sag basin, and therefore could explain the lack of serpentinisation.

We favour a tectonic scenario where a large part of the LCBs observed underneath the Cretaceous sag-basin mostly represents both inherited mid to lower crustal lenses as also suggested in the outer Vøring Basin farther north (Gernigon et al. 2003, Ebbing et al. 2006) Even if the crust has been considerably thinned beneath the Møre sag-basin, it is locally less compared to the hyperextended Iberia-type margin hyperextended system and the size of the structural blocks/rafts involved in the Møre margin area is much greater. For that reason, Gernigon et al. (2015) proposed a separate and intermediate superextension stage during crustal thinning between 10 and 4 km to avoid further confusion with the term hyper-extension and the exhumation phases often associated with zones of massive and pervasive serpentinisation which are not so obvious in the Møre margin. The nature of the crust close to the Tertiary basalts is also interpreted as a primary mixture of breakup-related intrusive and residual continental crust. Pre-rift and exhumed lower continental crustal rocks, more or less intruded and/or underplated by late-magmatic intrusions during the first phase of breakup and volcanic margin formation, might be a better option for the deep-crustal structures of the volcanic rifted system discussed in the present report. From a tectonic point of view, the outer Møre Basin probably represented the remnant of a continental marginal plateau before breakup (as defined by Lister et al. 1986), less thinned compared to the inland rift system that originally and mostly focused in the inner parts of the Møre Basin and along the Jan Mayen corridor. In the outer Møre Basin, the marginal plateau, partly covered by the Tertiary lava flows, represents for us a super-thinned plateau lying in the northern prolongation of the Fugløy Ridge clearly showing thicker continental crust, and a very abrupt magmatic continental-ocean transition (White et al. 2008). Preserved lower continental crust in a highly-extended regime has also been suggested and/or described beneath similar sag-basinal systems. These are interpreted as Type-II margins and has been described in the South Atlantic (e.g., Angola margin: Sibuet & Tucholke 2012, Brune et al. 2014, Huissmans & Beaumont 2014, Clerc et al. 2015).

Intense volcanism and typical SDR (Planke et al. 2000) recorded along the proto-breakup axis is a major difference compared to the conventional ´Iberian-type´ magma-poor system where such significant volcanic features are not observed (Brönner et al. 2011, Sibuet & Tucholke 2012). In the Vøring Marginal High, the geochemical signature of the silicic volcanism drilled underneath the tholeiitic basalts of the inner SDR wedge (Figures 9.1 & 9.2) suggests that

continental crustal anatexis has occurred and confirms the presence of underlying and preserved continental crust with a possible Caledonian affinity in very close proximity to the oceanic domain (Meyer et al. 2009). Even though the SDR of the Møre Marginal High has not yet been drilled, we may expect a similar configuration and preservation of the pre-existing continental crust in the outer Møre Basin (Figure 9.13). Here, we also interpret the substratum of the SDR wedges as stretched continental crust with basins moving gradually by increasing dyke injection towards a MORB-type igneous crust. This interpretation is quite similar to the volcanic margin and dyke systems described earlier and documented by field observations onshore East and West Greenland, where more than 90% of the upper continental crust is locally affected by gradual magmatic dilatation (Karson & Brooks 1999, Callot et al. 2001, Klausen & Larsen 2002, Geoffroy 2005). Magmatic underplating, plumbing and massive dyking of stretched continental crust can localize pulse and trigger a complete lithospheric rupturing of magma-rich margins, before and without necessarily involving a complete and syn-kinematic lamination of the continental crust before the pulse of volcanism (e.g., Nicolas et al. 1994, Ebinger & Casey 2001, Geoffroy 2005, Buck 2006, Gac & Geoffroy 2009, Franke 2013, Yamasaki & Gernigon 2009). Buck (2006) notably showed that lithosphere with a thicker continental crust should rift magmatically with much less force than for a lithosphere with thin crust. With a much larger volume of basalt erupted, this could be a non-negligible difference from Iberian-type hyperextended margins, where relatively continuous thinning and mantle denudation were observed before the (low to moderate) extrusion of breakup volcanic rocks on the surface (Brönner et al. 2011). In the case of the North Atlantic, the origin of the breakup magmatism and formations observed in the outer part of the Mid-Norwegian margin is also unclear and could have involved not only intrinsic (e.g., rift-related) but also extrinsic geodynamic processes including controversial plume and/or sub-lithospheric processes (Meyer et al. 2006, Hansen et al. 2009). Even the presence of preserved, fertile, sub-continental mantle material may have been involved, associated with pre-existing suture zones or old slabs preserved and now observed in the lithospheric mantle (Foulger et al. 2005, Schiffer et al. 2015).

9.7 Main conclusions

- In this phase 2 of the Coop project, we have investigated the onshore-offshore relationship observed in central Norway. We have shown a preliminary interpretation of the new Coop aeromagnetic surveys (SAS-11, TRAS-12 and STAS-13) in terms of structural inheritance and prolongation of the late post-orogenic detachments mapped onshore.
- On the new magnetic data, the newly defined Folda-Rørvik-Brønnøysund shear zone appears to represent an old and major continental, strike-slip feature that has been probably underestimated in previous studies. This shear zone probably influenced the prolongation of the Kollstraumen detachment, now slightly shifted in the offshore domain. The Høybakken detachment bifurcates towards this new shear zone and does not appear to extend towards the western basins.
- In the direct offshore prolongation of the new aeromagnetic survey, two recent 2D seismic lines provided by TGS have been modelled across the Møre Basin and the Jan Mayen corridor. They helped to constrain better some of the controversial crustal units together as well as the top basement and Moho depths.

- Lower crustal bodies (LCB) have been identified and modelled in many locations along the two transects. In the proximal domain, these structures are associated with pre-extension inherited crust and are unlikely to be related to syn-thinning (Mesozoic) serpentinised mantle.
- Locally, the LCB is overlapped by high-susceptibility upper-middle crust which help to explain notably the prominent magnetic signature of the Frøya High. The Frøya High is interpreted as a Precambrian granitic complex quite similar to the magnetic Transcandinavian Igneous Belt (TIB) granitoids observed in Sweden and Norway. This may indicate the existence of an inherited back-arc type of crust stretching from the northern North Sea up to the Frøya High and Froan Basin. This type of lower crust is apparently not observed beneath the Vingleia-Vikna magnetic high.
- In the distal parts of the Møre margin and adjacent Jan Mayen corridor, both lower and middle magnetic crust are likely preserved, at least up to the Vigra, Slettringen and Grip highs, which are interpreted as autochthonous continental crustal rafts. The Jan Mayen corridor is also a peculiar oblique margin segment probably affected by a component of higher lateral friction compared to the Møre Basin itself.
- Our model does not necessarily support any significant embrittlement or extensive mantle serpentinisation of the mantle east of that domain, where the preserved continental crust is still relatively thick (>4-5 km). Serpentinisation conditions could be present along the Jan Mayen corridor but would be local, rather limited and are still unconstrained by refraction seismic data.
- In the central/outer Møre Basin, we propose that some LCBs rather represent remnants of lower Caledonian crust exhumed during a phase of significant thinning of the crust and sag-basin formation. The inherited structures possibly control the late structural style and development of the Mid-Norwegian margin, at different levels and at different geological times. The deepest crustal structures seem to have influenced the overall style of crustal thinning of the rifted margin (e.g., the localisation and slope of the necking zone).
- As in recent tectonic discussions (Mohriak & Leroy 2012, Clerc et al. 2015), we believe that the inferred worldwide applicability of the Iberian magma-poor model also remains relatively ambiguous offshore Norway and is possibly model-driven. In terms of heat flow and preservation of potential pre-Cretaceous source rocks and reservoirs in the outer Møre Basin, our model is also more optimistic. Observations such as: 1) Preserved thicker continental and magnetic crust (superextension), 2) the great thickness of the syn-/post-rift sediments, 3) the long period of rifting with an intermediate cooling event and 4) the presence of a large volcanic SDRS near the continent-ocean transition have nothing in common with the magma-poor and sediment-starved Iberian margin. No zone of exhumed and denuded mantle has been observed and/or demonstrated clearly in the outer part of the Møre Basin, and both pre-Cretaceous sediments and underlying continental crust seem to be preserved up to the SDR area. The Møre margin is rather interpreted as an aborted type-II rifted margin (e.g., Angola) reactivated in Late Cretaceous time before the formation of the outer volcanic margin. The Jan Mayen corridor also shows an oblique component with peculiar tectonic characteristics and regional stress regime.
- Refined interpretations of the onshore-offshore relationships from the North Sea to Nordland will be presented in the Coop phase 3 report. We will also consider the new Frøya High aeromagnetic survey combined with an extra and more recent CFI seismic dataset already provided by TGS for our next Coop 3 investigation.

Table 9.1. Parameters used in the starting models.

Layers	Density (kg.m^{-3})	Average density	Susceptibility (SI)	Remanence (A/m)	Vp proxi (km/s)	Vp deep (km/s)
	SEDIMENTARY LAYERS					
Water	1030		0	0	1.45	
→	→ Sea floor					→
Neogene	1900	1900	0.001	0	1.8-1.9	1.8-1.9
Paleogene	2000	2000	0.001	0	2.0-2.2	2.0-2.2
Tare	2050	2050	0.001	0	2.1-2.45	2.1-2.45
Tang	2225-2260	2250	0.001	0	2.2-2.45	2.2-2.45
→	→ Base Tertiary Unconformity					→
Upper Cretaceous	2150-2350	2250	0.0002-0.003	0	2.4-3.0	3.1-3.2
Mid Cretaceous	2300-2375	2350	0.0002-0.003	0	3.0-3.8	3.8-4.2 (4.1)
Lower Cretaceous (Albien-Ceno)	2400-2500	2450	0.0002-0.003	0	2.8-4.2	4.2-4.4
Lowermost Cretaceous (BCU-Albien)	2300-2550	2500	0.0002-0.003	0	4.0-4.2	4.4-4.9
→	→ Base Cretaceous Unconformity					→
Jurassic	2600-2700	2650	0.0002-0.003	0	4.1-5.4	4.7-5.4
Trias	2600-2700	2650	0.0002-0.003	0	4.1-5.4	4.7-5.5
Phanerozoic Undifferentiated (Pre-Cretaceous)	2550-2600	2550-2600	0	0	4.1-5.5 (5.2)	5.5 (5.5)
Pre-Permian (TrØndelag)	2680	2680	0	0	4.5-5.5	
	BASEMENT-MANTLE LAYERS					
→	→ Magnetic top basement					→
Upper Basement (Caledonian nappes)	2700-2790	2750	0.005-0.01	0	5.6-6.2	6.0-6.5
Middle Crust	2790-2925	2800	0.01-0.035	0	6.3-6.6 (6.6)	6.0-6.5
Lower Crust	2940-3000	2950	0.005	0	6.6-6.9	6.6-6.9
CLCB type I	3100-3200	3150	0.002	0	7.1-8.0	7.1-8.0
CLCB type II	3000-3050	3150	0.005	0	7.1-7.4	7.1-7.4
OLCB type III	3000-3010	3150	0.005	0	7.0-7.5	7.0-7.5
→	→ Moho					→
Mantle	3240-3300	3275	0-0.0025	0	8.0-8.2	8.0-8.2
SDRS, basalts	2590-2750	2.65	0.015	-1	5.0	5.0
Upper Oceanic crust	2800	2800	0.04	+/- 1-5	4.9-5.1	4.9-5.1
Lower Oceanic crust	2900	2900	0.005	0	6.7-6.9	6.7-6.9

10. 3D DENSITY, MAGNETIC AND THERMAL MODELLING WITHIN THE MID-NORWEGIAN MARGIN AND ADJACENT AREAS OF THE MAINLAND

Yuriy Maystrenko & Laurent Gernigon

10.1 Introduction

To understand the regional-scale structural pattern of the crystalline crust within the Mid-Norwegian continental margin and the adjacent Norwegian mainland, a lithosphere-scale 3D model has been constructed, covering the area of interest in the frame of the Coop2 project. The 3D structural model covers the area from 60.6°N-62.15 °N to 65.3°N-67.1°N latitude and from 0.6°E-6.4°E to 7.5°E-14.1°E longitude (see orange frame in Figure 10.1). The Coop 2 study area overlaps partially with the northeastern corner of the Coop1 area where the geometry of the Coop1 model has been modified according to recently published results of the modelling of wide-angle seismic data (Kvarven et al. 2014). In addition, the geometries of the lithosphere-asthenosphere boundary and the Moho topography have been slightly modified compared to the Coop1 model (Maystrenko 2014). Furthermore, the northeastern part of the Coop2 model overlaps with the NEONOR2 3D structural model. The NEONOR2 model is in preparation for the scientifically-oriented 'NEOtectonics in NORdland 2' (NEONOR2) project which is aimed at investigating the neotectonics in Nordland.

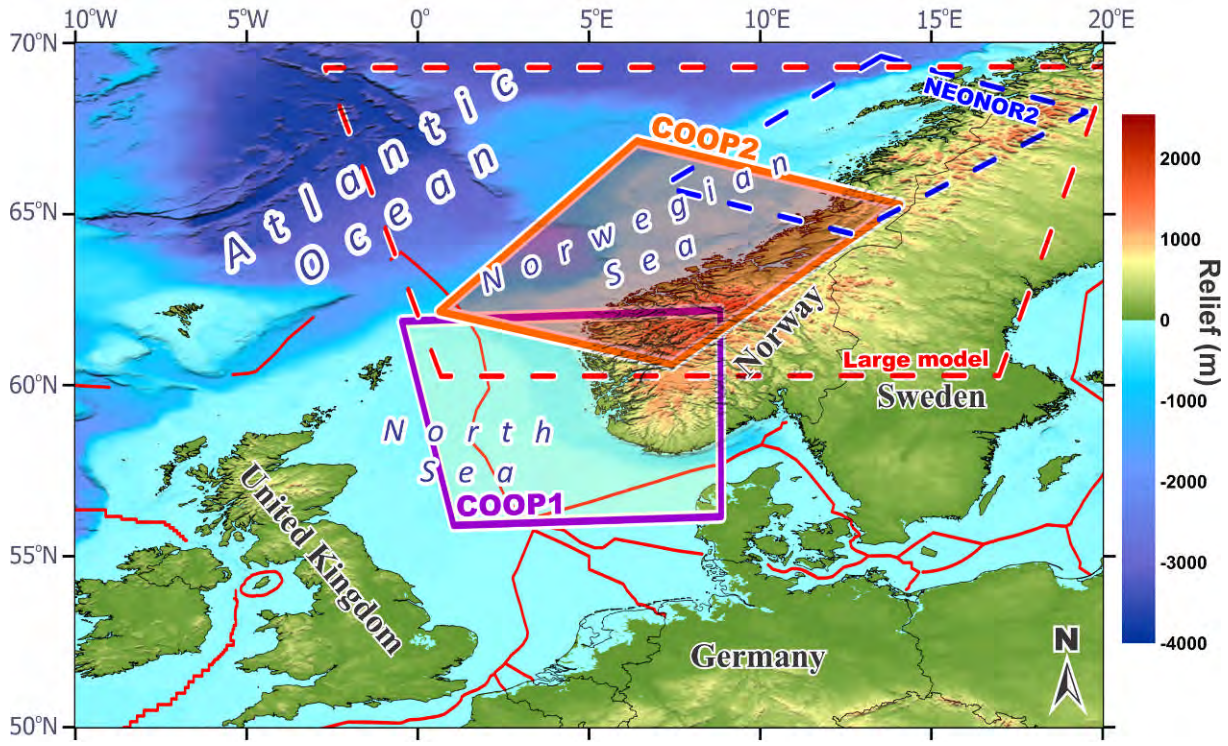

Figure 10.1. Overview map of northwestern Europe with location of the Coop*2 (orange frame),* Coop*1 (purple frame) and NEONOR2 (blue dashed frame) 3D structural models (bathymetry and topography from IOC, IHO, BODC 2003). In addition, the large-scale, low-resolution, NGU model is shown by the red dashed frame.*

Actually, the Mid-Norwegian continental margin is located between the Cenozoic oceanic domain of the North Atlantic region in the west and the exposed Fennoscandian Shield in the east. This specific location between two completely different tectonic elements implies that the

Coop2 study area is definitely affected in terms of gravity and temperature by the closely located thin oceanic lithosphere of the Atlantic Ocean and much thicker continental lithosphere of the Fennoscandian Shield. In order to consider the regional-scale effect from the oceanic and continental domains, the less detailed large 3D structural model (see red dashed frame in Figure 10.1) has been used. This large-scale, low-resolution, NGU model allows us to consider the gravity and thermal effects from the relatively shallow lithosphere-asthenosphere boundary and

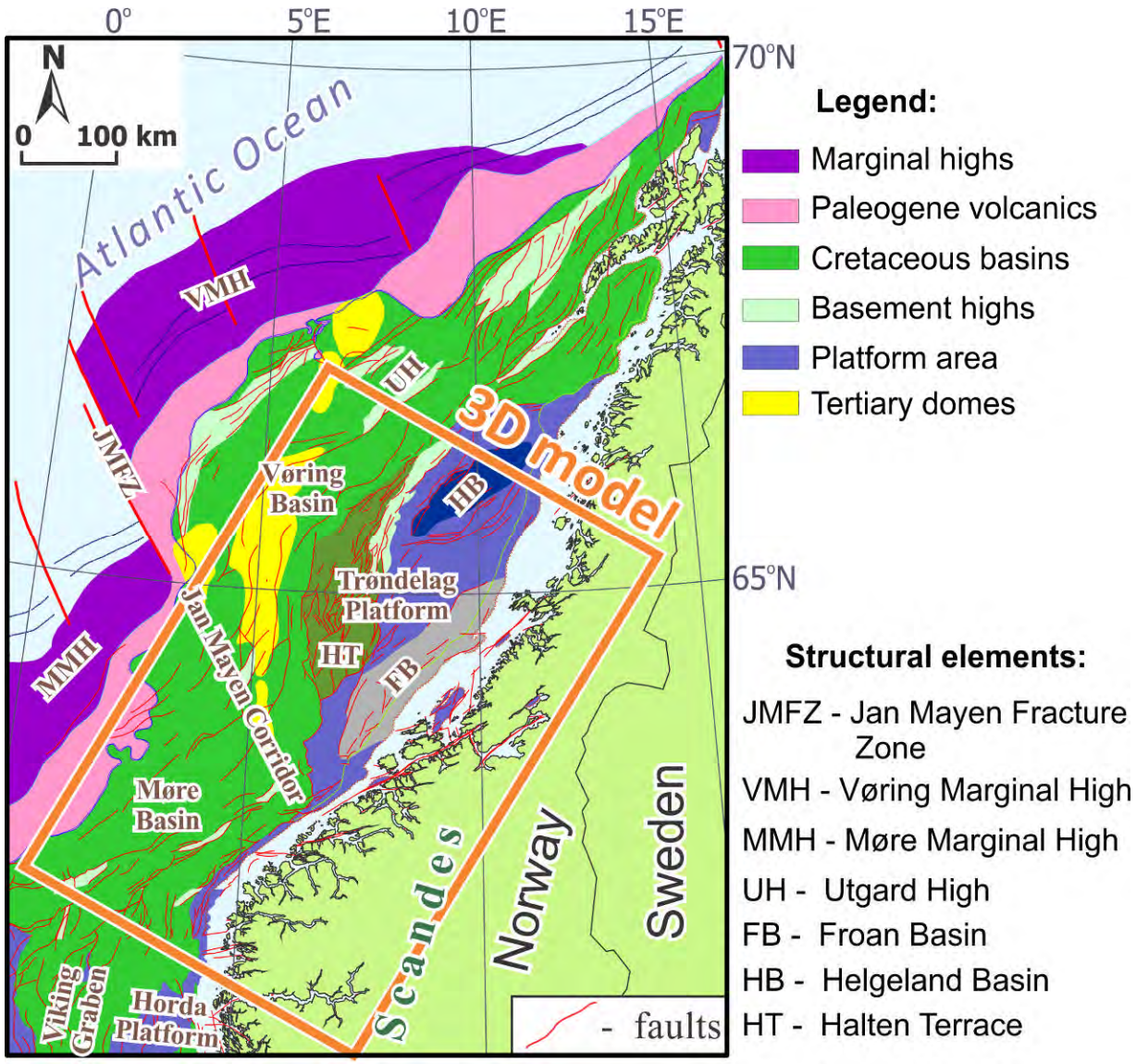

Figure 10.2. Tectonic settings within the Mid-Norwegian continental shelf with location of the 3D structural model (simplified after Blystad et al. 1995).

Moho beneath the ocean and the relatively deeply located interfaces beneath Fennoscandia. The large-scale 3D model has been used as a regional background during the 3D density and the 3D thermal modelling on the one hand. On the other hand, this large model is not a part of the Coop2 project and, therefore, the structure of the crystalline crust and sediments has not been resolved with the same details in this model as it has been done for the Coop2 model area.

The investigated area covered by the 3D model has a pronounced bathymetry within its western part (Figure 10.1). In addition, some fjords are also characterised by relatively deep locations of the sea bottom. Topography of the mainland is especially complex within the south-eastern part of the model area. There, the NE-SW-trending Scandes mountains are located with altitudes of more than 1500-2000 m.

The constructed 3D model covers the major tectonic elements of the Mid-Norwegian continental margin, including the Trøndelag Platform which contains thick pre-Cretaceous sedimentary rocks (Figure 10.2). The model also covers major Cretaceous sedimentary centres within the Møre and Vøring basins. Onshore, the sediments are mostly absent or relatively thin. There, the crystalline rocks are cropping out at the surface within a large part of the continent (Sigmond 2002).

At the first stage of the construction of the 3D structural model, all recently published/released structural data have been compiled and merged in order to construct an initial 3D model. This initial model has been validated during 3D density and magnetic modelling, allowing us to obtain a data-based, lithosphere-scale 3D model of the Mid-Norwegian continental margin and adjacent continent. The gravity and magnetic consistent 3D model has been used as a structural base during the 3D thermal modelling which has been performed in order to understand the major features of the 3D conductive thermal field within the sedimentary infill, the crystalline crust and the uppermost mantle. During the 3D thermal modelling, the geometry of the output model from the 3D density and magnetic modelling has been slightly modified and has been again validated by the 3D gravity and magnetic modelling.

The obtained, final, 3D structural model is 621 km long and 403 km wide (Figure 10.3). A horizontal grid spacing of the model is 4000 m. The final 3D model consists of 16 layers within the study area of the Coop2 model from the base of the lithosphere to the present-day Earth´s surface:

(1) Sea water;
(2) Naust-Kai (base Naust-sea floor);
(3) Brygge (top Paleocene-base Naust);
(4) Paleocene (base Tertiary unconformity-top Paleocene);
(5) Oceanic layer 2AB (basalts);
(6) Upper Cretaceous (near top Cenomanian-base Tertiary unconformity);
(7) Lower Cretaceous (base Cretaceous unconformity-near top Cenomanian);
(8) Pre-Cretaceous (Jurassic, Triassic and older sediments);
(9) upper-crustal high-density crystalline rocks;
(10) low-density upper-crustal body;
(11) regional upper-crustal layer;
(12) middle crust;
(13) lower crust;
(14) high-density crust;
(15) high-density lower-crustal layer;
(16) lithospheric upper mantle.

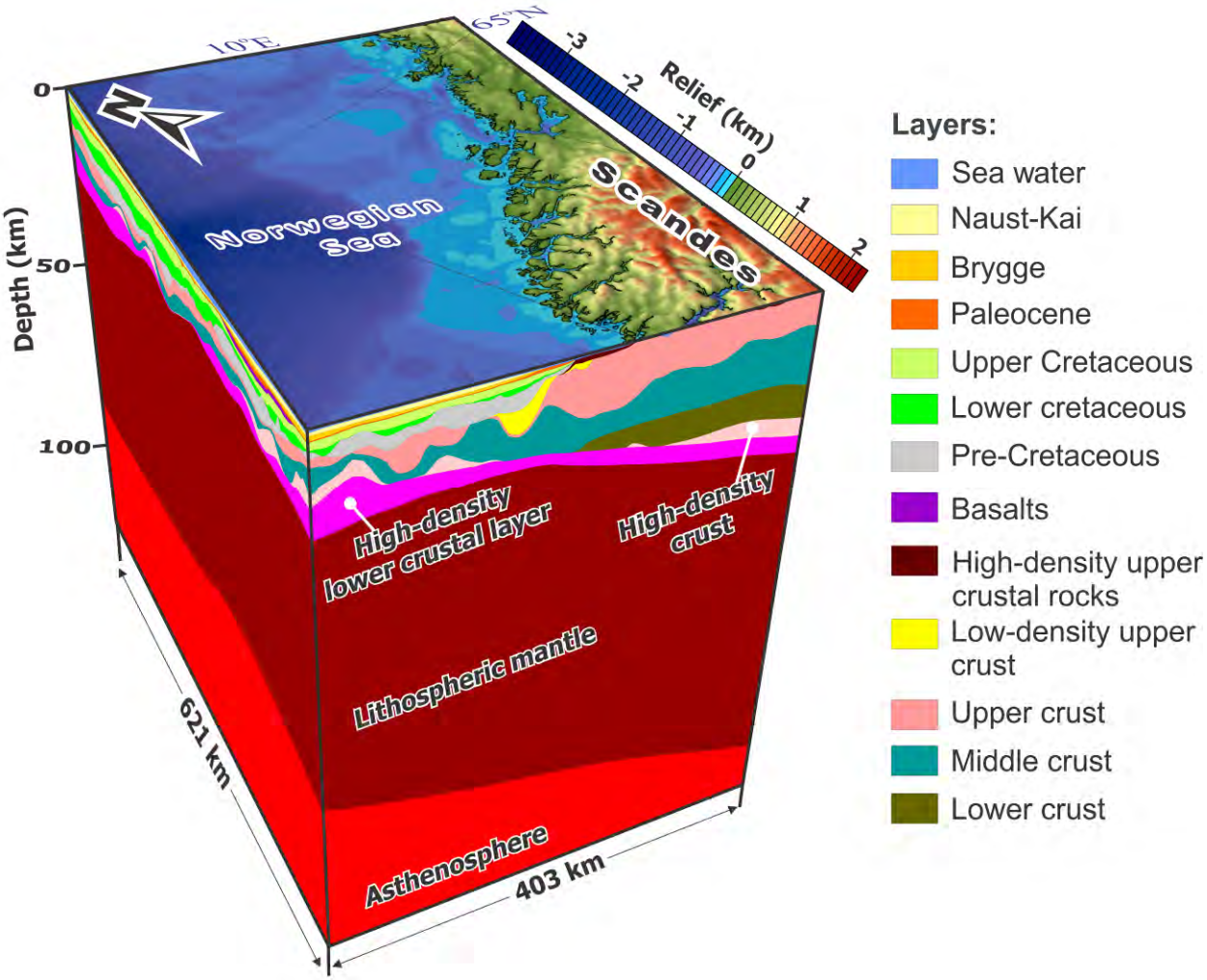

Figure 10.3. Lithosphere-scale 3D model of the Mid-Norwegian continental margin and adjacent areas of the continent (four times vertically exaggerated).

It is important to note that two additional layers have been included into the model within the oceanic domain which is not covered by the Coop2 model. These two layers represent the oceanic crystalline crust. In particular, oceanic layers 3A and 3B have been added to the model in addition to oceanic layer 2AB (basalts).

Model coordinates are based on the Universal Transverse Mercator (UTM) coordinate system zone 32 (Northern Hemisphere), using the World Geodetic System (WGS) 84 datum.

The main objective of this investigation is to understand the regional-scale structural and thermal patterns of the crystalline crust of the Mid-Norwegian continental margin and the adjacent Norwegian mainland. The information obtained about the major structural features and 3D temperature distribution within the sediments and crystalline crust at the regional scale can be used as a solid base for both more detailed local investigations within the present study area and for future large-scale studies within the Norwegian sector of the North Atlantic region.
The structure of the present lithospheric-scale 3D modelling chapter is compatible with the Coop1 report (Maystrenko 2014).

10.2 Datasets

10.2.1 Bathymetry and topography

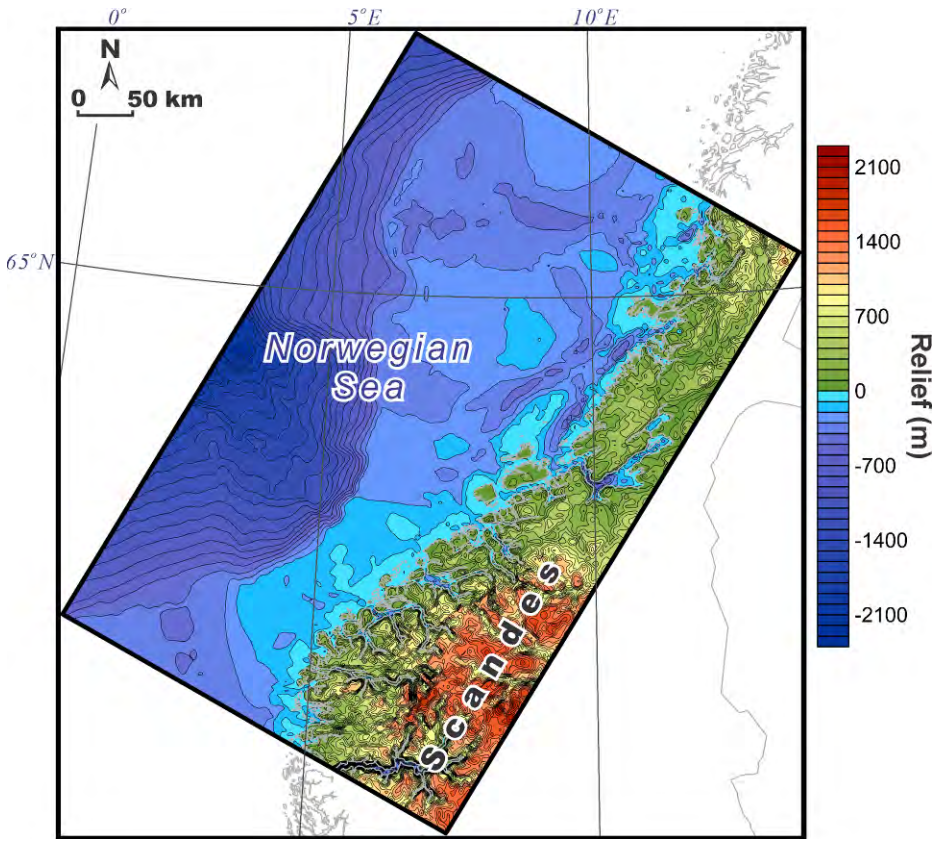

Figure 10.4. Bathymetry of the Coop*2 model area (from the Norwegian Mapping Authority).*

Bathymetry and topography for the study area have been taken from the Norwegian Mapping Authority. Depths to the sea bottom reach locally more than -2200 m and the altitude of the Scandes mountains is up to 2400 m (Figure 10.4), indicating an almost 5000 m difference in relief within the area under consideration. This large difference in topography between the Scandes mountains onshore and deep bathymetry offshore is one of the key factors which control distribution of the subsurface temperature at the shallow levels of the 3D model, implying that subsurface temperatures at shallow levels beneath the Scandes and in the areas with a deeply located sea bottom are partially controlled by the complex topography.

10.2.2 Structural data for the sedimentary infill

Construction of the 3D model has been done using all available structural data, such as 1D well data, 2D reflection seismic lines, geological maps and thickness and structural depth maps.

Table 10.1. Velocities for depth conversion

Layer	Vertical velocity V_0 [m/s]	Vertical velocity gradient k_z [1/s]
Water	1480	0
Naust-Kai	2050	0
Brygge	2000	0.05
Paleocene	2050	0.09
Upper Cretaceous (K_2)	2400	0.12
Lower Cretaceous (K_1)	2700	0.17

For the sedimentary infill (Figure 10.5), two major data sources are represented by the results of interpretation of reflection seismic lines by Gernigon (2014; NGU unpublished data) and Rise et al. (2005, 2006, 2010), Dowdeswell et al. (2006, 2010), Eidvin et al. (2007, 2014), Ottesen et al. (2009, 2012) and Chand et al. (2011). The data have been made available in terms of two-way travel time (TWT) structure maps. The TWT structure maps from Rise et al. (2005, 2006, 2010), Dowdeswell et al. (2006, 2010), Eidvin et al. (2007, 2014), Ottesen et al. (2009, 2012) and Chand et al. (2011) have been used for the Brygge-Naust interval, and the TWT structure maps from Gernigon (2014; NGU unpublished data) have been used for the Paleocene, Cretaceous and pre-Cretaceous sedimentary successions. The TWT thickness maps of the Naust-Kai (base Naust-sea floor), Brygge (top Paleocene-base Naust), Paleocene (base Tertiary unconformity-top Paleocene), Upper Cretaceous (near top Cenomanian-base Tertiary unconformity) and Lower Cretaceous (base Cretaceous unconformity-near top Cenomanian) have been calculated based on the previously mentioned data. The derived TWT thickness maps have then been depth-converted by use of interval velocities shown in Figure 10.6 by applying equation (10.1) according to parameters in Table 10.1.

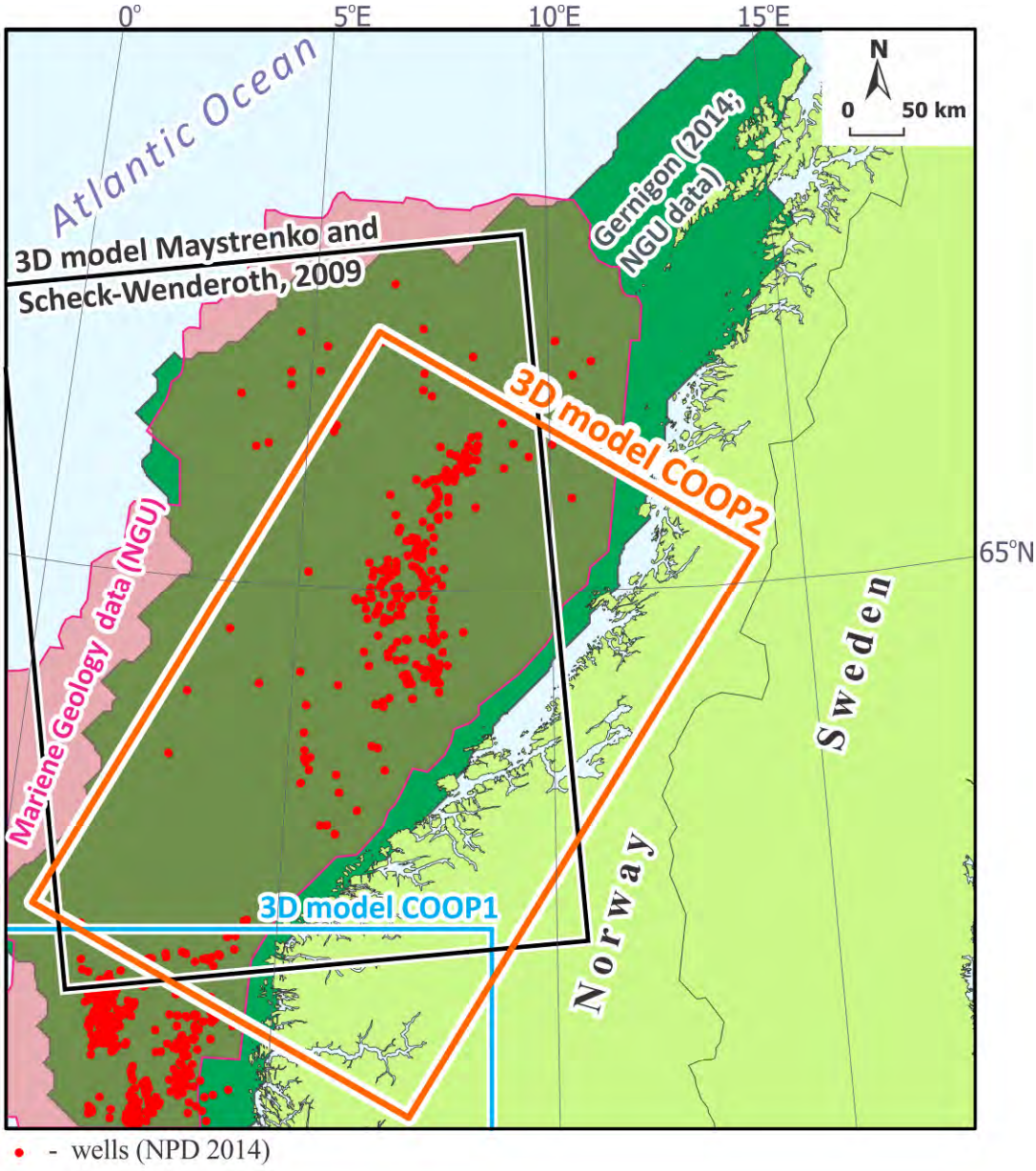

Figure 10.5. Datasets used for the sedimentary cover. Marine Geology data (NGU) are based on Rise et al. (2005, 2006, 2010), Dowdeswell et al. (2006, 2010), Eidvin et al. (2007, 2014), Ottesen et al. (2009, 2012), Chand et al. (2011) and Gernigon (2014; NGU unpublished data).

The interval velocities of the uppermost sedimentary interval, represented by Naust and Kai, have been taken to be constant and are equal to 2050 m/s (Table 10.1). On the other hand, the interval velocities for the Brygge, Paleocene and Cretaceous have been calculated according to a simplified linear function (10.1) (e.g., Sarkar & Tsvankin 2003, Takanashi & Tsvankin 2012).

$$V_i=V_0+k_z*z \quad (10.1)$$

where V_i is the interval velocity [m/s], V_0 is the initial vertical velocity [m/s], k_z is the vertical velocity gradient [1/s] and z is the depth [m].

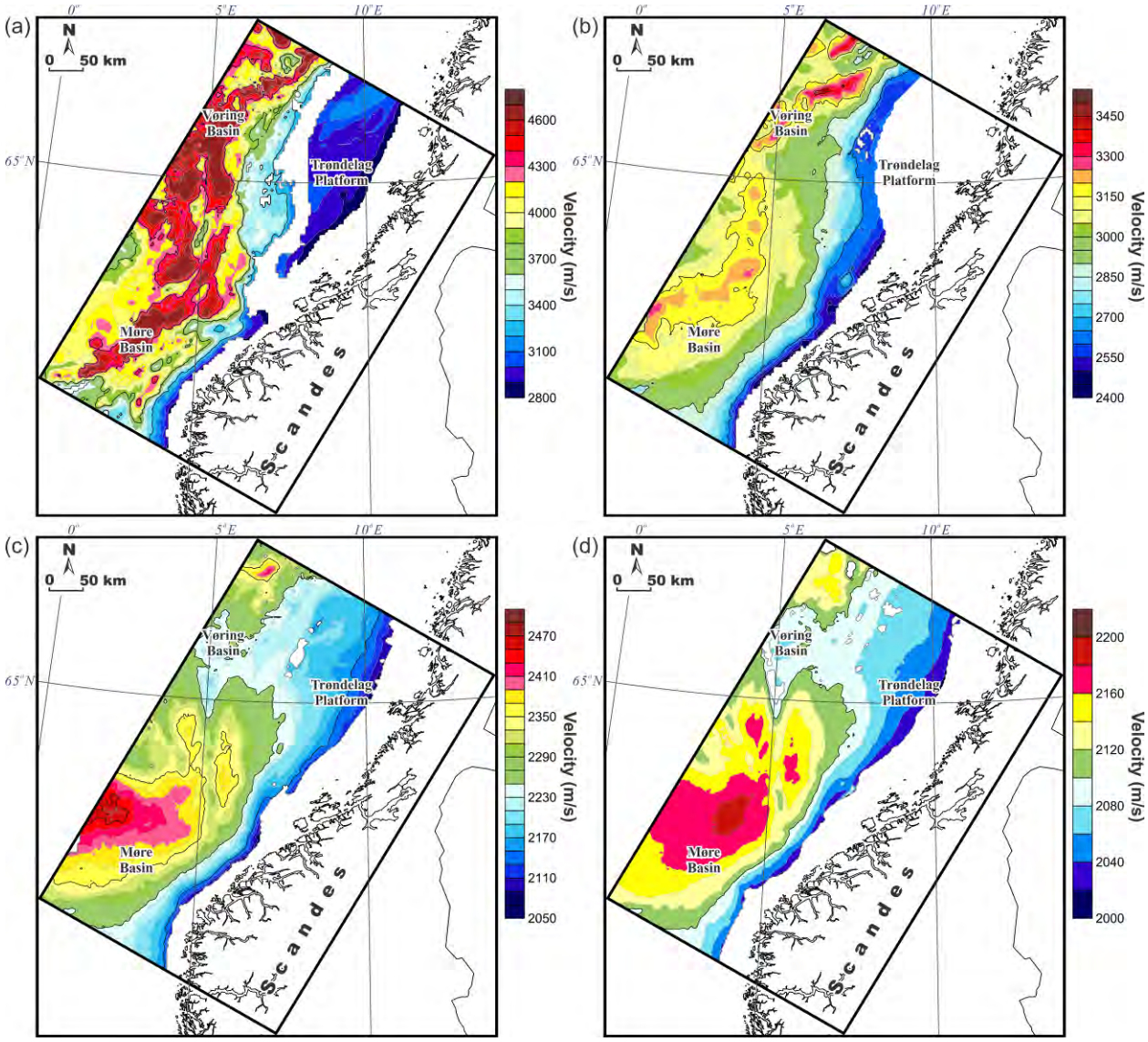

Figure 10.6. Interval velocities used for depth conversion of the data from Gernigon (2014; NGU unpublished data) and Rise et al. (2005, 2006, 2010), Dowdeswell et al. (2006, 2010), Eidvin et al. (2007, 2014), Ottesen et al. (2009, 2012) and Chand et al. (2011). (a) (7) Lower Cretaceous (base Cretaceous unconformity-near top Cenomanian); (b) Upper Cretaceous (near top Cenomanian-base Tertiary unconformity); (c) Paleocene (base Tertiary unconformity-top Paleocene); (d) Brygge (top Paleocene-base Naust).

Function (10.1) has the physical meaning that the interval velocities increase with depth according to different vertical gradients. Values of the initial vertical velocity and the vertical velocity gradient have been derived based on the best fit between the obtained thickness maps in metres and well data in places where well data are available. For the rest of the study area, these values have been chosen to obtain interval velocities similar to those from deep-seismic experiments (Mjelde et al. 1997, 2001, 2002, 2003, 2005, 2009; Raum et al. 2000, 2002, 2006; Breivik et al. 2006, 2009, 2011; Kvarven et al. 2014). The calculated velocities are shown in Figure 10.6, indicating that the highest velocities have been obtained for the Lower Cretaceous interval between the base of the Cretaceous unconformity and near the top of the Cenomanian. For this interval, velocities are locally more than 4500 m/s in the areas where sediments are particulary thick. In the case of the Upper Cretaceous interval (near top Cenomanian-base

Tertiary unconformity), the interval velocities vary from 2400 to maximum 3500 m/s within the Coop2 model area, reflecting a decrease of velocities compared to the Lower Cretaceous interval. Towards shallower levels, the interval velocities further decrease for the Paleocene (base Tertiary unconformity-top Paleocene) and Brygge (top Paleocene-base Naust) intervals, lying in the range of approximately 2050-2470 m/s within the Paleocene interval and approximately 2000-2200 m/s within the Brygge Formation.

In addition, the data from Maystrenko (2014) have been partially used within the area which is covered by the Coop1 3D structural model. A previous 3D structural model of the Mid-Norwegian margin (Scheck-Wenderoth et al. 2007, Maystrenko & Scheck-Wenderoth 2009) has been used mainly for the areas of the large NGU model which are not covered by the datasets described above.

The marginal limits of sediments have been taken from the Geological Map of Land and Sea Areas of Northern Europe (Sigmond 2002). Finally, all thicknesses have been cross-checked with the available well data (NPD 2014).

The above-described datasets have been merged and gridded in terms of thickness maps for the following five sedimentary intervals (Figures 10.7-10.11): the Naust-Kai (base Naust-sea floor), Brygge (top Paleocene-base Naust), Paleocene (base Tertiary unconformity-top Paleocene), Upper Cretaceous (near top Cenomanian-base Tertiary unconformity) and Lower Cretaceous (base Cretaceous unconformity-near top Cenomanian).

The uppermost sedimentary layer of the 3D model is represented by the Naust-Kai interval which is characterised by two clearly distinguished thickness maxima (Figure 10.7). One of these zones has an almost circular shape and is located in the Møre Basin where the Naust-Kai succession reaches more than 2000 m within the depocentre (Figure 10.7a). The second zone of thickening is located in the eastern part of the Vøring Basen and has a NNE-SSW-elongated form with a thickness maximum of around 1900 m. The structural pattern at the base of the Naust-Kai (Figure 10.7b) reflects the configuration of the thickness map in general. The depth to the base of the Naust-Kai is more than -2800 m within the Møre Basin where the Naust-Kai is thickest and the bathymetry is also deepest (Figure 10.4).

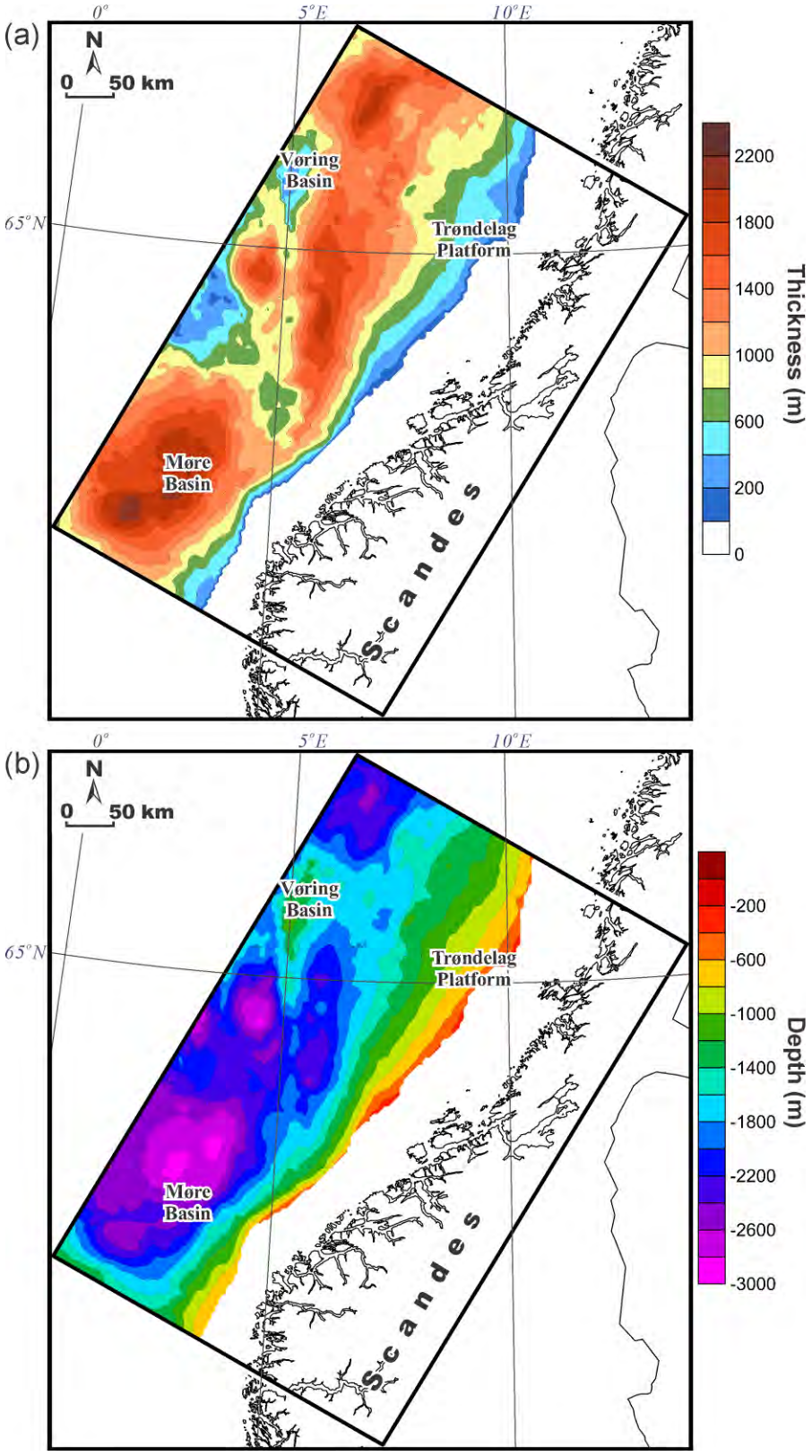

Figure 10.7. (a) Thickness map and (b) structural depth map (base of the layer) of the Naust-Kai (base Naust-sea floor; layer 2). Based on Rise et al. (2005, 2006, 2010), Dowdeswell et al. (2006, 2010), Eidvin et al. (2007, 2014), Ottesen et al. (2009, 2012) and Chand et al. (2011).

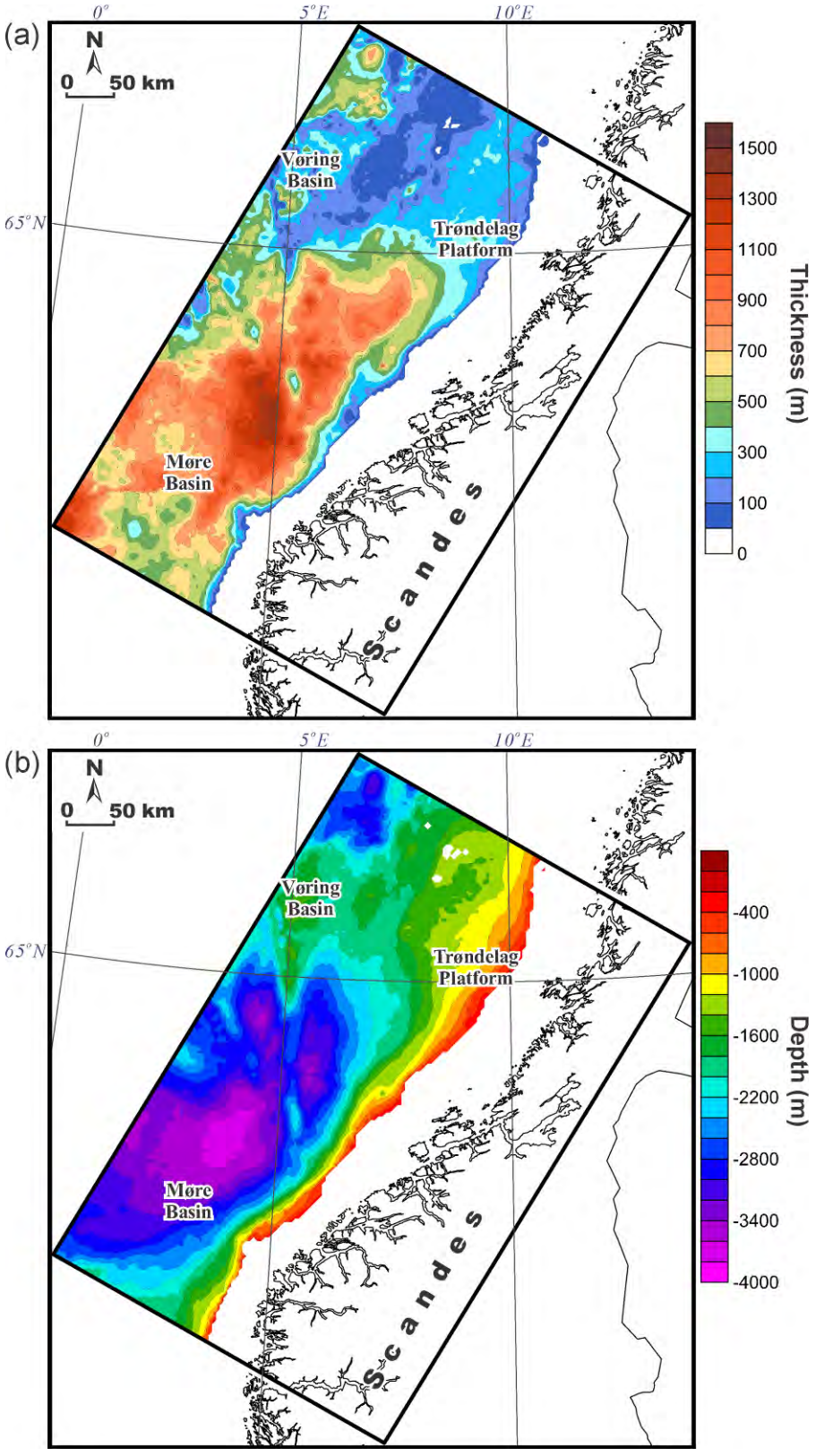

Figure 10.8. (a) Thickness map and (b) structural depth map (base of the layer) of the Brygge Formation (top Paleocene-base Naust; layer 3). Based on Rise et al. (2005, 2006, 2010), Dowdeswell et al. (2006, 2010), Eidvin et al. (2007, 2014), Ottesen et al. (2009, 2012) and Chand et al. (2011).

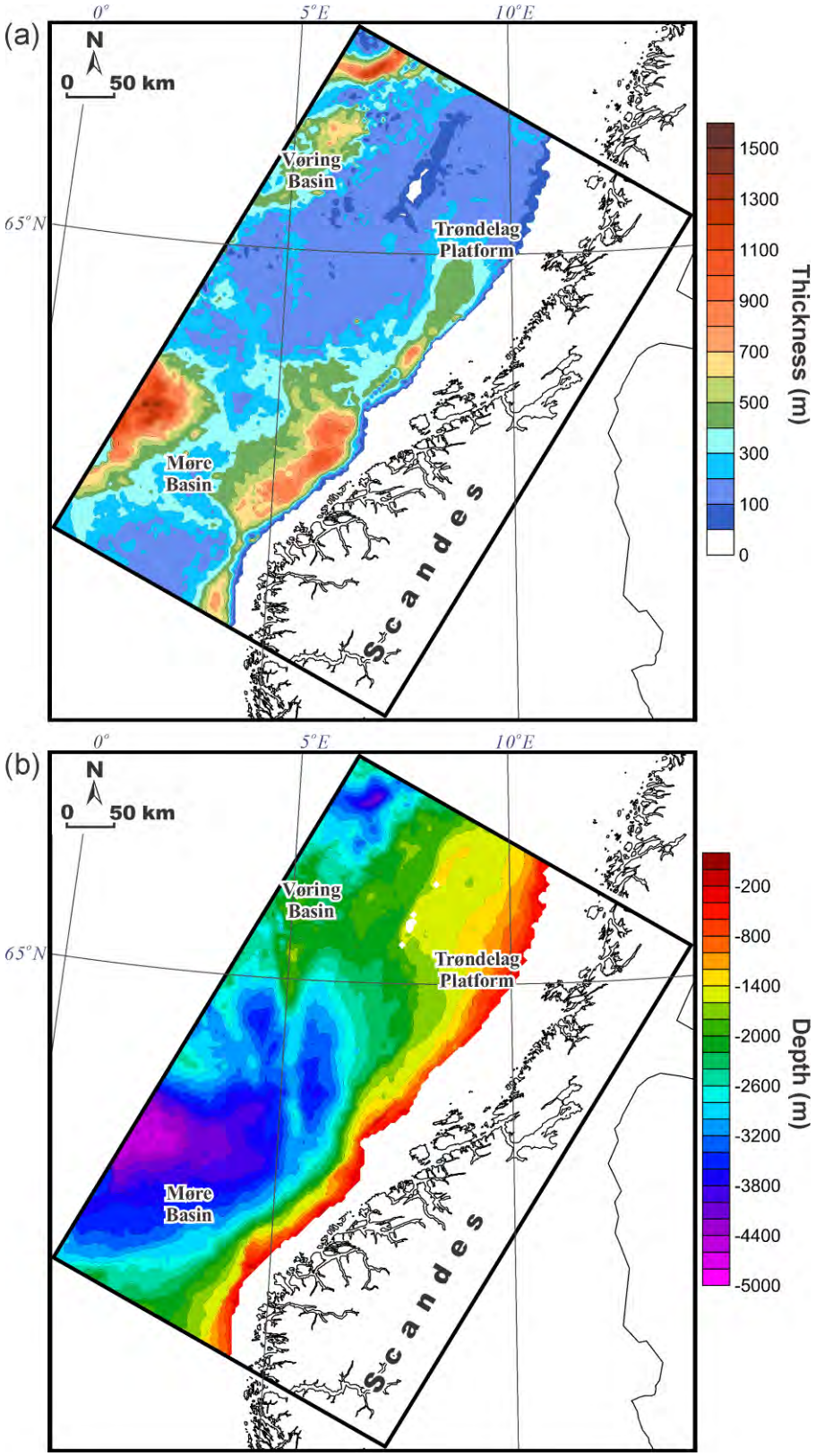

Figure 10.9. *(a) Thickness map and (b) structural depth map (base of the layer) of the Paleocene (base Tertiary unconformity-top Paleocene; layer 4). Based on Rise et al. (2005, 2006, 2010), Dowdeswell et al. (2006, 2010), Eidvin et al. (2007, 2014), Ottesen et al. (2009, 2012) and Chand et al. (2011) and Gernigon (2014, NGU unpublished data).*

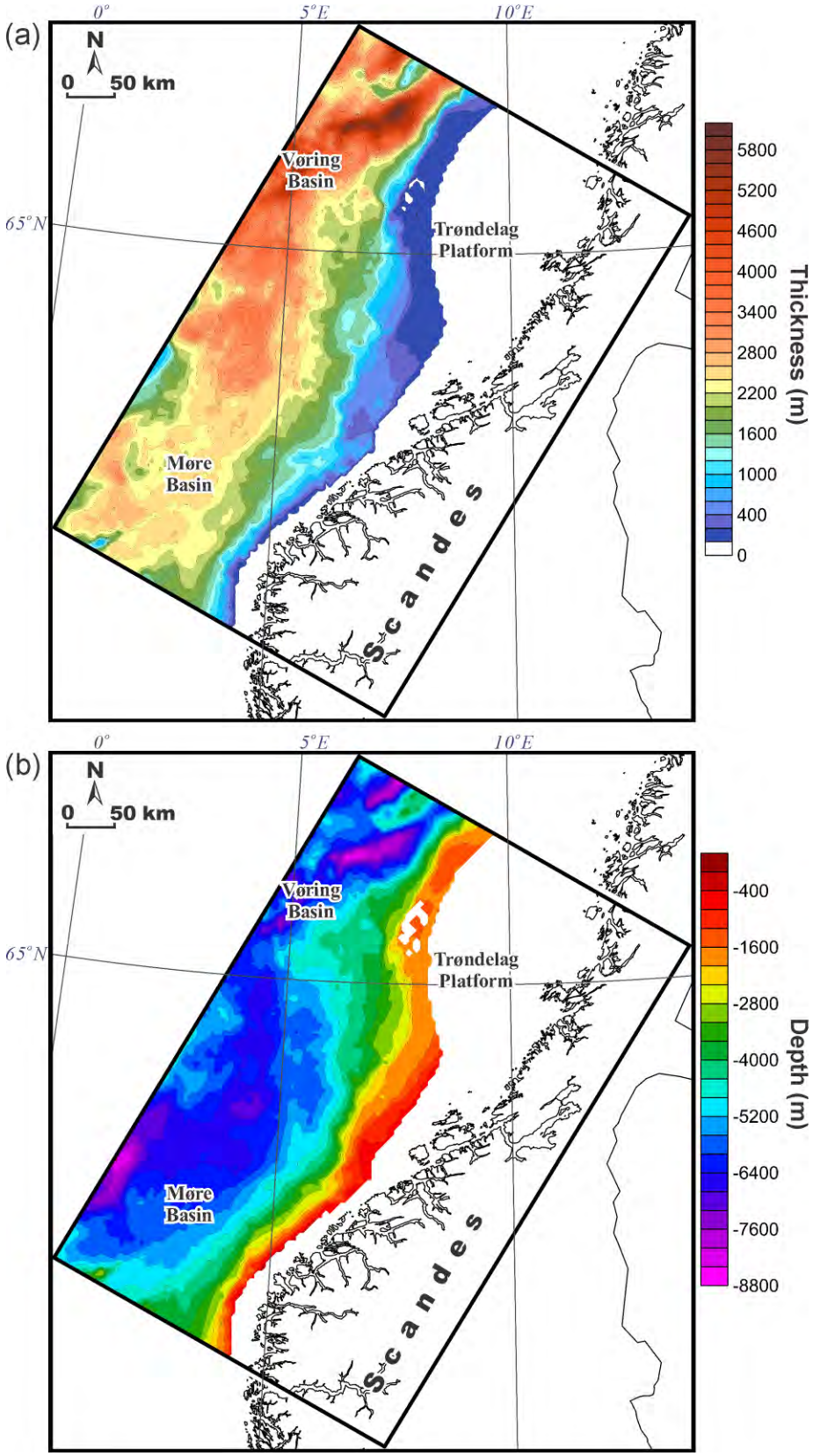

Figure 10.10. (a) Thickness map and (b) structural depth map (base of the layer) of the Upper Cretaceous (near top Cenomanian-base Tertiary unconformity; layer 6). Based on Gernigon (2014, NGU unpublished data).

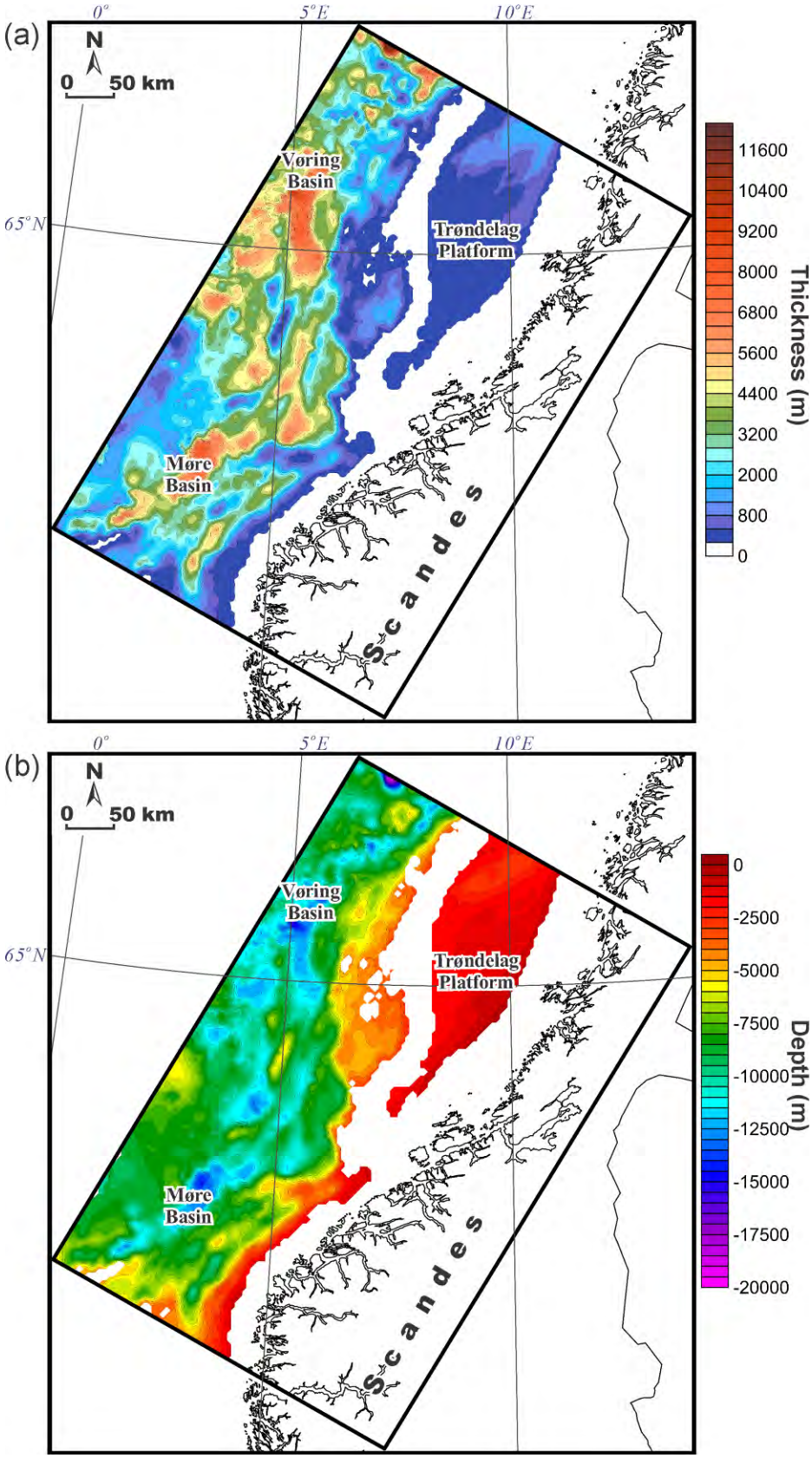

Figure 10.11. (a) Thickness map and (b) structural depth map (base of the layer) of the Lower Cretaceous (base Cretaceous unconformity-near top Cenomanian; layer 7). Based on Gernigon (2014, NGU unpublished data).

The Brygge Formation has the largest thickness of more than 1400 m at the transition zone from the Møre Basin to the Trøndelag Platform and the Vøring Basin (Figure 10.8a). Similarly to the Naust-Kai, the depth to the base of the Brygge is also located deeper within the Møre Basin, reaching almost -3800 m there (Figure 10.8b). This is again the result of a superimposed effect of the deep bathymetry within the Møre Basin and a fact that the Møre Basin is mostly characterised by the thicker Brygge Formation compared to the Trøndelag Platform and the Vøring Basin.

Distribution of the Paleocene succession shows three depocentres (Figure 10.9a), two of which are located within the western and eastern parts of the Møre Basin and the third one is located within the NW corner of the model area in the Vøring Basin. Thicknesses reach 1000-1400 m in these depocentres. In contrast, the transition from the Trøndelag Platform to the Vøring Basin is characterised by the very thin Paleocene sediments which are locally even absent in this area. The depth to the base of the Paleocene is greatest within a wide area in the Møre Basin as with the base of the Brygge and Naust formations (cf. Figure 10.9b and Figures 10.7b & 10.8b).

The thickness pattern of the Upper Cretaceous interval (Figure 10.10a) represents another structural level within the study area that is distinguished by a different thickness pattern compared to the overlying layers. The thickest Upper Cretaceous succession is observed within the Vøring Basin where it reaches more than 5900 m locally. In contrast, the Upper Cretaceous sediments are only 2300-2500 m thick on average within the Møre Basin. The depth to the base of the Upper Cretaceous (Figure 10.10b) is around -8000 m within the western part of the Møre Basin and reaches more than -7500–-8000 m within two, relatively narrow, SW-NE-trending zones in the Vøring Basin.

The next layer of the 3D structural model is the Lower Cretaceous which has a significantly thickened succession within several relatively narrow zones in the Møre and Vøring basins (Figure 10.11a), reflecting the fact that the highest rate of sedimentation was within the graben-like structures during the Early Cretaceous extensional event. The thickness of the Lower Cretaceous is more than 7000-8000 m within these zones. The mentioned zones with the thickened Lower Cretaceous are also clearly recognisable at the base of the Lower Cretaceous (Figure 10.11b) which is located at depths greater than -12000–-14000 m beneath the thickest Lower Cretaceous sediments

.

The depth to the top of the crystalline basement is based mainly on the OBS profiles (Mjelde et al. 1997, 2001, 2002, 2003, 2005, 2009; Raum et al. 2000, 2002, 2006; Breivik et al. 2006, 2009, 2011; Kvarven et al. 2014), interpretation of the reflection seismic lines (Gernigon 2014; NGU data) and deep transects from Nirrengarten et al. (2014) and Gernigon (2015, this report) (Figure 10.12). The top of the crystalline basement between the described datasets has been obtained by an extrapolation/interpolation of the existing data with partial use of data from the earlier 3D structural model of the Mid-Norwegian margin (Scheck-Wenderoth et al. 2007; Maystrenko & Scheck-Wenderoth 2009) and from the regional compilation of the basement topography by Ebbing & Olesen (2010). The top of the crystalline basement has also been cross-checked by deep wells (NPD 2014) which reached the crystalline basement (Figure 10.12). Finally, the basement topography has been validated and slightly modified during the 3D density and magnetic modelling.

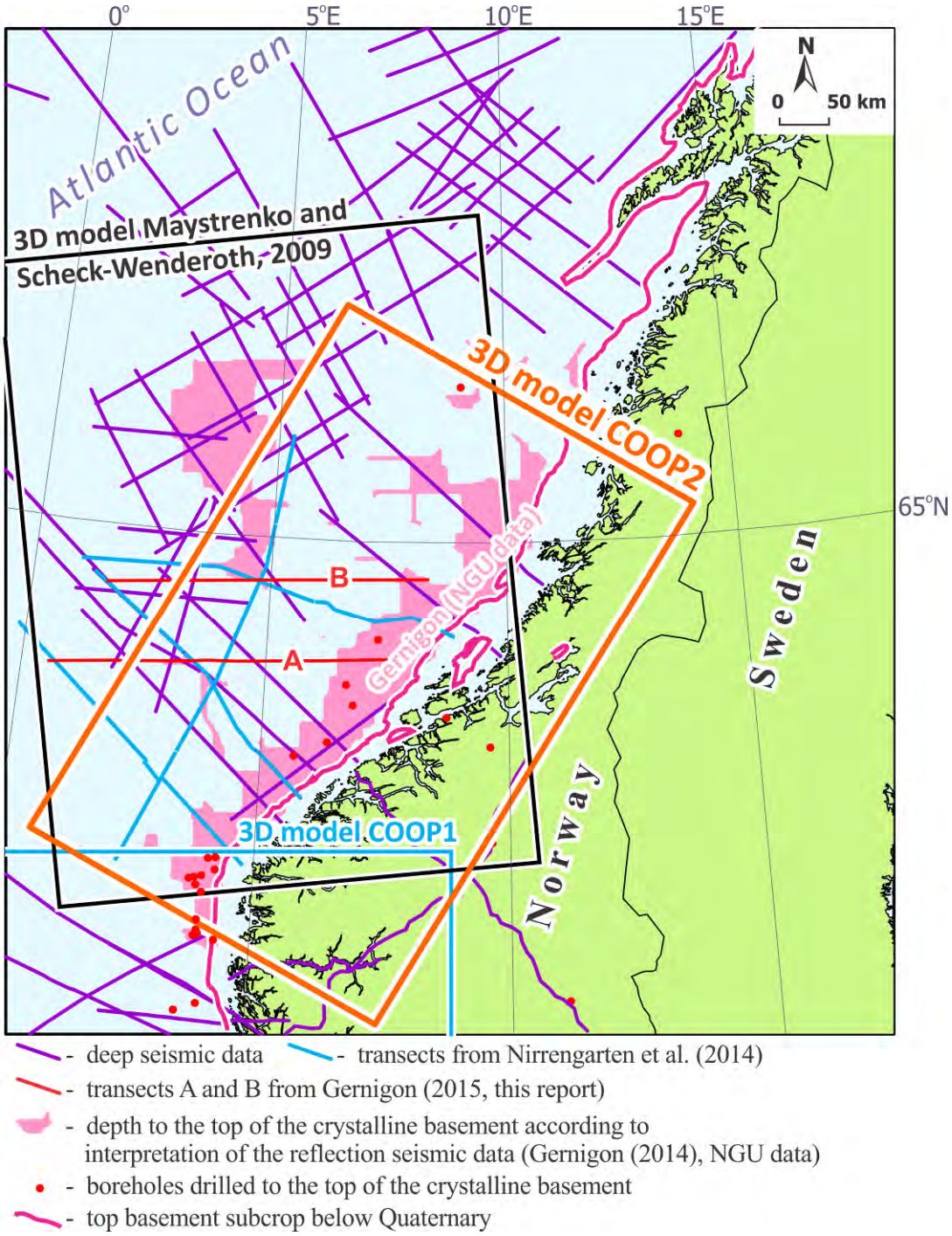

Figure 10.12. Datasets used for defining the depth to the top of the crystalline basement.

The structural pattern at the top of the crystalline basement is complex (Figure 10.13) due to the fact that it replicates the cumulative superimposed effects of all tectonic events that have affected the area under consideration during geological time. Three obvious zones can be distinguished at the top of the crystalline basement, such as (1) the Vøring and Møre basins with a very deeply located basement, (2) the Trøndelag Platform with moderate depths and (3) the Norwegian mainland and closely located shelf with very shallow basement. The depth to the top of the crystalline basement varies from -12000 to -15000 m on average within the Vøring and Møre basins, reaching locally more than -18000 m within the Vøring Basin (Figure 10.13).

On the other hand, the basement topography is relatively shallow within the Trøndelag Platform where depths to the base of sediments are mainly in the range -7000– -11000 m. Within the third tectonic zone, the crystalline basement crops out at the surface throughout a large part of the Norwegian mainland.

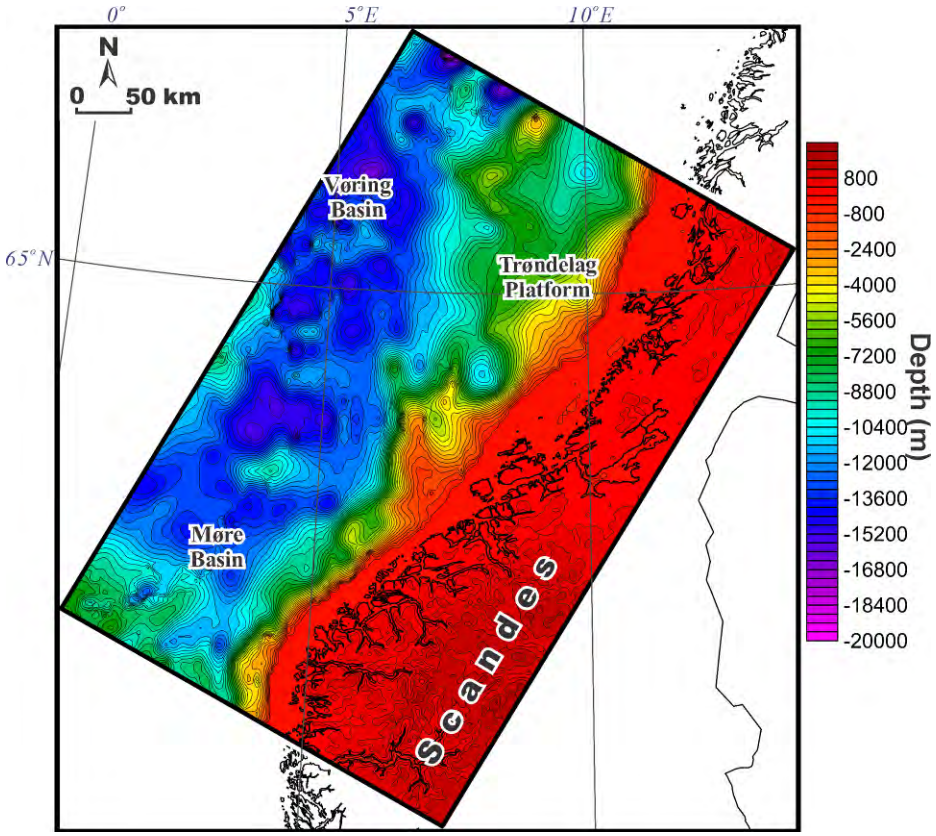

Figure 10.13. Depth to the top of the crystalline basement (based on Mjelde et al. 1997, 2001, 2002, 2003, 2005, 2009; Raum et al. 2000, 2002, 2006; Breivik et al. 2006, 2009, 2011; Ebbing & Olesen 2010, NPD 2014; Maystrenko & Scheck-Wenderoth 2009; Scheck-Wenderoth & Maystrenko 2011; Kvarven et al. 2014; Maystrenko 2014; Gernigon 2014 NGU unpublished data).

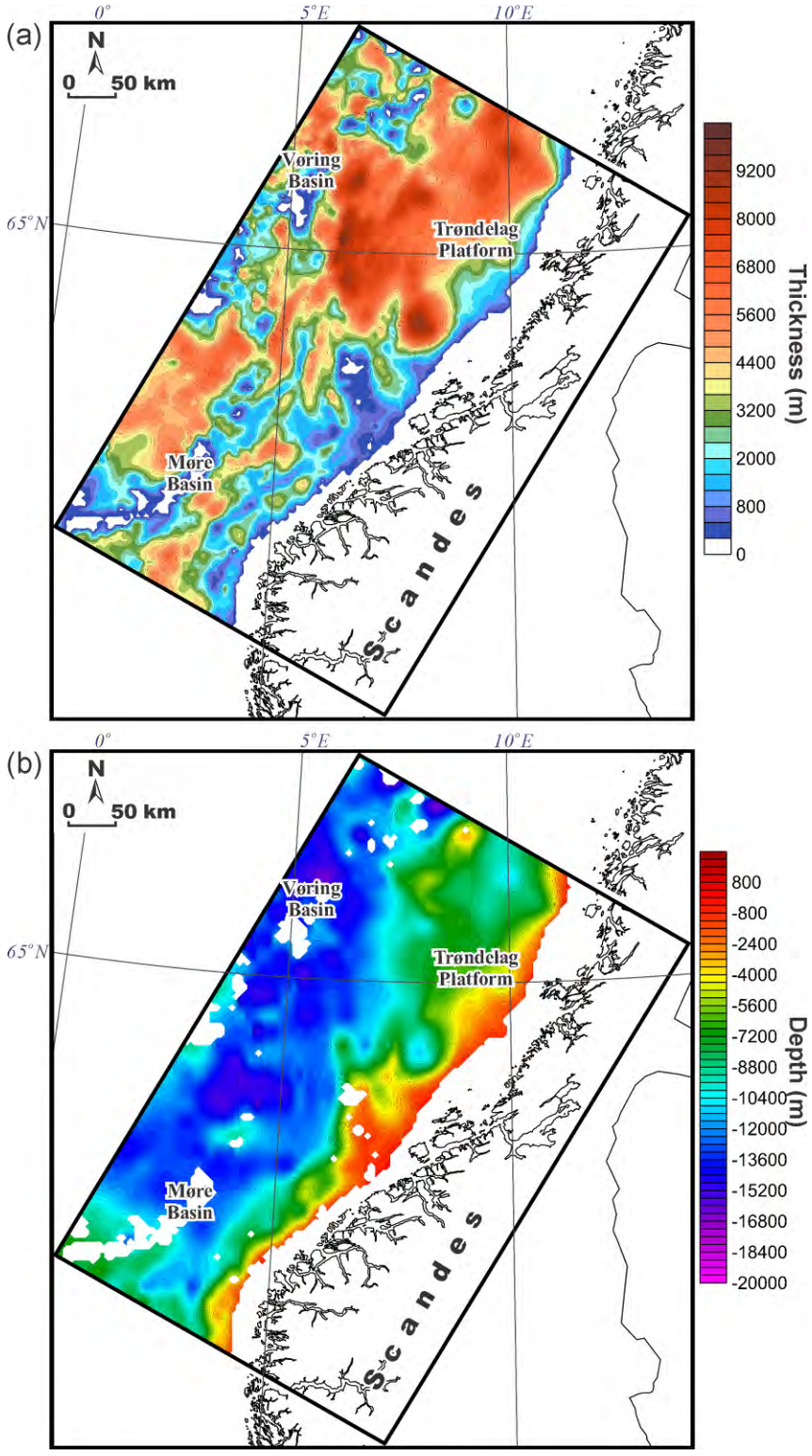

Figure 10.14. (a) Thickness map and (b) structural depth map (base of the layer) of the Pre-Cretaceous sedimentary rocks (layer 8; based on Mjelde et al. 1997, 2001, 2002, 2003, 2005; Raum et al. 2000, 2002, 2006; Breivik et al. 2006, 2009, 2011; Ebbing & Olesen 2010; NPD 2014; Maystrenko & Scheck-Wenderoth 2009; Scheck-Wenderoth & Maystrenko 2011; Kvarven et al. 2014; Maystrenko 2014; Gernigon 2014 NGU unpublished data).

The top of the crystalline basement has been used to obtain the thickness of the pre-Cretaceous sediments (Figure 10.14a) which are represented by Jurassic, Triassic, Permian

and older sedimentary rocks within the study area. The thickness of the pre-Cretaceous sedimentary rocks has been calculated as the difference between the base of the Cretaceous-Cenozoic sediments and the top of the crystalline basement (Figure 10.13). In addition, the thickness of the pre-Cretaceous has been cross-validated by wells which have been drilled into the pre-Cretaceous sedimentary rocks, keeping the pre-Cretaceous at least not thinner than the drilled pre-Cretaceous succession.

The thickness of the Pre-Cretaceous sediments (Figure 10.14a) is characterised by larger uncertainties compared to the Cretaceous and Cenozoic levels. This is especially true within the areas where the depth to the top of the crystalline basement is great, as in the Vøring and Møre basins. The thickness map of the pre-Cretaceous (Figure 10.14a) is characterised by a wide zone of significant thickening within the western part of the Trøndelag Platform and the eastern part of the Vøring Basin. There, the pre-Cretaceous layer is more than 9000 m thick within some of local depocentres. The thickness of this layer is 4500-6000 m on average within the western part of the Møre Basin. Depth to the base of the Pre-Cretaceous is shown in Figure 10.14b. Actually, the structural base map in Figure 10.14b is the same as the top of the crystalline basement in Figure 10.13 but in this case it is only displayed within the areas where Pre-Cretaceous rocks are present (Figure 10.14a).

The above-mentioned data for six sedimentary layers thus provide an excellent starting point for the regional-scale study of the deep structure of the crystalline crust within the Coop2 model area.

10.2.3 Structural data for the crystalline crust and Moho topography

The Mid-Norwegian margin is covered by several Europe-scale and smaller compilations of the Moho topography (Kelly et al. 2007; Tesauro et al. 2008; Grad et al. 2009; Ebbing & Olesen 2010; Artemieva et al. 2013). These regional-scale compilations demonstrate that the crust-mantle boundary is deeply located beneath the Norwegian mainland but is much shallower located beneath the Mid-Norwegian continental margin. However, the reported Moho topographies are not sufficiently detailed to resolve the major features of the crystalline crust within the study area, showing only a regional pattern for the Moho. In addition, there are several more detailed crustal-scale 3D models available for the study area (Ebbing et al. 2006; Scheck-Wenderoth et al. 2007; Maystrenko & Scheck-Wenderoth 2009; Reynisson 2010). In general, all these 3D models are based on OBS data and are validated by 3D density modelling. The most recent model was published in 2010 and was presumably constructed either in that year or in 2009. Since that time, additional deep-seismic data have been obtained within the study area, especially within the Møre Basin. Therefore, the present Coop2 model has been constructed mostly by use of the original deep seismic data rather than the earlier 3D structural models which have been partially used to constrain the areas where deep seismic lines are absent. Thus, configuration of the crystalline crust and depth to the Moho beneath the Mid-Norwegian continental margin (Figure 10.15) is mostly based on the wide-angle deep-seismic data (Mjelde et al. 1997, 2001, 2002, 2003, 2005, 2009; Raum et al. 2000, 2002, 2006; Breivik

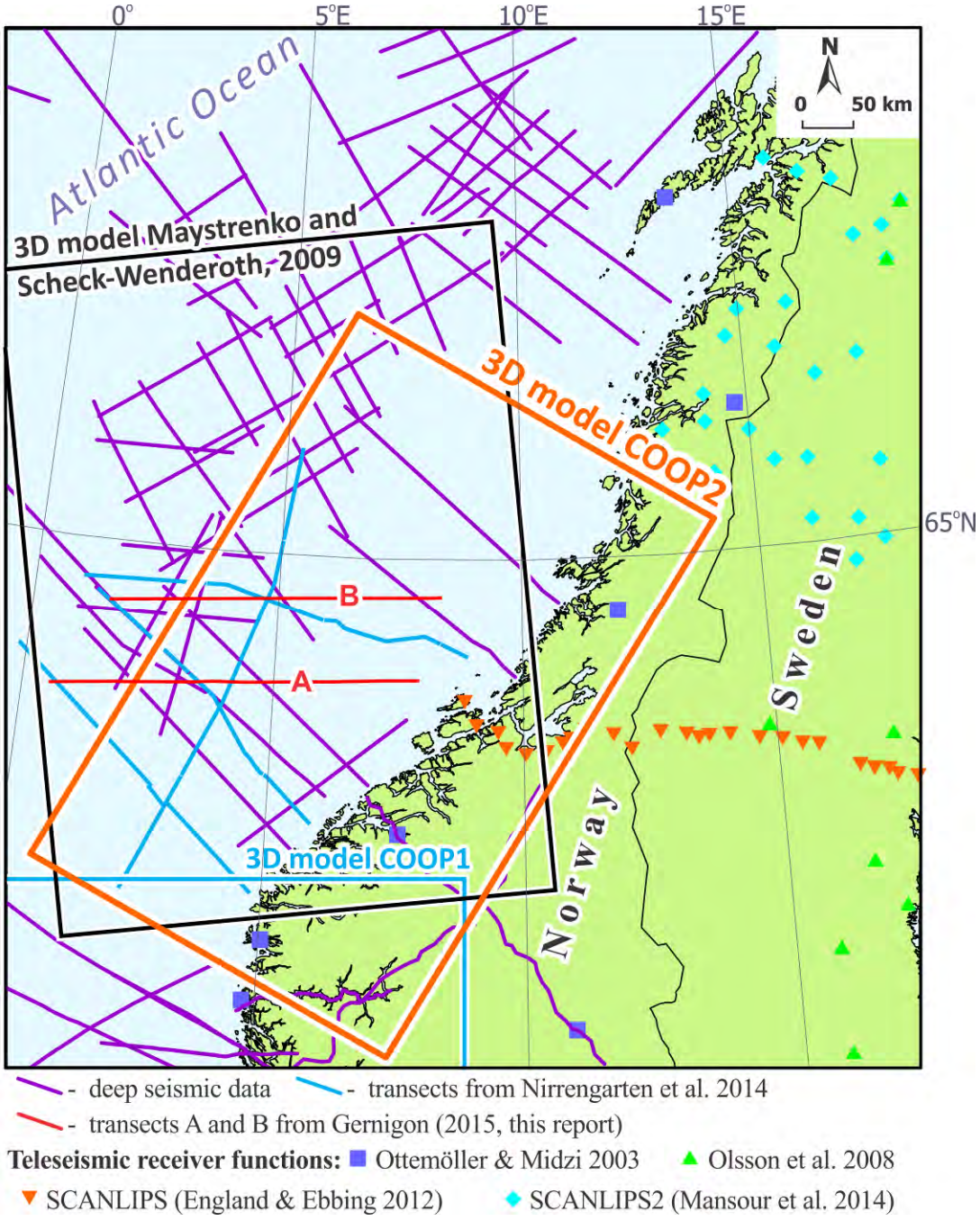

Figure 10.15. Datasets used for the internal configuration of the crystalline crust and for the Moho topography.

et al. 2006, 2009, 2011; Kvarven et al. 2014), the deep transects modelled by Nirrengarten et al. (2014) and Gernigon (2015, this report), as well as the Coop1 3D model (Maystrenko 2014) with some local adjustments from the previously published compilations and 3D structural models (Ebbing et al. 2006; Scheck-Wenderoth et al. 2007; Maystrenko & Scheck-Wenderoth 2009; Ebbing & Olesen 2010; Reynisson 2010). Onshore, the results of the deep seismic refraction experiment "Magnus-Rex" (Stratford et al. 2009) and the teleseismic receiver function data (Ottemöller & Midzi 2003; Olsson et al. 2008; England & Ebbing 2012; Mansour et al. 2014) have been applied to constrain the configuration of the crystalline crust and the Moho topography.

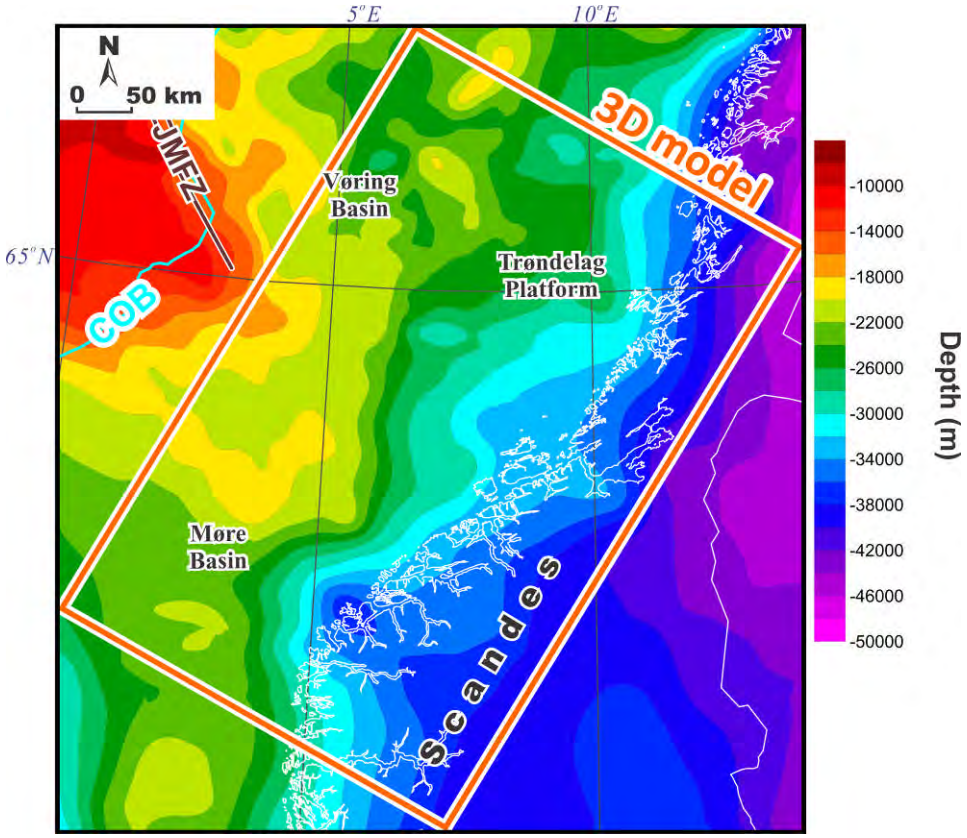

Figure 10.16. Moho topography beneath the study area (based on Mjelde et al. 1997, 2001, 2002, 2003, 2005, 2009; Raum et al. 2000, 2002, 2006; Ottemöller & Midzi 2003; Breivik et al. 2006, 2009, 2011; Olsson et al. 2008; Maystrenko & Scheck-Wenderoth 2009; Scheck-Wenderoth & Maystrenko 2011; England & Ebbing 2012; Kvarven et al. 2014; Mansour et al. 2014; Maystrenko 2014; Nirrengarten et al. 2014; Gernigon 2015 this report). COB - continent-ocean boundary (from Gernigon 2015; this report), JMFZ - Jan Mayen Fracture Zone (from Blystad et al. 1995).

The obtained Moho topography is displayed in Figure 10.16. The depth position of the Moho has been validated by 3D density modelling and this structural map therefore contains post-compilation modifications within the areas where coverage by seismic data is limited. The range of Moho depth is extremely wide from shallower than -10000 m beneath the oceanic domain to more than -45000 m beneath the continent. The Mid-Norwegian margin is characterised by a varying depth to the base of the crust, showing that the most shallow Moho (i.e., shallower than -20000 m) is beneath the northern part of the Møre Basin, whereas the Vøring Basin has a slightly deeper Moho position (20000-25000 m on average). The Trøndelag Platform is underlain by a 23000-2700-m-deep Moho on average.

10.2.4 Structural data for the lithosphere-asthenosphere boundary

In contrast to the sedimentary cover and the crystalline crust, information about the lithosphere-asthenosphere boundary is much less constrained by available data. The lithosphere-asthenosphere boundary beneath the continent has been derived from a 3D integrated geophysical modelling study by Gradmann et al. (2013), who used the lithospheric geometry from published datasets (Calcagnile 1982; Artemieva 2006; Ebbing et al. 2012) with adjustments applied to the depth of the lithosphere in order to match seismic velocity constraints. The depth to the lithosphere–asthenosphere boundary beneath the oceanic part

has been derived according to lithospheric age and Love and Rayleigh wave-phase velocity empirical relations from Zhang & Lay (1999), considering a gradual cooling of the oceanic lithosphere after the continental breakup. The age of oceanic lithosphere in North Atlantic has been taken from Müller et al. (2008). This kind of age-dependent depth of the lithosphere-asthenosphere boundary has already been examined by Scheck-Wenderoth & Maystrenko (2008) for the Mid-Norwegian continental margin.

The main problem is that there are no independent data on the depth to the lithosphere-asthenosphere boundary beneath the Mid-Norwegian continental margin. In this case, the base of the lithosphere beneath the margin has been obtained by interpolation between the calculated age-dependent oceanic lithosphere and the relatively well constrained lithosphere beneath the continent. However, there are several algorithms of interpolation/extrapolation data between two different lithospheric zones and these algorithms will provide diverse results. Therefore, two possible end-member configurations of the lithosphere-asthenosphere boundary beneath the continental margin have been tested by 3D density and 3D thermal modelling. The first configuration was with a sharp transition between the oceanic and continental lithospheres along the continent-ocean boundary (Figure 10.17a). This configuration for the base of the lithosphere is characterised by a relatively deep lithosphere beneath the margin with an average depth of around -110000 m. However, this is problematic for obtaining a fit between the major trends of the measured and modelled temperatures by the 3D thermal modelling. Therefore, the almost linear interpolation has been applied in order to fill the space between the ocean and the continent (Figure 10.17b). The final lithosphere-asthenosphere boundary has an average depth of around -97000 m beneath the continental margin, whereas the oceanic crustal domain is underlain by the -50000– -60000 m-deep base of the lithosphere. The lithosphere is more than 200000 m thick beneath the continent (Figure 10.17b), reflecting its Precambrian age in this area.

Finally, all described layers and interfaces have been set together to form the lithosphere-scale 3D structural model which has been used to understand the deep structure of the Mid-Norwegian continental margin.

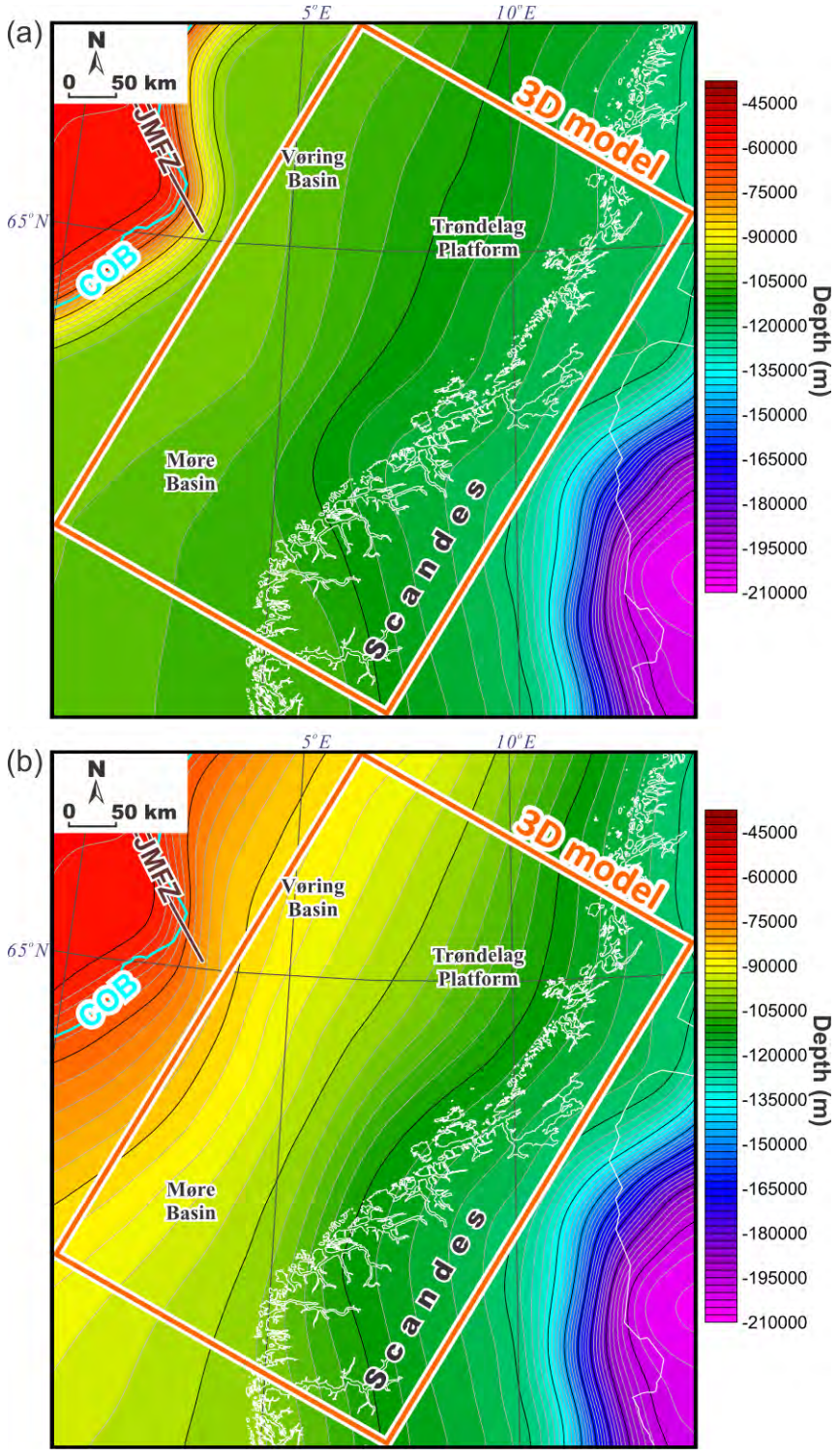

Figure 10.17. Depth to the lithosphere-asthenosphere boundary beneath the study area (based on Zhang & Lay 1999; Maystrenko & Scheck-Wenderoth 2009; Scheck-Wenderoth & Maystrenko 2011; Gradmann et al. 2013): (a) with the sharp transition along the COB and (b) linearly interpolated depth to the base of the lithosphere beneath the continental margin. COB - continent-ocean boundary (from Gernigon 2015; this report), JMFZ - Jan Mayen Fracture Zone (from Blystad et al. 1995).

10.3 3D DENSITY MODELLING

The key objective of the 3D density modelling was to evaluate the internal regional structure of the crystalline crust and sedimentary cover within the Mid-Norwegian continental margin and adjacent areas of the Norwegian mainland. The above-described input datasets have been used to constrain an input model for the 3D density modelling.

10.3.1 Observed gravity field

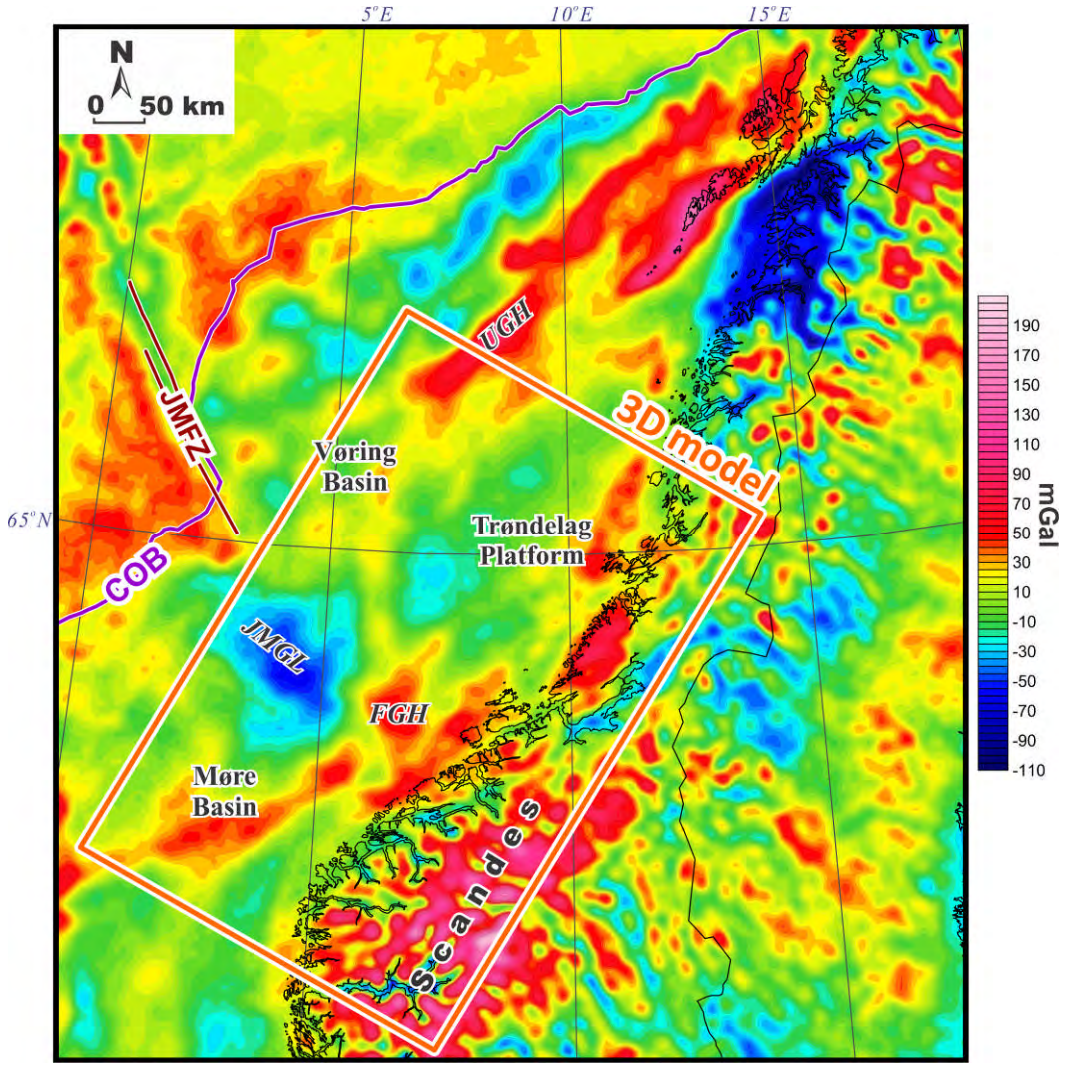

Figure 10.18. Observed gravity anomalies over the Mid-Norwegian continental margin and adjacent areas of the ocean and continent. Free-air gravity anomalies from the DTU13 gridded global gravity field (Andersen et al. 2013; ftp://ftp.space.dtu.dk/pub/DTU13/1_MIN/). COB - continent-ocean boundary (from Gernigon 2015; this report), FGH - Frøya gravity high, JMFZ - Jan Mayen Fracture Zone (from Blystad et al. 1995), JMGL - Jan Mayen gravity low, UGH - Utgard gravity high.

The free-air gravity anomalies offshore and onshore (Andersen et al. 2013) were used during the 3D density modelling. The free-air gravity anomalies are represented by the new global gravity field DTU13 from double retracked satellite altimetry (Andersen et al. 2013). The most prominent feature of the observed gravity field (Figure 10.18) is related to the wide gravity low over the Jan Mayen Corridor which represents a continental continuation of the Jan Mayen Fracture Zone. This Jan Mayen gravity low has less than -50 mGal within the central

part of the anomaly. Within the oceanic domain, the Jan Mayen Fracture Zone is characterised by the presence of the NW-SE-trending linear and narrow zone of negative gravity anomalies, separating two lithospheric blocks of positive anomalies with a distinctly marked horizontal shift (Figure 10.18). The complex topography and high altitude of the Scandes mountains are reflected by several strong, positive, free-air gravity anomalies. The Møre Basin is crossed by the NE-SW-elongated gravity high, and the Vøring Basin is characterised by a positive gravity anomaly over the Utgard High (Figure 10.18). Clearly visible positive anomalies bound the Trøndelag Platform to the east and the south.

10.3.2 Densities

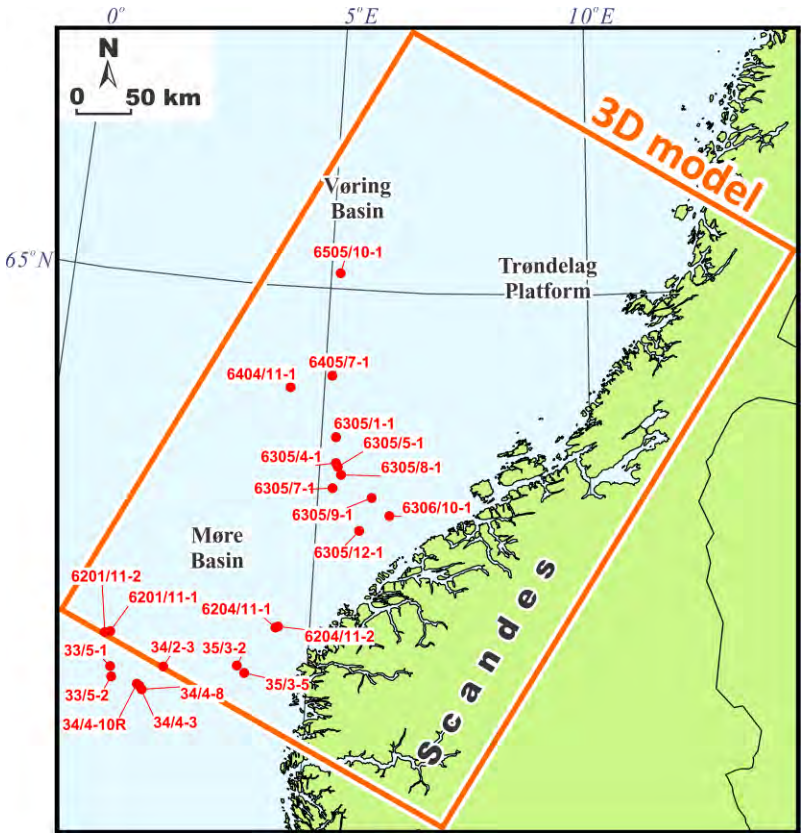

Figure 10.19. Location of the NPD wells with densities used in this study according to Reynisson (2010).

Table 10.2. Densities of the layers of the 3D structural model used during the 3D density modelling (lithology of sediments is derived from Bell et al. (2014) and from NPD (2014)).

Layer Number	Layer of the 3D structural model	Dominant lithology	Density ρ [kg/m^3]
1	Sea water		1030
2	Naust and Kai	92% shale, 8% sandstone	*Eq. (2)
3	Brygge	98% shale, 2% sandstone	*Eq. (3)
4	Paleocene	80% shale, 20% sandstone	*Eq. (2)
5	Oceanic layer 2AB	basalts and tuffs	2650
6	Upper Cretaceous	95% shale, 5% sandstone	*Eq. (4)
7	Lower Cretaceous	92% shale, 3% sandstone, 5% limestone	*Eq. (4)
8	Pre-Cretaceous	80% shale, 20% sandstone	*Eq. (5)
9	Upper-crustal high-density crystalline rocks	gabbro to anorthositic rocks, metamorphic rocks	2860
10	Low-density upper-crustal body	metasediments or granite	2655
11	Upper-crustal regional layer	granite and gneiss	2675
12	Middle crust	granitoids and/or gneiss	2740
13	Lower crust	metamorphic rocks	2845
14	High-density crust	mafic granulites, gabbros	2925
15	High-density lower-crustal layer	gabbros, high-grade metamorphic rocks	2985-3100
16	Lithospheric upper mantle	peridotite	3220

***Eq. is Equation**

During the 3D density modelling, densities have been assigned as constant values for each layer of the crystalline rocks (Table 10.2). On the other hand, densities of sediments have been set to be depth-dependent in order to reflect the compaction of sedimentary rocks with depth.

Several empirical equations have been derived for increasing densities with depth. This has been done based on the regional analysis of densities by Reynisson (2010) in some wells located within the Mid-Norwegian continental margin (Figure 10.19). The empirical functions

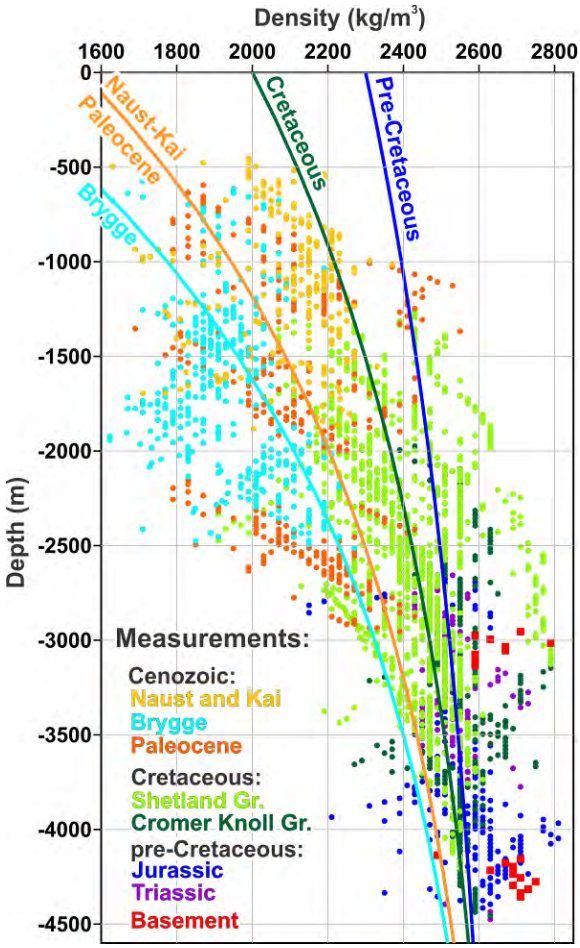

Figure 10.20. Distribution of the measured densities from the NPD wells from Reynisson (2010) with the averaged curves of depth-dependent densities used during 3D density modelling.

describe the exponential increase of densities with depth for sediments which have been assembled into four groups according to the characteristic distribution of the measured densities with depth and stratigraphy (Figure 10.20). These groups are the following: (1) Naust-Kai and Paleocene; (2) Brygge; (3) Cretaceous and (4) pre-Cretaceous.

The uppermost group of sediments is represented by the low-compacted Naust-Kai succession and the slightly more compacted Paleocene sediments, the measured densities of which form one cluster with similar densities (Figure 10.21a). Therefore, a single equation (10.2) has been derived for the Naust-Kai and Paleocene:

$$\rho(z)=2700-1150*\exp(0{,}00042*z) \quad (10.2)$$

where ρ is density [kg/m^3] and z is depth [m].

The obtained curve of the depth-dependent densities for the Naust-Kai and Paleocene is situated within the middle of the measured densities range at the same depth levels (Figure 10.21a) and, therefore, representing the average densities of these two layers.

Distribution of the measured densities for the Brygge Formation indicates that densities are shifted towards the lower values compared to densities of the rest of the layers (Figure 10.20). In particular, the measured densities of the Brygge vary from 1623 to 2270 kg/m^3 (Figure 10.21b). This specific feature has been reflected by the empirical function (10.3):

$$\rho(z)=2700-1450*exp(0,00045*z) \quad (10.3)$$

where ρ is density [kg/m^3] and z is depth [m].

The numbers in the function (10.3) have been chosen to produce a curve for depth-dependent densities which predict the major trend in the measured densities of the Brygge Formation (Figure 10.21b).

The measured densities of the Cretaceous are characterised by a wide range of values, varying from 1910 to 2790 kg/m^3 (Figure 10.21c). The derived function (10.4) for the Cretaceous has been set to reproduce more or less average densities of this wide range:

$$\rho(z)=2700-700*exp(0,00037*z) \quad (10.4)$$

where ρ is density [kg/m^3] and z is depth [m].

The last group of sediments is the pre-Cretaceous which consists of the Jurassic, Triassic, Permian and older sedimentary rocks in general. However, the measured densities are only available for the Jurassic and Triassic (Figure 10.21d). Therefore, the empirical function (10.5) is mainly representative for the Jurassic-Triassic interval (and mainly for the upper parts of these stratigraphic units):

$$\rho(z)=2700-400*exp(0,00027*z) \quad (10.5)$$

where ρ is density [kg/m^3] and z is depth [m].

Due to an absence of information for the underlying older layers, the function (10.5) has been used for all pre-Cretaceous strata, assuming that the major trend in density distribution with depth of the compacted old sediments is similar to the Jurassic and Triassic densities within the Mid-Norwegian continental margin. This assumption is supported by the fact that the distribution of the Jurassic and Triassic densities forms a rather narrow zone of the relatively slowly increasing measured densities with depth due to their high degree of compaction (Figure 10.21d). A similar degree of compaction is inferred for the lower part of the Triassic and older sediments. The obtained curve of densities according to equation (10.5) is located within the middle part of this narrow zone (Figure 10.21d), showing that the calculated densities are suitable for the main tendency in distribution of the measured ones.

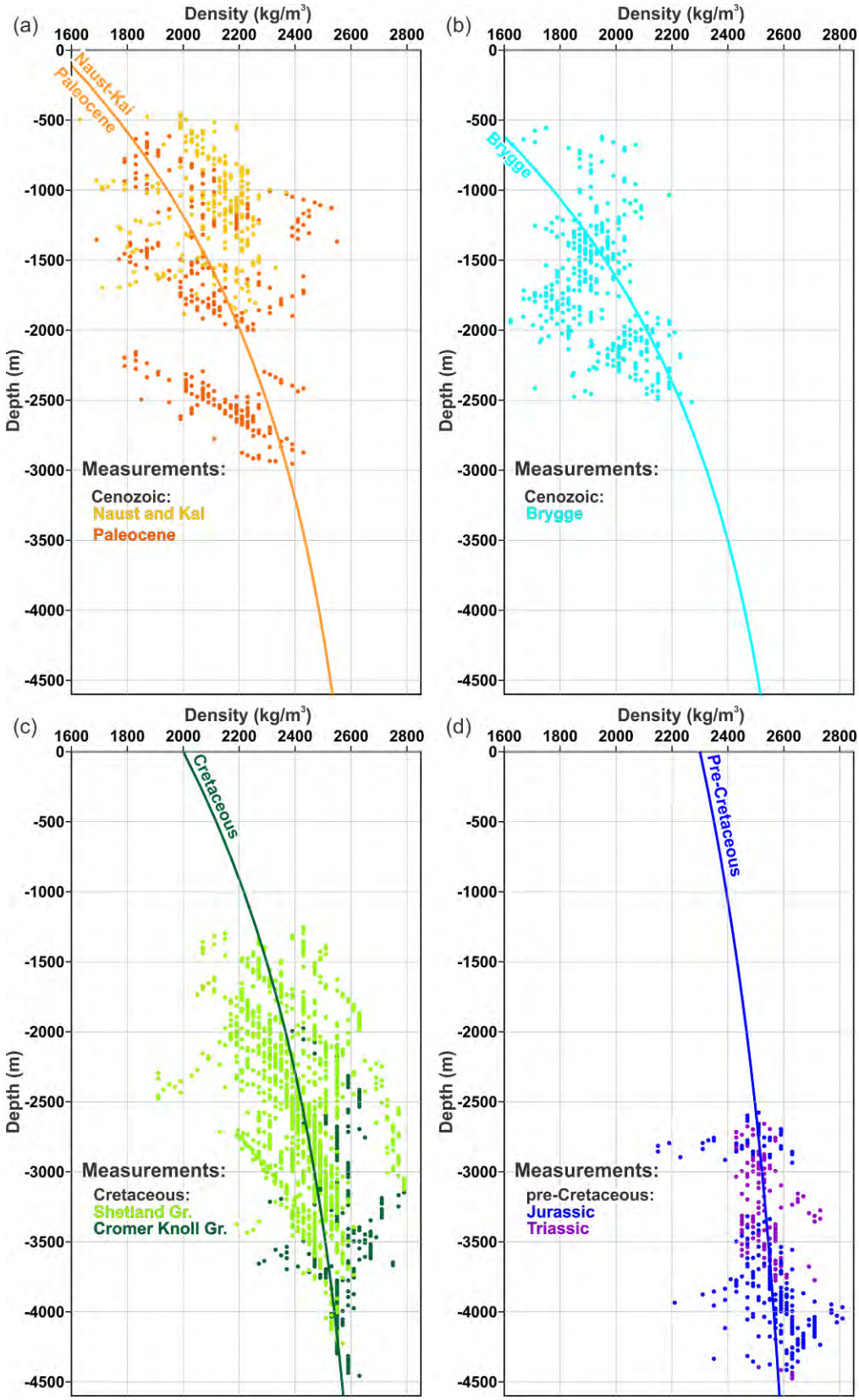

Figure 10.21. Measured densities from the NPD wells (Reynisson 2010) with the averaged curves of depth-dependent densities shown separately for (a) Naust-Kai and Paleocene, (b) Brygge, (c) Cretaceous and (d) pre-Cretaceous.

It is important to note that some of the measured densities of the crystalline basement are locally lower than the densities of sediments (Figure 10.20), implying that densities of sediments can be theoretically higher than densities of the crystalline crust at great depths where sediments are strongly compacted. Consequently, the typical density contrast between sediments and crystalline rocks can be inverted within the deepest parts of the Vøring and Møre basins and the Trøndelag Platform.

As a general rule, the chosen densities of the crystalline crust (Table 10.2) have been taken to represent the major lithological composition of each layer. The uppermost crystalline layer is the high-density, present-day, upper-crustal rocks which are mostly represented by former lower-middle-crustal gabbro to anorthosite and metamorphic rocks with a high density of 2860 kg/m^3. These former lower-middle-crustal rocks were brought close to the surface mainly during the Caledonian Orogeny. In contrast, the next layer is the low-density upper-crustal layer with density of 2655 kg/m^3. This low-density layer can be represented by metasediments or granite and is spatially restricted to the southeastern corner of the model area. A typical upper-crustal density of 2675 kg/m^3 has been assigned to the regional upper-crustal layer which is characterised by the broad distribution beneath the greater part of the study area. The middle crystalline crust has an average density of 2740 kg/m^3. The assigned density for the lower crystalline crust has been chosen to be 2845 kg/m^3. On the other hand, the high-velocity lower-crustal layer is in general characterised by velocities which exceed 6.7-6.8 km/s. These velocities can locally be even higher than 8 km/s in places where eclogitised rocks are possibly present, according to Mjelde et al. (2009). In addition, the high-velocity lower-crustal layer is represented by the magmatically underplated lower crust in the vicinity of the oceanic crustal domain (e.g., Mjelde et al. 2002). Consequently, the average density of this high-velocity, lower-crustal layer has been taken to be in the range of 2985-3100 kg/m^3. A density of 2925 kg/m^3 has been additionally assigned to high-density crust which differs from the high-density lower-crustal layer and the rest of the crust. In general, these assigned densities for the crystalline rocks (Table 10.2) are similar to those which were used during previous density modelling within the Coop2 model area (e.g., Tsikalas et al. 2005, Ebbing et al. 2006, Maystrenko & Scheck-Wenderoth, 2009, Raynisson 2010, Nirrengarten et al. 2014, Gernigon, 2015 this report). In addition, two crustal layers have been included into the model within the oceanic crustal domain which is not covered by the Coop2 model. These two layers are represented by the oceanic layers 3A and 3B. The middle-crustal oceanic layer 3A is considerred to be a mixture of sheeted dykes and gabbroic intrusions and has therefore been assigned a density of 2890 kg/m^3. The lowest oceanic crustal layer 3B has properties of gabbros and ultramafic rocks. Actually, the lower-crustal oceanic layer 3B is continuous with the high-velocity lower-crustal layer beneath the western parts of the Møre and Vøring basins in terms of seismic velocities and spatial position (Mjelde et al. 1997, 2005, 2009; Raum et al. 2002, 2006; Scheck-Wenderoth et al. 2007; Maystrenko & Scheck-Wenderoth, 2009). Therefore, a density of 3100 kg/m^3 has been set for this layer which is the same as the density of the high-density lower crust which was underplated during the breakup.

A strong velocity change from around 7.0 km/s within the lower crust to more than 8.0 km/s within the uppermost mantle is observed at the Moho (Mjelde et al. 1997, 2001, 2002, 2003, 2005, 2009; Raum et al. 2000, 2002, 2006; Breivik et al. 2006, 2009, 2011; Kvarven et al.

2014). This prominent jump in P-velocities indicates a discrete increase of densities within the uppermost mantle compared to the lower crust. Considering the thermal state of the whole lithospheric mantle, an average density of the lithospheric mantle has been set to be 3220 kg/m^3. Finally, an average density of 3160 kg/m^3 has been assigned to the uppermost asthenosphere in order to mimic differences in the thermal state between the oceanic and continental lithospheres.

10.3.3 Method

The 3D density modelling has been carried out by using the IGMAS plus software (the Interactive Gravity and Magnetic Application System; Götze 1978, Götze & Lahmeyer 1988, Schmidt & Götze 1998, Götze & Schmidt 2010). The oceanic and continental lithospheric domains are not fully covered by the Coop2 3D model. Therefore, the less constrained, large-scale, NGU 3D structural model (Figure 10.22a) has been used in order to take into account the regional gravity effects from the oceanic and continental domains. This large-scale NGU model allows us to consider the gravity effects from the relatively shallow Lithosphere-Asthenosphere boundary and Moho beneath the ocean and the relatively deep locations of the interfaces beneath Fennoscandia. On the other hand, the 3D density modelling has been conducted only for the Coop2 model area (Figure 10.22b), whereas the input geometry of the NGU model (Figure 10.22a) has been only slightly modified during the modelling.

During the 3D density/structural model preparation, a triangulation between structural depth maps and predefined 2D vertical slices has been applied in order to obtain the 3D geometry of the model. The geometrical approximation for the layers of the 3D model is determined by multiple polyhedra with triangulated planes between the top and the base of each layer. Constant and depth-dependent densities have been assigned to those polyhedra. As a final point, the integral gravity effect of all triangulated polyhedra gives the total gravity effect of the 3D density/structural model. The procedure of 3D gravity modelling is based on interactive changes of the geometry and density of the layers. In particular, the 3D gravity modelling was carried out by interactive changes of the geometry and densities along 46 E-W-oriented vertical slices through the 3D model of the Coop2 study area (Figure 10.23). The distance between these 2D working planes is 16 km which is sufficient to model the major crustal features of the model area. The 2D working slices are parallel to each other and cross the most important gravity anomalies and the major structural elements of the study area to avoid potential artifacts due to 3D triangulation between the slices. In addition, the sedimentary cover has been voxelised in order to consider the increase of densities with depth according to empirical functions (10.2-10.5). Furthermore, the 3D model has been laterally extended in all directions in addition to the above-mentioned, large-scale, NGU model, exceeding the actual model area. Thereby, the major structural features of the North Atlantic region and Fennoscandia have been schematically included to the extended parts of the 3D structural model to avoid boundary gravity effects.

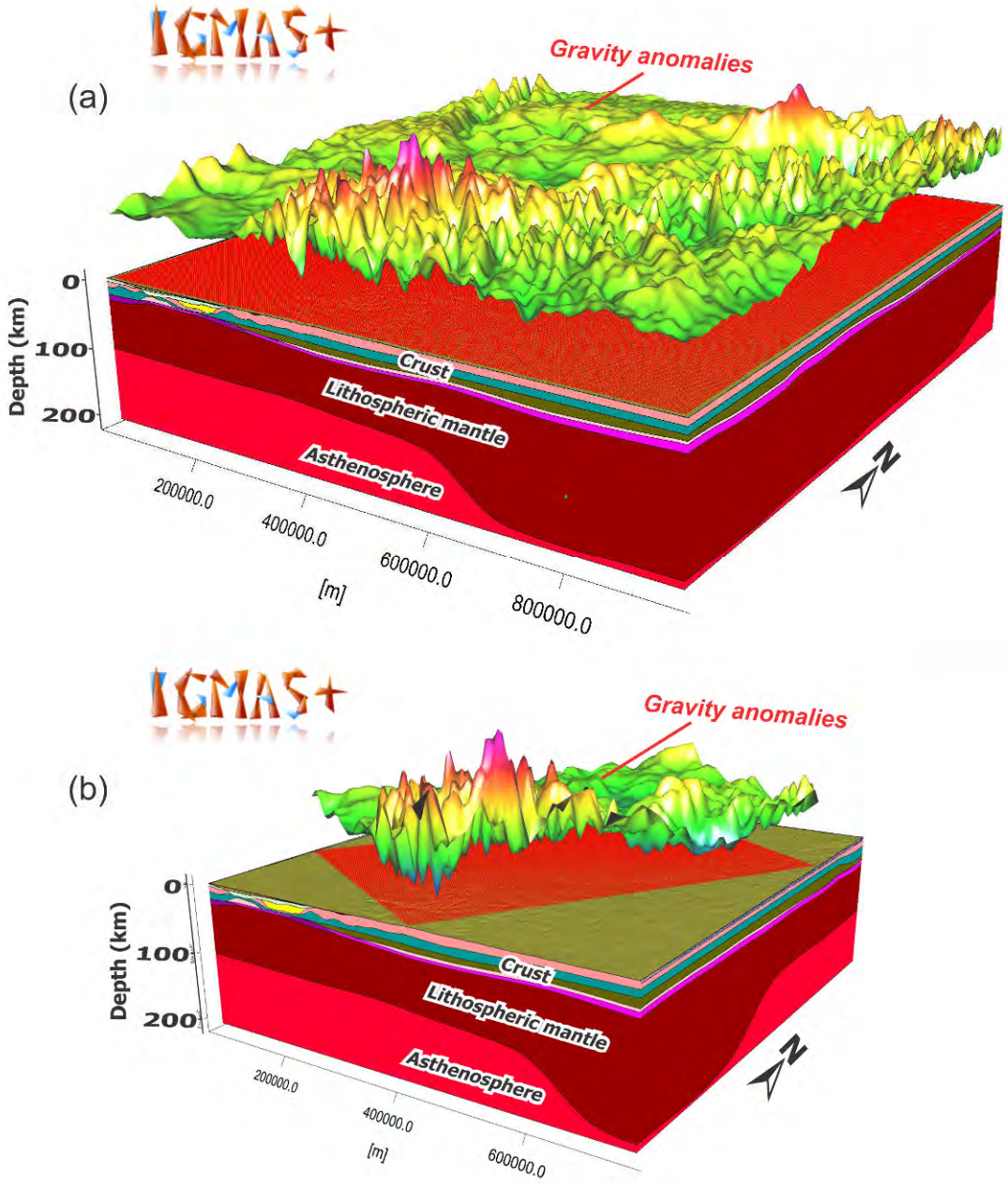

Figure 10.22. (a) Large-scale NGU 3D density/structural model and (b) Coop*2 3D density/structural model. For the location of the models, see Figure 10.1.*

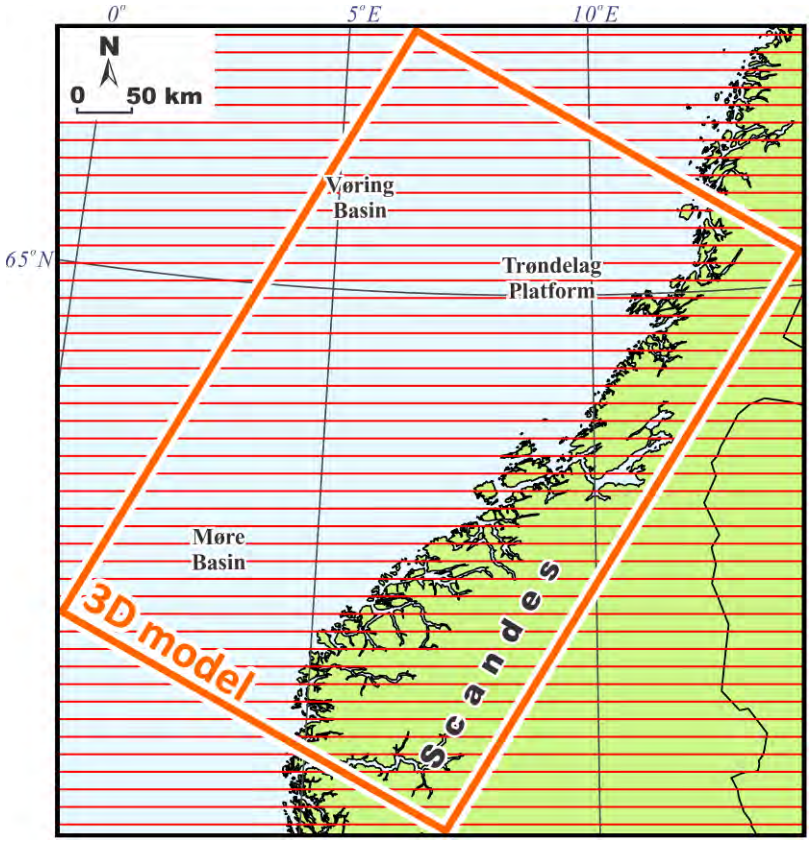

Figure 10.23. Location of the 2D vertical slices (red lines) through the 3D density-structural model.

Furthermore, an inherent non-uniqueness of the modelling approach has to be mentioned. It is known that numerous density and structural models can produce the same or similar modelled gravity. In this study, these objective limitations of the method have been considerably reduced by use of additional constraining data. Besides, the 3D density modelling assumes that the lateral influence of masses is considered in three dimensions, thus reducing a number of possible solutions. Sensitivity tests have shown that the modelled gravity response is most sensitive to geometrical modifications of interfaces where the strongest density contrast is present, such as at the base of sediments/the top of crystalline crust at a shallow level and at the Moho discontinuity. The depth position of the Moho is relatively well constrained by deep-seismic data over large parts of the modelled area (Figure 10.15). The top of the crystalline basement at shallow levels is also in good agreement with borehole and seismic data. However, the boundary between the pre-Cretaceous sediments and the crystalline crust is not always properly defined by seismic *data* within the deeper parts of the sedimentary cover. The problem is that the sediments are highly compacted within the deep parts of the Vøring and Møre basins and the Trøndelag Platform and therefore the density contrast between the sedimentary infill and the crystalline crust is smoothed or even inverted. Consequently, similar densities of the highly compacted sedimentary rocks and the crystalline crust increase the uncertainties in determining the depth to the top of the crystalline basement by the 3D density modelling within the deepest

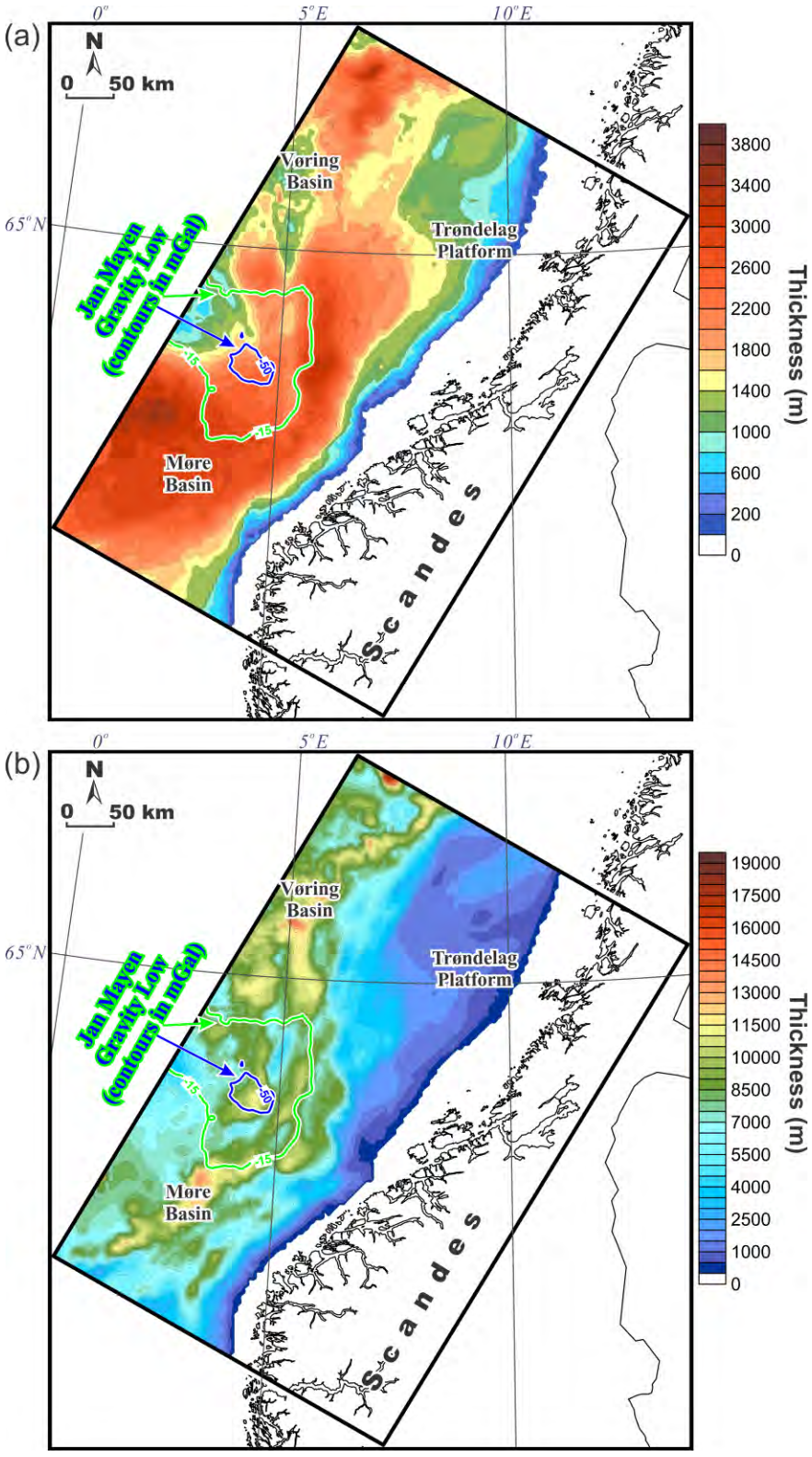

Figure 10.24. (a) Cumulative thickness of the Cenozoic and (b) cumulative thickness of Cenozoic, Cretaceous and basalts. Based on Rise et al. (2005, 2006, 2010), Dowdeswell et al. (2006, 2010), Eidvin et al. (2007, 2014), Ottesen et al. (2009, 2012), Chand et al. (2011) and Gernigon (2014; NGU unpublished data). The Jan Mayen gravity low is from Figure 10.18.

parts of the of the study area. In this case, the accuracy of the 3D density modelling is strongly dependent on the quality of the input data. In fact, the uncertainties in geometry and densities increase with depth, mostly due to the decreasing resolution of the input data. This is especially true in the case of the depth to the lithosphere-asthenosphere boundary which is the deepest boundary in the model. To remove all these uncertainties, additional data would be required.

10.3.4 Jan Mayen gravity low

There is a dilemma as to how to model the Jan Mayen gravity low according to the previous and the present-day attempts in order to achieve the consistent 3D density model within the study area. The Jan Mayen gravity low is a well pronounced feature of the observed gravity field over the continental continuation of the Jan Mayen Fracture Zone (Figure 10.18). There is a clear spatial correlation between the position of the Jan Mayen gravity low (Figure 10.18) and deepening of the sea floor (Figure 10.4). Therefore, one could expect that the density contrast between the sea water and the sedimentary cover within the local deepening of the sea floor might be fully responsible for the Jan Mayen gravity low. However, the jump in density from 1030 kg/m3 at the sea water level to approximately 1600-2000 kg/m3 at the level of the uppermost sediments is not sufficient to produce more than a -50 mGal gravity low over the deeply located sea floor within the Jan Mayen Corridor. Therefore, another density contrast is required in order to produce the Jan Mayen gravity low. This additional density contrast can be associated with either a structural feature or a lithological one, or both, in the layers of the 3D density model. In actual fact it is difficult to find an additional structural element at the crustal level which is solely related to this pronounced negative gravity anomaly. For instance, there is no real correlation between the Jan Mayen gravity low and the thickness pattern at the level of the Cenozoic (Figure 10.24a), with the exception of a thinning of sediments towards the Jan Mayen Fracture Zone. However, this thinning is located within the area where the intensity of this wide gravity low decreases (cf. Figures 10.18 & 10.24a). The next possible pretender is the level of the Cretaceous (Figure 10.24b), but the outline of the Jan Mayen negative gravity crosses areas with different thicknesses at this level. There is only one apparent coincidence between the local thickening of the Cretaceous-Cenozoic sediments and the -50 mGal contour of the anomaly (Figure 10.24b). However, this coincidence cannot explain the whole anomaly and, therefore, cannot be considered as a source of the gravity low. Furthermore, there is no clear correlation between the gravity low under discussion and the cumulative thickness of the entire sedimentary cover (Figure 10.25a). The negative gravity overlies both thickened and thinned sedimentary cover. Actually, there is a possibility to model this gravity low along the E-W-trending 2D profile because thickening of the sediments would be more or less spatially coincident with the negative gravity, and thinning with a diminishing magnitude of this anomaly. However, there is no chance of reproducing this anomaly along the N-S-trending 2D profile which crosses a few zones of thickening and thinning without any real correlation with the pattern of the observed gravity. Actually, this is an advantage of the modelling in 3D in that it provides a possibility to perform a gravity analysis by considering the gravity effect in all directions, allowing us to avoid possible mistakes in interpretation of the speculative gravity anomalies. Moreover, there is no way to find a direct structural signature of the Jan Mayen gravity low

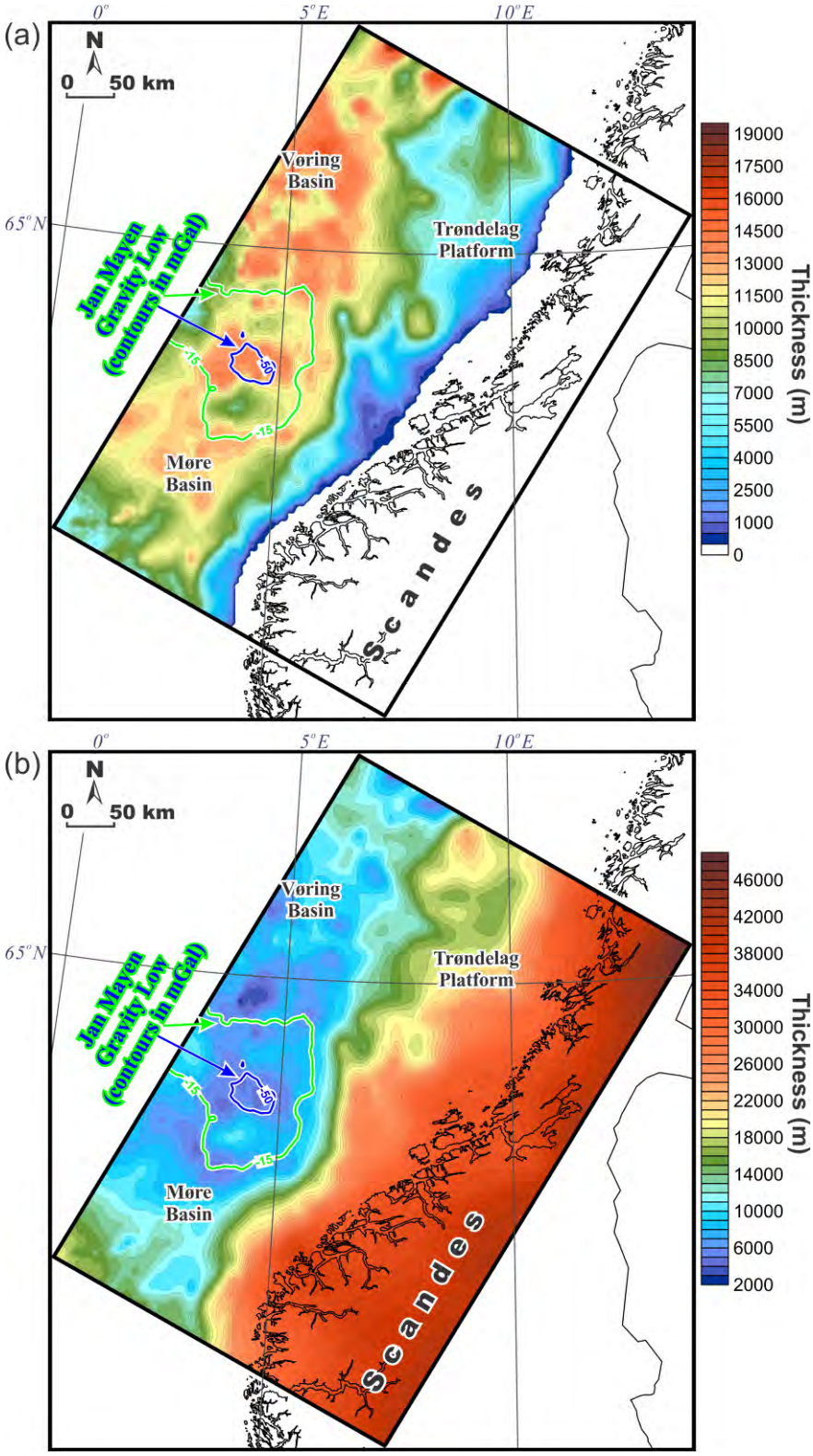

Figure 10.25. (a) Cumulative thickness of all sediments with basalts (based on Rise et al. 2005, 2006, 2010; Dowdeswell et al. 2006, 2010; Eidvin et al. 2007, 2014; Ottesen et al. 2009, 2012; Chand et al. 2011 and Gernigon 2014, NGU unpublished data) and (b) cumulative thickness of the whole crystalline crust. The Jan Mayen gravity low is from Figure 10.18.

at the level of the whole crystalline crust which is only 4000-10000 m thick in that area (Figure 10.25b). The -15 mGal contour of the Jan Mayen negative gravity anomaly crosses the region with different thicknesses of the crystalline crust without any clear regularity

between the thickness of the crust and the shape of the anomaly. The -50 mGal contour is actually restricted to the area with the minimal thickness of the crystalline crust where the sedimentary cover thickens (cf. Figures 10.25a & 10.25b), implying that there is some gravity effect which may be related to a possible density contrast between the sediments and the crystalline rocks within the central part of the Jan Mayen gravity anomaly. On the other hand, the depth to the top of the crystalline basement is around -15000 m and

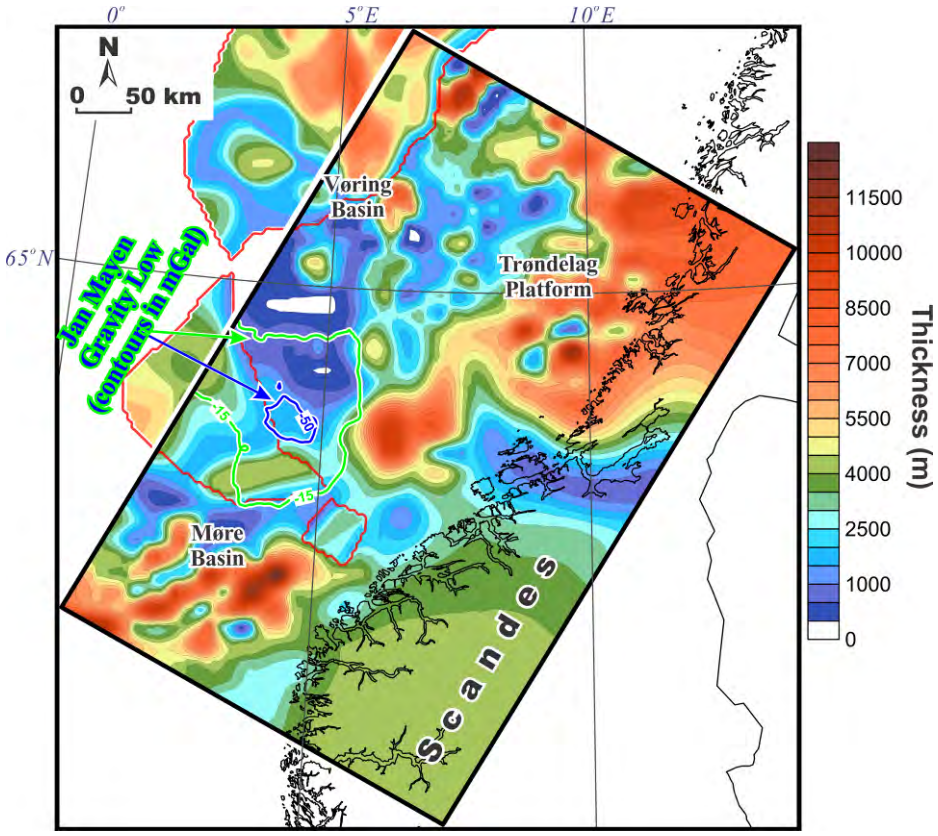

Figure 10.26. The modelled thickness of the high-density lower-crustal layer (this study) with the superimposed thickness of the high-velocity lower-crustal bodies from Mjelde (2009). The previously published limits of the high-velocity bodies are outlined by red lines. The Jan Mayen gravity low from Figure 10.18 is outlined with green (-15 mGal) and blue (-50 mGal) contours.

the sediments are highly compacted there, assuming a very low or even absent density contrast at the sediments-crystalline rocks interface. In addition, there are some structural inhomogeneities internally within the crystalline crust. The largest density contrast within the crystalline crust occurs between the high-density/velocity lower-crustal layer and the rest of the crust. The high-density/velocity lower-crustal layer is characterised by the presence of two zones with pronounced thickening beneath the Vøring and Møre basins (e.g., Ebbing et al. 2006; Mjelde et al. 2009; Maystrenko & Scheck-Wenderoth 2009). These two zones are separated by a strong thinning of this high-density layer in the vicinity of the Jan Mayen Corridor and can be related to the origin of the Jan Mayen gravity low. However, the detailed analysis demonstrates that the Jan Mayen gravity anomaly is shifted to the south from the strongly thinned high-density/velocity lower-crustal layer (Figure 10.26). Consequently, thinning of the high-density lower-crustal layer cannot be considered as the only reason for the wide gravity low over the Jan Mayen Corridor.

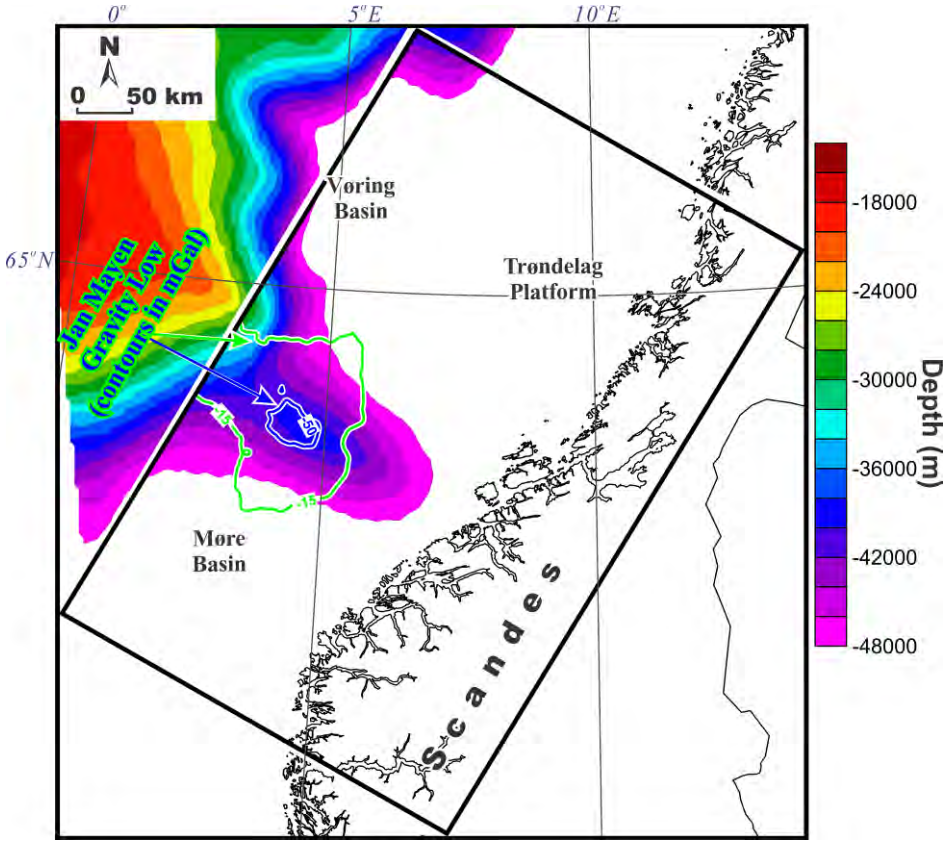

Figure 10.27. Top of the lower density mantle in the modelled end-member geometry according to Maystrenko & Scheck-Wenderoth (2009). The Jan Mayen gravity low from Figure 10.18 is outlined with green (-15 mGal) and blue (-50 mGal) contours.

An overview of the previously published attempts to reproduce the Jan Mayen gravity anomaly by density modelling shows that Maystrenko & Scheck-Wenderoth (2009) have associated this gravity low with a mantle wedge of reduced density which extends from the oceanic Jan Mayen Fracture Zone to the continental Jan Mayen Corridor, and can be related to increased mantle temperatures and/or compositional changes in the mantle beneath the lineament (Figure 10.27). The Jan Mayen Fracture Zone is in fact characterised by a linear negative gravity anomaly (Figure 10.18). Based on plate reconstructions (Gernigon et al. 2009, 2015), the last movements along the Jan Mayen Fracture Zone occurred during the final separation of the Jan Mayen microcontinent from East Greenland, indicating that this oceanic fracture zone is tectonically younger than the neighbouring Mid-Norwegian margin. In contrast, the continental Jan Mayen Corridor or Jan Mayen Lineament may be of pre-breakup age according to Torske & Prestvik (1991) and Gernigon et al. (2015). Torske & Prestvik (1991) proposed that the continental Jan Mayen Corridor may have acted as a lithosphere-penetrating, strike-slip transfer fault or accommodation zone during Mesozoic phases of extension and thus would be older than the breakup. Gernigon et al. (2015) have a very similar view on the pre-breakup history of the Jan Mayen Corridor and have assumed that it was a large crustal and basin-scale accommodation and transfer zone between the Møre and Vøring margins that is reflected by the structural style of the pre-Cretaceous and Early Cretaceous rift system. In this case, the continental Jan Mayen Corridor may have been the precursor of the Jan Mayen Fracture Zone and could represent a deep lithospheric conduit which is responsible for transport of volatiles from the asthenosphere to the upper mantle (Torske & Prestvik 1991). Therefore, it is reasonable to suggest that the reduced

mantle densities within the Jan Mayen gravity low can be associated with the superimposed complex effects of pre-breakup tectonic activity along the Jan Mayen Corridor and possible later reactivation related to the development of the Jan Mayen Fracture Zone.

In an alternative interpretation, Reynisson (2010) has suggested the presence of a relatively deep crustal root beneath the Jan Mayen negative gravity anomaly (Figure 10.28) which can produce a similar gravity signal as in a zone of reduced upper mantle density (Figure 10.27). This hypothesis, however, is not supported by the recently obtained deep seismic data (Kvarven et al. 2014) which do not show a significant deepening of the Moho within the area of the Jan Mayen gravity anomaly.

Although Maystrenko & Scheck-Wenderoth (2009) and Reynisson (2010) demonstrated a need for an upper mantle and/or deep crustal mass deficit within the Jan Mayen gravity low, the sediment-related origin of this negative anomaly cannot be ignored and has to be investigated in detail. In order to investigate this possibility, the NPD wells with the measured densities from Reynisson (2010) have been plotted in relation to the position of the Jan Mayen negative gravity anomaly (Figure 10.29). There are four wells which are clearly located within the area of the negative gravity anomaly (Figure 10.29). These wells are the following: 6305/5-1, 6305/4-1, 6405/7-1 and 6404/11-1 (highlighted in magenta in Figure 10.29).

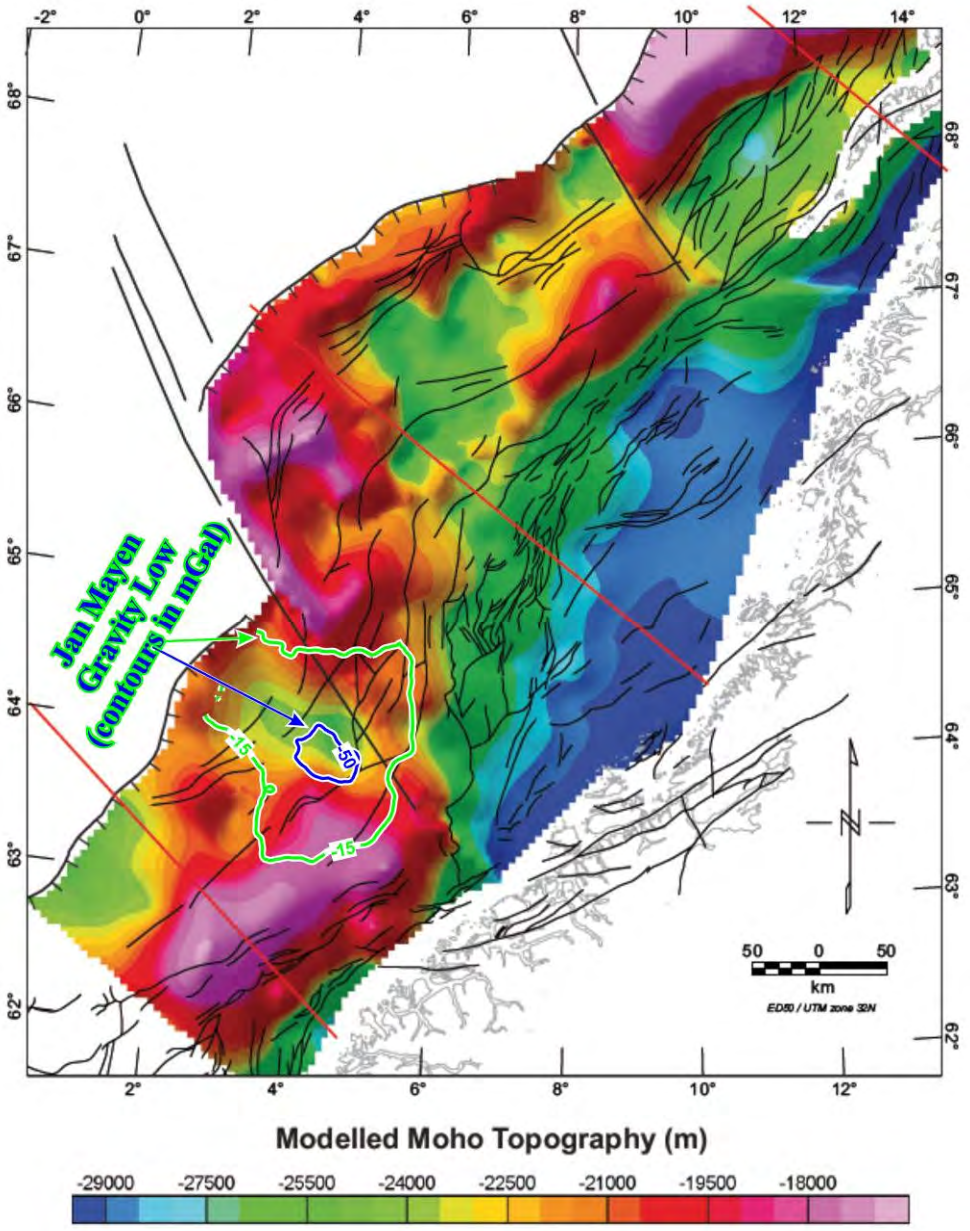

Figure 10.28. Moho topography from the model by Reynisson (2010). The Jan Mayen gravity low from Figure 10.18 is outlined with green (-15 mGal) and blue (-50 mGal) contours.

The next step of this analysis was an extraction and plotting of the measured densities from the wells, located within the gravity low, in comparison with the densities from the rest of the wells. This has been done separately for three groups of sediments (Figure 10.30), such as the Naust-Kai and the Paleocene, the Brygge and the Cretaceous. The results of the analysis clearly demonstrate that the measured densities from wells 6305/5-1, 6305/4-1, 6405/7-1 and 6404/11-1 are characterised by lower values compared to the densities from the wells located outside or at the outer edge of the Jan Mayen gravity low. The reduction of densities is especially pronounced for the Brygge (Figure 10.30b) and the Cretaceous (Figure 10.30c).

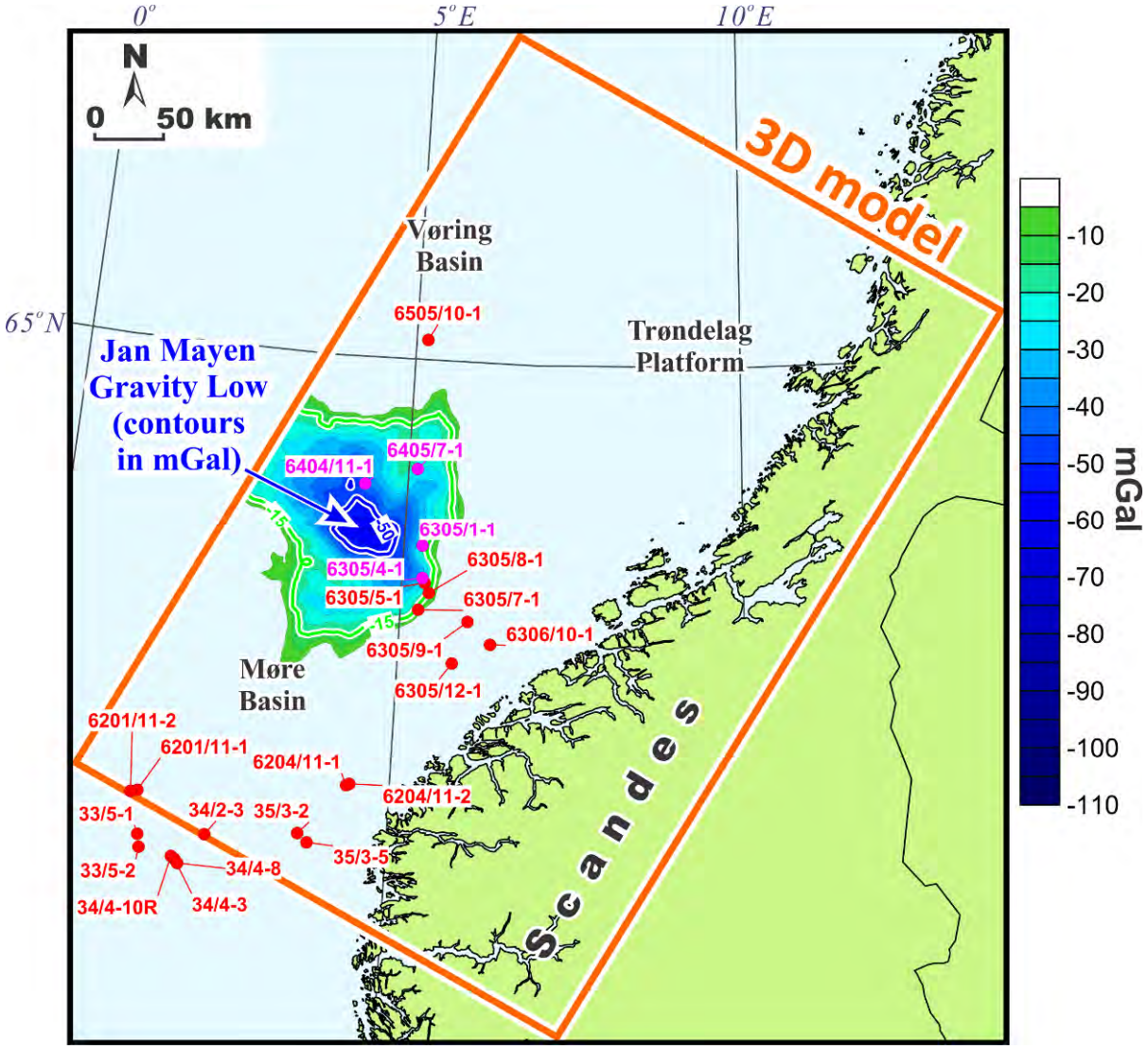

Figure 10.29. Location of the NPD wells with densities used in this study according to Reynisson (2010). The NPD wells are shown in relation to the Jan Mayen gravity low from Andersen et al. (2013; ftp://ftp.space.dtu.dk/pub/DTU13/1_MIN/).

Therefore, this reduction in densities within the sedimentary cover within the area of the Jan Mayen gravity low has been included into the 3D density/structural model. This has been done by dividing the sedimentary layers into several blocks within the Jan Mayen gravity low in order to consider the gradual decrease of densities toward the centre of this wide negative gravity anomaly.

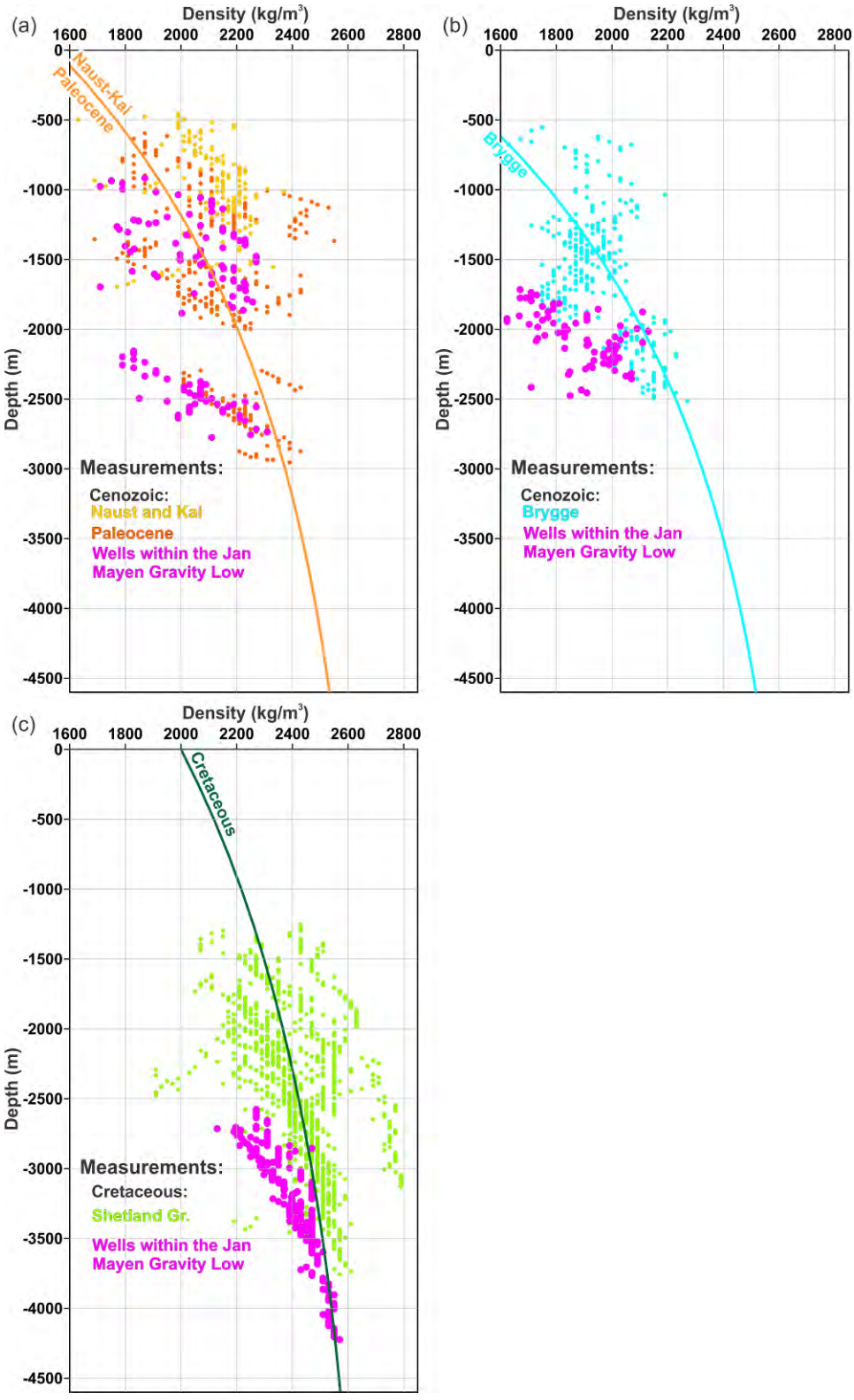

Figure 10.30. Measured densities from the NPD wells (Reynisson 2010) with the averaged curves of depth-dependent densities for (a) Naust-Kai and Paleocene, (b) Brygge and (c) Cretaceous. Magenta symbols represent measurements from the wells marked by magenta in Figure 10.29 from the internal area of the Jan Mayen gravity low.

It is important to note that the problem regarding the origin of the Jan Mayen gravity low still remains unresolved. As the real internal configuration and composition of the upper mantle at the transition from the oceanic domain to the continental one between the Vøring and Møre

basins is unknown in detail, the gravity inversion is thus non-unique. Only one of the possible end-members has been examined during the present 3D density modelling. Only the gravity effect of the low-density sediments has been used to explain the Jan Mayen gravity low in addition to the deep bathymetry. This has been done in order to demonstrate an alternative upper-crustal possibility for the nature of the gravity low compared to upper mantle or deep crustal origin (Maystrenko & Scheck-Wenderoth 2009, Reynisson 2010). On the other hand, this does not exclude at least an upper mantle origin for the Jan Mayen gravity low in addition to the deep bathymetry and the low densities within the sedimentary cover. The Jan Mayen gravity low can be related to a cumulative effect of the density contrasts at the upper mantle level, within the sediments and at the deep sea floor. Unfortunately, there is no way to estimate the precise separate contributions from the upper mantle and sedimentary cover, as this would require additional constraints and more detailed density modelling.

10.3.5 Results of the 3D density modelling

The results of the 3D density modelling demonstrate that the calculated gravity effect of the final 3D density/structural model (Figure 10.31b) is in good agreement with the long-wavelength component of the observed free-air gravity anomalies (Figure 10.31a) over the Coop2 model area. The difference between observed and modelled gravity (observed gravity minus the modelled version; Figure 10.31c) demonstrates that some of local gravity anomalies have not been reproduced during the 3D density modelling. Most of these residual misfits are in the range of less than ±10 mGal and have a rather small size. On the other hand, these short-wavelength local misfits do not have a marked impact on the regional gravity field and, therefore, do not have any strong influence the structure of the study area at the regional scale. Over the Scandes mountains, a number of short-wavelength misfits between the observed and the modelled gravity anomalies are locally more than ±25 mGal. These large misfits can be related to the fact that the gridded topography and the gridded free-air gravity anomalies have been used during the 3D density modelling. However, the free-air gravity anomalies are very sensitive to the gravity effect of the topography and, unfortunately, in the case of the gridded topography and the gridded free-air gravity, the local lack of coincidence between topography and gravity cannot be avoided. In this case, the main effort has been directed to fit the long-wavelength component of the observed gravity over the mainland rather than to fit the short-wavelength components. The free-air gravity anomalies onshore have been used instead of the Bouguer gravity anomalies in order to make a parallel 3D magnetic modelling possible that also requires the inclusion of the mainland topography.

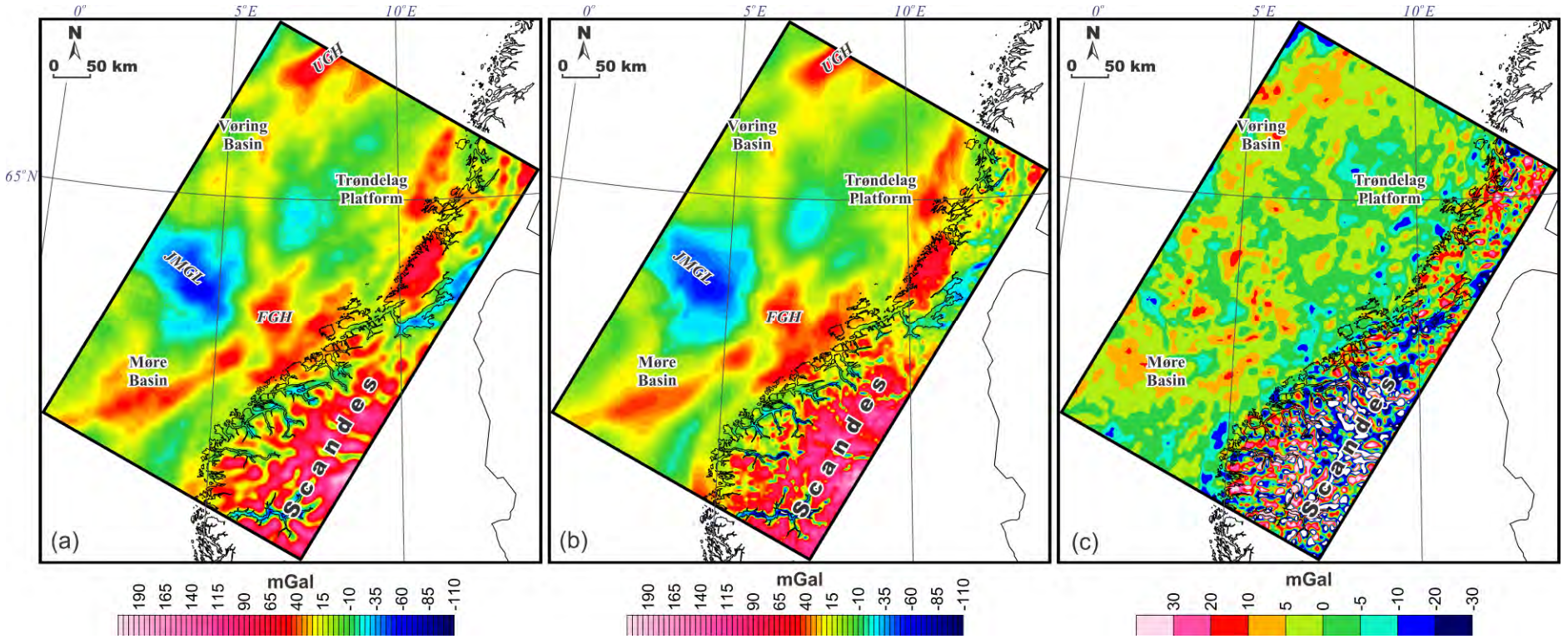

Figure 10.31. (a) Observed gravity anomalies over the study area (Andersen et al. 2013), (b) modelled gravity anomalies and (c) residual gravity anomalies demonstrating the difference between the observed gravity field (Figure 10.31a) and the modelled one (Figure 10.31b). FGH - Frøya gravity high, JMGL - Jan Mayen gravity low, UGH - Utgard gravity high.

During the 3D density modelling, the crystalline crust of the study area has been subdivided into several layers according to seismic data and the generally accepted geological conception of the deep structure of the study area. In contrast to the sedimentary cover, the constant average densities have been assigned to each layer of the crystalline crust.

The modelled upper crystalline rocks have been subdivided into four layers. The uppermost layer of the crystalline rocks is represented by the oceanic layer 2AB (Figure 10.32; layer 5 in Table 10.2) and consists mainly of flood basalts. The average density of this layer has been chosen to be 2650 kg/m^3 within the model area, assuming the presence of tuffs in addition to the basalts. Within the Coop2 study area, the edge of this layer is only present within the western margin of the Møre Basin and has an average thickness of 1000-1100 m (Figure 10.32a). The base of the basalts is mainly located at -4500–-5500 m depth (Figure 10.32b). The next upper-crustal layer consists of the upper-crustal high-density crystalline rocks (Figure 10.33; layer 9 in Table 10.2). This layer is represented by gabbroic to anorthositic and metamorphic rocks which are mapped at the surface along the western coast of Norway and within the southeastern corner of the model where the Jotun Nappe Complex is present (Sigmond 2002). The Jotun Nappe Complex has already been covered by the Coop1 3D model (Maystrenko 2014) and has a thickness pattern which is similar to the one obtained during the previous attempt at gravity modelling in this area by Skilbrei (1990). In contrast to the mainland, the distribution of the gabbroic-anorthositic and metamorphic rocks is not so obvious within areas covered by sedimentary rocks in the northern North Sea and the Norwegian Sea. The third upper-crustal layer is the northern continuation of the previously modelled low-density body beneath the Horda Platform in the northern North Sea (Maystrenko 2014). This low-density upper-crustal layer (layer 10 in Table 10.2) is locally more than 15000 m thick (Figure 10.34) and has a relatively low density of 2655 kg/m^3 which can correspond to either metasediments or granite. The last upper-crustal layer (Figure 10.35; layer 11 in Table 10.2) has a regional distribution and has been assigned a typical upper-crustal density of 2675 kg/m^3. This regional upper-crustal layer is thickest beneath the Scandes mountains on the Norwegian mainland and beneath the Trøndelag Platform (Figure 10.35a). The thickness of the layer is locally up to 20000 m. On the contrary, outlines of the Møre and Vøring basins are clearly distinguished by either strong thinning or even the absence of this layer, implying that a large part of the crystalline crust is more dense beneath the Cretaceous depocentres where thick sedimentary successions have been reported.

The modelled middle crust of the Coop2 model area (Figure 10.36; layer 12 in Table 10.2) can be lithologically represented by granitoids and gneisses, having an average density of 2740 kg/m^3. The thickest middle-crustal layer (more than 18000-19000 m thick) is modelled within the northeastern part of the study area beneath the Norwegian mainland and adjacent shelf (Figure 10.36a). The Trøndelag Platform and the area beneath the Scandes Mountains are characterised by a moderate thickness of this middle-crustal layer which varies from 6000 to 12000 m on average. On the other hand, as in the case of the regional upper-crustal layer (cf. Figures 10.35 & 10.36), the middle-crustal layer is very thin or absent beneath the Møre and Vøring basins.

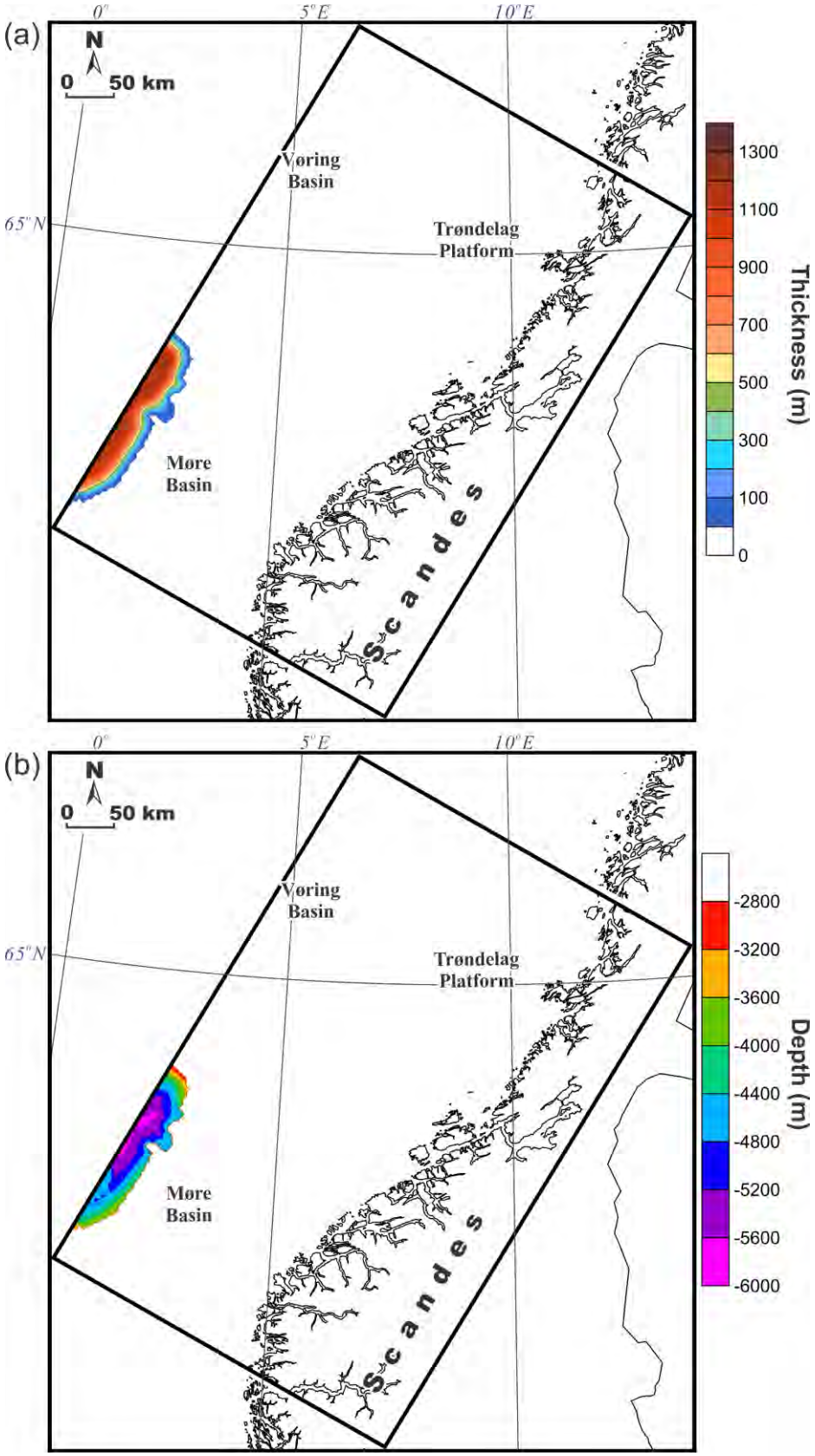

Figure 10.32. Upper crystalline crust: (a) thickness map and (b) structural depth map (base of the layer) of the oceanic layer 2AB (basalts)(layer 5).

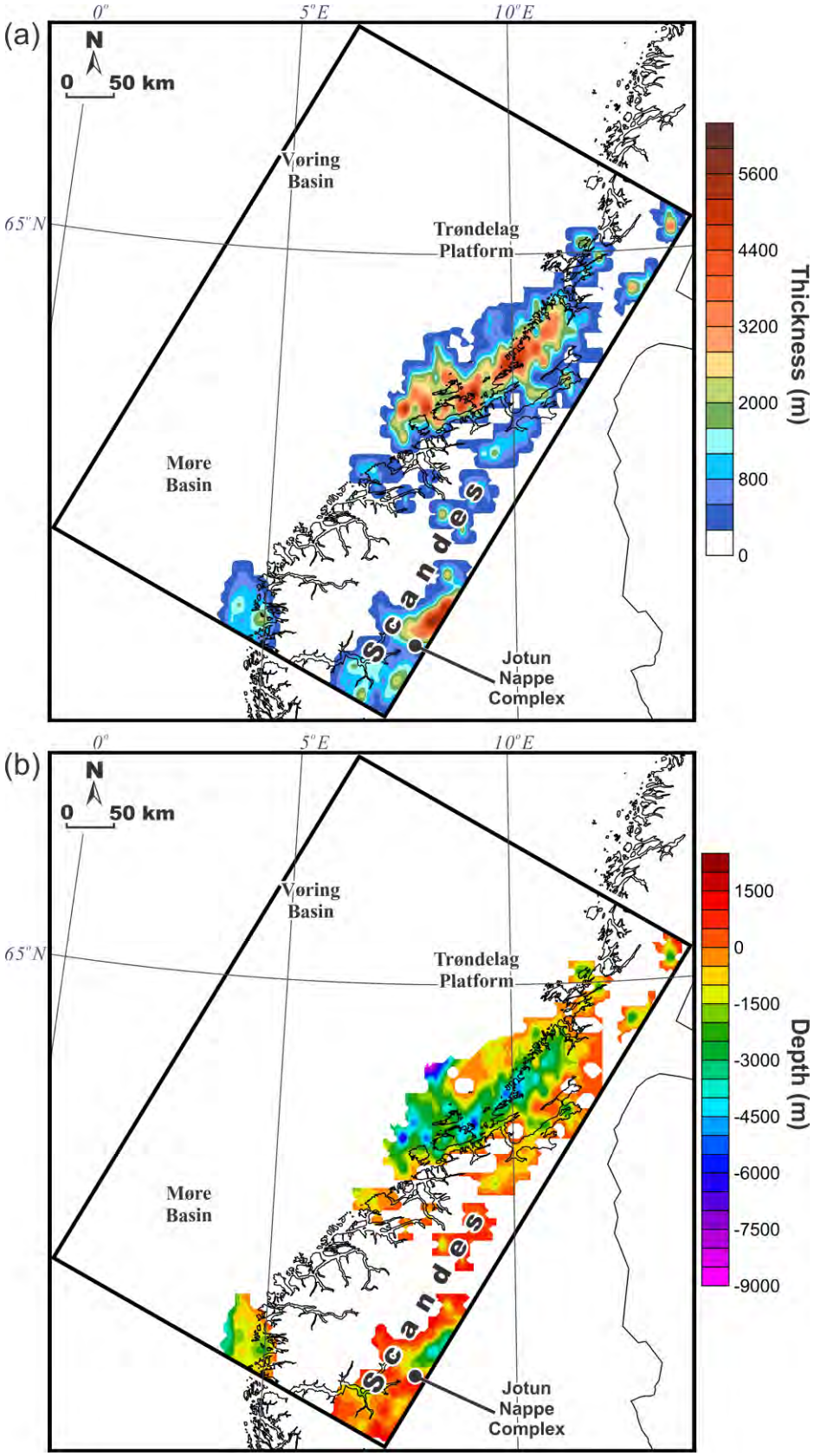

Figure 10.33. Upper crystalline crust: (a) thickness map and (b) structural depth map (base of the layer) of the upper-crustal high-density crystalline rocks (layer 9).

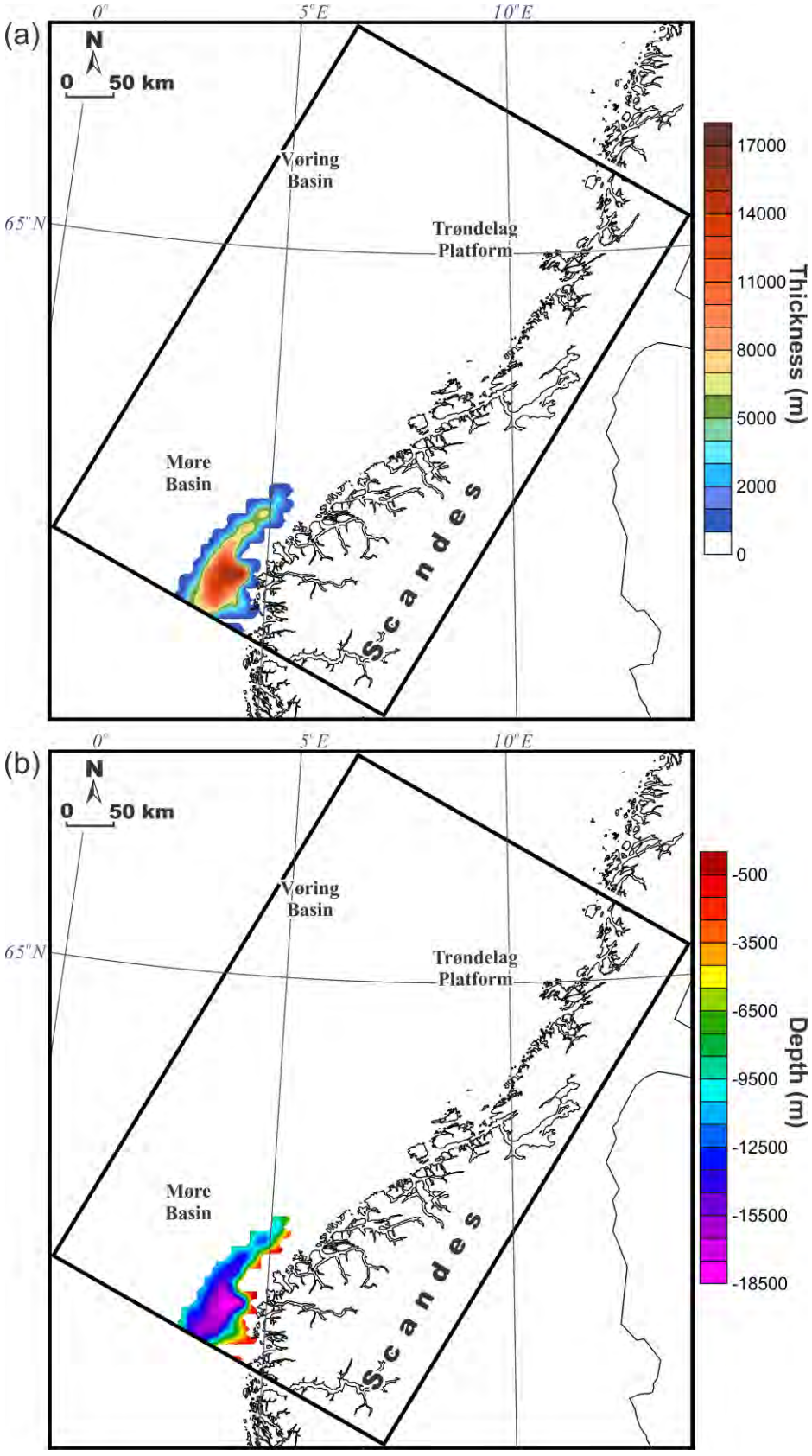

Figure 10.34. Upper crystalline crust: (a) thickness map and (b) structural depth map (base of the layer) of the low-density upper-crustal body (layer 10).

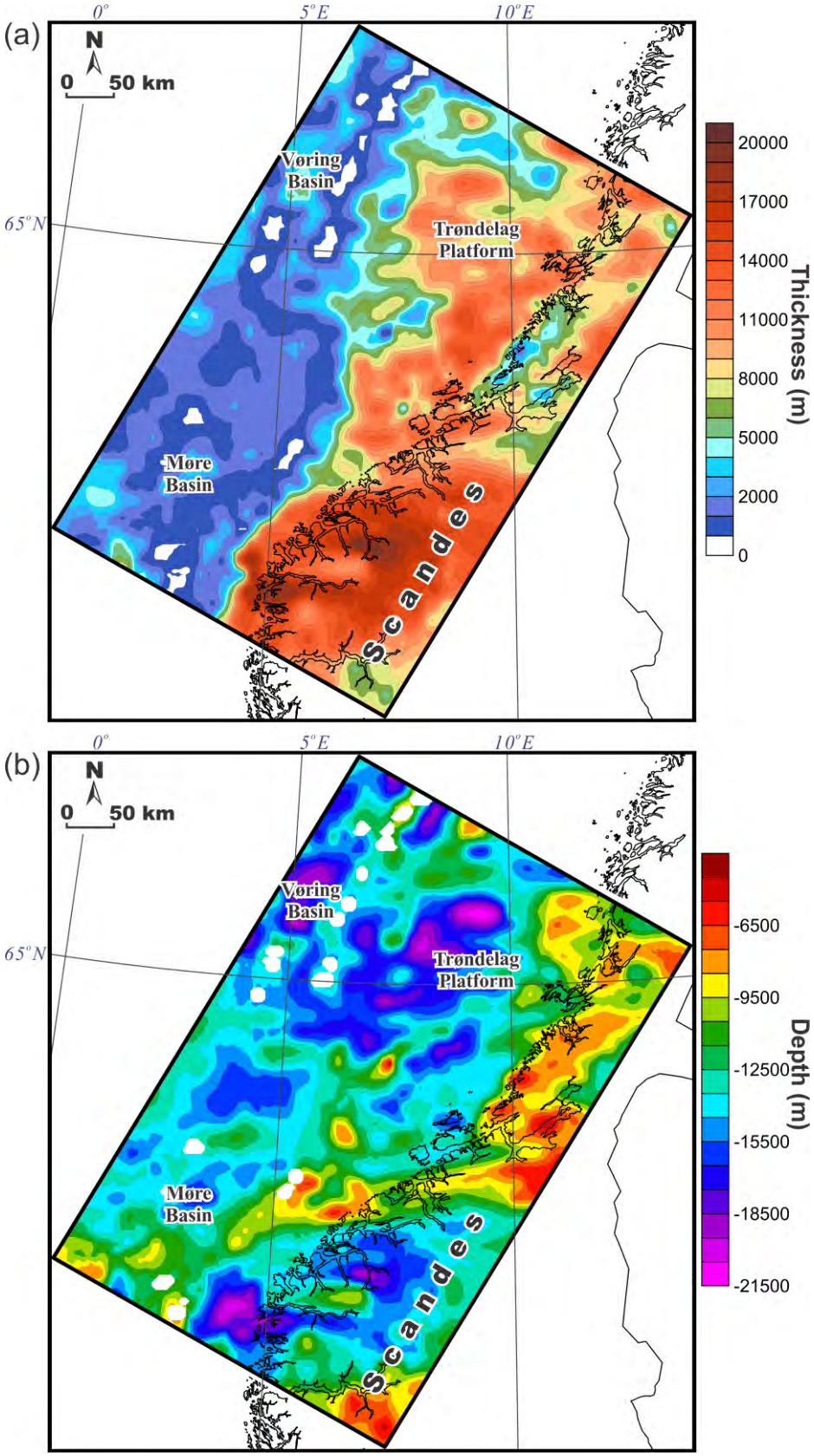

Figure 10.35. Upper crystalline crust: (a) thickness map and (b) structural depth map (base of the layer) of the regional upper-crustal layer (layer 11).

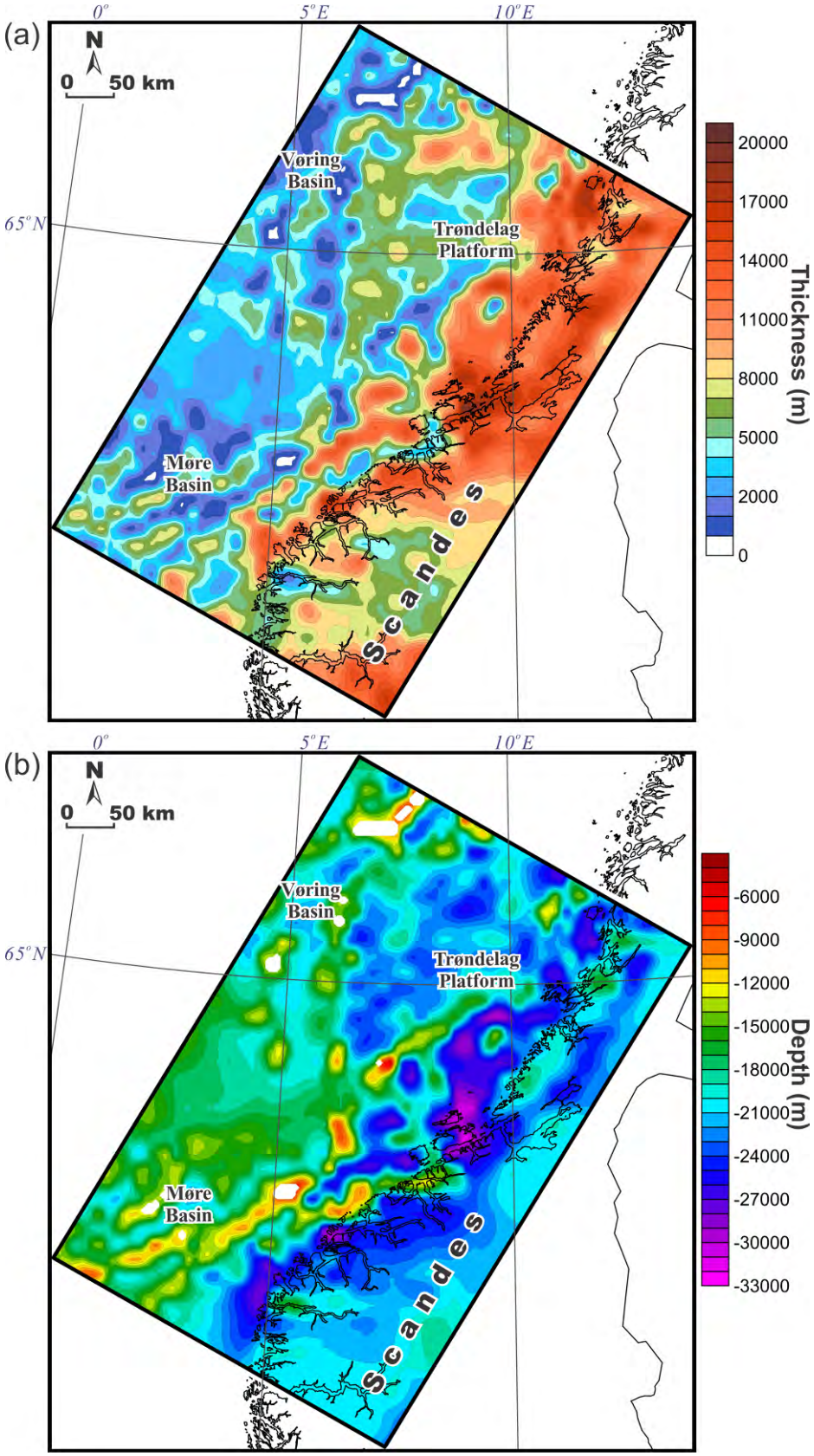

Figure 10.36. Middle crystalline crust: (a) thickness map and (b) structural depth map (base of the layer) of the middle crust (layer 12).

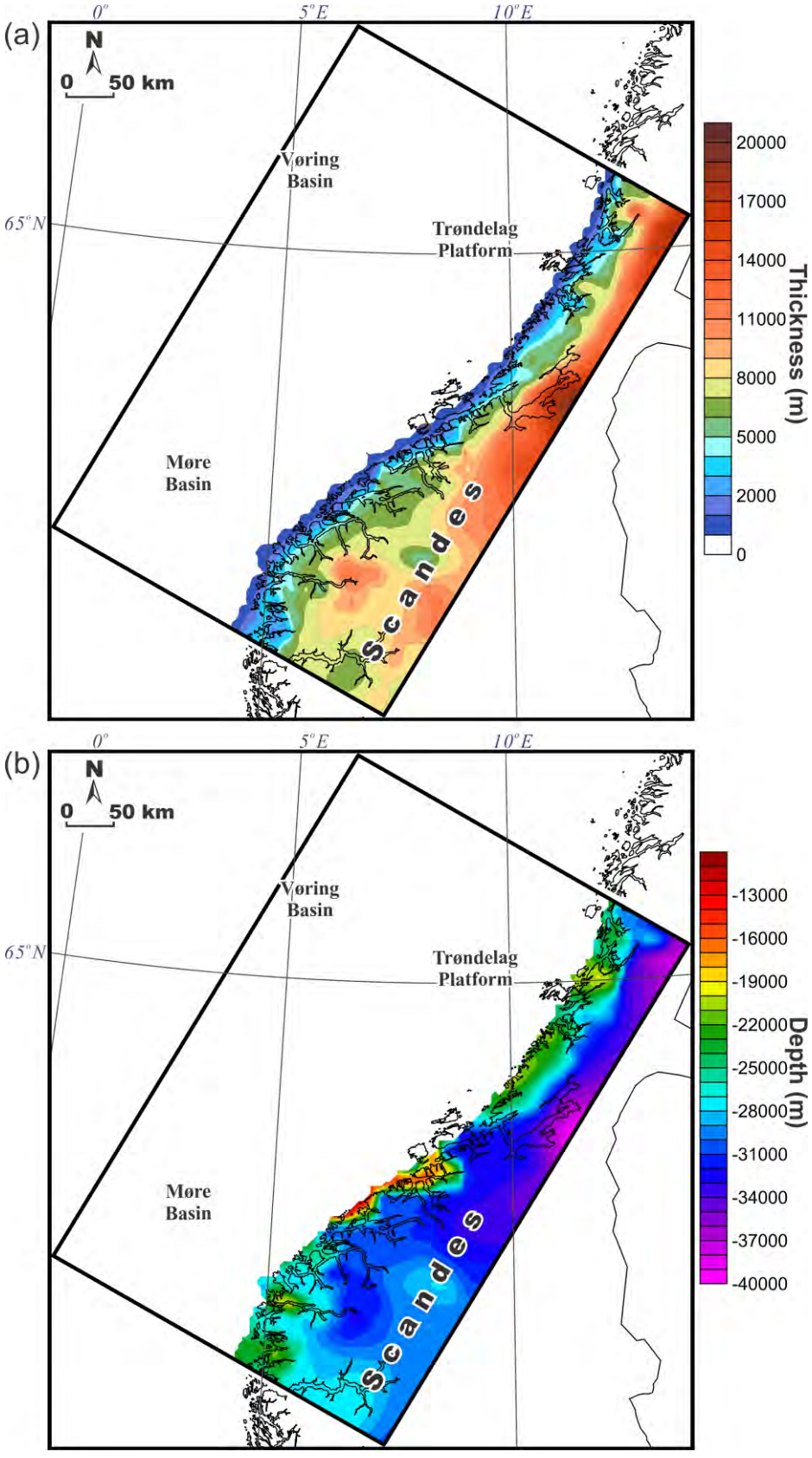

Figure 10.37. Lower crystalline crust: (a) thickness map and (b) structural depth map (base of the layer) of the lower crust (layer 13).

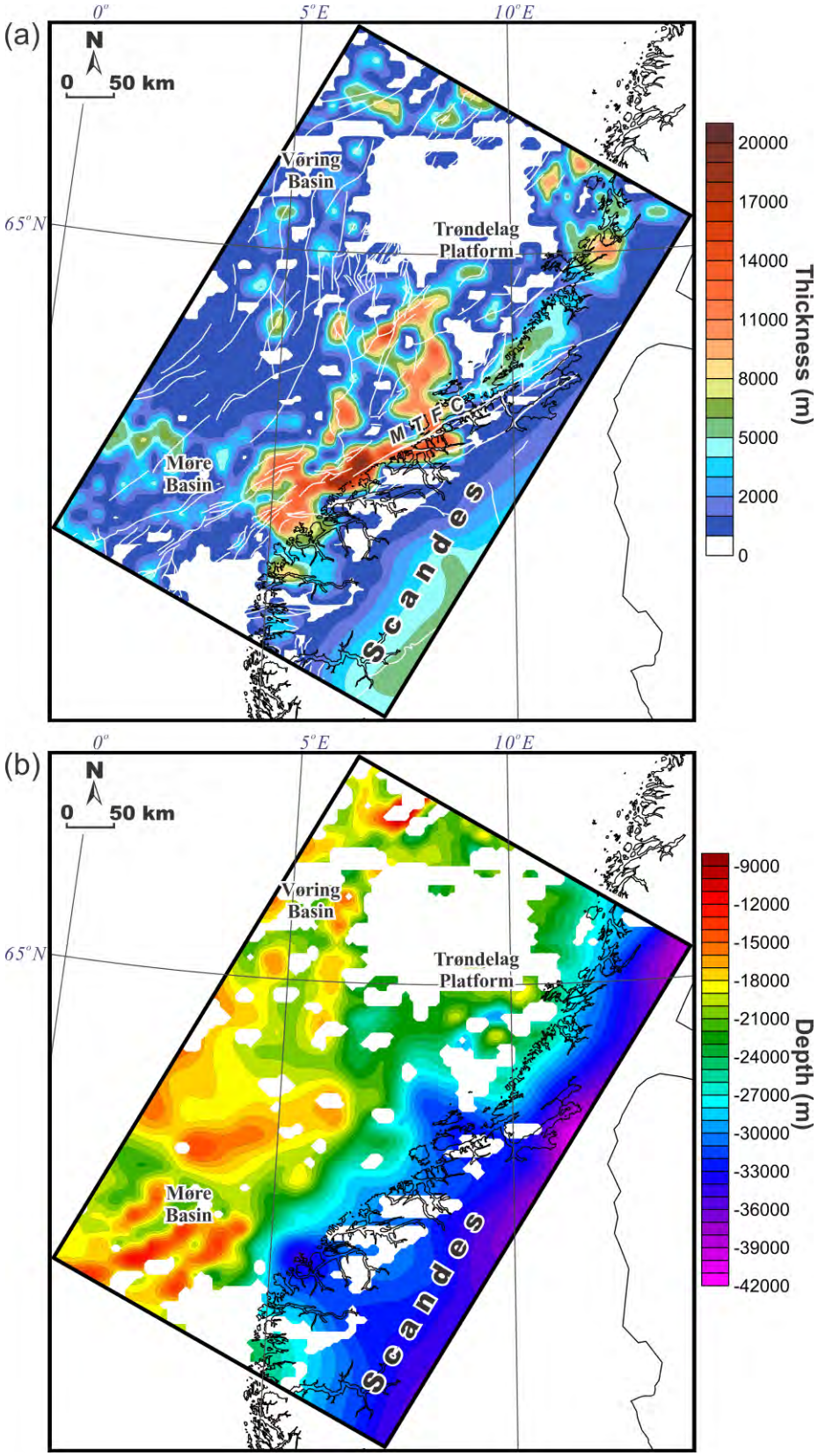

Figure 10.38. Lower crystalline crust: (a) thickness map and (b) structural depth map (base of the layer) of the high-density crust (layer 14). White lines are the major faults (Blystad et al. 1995, Sigmond 2002). MTFC - Møre-Trøndelag Fault Complex.

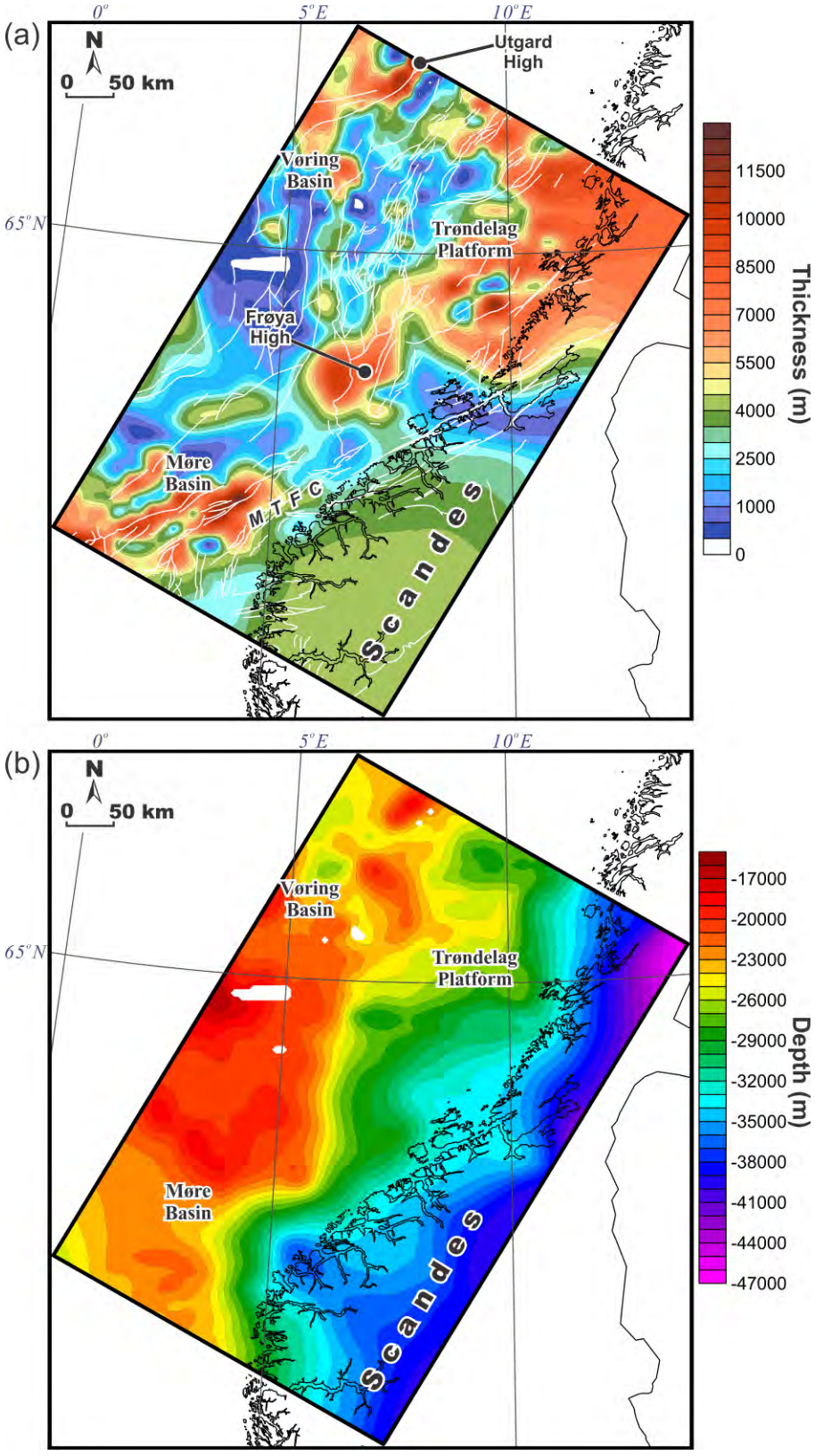

Figure 10.39. Lower crystalline crust: (a) thickness map and (b) structural depth map (base of the layer; Moho) of the high-density lower-crustal layer (layer 15). White lines are the major faults (Blystad et al. 1995, Sigmond 2002). MTFC - Møre-Trøndelag Fault Complex.

The modelled lower crust consists of three layers within the study area. The uppermost lower-crustal layer is the lower crust of Baltica (Figure 10.37; layer 13 in Table 10.2). This layer is only present beneath the Norwegian mainland and its northwestern limit of distribution coinsides almost precisely with the present-day coastline of Mid Norway. This layer is the thickest in the northeastern part of the model where it is more than 18000-19000 m thick (Figure 10.37a), and the depth to the base of the layer is -38000–-39000 m (Figure 10.37b). The next lower-crustal layer is represented by a high-density zone within the crystalline crust of the area under investigation (Figure 10.38; layer 14 in Table 10.2). The high-density crust has been included into the 3D density model in order to fit the observed and calculated gravity where the presence of the more dense high-density/velocity lower-crustal layer is not sufficient. The pronounced characteristic of this layer is the thick NE-SW-elongated zones within the middle of the model almost parallel to the coast of Norway (Figure 10.38a). There, the high-density crust is 13000-18000 m thick on average and spatially coincides with the location of the Møre-Trøndelag Fault Complex of Mid Norway. The Møre-Trøndelag Fault Complex is one of the deepest polyphase fault systems of Mid Norway (e.g., Oftedahl 1975, Gabrielsen & Ramberg 1979, Bukovics et al. 1984, Grønlie & Roberts 1989, Gabrielsen et al. 1999, Nasuti et al. 2012) and is possibly responsible for the position of the Norwegian coastline between northern latitudes 62° and 64° (Nasuti et al. 2012). This ENE-WSW trending fault complex extends from the Norwegian mainland towards the transition zone between the Møre Basin and the northern Viking Graben and can therefore control the structural style of the eastern margin of the Møre Basin. The presence of the high-density crust along a large part of the Møre-Trøndelag Fault Complex indicates that contrasting physical properties within the crystalline crust can represent rheological heterogeneities that could have controlled stress and strain localisation within this large-scale crustal deformation zone during the Mesozoic tectonic events. Furthermore, the thickest high-density crust is localised within the areas where no breakup-related magmatic activity is observed and, therefore, this would imply a pre-breakup age for its origin. In general, these high-density zones can also be related to inherited Caledonian or older structure. The lowest crustal layer is the high-density lower-crustal layer (Figure 10.39; layer 14 in Table 10.2) which corresponds to the high-velocity layer where observed P-wave velocities exceed 6.7-6.8 km/s. The density of this layer varies from 2985 to 3100 kg/m^3. The highest densities have been assigned mainly within the northwestern part of the layer where the lower crust could have undergone magmatic underplating during the breakup. The wide zone of significant thickening (6000-8000 m on average) is located within the northeastern part of the model beneath the Norwegian mainland and the eastern part of the Trøndelag Platform (Figure 10.39a). The E-W trending linear zone with a thinned layer borders the above-mentioned wide thickening from the south. This local thinning is based on the recently obtained seismological data by England & Ebbing (2012) along the SCANLIPS profile. The southeastern part of the model is characterised by an almost constant thickness of this layer which is around 4000 m. The Møre Basin is characterised by the presence of the NE-SW trending narrow areas with the thickened high-density lower-crustal layer which is more than 11000-12000 m thick. These thickened NE-SW-trending areas in the Møre Basin appear to be a southwestern continuation of the thickened high-density crust (layer 14) along the Møre-Trøndelag Fault Complex (cf. Figures 10.38a & 10.39a), implying a southwestward increase in density of the lower-middle-crustal heterogeneities which control the location of the fault complex. The Frøya High is underlain by an up to 8000 m-thickened, high-density, lower-

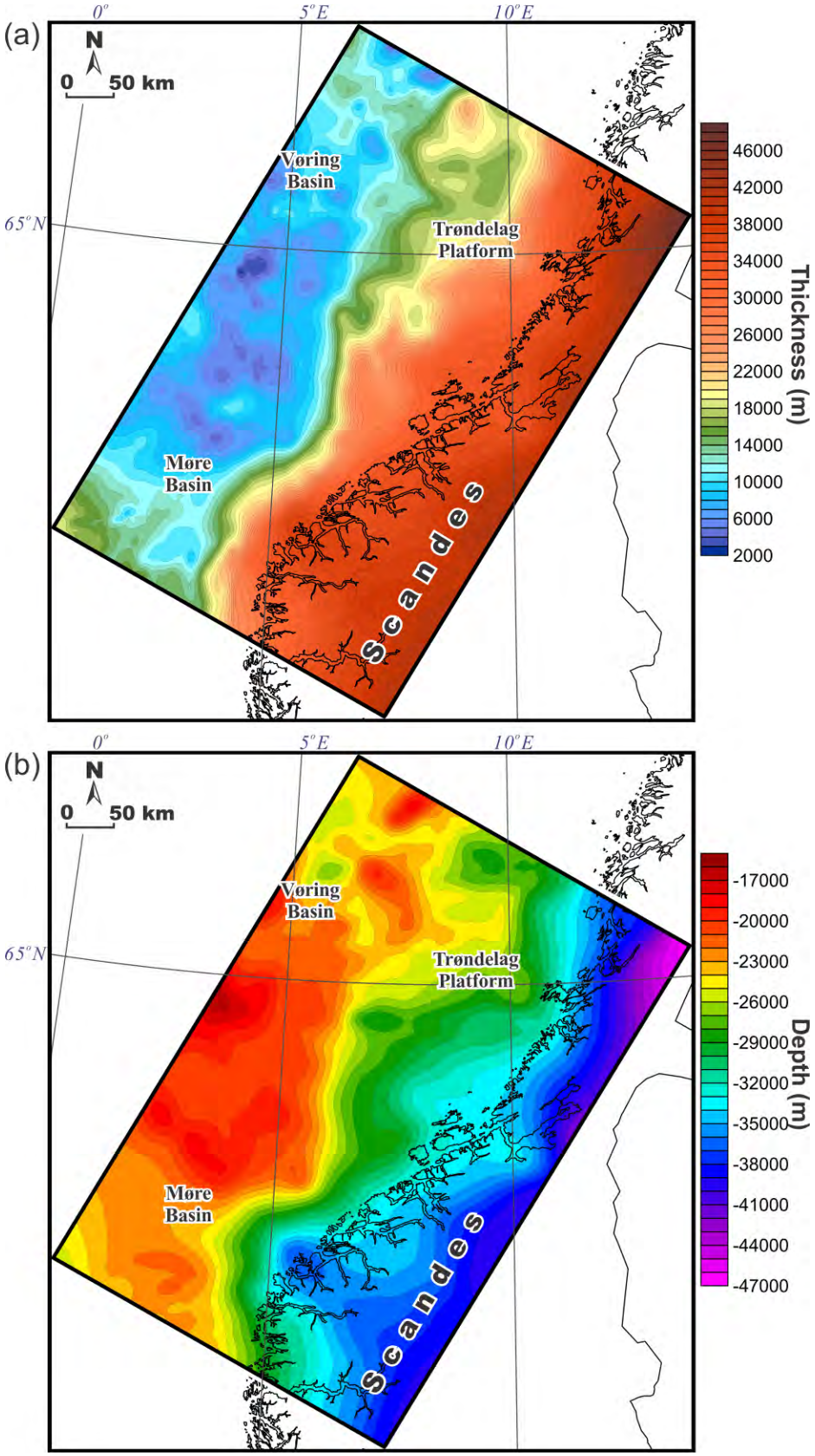

Figure 10.40. (a) thickness of the whole crystalline crust and (b) depth to Moho within the Coop*2 study area.*

crustal layer and is located in between two thickness maxima in the southwest and the northeast (Figure 10.39a). The next prominent basement high is the Utgard High which is characterised by a thickening of the high-density lower-crustal layer to more than 10000-11000 m where the observed gravity field is characterised by the highest values of around 80 mGal in the Vøring Basin (Figures 10.18 & 10.31a). Within the Utgard High, the crystalline crust reaches a very shallow depth and is extensively intruded by magmatic sills with P-wave velocities of more than 7000 m/s according to Berndt et al. (2000). The base of the high-density lower-crustal layer represents the base of the crust, i.e. the Moho discontinuity (Figure 10.39b).

The obtained thickness of the whole crystalline crust is shown in Figure 10.40a, demonstrating a strong thinning within the Møre and Vøring basins where it is from 5000 to 9000 m thick on average. In contrast, the thickness of the crystalline crust reaches more than 40000 m on the mainland. The Trøndelag Platform is characterised by a transition from the thick crust beneath the continent to the thin one beneath the Vøring Basin.

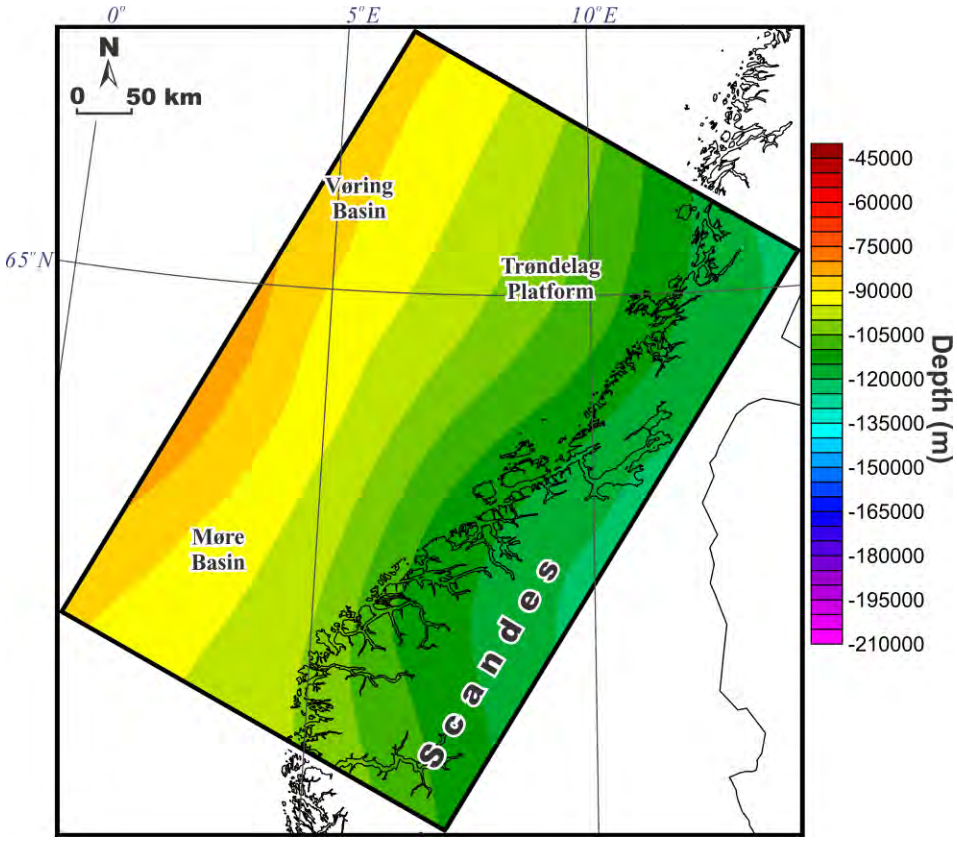

Figure 10.41. Depth to the lithosphere-asthenosphere boundary within the Coop*2 study area.*

The final Moho topography (Figure 10.40b) reflects to a large extent the thickness pattern of the whole crystalline crust (Figure 10.40a): where the crust is thick, the Moho is deeply located and vice versa. Consequently, the Moho is located at more than -40000 m depth beneath the continent and is locally less than -16000–-17000 m deep between the Vøring and Møre basins.

The obtained base of the lithosphere (Figure 10.41) correlates clearly with the tectonic structure of the Coop2 model area. The lithosphere-asthenosphere boundary is located at depths of around -120000 m beneath the mainland and becomes relatively shallow towards the oceanic lithospheric domain beneath the northwestern part of the model where it is only -83000–-85000 km deep.

A cross-sectional view across the major structural units of the Coop2 model area is displayed along five selected 2D vertical slices through the 3D density/structural model. The locations of these vertical slices 1, 2, 3, 4 and 5 (Figure 10.42) have been chosen to demonstrate the structural features of the tectonically and structurally different parts of the model area (Figures 10.43-10.47).

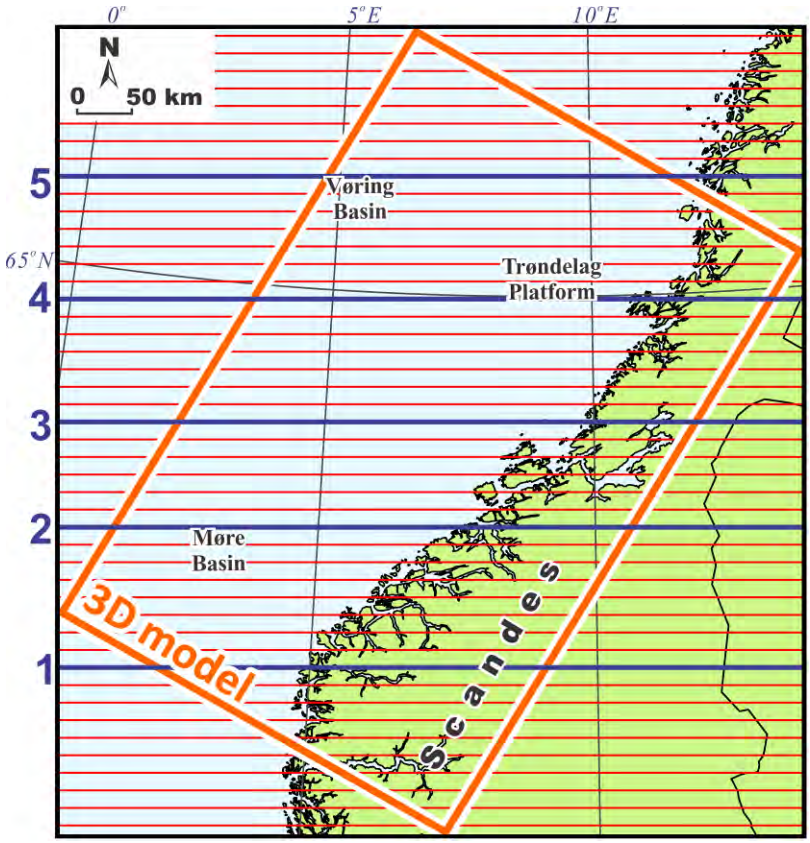

Figure 10.42. Location of the 2D vertical slices (red lines) through the 3D density-structural model. Five selected 2D slices (shown in Figures 10.43-10.47) are highlighted by bold blue lines and numbering.

The first selected vertical slice 1 is located within the southern part of the Coop2 study area (Line 1 in Figure 10.42), crossing the Norwegian mainland and the adjacent transition zone from the eastern part of the Møre Basin towards the northern parts of the Viking Graben and the Horda Platform. Along this line (Figure 10.43), a remarkable thickening of the low-density upper-crustal layer (the yellow body) has been modelled beneath the eastern part of the basin area near the coastline. This line also shows a significant uplift of the Moho which is observed beneath the sedimentary basin. The crystalline crust beneath the continent is mostly characterised by the subhorizontal layering.

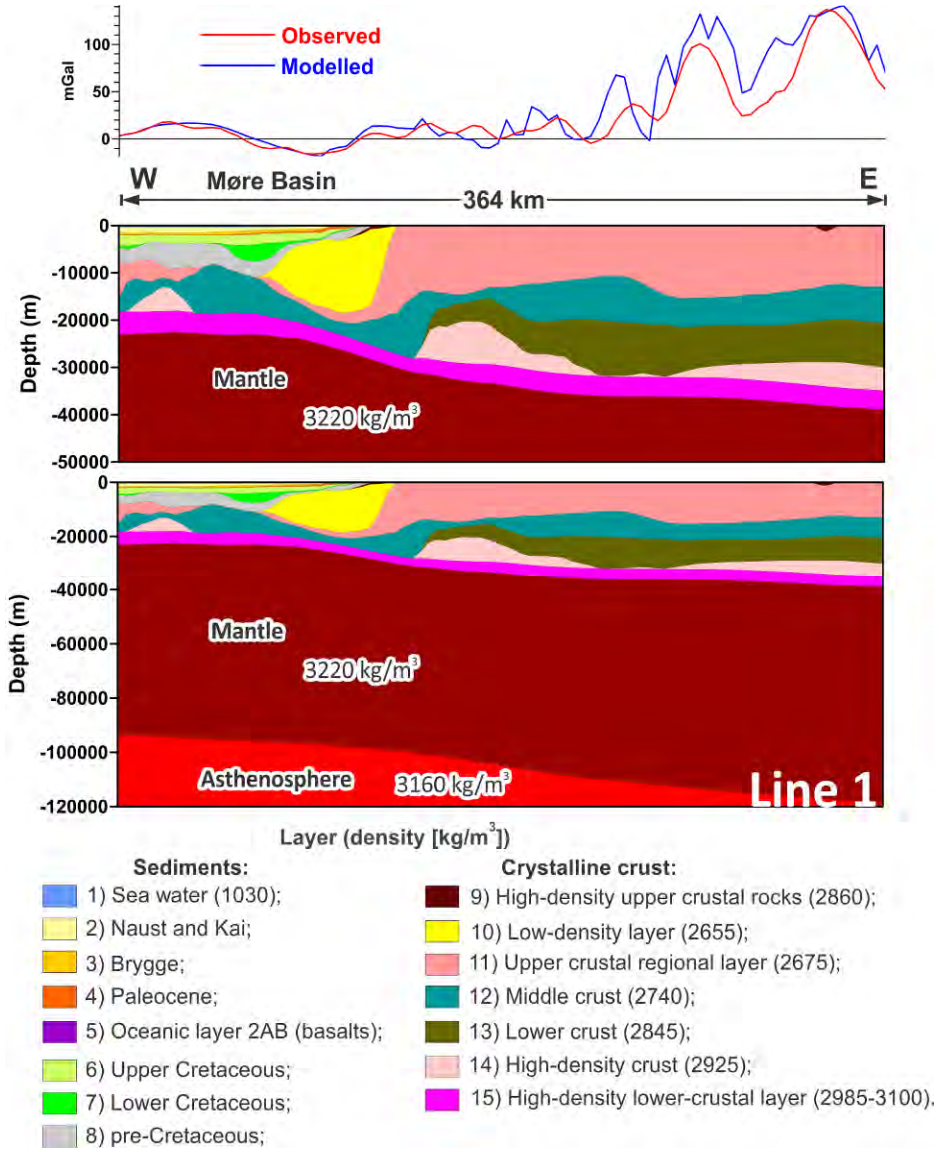

Figure 10.43. Selected vertical slice 1 through the 3D density model of the Coop*2 study area. Layer numbering is the same as in Table 10.2. The location of this slice is shown in Figure 10.42.*

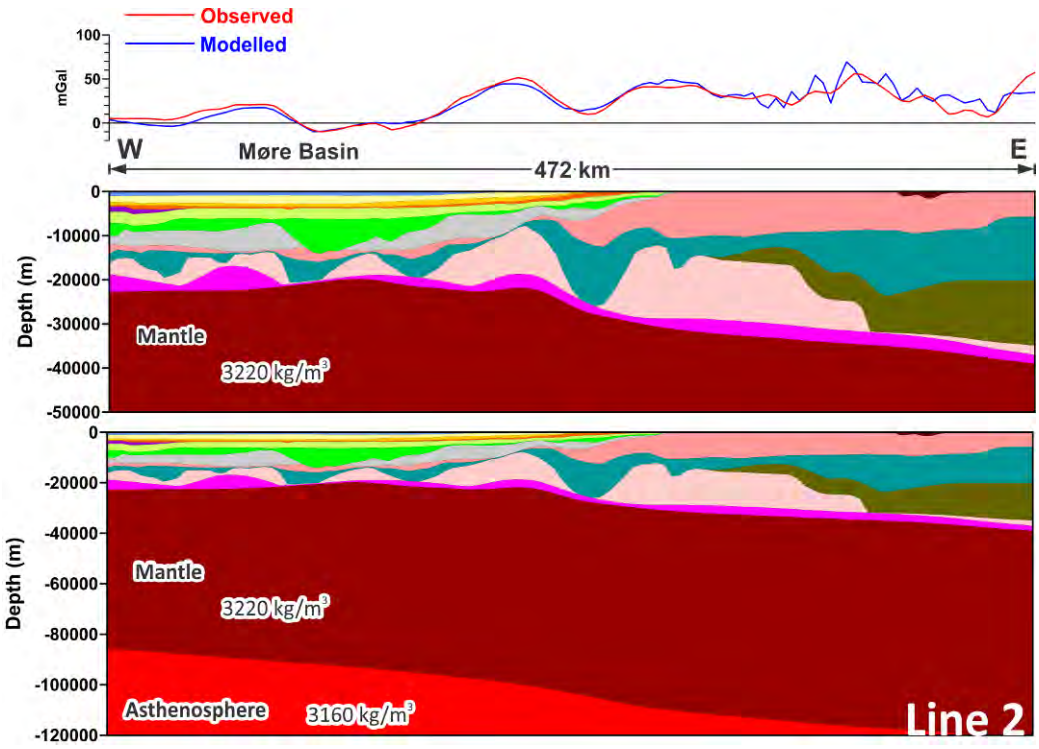

Figure 10.44. Selected vertical slice 2 through the 3D density model of the Coop*2 study area (for the legend, see Figure 10.43). The location of this slice is shown in Figure 10.42.*

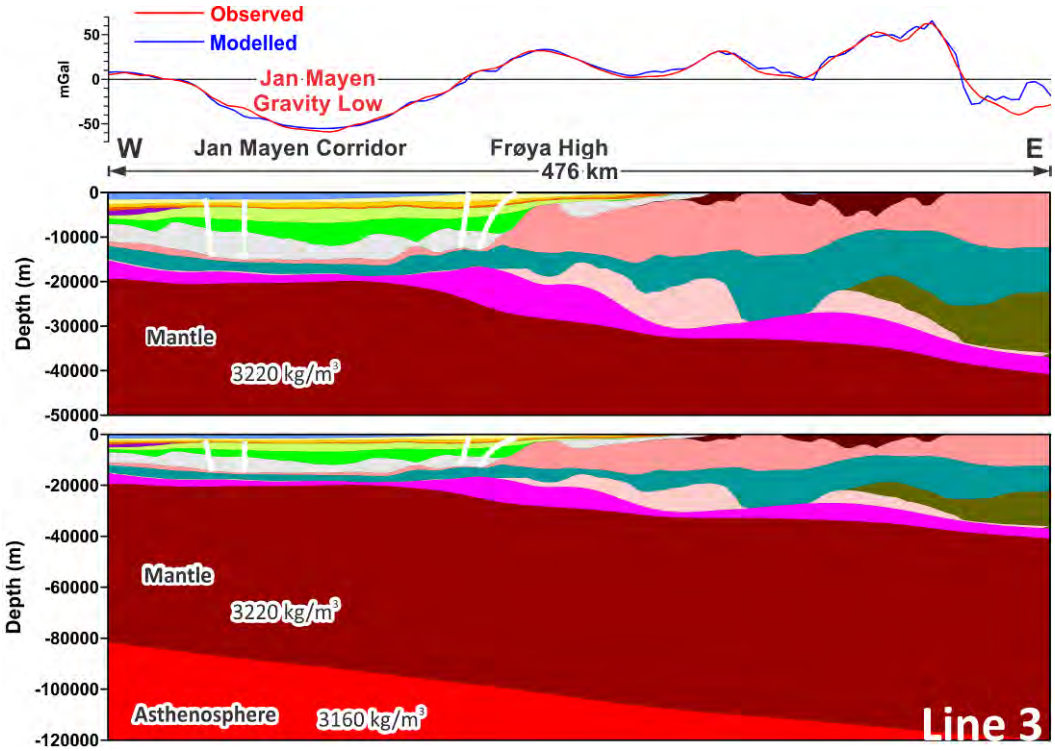

Figure 10.45. Selected vertical slice 3 through the 3D density model of the Coop*2 study area (for the legend, see Figure 10.43). White lines outline the zones of the low-density sediments related to the Jan Mayen gravity low. The location of this slice is shown in Figure 10.42.*

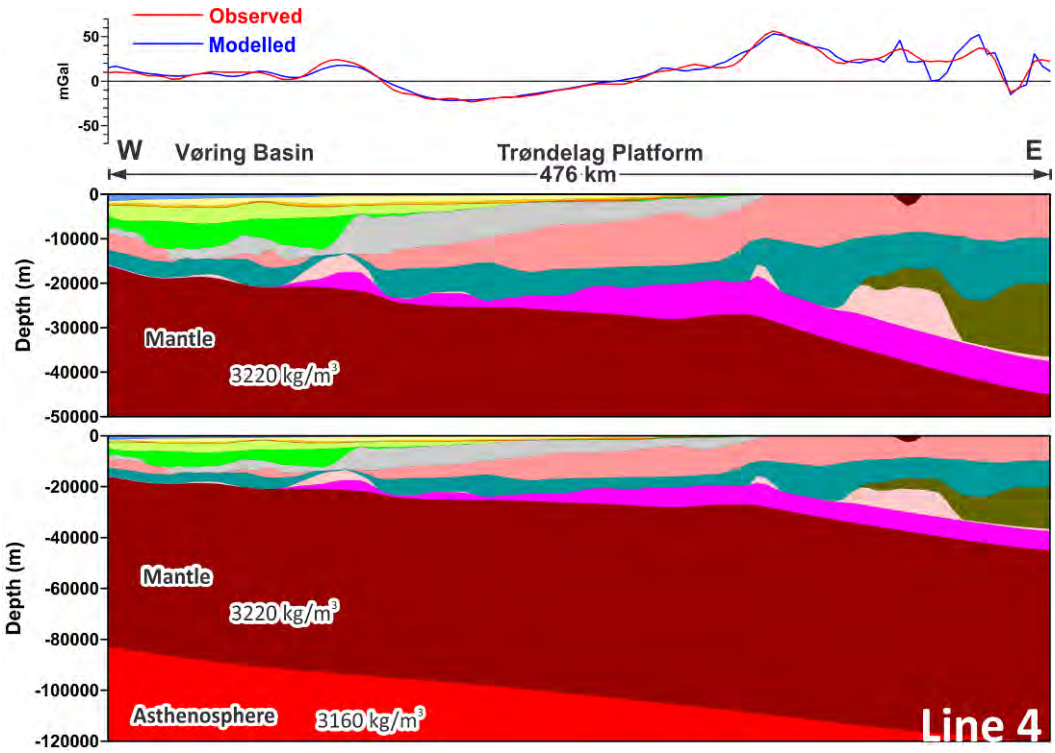

Figure 10.46. Selected vertical slice 4 through the 3D density model of the Coop*2 study area (for the legend, see Figure 10.43). The location of this slice is shown in Figure 10.42.*

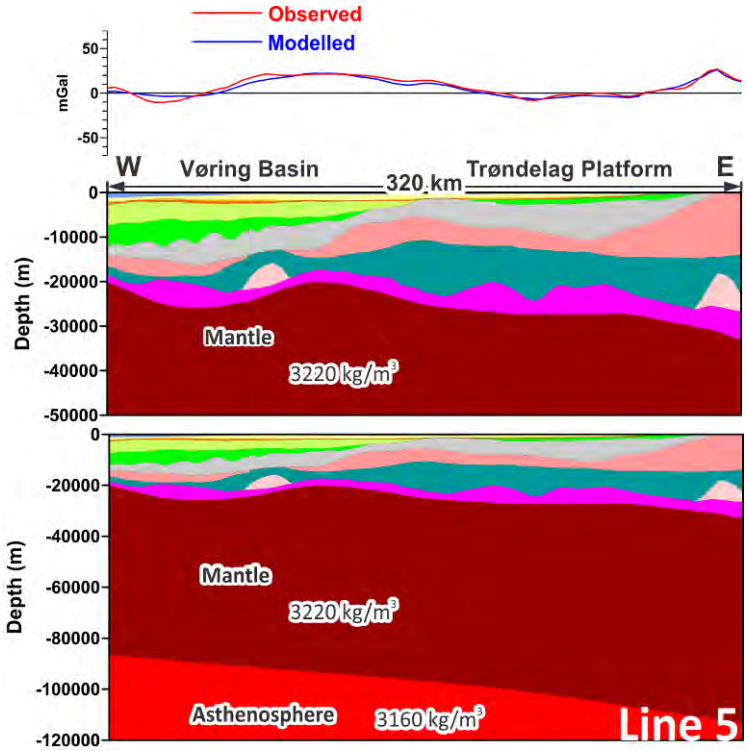

Figure 10.47. Selected vertical slice 5 through the 3D density model of the Coop*2 study area (for the legend, see Figure 10.43). The location of this slice is shown in Figure 10.42.*

Along vertical slice 2 (Line 2 in Figure 10.42), the internal structure of the Møre Basin is shown (Figure 10.44). This basin is characterised by the Moho uplift beneath the strongly

thickened Lower Cretaceous succession. The exceptionally thick high-density crust (layer 14) is clearly visible within the eastern part of the Møre Basin and beneath the adjacent continent where the Møre-Trøndelag Fault Complex is located. There, the presence of the strongly thickened high-density crust is essential in order to fit the observed and modelled gravity fields.

Towards the north, the next slice 3 (Line 3 in Figure 10.42) crosses the pronounced Jan Mayen gravity low over the Jan Mayen Corridor (Figure 10.45). Based on the results of the 3D density modelling, this wide, basin-scale, negative gravity anomaly is partially related to the less dense sediments compared to the neighbouring Møre and Vøring basins. A local decrease in the density of the sediments can be related to a lesser degree of compaction and possible lithological differentiation within the Jan Mayen Corridor which represents a continental continuation of the Jan Mayen Fracture Zone.

Vertical slice 4 (Line 4 in Figure 10.42) is interesting in terms of the internal structure of both the Vøring Basin and the Trøndelag Platform. Along this line (Figure 10.46), the Vøring Basin is characterised by an increased thickness of the Cretaceous (especially the Lower Cretaceous), whereas the Trøndelag Platform has thick pre-Cretaceous sedimentary strata. The important structural feature along this line is associated with an absent or very thin high-density crust (layer 14) and high-density lower-crustal layer (layer 15) beneath a large part of the Vøring Basin.

The northernmost selected vertical slice 5 (Line 5 in Figure 10.42) crosses the northern part of the Vøring Basin, demonstrating an increased thickness of the pre-Cretaceous in that area (Figure 10.47). In addition, there is a local thickening of the crust beneath the Vøring Basin. The northern part of the Trøndelag Platform is characterised by the thick pre-Cretaceous sediments.

The vertical slice 3 across the Jan Mayen gravity low has been chosen to demonstrate the gravity effect of the oceanic lithosphere (Figure 10.48). A uniform density in the upper mantle below the continental and the oceanic lithospheric domains imposes a long-wavelength misfit between the observed and modelled gravity which is more than 100 mGal in the western part of the profile (Figure 10.48b). Therefore, the oceanic mantle has to be less dense than the continental one, a feature that is in agreement with previous 2D density models by Breivik et al. (1999), Ritzmann et al. (2002), Schmidt-Aursch & Jokat (2005) and a 3D density model by Maystrenko & Scheck-Wenderoth (2009) who have shown that the thermal effect of the oceanic lithosphere is significant within the North Atlantic region. In order to consider the thermal effect of the oceanic lithosphere, the base of the lithosphere-asthenosphere boundary (Figure 10.17) has been included into the Coop2 model with a density jump from 3160 to 3220 kg/m^3 at this boundary. In this case, the varying depth to the base of the lithosphere represents different thermal gradients within the crust: where lithosphere is thick, the thermal gradient is low, and where the lithosphere is thin, the thermal gradient is high.

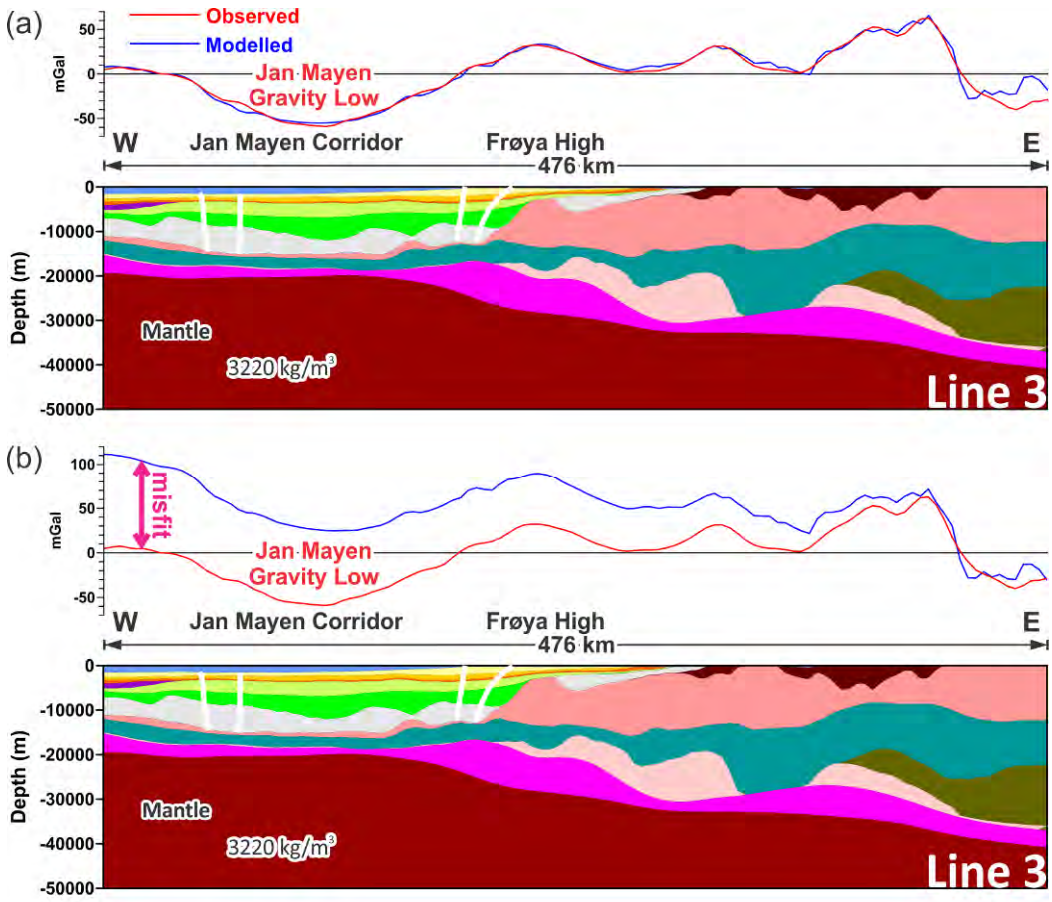

Figure 10.48. Selected vertical slice 3 through the 3D density-structural model of the Coop*2 study area (for the legend, see Figure 10.43). (a) Model with thermal effect of the oceanic lithosphere and (b) model without thermal effect of the oceanic lithosphere considering the homogeneous mantle below the continental and oceanic crust. The location of this slice is shown in Figure 10.42.*

To summarise, the integration of all available structural data in combination with the 3D density modelling provides a first-order configuration of the crystalline crust within the Mid-Norwegian continental margin and adjacent areas of the continent. According to the results of the 3D density modelling, the input structural data have been refined in terms of the lithosphere-scale 3D density/structural model (Figure 10.3). The output 3D model includes sixteen layers:

(1) Sea water (layer 1);
(2) Naust-Kai (base Naust-sea floor) (layer 2);
(3) Brygge (top Paleocene-base Naust) (layer 3);
(4) Paleocene (base Tertiary unconformity-top Paleocene) (layer 4);
(5) Oceanic layer 2AB (basalts) (layer 5);
(6) Upper Cretaceous (near top Cenomanian-base Tertiary unconformity) (layer 6);
(7) Lower Cretaceous (base Cretaceous unconformity-near top Cenomanian) (layer 7);
(8) Pre-Cretaceous (Jurassic, Triassic and older sediments) (layer 8);
(9) upper-crustal high-density crystalline rocks (layer 9);
(10) low-density upper-crustal body (layer 10);
(11) upper-crustal regional layer (layer 11);
(12) middle crust (layer 12);

(13) lower crust (layer 13);
(14) high-density crust (layer 14);
(15) high-density lower-crustal layer (layer 15);
(16) lithospheric upper mantle (layer 16).

This data-constrained, 3D density/structural model (Figure 10.3) has been used during the next step of this integrated study: 3D magnetic modelling.

10.4 3D magnetic modelling

The second step of the 3D analysis was the crustal-scale 3D magnetic modelling which has been performed in order to understand some regional structural features of the crystalline crust in accordance with magnetic properties of rocks, as well as the results of the 3D density modelling within the Mid-Norwegian continental margin and adjacent areas of the Norwegian mainland. During the 3D magnetic modelling, the layers of the 3D density/structural model have been subdivided into additional crustal blocks according to the magnetic properties of the rocks which are required in order to fit the modelled magnetic anomalies with the observed ones.

10.4.1 Observed magnetic field

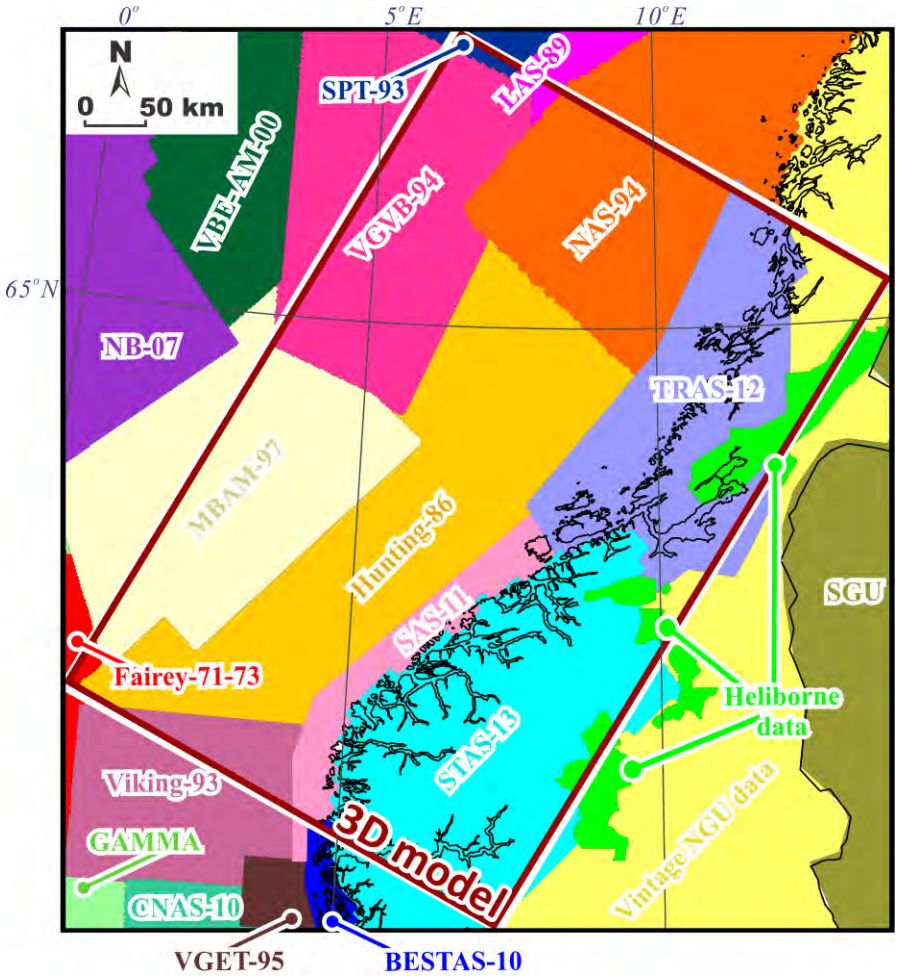

Figure 10.49. Aeromagnetic data, merged from the Coop *Phase 1 and Phase 2 compilations over the Mid Norwegian margin (from Nasuti et al. 2013, 2015; this report). For details see Table 10.3.*

Table 10.3. Aeromagnetic surveys used during the 3D magnetic modelling.

Year	Area	Operator and/or reference	Survey name	Sensor elevation [m]	Line spacing [km]
1955-65	NW North Sea	British Geol. Survey	GAMMA	300	2
1971-73	Shetland Basin	Fairey, Verhoef et al. 1996	Fairrey-71-73	500	5-15
	Sweden	Geological Survey of Sweden	SGU		
1960-73	Norwegian mainland	NGU	Vintage	300 m a. ground	1
1964-76	Norwegian mainland	NGU	NGU data	150 m a. ground	0.4-0.5
1979-2010	Western Norway	NGU heliborne data	Heliborne data		0.2-0.25
1986	Trøndelag Platform	Hunting, Skilbrei & Kihle 1995	Hunting-86	200	2
1989	Lofoten	NGU, Olesen et al. 2002	LAS89	250	2
1993	N. Viking Graben	NGU, 20	Viking-93	150	0.5-2
1993	Hel Graben- Nyk High	World Geoscience, 21	SPT-93	80	0.75
1994	Nordland Ridge- Helgeland Basin	NGU, Olesen et al. 2002	NAS-94	150	2
1994	Vøring Basin	Amarok/TGS, 22	VGVB-94	140	1-3
1995	East Troll, North Sea	TGS,1995	VGET-95		0.2-0.6
1997	Møre Basin	Amarok/TGS, 26	MBAM-97	220	1-2
2000	Vøring Basin	TGS, Olesen et al. 2007b	VBE-AM-00	130	1-4
2007	Norway Basin	NGU, Gernigon et al., 2008	NB-07	230	5
2010	Central North Sea	NGU, Nasuti et al., 2012	CNAS-10	115	1
2010	Bergen-Stavanger Region	FUGRO, 2010	BESTAS-10	120	0.25
2011	Stat region (western coast)	Novatem C11089, 2012	SAS-11	140-1450	0.25
2012-14	Mid Norway	Novatem C12095, 2014	TRAS-12	60	0.25
2013	Western Norway	EON Geosciences Inc	STAS-13	200-700	1

Aeromagnetic data have been mostly compiled by use of the Coop Phase 2 compilation over the Mid-Norwegian continental margin (Nasuti et al. 2015; this report) and the Coop phase-1 compilation over the northern North Sea (Nasuti et al. 2013). In addition, magnetic data from NGU-60-73 and NGU-64-76 have been partially used over the Norwegian mainland (Figure 10.49). Detailed information about each particular survey is given in Table 10.3 and can also be obtained from Nasuti et al. (2013 and 2015). Consequently, the horizontal resolution (line spacing) of the merged surveys varies from 0.2-0.6 km to 2-15 km. The spacing of the merged grid with aeromagnetic anomalies (Figure 10.50) has been set to 4000 m for the 3D magnetic modelling which is sufficient for a regional-scale analysis.

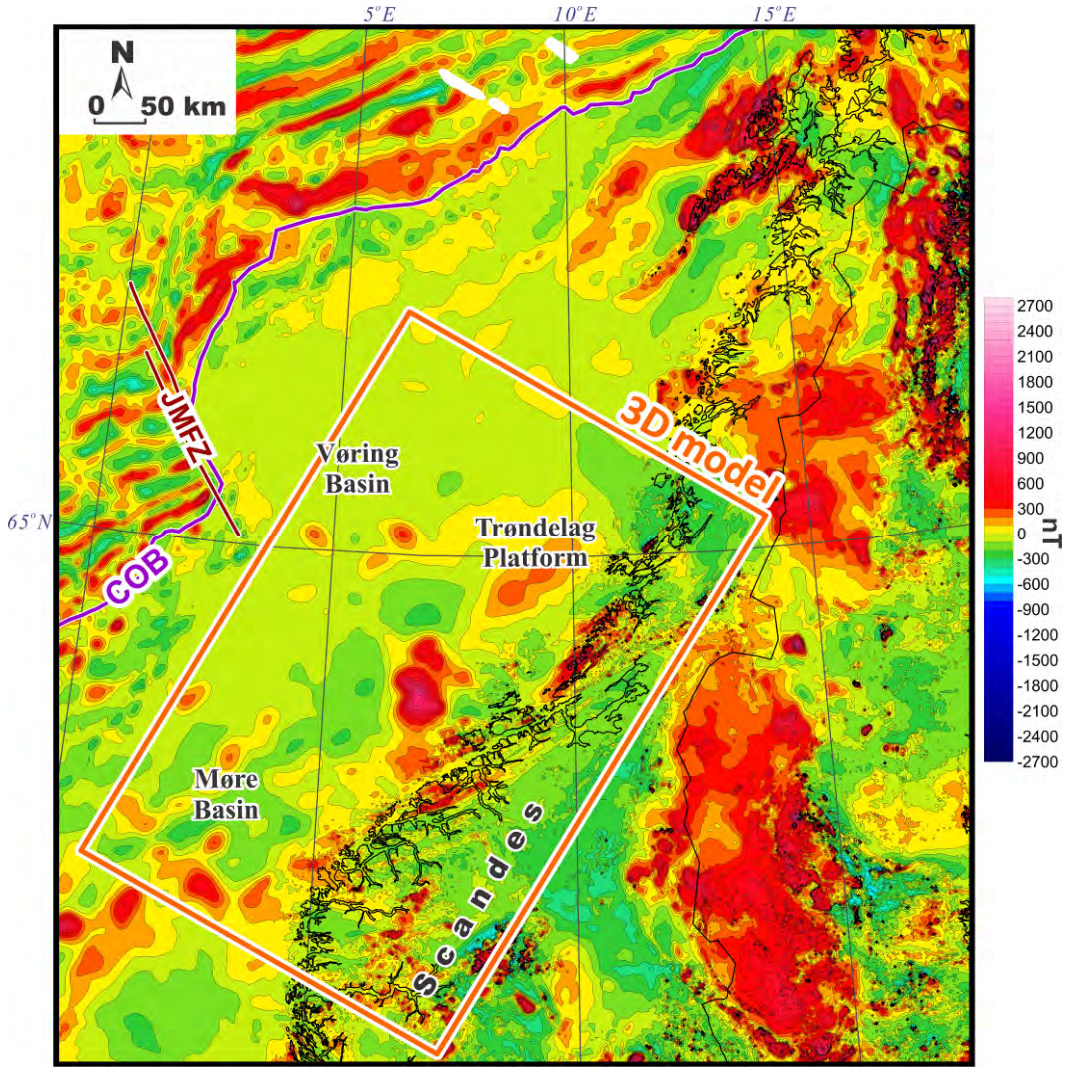

Figure 10.50. Observed magnetic field over the Mid-Norwegian continental margin and adjacent areas of the ocean and the continent (compiled and processed by Nasuti et al. 2015; this report). COB - continent-ocean boundary (from Gernigon 2015; this report), JMFZ - Jan Mayen Fracture Zone (from Blystad et al. 1995).

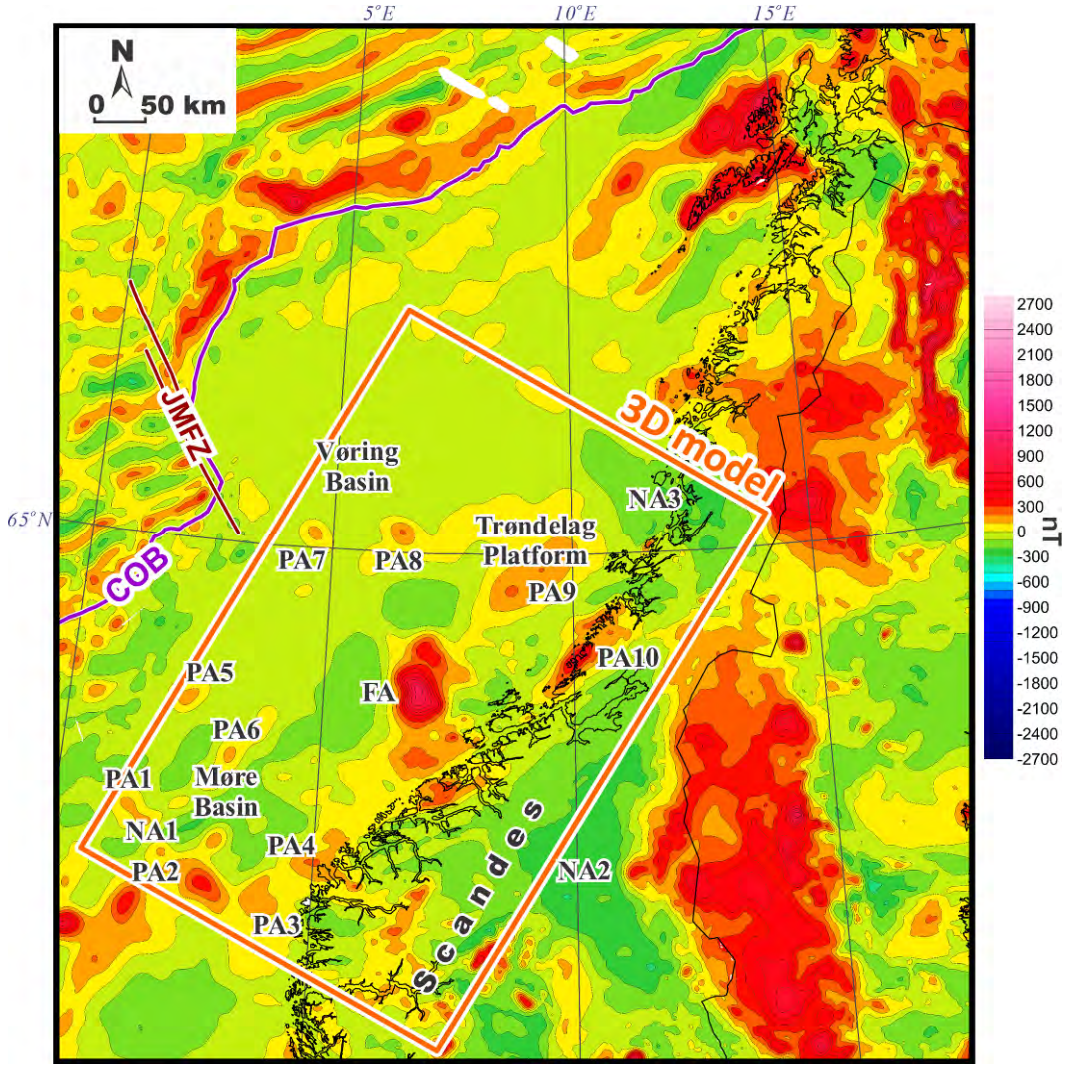

Figure 10.51. Upward-continued observed magnetic field in Figure 10.50 to altitude of 3000 m above sea level (a.s.l.) (compiled and processed by Nasuti et al. 2015; this report). PA - positive anomaly, NA - negative anomaly and FA - magnetic anomaly over the Frøya basement high. COB - continent-ocean boundary (from Gernigon 2015; this report), JMFZ - Jan Mayen Fracture Zone (from Blystad et al. 1995).

The main goal of the present study has been to analyse the regional-scale structure of the crystalline crust rather than small features associated with some local inhomogeneities in the crust of the area under consideration. Moreover, the horizontal resolution of the 3D structural model is 4 km and the distance between vertical slices of the 3D magnetic model is 16 km. Therefore, short-wavelength anomalies cannot be accurately modelled at this scale. In order to decrease the intensity of the short-wavelength component of the observed magnetic anomalies (Figure 10.50), the observed magnetic field has been upward-continued to an altitude of 3000 m a.s.l. (Figure 10.51). The upward continuation of the magnetic field has been done by use of the commercial software package Geosoft Oasis Montaj.

Comparative analysis of the magnetic fields in Figures 10.50 & 10.51 notably shows that the wavelength of the upward-continued magnetic anomalies is characterised by a more smoothed magnetic field that is especially pronounced over the continent and the adjacent Norwegian shelf in the vicinity of the coastline (Figure 10.50). In contrast, the difference between magnetic fields offshore is not so prominent. Accordingly, the upward-continued

magnetic anomalies to an altitude of 3000 m a.s.l. (Figure 10.51) have been used during the 3D magnetic modelling to model the regional-scale structural features of the Mid-Norwegian continental margin and adjacent areas of the mainland.

On a large scale, the observed magnetic field (Figures 10.50 & 10.51) can be subdivided into three distinct areas, such as the oceanic domain, the Mid-Norwegian continental margin and the continent. The magnetic field over the oceanic lithospheric domain has a clearly recognisable linear pattern which is related to the formation of the oceanic crust during the Cenozoic. These linear anomalies are generally parallel to the Mid-Atlantic Ridge (Mohns Ridge) and the extinct Aegir Ridge, representing magnetic spreading anomalies, the intensity of which reflects changes in polarity of the Earth's magnetic field during the seafloor spreading. On the other hand, the Mid-Norwegian continental margin is characterised by the predominance of long-wavelength magnetic anomalies offshore, whereas short-wavelength anomalies are present over the Norwegian mainland (Figure 10.50). This difference in wavelength distribution between offshore and onshore areas is mostly related to the fact that crystalline rocks are exposed on the mainland. In contrast, the low-magnetic sediments are very thick offshore (Figures 10.7-10.11, 10.14) and, for that reason, magnetic crystalline rocks are deeply located beneath the Møre and Vøring basins and the Trøndelag Platform (Figure 10.13). Therefore, the short-wavelength component of the observed magnetic signal is weak offshore due to the presence of the thick sediments. In addition, the crystalline crust is relatively thin beneath the Møre and Vøring basins (Figure 10.40a).

In particular, the observed magnetic field over the Mid-Norwegian continental margin (Figures 10.50 & 10.51) is very smooth over a large part of the Vøring Basin, reflecting the influence of the thickest sedimentary infill within the study area (Figure 10.25a). On the other hand, the magnetic field of the Møre Basin is complicated by several magnetic highs and lows. The presence of the anomalies is especially pronounced over the southwestern part of the Møre Basin where the sedimentary cover is slightly thinner (cf. Figures 10.25a & 10.50). The prominent magnetic feature of the Trøndelag Platform is associated with the long-wavelength magnetic high (PA9 in Figure 10.51) which is located in the centre of the platform. The highest intensity of the magnetic field is observed over the Frøya High where a relatively broad magnetic positive anomaly is present over the strongly uplifted crystalline rocks. The magnetic field over the offshore areas close to the western coast of Norway has a more complex pattern compared to the rest of the basin area, reflecting a shallow position of the crystalline basement and partial absence of sediments. The magnetic field over the continent is characterised by the presence of two long-wavelength magnetic lows (NA2 and NA3 in Figure 10.51) which are separated by a relatively narrow area with positive magnetic anomalies. In addition, several positive magnetic anomalies are visible within the south-eastern part of the model area over the continent.

10.4.2 Magnetic properties

Variations in the assigned values of magnetic susceptibility are shown in Table 10.4. The upper-crustal magnetic susceptibilities are based on the measured magnetic susceptibilities according to the NGU petrophysical electronic database, called "PETBASE" (Olesen et al. 1993). During the 3D magnetic modelling, the average constant values for each crustal block

have been assigned according to the location of the individual sampling points in the major lithology-tectonic units shown on the geological map of Norway (Sigmond 2002, Lauritsen et al. 2015; this report). If information about the required property is absent in the NGU database or the structural layer is deeply located, the published values for similar assumed lithologies have been used. In particular, magnetic susceptibilities of the middle and lower crystalline crust are mostly adopted from the previously published estimations (e.g., Ebbing et al. 2009, Fichler et al. 2011, Ebbing et al. 2012, Nirrengarten et al. 2014 and Gernigon 2015, this report). Sedimentary layers have been assumed to be low-magnetic with the same magnetic susceptibility which is equal to 0.0003 SI. These low values of the magnetic susceptibility are in agreement with the total average value of 0.000288 SI according to results of well-core measurements within the northern North Sea-Norwegian Sea area (Mørk et al. 2002). In contrast, the crystalline crust is characterised by a widely varying magnetic susceptibility from 0.0001 to 0.085 SI (Table 10.4).

The geomagnetic reference field parameters have been chosen to be mean values for the largest magnetic survey (Hunting-86) which is located in the centre of the used compilation for the Coop2 model area (Figure 10.49). This mean value of the geomagnetic reference field has been set constant for the whole model area: total intensity of the magnetic field is 50860 nT, declination is -4^{o} and inclination is 74^{o}. This has been done in agreement with previously performed sensitivity tests by Marello et al. (2013) who have shown that spatially varying parameters of the geomagnetic reference field, calculated separately for each particular magnetic survey, do not strongly affect the modelled magnetic field. Actually, in order to consider spatially variable parameters of the geomagnetic reference field for each survey, the observed magnetic anomalies can be reduced to the pole. On the other hand, the difference between calculated magnetic anomalies using a constant mean value of the reference field and magnetic anomalies reduced to the pole demonstrates that the inaccuracy is about 2 nT according to Marello et al. (2013). Consequently, this value for the inaccuracy is much lower than the uncertainties of the 3D magnetic/structural model and can simply be neglected in this regional-scale investigation. The magnetic susceptibility for the upper mantle layer has been assigned to be 0, supposing that paramagnetic minerals predominate in the upper mantle. Most of paramagnetic minerals are characterised by very low values of the magnetic susceptibility on average (e.g., Clark 1997). A possible dominance of paramagnetic minerals within the deep part of the 3D model is straightforwardly related to the Curie temperature or Curie Point if pressure is also considered. The reason is that 'ferromagnetic' (mostly ferrimagnetic and antiferromagnetic) minerals lose their magnetic properties at temperatures higher than the Curie Point. In this case, a right way would be to define the Curie Point isotherm and set a boundary at depth for this isotherm. The Curie Point isotherm marks changes in the magnetic properties of rocks, implying an occurrence of relatively high magnetic properties above depth to this isotherm due to a presence of 'ferromagnetic' minerals and very low magnetic properties below depth to the isotherm. Unfortunately, the Curie point varies over a wide range for different minerals depending on their chemical composition (e.g., Clark 1997, Pasquale 2011) and, therefore, detailed information on the composition of lower-crustal and upper mantle rocks is required for a reliable determination of the Curie Point isotherm. This kind of information is not available at the moment. Therefore, to solve this problem, an assumption has been

Table 10.4. Magnetic susceptibilities of the layers of the 3D model used during the 3D magnetic modelling (lithology of sediments is from Bell et al. (2014) and from NPD (2014)).

Layer num-ber	Layer of the 3D structural model	Dominant lithology	Dominant magnetic susceptibility χ_m [SI]	Anomalous magnetic susceptibility χ_m [SI]
1	Sea water		0	-
2	Naust and Kai	92% shale, 8% sandstone	0.0003	-
3	Brygge	98% shale, 2% sandstone	0.0003	-
4	Paleocene	80% shale, 20% sandstone	0.0003	-
5	Oceanic layer 2AB	Basalts and tuffs	0.001	-
6	Upper Cretaceous	95% shale, 5% sandstone	0.0003	-
7	Lower Cretaceous	92% shale, 3% sandstone, 5% limestone	0.0003	-
8	Pre-Cretaceous	80% shale, 20% sandstone	0.0003	-
9	Upper-crustal high-density crystalline rocks	gabbro to anorthositic rocks, metamorphic rocks	0.0001-0.03	0.035-0.07
10	Low-density upper-crustal body	metasediments or granite	0.005-0.025	0.03-0.055
11	Upper-crustal regional layer	granite and gneiss	0.0001- 0.025	0.03-0.085
12	Middle crust	granitoids and/or gneiss	0.0002-0.012	0.02-0.07
13	Lower crust	metamorphic rocks	0.0001- 0.006	0.01-0.03
14	High-density crust	mafic granulites, gabbros	0.0001- 0.022	0.025- 0.075
15	High-density lower-crustal layer	gabbros, high-grade metamorphic rocks	0.0001-0.02	0.025- 0.075
16	Lithospheric upper mantle	peridotite	0	-

made that 'ferromagnetic' minerals are still present in the lower crust, whereas they are absent in the upper mantle, assuming that the upper mantle rocks are very low magnetic ones with a value of magnetic susceptibility close to 0 SI and do not have significant remanent magnetisation.

Remanent magnetisation of the upper-crustal rocks has been included into the model by assigning remanent declination, remanent inclination and a Königsberger ratio (Q-value - ratio of remanent to induced magnetisation) to some crustal rocks in order to fit the observed and modelled magnetic anomalies. Measured values of remanent declination and remanent

inclination have been used for the Jotun Nappe Complex according to values published by Piper and Poppleton (1990). Remanent declination and inclination of the Jotun Nappe rocks have been chosen from the relatively wide range in Piper and Poppleton (1990) to be 251° and -1° respectively. The Q-value for the magnetically anomalous Jotun Nappe Complex has been taken to be 2.0. Furthermore, anomalous total magnetisation of some lower-crustal blocks cannot be explained by suitable values of the induced magnetisation alone, implying an influence of remanent magnetisation as well. However, there are no data about remanent declination and inclination for the lower-crustal rocks due to their very deep location. Accordingly, Q-values have been considered only for the remanent magnetisation of the anomalous lower-crustal rocks (Q-values have been taken to be 2.0-3.0). In the case of positive magnetic anomalies, the direction of the remanent magnetisation has been assumed to be similar to the configuration of the present-day magnetic field and, therefore, the declination and inclination of the present-day geomagnetic reference field have been used for these anomalous lower-crustal blocks during the 3D magnetic modelling. On the other hand, some large-scale negative magnetic anomalies (NA1, NA2 and NA3 in Figure 10.51), assumed to be related to remanent magnetisation, require an inverted direction of the remanent magnetisation. Due to an absence of any other reliable data, remanent declination and inclination have been taken to be 293° and -64°, respectively, for these lower-crustal rocks that is in accordance with values from Olesen et al. (2004), assuming similar paleomagnetic conditions for these lower-crustal rocks as in the case of Sveconorwegian magmatic rocks from the Rogaland Igneous Province.

10.4.3 Method

The 3D modelling has been performed by using the IGMAS plus software (the Interactive Gravity and Magnetic Application System; Götze 1978, Götze & Lahmeyer 1988, Schmidt & Götze 1998, Götze & Schmidt 2010). Accordingly, the methodology is almost the same as the one which is described in Subchapter 3.3 for the 3D density modelling. It is important to note that the final outcome of the 3D density/structural model has been used as an initial structural skeleton for the 3D magnetic modelling.

The horizontal resolution of the model and the number of vertical slices have been kept the same as during the 3D density modelling. Therefore, the 3D magnetic modelling was performed by interactive changes of the geometry and magnetic properties along 46 E-W-oriented vertical slices through the 3D density/structural model of the Mid-Norwegian continental margin and adjacent areas of the mainland (Figure 10.52). During the 3D magnetic modelling, almost 350 crustal blocks have been included in the model in addition to the layers of the 3D density model. This has been done in order to obtain a good fit between the observed and modelled magnetic fields. In contrast, the 3D density model has only 16 layers and a relatively large number of blocks (114) due to a differentiation of sediments within the Jan Mayen gravity low.

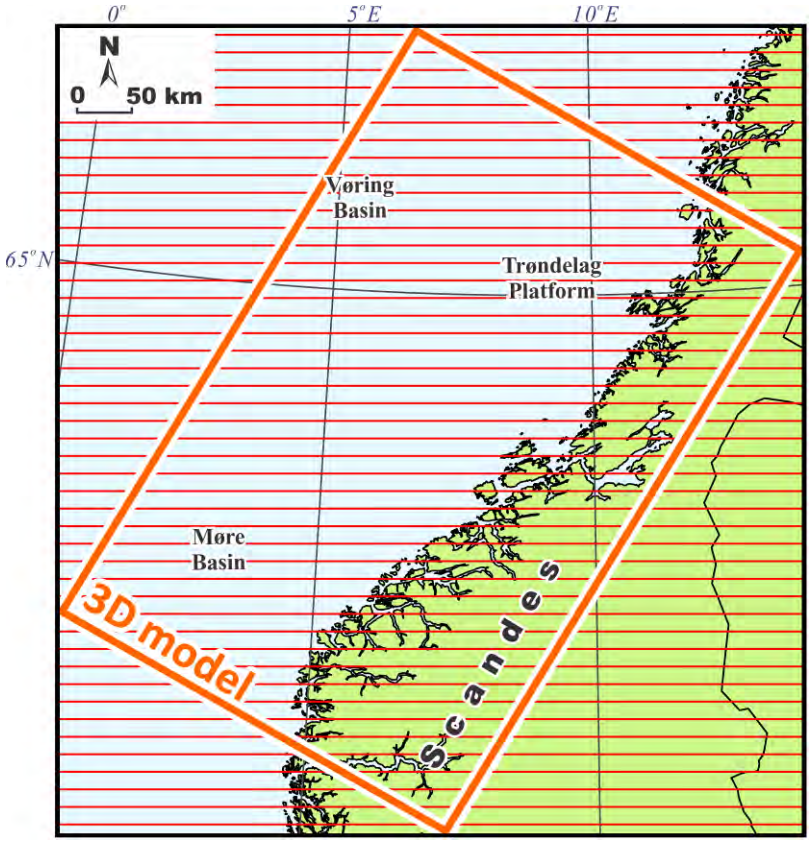

Figure 10.52. Location of the 2D vertical slices (red lines) through the 3D magnetic/structural model.

10.4.4 Results of the 3D magnetic modelling

The results of the 3D magnetic modelling indicate that the modelled induced plus remanent magnetic anomalies (Figure 10.53b) are in fine agreement with the long-wavelength signal of the 3000 m-upward-continued observed magnetic field (Figure 10.53a). The solitary modelled induced magnetic anomalies are also shown in Figure 10.53c, allowing us to see the difference if remanent magnetisation is not considered during the 3D magnetic modelling. The difference between the modelled induced and remanent magnetic anomalies and the solitary modelled induced ones is mostly related to the intensity of several positive magnetic anomalies (PA1, PA2 and PA5-PA8) and two negative anomalies (NA1 and NA3). In addition, the negative magnetic anomaly NA2 over a large part of the continent is almost completely caused by a remanent magnetisation in the case of the present 3D magnetic anomaly (cf. Figures 10.53b & 10.53c).

It should be mentioned that some short-wavelength restricted misfits are locally characterised by a relatively high amplitude. On the other hand, these misfits do not have a significant impact on the regional-scale component of the magnetic field, which has been reproduced almost completely during the 3D magnetic modelling. Furthermore, some of these high-amplitude misfits are associated with the presence of remanent magnetisation which can vary at short distances and, therefore, cannot be properly considered in this

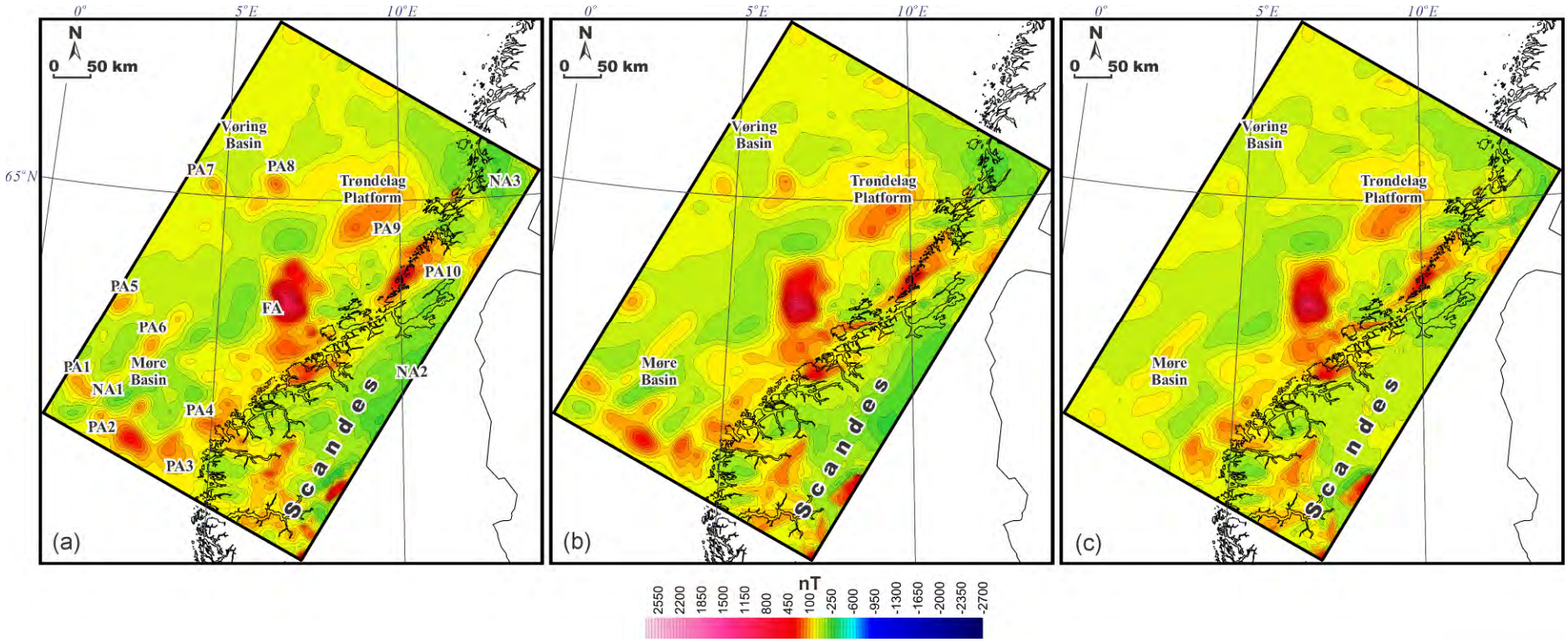

Figure 10.53. (a) Upward-continued observed magnetic field to an altitude of 3000 m a.s.l. (compiled and processed by Nasuti et al. 2015; this report), (b) modelled induced and remanent magnetic anomalies and (c) modelled induced magnetic anomalies. PA - positive anomaly, NA - negative anomaly and FA - Frøya magnetic anomaly over the Frøya basement high.

regional study. For example, according to Piper and Poppleton (1990) the paleomagnetic declination and inclination vary from 3° and -52° to 359° and 81°, respectively. This is also true for the Q-value which can vary within a wide range from close to 0 to high values like 77 or 148 within the Rogaland Igneous Province (Olesen et al. 2004, Brown & McEnroe 2004). Thus, a significant variability of the paleomagnetic field parameters may locally disturb the modelled detailed configuration of the total observed magnetic field.

During the 3D magnetic modelling, some layers, validated by the 3D density modelling, have been subdivided into several blocks with different magnetic properties in order to fit the observed and modelled magnetic fields. Therefore, reproducing the observed magnetic field has been done mainly by changes in magnetic susceptibilities which were kept in the range of measured values according to the NGU petrophysical electronic database "PETBASE" (Olesen et al. 1993). Some anomalous zones have been modelled to be cross-cutting through several layers in order to obtain a good fit between the observed and modelled magnetic fields. The results of the 3D magnetic modelling have also been used to improve the 3D density model where necessary. Consequently, the final, density-derived, crustal layers, based on results of the 3D density/magnetic modelling, are shown in map view, highlighting magnetically anomalous parts by additional maps (Figures 10.54-10.60). The results are also displayed in cross-sectional view by colour-scaled magnetic susceptibilities (Figures 10.62-10.67).

According to the 3D magnetic modelling, five anomalous blocks of upper-crustal high-density rocks (layer 9) with increased magnetic susceptibilities have been included into the 3D magnetic model (Figure 10.54b). The southeastern block has been defined within the northeastern part of the Jotun Nappe Complex (Figure 10.54b) and can be represented by metaplutonic rocks. This magnetically anomalous crustal block is characterised by the presence of remanent magnetisation with the assigned declination of 251° and inclination of -1° according to values in Piper and Poppleton (1990), and a chosen Q-value of 2.0. Towards the north from the Jotun Nappe, seven zones with increased magnetic susceptibility have been modelled, the largest of which coincides spatially with the large positive gravity anomaly (cf. Figures 10.31a & 10.54b). In that place, the high-grade metamorphic rock complexes of the ancient middle or lower crust are exposed at the present-day surface, causing both gravity and magnetic positive anomalies (Möller 1988, Skilbrei et al. 1991).

The low-density upper-crustal layer (layer 10; Figure 10.55) is characterised by the presence of one zone with increased magnetic susceptibility in the place where a positive magnetic anomaly PA3 is located (cf. Figures 10.53a & 10.55b). Actually, the greater part of the low-density upper-crustal layer of the Coop2 3D model (Figure 10.55) was, in the case of the Coop1 3D model, magnetically anomalous, with a magnetic susceptibility of 0.022 SI in comparison with less magnetic parts of this layer with magnetic susceptibility of around 0.006

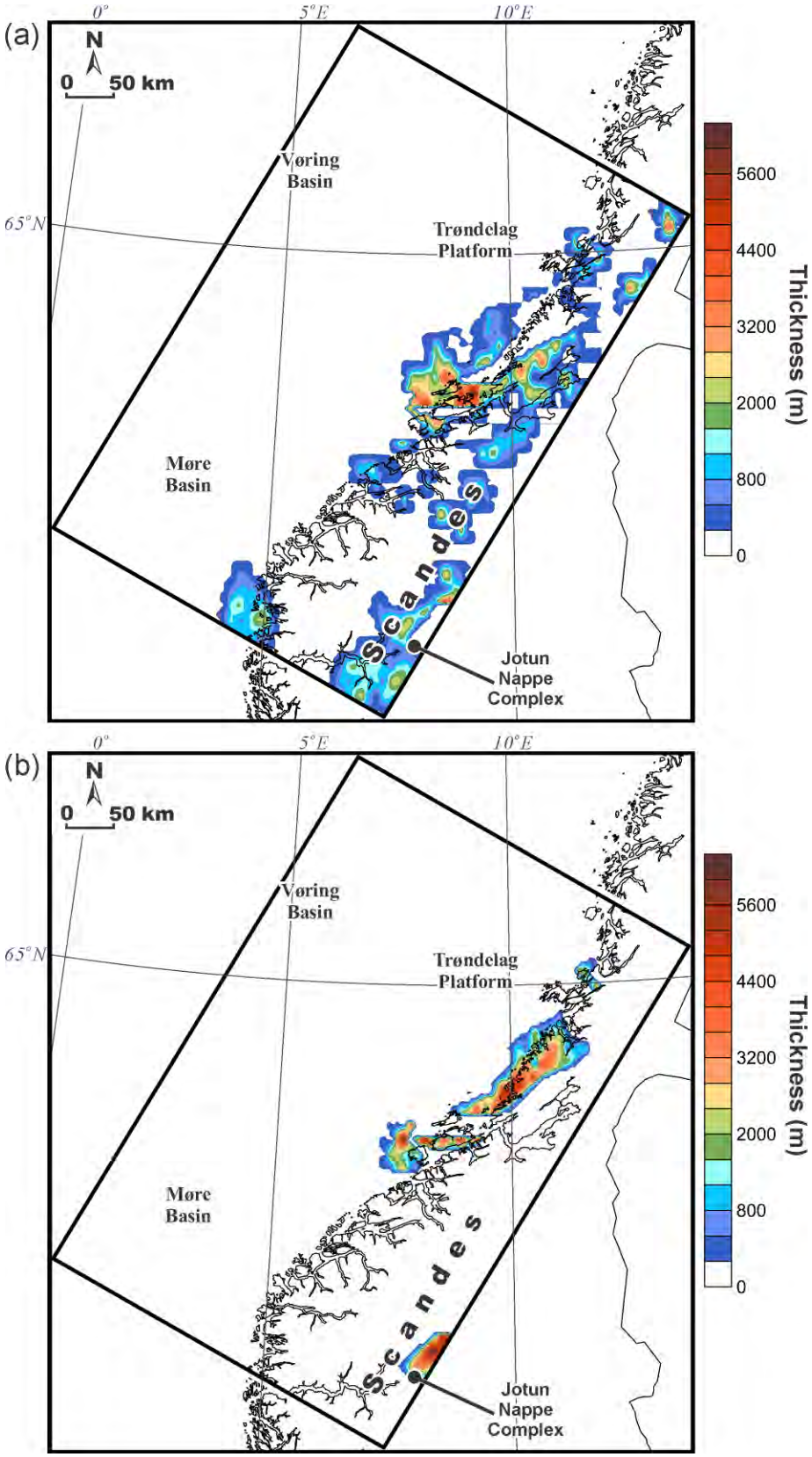

Figure 10.54. Thickness of the upper-crustal high-density crystalline rocks (layer 9): (a) main body of the layer without blocks with increased magnetic susceptibility and (b) blocks with increased magnetic susceptibility.

.

SI (Maystrenko 2014). On the other hand, the Coop2 low-density upper-crustal layer in Figure 10.55a has a magnetic susceptibility of around 0.025 SI with the highest one at 0.055 SI. Therefore, this variable magnetic susceptibility can indicate that the lithological composition of the magnetically anomalous layer in Figure 10.55b may even differ more significantly from the rest of the layer beneath the central part of the Horda Platform in the Coop1 3D model (Maystrenko 2014).

The regional upper-crustal layer (layer 11) has one of the strongest impacts on the magnetic field within the Coop2 model area (Figure 10.56). This layer is characterised by the presence of several magnetically anomalous crustal blocks offshore and within the mainland (Figure 10.56b). The largest crustal block with the increased magnetic susceptibility is located beneath the Trøndelag Platform where a large-scale magnetic high is located as a background for the positive anomaly PA9 (cf. Figures 10.52a & 10.56b). The next prominent magnetically anomalous zone has been modelled beneath the chain of positive magnetic anomalies which reach their culmination within a magnetic anomaly over the Frøya basement high. The magnetic susceptibility of the upper-crustal blocks has been set to be up to 0.085 SI beneath the most intensive magnetic anomaly related to the Frøya High. Several blocks with increased magnetic susceptibility have been modelled to reproduce magnetic highs PA4, PA10 and other positive anomalies over the Norwegian mainland. In this case, the origin of the positive magnetic anomaly PA10 is not only related to the crustal high-density crystalline rocks (layer 9) but it is also partially cased by the regional upper-crustal layer (layer 11) (cf. Figures 10.52a, 10.54b & 10.56b). One relatively small anomalous zone is located within the north-western corner of the model area, being associated with a low-intensive magnetic high in the same place. There is a clear correlation between the thickness of the regional upper-crustal layer (Figure 10.35a), the total thickness of sedimentary rocks (Figure 10.25a) and the location of the upper-crustal blocks with anomalous magnetic susceptibility (Figure 10.56b). Almost all blocks of the anomalous regional upper-crustal layer are located within the areas where the regional upper-crustal layer is relatively thick (cf. Figures 10.35a & 10.56b). On the other hand, areas with the thickest sedimentary cover are characterised by the absence of the anomalous regional upper-crustal layer (cf. Figures 10.25a & 10.56b). This fact can be explained, on the one hand, by the presence of the thick low-magnetic sediments within the Vøring and Møre basins that can partially hide the magnetic signal from the great depths. On the other hand, the thickness of the regional upper-crustal layer is only around 2000-3000 m beneath the Cretaceous depocentres of the Vøring and Møre basins and, therefore, it is possibly not sufficient to produce a significant magnetic anomaly if there are no crustal blocks with the extremely high magnetic susceptibilities in those areas. The upper-crustal blocks with increased magnetic susceptibility beneath the Trøndelag Platform and the Frøya basement high may indicate the presence of the Precambrian granitic and/or granodioritic rocks (Gernigon, 2015; this report) which are mapped at the surface on the mainland (Sigmond 2002) and are also magnetically anomalous (Maystrenko 2014).

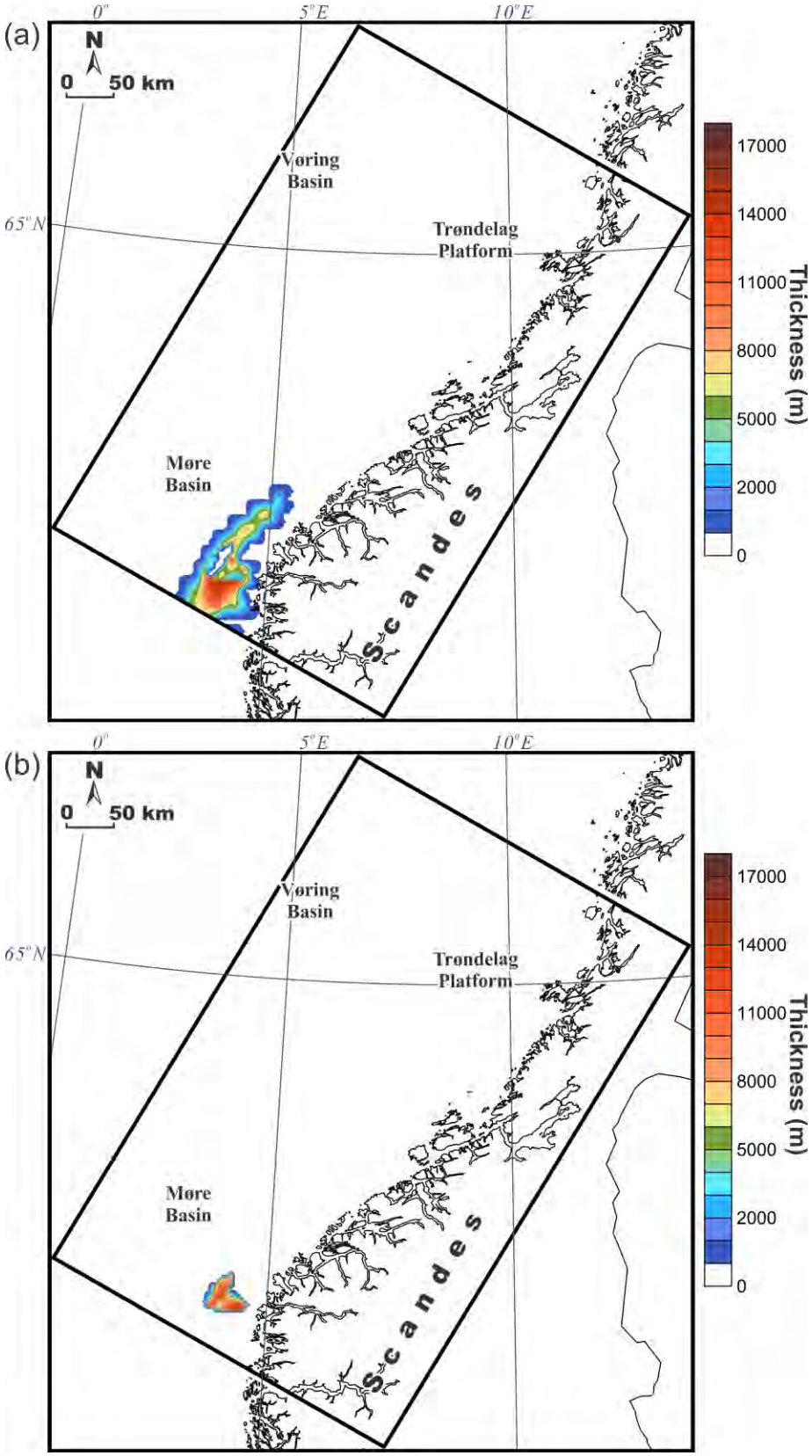

Figure 10.55. Thickness of the low-density upper-crustal body (layer 10): (a) main body of the layer without blocks with increased magnetic susceptibility and (b) blocks with increased magnetic susceptibility.

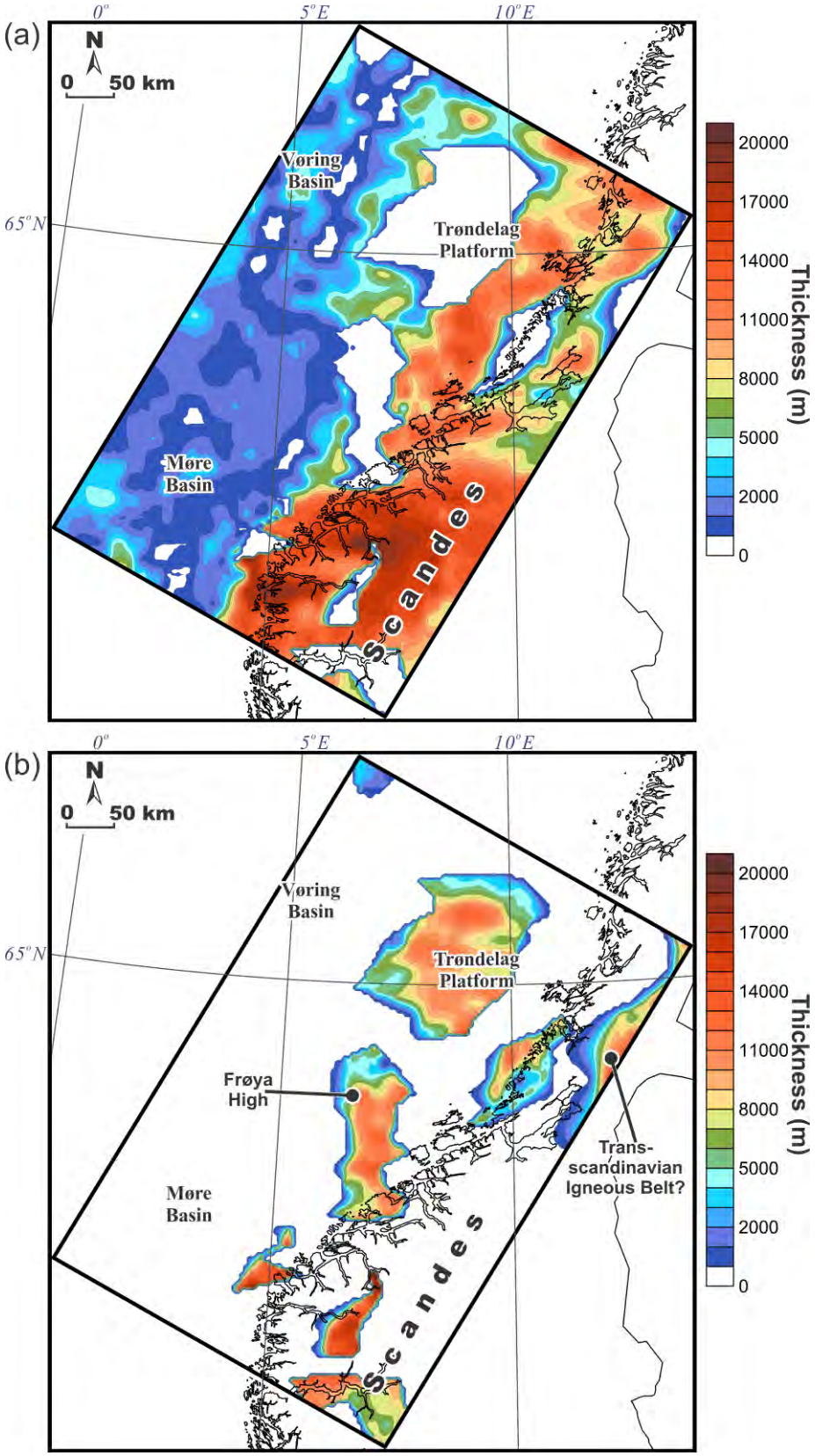

Figure 10.56. Thickness of the regional upper-crustal layer (layer 11): (a) main body of the layer without blocks with increased magnetic susceptibility and (b) blocks with increased magnetic susceptibility.

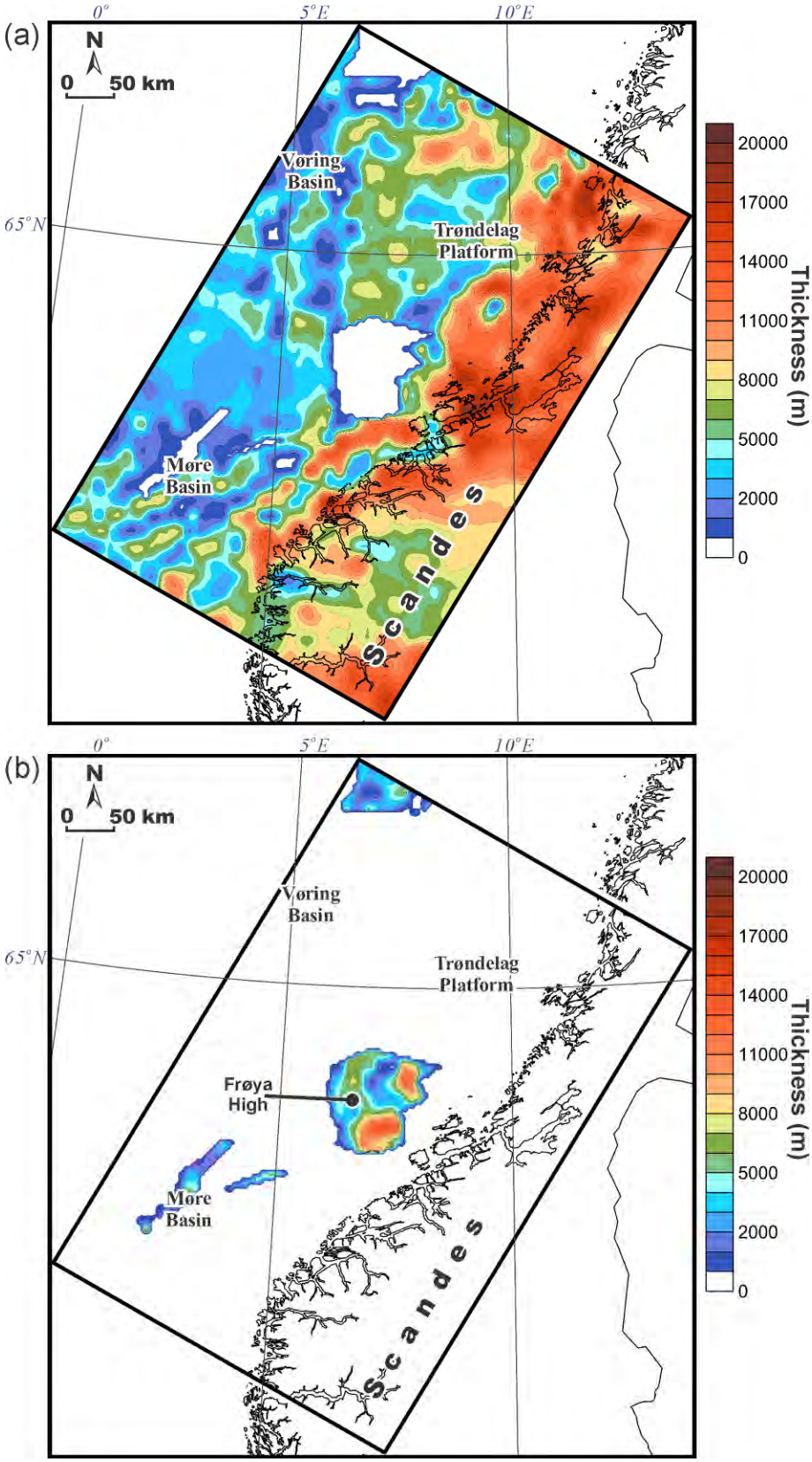

Figure 10.57. Thickness of the middle crystalline crust (layer 12): (a) main body of the layer without blocks with increased magnetic susceptibility and (b) blocks with increased magnetic susceptibility.

The results of the 3D magnetic modelling for the middle crystalline crust (layer 12) are shown in Figure 10.57. It is clearly visible that the anomalous middle crust is also involved in the origin of the magnetic anomaly over the Frøya High and the neighbouring positive magnetic anomalies within that area (cf. Figures 10.52a & 10.57b). Two blocks of the middle crust with the increased magnetic susceptibility are associated with the positive anomaly PA6 (cf. Figures 10.52a & 10.57b) and a low-intensive magnetic high within the northwestern corner of the study area where the magnetically anomalous upper crust is also present (cf. Figures 10.56b & 10.57b).

The lower crystalline crust (layer 13; Figure 10.58) is characterised by the presence of only two magnetically anomalous zones which are associated with negative magnetic anomalies NA2 and NA3 (cf. Figures 10.52a & 10.58b), in contrast to the above-described anomalous crustal blocks which are related to the positive magnetic anomalies. During the 3D magnetic modelling, it has been realised that the two magnetic lows NA2 and NA3 cannot be modelled without including the remanant magnetisation into the crystalline crust. The problem is that the intensity of the surrounding positive anomalies is not high enough to produce the associated magnetic lows which would fit the observed magnetic field (Figures 10.50-10.52). In general, this works perfectly in the vicinity of the high-amplitude positive magnetic anomaly over the Frøya High where two wide magnetic lows can be easily modelled in connection with the Frøya magnetic high. However, this is not the case for the magnetic lows NA2 and NA3 (cf. Figures 10.52b & 10.52c). The question was where to place the remanent magnetisation in order to explain the origin of the NA2 and NA3 lows. From a theoretical point of view, the remanent magnetisation is not typical for granites, gneisses or granodiorites but is more frequently associated with different kinds of mafic rocks. On the other hand, the problematic magnetic lows NA2 and NA3 do not coincide with the positive gravity anomalies (cf. Figures 10.18 & 10.50-10.52) as one would expect in the presence of reasonably thick magmatic rocks of mafic composition within the upper or middle crust of the study area. Therefore, these magnetic lows over the continent may be related to the lower-crustal gabbroic body which is not reflected in the observed gravity due to its similar density to lower-crustal rocks (eclogites or granulites). Consequently, the source for the remanent magnetisation has been assumed to be related to the lower crust where the density of the crystalline rocks is already relatively high and, therefore, the presence of the magmatic rocks would not create a significant density contrast to the associated positive gravity anomaly in the observed gravity. According to 3D magnetic modelling, the required anomalous lower-crustal bodies have a relatively high remanent magnetisation (Q-factor is 3.0). The origin of these negative magnetic anomalies is mostly related to a difference in direction and intensity between the present-day Earth's magnetic field and the paleomagnetic one. Therefore, the paleomagnetic declination and inclination have been set to be 293^{o} and -64^{o}, respectively, as was done for the Rogaland Igneous Province in the Coop1 3D model (Maystrenko 2014), thus reflecting a paleo-position and time of formation similar to the Rogaland Igneous Province. The main point is that the paleomagnetic field has to be reversed in relation to the present-day one and, therefore, the paleodeclination and paleoinclination for the Rogaland Igneous Province given by Olesen et al. (2004) are not necessarily correct but are very reasonable values. The

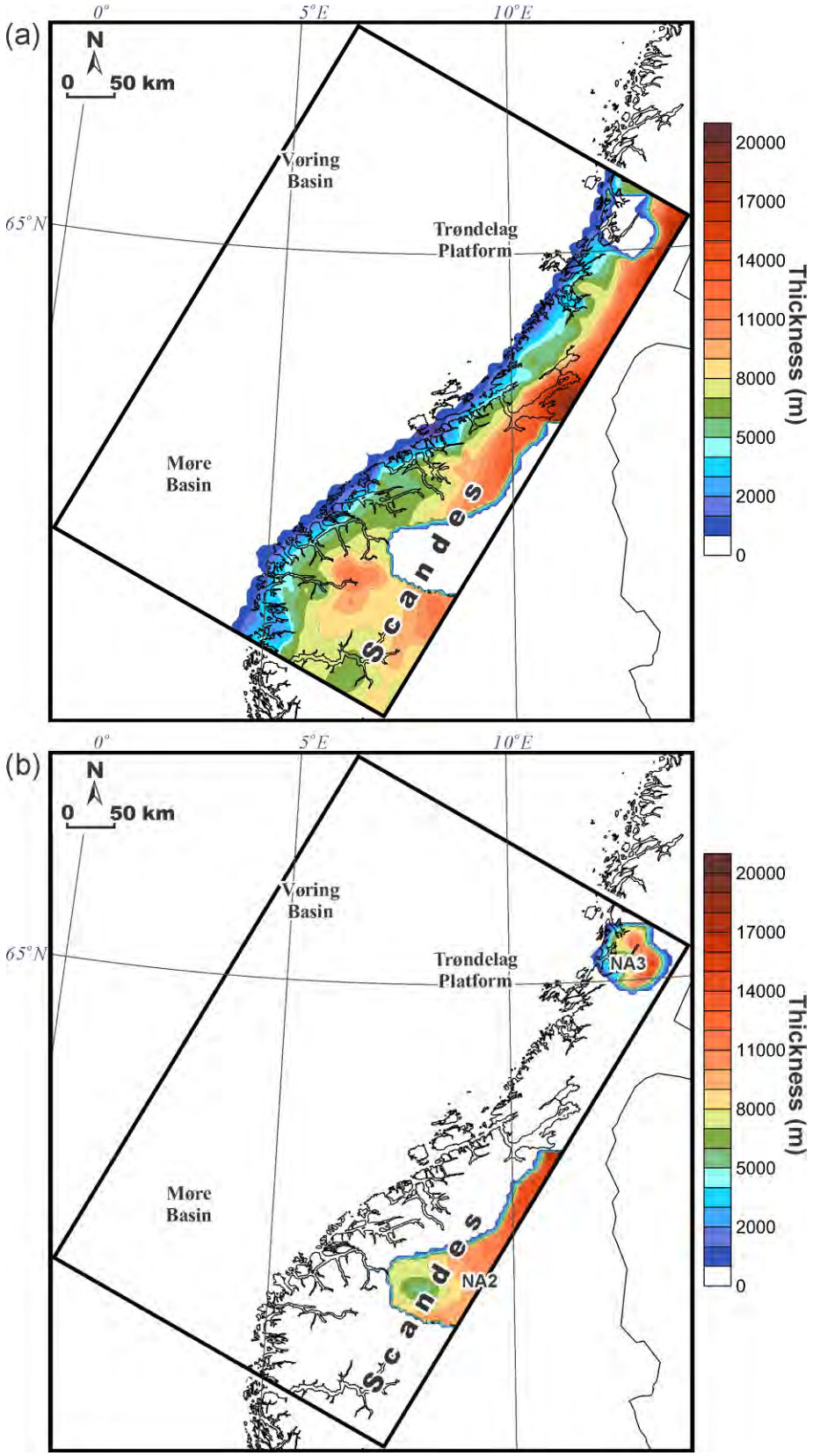

Figure 10.58. Thickness of the lower crystalline crust (layer 13): (a) main body of the layer without magnetically anomalous blocks and (b) blocks with significant remanent magnetisation.

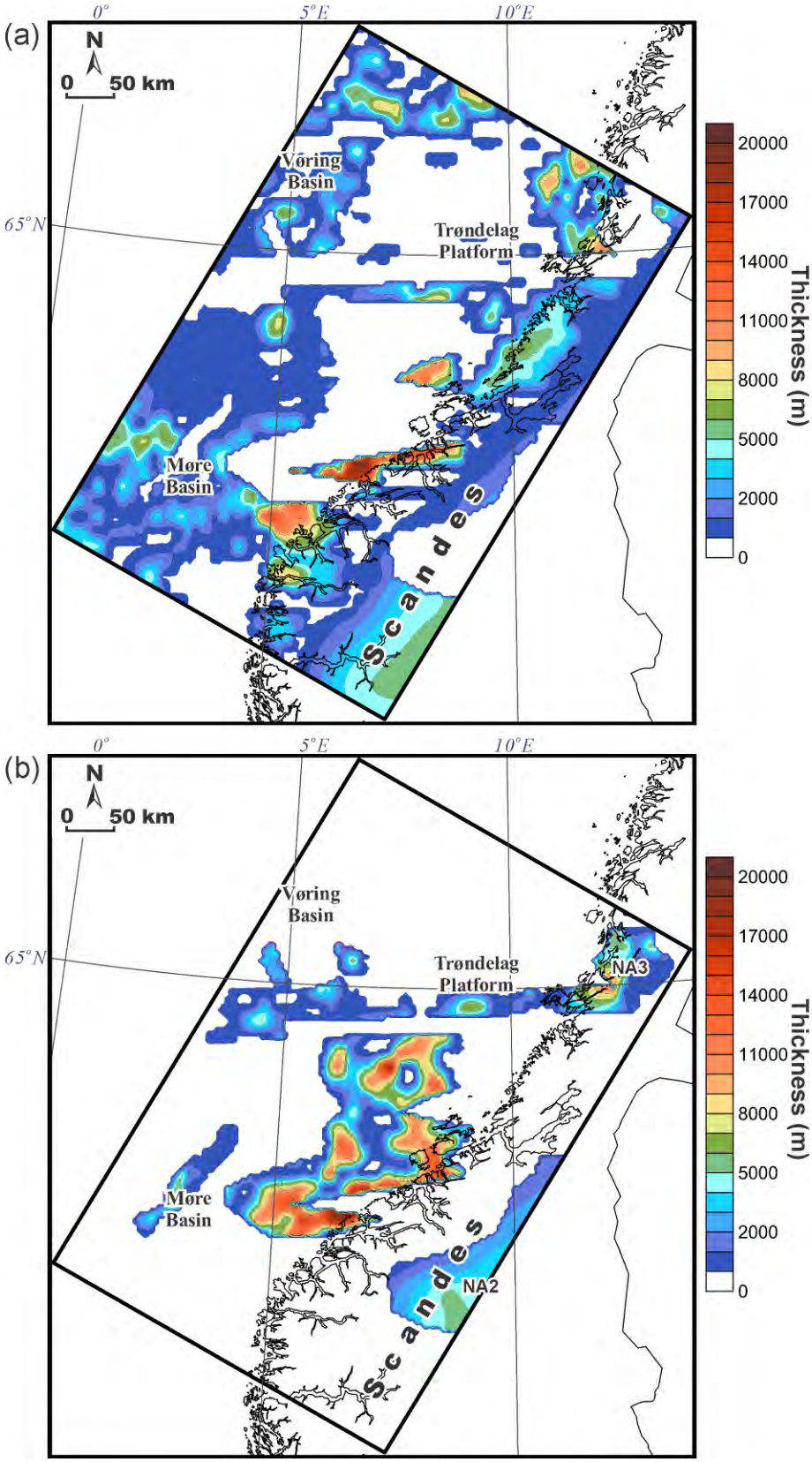

Figure 10.59. Thickness of the high-density crust (layer 14): (a) main body of the layer without blocks with increased magnetic susceptibility and (b) blocks with increased magnetic susceptibility, including blocks with significant remanent magnetisation.

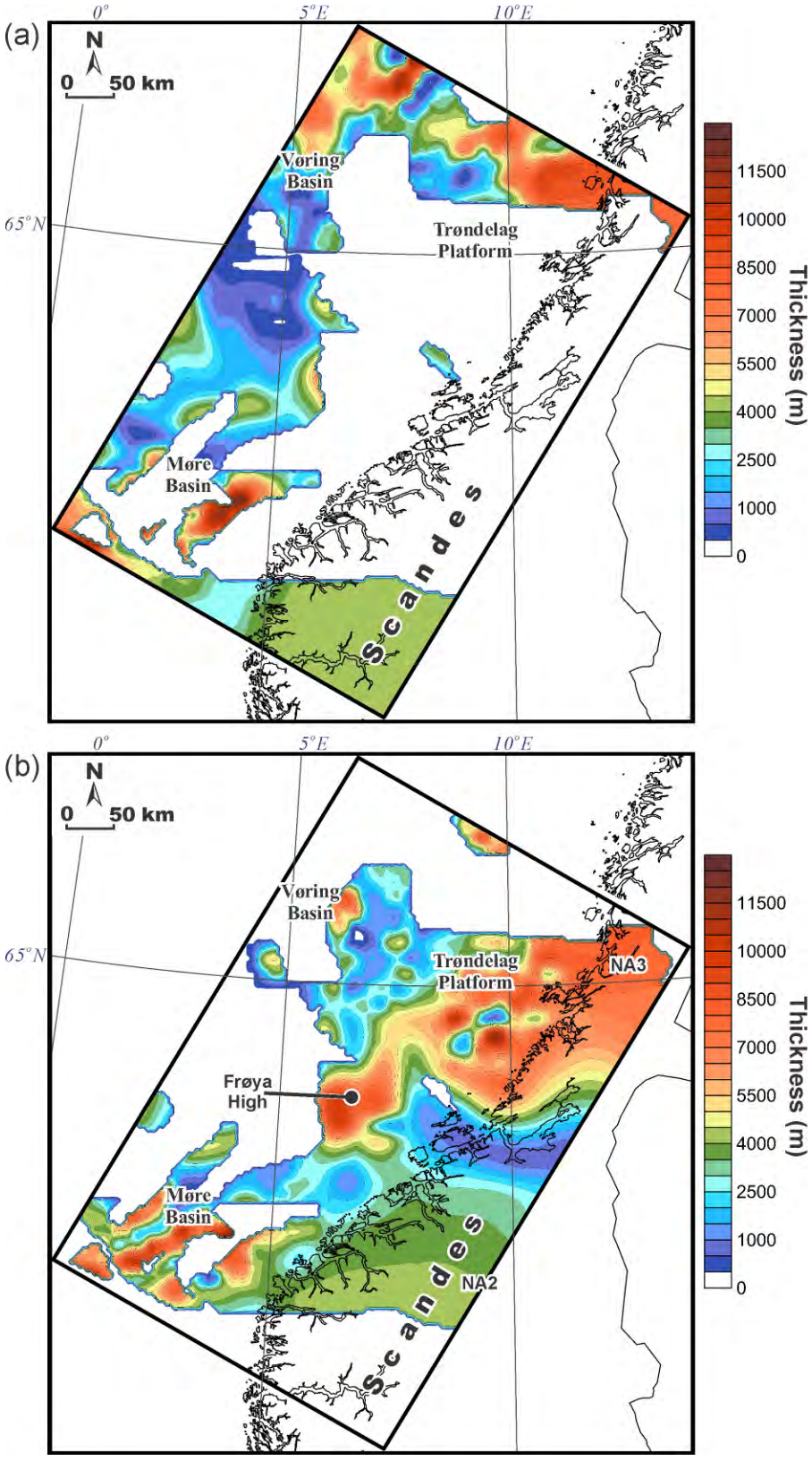

Figure 10.60. Thickness of the high-density lower-crustal layer (layer 15): (a) main body of the layer without blocks with increased magnetic susceptibility and (b) blocks with increased magnetic susceptibility, including blocks with significant remanent magnetisation.

same bodies have been included into the rest of the lower crust, represented by the high-density crust (layer 14) and the high-density lower-crustal layer (layer 15) (Figures 10.59b & 10.60b). The presence of these bodies can be related to the formation of the 'Sparagmite Basin' of South Norway (the Neoproterozoic, 750 to 590 Ma 'Sparagmite Basin'; e.g., Bjørlykke et al. 1976; now called the Hedmark Basin, Nystuen 1987) and/or to the Sveconorwegian orogeny. If the anomalous lower crust really is related to the formation of the Hedmark Basin, the autochthonous origin of this basin is more reasonable compared to the horizontally displaced upper-crustal part of the basin during the Caledonian Orogeny (Nystuen 1987). However, there is no single answer to the question about the origin of the Hedmark Basin even though most geologists regard it as allochtonous. Actually, the remanent magnetisation of the lower crust can be related to the lamellar magnetism, which is suggested to occur at the interfaces between fine precipitates of ilmenite and hematite (e.g., McEnroe et al. 2005). McEnroe et al. (2005) proposed that the lamellar, magnetism-related, natural remanent magnetisation can be stable over billions of years and, therefore, can be a reasonable explanation for the natural remanent magnetisation of the deeply located lower-crustal rocks beneath the mainland.

The next lower-crustal layer is represented by the high-density crust (layer 14; Figure 10.59) which is also responsible for the origin of the negative magnetic anomalies NA2 and NA3 (Figure 10.59b). In addition, positive magnetic anomalies PA6, PA7, PA8, PA9 and FA are fully or partially associated with the magnetically anomalous parts of this layer (cf. Figures 10.52a & 10.59b). In particular, the largest anomalous block of the high-density crust is partially responsible for the chain of positive anomalies associated with the extremely intense anomaly over the Frøya High (FA), and is also responsible for a broad low-intensive positive anomaly located to the south of the magnetic high on Frøya. A small, circular, magnetic high PA8 is associated with the rounded zone of thickening of the high-density crust (cf. Figures 10.52a & 10.59b), implying a possible intrusive origin for of the high-density crust in that area.

The deepest crustal layer is the high-density lower-crustal layer (layer 15; Figure 10.60). As already mentioned above, the anomalous part of this layer contributes to the origin of the negative magnetic anomalies NA2 and NA3. In addition, the anomalous crustal block of this layer with the remanent magnetisation is responsible for the origin of the narrow, negative, magnetic anomaly NA1, which is located in the southern part of the Møre Basin and cannot be modelled by purely induced magnetisation due to the very low intensity of the observed magnetic field (less than -200 nT) in that area. The positive magnetic anomalies PA7 and PA8 are partially related to the high-density lower-crustal layer (layer 15) in addition to the high-density crust (layer 14). Layer 15 is also responsible for the origin of the positive anomaly over the Frøya High and the positive anomaly PA9 over the Trøndelag Platform (cf. Figures 10.52a & 10.60b). Beneath the Frøya High and the Trøndelag Platform, almost the whole crystalline crust is magnetically anomalous, and the remanent magnetisation of some of the layers is not significant. Here, some explanations from the Coop1 report are partly repeated due to the reason that the positive anomalies PA2 and PA3 in the present study correspond to the positive anomalies A7 and A8 in the Coop1 report (Maystrenko 2014). Magnetic anomalies PA1, PA2, PA3 and PA5 have been modelled to have originated completely inside this layer 15, which has been assigned very high values of magnetic

susceptibilities (0.055-0.075 SI) and a Q-factor of 2.0. The reason is that there is not enough space for some parts of the prominent anomaly PA2 to have been caused by magnetic rocks in the middle or upper crust due to a strong thinning of the crystalline crust beneath the transition from the southern Møre Basin to the northern East Shetland Basin (Figure 10.62). Sources for anomalies PA1 and PA3, according to the model, must be located in the high-density lower-crustal layer in view of their close proximity to anomaly PA2 and some similarities in magnetic style of these anomalies with anomaly PA2. On the other hand, the magnetic anomaly PA6 has been modelled to be associated with the anomalous high-density lower-crustal layer, high-density and middle crust (layers 15, 14 and 12, respectively), which are thick enough to reproduce this anomaly without involving remanent magnetisation.

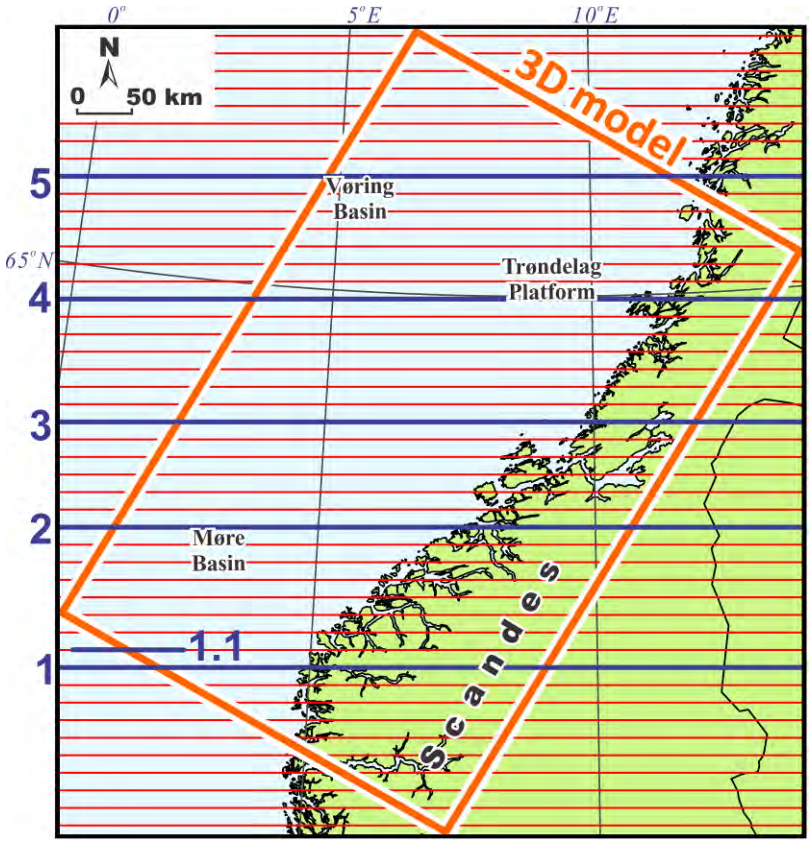

Figure 10.61. Location of the 2D vertical slices through the 3D magnetic model (red lines). Five selected slices are highlighted by bold blue lines and numbering.

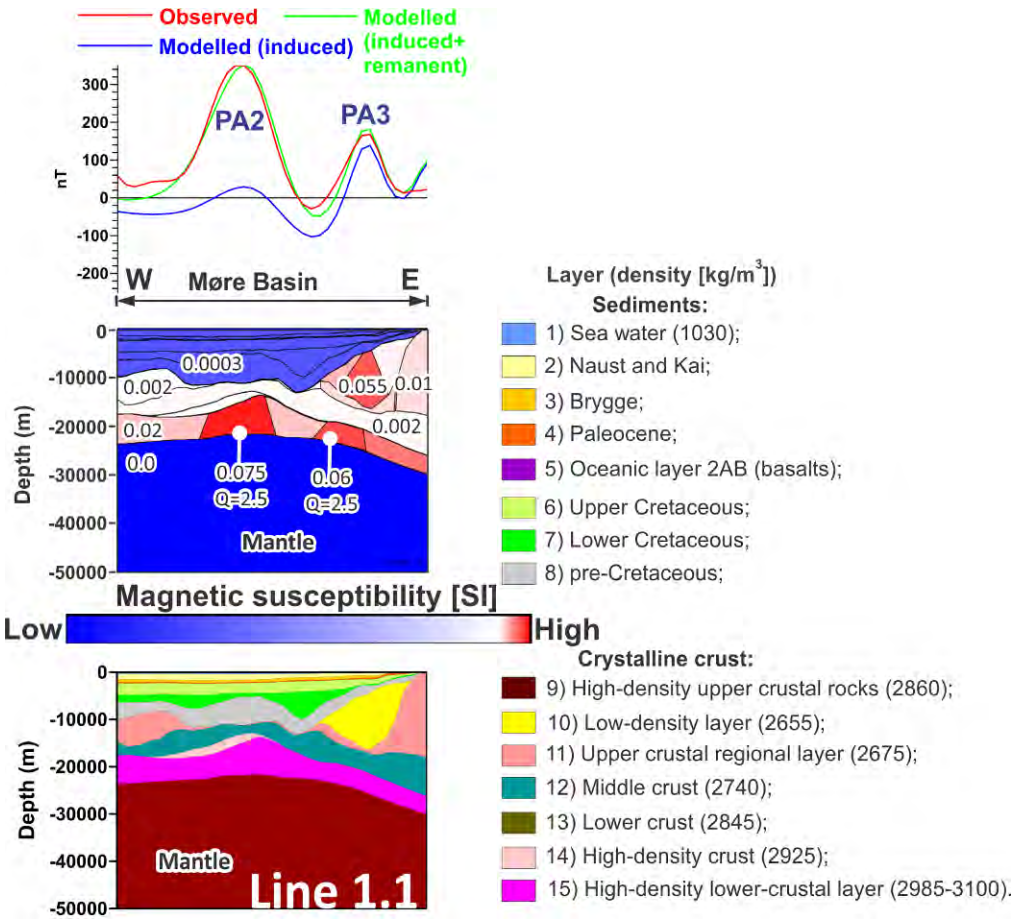

Figure 10.62. Selected fragment of vertical slice 1.1 through the 3D magnetic/structural model of the Mid-Norwegian continental margin and adjacent areas of the continent. Layer numbering is the same as in Tables 10.2 and 10.4. For the location, see Figure 10.61. PA - positive anomaly.

This assumption about the origin of magnetic anomaly PA2 has already been tested during the Coop1 study (Maystrenko 2014) and was originally proposed by Fichler et al. (2011) who suggested that the lower-crustal block with high magnetic susceptibility, associated with the positive anomaly PA2, is possibly represented by inherited serpentinites. According to Fichler et al. (2011), serpentinization of the lower crust was caused by subduction and generation of an island arc prior or during the Caledonian Orogeny. In this case, a similar mechanism can be proposed for the origin of anomalies PA1 and PA3.

The structural style associated with some of the magnetic anomalies is described below by use of five selected, W-E-oriented, 2D vertical slices across the 3D magnetic/structural model (Figure 10.61). The positions of vertical slices 1-5 are the same as for the five vertical slices illustrating the 3D density/structural model (Figure 10.42).

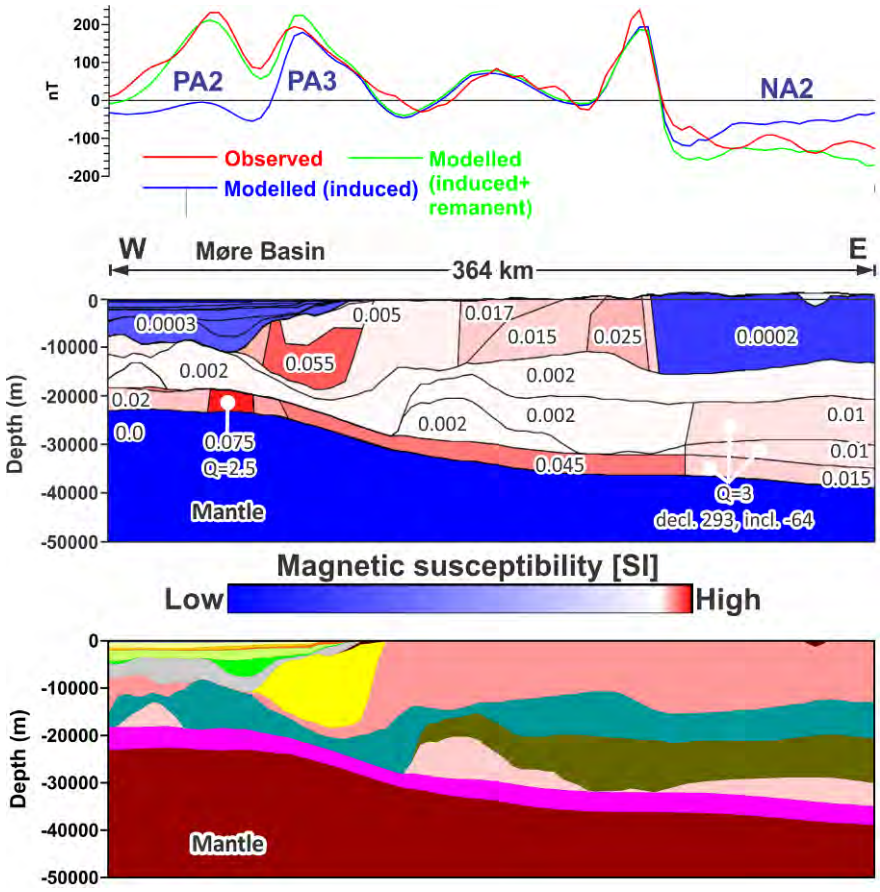

Figure 10.63. Selected vertical slice 1 through the 3D magnetic/structural model of the Mid-Norwegian continental margin and adjacent areas of the mainland. Layer numbering is the same as in Tables 10.2 and 10.4 (for the legend, see Figure 10.62 and for the location, see Figure 10.61). PA - positive anomaly and NA - negative anomaly.

2D vertical slice 1 is located within the southern part of the study area (Figure 10.56), demonstrating the origin of the positive magnetic anomaly PA3. This magnetic high is associated with the block of the lower-density upper-crustal layer (layer 10) which has an increased magnetic susceptibility (0.055 SI). In addition, the southeastern edge of the anomaly PA2 is also crossed by this vertical slice, indicating that this anomaly originates from the high-density lower-crustal layer (layer 15) where a small block with a high value of magnetic susceptibility (0.075 SI) and a Q-factor of 2.5 has been included during the 3D magnetic modelling. Furthermore, vertical slice 1 crosses the southern part of the negative anomaly NA2 (Figure 10.63) which is modelled by assigning a remanent magnetisation for all three layers of the lower crust (layers 13, 14 and 15). Actually, there is no real necessity to assign remanent magnetisation to all these lower-crustal layers because an increase of the magnetic susceptibility and/or Q-factor would allow us to localise the origin of the negative anomaly NA2 in one of those layers. However, there are no constraints on the induced and remanent magnetisation of these layers. As has already been noted above, the remanent magnetisation can most likely be associated with different kind of magmatic rocks, but magnetic lows NA2 does not coincide with the positive gravity anomalies (cf. Figures 10.18 & 10.50-10.52). In this case, the source for the remanent magnetisation has been set within the lower crust without creating a density contrast because the density of the lower-crustal rocks

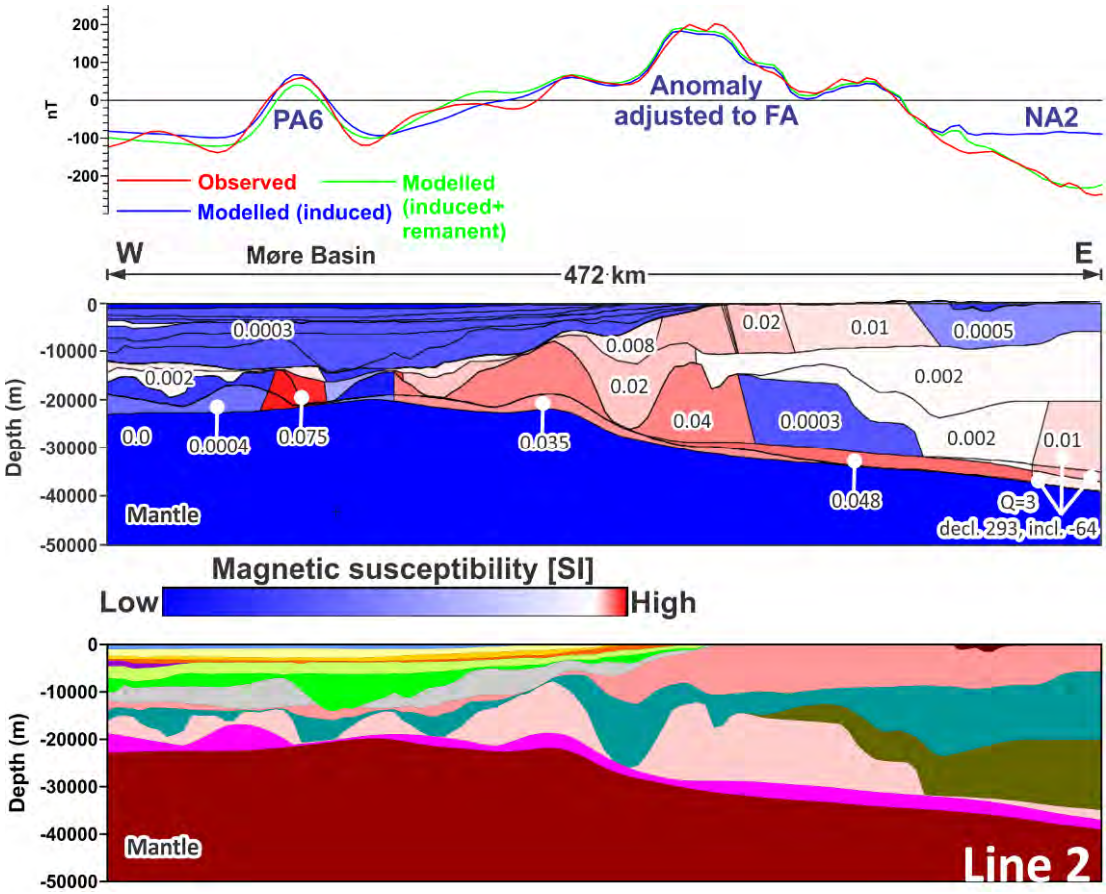

Figure 10.64. Selected vertical slice 2 through the 3D magnetic/structural model of the Mid-Norwegian continental margin and adjacent areas of the continent (for the legend, see Figure 10.62 and for the location, see Figure 10.61). PA - positive anomaly, NA - negative anomaly and FA - Frøya magnetic anomaly over the Frøya basement high.

is already relatively high. Along this vertical slice, the high-amplitude magnetic anomaly, located between the anomalies PA3 and NA2, is related to the anomalous block of the regional upper-crustal layer (layer 11). The second vertical slice (slice 2) is interesting in terms of the origin of the positive magnetic anomaly PA6, a negative magnetic anomaly NA2 and a broad positive anomaly adjusted by magnetics to the Frøya High in the south. The structural pattern of the crystalline crust in the area of the positive anomaly PA6 indicates that this magnetic high represents a cumulative magnetic effect from at least three layers (Figure 10.64): the middle crust, the high-density crust and the high-density lower-crustal layer (layers 12, 14 and 15, respectively). These magnetically anomalous blocks are characterised by a high magnetic susceptibility (ranging from 0.07 to 0.075 SI) which has been assigned during the 3D magnetic modelling. The next important anomaly along this vertical slice is the positive anomaly which was adjusted to the magnetic anomaly over the Frøya High from the

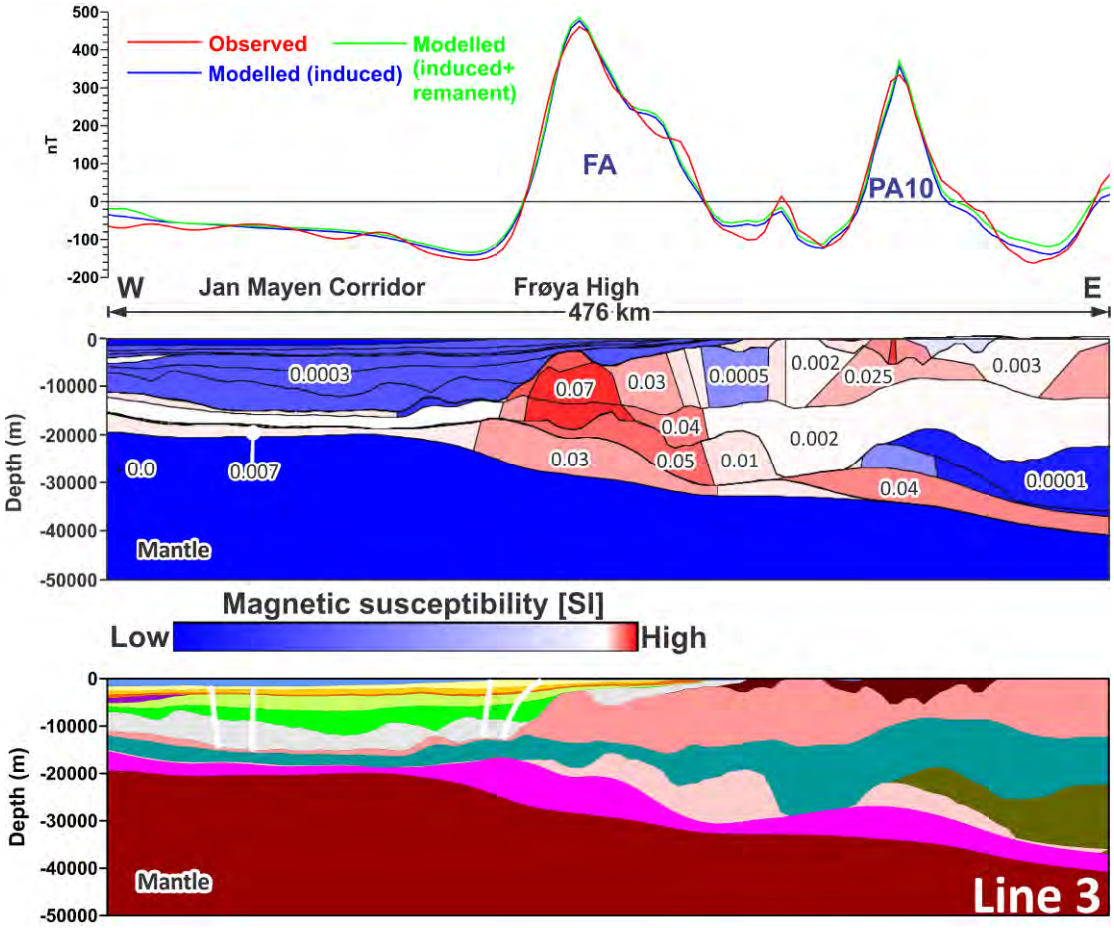

Figure 10.65. Selected vertical slice 3 through the 3D magnetic/structural model of the Mid-Norwegian continental margin and adjacent areas of the mainland (for the legend, see Figure 10.62 and for the location, see Figure 10.61). PA - positive anomaly, NA - negative anomaly and FA - Frøya magnetic anomaly over the Frøya basement high.

south. This anomaly is mostly associated with the increased magnetic susceptibility within several blocks of the regional upper-crustal layer (layer 11) on the one hand. On the other hand, there is also an input from the magnetically even more anomalous high-density crust (layer 14) which strongly thickens beneath the centre of the anomaly (Figure 10.64). In addition, blocks with increased magnetic susceptibility of the middle crust (layer 12) and the high-density lower-crustal layer (layer 15) are also partially responsible for this broad anomaly in places where the regional upper-crustal layer and the high-density crust are relatively thin. Within the eastern part of this vertical slice, the lower-crustal blocks with remanent magnetisation have been included into the lower crust in order to remove more than 100-nT of misfit in the case of only induced magnetisation for those lower-crustal blocks. Actually, the misfit becomes larger towards the east where negative anomaly NA2 reaches a culmination out of vertical slice 2.

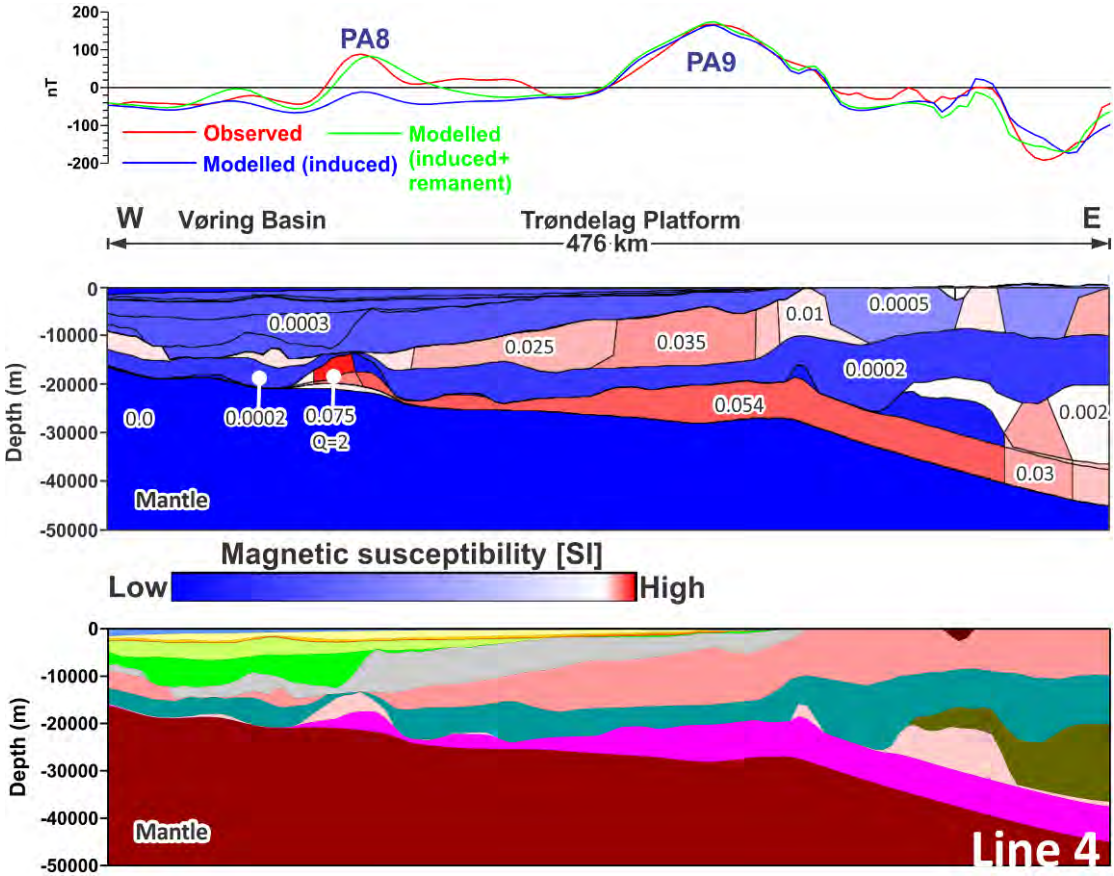

Figure 10.66. Selected vertical slice 4 through the 3D magnetic/structural model of the Mid-Norwegian continental margin and adjacent areas of the mainland (for the legend, see Figure 10.62 and for the location, see Figure 10.61). PA - positive anomaly.

The third vertical slice (slice 3) is located in the middle of the Coop2 model area (Figure 10.61). This vertical slice clearly demonstrates the structural style of the crystalline crust related to the magnetic anomaly over the Frøya High (Figure 10.65), which has mostly originated from the anomalous blocks of the regional upper-crustal layer and the middle crust (layers 11 and 12, respectively). Magnetic susceptibility in these anomalous blocks varies from 0.03 at the slopes of the anomaly to 0.07 SI within the core of the Frøya High. Additionally, blocks of the high-density crust (layer 14) and the high-density lower-crustal layer (layer 15) have been assigned by an increased magnetic susceptibility (0.05 and 0.03 SI, respectively) in order to fit the modelled and observed magnetic fields in that area. Alternatively, natural remanent magnetisation can be included into the upper and/or middle-crustal blocks with a Q-factor around 2 or more in order to model the high-amplitude magnetic anomaly over the Frøya High without involving the lower crust. The next important, high-amplitude, magnetic anomaly along slice 3 is the magnetic high PA10 (Figure 10.65) which has been modelled to be mostly associated with the anomalous blocks of the high-density upper-crustal layer (layer 9). Vertical slice 3 is also interesting in terms of an absence of magnetic anomalies within the western part of the profile where the Jan Mayen corridor is

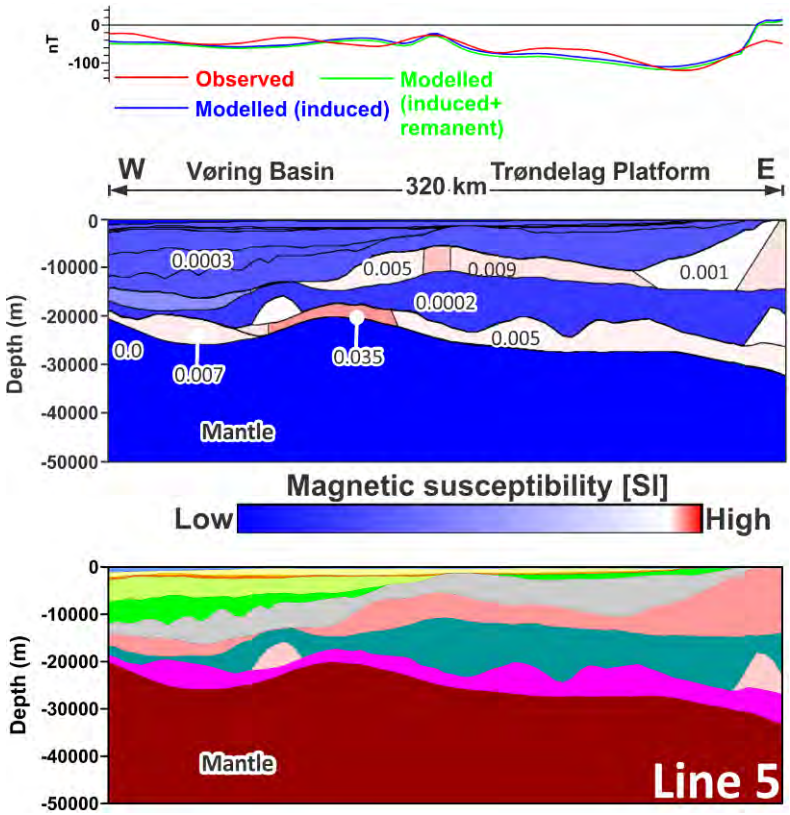

Figure 10.67. Selected vertical slice 5 through the 3D magnetic/structural model of the Mid-Norwegian continental margin and adjacent areas of the mainland (for the legend, see Figure 10.62 and for the location, see Figure 10.61).

located. The observed magnetic field is almost flat without any strong anomalous deviations over the Jan Mayen corridor. This is mostly due to the fact that magnetically roughly neutral sediments are very thick in this area. On the other hand, the crystalline crust is relatively thin and is deeply located there.

Farther north, vertical slice 4 demonstrates the structural pattern related to positive magnetic anomalies PA8 and PA9 (Figure 10.66). The origin of the wide positive anomaly PA9 has been modelled to be related to the large block of the regional upper-crustal layer (layer 11) with increased magnetic susceptibility (0.035 SI). The magnetic anomaly PA8 is mostly associated with an anomalous block of the high-density crust (layer 14) which represents the thickest crystalline crustal layer beneath the anomaly. In addition, this anomaly PA8 is also related to the high-density lower-crustal layer (layer 15). The assigned magnetic susceptibility is relatively high (0.075 SI for layer 14 and 0.045 for layer 15) within the rocks associated with the anomaly PA8 but this does not allow us to fit the observed and modelled magnetic fields within this anomaly. Therefore, the Q-factor of these anomalous lower-crustal blocks has been set at 2.0, allowing a reasonable coincidence of the observed and modelled fields within the area where the sediments are relatively thick. The western part of vertical slice 4 is also characterised by a very smooth observed magnetic field as in the case of the western part of vertical slice 3. The reason for this non-anomalous magnetic field is also the same as in the case of slice 3: thick low-magnetic sediments and thin deeply seated crystalline crust (cf. Figures 10.65 & 10.66).

The northernmost selected vertical slice 5 (Figure 10.67) is characterised by a very smooth magnetic field over almost the whole profile. The exception is at the easternmost end of the slice where a low-amplitude positive magnetic anomaly is located, having an origin from the anomalous block of the upper crust (Figure 10.67). The modelled anomalous upper-crustal blocks within the middle part of the slice are reflected by a very smooth positive magnetic anomaly due to the fact that the relatively thick sedimentary cover decreases the intensity of the observed magnetic effect from the crystalline crust. The crystalline crust is relatively thin and deeply located beneath the Vøring Basin (Figure 10.67) and, therefore, there are only very smooth and hardly recognisable magnetic anomalies in the observed magnetic field that actually support a deep position of the top crystalline basement there and this also supports the presence of very thick sediments.

For completeness should be mentioned that the origin of some observed anomalies can have alternative explanations by comparison comparison with interpretations outlined above. For instance, positive magnetic anomalies PA1, PA2, PA3 and PA5 can also be associated with the upper-mantle rocks in view of the fact that the Curie isotherm for the dominant magnetic minerals can be theoretically located slightly deeper than the strongly uplifted base of the crystalline crust (Moho discontinuity). Furthermore, negative magnetic anomalies NA2 and NA3 can also be explained by the presence of the thin magmatic rocks with high Q-factor within the upper crust. In this case, the density contrast would be not be significant at the regional scale and, therefore, the observed gravity would not contain a positive anomaly related to these magmatic rocks. To summarise, the origin of anomalies NA2 and NA3 requires additional investigations, including both sampling rocks from the Earth's surface and boreholes and a more detailed study on the remanent magnetisation of the lower crust. The important fact is that there is no correlation between the prominent Jan Mayen gravity low and the observed magnetic anomalies (cf. Figures 10.18, 10.31 & 10.50-10.52), indirectly supporting the origin of the Jan Mayen gravity low as deriving from the density contrast within the sediments rather than from inhomogeneities in the crystalline crust. However, this does not allow us to exclude an upper-mantle origin for that broad gravity low because an upper mantle density contrast can be located below the Curie isotherm.

Furthermore, there is also a very weak correlation between the strong positive gravity anomaly over the Utgard High and the anomalous pattern of the observed magnetic field in that area (cf. Figures 10.18, 10.31 & 10.50-10.52), implying that crystalline rocks of the Utgard High are low-magnetic in contrast to the high-magnetic susceptibility of crystalline rocks of the Frøya basement high where the observed gravity and magnetic anomalies coincide spatially. The particulary low-magnetic crystalline rocks of the Utgard High can indicate that the entire crystalline crust is not so strongly magnetic beneath the greater part of the Vøring Basin and the northern part of the Møre Basin, assuming that the absence of the observed strong magnetic anomalies there is not only due to the very thick sedimentary cover but also can be related to some lithological features of the crystalline crust in that area. In addition, the deeply located crystalline crust can be affected by temperatures which are higher than the Curie temperature isotherm and, therefore, crystalline rocks can at least partially lose their magnetisation beneath the deepest parts of the Vøring and Møre basins.

To summarise, the observed magnetic anomalies over the study area have different origins, strongly dependent on both the structural style of the crystalline crust and the magnetic properties (lithology) of the rocks. According to the results of the 3D magnetic modelling, the 3D density/structural model has been accomplished by including into layers of the model magnetically anomalous blocks which are characterised by increased magnetic susceptibility. Thus, these blocks can be lithologically different from the remainder of the original density-derived layers.

10.5 3D THERMAL MODELLING

The last step of the integrated regional-scale 3D analysis involved the 3D thermal modelling which has been carried out in order to understand the conductive thermal regime beneath the Mid-Norwegian continental margin and adjacent areas of the continental mainland (Figure 10.68). Results of the 3D conductive thermal modelling reveal the temperature distribution and pattern of the subsurface within the Coop2 3D model (Figure 10.69).

10.5.1 Structural data

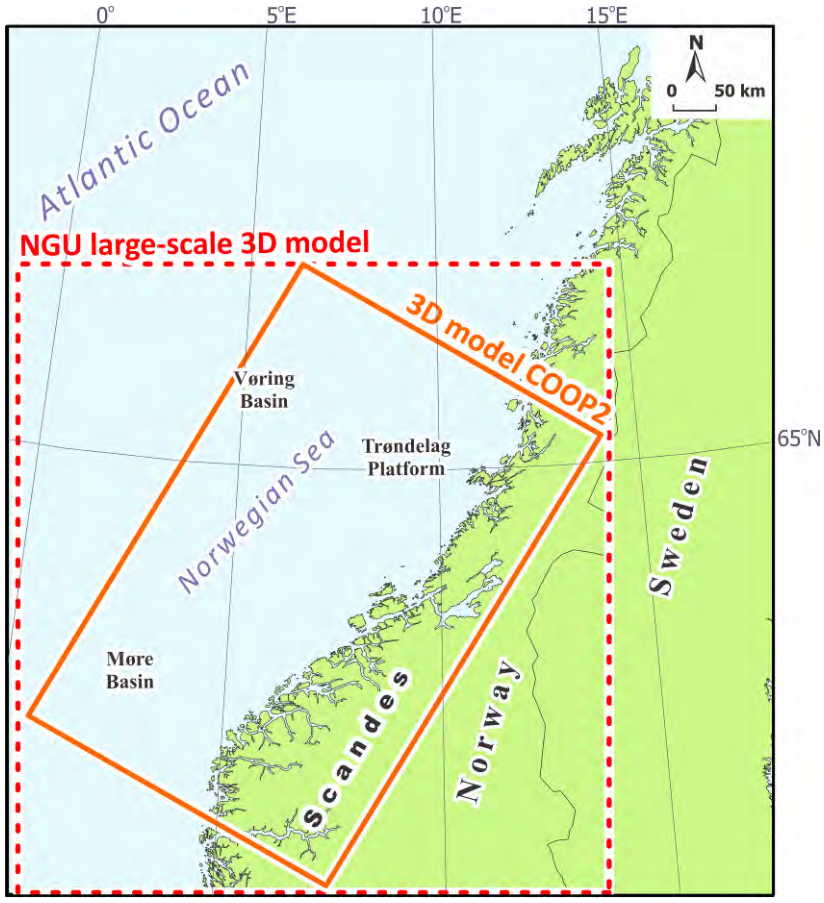

Figure 10.68. Location of the C Coop2 3D structural model (the orange frame) in relation to the location of the NGU large-scale 3D structural model (the red dashed frame).

The 3D thermal modelling has been performed for the area covered by the large-scale NGU 3D structural model (Figure 10.68). This has been done in order to consider the thermal influence of both the oceanic and the continental lithospheric domains which are not completely covered by the NE-SW-oriented rectangular Coop2 3D model. Use of the NGU

3D model makes it possible to consider, at least partially, the thermal effects from the relatively shallow lithosphere-asthenosphere boundary and Moho beneath the ocean and the relatively deep location of these interfaces beneath the Fennoscandian Shield. The regional thermal pattern associated with the position of the lithosphere-asthenosphere boundary is actually one of the key factors for performing a proper and detailed 3D model of temperature distribution within the Coop2 study area. Nevertheless, the comprehensive 3D thermal modelling has been restricted to the Coop2 3D model, whereas the NGU model has been used only to consider the large-scale thermal influence. Therefore, the results of 3D thermal modelling are mainly presented and described in this report for the Coop2 model area with some minor information from the areas located outside of the Coop2 3D model. The main point is that the NGU large-scale 3D structural model is less constrained by existing data

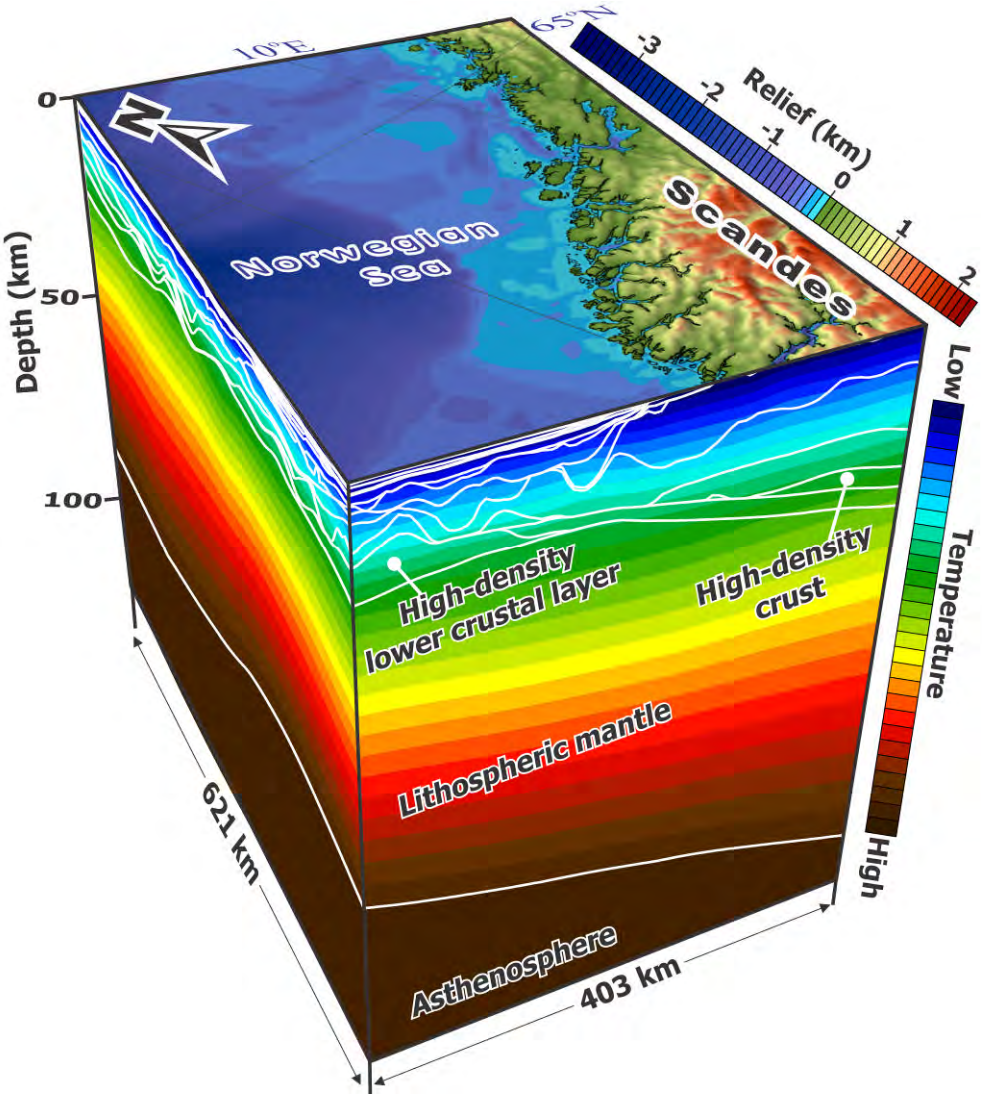

Figure 10.69. 3D temperature distribution within the lithosphere-scale 3D structural model of the Mid-Norwegian continental margin and adjacent continent (four times vertically exaggerated).

compared to the Coop2 3D model and, therefore, cannot be used to actually verify or investigate the detailed configuration of the 3D conductive thermal field beneath the Earth's surface outside the Coop2 study area. In particular, the NGU 3D model is used to consider the long-wavelength thermal pattern at the continent-ocean system rather than to understand

the local details of the subsurface temperature. Consequently, the NGU large-scale 3D model with its better constrained part for the Coop2 study area, which has been validated by the 3D density and magnetic modelling, has been used as a first-order structural representation for geometries of the sedimentary cover, crystalline crust and lithospheric mantle during the 3D thermal modelling.

10.5.2 Method

The 3D temperature distribution within the structurally complex 3D model of the Mid-Norwegian continental margin and adjacent mainland has been calculated using the commercial software package COMSOL Multiphysics. COMSOL Multiphysics is a finite-element analysis software package for a variety of physical processes. During the 3D thermal modelling, the Heat Transfer Module was used to simulate the stationary and time-dependent heat transfer in solid materials by heat conduction, which is considered to be the dominant mechanism of heat transfer at the regional scale within the subsurface of the investigated area. Therefore, these calculations have been performed based on physical principles of the conductive 3D thermal field by solving the heat equation (10.6):

$$\rho C_p \, (\delta T/\delta t) = \nabla \cdot (k \, \nabla T) + Q \qquad (10.6)$$

where ρ is the density [kg/m^3], C_p is the specific heat capacity [J/kgK], T is the temperature [K], k is the thermal conductivity [W/mK], ∇T is the temperature gradient [K/m], t is the time [s], Q is the heat source (radioactive heat production) [W/m^3], δT is the change in temperature per time interval δt, and $\nabla \cdot$ is the operator giving the spatial variation in temperature. Consequently, the solution of the heat equation (10.6) is sensitive to the values of the thermal properties (specific heat capacity, thermal conductivity and radiogenic heat production) and density as well as the thermal boundary conditions.

During the thermal simulation, the heat flux q [W/m^2] has been calculated according to Fourier's law of heat conduction (10.7):

$$q = - k \nabla T \qquad (10.7)$$

where k is the thermal conductivity [W/mK] and ∇T is the temperature gradient [K/m].

The 3D thermal modelling has been carried out by means of a finite-element method in 3D which is a suitable approach for a rather complex geometry like the lithosphere-scale 3D model of the Mid-Norwegian continental margin and adjacent areas (Figure 10.3). The lateral boundaries are closed to heat transfer, assuming that the temperature gradient is zero across the thermally insulated lateral boundaries. The time-dependent temperatures at the sea floor and at the Earth´s surface (Figure 10.70) have been set as the upper thermal boundary condition, whereas the base of the lithosphere (Figure 10.71) has been taken as a lower thermal boundary, assuming that the lower thermal boundary corresponds to the 1300 °C isotherm (e.g., Turcotte & Schubert 2002). The importance of the lower thermal boundary configuration within the continent-ocean transition has been examined by Scheck-Wenderoth & Maystrenko (2008).

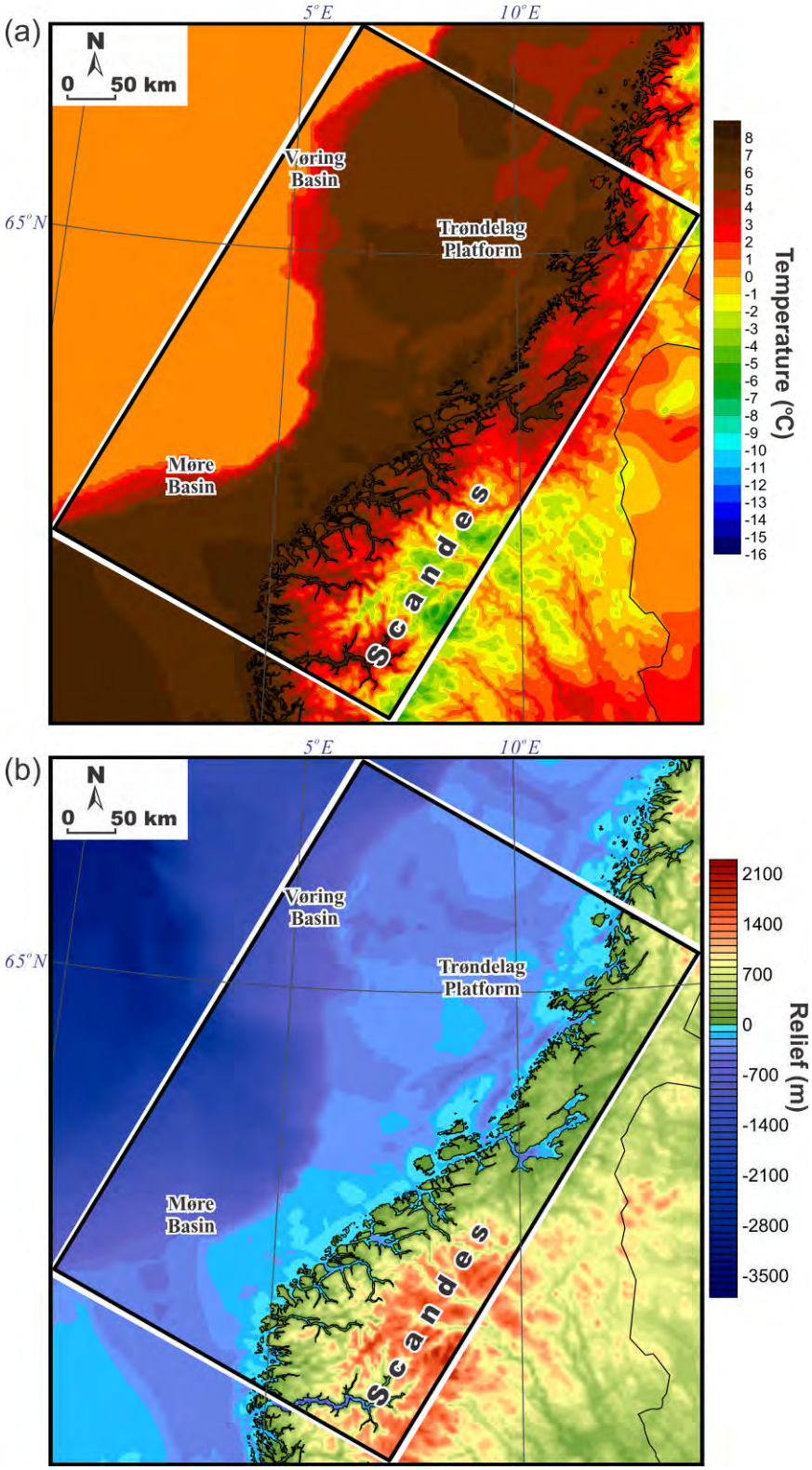

Figure 10.70. Present-day upper thermal boundary: (a) annual average air temperatures during 1961-1990 for Norway (Tveito et al. 2000) and for Sweden (Raab & Vedin 1995) and average sea-bottom temperature, derived from Ottersen (2009), ICES (2012) and Korablev et al. (2014); (b) depth to the sea floor and the Earth´s surface (from the Norwegian Mapping Authority).

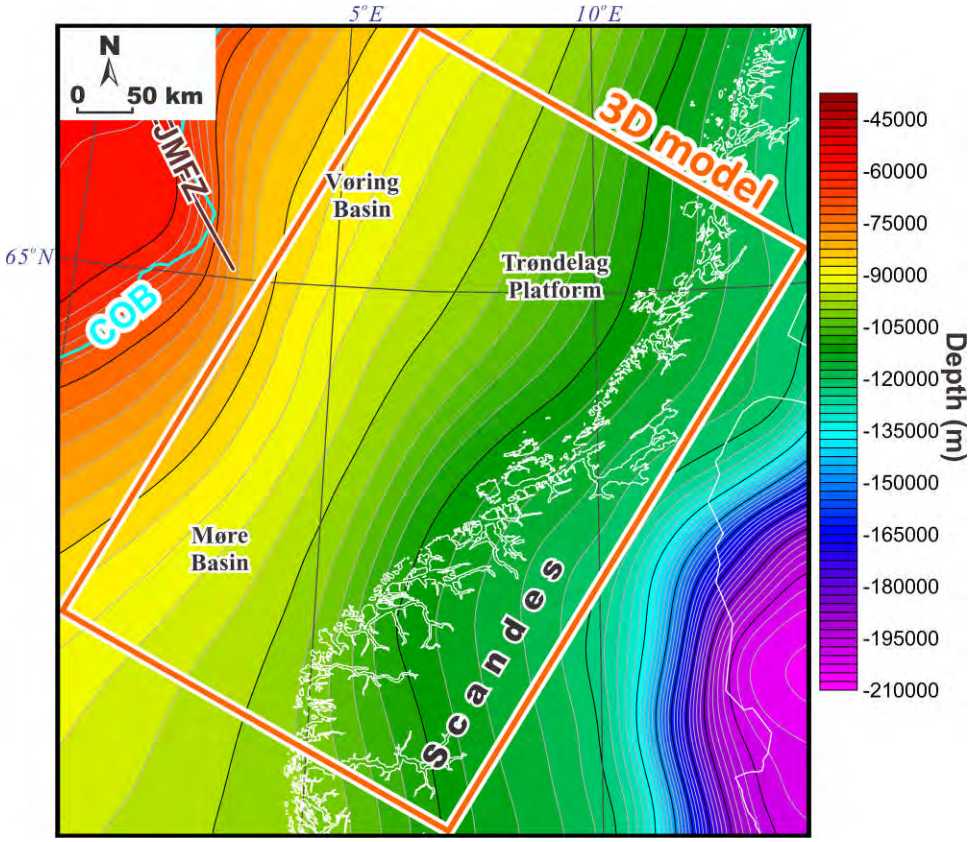

Figure 10.71. Present-day lower thermal boundary: 1300°C isotherm at the lithosphere-asthenosphere boundary. COB - continent-ocean boundary (from Gernigon 2015; this report), JMFZ - Jan Mayen Fracture Zone (from Blystad et al. 1995).

The present-day temperature at the Earth´s surface (Figure 10.70a) is represented by the annual average air temperatures during 1961-1990, which are taken from the database at the Norwegian Meteorological Institute (Tveito et al. 2000) and the National Atlas of Sweden (Raab & Vedin 1995). The temperature at the sea floor (Figure 10.70a) has been inferred from published values of bottom temperatures within the Norwegian Sea (Ottersen 2009, Korablev et al. 2014), being set to be dependent on the bathymetry (Table 10.5) with a slight decrease of temperature towards the northeast (Figure 10.70a). In addition, published values of average sea-bottom temperatures in winter and in summer within the North Sea during 1997-2002 (ICES 2012) have been used to cross-check the sea-bottom temperature within the northernmost part of the North Sea.

Table 10.5 Average annual temperature at the sea floor of the Norwegian Sea.

Bathymetry, m	100	300	500	600	700	750	800	850 and deeper
Temperature, °C	7	6	5	4	3	2	1	0

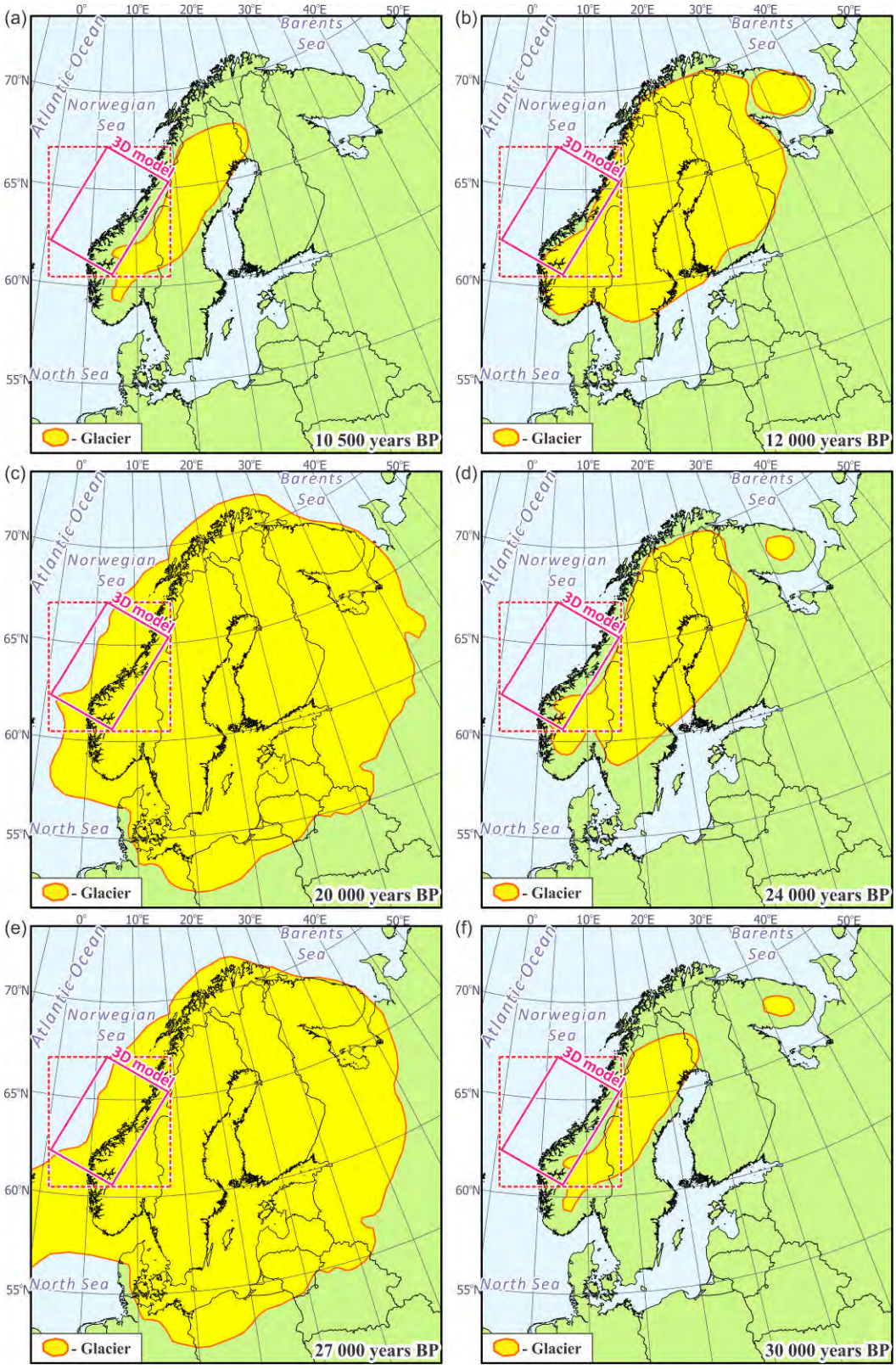

Figure 10.72. Ice cover during the Weichselian glaciation (after Olsen 2006, Slagstad et al. 2009, Olsen et al. 2013). The Coop2 model is shown by the magenta frame. The southern part of the large-scale NGU structural model is shown by the red dashed frame.

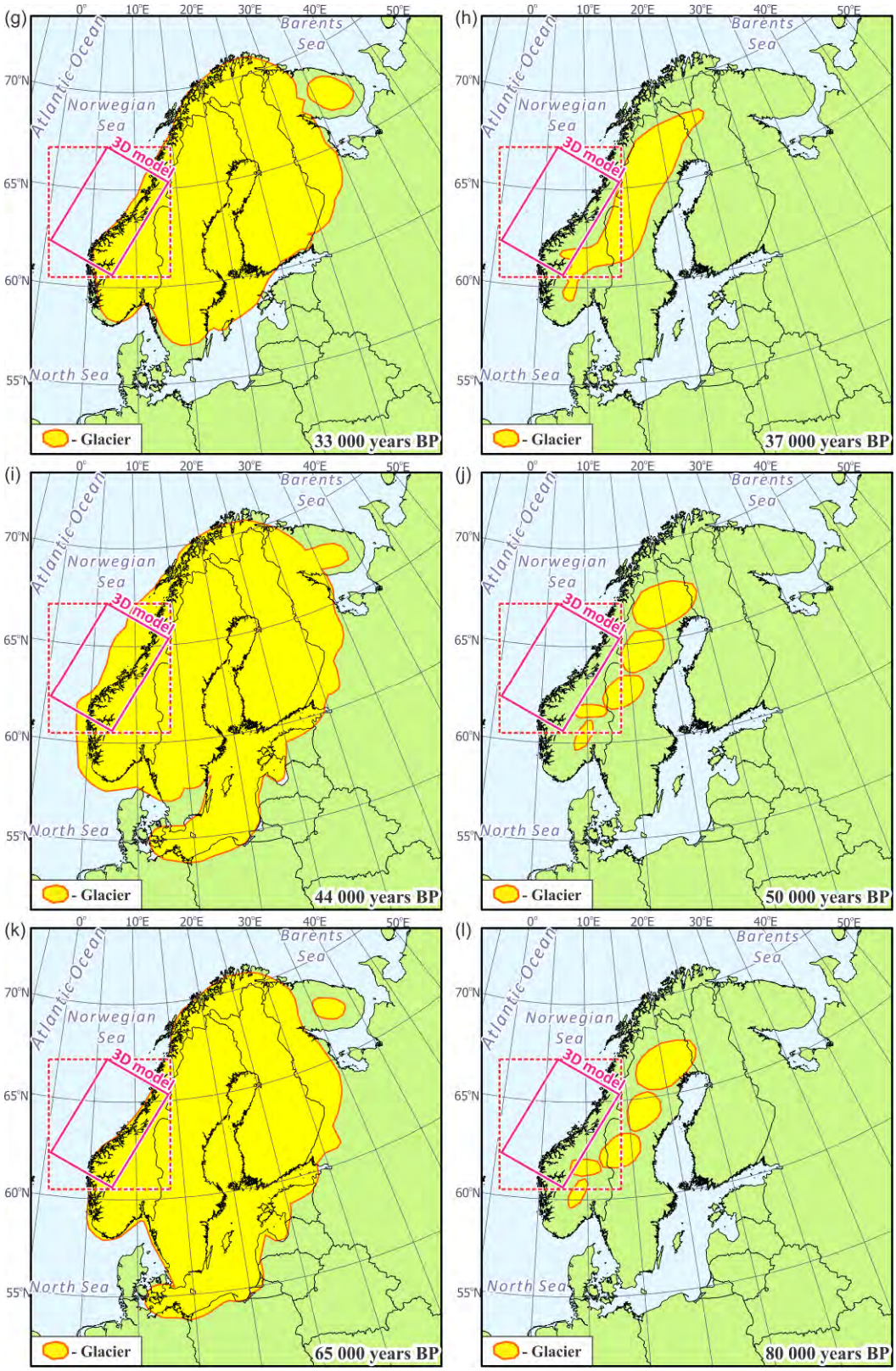

Figure 10.72. Continued. Ice cover during the Weichselian glaciation (after Olsen 2006, Slagstad et al. 2009, Olsen et al. 2013). The Coop2 model is shown by the magenta frame. The southern part of the large-scale NGU structural model is shown by the red dashed frame.

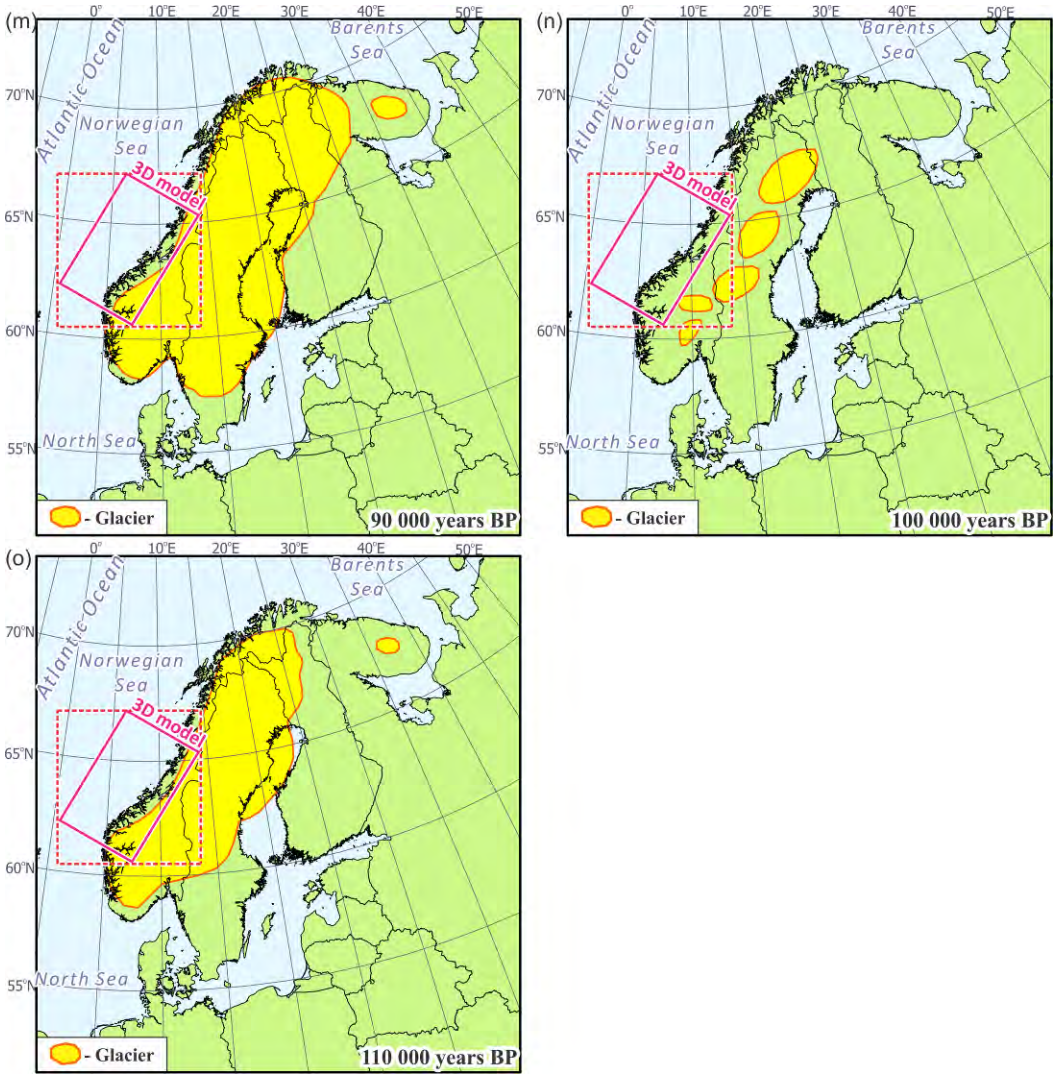

Figure 10.72. Continued. Ice cover during the Weichselian glaciation (after Olsen 2006, Slagstad et al. 2009, Olsen et al. 2013). The Coop2 model is shown by the magenta frame. The southern part of the large-scale NGU structural model is shown by the red dashed frame.

The 3D thermal modelling has been carried out taking into account the palaeoclimatic changes of the surface temperature during the last 220,000 years before present (BP). During this time interval, the study area was affected by glaciations during the Saalian glacial period with interruption during the Eemian interglacial period (220,000-110,000 years BP) and the Weichselian glacial period (~110,000–10,000 years BP; Figure 10.72), as well as by the Holocene interglacial period (10,000 years BP to present day).

The palaeotemperatures during the last 8000 years (Table 10.6) are represented by almost 0.4◦C below the present-day average air temperature during the Little Ice Age (Nesje et al. 2008; Mann et al. 2009; Figure 10.73a) and by 1◦C above the present-day average air temperature during the Holocene Climate Optimum (e.g., Seppä et al. 2009; Figure 10.73b). Palaeotemperature at 8,000 years BP (Figure 10.73c) has been set to be 1 °C below the present-day surface temperature (Figure 10.70a). This difference between the present-day temperature and that at 8,000 years BP has been derived from the reconstructed, area-average, mean annual temperature anomalies for northwestern Europe (Davis et al. 2003).

Table 10.6. Difference between palaeotemperatures and the present-day temperature for the last 8000 years.

Time, years before present BP	0 Present day	400 Little Ice Age	7500 Holocene Climate Optimum	8000
Temperature difference in relation to present day, °C	0	-0.4	+1	-1

To reconstruct the earlier palaeoclimatic thermal conditions at the Earth's surface within the Mid-Norwegian continental margin and adjacent areas of the continent and the ocean, a model of temporal and spatial variations of the ice cover within Scandinavia during the Weichselian glacial period (Olsen 2006, Olsen et al. 2013) has been used according to the set of maps published in Slagstad et al. (2009). The spatial distribution of an ice cover through time is reproduced in Figure 10.72, showing the position of the NGU large-scale and Coop2 3D structural models. According to these data (Olsen 2006, Olsen et al. 2013; Figure 10.72), the continent within the study area was almost continuously covered by a variably shaped Weichselian ice sheet which could have reached up to 3,000 m thickness during the Last Glacial Maximum (Siegert et al. 2001). The same palaeoclimatic scenario was also applied for the Saalian glacial/Eemian interglacial period (220,000-110,000 years BP), taking into account that paleoclimatic conditions were relatively similar during the Weichselian glacial/Holocene interglacial and the Saalian glacial/Eemian interglacial periods (Andersen & Borns 1994, Slagstad et al. 2009).

At times when the study area was glaciated, a temperature of -0.5 °C has been set at the Earth´s surface beneath the ice cover. This is a similar assumption as used by Slagstad et al. (2009) for palaeoclimatic corrections of heat-flux measurements from several sites in Norway. A near-melting point temperature of -0.5 °C is in agreement with published estimates of the subglacial thermal regime beneath the large polar ice sheets in Antarctica, which can be taken as comparable analogues of ice sheets developed during the Quaternary glacial cycles in northern Europe. The main features of the Antarctic subglacial conditions have been discussed by Pattyn (2010) who has shown that the mean ice basal temperature is in the range of -1-0 °C for the greater part of Antarctica. Besides, an airborne radar survey detected approximately 100 lakes under the Antarctic ice cap (Price et al. 2002), the largest of which, Lake Vostok, has already been drilled (Jones, 2012, Lake Vostok Drilling Project, 2014).

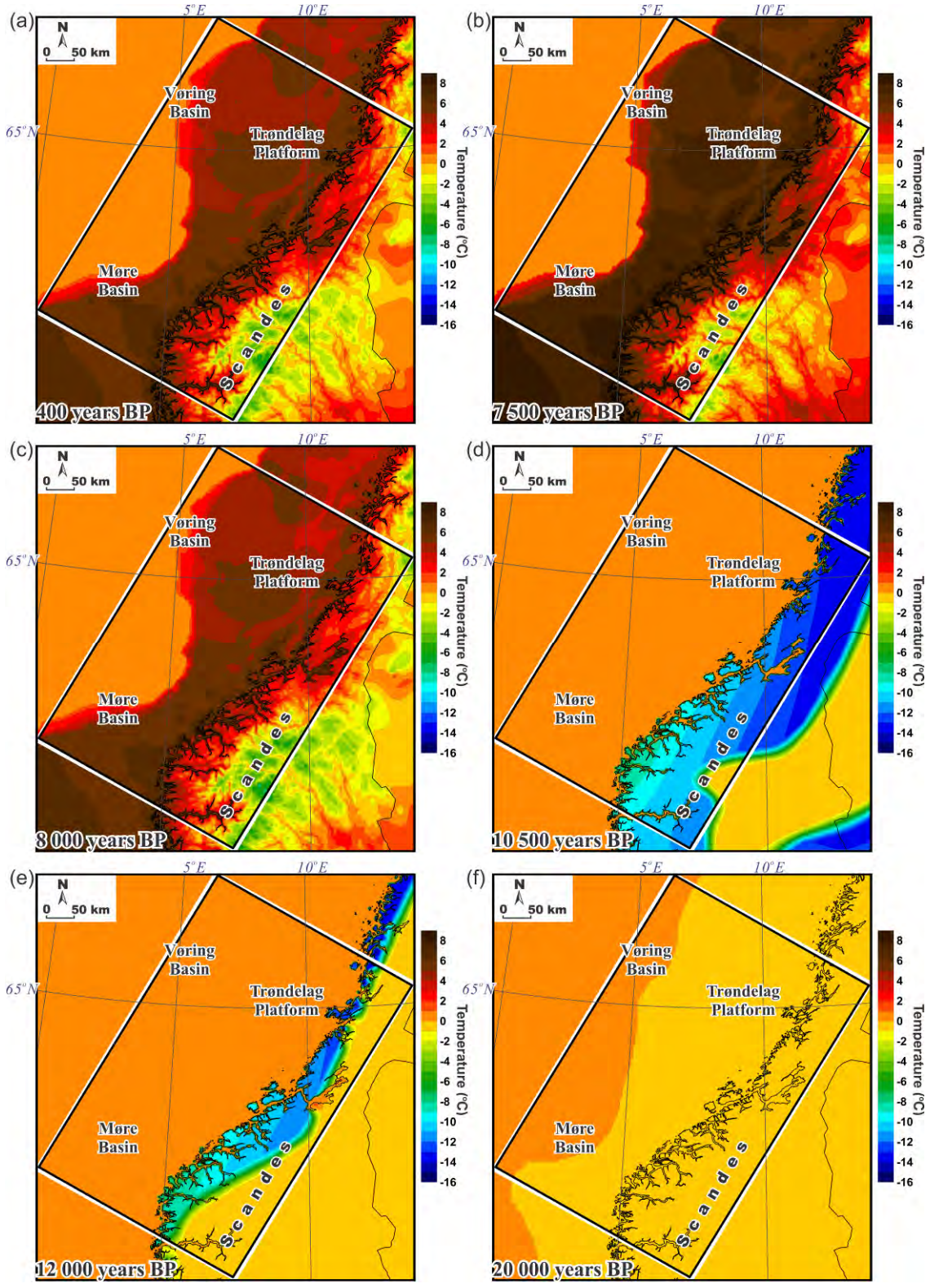

Figure 10.73. Annual average palaeotemperatures at the sea bottom and the Earth´s surface during the Weichselian glaciation (after Raab & Vedin 1995, Renssen & Isarin 1998, Tveito et al. 2000, Davis et al. 2003, Hohl 2005, Nesje et al. 2008, Mann et al.2009, Ottersen 2009, Seppä et al. 2009, Schmittner et al. 2011, ICES 2012, Eldevik 2014, Korablev 2014).

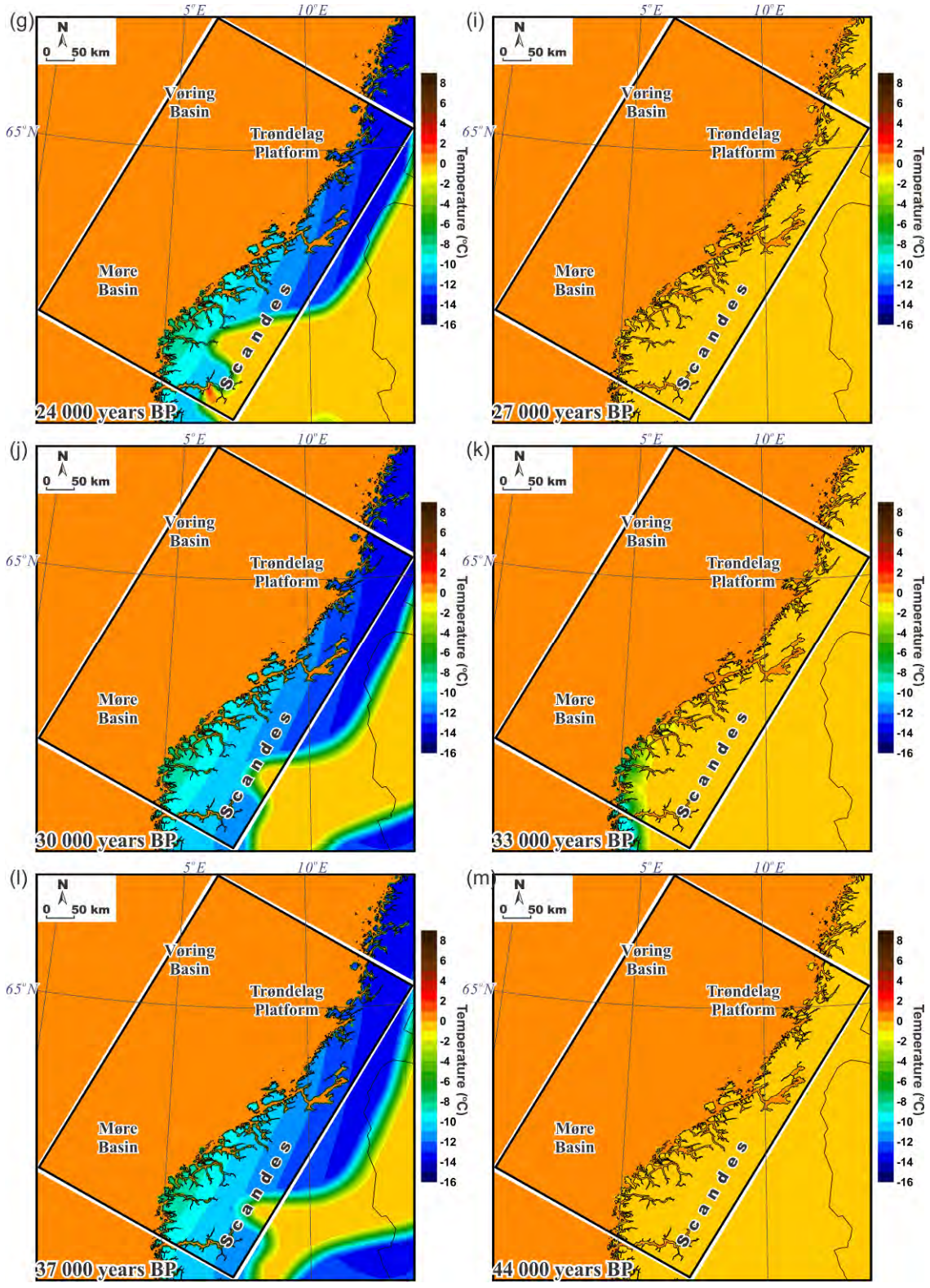

Figure 10.73. Continued. Annual average palaeotemperatures at the sea bottom and the Earth´s surface during the Weichselian glaciation (after Raab & Vedin 1995, Renssen & Isarin 1998, Tveito et al. 2000, Davis et al. 2003, Hohl 2005, Nesje et al. 2008, Mann et al.2009, Ottersen 2009, Seppä et al. 2009, Schmittner et al. 2011, ICES 2012, Eldevik 2014, Korablev 2014).

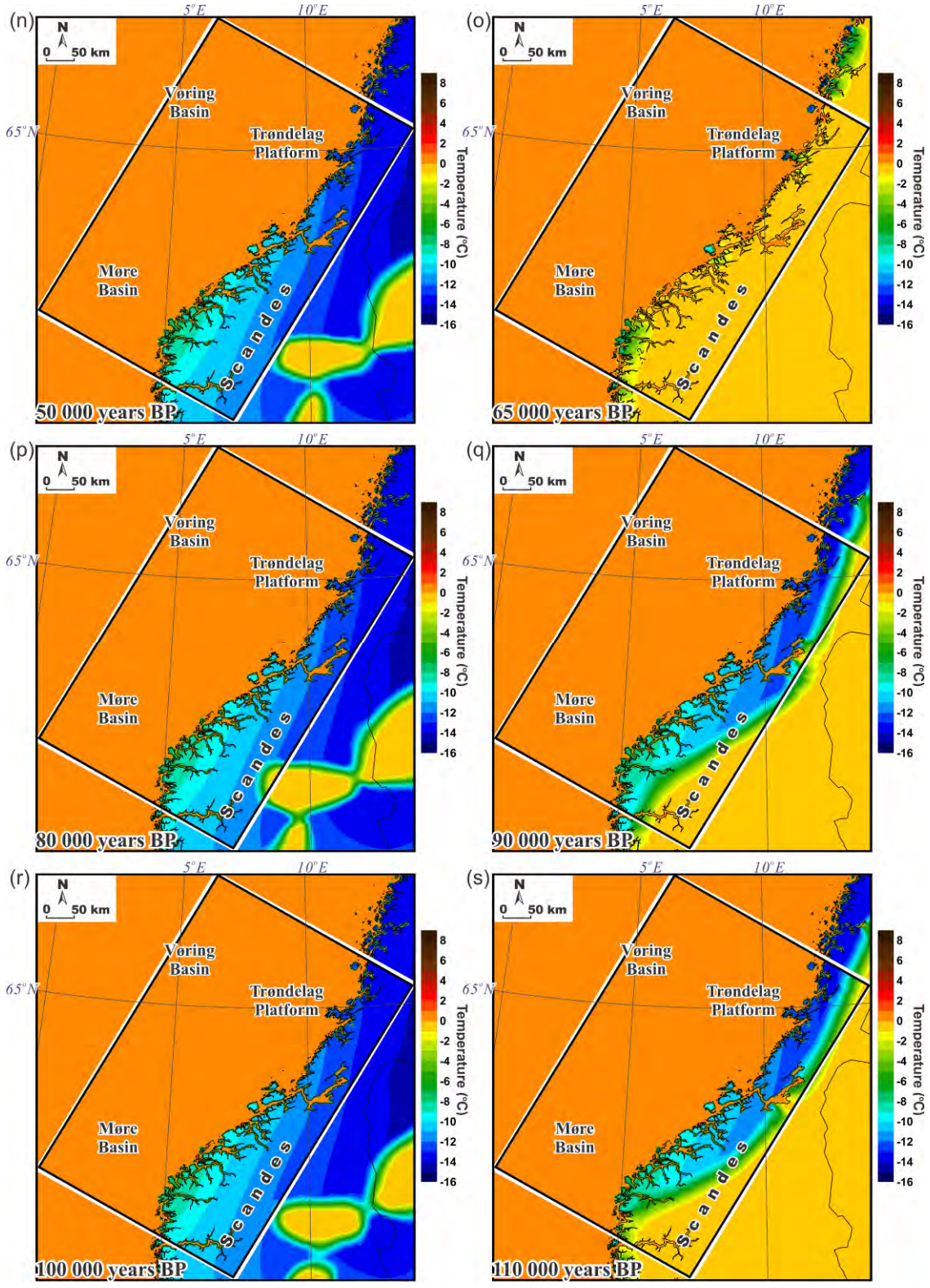

Figure 10.73. Continued. Annual average palaeotemperatures at the sea bottom and the Earth´s surface during the Weichselian glaciation (after Raab & Vedin 1995, Renssen & Isarin 1998, Tveito et al. 2000, Davis et al. 2003, Hohl 2005, Nesje et al. 2008, Mann et al.2009, Ottersen 2009, Seppä et al. 2009, Schmittner et al. 2011, ICES 2012, Eldevik 2014, Korablev 2014).

Paleotemperature at the sea floor has been taken as 0 °C which is in agreement with reconstructed temperature anomalies for the Norwegian Sea during the period 12,000-

23,000 years BP (Eldevik et al. 2014). According to Eldevik et al. (2014), the paleotemperatures were 6-7 °C less than the present-day temperatures within the Norwegian Sea.

In general, a more complex paleoclimatic scenario should be applied for time intervals when some parts of the Mid-Norwegian continental margin were free of ice and sea water. However, there are no obtainable regional-scale data on the position of shorelines within the study area and, therefore, possible local fluctuations of the sea level have not been considered during the 3D thermal modelling. This means that a real temperature near the coastline within the areas with shallow bathymetry can differ from the temperatures which have been obtained during the thermal simulations for the uppermost levels of the model.

For the Coop1 3D model, simulated mean annual temperatures for the Younger Dryas by Renssen & Isarin (1998) were used. Unfortunately, the greater part of the Coop2 study area is not covered by the simulated mean annual temperatures for the Younger Dryas by Renssen & Isarin (1998) and, therefore, paleotemperatures have been taken from Schmittner et al. (2011) who have modelled the annual mean surface temperatures during the Last Glacial Maximum. The estimated temperatures from Schmittner et al. (2011) are similar to other estimations of the surface temperatures during the Last Glacial Maximum (e.g., Otto-Bliesner & Brady 2006, Bartlein et al. 2010, Hofer et al. 2012, Ziemen et al. 2012), showing that the near-surface air temperature difference could be less than -20 °C compared to the pre-industrial period (present day before the industrial revolution). However, this estimation is only valid for the Last Glacial Maximum when the air temperatures were the lowest during the Weichselian glaciation and, in order to consider this fact, temperatures lower than -11 °C from Schmittner et al. (2011) have been reduced slightly by 1-4 °C to become more similar to the modelled mean annual temperatures for the Younger Dryas (Renssen & Isarin 1998) when the paleoclimate was warmer. Consequently, the reduced paleotemperatures from Schmittner et al. (2011) have been taken as representative temperatures at the Earth´s surface where the ice cover was absent. Temperatures along the marginal parts of the ice sheet are unknown in detail and, for that reason, these temperatures have been obtained by a simple interpolation between -0.5 °C beneath the internal parts of the ice cover and the derived temperature over the remaining land areas.

The reconstruction of the annual average palaeotemperatures at the sea bottom and the Earth´s surface demonstrates that the Coop2 3D model area is characterised by essentially lower palaeotemperatures during the Weichselian glaciation compared to the present day (cf. Figures 10.70 & 10.73). In particular, the surface temperature could be locally less than -15 °C over the continent where the ice cover was absent or very thin. These low negative temperatures imply the existence of permanently frozen ground during the glacial periods. From a theoretical point of view, the paleo-permafrost could have reached a depth of more than 1-2 km by analogy with present-day variations of the permafrost (e.g., Dobinski 2011).

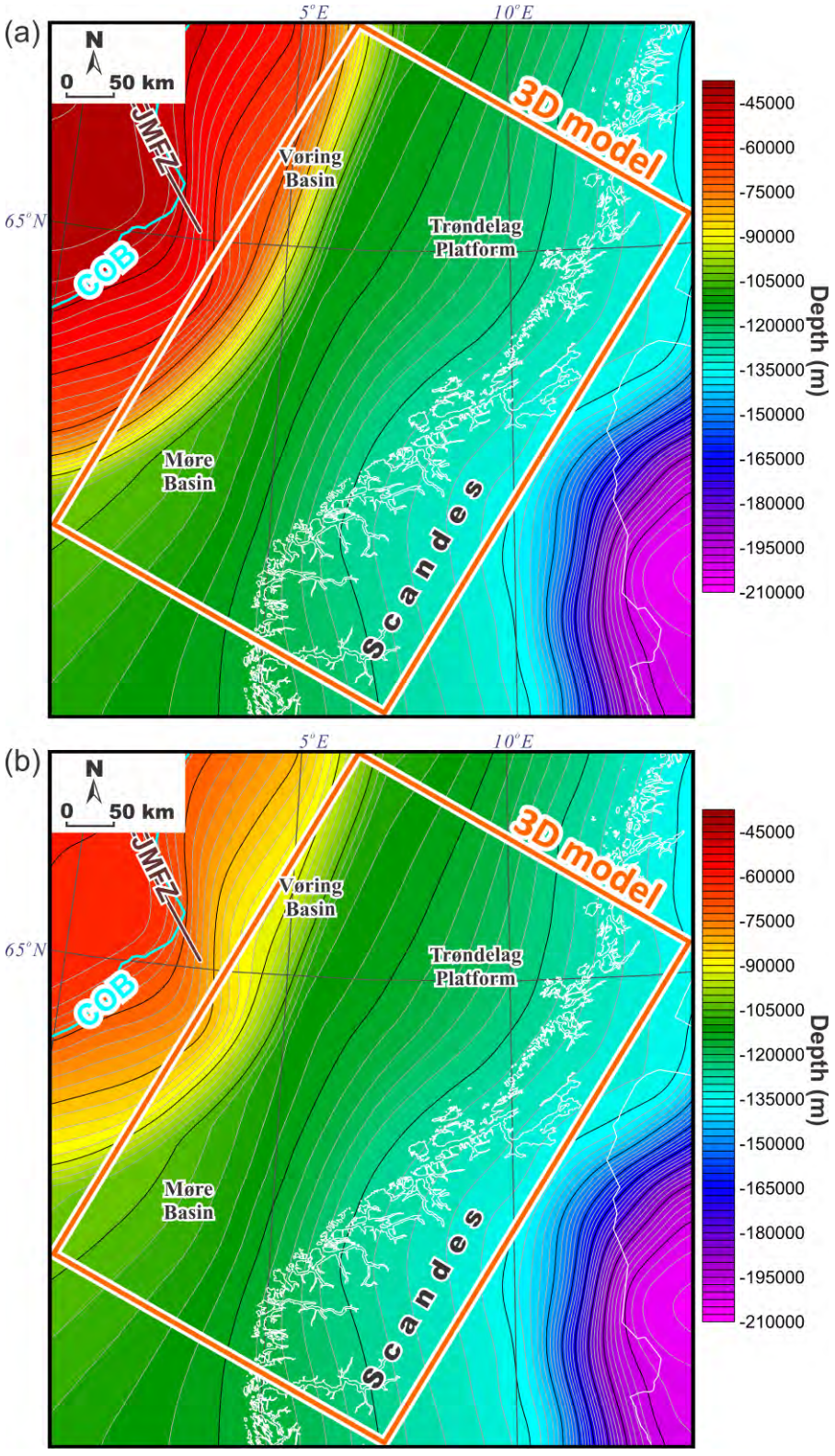

Figure 10.74. Lower thermal paleo-boundaries represented by rough estimations of the depth to the lithosphere-asthenosphere boundary in the vicinity of the oceanic crustal domain at the end of the Paleocene (a) and at the end of the Paleogene (b). COB - continent-ocean boundary (from Gernigon 2015; this report), JMFZ - Jan Mayen Fracture Zone (from Blystad et al. 1995).

In addition to the described paleoclimatic scenario, the influence of early Cenozoic continental breakup has been roughly taken into account during the 3D thermal modelling.

This has been done by including into the model two additional configurations of the lithosphere-asthenosphere boundaries, are at the end of the Paleocene (Figure 10.74a) and another at the end of the Paleogene (Figure 10.74b). The additional two paleopositions of the lithosphere-asthenosphere boundary in the vicinity of the oceanic crustal domain have been used to adjust the shallower position of the lower thermal boundary in the past compared to the present-day situation (cf. Figures 10.41 & 10.74). These two time-steps (55 Ma and 23 Ma years ago) provide an opportunity to include the effect of the increased geothermal gradient due to continental breakup in the early Cenozoic with subsequent cooling of the lithosphere in the vicinity of the oceanic domain during the rest of the Cenozoic. However, the position of the base of the lithosphere at the end of the Paleocene is not known in detail. On the other hand, most of numerical models predict a relatively shallow position of the 1300-°C -isotherm within the present-day axis of the oceanic spreading centre beneath the mid-oceanic ridges (e.g., Chen & Lin 2004). In the case of this study, the depth position of the lithosphere-asthenosphere boundary at the end of the Paleocene has been set to be around 14-15 km deeper beneath the present-day oceanic domain, representing the formation of new oceanic lithosphere there. Moreover, the depth position of the base of the lithosphere, which is deeper than 85-95 km, has been kept constant beneath the mainland and over a large part of the continental margin. The depth to the lithosphere-asthenosphere boundary between the oceanic domain and the more than 85-95 km-deep continental lithosphere has been obtained by linear interpolation, assuming that the adjacent continental lithosphere has also been thinned in the vicinity of the oceanic domain (Figure 10.74a). The lithosphere-asthenosphere boundary at the end of the Paleogene (Figure 10.74b) has been calculated as a half of the difference between the present-day base of the lithosphere (Figure 10.41) and the base at the end of the Paleocene (74a) within the oceanic domain and the adjacent continental part. However, there are definitely some large uncertainties in these estimations of the paleo-depths to the base of the lithosphere in Figure 10.74. Therefore, these paleo-configurations of the lithosphere-asthenosphere boundary are rough approximations of the thinner lithosphere in the past after the continental breakup rather than more accurate data-constrained ones. The next factor involving the thermal disturbance of the study area in the vicinity of the oceanic domain is related to the syn-breakup magmatism represented by the lower-crustal underplating, middle-upper-crustal dykes and surface volcanic activity. The problem is that magmatic activity can locally increase the geothermal gradient but the process itself is very complex and requires more detailed investigations which are outside the scope of the present study. For that reason, an influence of the syn-breakup magmatic activity has been neglected in the present study.

In addition to the above factors, an influence of the post-breakup deposition of the Brygge and Naust-Kai formations has been roughly included into the 3D thermal modelling by setting the upper thermal boundary to the base of the Brygge at the end of the Paleocene and to the base of the Naust-Kai at the end of the Paleogene. This helps in considering the transient perturbations in the near-surface thermal regime as a result of the post-Paleocene sedimentation. However, the effect of the simultaneous erosion over the mainland has not been considered because additional data would be required to constrain a differentiation of the erosional rate in time and space within the continental mainland.

10.5.3 Thermal properties

Prior to the 3D thermal modelling, thermal properties represented by specific heat capacity, thermal conductivity and radiogenic heat production have been assigned for each layer of the 3D model (Table 10.7).

The values of a thermal conductivity for the sedimentary cover are represented by the scale values which are close to the thermal conductivity of the matrix. These thermal conductivities have been mostly derived from the previous estimations of the matrix thermal conductivity within the northern Viking Graben (Brigaud et al. 1992) and in the wells which are located within the Mid-Norwegian continental margin (Pascal & Midttømme 2006, Pascal 2015), and are also based on sampling the unconsolidated sediments from the Vøring Basin (Midttømme et al. 1995). In addition, the obtained porosity- and temperature-dependent thermal conductivities of sediments have been cross-validated with the measured thermal conductivities from the North Sea (Evans 1977), laboratory measurements of rock samples with similar lithology (Čermak & Rybach 1982, Clauser 2011) and a comprehensive overview of thermal conductivities of the sedimentary rocks (Midttømme & Roaldset 1999). The thermal conductivity of basalts (layer 5) has been set to be 1.8 W/mK on average according to Balling et al. (2006) who measured thermal conductivity of basalts and tuffs for the depth interval of more than 3000 m in the Lopra-1/1A borehole on the Faroe Islands. Thermal conductivities of the upper crystalline crustal rocks have been set to be in the range of the rock-sample measurements within the Norwegian mainland (e.g., Slagstad et al. 2009, Maystrenko et al. 2015). The mentioned thermal conductivities of the sedimentary infill, basalts and upper-crustal rocks have been supplemented with published values for the deeper crystalline crust and the lithospheric mantle (Čermak & Rybach 1982, Wollenberg & Smith 1987, Hofmeister 1999, Artemieva et al. 2006, Scheck-Wenderoth & Maystrenko 2008, 2013, Maystrenko et al. 2014, 2015).

During the present study, the thermal conductivities of rocks have been set to be dependent on temperature. In the case of sediments, the thermal conductivity is additionally dependent on compaction. This has been done in order to consider a significant change in the thermal conductivities of rocks and groundwater as a result of increasing temperature and decreasing porosity of sediments with depth. In fact, the conductive heat transfer is very responsive to variations in values of thermal conductivities because the thermal conductivity represents the rate at which heat is conducted through a material.

Temperature-dependent values of the thermal conductivities for the uppermost crystalline crust have been calculated according to the empirical equations (10.8) and (10.9) from Sass et al. (1992):

$$k(T) = k_o / (1.007+T(0.036-0.0072/k_o)) \quad (10.8)$$

$$k_o = k_r(1.007+25(0.0037-0.0074/k_r)) \quad (10.9)$$

where k(T) is the thermal conductivity [W/mK] at temperature T in [°C], k(0) is the thermal conductivity [W/mK] at 0 °C, k_r is the thermal conductivity [W/mK] at room temperature and T is the temperature [°C].

The empirical equations (10.10) and (10.11) from Vosteen & Schellschmidt (2003) have been used to calculate the temperature-dependent thermal conductivities for the rest of the crystalline crust where temperature is higher than 300 °C:

$$k(T) = k_o / (0.99+T(a-b/k_o)) \quad (10.10)$$

where k(T) is the thermal conductivity of crystalline rocks [W/mK] at temperature T in [K], k_o is the thermal conductivity [W/mK] at 0 °C, k_r is the thermal conductivity [W/mK] at room temperature, T is the temperature [K], a and b are constants: a = 0.0030±0.0015 and b = 0.0042±0.0006.

$$k_o = 0.54k_r + 1/2(1.16(k_r)^2-0,39k_r)^{1/2} \quad (10.11)$$

where k_o is the thermal conductivity of crystalline rocks [W/mK] at 0 °C and k_r is the thermal conductivity [W/mK] at room temperature.

To define the temperature- and pressure-dependent thermal conductivities within the lithospheric mantle, the empirical equations (10.12) and (10.13) from Hofmeister (1999) have been taken:

$$k(T,P) = k_r(298/T)^a exp[-(4\gamma+1/3)\alpha(T-298)](1+K'_oP/K_o) + k_{rad} \quad (10.12)$$

$$k_{rad} = 4.7(0.01753-0.00010365T+2.2451T^2/10^7-3.407T^3/10^{11}) \quad (10.13)$$

where k(T,P) is thermal conductivity [W/mK] at temperature T in [K] and under pressure in [Pa], k_r is the thermal conductivity [W/mK] at room temperature, T is the temperature [K], γ is Grueneisen parameter (γ =1 to 1.4), a is the phonon fitting parameter (a = 0.25 to 0.45), α(T-298) is the volume coefficient of thermal expansion as a function of temperature, K_o is the bulk modulus [Pa](K_o=261 GPA), K'_o is the pressure derivative of the bulk modulus (K'_o=5) and k_{rad} is the radiative component of the thermal conductivity, enhanced according to van den Berg et al. (2001).

In addition, the empirical equation (10.10) has been used to calculate the temperature-dependent thermal conductivities for the solid material (porous matrix) of the sedimentary cover. In this case, constants a and b vary within the following range: a = 0.0034±0.0006 and b = 0.0039±0.0014.

$$k_o = 0.53k_r + 1/2(1.13(k_r)^2-0,42k_r)^{1/2} \quad (10.14)$$

where k_o is the thermal conductivity of sedimentary rocks [W/mK] at 0 °C and k_r is the thermal conductivity [W/mK] at room temperature.

Table 10.7. Thermal properties of the layers of the 3D structural model used during the 3D thermal modelling (lithology of sediments is derived from Bell et al. (2014) and from NPD (2014)).

N	Layer of the 3D structural model	Dominant lithology	Specific heat capacity C_p [J/kgK]	Thermal conductivity scale value k_r [W/mK]	Radiogenic heat production S [$\mu W/m^3$]
2	Naust and Kai	92% shale, 8% sandstone	1180	3.1	0.5-1.5
3	Brygge	98% shale, 2% sandstone	1180	3.1	0.47-1.5
4	Paleocene	80% shale, 20% sandstone	1180	3.6	0.6-1.39
5	Oceanic layer 2AB	Basalts and tuffs	880	1.8	0.4
6	Upper Cretaceous	95% shale, 5% sandstone	1180	3.0	0.7-1.68
7	Lower Cretaceous	92% shale, 3% sandstone, 5% limestone	1180	3.1	0.81-1.83
8	Pre-Cretaceous	80% shale, 20% sandstone	1180	3.6	0.8-1.64
9	Upper-crustal high-density crystalline rocks	gabbro to anorthositic rocks, metamorphic rocks	880	2.9	0.4
10	Low-density upper-crustal body	metasediments or granite	880	3.0	0.4-2.2
11	Upper-crustal regional layer	granite and gneiss	880	3.2	1.5 (0.9-2.5)
12	Middle crust	granitoids and/or gneiss	950	3.1	0.9 (0.4-2.5)
13	Lower crust	metamorphic rocks	1050	3.0 (3.00-3.20)	0.32 (1.3-3.3)
14	High-density crust	mafic granulites, gabbros	1050	3.0 (2.95-3.35)	0.32 (0.3-3.0)
15	High-density lower-crustal layer	gabbros, high-grade metamorphic rocks	1100	2.8 and 3.2	0.2
16	Lithospheric upper mantle	peridotite	1200	4.79	0.03

In addition, the thermal conductivity of the sedimentary rocks has also been set to be dependent on compaction by introducing the equivalent thermal conductivity. The thermal conductivity of the solid-fluid system k_{eq} is the so-called equivalent thermal conductivity and can be inferred by use of this equation:

$$k_{eq} = \theta_s k_s + \theta_f k_f \qquad (10.15)$$

where k_s is the thermal conductivity of the solid material (porous matrix) and k_f is the thermal conductivity of the fluid (water in the case of the present study), θ_s is the solid material's volume fraction, which is related to the volume fraction of the fluid θ_f as in the following:

$$\theta_s + \theta_f = 1 \qquad (10.16)$$

Table 10.8. Dominant lithology and matrix densities (according to Sclater & Christie 1980) of sedimentary layers.

N	Sedimentary layer	Dominant lithology (according to Bell et al. 2014 and NPD 2014)	Matrix density ρ_r (kg/m^3)
1	Naust and Kai	92% shale, 8% sandstone	2711
2	Brygge	98% shale, 2% sandstone	2719
3	Paleocene	80% shale, 20% sandstone	2706
4	Upper Cretaceous (post-Cenomanian)	95% shale, 5% sandstone	2717
5	Lower Cretaceous (pre-Cenomanian)	92% shale, 3% sandstone, 5% limestone	2717
6	Pre-Cretaceous	80% shale, 20% sandstone	2706

The thermal conductivity of the fluid in the pores of sedimentary rocks has been taken as the temperature-dependent thermal conductivity of water based on the thermodynamic properties of water and steam according to the International Association for Properties of Water and Steam Industrial Formulation 1997 (Wagner & Kretzschmar 2008).

The volume fraction of the fluid θ_ϕ is represented by porosity. Porosities of sedimentary rocks have been calculated according to Sclater & Christie (1980). Therefore, porosity Φ is assumed to decrease with depth according to the equation (10.17):

$$\Phi = 1 - \rho(z)/\rho_r \qquad (10.17)$$

where Φ is the porosity, $\rho(z)$ is depth-dependent density [kg/m^3] which is specified for each layer according to equations (10.2-10.5), z is depth [m], and ρ_r is matrix density [kg/m^3] from Table 10.8. Matrix density has been calculated according to the lithological composition of rocks derived from Bell et al. (2014) and from NPD (2014) based on the parameters for each lithology from Sclater & Christie (1980) and is given in Table 10.8.

It is important to note that densities of the sedimentary cover have been set to be reduced within the Jan Mayen gravity low compared to the rest of the study area. This has been done in accordance with the results of 3D density analysis and, therefore, the calculated thermal conductivities are also reduced within the Jan Mayen gravity low.

In contrast, porosities of the crystalline rocks have been neglected during the 3D thermal modelling because porosities of the these rocks are extremely low compared to the sediments. For instance, according to the porosity measurements of crystalline rocks in Sweden (Tullborg & Larson 2006), porosities of crystalline rocks vary from 1.5% at the relatively shallow level to 0.98% in the deep crust. Therefore, the influence of these low porosities can be ignored for the thermal conductivities of crystalline rocks during purely conductive heat transfer due to the fact that uncertainties in values of the thermal conductivities of the rock matrix are much larger than the effect of thermal conductivities of fluids in these very small pores. Consequently, densities of the crystalline rocks have been taken from the results of the 3D density modelling (Table 10.2). Using average constant densities for each crystalline layer is a reasonable way to represent the major structural features of the crystalline crust which is characterised by an extremely low porosity (typically less than 1-2%; e.g., Tullborg & Larson 2006).

The assigned values of the specific heat capacity have also been set to be constant during the 3D thermal modelling (Table 10.7) and have been derived mainly from values published in Clauser (2011). For the specific heat capacity of rock matrix, the dependence on temperature has been considered in terms of significant changes by assigning the average values for the layers at different temperature intervals, depending on the depth of the layer. These temperature-dependent average values of the specific heat capacity have been derived from the literature based on laboratory measurements at different temperature conditions (e.g., Čermak & Rybach 1982, Fernandez et al. 2005, Clauser 2011).

The used radiogenic heat productions of the upper and middle-crustal layers are derived mainly from average values which are calculated from airborne gamma spectrometry surveys and/or based on average heat production for geological units in Norway according to rock sample measurements (Slagstad 2008, Slagstad et al. 2009, Slagstad & Lauritsen 2013, Lauritsen 2015; this report). The values of the radiogenic heat production for the lower-crustal layers and the lithospheric mantle have been considered to be constant (Table 10.7). The problem is that in the case of the radiogenic heat production, there is no accurate mathematical way to predict the content of radiogenic elements within the deep crustal layers. The radiogenic heat production is mostly dependent on the specific lithological composition of the layer rather than on depth, pressure and/or temperature. There is only a general tendency for a decreasing content of the radiogenic elements with depth. In this case, the average constant values of the radiogenic heat production have been used

according to published values for the assumed lithological composition of the layers (e.g., Čermak & Rybach 1982, Scheck-Wenderoth & Maystrenko 2008, Vila et al. 2010).

In order to obtain a better fit between the observed and modelled temperatures in the available boreholes offshore, differentiation of the radiogenic heat production has been applied for the low-density upper-crustal body (layer 10; Figure 10.75), upper-crustal regional layer (layer 11; Figure 10.76) and middle crust (layer 12; Figure 10.77). The variable radiogenic heat production is one of the most suitable candidates which can be responsible for local changes of temperatures measured in the borehole. On the other hand, some other possible reasons for local changes of the measured temperature should not be excluded, such as enforced fluid flow (convection and/or advection), significant variations in thermal conductivities, structural uncertainties and limited horizontal resolution of the 3D model. However, these additional reasons require supplementary structural data, sampling material and including extra physical processes (e.g., fluid flow) into the 3D thermal modelling workflow. More to the point, an absence of reliable data and difficulties in the 3D modelling approach do not allow us to test the above-mentioned reasons during the present study. Moreover, relatively strong variations in the radiogenic heat production of the crystalline rocks within the mainland (e.g., Slagstad & Lauritsen 2013) provide a possibility to assume that a similar situation can also obtain within the crystalline rocks offshore. Consequently, the variable radiogenic heat production within the crystalline crust is the most reasonable and easily applicable procedure for the 3D thermal modelling technique. Several testing models with different values of the radiogenic heat production have been generated and validated during the 3D thermal modelling to obtain a reasonable fit between the modelled and measured temperatures in the available boreholes.

In particular, the low-density upper-crustal body (layer 10) has been subdivided into two blocks with different radiogenic heat production (Figure 10.75a). The southwesternmost part of this layer has been assigned a radiogenic heat production of 2.2 $\mu W/m^3$ that is similar to the value (2.0 $\mu W/m^3$) used in the Coop1 3D thermal model (Maystrenko 2014). In contrast, the rest of this layer has been set to have a reduced value (0.4 $\mu W/m^3$) of radiogenic heat production, implying possible lithological changes within this layer towards the northeast.

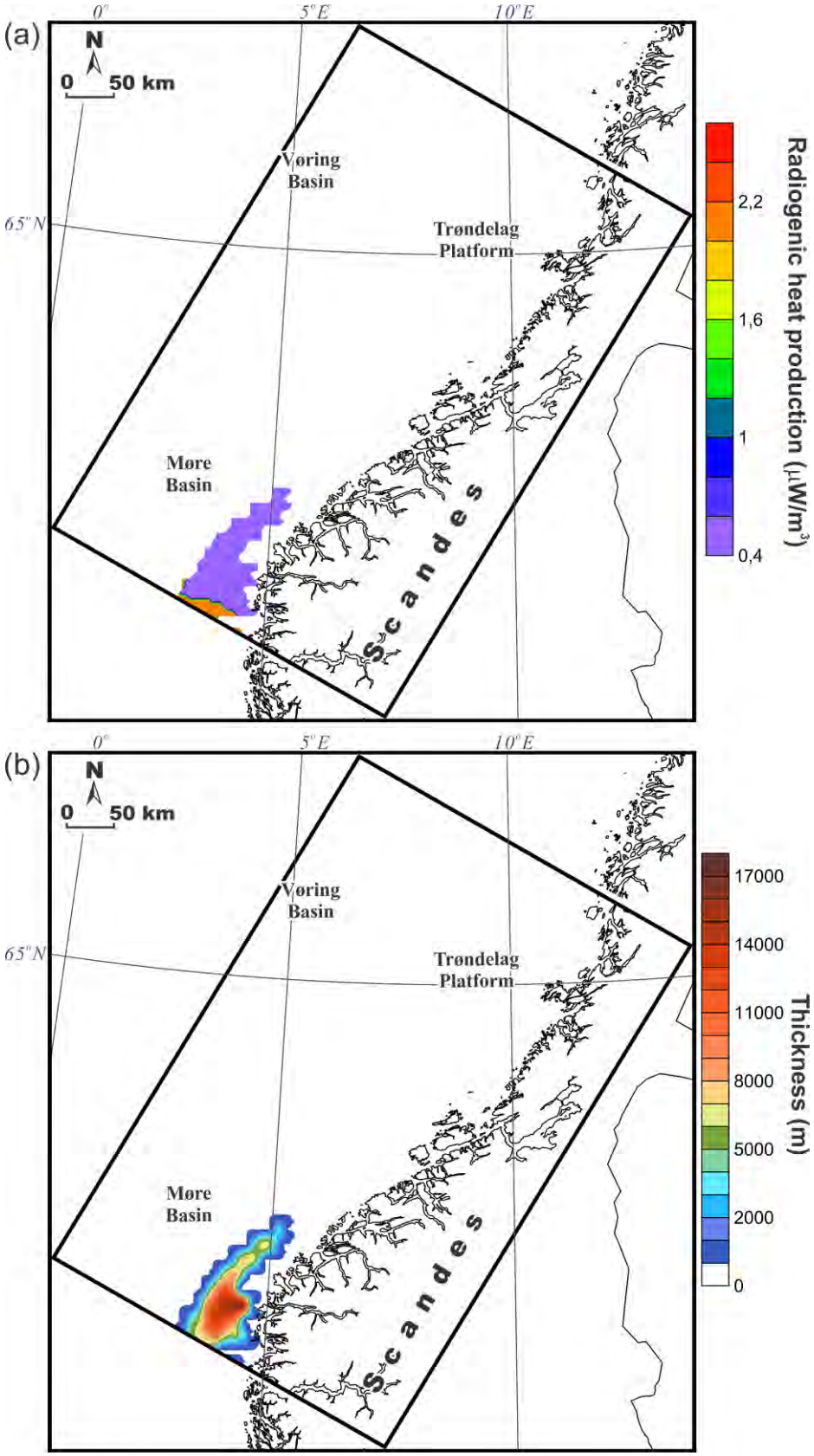

Figure 10.75. (a) Radiogenic heat production and (b) thickness map of the low-density upper-crustal body (layer 10).

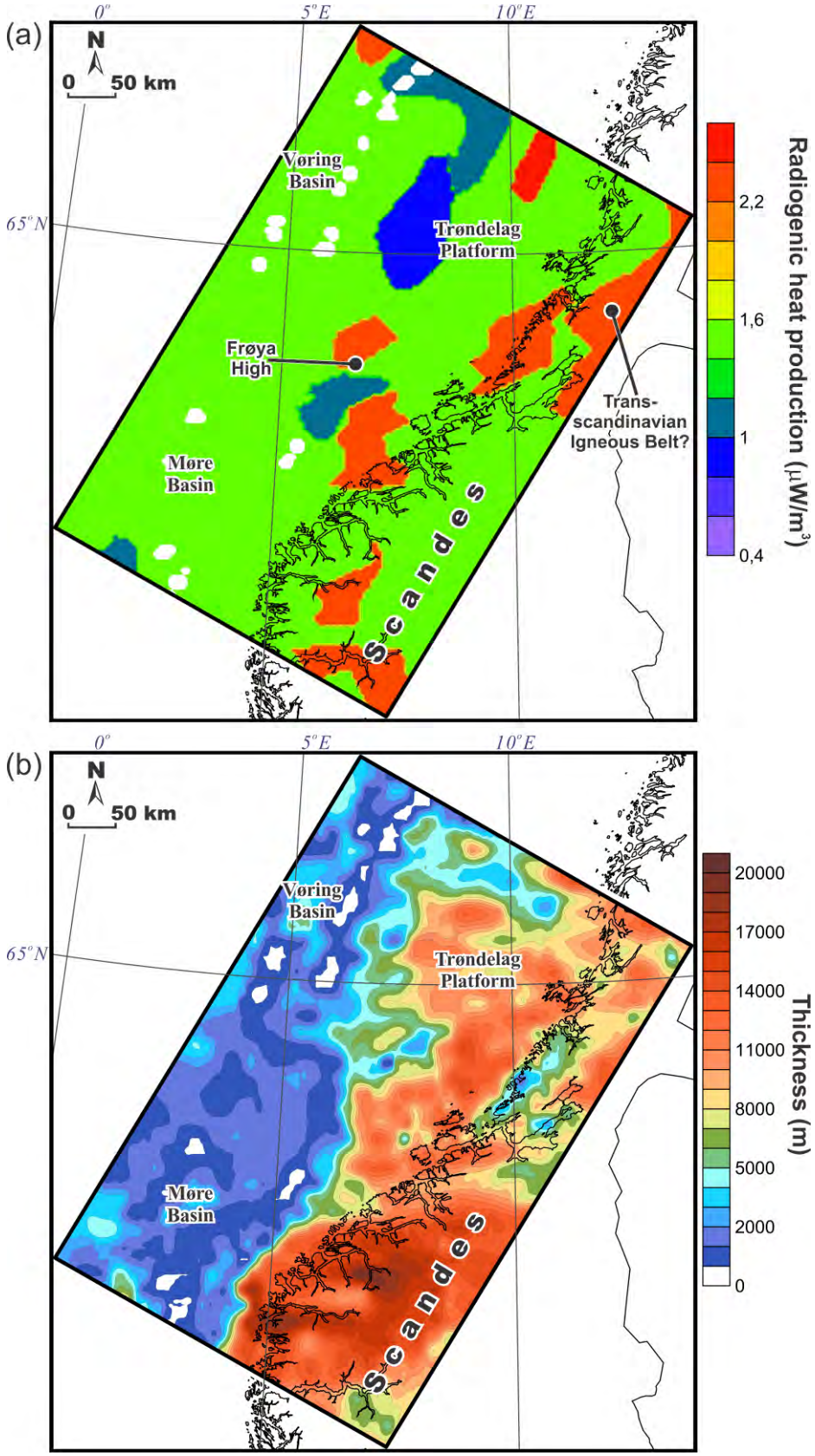

Figure 10.76. (a) Radiogenic heat production and (b) thickness map of the regional upper-crustal layer (layer 11).

The upper-crustal regional layer (layer 11) is characterised by a relatively complex pattern of the assigned values of radiogenic heat production (Figure 10.76a). Different blocks with

increased or decreased values of radiogenic heat production have been defined mainly based on the results of the 3D magnetic modelling (cf. Figures 10.56 & 10.76a). The block with increased radiogenic heat production within the northeastern part of the Coop2 model area is most likely related to the Transscandinavian Igneous Belt which is mainly composed of granitoid rocks (Åhäll & Larson 2000). Based on more than 500 samples (Slagstad et al. 2008), the Transscandinavian Igneous Belt has a median heat production of 2.57 $\mu W/m^3$. In the case of the present study, a lower value of 2.2 $\mu W/m^3$ compared to the median heat production (Slagstad et al. 2008) has been assigned to the Transscandinavian Igneous Belt. This lower value of the radiogenic heat production has been chosen to represent a possible decrease of radiogenic heat production with depth within the Transscandinavian Igneous Belt. To the west of the Transscandinavian Igneous Belt, a second block with anomalous magnetic susceptibility has been set to have an increased value of radiogenic heat production (2.2 $\mu W/m^3$) and can also be associated with the Transscandinavian Igneous Belt which is covered by the relatively thick Caledonides represented by the upper-crustal high-density crystalline rocks (layer 9) in that area (cf. Figures 10.33, 10.54 & 10.76a).

The two blocks within the southeastern corner of the Coop2 study area (Figure 10.76a) are probably related to granitoids which are in general characterised by relatively high contents of the radiogenic elements responsible for the increased values of radiogenic heat production towards the south from the Coop2 study area (e.g., Killeen & Heier 1975, Wilson et al. 1977, Slagstad & Lauritsen, 2013).

The Frøya High and the neighbouring, magnetically anomalous, upper-crustal blocks (Figure 10.56) have been subdivided into three blocks (Figure 10.76a): two blocks with increased radiogenic heat production (2.2 $\mu W/m^3$) and one block in between with decreased heat production (1.2 $\mu W/m^3$).

A speculative small block with on increased radiogenic heat production (2.5 $\mu W/m^3$) has been set within the northern part of the Trøndelag Platform (Figure 10.76a) in order to raise the modelled temperatures. However, this upper-crustal block is not reflected by either gravity or magnetic data and, thus, there is possibly another reason for the increased measured temperatures in that area.

The transition zone from the Trøndelag Platform to the Vøring Basin is characterised by the presence of the hypothetical zone with very low values of radiogenic heat production, ranging from 0.9 to 1.1 $\mu W/m^3$.

In addition, a small crustal block with increased radiogenic heat production (2.2 $\mu W/m^3$) has been included into the regional upper-crustal layer in the northwestern corner of the model area and a small block with decreased radiogenic heat production (1.0 $\mu W/m^3$) has been set within the southern part of the Møre Basin (Figure 10.76a).

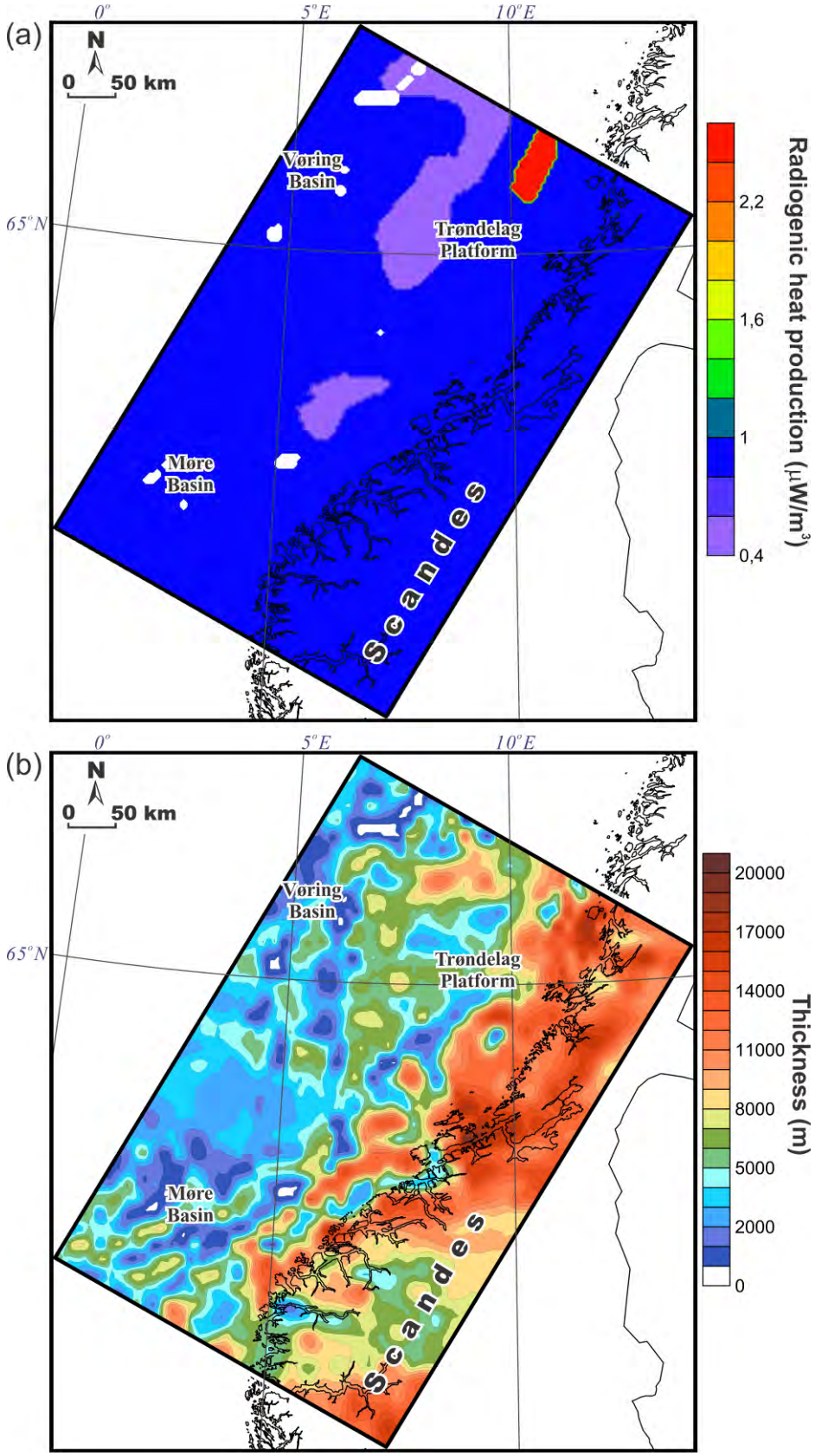

Figure 10.77. (a) Radiogenic heat production and (b) thickness map of the of the middle crust (layer 12).

A differentiation of the middle crust (layer 12) in terms of the radiogenic heat production has been achieved only in places where either a decreased or increased heat production has been assigned to the previously described layer (layer 11, cf. Figures 10.76a & 10.77a).

Consequently, the block with increased values of radiogenic heat production (2.5 μW/m^3) has been hypothetically distinguished within the northern part of the Trøndelag Platform, and crustal blocks with the reduced property (0.4-0.6 μW/m^3) are located at the transition from the Trøndelag Platform to the Vøring Basin and in the vicinity of the Frøya High (Figure 10.77a). It is important to mention that the necessity to include these middle-crustal blocks with the variable radiogenic heat production is partially related to the fact that the regional upper-crustal layer is locally not thick enough to reduce the misfit between the measured and modelled temperatures, if a more or less realistic heat production has been assigned to this layer.

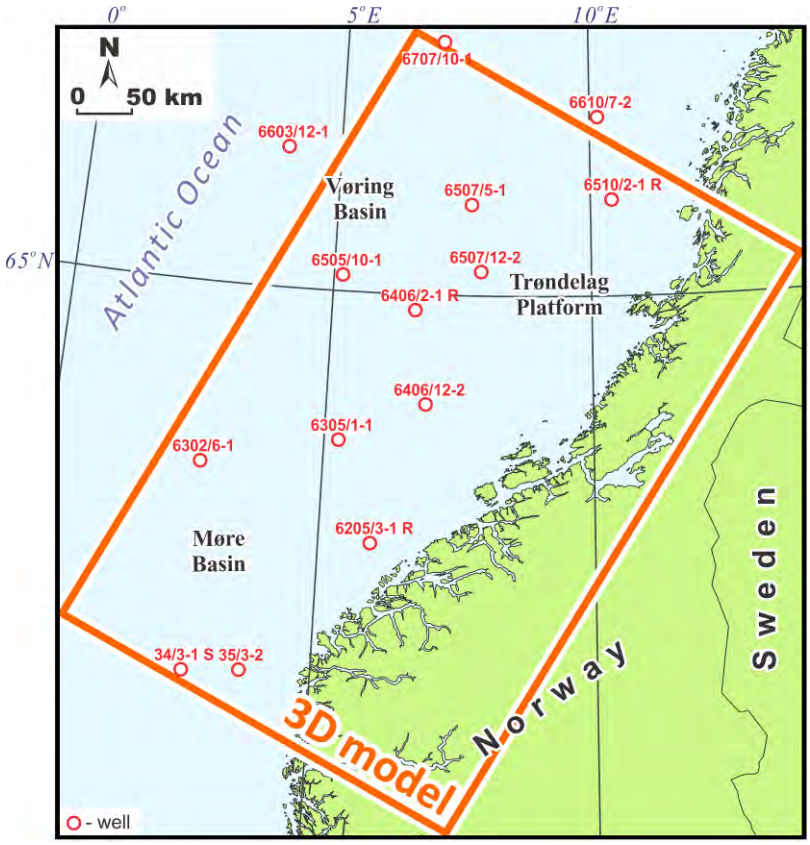

Figure 10.78. Location of the wells used to estimate the radiogenic heat production of sedimentary layers in the Coop2 3D model.

Moreover, there is not really enough room to set the radiogenic heat production for differentiated blocks within the crystalline crust beneath the Vøring and Møre basins for one simple reason - the crystalline crust is very thin there (Figure 10.40a). On the other hand, the sedimentary cover is extremely thick in that area as well as in the Trøndelag Platform. Therefore, radiogenic heat production of sedimentary rocks could play an important role as an additional heat source in the 3D thermal model of the Mid-Norwegian continental margin. According to studies within other sedimentary basins of the world, the radiogenic heat production of sediments can vary significantly. For instance, heat production varies from approximately 0.07 μW/m^3 to about 2.21 μW/m^3 in the Gulf of Mexico (McKenna & Sharp 1998) and has an average range of 0.4-2.1 μW/m^3 in the Northeast German Basin (Norden & Förster 2006). The radiogenic heat production of sediments can therefore be relatively high and has to be considered in a proper way during the 3D thermal modelling.

In the case of the present study, all sedimentary layers of the 3D model have been assigned by variable radiogenic heat production values in order to differentiate the layer into different parts with specified radiogenic heat production. This kind of differentiation provides a support for including more realistic values of radiogenic heat production within the sedimentary cover based on the results of gamma-ray logging in the selected wells which are shown in Figure 10.78. These wells have been chosen to cover the whole model area, giving a range of values which are assumed to be representative for the neighbouring area in the vicinity of each well. The average values of the radiogenic heat production for every sedimentary layer have been derived (Table 10.9) based on the calculated values in Figure 10.79. Finally, the average radiogenic heat production has been used to produce maps by interpolation between the existing values in the wells (Figures 10.80-10.85). It is obvious that a larger number of the analysed wells would lead to more consistent maps. However, the procedure for the obtaining data for each well is time-consuming and could not be done in any detail in the present study. Moreover, the selected wells are located within different parts of the study area and, therefore, these wells are cosidered to be representative enough for this kind of regional study.

In order to obtain values of the radiogenic heat production for sedimentary rocks, natural gamma ray logs have been collected from the NPD web site and were ultimately digitised (Figure 10.79). The empirical relationship between total natural gamma and radiogenic heat production (18) from Bücker & Rybach (1996) has been applied to calculate the radiogenic heat production of the sedimentary infill in the selected wells (Figure 10.78).

$$S=0.0158\,(GR-0.8) \qquad (18)$$

where S is the radiogenic heat production (μW/m3) and GR is the total gamma (API units). The results of the calculation are scaling values of the radiogenic heat production rather than precise ones. Actually, the empirical relationship (18) has been derived by Bücker & Rybach (1996) based on the data from the following boreholes: Soultz-Sous-Forêts, Sancerre-Couy and BALAZUC- I, France; KTB, Germany; ODP 834B, Ocean Drilling Program; and three different NAGRA boreholes (Switzerland). The 160 data points cover the range of 0-350 API. In the case of the sedimentary cover of the Mid-Norwegian continental margin, values of the total natural gamma are mainly in the range 0-150 API (Figure 10.79) and, therefore, the results of the calculation should provide values for the radiogenic heat production which are reasonably realistic.

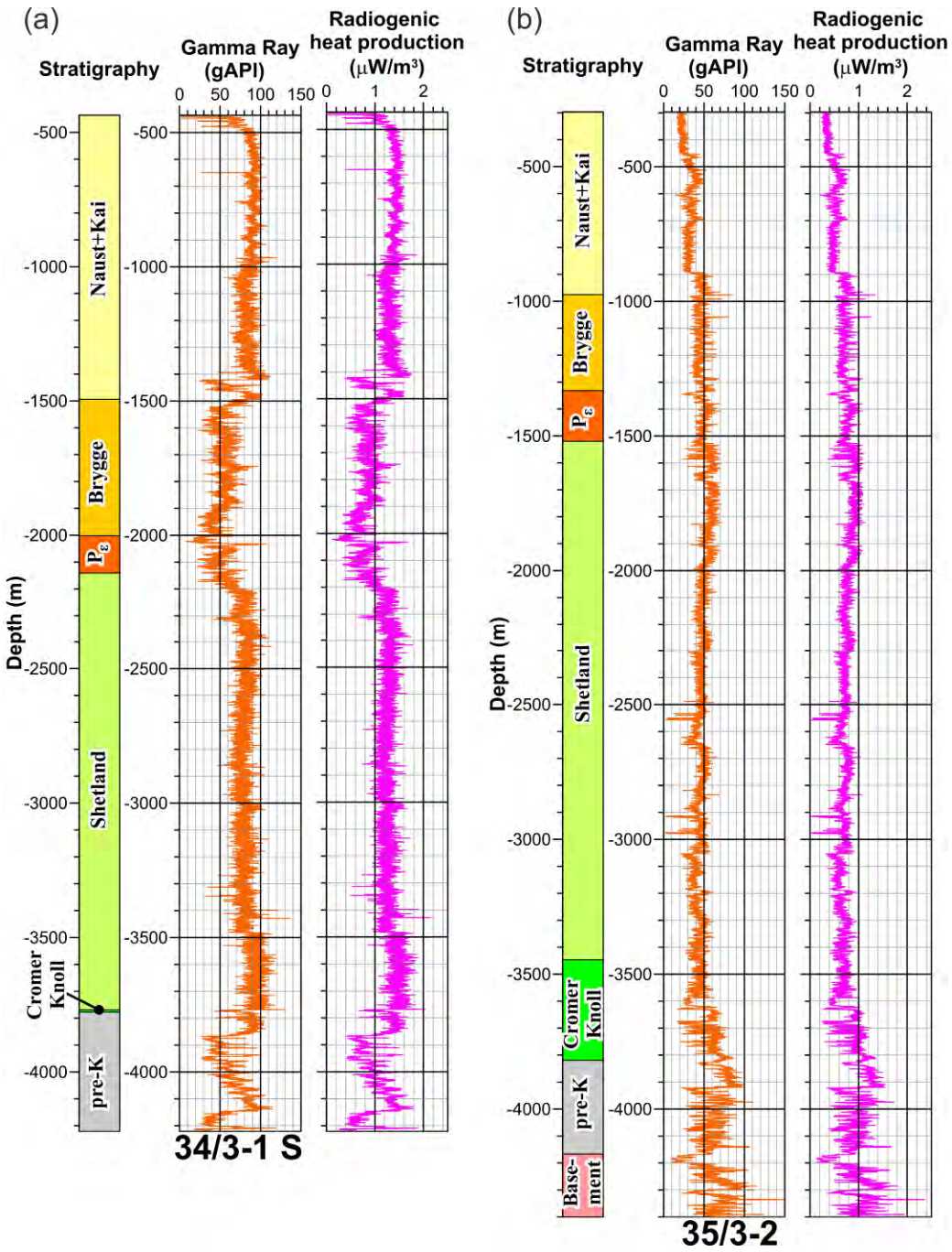

Figure 10.79. Plot showing stratigraphy, measured total natural gamma and derived radiogenic heat production for the wells shown in Figure 10.78. (a) 34/3-1 S, (b) 35/3-2, (c) 6205/3-1 R, (d) 6302/6-1, (e) 6305/1-1, (f) 6406/2-1 R, (g) 6406/12-2, (h) 6505/10-1, (i) 6507/5-1, (j) 6507/12-2, (k) 6510/2-1 R, (l) 6603/12-1, (m) 6610/7-2 and (n) 6707/10-1.

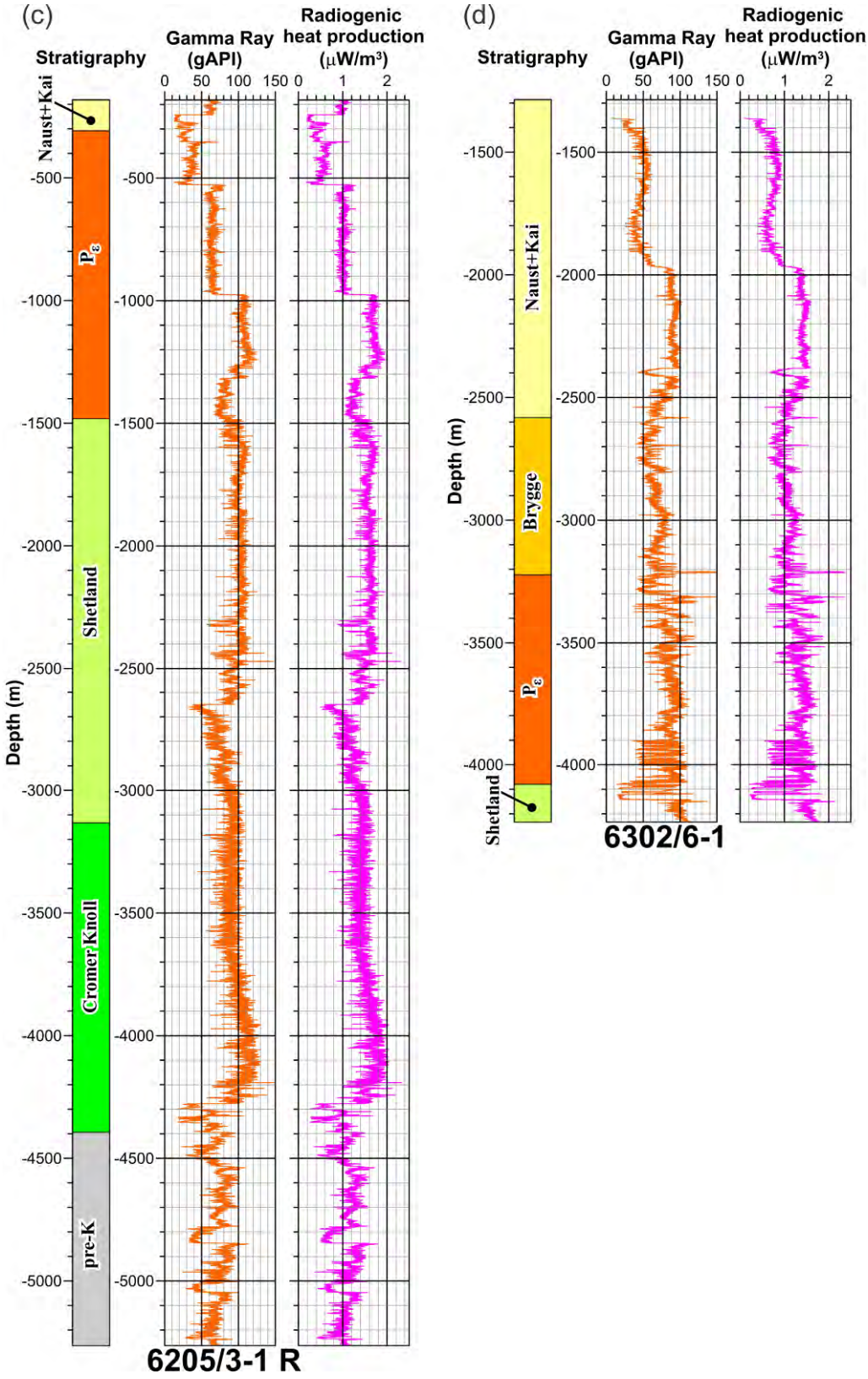

Figure 10.79. Continued. Plot showing stratigraphy, measured total natural gamma and derived radiogenic heat production for the wells shown in Figure 10.78. (c) 6205/3-1 R and (d) 6302/6-1.

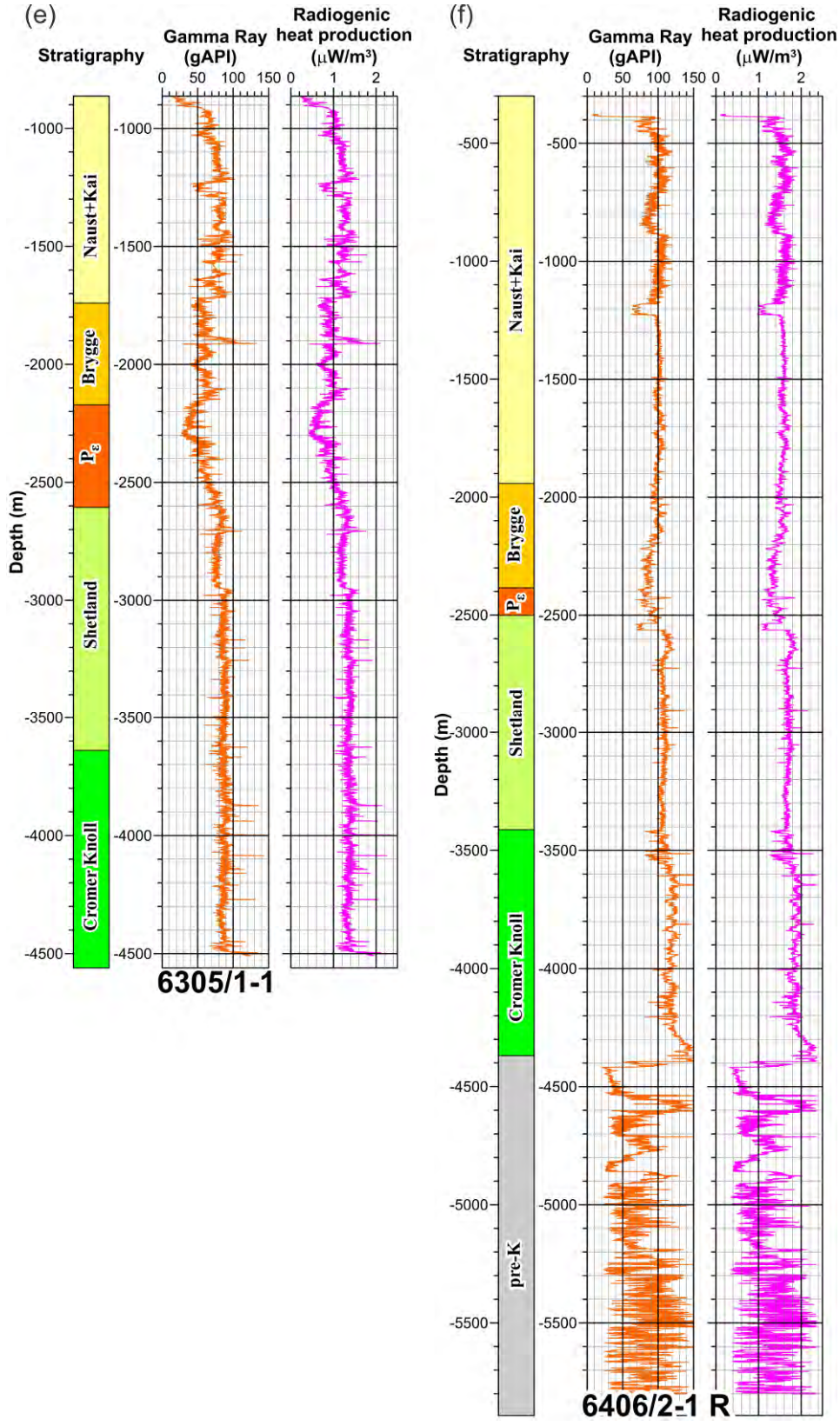

Figure 10.79. Continued. Plot showing stratigraphy, measured total natural gamma and derived radiogenic heat production for the wells shown in Figure 10.78. (e) 6305/1-1 and (f) 6406/2-1 R.

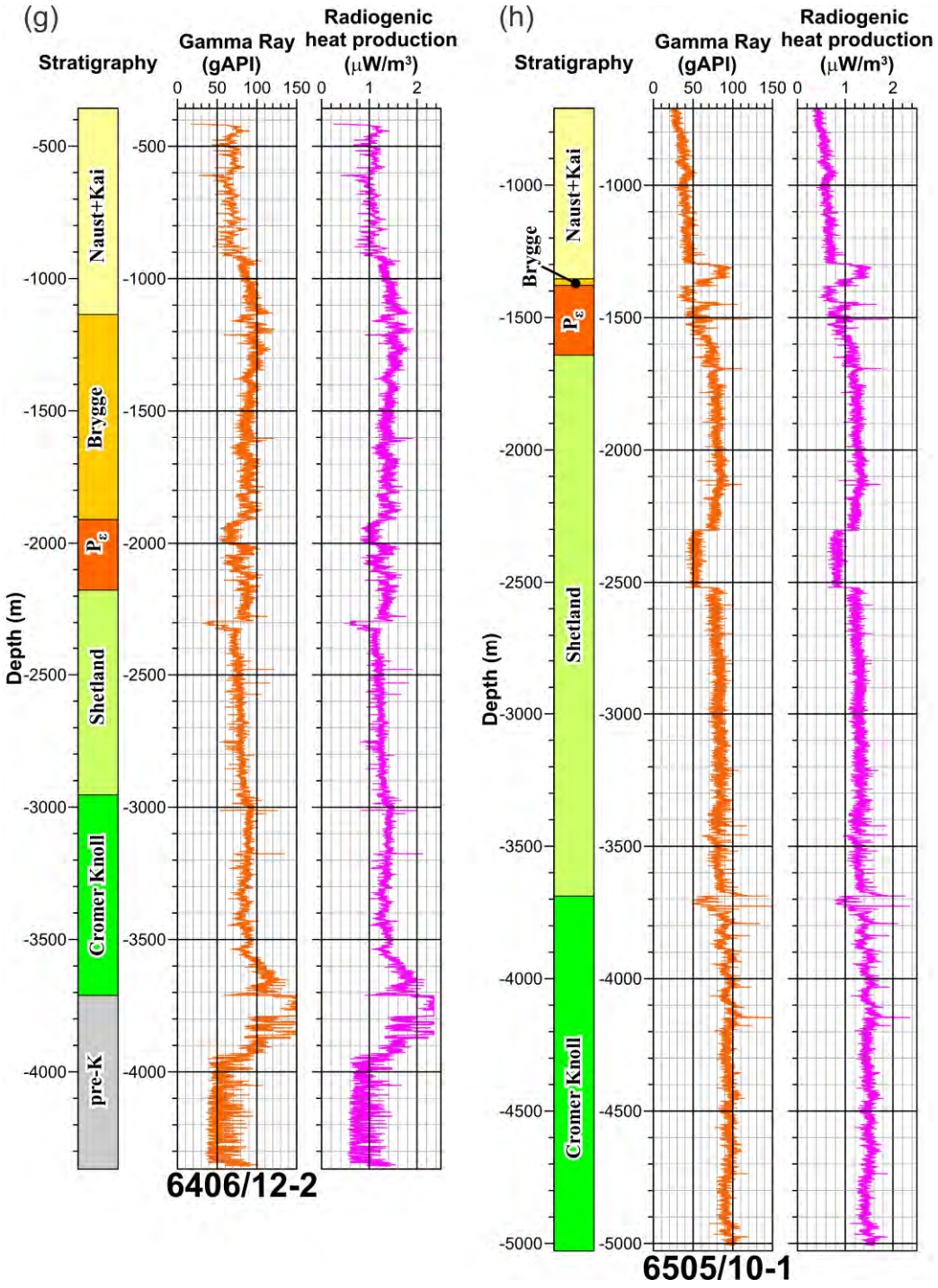

Figure 10.79. Continued. Plot showing stratigraphy, measured total natural gamma and derived radiogenic heat production for the wells shown in Figure 10.78. (a) 34/3-1 S, (b) 35/3-2, (c) 6205/3-1 R, (d) 6302/6-1, (e) 6305/1-1, (f) 6406/2-1 R, (g) 6406/12-2, (h) 6505/10-1, (i) 6507/5-1, (j) 6507/12-2, (k) 6510/2-1 R, (l) 6603/12-1, (m) 6610/7-2 and (n) 6707/10-1.

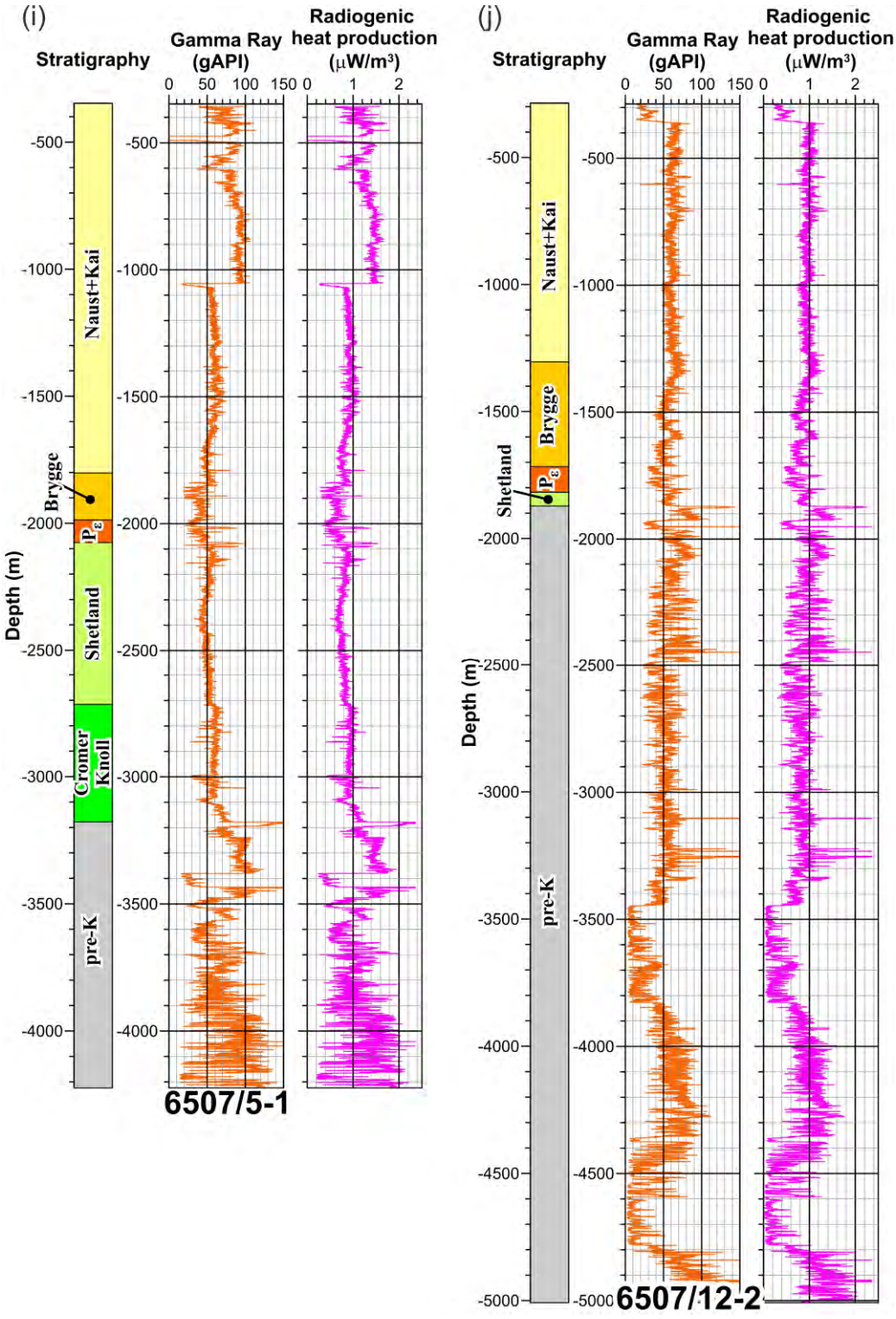

Figure 10.79. Continued. Plot showing stratigraphy, measured total natural gamma and derived radiogenic heat production for the wells shown in Figure 10.78. (a) 34/3-1 S, (b) 35/3-2, (c) 6205/3-1 R, (d) 6302/6-1, (e) 6305/1-1, (f) 6406/2-1 R, (g) 6406/12-2, (h) 6505/10-1, (i) 6507/5-1, (j) 6507/12-2, (k) 6510/2-1 R, (l) 6603/12-1, (m) 6610/7-2 and (n) 6707/10-1.

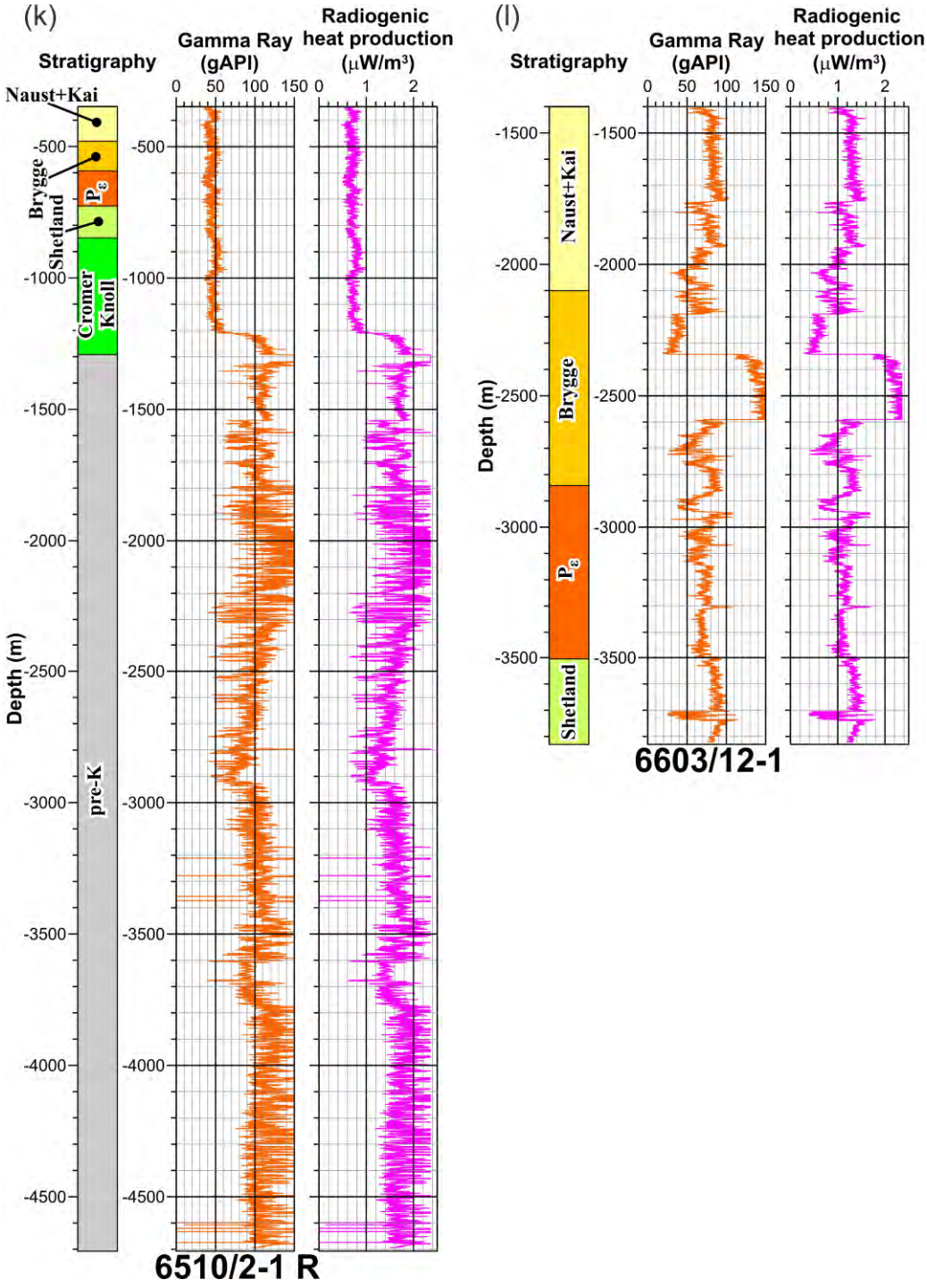

Figure 10.79. Continued. Plot showing stratigraphy, measured total natural gamma and derived radiogenic heat production for the wells shown in Figure 10.78. (a) 34/3-1 S, (b) 35/3-2, (c) 6205/3-1 R, (d) 6302/6-1, (e) 6305/1-1, (f) 6406/2-1 R, (g) 6406/12-2, (h) 6505/10-1, (i) 6507/5-1, (j) 6507/12-2, (k) 6510/2-1 R, (l) 6603/12-1, (m) 6610/7-2 and (n) 6707/10-1.

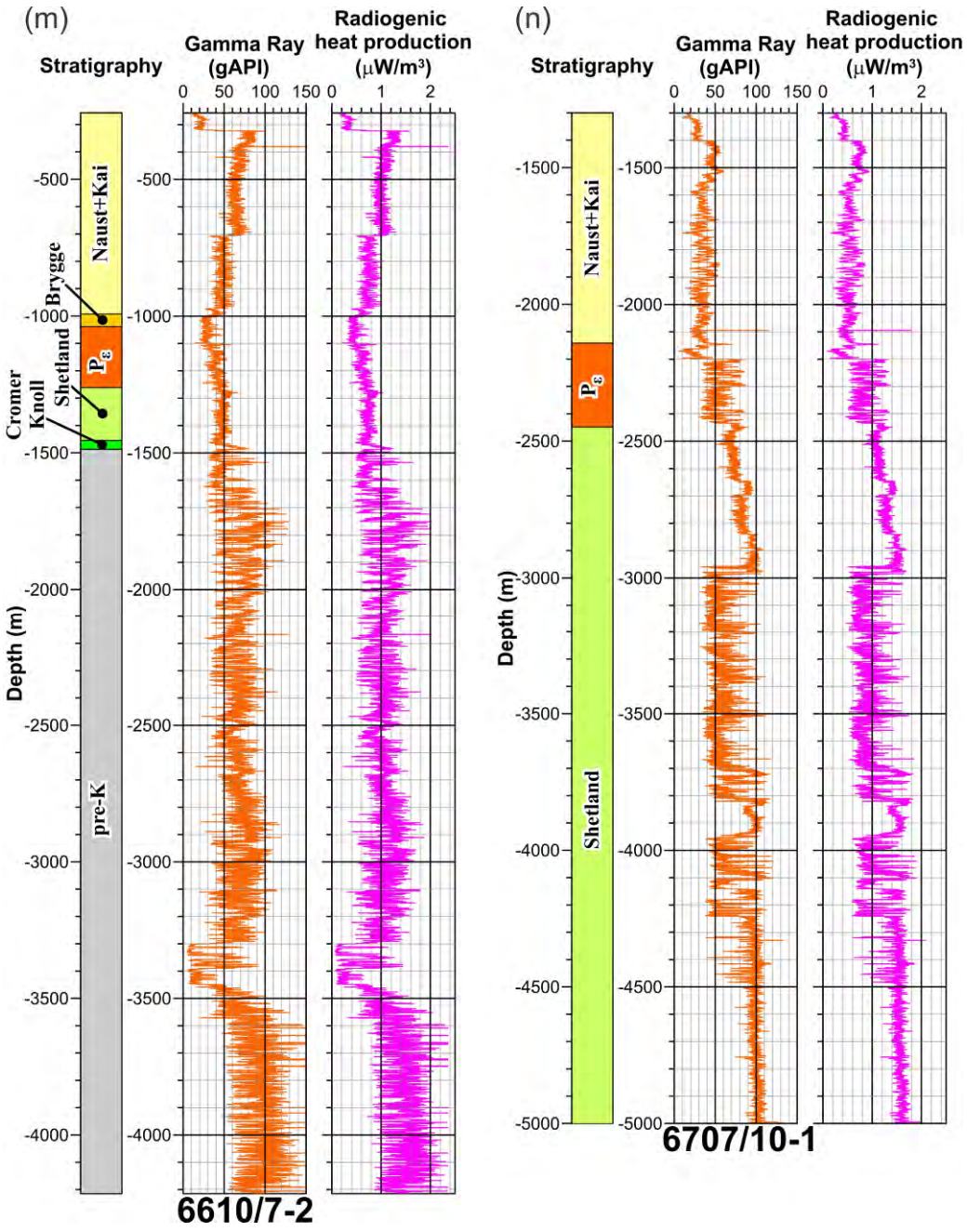

Figure 10.79. Continued. Plot showing stratigraphy, measured total natural gamma and derived radiogenic heat production for the wells shown in Figure 10.78. (a) 34/3-1 S, (b) 35/3-2, (c) 6205/3-1 R, (d) 6302/6-1, (e) 6305/1-1, (f) 6406/2-1 R, (g) 6406/12-2, (h) 6505/10-1, (i) 6507/5-1, (j) 6507/12-2, (k) 6510/2-1 R, (l) 6603/12-1, (m) 6610/7-2 and (n) 6707/10-1.

Table 10.9. Average radiogenic heat production of sedimentary rocks, derived from gamma ray logs, in the selected wells. Units of radiogenic heat production are $\mu W/m^3$.

Well	Nordland (layer 2)	Hordaland (layer 3)	Rogaland (layer 4)	Shetland (layer 6)	Cromer Knoll (layer 7)	Pre-Cretaceous (layer 8)
34/3-1 S	1.33	0.84	0.73	1.3	1.03	1.1
35/3-2	0.5	0.72	0.76	0.74	0.8	1.0
6205/3-1R	0.7	-	1.2	1.5	1.5	1.1
6302/6-1	1.03	1.04	1.3	1.24	-	-
6305/1-1	1.22	1.0	0.9	1.32	1.4	
6406/2-1R	1.53	1.5	1.4	1.7	1.85	1.14
6406/12-2	1.2	1.42	1.21	1.23	1.42	1.11
6505/10-1	0.7	1.2	0.91	1.23	1.46	-
6507/5-1	1.1	0.7	0.7	0.8	0.93	1.13
6507/12-2	0.92	0.88	0.76	0.92	-	0.78
6510/2-1R	0.68	0.72	0.68	0.7	0.94	1.65
6603/12-1	1.2	1.31	1.1	1.31	-	-
6610/7-2	0.86	0.47	0.6	0.74	0.82	1.1
6707/10-1	0.54	-	0.8	1.24	-	-

Furthermore, the reliability of radiogenic heat production obtained from the gamma ray logs according to the empirical equation (10.18) has been recently verified in the Fyllingsdalen and Årvollskogen boreholes, which have been drilled through crystalline rocks on the Norwegian mainland (Maystrenko et al. 2014, 2015). In addition to natural gamma ray logging, gamma spectrometry logging in the Årvollskogen borehole has been used to obtain values of radiogenic heat production based on concentrations of uranium (U), thorium (Th) and potassium (K). Comparative analysis indicates that curves of radiogenic heat production, calculated based on natural gamma ray and gamma spectrometry loggings, demonstrate a very good qualitative fit as the shapes of graphs are very similar. However, these two graphs differ quantitatively in some places where values of radiogenic heat production obtained from the natural gamma log are locally lower compared to those obtained from gamma spectrometry. These local mismatches are mainly related to differences in the resolvability of the two methods and, therefore, radiogenic heat production based on gamma ray logging is representative for the drilled rocks in the tested Årvollskogen borehole. In the case of the Fyllingsdalen borehole, most of the values of the radiogenic heat production according to whole-rock chemical analyses of core samples are in the range of radiogenic heat production derived from gamma ray loging (Maystrenko et al. 2015).

The results of calculations of the radiogenic heat production within the Mid-Norwegian continental margin are displayed in Figure 10.79 for each well, and average values of the radiogenic heat production for sedimentary layers of the 3D structural model in the selected wells are shown in Table 10.9. According to these results, the average radiogenic heat

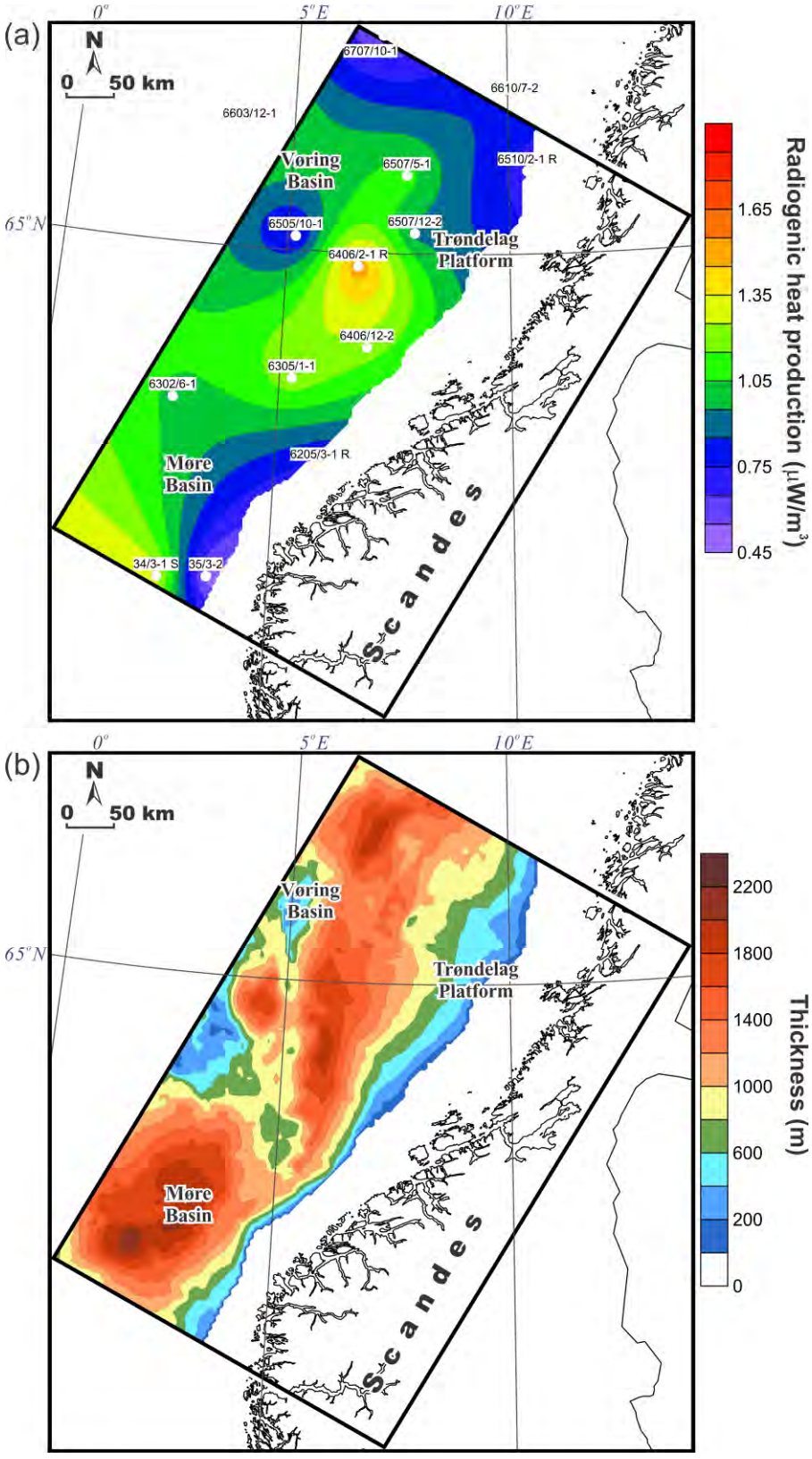

Figure 10.80. (a) Radiogenic heat production and (b) thickness map of the Naust-Kai (base Naust-sea floor; layer 2; (based on Rise et al. 2005, 2006, 2010; Dowdeswell et al. 2006, 2010; Eidvin et al. 2007, 2014; Ottesen et al. 2009, 2012 and Chand et al. 2011).

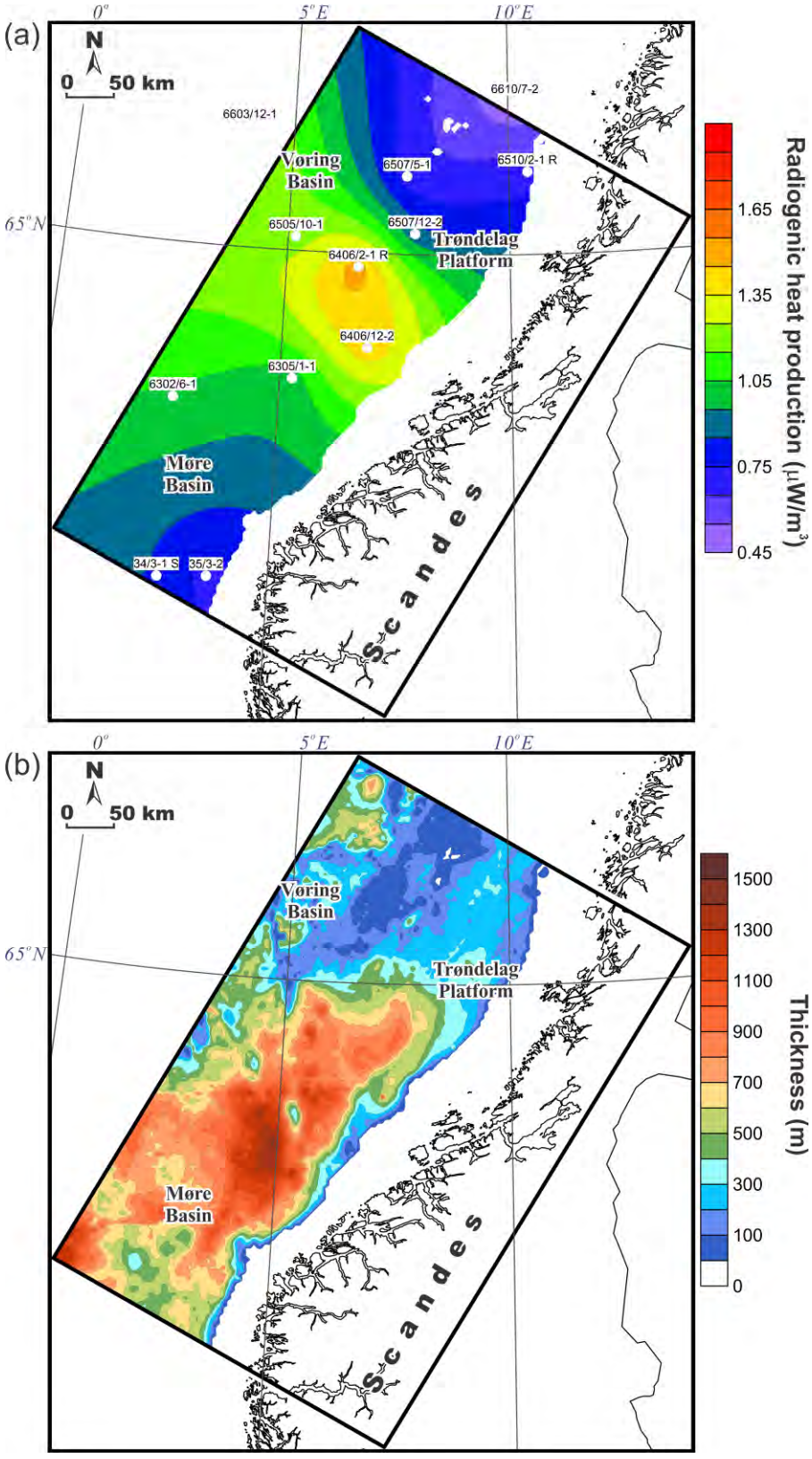

Figure 10.81. (a) Radiogenic heat production and (b) thickness map of the Brygge (top Paleocene-base Naust; layer 3; based on Rise et al. 2005, 2006, 2010; Dowdeswell et al. 2006, 2010; Eidvin et al. 2007, 2014; Ottesen et al. 2009, 2012 and Chand et al. 2011).

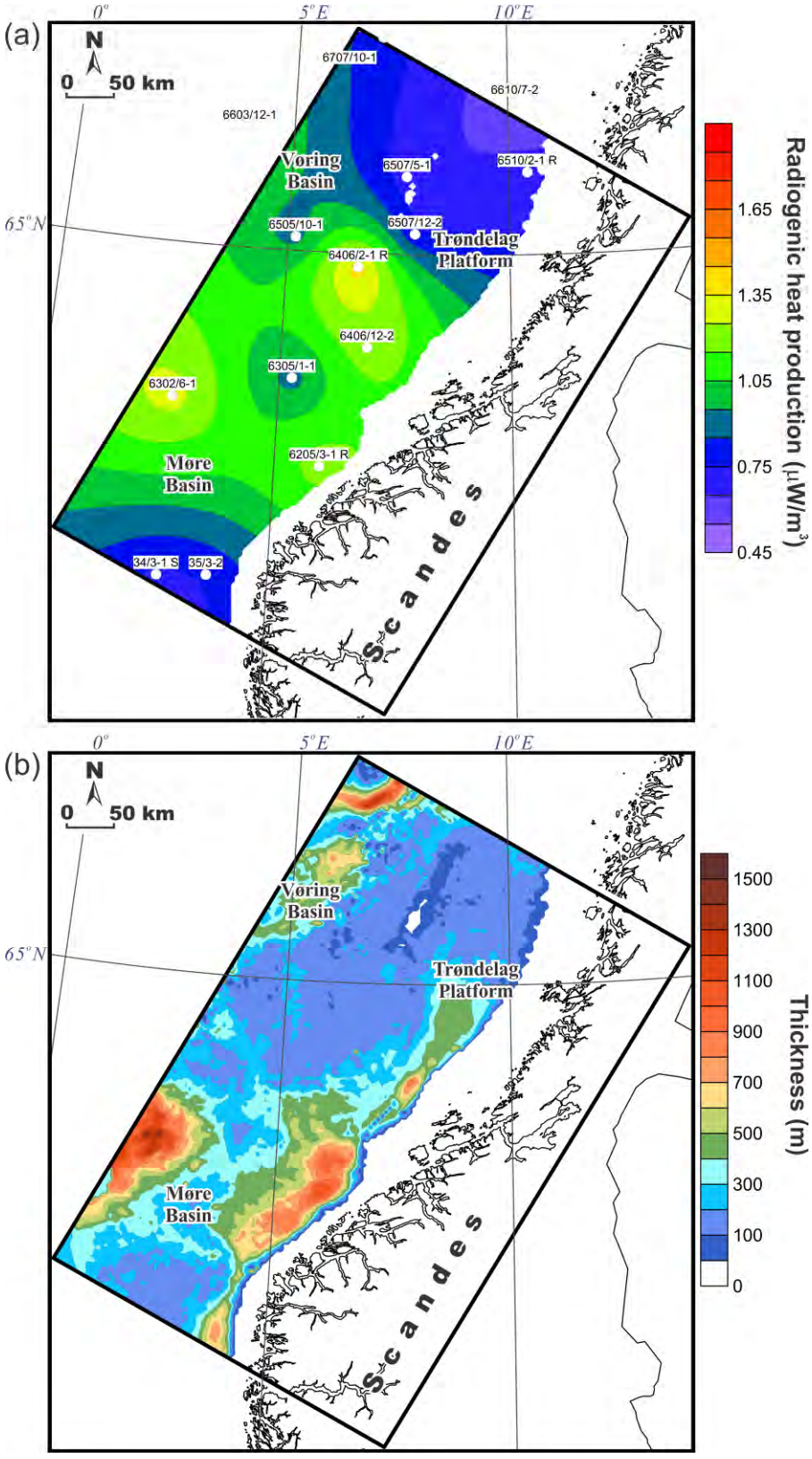

Figure 10.82. (a) Radiogenic heat production and (b) thickness map of the Paleocene (base Tertiary unconformity-top Paleocene; layer 4; based on Rise et al. 2005, 2006, 2010; Dowdeswell et al. 2006, 2010; Eidvin et al. 2007, 2014; Ottesen et al. 2009, 2012; Chand et al. 2011 and Gernigon 2014, NGU unpublished data).

production of the sedimentary layers varies from 0.92 $\mu W/m^3$ to 1.85 $\mu W/m^3$ (Table 10.9), indicating relativel strong variations within different parts of the study area and within different layers of the 3D model. The NPD nomenclature has been partially used in Figure 10.79 and in Table 10.9 for stratigraphic intervals. In this case, it is important to clarify that the Nordland, Hordaland and Rogaland groups correspond to the Naust-Kai (base Naust-sea floor; layer 2), Brygge (top Paleocene-base Naust; layer 3) and Paleocene (base Tertiary unconformity-top Paleocene; layer 4), respectively, whereas the Shetland and Cromer Knoll groups are not exactly correlated with the Upper Cretaceous (near top Cenomanian-base Tertiary unconformity; layer 6) and the Lower Cretaceous (base Cretaceous unconformity-near top Cenomanian; layer 7) in some regions of the Coop2 study area. On the other hand, the difference in average values of the radiogenic heat production between the Shetland and Cromer Knoll groups is rather small (Table 10.9) and, therefore, an average radiogenic heat production for the Shetland and Cromer Knoll groups has been assigned to the Upper Cretaceous (layer 6) and the Lower Cretaceous (layer 7), respectively.

In particular, the uppermost stratigraphic intervals, represented by Naust-Kai (layer 2) and Brygge (layer 3), are characterised by a similar range of values for the derived radiogenic heat production, varying from 0.5 $\mu W/m^3$ to 1.53 $\mu W/m^3$ for layer 2 and from 0.47 $\mu W/m^3$ to 1.5 $\mu W/m^3$ for layer 3 (Table 10.9). Nevertheless, the maps in Figures 10.80a & 10.81a demonstrate easily recognisable differences in the local pattern of radiogenic heat production. On the other hand, the general pattern is relatively similar, displaying low values within the northeastern and the southeastern parts of the Coop2 model area which are separated by a zone with increased radiogenic heat production (c.f. Figures 10.80a & 10.81a). The above-described general trend in radiogenic heat production is also recognisable at the level of the Paleocene (Figure 10.82a) with the average values ranging from 0.6 $\mu W/m^3$ to 1.4 $\mu W/m^3$ (Table 10.9). Moreover, this pattern is still clearly visible at the level of the Upper Cretaceous (layer 6) and Lower Cretaceous (layer 7) where a zone of increased radiogenic heat production in the central part of the Coop2 model area is bounded in the northeast and the southeast by reduced values (Figures 10.83a & 10.84a). Compared to the Cenozoic stratigraphic intervals (Figures 10.80a, 10.81a & 10.82a), the Cretaceous maps show more intensive radiogenic heat production which ranges from 0.7 $\mu W/m^3$ to 1.7 $\mu W/m^3$ for the Upper Cretaceous and from 0.8 $\mu W/m^3$ to 1.85 $\mu W/m^3$ for the Lower Cretaceous (Table 10.9). In the case of the pre-Cretaceous, the general pattern that reflects structural changes in deposition and present-day distribution between the pre-Cretaceous and the Cretaceous-Cenozoic sediments is not more indentifiable. The data on the pre-Cretaceous radiogenic heat production are mostly limited to the uppermost part of the pre-Cretaceous (Figure 10.79) and, therefore, it is obvious that these data cannot be really representative for the whole of the pre-Cretaceous interval. However, the absence of complete data, existing sparse data for the drilled pre-Cretaceous in selected wells (Figure 10.79) have been used to estimate the radiogenic heat production for this interval (Figure 10.85a). A large part of the pre-Cretaceous in Figure 10.85a is characterised by values of heat production which are around 1μW/m3. In the northeast, an increase of the radiogenic heat production in well 6510/2-1R is bounded by reduced values in well 6507/12-2. The investigated pre-Cretaceous succession is the thickest one in these two wells (6507/12-2 and 6510/2-1R), implying that the average radiogenic heat production of the whole of the

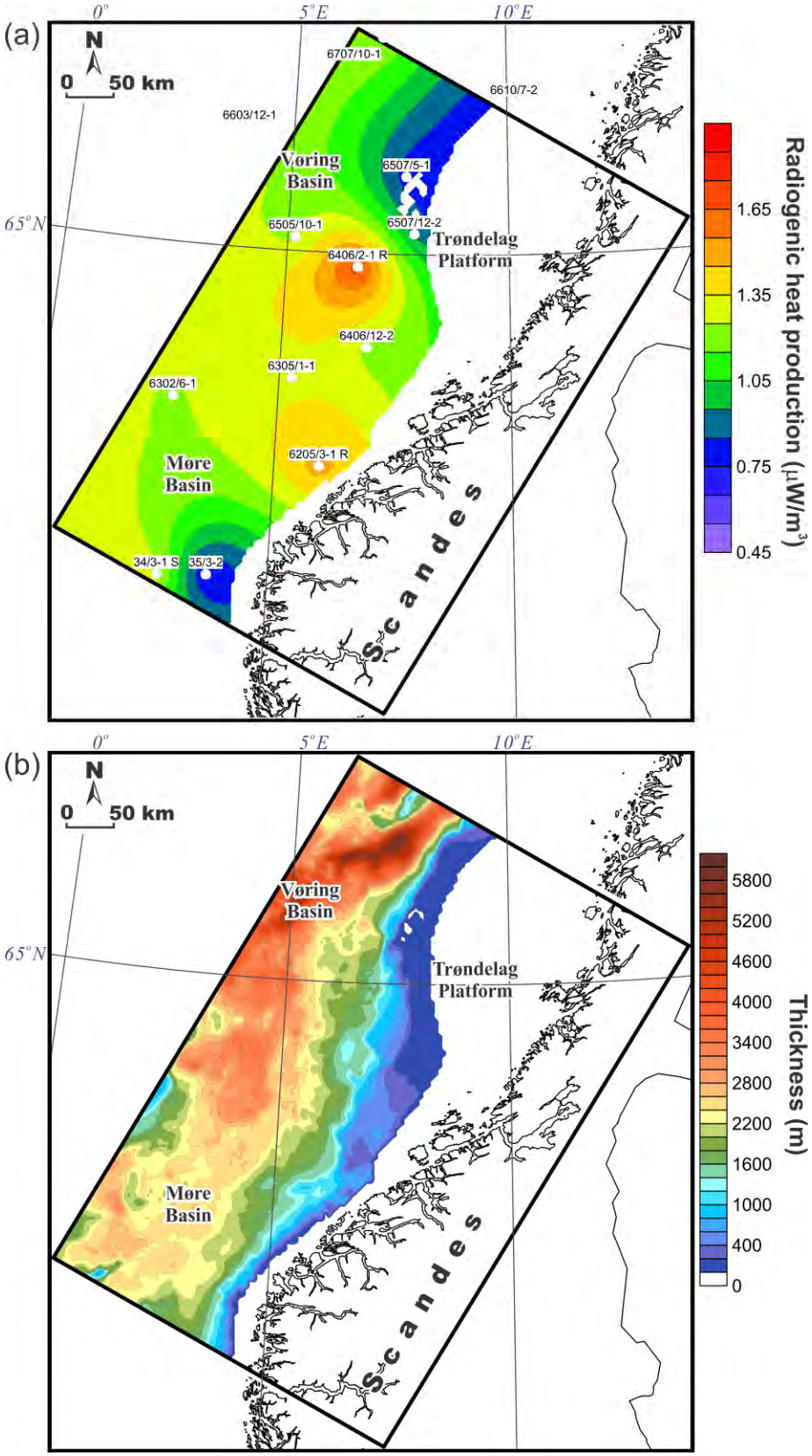

Figure 10.83. (a) Radiogenic heat production of the Shetland group and (b) thickness map of the Upper Cretaceous (near top Cenomanian-base Tertiary unconformity; layer 6; based on Gernigon 2014, NGU unpublished data).

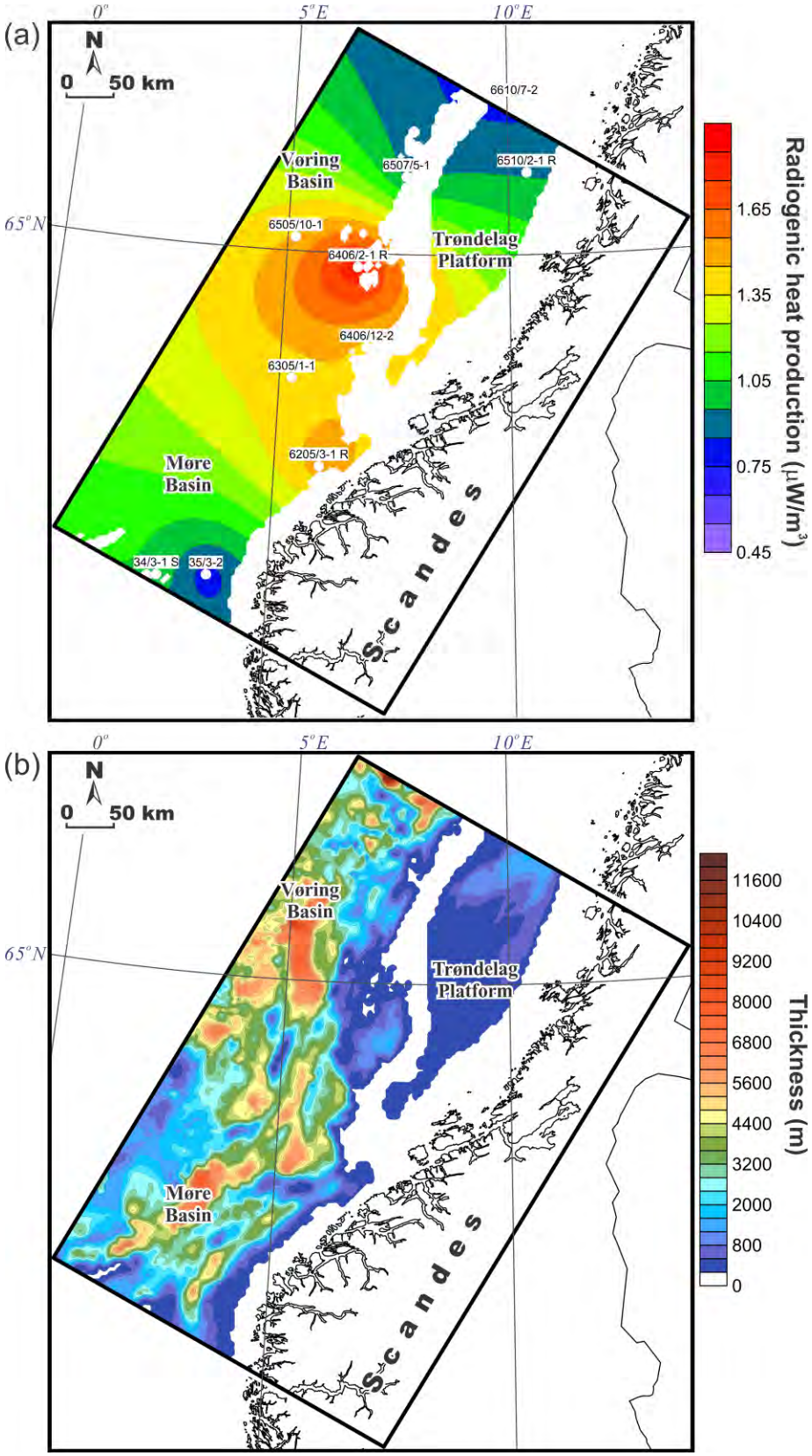

Figure 10.84. (a) Radiogenic heat production of the Cromer Knoll Group and (b) thickness map of the Lower Cretaceous (base Cretaceous unconformity-near top Cenomanian; layer 7; based on Gernigon 2014, NGU unpublished data).

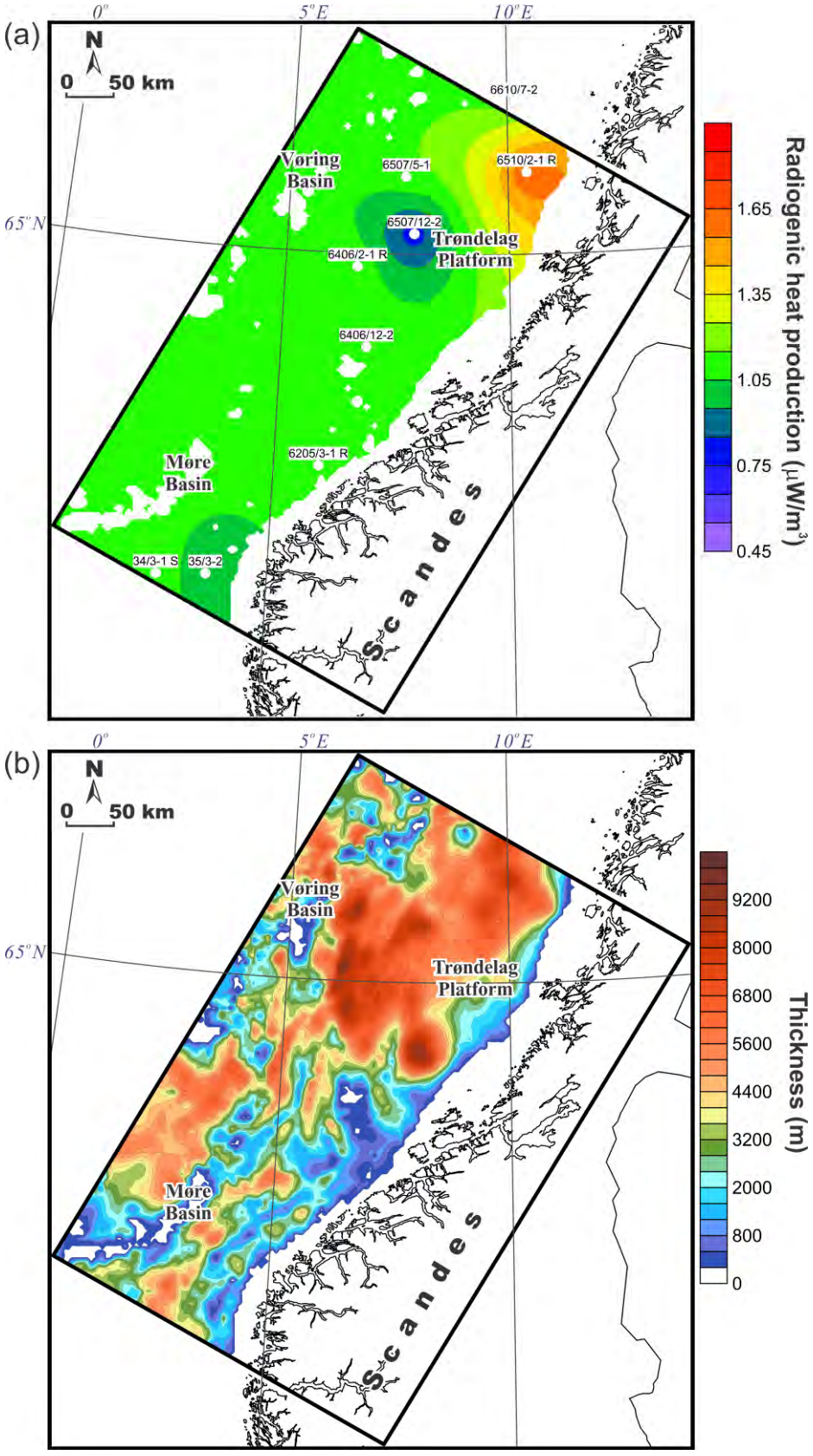

Figure 10.85. (a) Radiogenic heat production and (b) thickness map of the pre-Cretaceous sedimentary rocks (layer 8).

pre-Cretaceous can be more variable than it appears from the map in Figure 10.85a. The studied radiogenic heat production of the pre-Cretaceous varies from 0.78 $\mu W/m^3$ to 1.65 $\mu W/m^3$ (Table 10.9).

Coming back to the Cretaceous-Cenozoic interval (Figures 10.80-10.84), the interesting common feature with increased values of radiogenic heat production in the vicinity of wells 6406/2-1R and 6406/12-2 is characteristic for this more than 100-million-years-long stratigraphic interval. The zone of the increased radiogenic heat production with a culmination in well 6406/2-1R is easily traceable on all Cretaceous-Cenozoic maps (Figures 10.81a, 10.82a, 10.83a & 10.84a), implying a possible inheritance in clastic material transport from the same erosional locality onshore where crystalline rocks are or were characterised by an increased content of radiogenic elements. According to McKenna & Sharp (1998), mudrocks produce about 30-40% more radiogenic heat than stratigraphically equivalent sandstones. Therefore, the inherited zone with the increased radiogenic heat production can also represent the result of differentiation of the eroded clastic material during transportation with deposition of more argillaceous fractions in this particular area. Nevertheless, it is obvious that this remarkable feature requires additional investigation and cannot be unambiguously explained based just on several wells. Therefore, a more detailed study is required in order to analyse this specific pattern of radiogenic heat production within the sedimentary cover by including smaller stratigraphic intervals and by use of a larger number of wells with an attempt to correlate the radiogenic pattern of sediments with potential sources for eroded material within the mainland.

10.5.4 Results of 3D thermal modelling

The results of the transient 3D thermal modelling provide an overview of the present-day temperature distribution beneath the Earth's surface within the Mid-Norwegian continental margin and adjacent areas of the Norwegian mainland. Major features of the temperature pattern within the Coop2 study area are demonstrated by use of selected 2D horizontal slices through the obtained 3D conductive thermal field (Figures 10.86 & 10.87). Figure 10.86 shows the pattern of subsurface temperature at six chosen depth levels within the upper part of the 3D thermal/structural model where relatively low thermally conductive sedimentary rocks are present. In addition, Figure 10.87 illustrates the temperature distribution within the deeper parts of the Coop2 model area; near the crust-mantle boundary (Figure 10.87a, b) and within the lithospheric mantle (Figure 10.87c, d).

At a large scale, the mainland is generally colder compared to the Mid-Norwegian continental margin (Figure 10.86). Within the upper part of the 3D thermal model, this regional trend of the modelled temperatures is associated mainly with the high thermal conductivity of crystalline crustal rocks (Table 10.7) which crop out over large parts of the mainland. This interaction

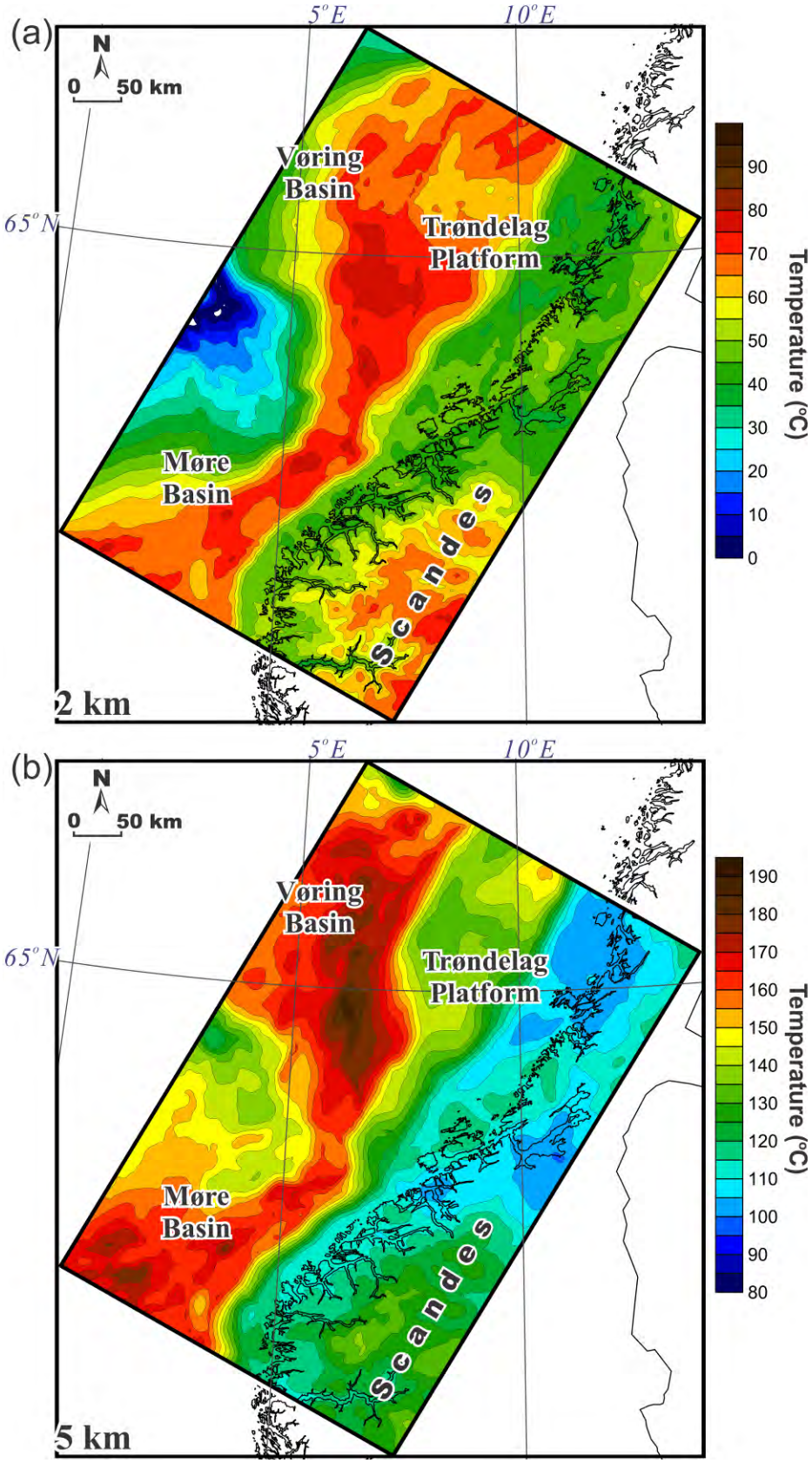

Figure 10.86. Modelled temperatures within the upper part of the Coop2 model area. Temperature maps for the depths of 2 km (a), 5 km (b), 7 km (c), 10 km (d), 15 km (e) and 18 km (f) extracted from the 3D thermal model.

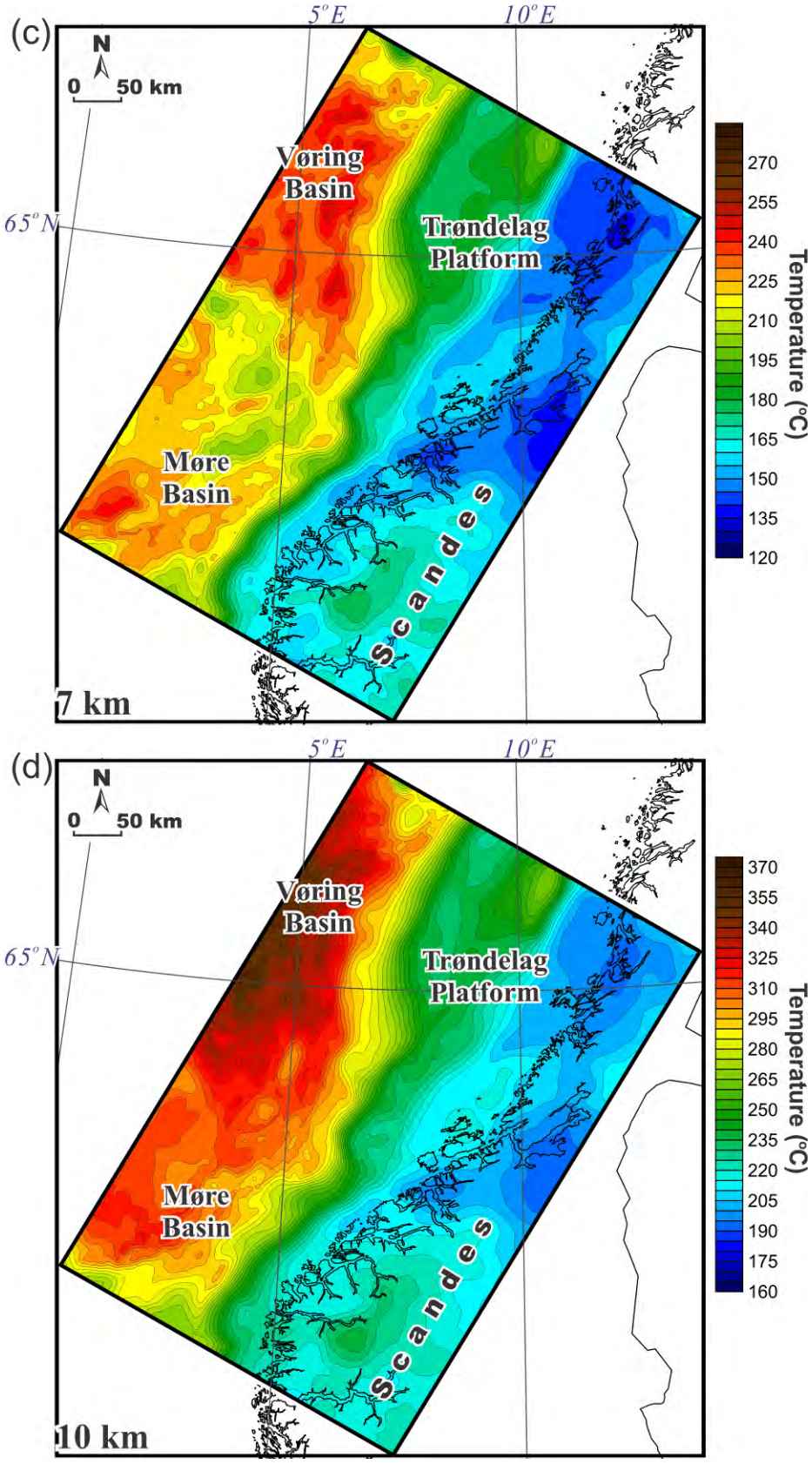

Figure 10.86. Continued. Modelled temperatures within the upper part of the Coop2 model area. Temperature maps for the depths of 2 km (a), 5 km (b), 7 km (c), 10 km (d), 15 km (e) and 18 km (f) extracted from the 3D thermal model.

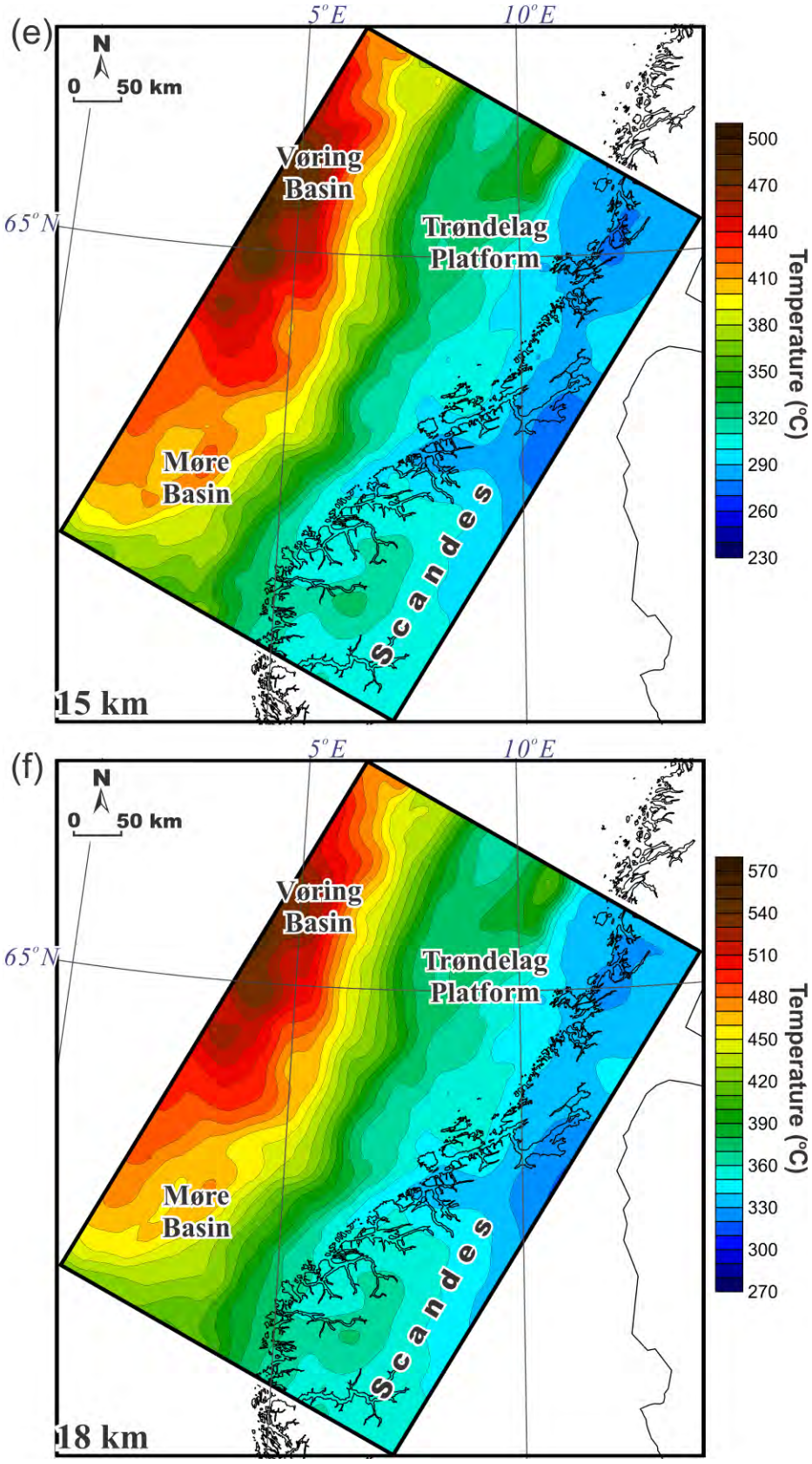

Figure 10.86. Continued. Modelled temperatures within the upper part of the Coop2 model area. Temperature maps for the depths of 2 km (a), 5 km (b), 7 km (c), 10 km (d), 15 km (e) and 18 km (f) extracted from the 3D thermal model.

between the relatively high values of thermal conductivities of the crystalline rocks and specific structural patterns is responsible for a chimney effect within the areas where the crystalline rocks are exposed at the surface. The thermal pattern related to the chimney effect within the mainland is complicated by a zone with increased temperatures beneath the Scandes mountains that is especially pronounced at a depth of 2000 m (Figure 10.86a). This is mainly due to a presence of the Scandes mountains which are more than 1500-2000 m in altitude. The upper thermal boundary at the Earth's surface is therefore also uplifted by more than 1500-2000 m under the Scandes mountains compared to the rest of the mainland where the relief is lower and more smooth. The topographic effect of the Scandes mountains is clearly recognisable at a depth of 7000 m and even deeper where it is disturbed by structural interaction between the middle and upper crystalline crustal layers (cf. Figures 10.35-10.36 & 10.86e-f) which have different thermal properties (Table 10.7). The thermal effect associated with changes of the topography is also prominent at the shallow levels offshore where the bathymetry is deep (cf. Figures 10.4 & 10.86a, b). In contrast to the Scandes mountains, the modelled temperatures are notably lower within the wide area of deep bathymetry compared to the rest of the Norwegian continental shelf (e.g., Figure 10.86a), reflecting the fact that the upper thermal boundary at the sea floor sinks together with the bathymetry and, therefore, brings low surface temperatures down to greater depths.

The next feature of the thermal pattern within the upper crust concerns the a direct relationship between areas with a thick sedimentary cover and areas with increased temperatures (cf. Figures 10.7a-10.11a, 10.14a, 10.25a & 10.86). This large-scale trend of temperature distribution is related to the low thermal conductivity of sedimentary rocks which increases the heat storage within the areas characterised by a thick sedimentary cover. In other words, the relatively thick, low thermally conductive, sedimentary rocks lessen the rate of heat transfer, acting like the thermal insulation in a vacuum flask. This thermal effect is particularly prominent within the Vøring Basin where the sedimentary infill is thickest (Figure 10.25a). Actually, the values of thermal conductivities of sediments are dependent on both temperature and compaction during the 3D thermal modelling and, therefore, the uppermost sedimentary layers of the Coop2 model, represented by the Brygge, Naust and Kai formations, are characterised by the lowest thermal conductivities. This fact is partially reflected by distribution of the modelled temperature at depths of 2000 and 5000 m where the thickness pattern of the Brygge, Naust and Kai formations is still recognisable (cf. Figures 10.7a, 10.8a & 10.86a, b). The blanketing effect of sediments becomes reasonably more smooth in the areas with thinner sediments within the Trøndelag Platform and within the eastern part of the Møre Basin where a strong thinning of the sediments occurs towards the mainland. The Møre Basin itself is characterised by slightly lower temperatures compared to the Vøring Basin. The latter is mainly due to thermal blanketing effect of thicker sediments within the Vøring Basin on the one hand. On the other hand, the variable radiogenic heat production of the sedimentary rocks makes its own contribution to the modelled temperatures. Furthermore, the above-mentioned topographic thermal effect of deepening bathymetry affects the modelled temperature within the Møre Basin, causing an easily recognisable decrease in temperatures within the northwestern part of the Møre Basin even

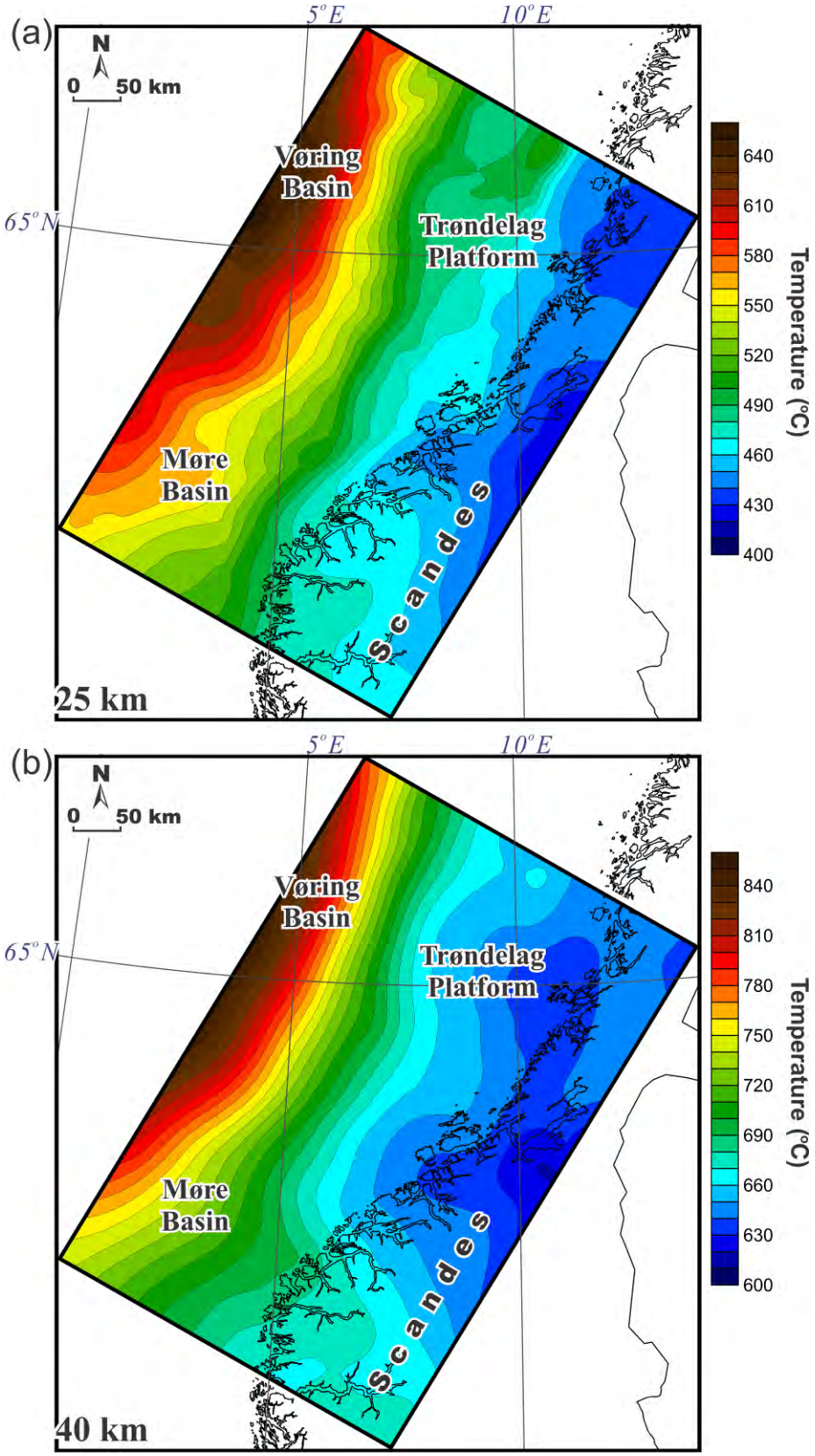

Figure 10.87. Modelled temperatures within the deep part of the Coop2 model area. Temperature maps for the depths of 25 km (a), 40 km (b), 80 km (c) and 100 km (d) extracted from the 3D thermal model.

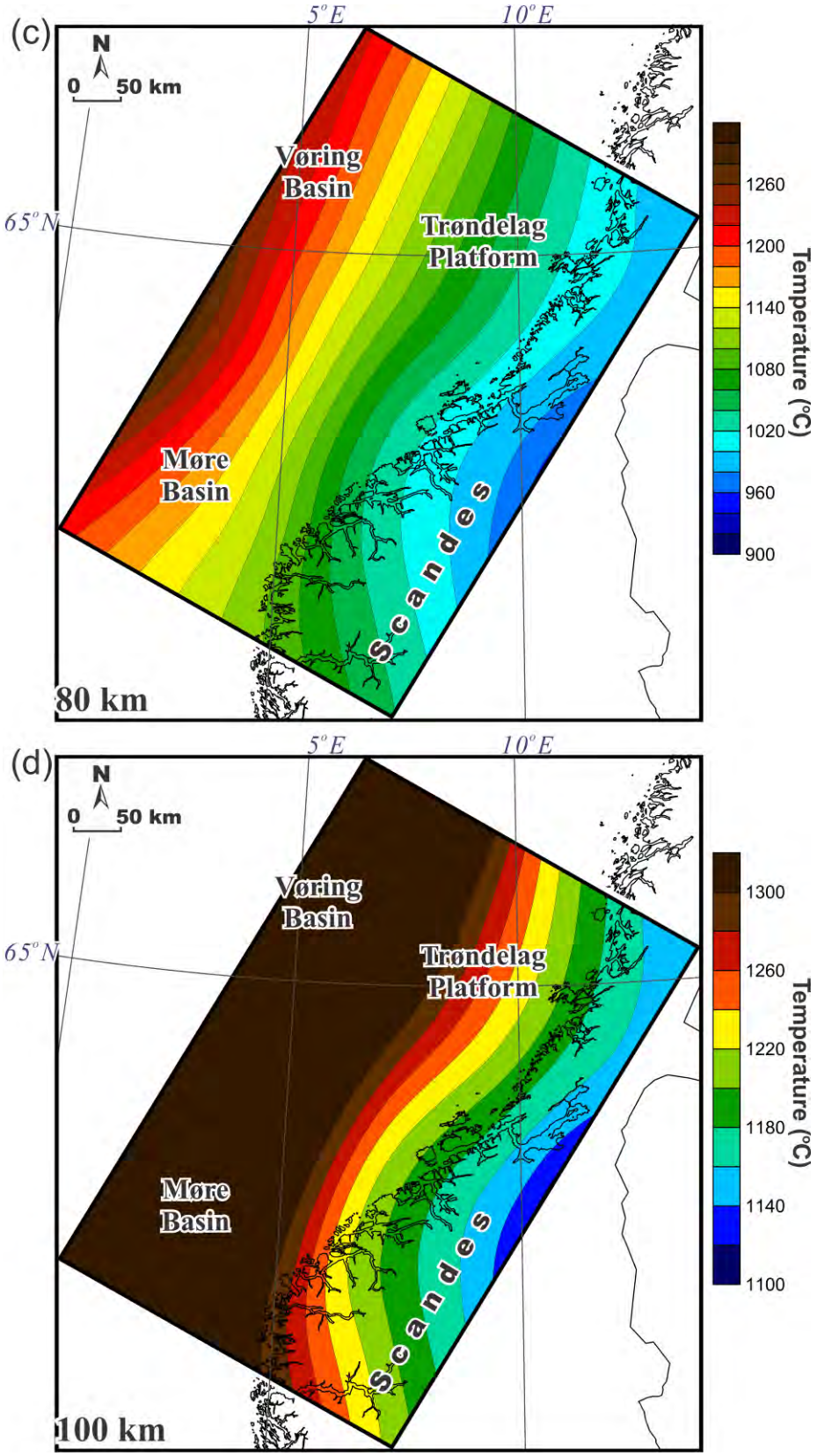

Figure 10.87. Continued. Modelled temperatures within the deep part of the Coop2 model area. Temperature maps for the depths of 25 km (a), 40 km (b), 80 km (c) and 100 km (d) extracted from the 3D thermal model.

at a depth of 5000 m (Figure 10.86b). Besides, the distribution of the subsurface temperatures along the northwestern limit of the Coop2 model area is strongly affected by the gradual uplift of both the present-day lower thermal boundary (Figure 10.71) and paleo-thermal boundaries (Figure 10.74) at the base of the lithosphere towards the oceanic lithospheric domain.

The thermal influence of the lower thermal boundary configuration becomes more and more noticeable at greater depths where the modelled temperature increases due to the uplift of the lithosphere-asthenosphere boundary towards the Atlantic Ocean. The results of the 3D thermal modelling within the deeper part of the 3D thermal model are presented in Figure 10.87 by four 2D horizontal slices of the temperature distribution at depths of 25, 40, 80 and 100 km. The major feature of the 3D conductive thermal field in these maps is the change of temperatures from the relatively low values within the southeastern part of the Coop2 model area to the higher ones in the northwest (Figure 10.87). At depths of 80 and 100 km (Figures 10.87c, d) the distribution of the modelled temperature generally reflects the configuration of the lower thermal boundary, which is represented by the base of the lithosphere. It is important to note that the modelled temperature beneath the mainland is already lower than the temperature beneath the Mid-Norwegian continental margin at depths of 25 and 40 km (Figure 10.87a, b), where the mantle material partially or fully predominates beneath the continental margin, whereas the crystalline crustal rocks are still present beneath the mainland at these depth levels (Figure 10.39). There are some complications in the modelled thermal pattern beneath the mainland (Figures 10.87a, b) as a result of the interaction between crustal and mantle thermal properties (Table 10.7). However, the influence of this interaction is strongly smoothed by the topography of the lower thermal boundary which is deeply located beneath the mainland and is significantly uplifted beneath the oceanic domain. Therefore, an increased radiogenic heat production of the crystalline crust compared to the mantle material at 25 and 40 km depth levels is not large enough to overcome the thermal pattern of the heat coming from deeper parts of the Earth's interior within the study area. In this case, the configuration of the lithosphere-asthenosphere boundary is the key factor controlling the temperature distribution within the deeper levels of the Coop2 3D thermal model.

The modelled temperatures at the top of the crystalline basement (Figure 10.88) reflect the configuration of the depth to the top of this basement (Figure 10.13). There is a straightforward relationship between the distribution of the modelled temperatures (Figure 10.88) and the depth to the top of the crystalline basement (Figure 10.13): if the top of the crystalline rocks is deeply situated, the modelled temperatures are increased and vice versa (cf. Figures 10.13 & 10.88). Consequently, the modelled temperature maxima coincide with the deepest parts of the Vøring Basin. There, the temperatures are more than 450 °C (Figure 10.88). Actually, the top of the crystalline basement beneath the Vøring Basin is characterised by higher modelled temperatures (350-450 °C on average) compared to the Møre Basin which is slightly colder with average temperatures varying from 250 to 350 °C in the southwestern part of this basin to values similar to those of the Vøring Basin in the northeastern part. The Trøndelag Platform is clearly distinguished by its lower temperatures in comparison to the Vøring and

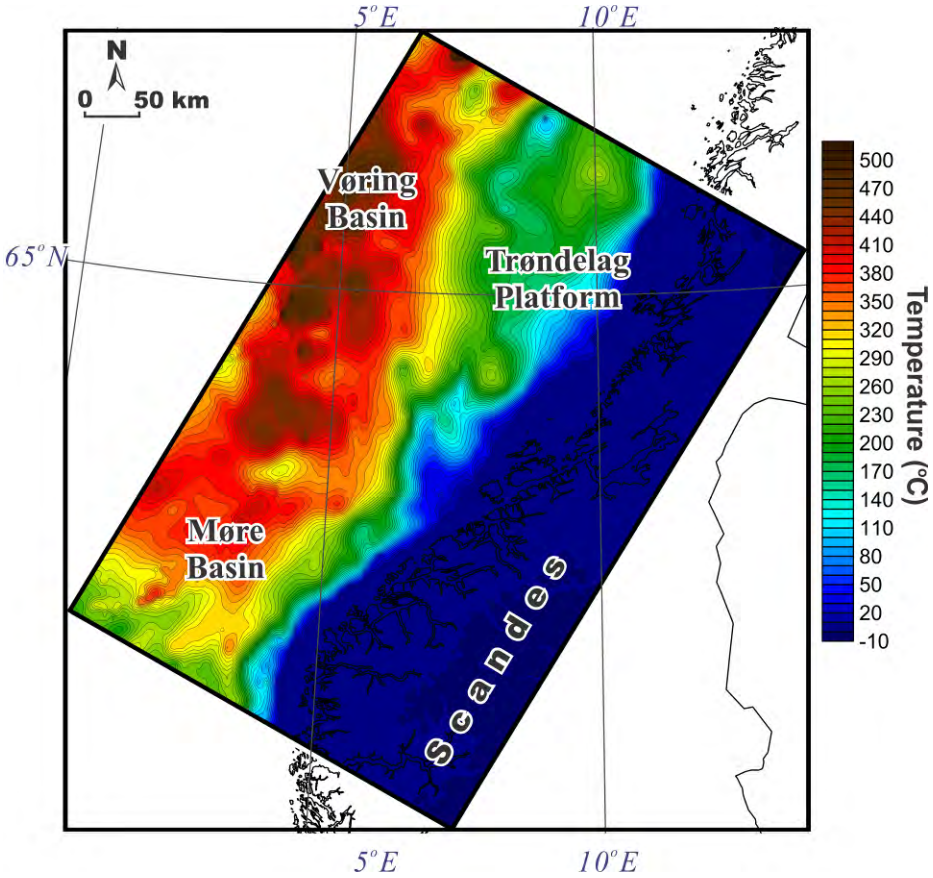

Figure 10.88. Modelled temperatures at the top of the crystalline basement within the Coop2 model area.

Møre basins. The average modelled temperatures are in the range of 200-230 °C at the top of basement beneath the Trøndelag Platform. The modelled temperatures on the mainland simply reproduce the Earth´s surface temperatures (Figure 10.70a) due to the fact that the crystalline basement is exposed at the surface there.

In contrast, the modelled heat flux at the top of the crystalline basement (Figure 10.89) has a more complex pattern compared to the distribution of temperature (Figure 10.88). First of all, it has to be mentioned that the complex image of heat flux over the mainland is partially controlled by abrupt changes in the topography (Figure 10.4). In addition, there is strong influence of the paleoclimatic conditions related to the Saalian and Weichselian glaciations. The effect of these two cooling events is recognisable in terms of the decreased modelled heat flux (around 40 mW/m^2) over those parts of the continent which were mostly ice-free during the glaciations (cf. Figures 10.72 & 10.89a) and, therefore, were affected by low surface temperatures similar to the present-day tundra conditions (Figure 10.73). On the other hand, the influence of the Saalian and Weichselian glaciations is smoothed within the areas which were covered by ice sheets or sea water. For instance, there is an increased heat flux of up to 60-70 mW/m^2 within the part of Scandes (Figure 10.89a) which was almost permanently covered by ice, being partially insulated from the ice-free low surface paleo-temperatures during the glacial periods. A similar situation occurs for the areas in the vicinity

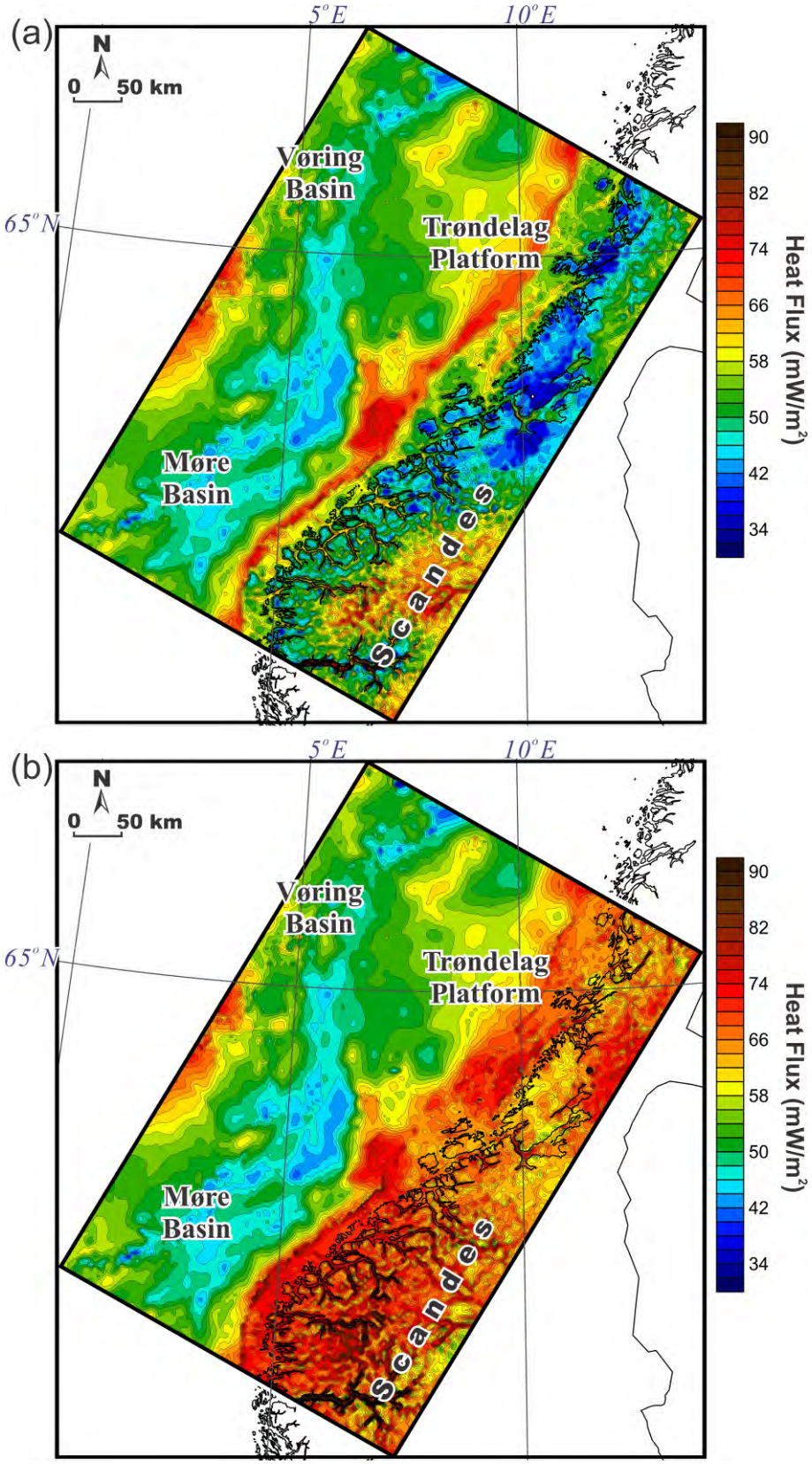

Figure 10.89. Modelled heat flux at the top of the crystalline basement: (a) with influence of the Saalian and Weichselian glaciations and (b) without influence of those glaciations.

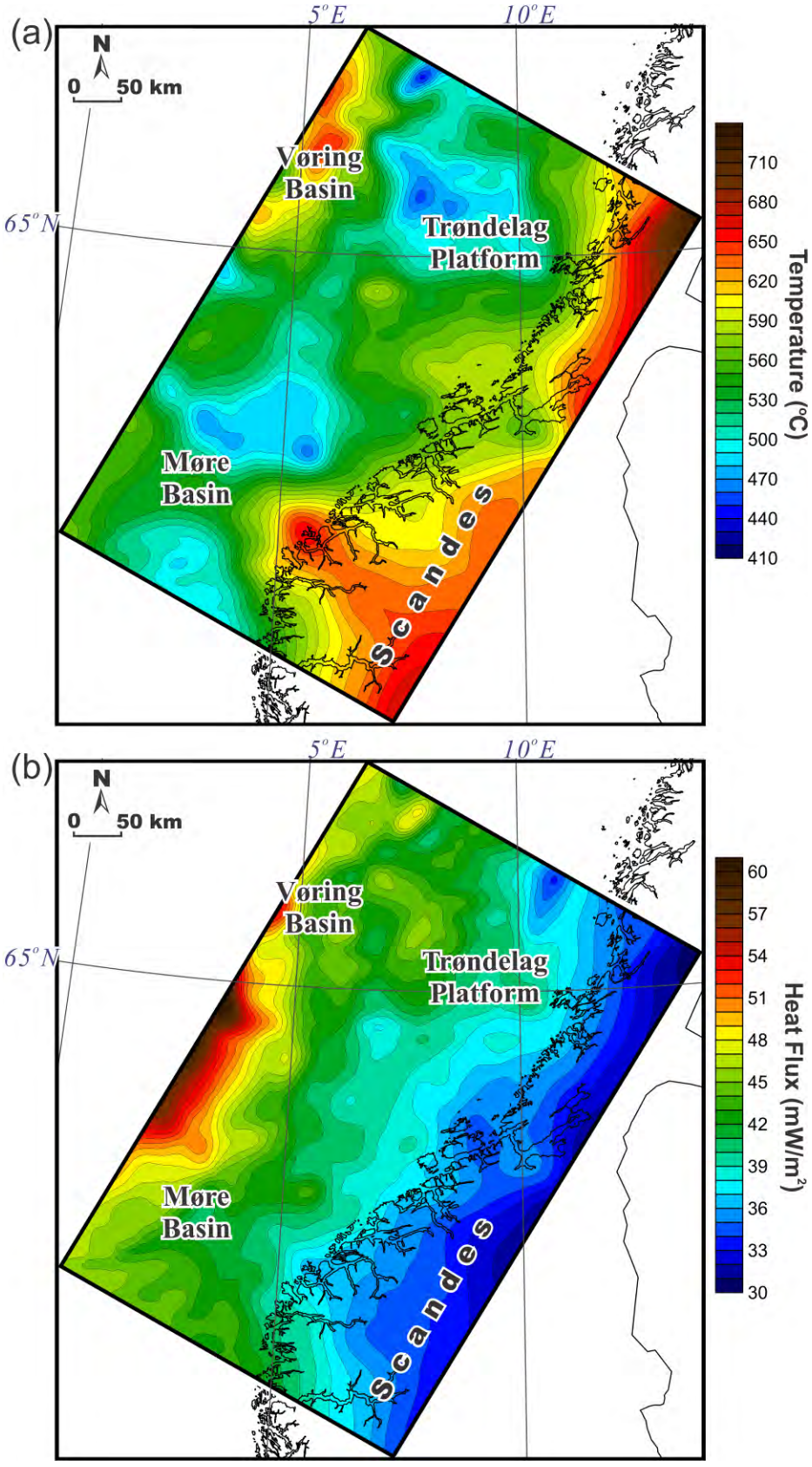

Figure 10.90. Modelled temperatures (a) and heat flux (b) at the base of the crust (Moho).

of the coastline which have been thermally insulated by the sea water. However, the NE-SW-trending narrow zone with the increased heat flux along the coastline (Figure 10.89a) is

mainly controlled by the present-day sea level which could have varied during the Saalian and Weichselian glacial periods. As noted earlier there are unfortunately no regional-scale data on the paleo-position of shoreline within the study area and, therefore, the modelled heat flux near the coastline within the areas with shallow bathymetry is at least partially uncertain within the uppermost levels of the 3D thermal model. Figure 10.89b shows the modelled heat flux without the influence of the Saalian and Weichselian glaciations, indicating that the heat flux is relatively high over the entire mainland. This increased heat flux is mainly caused by the thickened crystalline crust beneath the mainland (Figure 10.40a) which acts as an additional heat source due to its increased content of radiogenic elements and, therefore, contributes significantly to a deep heat flux (cf. Figures 10.89b & 10.90b). The same reason, associated with the thickness of the crystalline crust, helps to explain the increased modelled heat flux (around 55-60 mW/m^2) beneath the Trøndelag Platform in comparison with the Vøring and Møre basins which are underlain by a much thinner crystalline crust. Consequently, the heat flux is relatively low within the eastern parts of the Vøring and Møre basins, being in the range of 42-50 mW/m^2. These low values of the simulated heat flux are due to the presence of a thin crystalline crust in those areas (Figure 10.40a). The crystalline crust is actually quite thin beneath almost the entire Vøring and Møre basins but the northwestern part of the Coop2 model area is characterised by an increased heat flux. This is because of its proximity to the oceanic domain where both the Moho and the lithosphere-asthenosphere boundary are uplifted (Figures 10.40b & 10.41). The increased modelled heat flux is especially pronounced within the northwestern part of the Møre Basin, there reaching more than 70 mW/m^2.

The modelled temperatures at the Moho (Figure 10.90a) partially replicate the configuration of the Moho topography (Figure 10.40b), indicating that the key controlling factor, as in the case of the top of the crystalline basement, is again the depth position of the selected boundary. For that reason, the highest temperatures (more than 700 °C) are obtained beneath the northeastern part of the model area where the Moho is deepest. In contrast, this correlation between the depth position of the Moho and the modelled thermal pattern is not completely valid for the modelled heat flux (Figure 10.90b) which is more sensitive to the configuration of the lower thermal boundary. There is a zone with highly increased heat flux within the northwestern part of the Møre Basin. There, the heat flux varies from 50 to more than 60 mW/m^2, reflecting the influence of the early Cenozoic continental breakup and present-day position of the base of the lithosphere. The lowest values of the modelled heat flux have been obtained beneath the mainland where these values are in the range of 30-35 mW/m^2 on average.

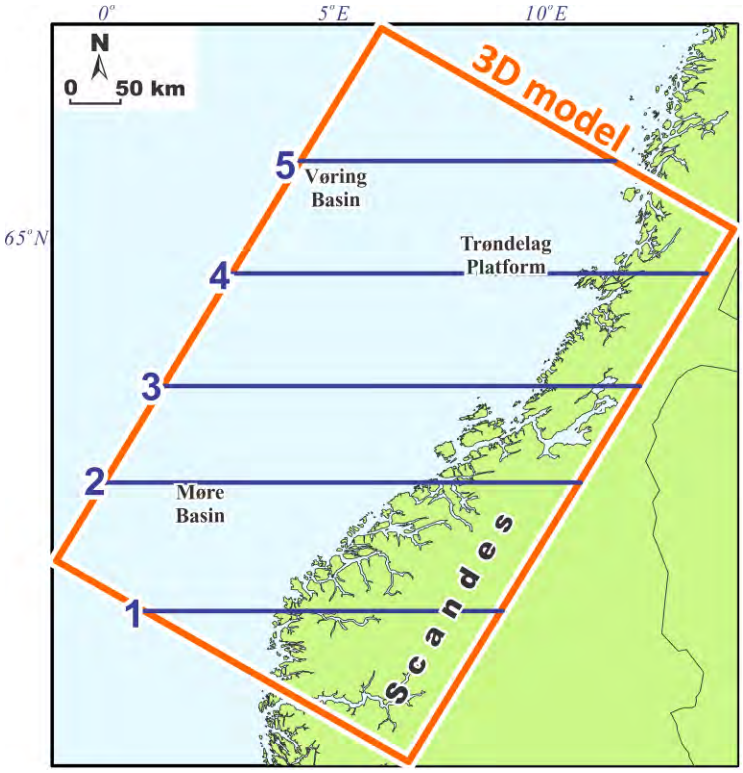

Figure 10.91. Location of the selected 2D vertical slices (blue lines) through the Coop2 3D thermal-structural model.

Five selected five 2D vertical slices (Figure 10.91) have been extracted from the 3D thermal model in order to show the cross-sectional view of the modelled subsurface temperatures (Figure 10.92). The locations of these cross-sections are the same as those through the 3D density and magnetic models (Figures 10.42 & 10.61). The interesting feature along the vertical slices 1, 2 and 4 is that an uplift of the modelled isotherms does not always correlate with the shallow position of the Moho (Figure 10.92). This is due to the relatively shallow paleo- and present-day positions of the lower thermal boundary at the base of the lithosphere within the western part of the Coop2 model area (Figures 10.17b, 10.41 & 10.74). This means that the long-wavelength component of the deep heat from the Earth's interior, controlled by the geometry of the lithosphere-asthenosphere boundary, prevails over the thermal disturbance related to the Moho topography within the Coop2 model area. For instance, the subhorizontal calculated isotherms are intersected by a rapidly deepening Moho within the eastern parts of lines 3 and 4 (Figure 10.92). The large-scale deep thermal pattern is disturbed mainly in places where significant contrasts occur in the thermal properties of the upper mantle material, crystalline crustal rocks and/or sediments. For example, the modelled isotherms mainly follow the depth position of the Moho along the western parts of the vertical slices 3 and 4 (Figure 10.92). There, the uplift of the modelled temperatures within the crust spatially coincide with the areas where the Moho is shallow and the sediments are thickest. Consequently, a superposition of the chimney effect of the high thermally conductive upper mantle material in the areas with the uplifted Moho and thermal blanketing of the low thermally conductive thick sedimentary infill results in the increased modelled temperatures within the crystalline crust.

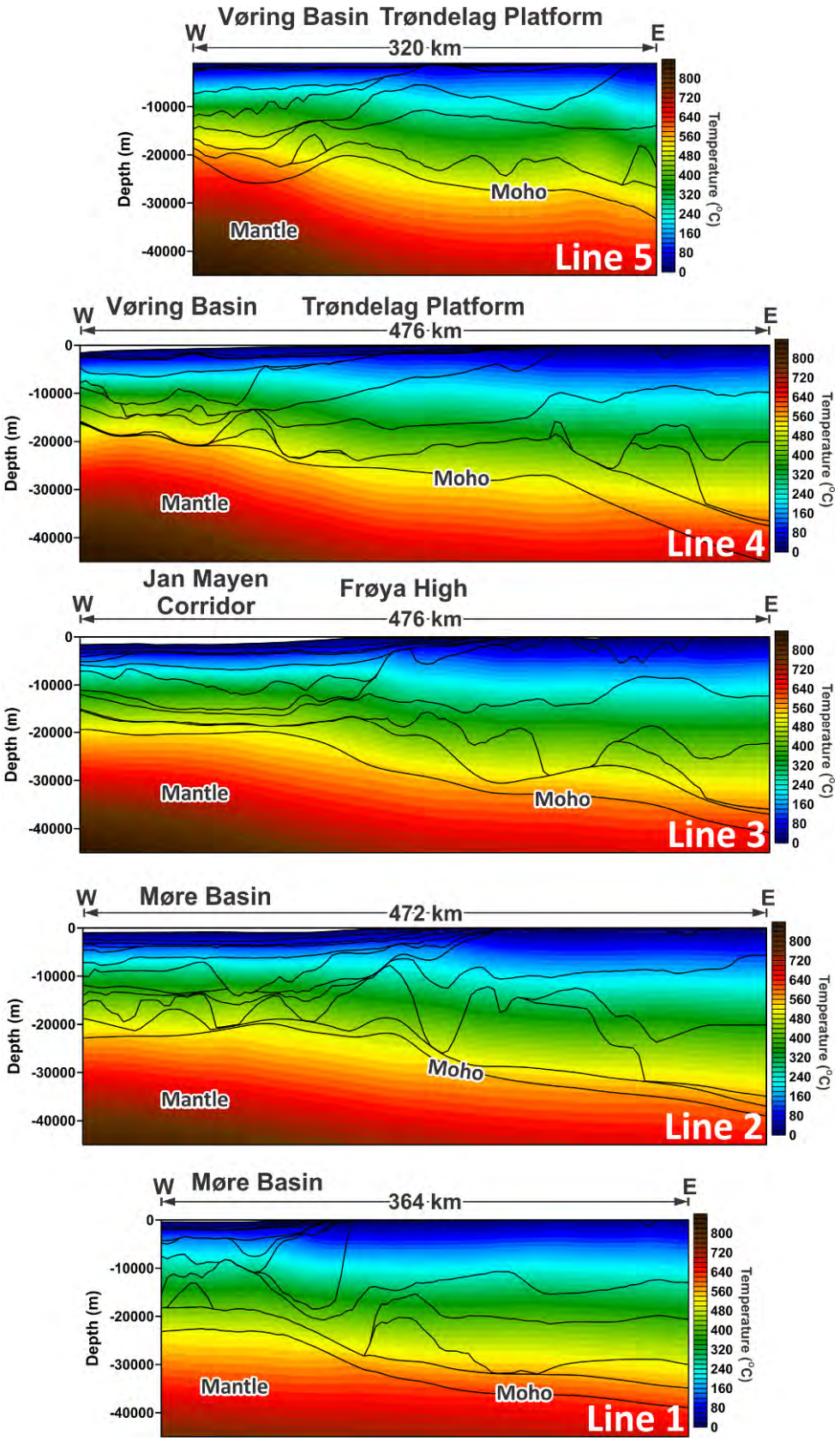

Figure 10.92. Subsurface modelled temperatures along five selected 2D vertical slices through the Coop2 3D thermal model (for the location of these slices, see Figures 10.42, 10.61 & 10.91). The vertical exaggeration is 3.3 times.

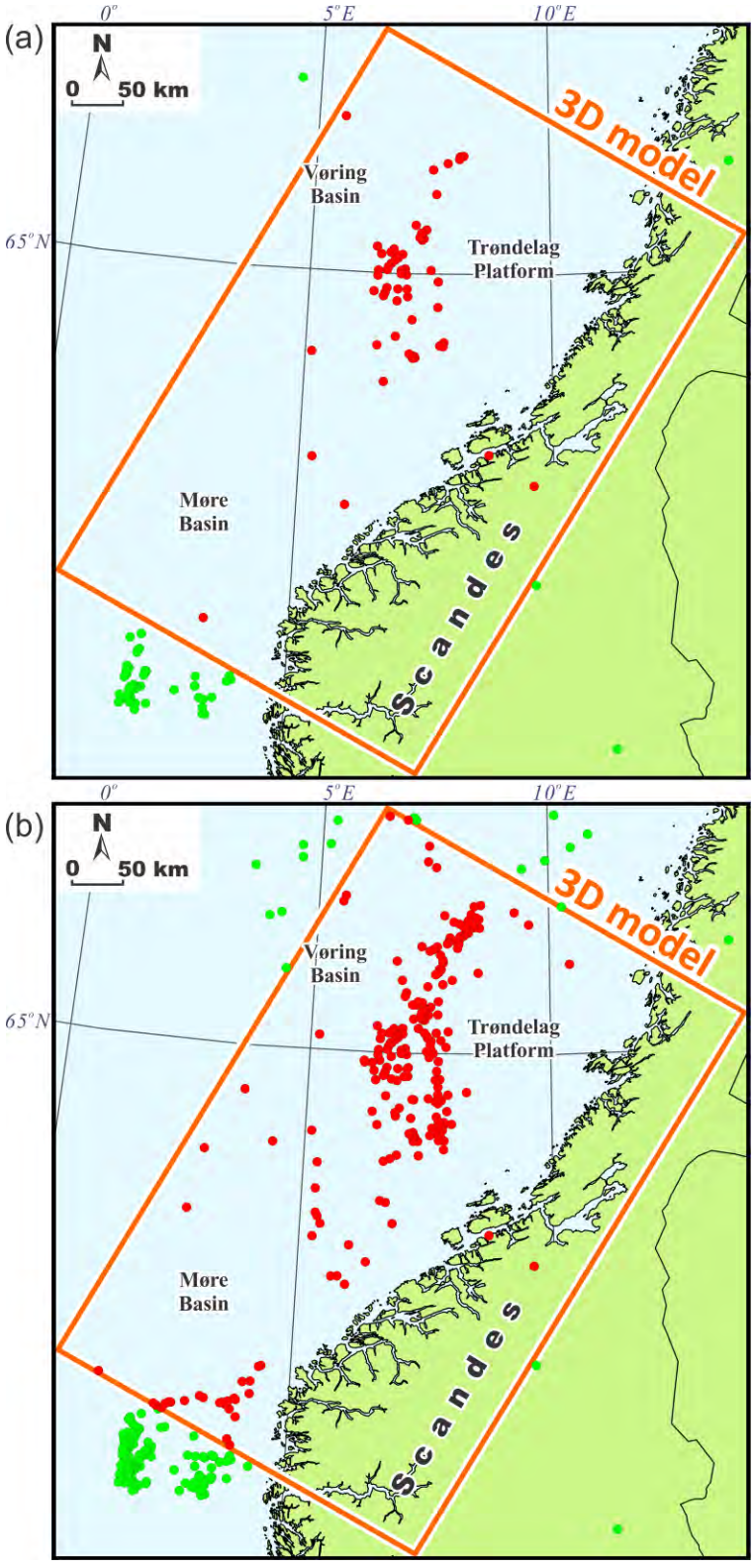

Figure 10.93. Location of the available wells with the measured temperatures. (a) Wells with DST (drill-stem test) temperatures. (b) Wells with less reliable bottom-hole temperatures (BHT) are also shown in addition to the DST temperatures. Wells in red are located inside of the Coop2 model area, and the green ones are located outside of the model area.

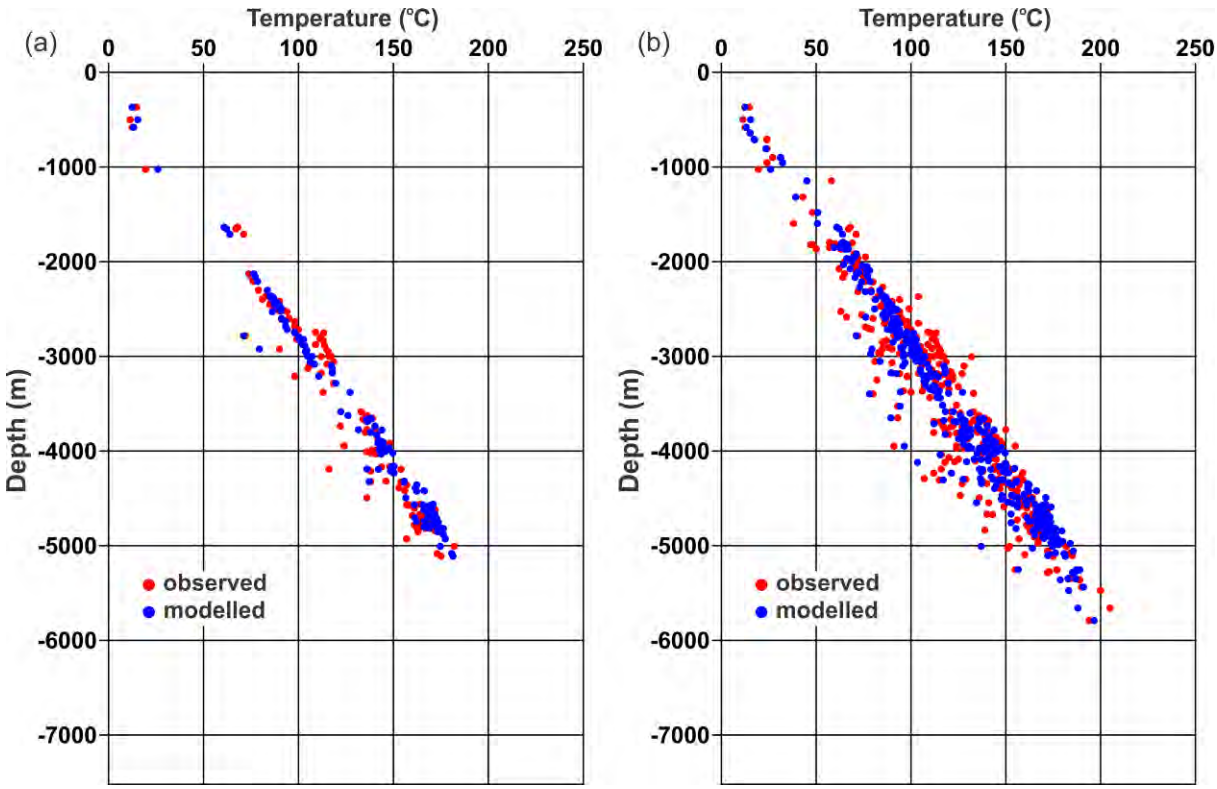

Figure 10.94. Misfit between the calculated (blue dots) and the observed (red dots) temperatures for the wells which are located inside of the Coop2 model area. (a) Only wells with DST (drill-stem test) temperatures are used. (b) Wells with less reliable bottom-hole temperatures (BHT) are also included in addition to the wells with DST.

The variations of the modelled temperatures within the uppermost part of the 3D thermal/structural model have been compared with measured temperatures in available wells. The locations of all accessible wells with the measured temperatures are shown in Figure 10.93. For the Mid-Norwegian continental margin, positions of the wells with only DST (drill-stem test) temperatures, and temperatures from well loggings are shown in Figure 10.93a, whereas the positions of the wells with less reliable bottom-hole temperatures (BHT) in addition to the previous wells are shown in Figure 10.93b. The wells are highlighted by different colours depending on their location in relation to the Coop2 model area. Wells indicated by red colour are located inside the Coop2 model area, and the green wells are from external areas. This has been done in order to separate the external wells which have been used as supplementary data to constrain the thermal regime in the regions adjacent to the Coop2 model area (Figure 10.93). The complexity with bottom-hole temperatures (BHT) values is that these values were measured near the bottom of the wells either during drilling or shortly after the drilling process was finished. In this case, these temperatures contain an element of thermal disturbance within the boreholes due to circulation of the drilling fluid. For that

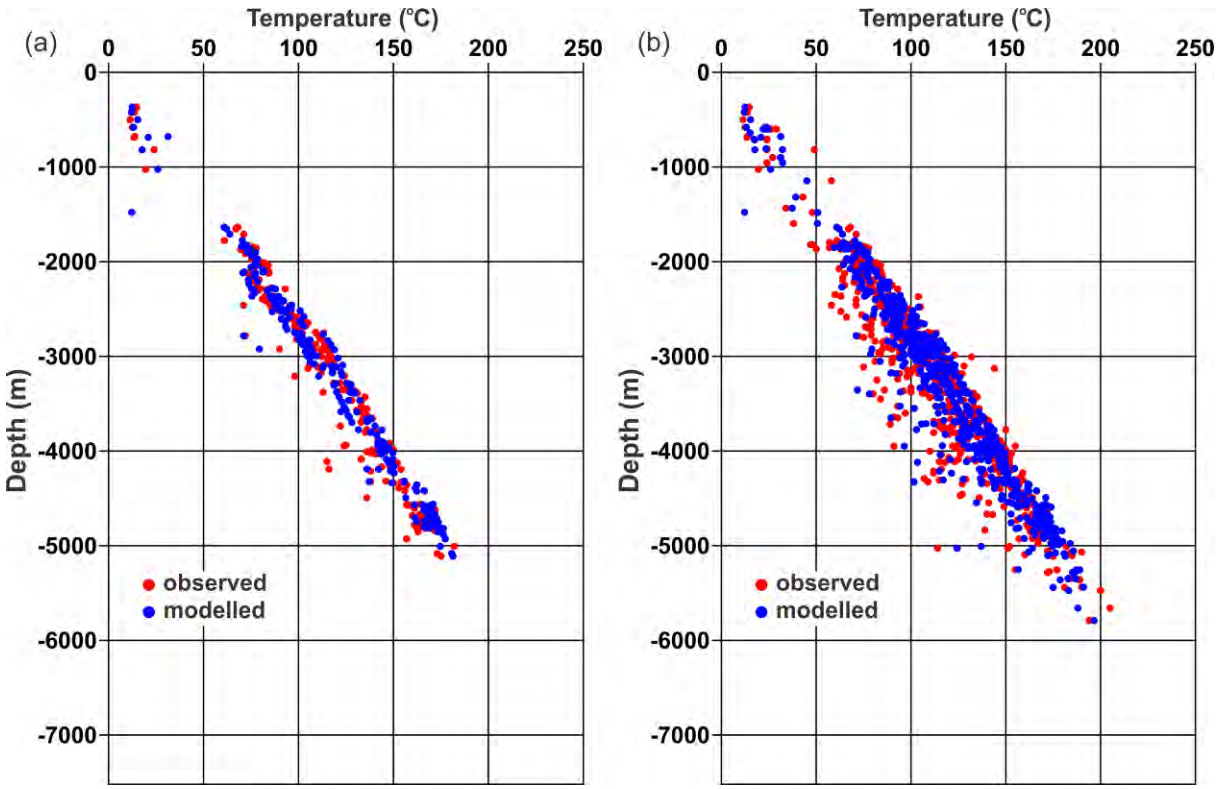

Figure 10.95. Misfit between the calculated (blue dots) and the observed (red dots) temperatures for the wells which are located inside and outside of the Coop2 model area. (a) Only wells with DST (drill-stem test) temperatures are used. (b) Wells with less reliable bottom-hole temperatures (BHT) are also included in addition to the wells with DST.

reason, bottom-hole temperatures (BHT) are unfortunately not totally reliable even if these temperatures are the Horner-corrected values. On the contrary, drill-stem test (DST) temperatures and temperatures from well logs are generally obtained after reaching thermal equilibrium in the wells and, accordingly, are more reliable for constraining the subsurface thermal field of the study area. Nevertheless, due to a shortage of drill-stem test (DST) data within the Mid-Norwegian continental margin (Figure 10.93a), bottom-hole temperatures (BHT) have also been used to compare the modelled temperatures with the measured ones. In order to separate these two datasets with different reliabilities, the results of the comparison are provided separately for drill-stem test (DST) temperatures (Figures 10.94a, 10.95a, 10.96a, 10.97a & 10.98a; Table 10.10) and for drill-stem test (DST) temperatures together with bottom-hole temperatures (BHT) (Figures 10.94b, 10.95b, 10.96b, 10.97b & 10.98b; Table 10.11). Furthermore, a comparison of the obtained results with the observations has been separately provided for the wells which are located inside (Figures 10.94 & 10.96) and outside (Figures 10.95 & 10.97) of the Coop2 model area.Comparison of the measured and modelled values of temperature indicates that the results of the 3D conductive thermal modelling are in a reasonable agreement with the general trends of the measured temperatures (Figures 10.94 & 10.95). In spite of a good general fit, there are also clearly visible large misfits in Figures 10.94 and 10.95. In order to understand the magnitude of these large misfits, a more detailed analysis has been performed by plotting the difference between the measured and modelled temperatures (the measured temperatures minus the modelled ones) in relation to depth (Figures 10.96 & 10.97). From these plots it is obvious

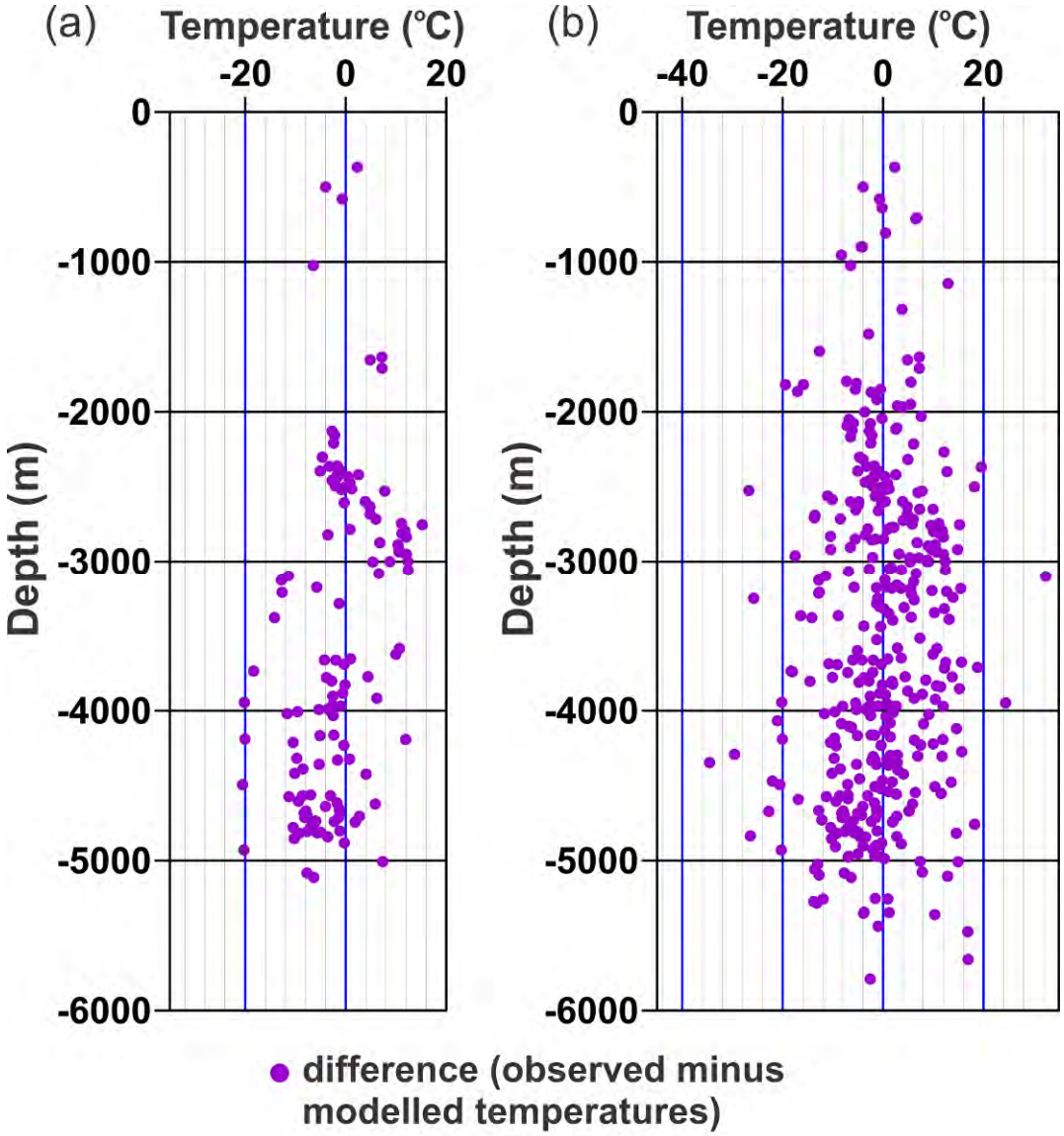

Figure 10.96. Temperature difference values (measured temperature minus the modelled one) for the wells which are located inside of the Coop2 model area. (a) Only wells with DST (drill-stem test) temperatures are used. (b) Wells with less reliable bottom-hole temperatures (BHT) are also included in addition to the wells with DST.

that most of the misfits between the modelled and measured temperatures are in the range of ±10 °C. In the case of the wells located inside the Coop2 model area, around 78% of the misfits are in the range of -10–+10 °C, if the wells with only the drill-stem test (DST) temperatures are considered (Table 10.10). Those misfits with a range of ±10 °C are slightly lower at around 73% (Table 10.11), if the wells with bottom-hole temperatures (BHT) are considered as well. This large portion of the difference in the range of ±10 °C implies that thermal conduction is the dominant mechanism of heat transfer at the large scale within the Mid-Norwegian continental margin. However, according to Figures 10.96 and 10.97 and Tables 10.10 and 10.11, misfits of more than ±10 °C between the modelled and measured temperatures are also recorded. Moreover, some of the misfits are even greater than ±20 °C and even up to 40 °C locally.

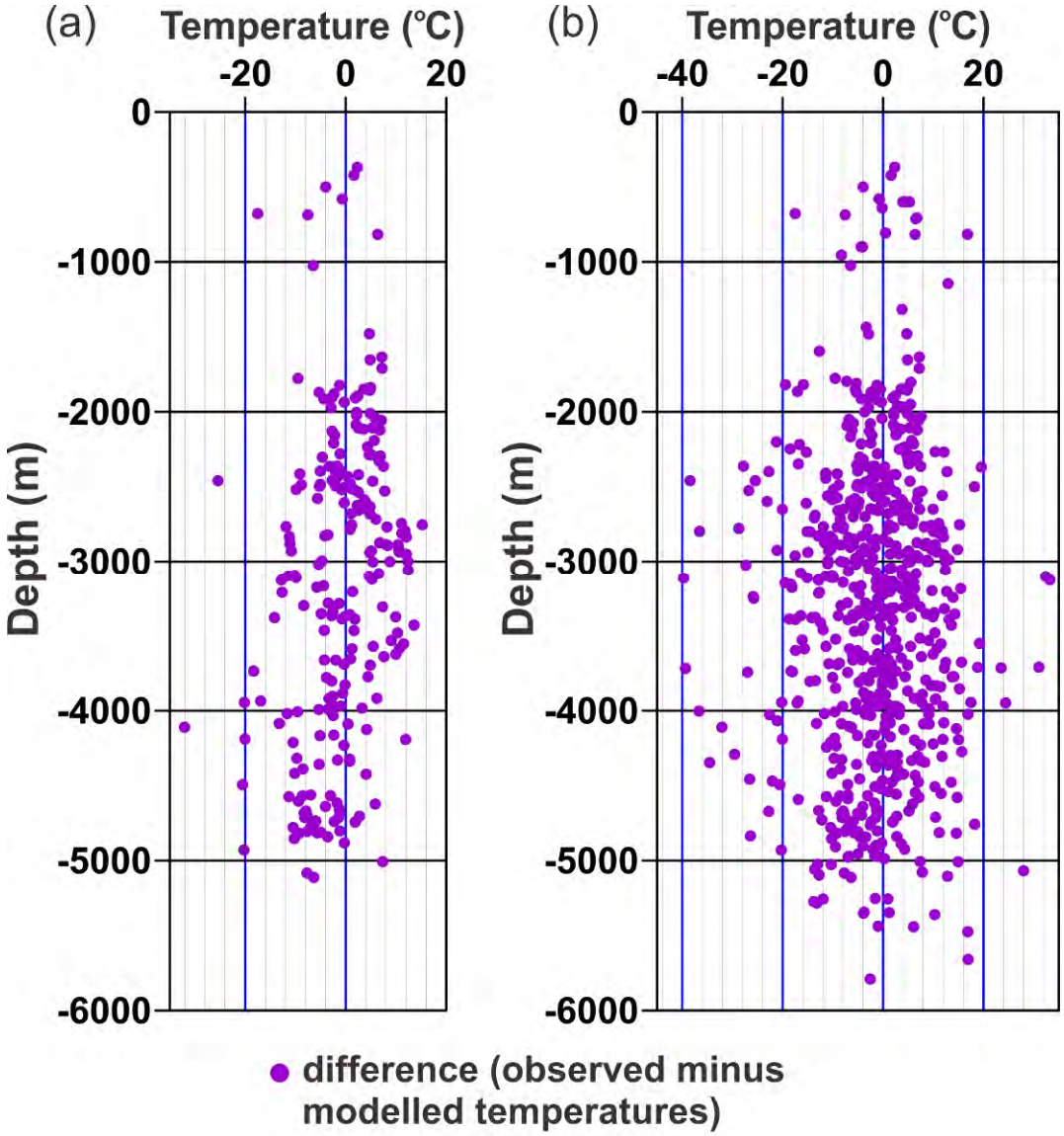

Figure 10.97. Temperature difference values (measured temperature minus the modelled one) for the wells which are located inside and outside of the Coop2 model area. (a) Only wells with DST (drill-stem test) temperatures are used. (b) Wells with the less reliable bottom-hole temperatures (BHT) are also included in addition to the wells with DST.

Table 10.10. Comparison of the difference between modelled temperatures and measured ones (measured values minus the modelled ones) in available deep boreholes obtained for the wells which are located inside the Coop2 model area. Only the DST (drill-stem test) temperatures are used.

N	Temperature range of differences between modelled and measured temperatures	Percentage of values, %	Number of values
1	from -25 to -20	3.1	4
2	from -20 to -10	8.5	11
3	from -10 to -5	19.2	25
4	from -5 to 5	50.0	65
5	from 5 to 10	9.2	12
6	from 10 to 20	10.0	13

Table 10.11. Comparison of the difference between modelled temperatures and measured ones (measured values minus the modelled ones) in available deep boreholes obtained for the wells which are located inside the Coop2 model area. In addition to the DST (drill-stem test) temperatures, the less reliable bottom-hole temperatures (BHT) are also included.

N	Temperature range of differences between modelled and measured temperatures	Percentage of values, %	Number of values
1	from -35 to -25	1.3	5
2	from -25 to -20	1.8	7
3	from -20 to -10	9.8	38
4	from -10 to -5	15.3	59
5	from -5 to 5	45.9	177
6	from 5 to 10	12.2	47
7	from 10 to 20	13.0	50
8	from 20 to 25	0.3	1
8	from 25 to 40	0.5	2

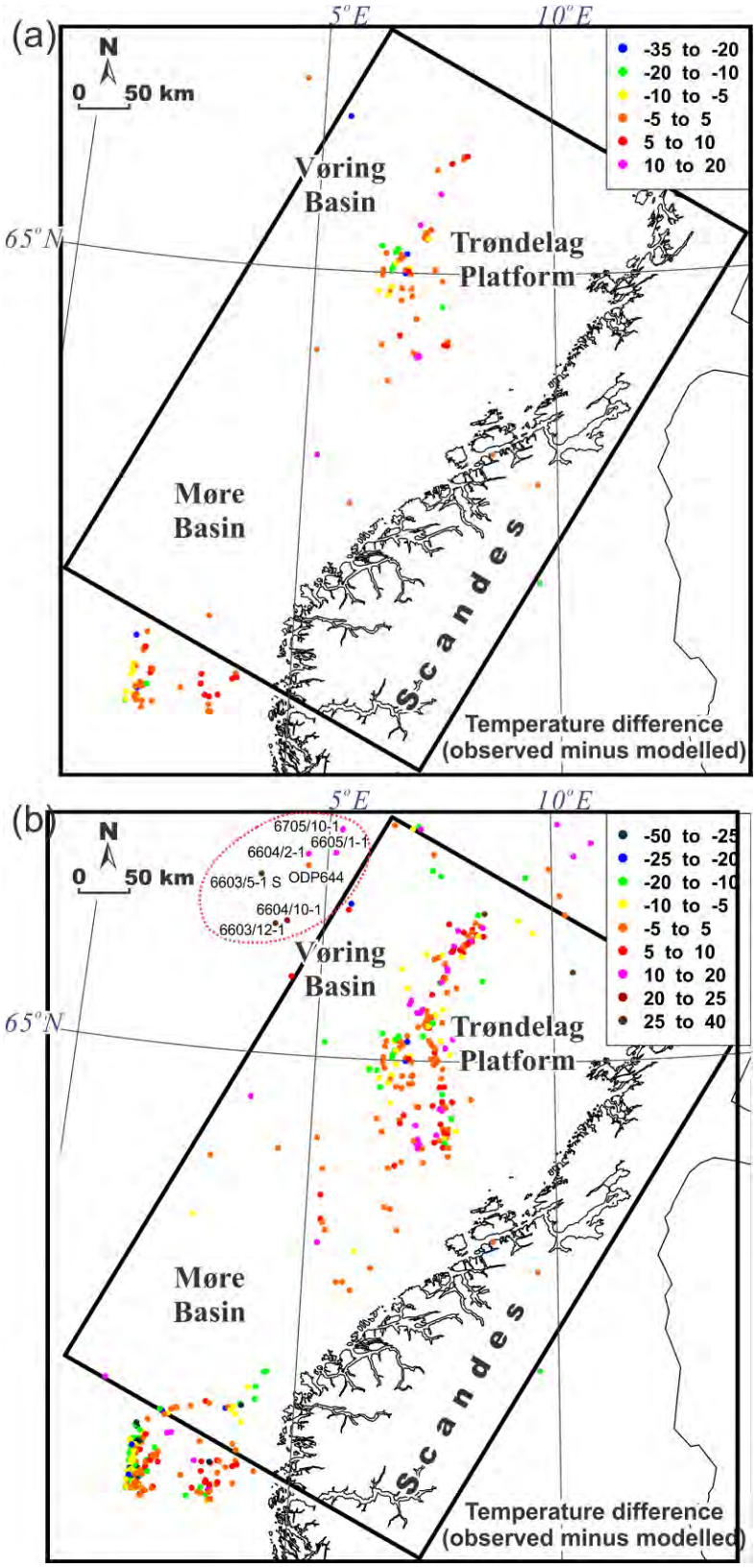

Figure 10.98. Spatial distribution of temperature difference values (measured temperature minus the modelled one) within the whole study area. (a) Only wells with the DST (drill-stem test) temperatures are used. (b) Wells with the less reliable bottom-hole temperatures (BHT) are also included in addition to the wells with DST.

The spatial distribution of the differences between the modelled and the measured wells demonstrates that some wells with large misfits are located relatively close to the wells where the misfits are suitable for this kind of regional-scale study (Figure 10.98). In some places, the distance between wells with different values of the misfits is comparable to the horizontal resolution of the Coop2 3D structural model and, for that reason, an improvement of the temperature fit in one well will automatically lead to an increase of misfit in the neighbouring one and vice versa. Moreover, local structural features of the Mid-Norwegian continental margin could not be resolved with sufficient detail to represent the complete lithological section of any one particular well in the places where these wells are located. Therefore, in these specific locations the measured temperatures cannot be correctly reproduced by the purely conductive 3D thermal modelling. Actually, some or even most of the large misfits are probably associated with the convective or advective heat transfer which is superimposed on the regional conductive thermal field in the areas where geothermally heated or cooled fluids circulate through the sedimentary succession.

A fluid-related thermal disturbance is most likely responsible for the large misfits in the external wells which are located in the vicinity of the northwestern corner of the Coop2 model area (see an area outlined by the red dashed line in Figure 10.98b). There, the relatively large residual misfits between the modelled and measured temperatures are still present in the wells located within the western part of the Vøring Basin. These residual misfits are especially large in wells 6603/5-1S and 6603/12-1, reaching around 30 °C there. In other boreholes (6604/2-1, 6604/10-1, 6605/1-1 and 6705/10-1), the residual misfits are in the range of 14-24 °C. The misfits are called residual because they were almost two times larger in the 3D thermal models without taking into account the influence of the early Cenozoic continental breakup during the 3D thermal modelling procedure. The difference in temperature between the thermal models with and without taking into account the influence of the strongly uplifted isotherms during the continental breakup are shown in Figure 10.99. According to the maps in Figure 10.99, the considerable influence of the continental breakup is mostly restricted to the northwestern side of the Coop2 model area. There, the residue of the breakup-related heating is still recognisable in terms of the increased temperatures within the positive thermal anomaly represented by the thermal difference between the modelled temperatures with the influence of the continental breakup and those without including the breakup into the modelling procedure. This difference is more than 50 °C at the top of the crystalline basement (Figure 10.99a) and reaches more than 70 °C at the level of Moho (Figure 10.99b). However, this attempt was not really successful for reproducing the measured temperatures in the problematic wells by purely conductive heat transfer in the area, highlighted by the red dashed ellipsoid in Figure 10.98b, if the reasonable thermal properties are assigned and a realistic structural configuration is used. The modelled temperatures have only been moved much closer to the measured ones but an acceptable fit has not been achieved in those wells. The measured temperature in well 6603/12-1 is already 139 °C at only 2335.5 m of the true vertical depth below the sea floor (absolute depth is 3736.5 m), assuming a linear geothermal gradient from the sea bottom of 60 °C/km, which is the highest

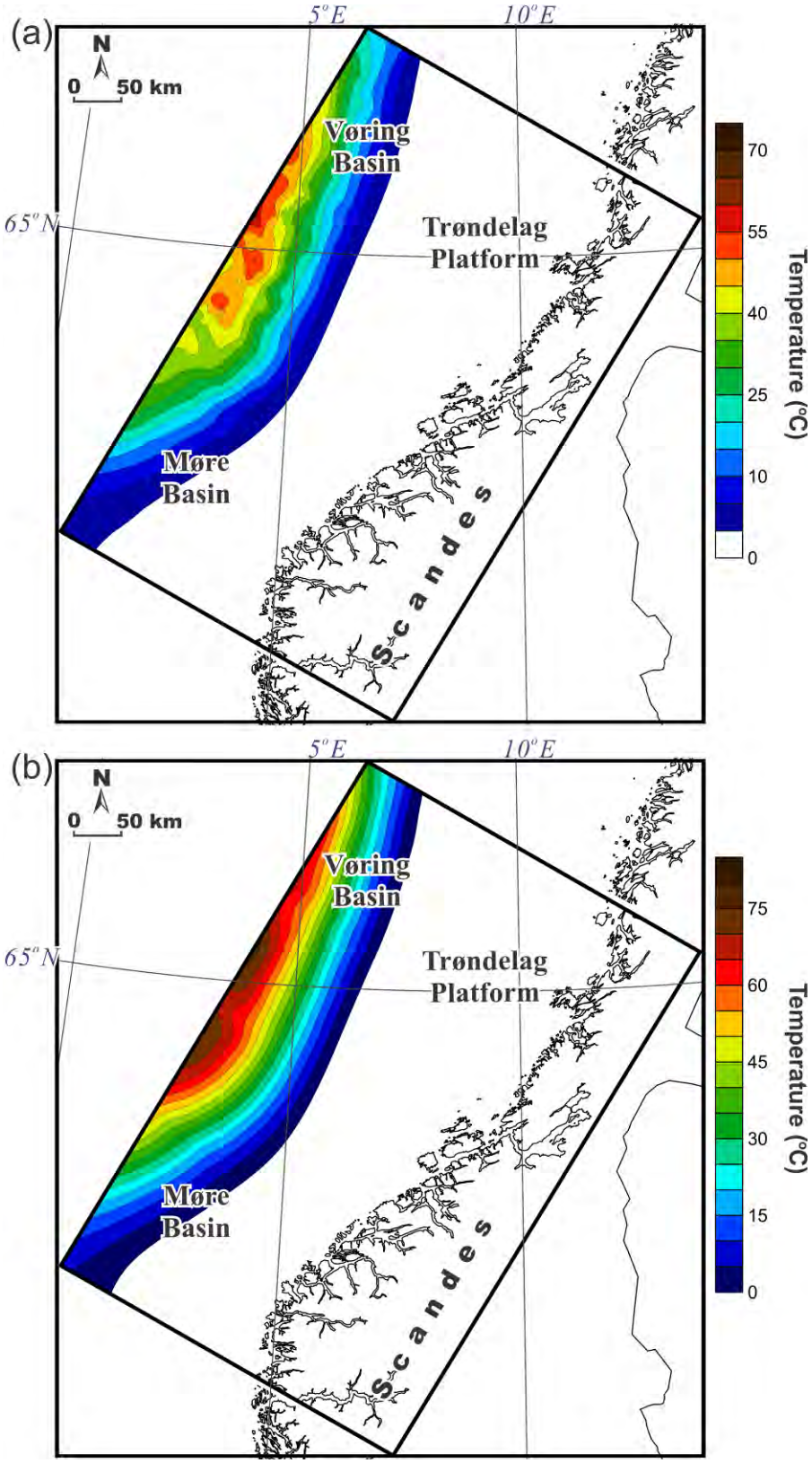

Figure 10.99. Temperature difference between the modelled temperatures with an influence of the continental breakup and without including the breakup (temperature with breakup minus temperatures without breakup): (a) at the top of the crystalline basement and (b) at the Moho.

value in the case of the Norwegian exploration wells (NPD, 2014). In well 6603/5-1 S, the estimated temperature is 190 ± 5 °C at the absolute depth of 5254 m. These temperatures are bottom-hole temperatures (BHT) and, therefore, can differ from the equilibrium temperatures. On the other hand, from the theoretical point of view, these temperatures can be even higher rather than lower, if the equilibrium temperatures would be reached after stopping circulation of the drilling fluid. There is only one suitable fit between the modelled and the measured temperatures in the scientific well ODP Site 644 (Eldholm et al. 1987), being around 5 °C at a total depth of 1479 m that is only slightly more than 200 m below the sea floor. Therefore, the temperature in this well represents a rather shallow temperature compared to the temperatures measured in the deep exploration wells. Another well from the ocean drilling program (ODP Site 642) is located on the Vøring Plateau which is outside of the NGU large-scale 3D structural model, but this borehole is interesting in terms of the fluid inflow. In this well, a positive temperature excursion at a depth of around 500 m below the sea floor may indicate a significant fluid in-flow which is also supported by the other logs in this well (Channell et al. 2006). A similar situation can also be suggested for the external wells near the northwestern corner of the Coop2 model area but, in this case, the origin of the fluid flow can differ from the ODP Site 642 due to the greater depth and different structural domain. Moreover, hydrothermal activities have been reported at the Gjallar Ridge (e.g., Njone 2014), indicating that the presence of hydrothermal vent and sill complexes together with accompanying faults could create favourable conditions for the convective heat transfer by fluid flow within the northwestern part of the Vøring Basin.

A comparative analysis of the results of 3D thermal modelling with the measured temperatures therefore indicates that there is a good correlation between the measured and modelled temperatures in general, with some large misfits which cannot be reduced by the purely conductive heat transfer with the present resolution of the 3D structural model. In other words, a significant improvement can only be obtained by increasing the horizontal resolution and number of the lithologically differentiated layers of the 3D structural model, involving simulations of fully coupled fluid flow and heat transfer in 3D with a more detailed paleo-scenario for the continental breakup. However, 3D thermal models that take into account the influence of fluid flow cannot be correctly established without detailed hydrogeological, lithological and structural constraints for the deeper parts of the study area and, therefore, cannot be performed within the framework of the present study.

10.6 SUMMARY

In summary it can be stated that the lithosphere-scale 3D structural model of the Mid-Norwegian continental margin and the adjacent areas of the continent has been constructed by using both previously published, publically available datasets and recently obtained confidential data. This data-based 3D model has been successfully validated by the 3D density modelling and has been modified in detail during the 3D magnetic modelling. Consequently, the constructed 3D structural model represents the present-day state of our knowledge about the structure of the sedimentary infill and the crystalline crust within the Coop2 model area. Finally, the 3D subsurface temperature distribution within the study area has been obtained by the 3D thermal modelling.

In particular, the 3D density analysis incorporates all available structural data for the deep part of the study area by a density/structure-controlled filling of the gaps between the existing data sets. Therefore, the results of the 3D density modelling provide a first-order configuration of the crystalline crust that is consistent with the long-wavelength characteristics of the observed gravity over the Mid-Norwegian continental margin and adjacent areas. The obtained Moho topography clearly correlates with the major tectonic units of the continental margin where a deep Moho corresponds to Precambrian continental crust and the shallower one is located in close proximity to the younger oceanic lithospheric domain. The 3D density modelling is in accordance with previous studies which indicate the presence of a high-density/high-velocity lower-crustal layer beneath the Mid-Norwegian continental margin. Local thickening of the high-density lower-crustal layer is partially due to a magmatic underplating within the western parts of the margin as a result of the continental breakup in the early Cenozoic. On the other hand, the eastern parts of the high-density lower-crustal layer are most likely related to the pre-breakup compositional heterogeneities in the lower continental crust. The presence of the thickened zones of the high-density lower-crustal layer and high-density zones of the crust could have played an important role in strain localisation during the Mesozoic-Cenozoic and earlier tectonic events, being a rheological heterogeneity with contrasting physical properties within the crystalline crust. For example, the location of the Møre-Trøndelag Fault Complex coincides spatially with the strong thickening of the high-density lower-crustal layer and high-density zones and, therefore, this fault zone is most likely controlled by the configuration of the high-density crustal heterogeneities internally within the crust. The important outcome of the 3D density modelling is that the crystalline crust is relatively thin and dense beneath the Møre and Vøring basins. Furthermore, the broad Jan Mayen gravity low is partially related to the decreasing density of the sedimentary layers within the Jan Mayen tectonic corridor, assuming a lesser degree of compaction and therefore a higher porosity of the sedimentary rocks in that area compared to the rest of the margin. This feature can be considered as favourable for hydrocarbon accumulations on the one hand. On the other hand, the Cenozoic tectonic activity along the oceanic Jan Mayen Fracture Zone could also have affected the adjacent Jan Mayen Corridor and destroyed at least partially the possible reservoirs there. Moreover, the Jan Mayen gravity low has also to be considered in relation to a possible low-density composition- and/or temperature-related zone in the lithospheric mantle, in addition to the low density of the sedimentary infill. This complex dilemma cannot be resolved by the present study and requires

additional constraints and/or a more detailed analysis, involving a structural, possibly thermo-mechanical, modelling of the paleo-tectonic movements along the oceanic Jan Mayen Fracture Zone, in order to understand the present-day configuration of the lithospheric mantle beneath the continental Jan Mayen Corridor.

According to the results of the 3D magnetic modelling, magnetically anomalous parts of the layers from the 3D density/structural model have been differentiated into crustal blocks with differing magnetic susceptibility, implying that these blocks lithologically differ from the rest of the initial density/structurally-derived layers. The absence of a strong magnetic anomaly over the Utgard High indicates that the uplifted crystalline rocks are not so magnetic there, supporting a suggestion that the entire crystalline crust has a low magnetisation beneath the greater part of the Vøring Basin and the northern part of the Møre Basin. In this case, the absence of any significant magnetic anomalies there is not only due to the fact that magnetic crystalline rocks are deeply located within the Møre and Vøring basins, but it can also be associated with a specific lithological composition of the crystalline crust in that area. In contrast, the crystalline crust is much more magnetic beneath the Trøndelag Platform, the southern part of the Møre Basin and within the mainland, reaching a culmination within the Frøya High where the most intensive magnetic anomaly is observed within the study area. During the 3D magnetic modelling, a large area of the lower crystalline crust beneath the continent has been assumed to be a source for the remanent magnetisation, which can explain the origin of the observed large-scale magnetic lows in the area where the Hedmark Basin is located and, therefore, these anomalies can possibly be related to the formation of this basin. However, the Hedmark Basin was involved in thrusting during the Caledonian Orogeny, implying that the origin of the remanent magnetisation may have another cause. Therefore, the large negative magnetic anomalies over the mainland have to be investigated in more detail, including an additional rock sampling at the present-day surface in order to exclude, or possibly even include, the near-surface origin of the remanent magnetisation in that area. Moreover, the origin of the magnetic remanence can be additionally tested by use of satellite magnetic data for global models involving the entire Fennoscandian Shield.

In general, the results of the 3D thermal modelling have taken us a step further in understanding the major features of the 3D conductive thermal field within the Mid-Norwegian continental margin and the adjacent areas of the mainland. The obtained first-order characteristics of the subsurface thermal pattern can be used to estimate the maturation of organic matter and, therefore, to make progress in regional strategies for hydrocarbon exploration within the Trøndelag Platform and Vøring and Møre basins, as well as to evaluate the geothermal potential within the mainland. Actually, during preparation of the input data for the 3D thermal modelling, interesting results have already been obtained about the spatial and temporal distribution of radiogenic heat production of the sedimentary rocks. A clearly distinguished zone of increased radiogenic heat production is easily traceable through the Cretaceous and Cenozoic stratigraphic intervals, implying a possible inheritance from the transport of eroded clastic material from the same erosional area within the continent where crystalline rocks with high or enhanced contents of the radiogenic elements were once exposed. Besides, the radiogenic pattern of sedimentary rocks may indicate a differentiation of the eroded

clastics by grain size during their transportation. Therefore, a more detailed study on radiogenic heat production of sedimentary successions could provide a much better knowledge of sediment transport and differentiation of the eroded material during at least the Cretaceous and the Cenozoic. Consequently, including a large number of the analysed wells for smaller stratigraphic intervals may possibly reveal the true provenance of the variably-sorted clastic material, thus providing, in combination with other methods, a possibility to correlate the radiogenic pattern of the sedimentary infill with probable sources for eroded material on the mainland. Moreover, this kind of analysis can also be performed for the entire Norwegian shelf by use of all available wells with their natural gamma logs. Coming back to the results of the 3D thermal modelling, it has to be emphasised that a comparison of the modelled temperatures with the measured ones in the wells indicates that there is a good correlation between the measurements and the present results of the simulations. However, the purely conductive thermal field within the Mid-Norwegian continental margin is most likely disturbed by fluid flow (convection and/or advection), as is indicated by large residual misfits between the measured and the modelled temperatures in some of the boreholes. Finally, including the paleo-scenario for the continental breakup with different depths to the lower thermal boundary into the modelling procedure improves the modelled temperatures, indicating that the thermal influence of the early Cenozoic continental breakup is still significant within the western part of the Coop2 model area. Further improvements to the results can be achieved by increasing the horizontal and vertical resolutions of the 3D structural model, as well as by involving simulations of fully coupled fluid flow and heat transfer with a better constrained paleo-scenario for the continental breakup and the post-break relationship between erosion onshore and sedimentation offshore.

11. CONCLUSIONS

1) An updated and seamless map of the basement geology and subcrop pattern along the coast of Western and Mid Norway is based on the new Coop aeromagnetic and batymetry/topography compilations and existing 1:250.000 bedrock maps.
2) The onshore-offshore relationship has been interpreted in terms of structural inheritance and prolongation of the late post-orogenic detachments mapped onshore. The newly identified Folda-Rørvik-Brønnøysund shear zone appears to represent an old and major continental, strike-slip feature along the coast of Mid Norway. This shear zone probably influenced the prolongation of the Kollstraumen detachment, now slightly shifted in the offshore domain. The Høybakken detachment bifurcates towards this newly defined shear zone and may extend towards the western basins.
3) The heat-production mapping of the mainland basement rocks has been extended to Mid Norway. The results show variations by one order of magnitude, from less than 0.5 $\mu W/m^3$ to more than 4 $\mu W/m^3$.
4) Granitic rocks with high radiogenic heat production generate an increased heat flow in the Namdal-Vikna area in Nord-Trøndelag. The aeromagnetic map indicates that these Precambrian rocks extends to the west below the Halten-Frøya High area and can consequently explain an increased temperature within this area.
5) A zone of increased radiogenic heat production dominates the central part of the studied offshore area through the Cretaceous and Cenozoic stratigraphic intervals and implies a possible inheritance from the transport of eroded clastic material from the same erosional area.
6) The AMAGER mapping has been extended to Mid Norway and indicates that the Norwegian strandflat is an exhumed, weathered and peneplaned surface. We suggest that this Late Triassic to Early Jurassic surface was modified and levelled during Pleistocene erosion.
7) The studied weathering zones are developed in a wide variety of rock types. All of the weathered samples, even the greenstones, are characterised by being sandy and having low clay contents. This is typical for weathering processes at depth in regoliths, termed arenisation; commonly found in the Mediterranean climate zone.
8) Some of the weathered samples contain smectite and kaolinite, which indicates a formation in warmer climate, e.g. the climate in the Early Tertiary and Mesozoic. The accumulation of lanthanides in some of the weathering zones is supporting that the weathering occurred in a warm (sub-tropical) climate.
9) The composition of the weathered samples is different from the pre-Jurassic weathering profiles on Andøya, which show a pervasive weathering with almost complete dissolution of feldspars in the gneiss and the simultaneous authigenic formation of kaolinite. It is therefore suggested that the samples investigated in the present report, are from the deepest parts of a pre-Quarternary regolith, characterised by arenisation.
10) The Frøya High is interpreted as a Precambrian granitic complex quite similar to the magnetic Transcandinavian Igneous Belt (TIB) granitoids observed in Sweden and Norway.
11) Both lower and middle magnetic crust are likely preserved in the distal parts of the Møre margin and adjacent Jan Mayen corridor, at least up to the Vigra, Slettringen and Grip highs, which are interpreted as autochthonous continental crustal rafts.
12) Our model does not support any extensive syn-thinning (Mesozoic) serpentinisation of the mantle to the east where the preserved continental crust is still relatively thick

(>4-5 km). Serpentinisation conditions could be present along the Jan Mayen corridor but would be local and rather limited.

13) The Møre margin is interpreted as an aborted type-II rifted margin (e.g. Angola) reactivated in Late Cretaceous time before the formation of the outer volcanic margin.
14) The 3D density modelling indicates local thickening of the high-density lower-crustal layer partially due to a magmatic underplating within the western parts of the Mid-Norwegian continental margin as a result of the continental breakup in the early Cenozoic.
15) The high-density lower-crustal bodies in the central/outer Møre Basin, are most likely related to the pre-breakup (Caledonian?) heterogeneities in the lower continental crust.
16) The inherited structures possibly control the late structural style and development of the Mid-Norwegian margin and seem to have influenced the overall style of crustal thinning of the rifted margin.
17) The broad Jan Mayen Lineament gravity low is partially related to the decreasing density of the sedimentary layers within the Jan Mayen tectonic corridor, assuming a lesser degree of compaction and therefore a higher porosity of the sedimentary rocks. The gravity low may also be related to a possible low-density composition- and/or temperature-related zone in the lithospheric mantle.
18) A comparison of the 3D modelled temperatures with the measured ones in wells indicates that there is a good correlation between the measurements and the results of the simulations. The conductive thermal field within the Mid-Norwegian continental margin is most likely disturbed by fluid flow, as is indicated by large residual misfits between the measured and the modelled temperatures in some of the boreholes.
19) The thermal influence of the early Cenozoic continental breakup is still significant within the western part of the model area.

12. RECOMMENDATION FOR COOP PHASE 3

1. Extend the aeromagnetic coverage offshore central and western Norway to cover the Frøya High - Froan Basin area and southwards to the Måløy Terrace - Sogn Graben area by acquisition of the Coop Aeromagnetic Survey 2015 West (CAS-15W) consisting of 80.000 profile km.
2. Purchase the VGET-95 aeromagnetic survey from TGS Geophysical Company. A reprocessing of the 22 000 profile km will most likely be necessary.
3. Upgrade the Coop aeromagnetic compilation by adding the CAS-15W survey, an updated version of VGET-95, the Moldefjord Aeromagnetic Survey 2014 and the Helgeland Aeromagnetic Survey 2014 South (HAS-14S).
4. Improve the coastal gravity coverage by airborne and marine measurements in collaboration with the Norwegian Mapping Authority, the Norwegian Coast Guard and the Coastal Express (Hurtigruten). The airborne CAS-15E survey offshore Smøla consists of 2400 profile km with a line spacing of 2 km.
5. Compilation of data on weathered basement in the Ukrainian Shield as an analogue to deep weathering on the Fennoscandian Shield.
6. Drill an 800 m deep borehole on Veidholmen to the north of Smøla to check the possibility that the observed high heat flow on the Haltenbanken can be attributed to a westward extension of the Transcandinavian Igneous Belt (TIB) from the mainland of Trøndelag.
7. A study of the Cenozoic evolution of the NE Atlantic flexural strength including a detailed structural and thermo-mechanical modelling of the tectonic movements along the Jan Mayen Fracture Zone to help understanding the origin of the Cenozoic compressional domes and the Jan Mayen Lineament gravity low.
8. An in-depth study on the radiogenic heat production of the sedimentary successions on the Mid Norwegian margin to gain a better knowledge of the sediment transport and differentiation of the eroded material during the Cretaceous and the Cenozoic.
9. Generate a more detailed crustal and thermal model of the Frøya High and adjacent areas by increasing the horizontal and vertical resolutions of the 3D structural model.
10. Refined interpretations of the onshore-offshore relationships from the Rogaland area Sea to Helgeland including the new Coop Aeromagnetic Survey 2015 (CAS-15) High. The study will be combined with an extra and more recent CFI seismic dataset provided by TGS.
11. Modelling of the thermal effects of Neogene erosion/sedimentation in the North Sea.

Work tasks 1-5 are already underway. GeoDrilling will commence the drilling of an 800 m deep well on Veidholmen in January next year.

Acknowledgements

Novatem and EON Geosciences from from Mont-Saint-Hilaire and Montral in Québec, respectively carried out the airborne surveys. Clea Fabian, Henry Kalvøy and Melanie Mesli carried out the measurements of density and magnetic properties in NGUs laboratory. Jasmin Schönenberger and Bjørn Nilsen at NGU carried out the XRD and XRF analysis of weathered and 'fresh' rock samples. The sample preparation was performed by Wieslawa Koziel and Ann Elisabeth Karlsen. BayernGas, Centrica, ConocoPhillips, Det norske oljeselskap, DONG, Eni, E.ON, GdF Suez, Lundin Norway, Maersk Oil, NGU, Noreco, NPD, Repsol, Dea, Statoil, Suncor, Total, VNG and Wintershall funded the Coop Project. The sponsor representatives Tanni Juul Abramovitz, Gunnar Aschjem, Mats Andersson, Gunnar Aschjem, Dag Bering, Tom Bugge, Carlo Cavalli, Michele Marco Comisso, Ben De Mol, Ralf Ehrlich, Christine Fichler, Grim Gjeldvik, Christian Gram, Ebbe Hartz, Henning Hovland, Robert P. Johannessen, Åge Karlsen, Dirk Knaust, Ivar B. Kristvik, Marcus Lang, Jan Erik Lie, Anne-Lise Jensen Lysholm, Ingrid Magnus, Kathrin Mälzer, Chris Parry, Jochen Rappke, Jörgen Samuelsson, Morten Sand, Arnaud Santoire, Craig Schneider, Reinert Seland, Inger Flesland Strass, Jan Strømmen, Stephen Tarran, Filippos Tsikalas, Michael Young, Alastair Welbon, Tor Atle Wicklund and Alv Aanestad followed the progress of the project and gave advice during the different stages of the work tasks. TGS-NOPEC Geophysical Company (Reidun Myklebust) permitted us to display the Hunting-86, VGVB-94, VGCG-94, CGAM-95, VGET-95, Q17, MBAM-97, UHAM-09 and the two seismic lines, CFI-MNR-7086 and CFI-MNR-7179 in the present report. Åse Minde compiled the report. David Roberts read the report and improved the English text. We express our sincere thanks to all these persons, companies and institutions.

REFERENCES

Abdelmalak, M.M., Andersen, T.B., Planke, S., Faleide, J.I., Corfu, F., Tegner, C., Shepard, G.E., Zastrozhnov, D. & Mykelbust, R. 2015: The ocean-continent transition in the mid-Norwegian margin: Insight from seismic data and an onshore Caledonian field analogue. *Geology.* doi: 10.1130/G37086.1, 1-5.

Andersen, B.G. & Borns Jr., H.W. 1994: *The Ice Age World*. Scandinavian University Press (Universitetsforlaget AS), Oslo. 208 pp.

Andersen, O.B., Knudsen, P., Kenyon, S. & Holmes, S. 2014: Global and Arctic Marine Gravity Field From Recent Satellite Altimetry (DTU13). 76th EAGE Conference and Exhibition 2014. Amsterdam, *EAGE*.

Andersen, O.B., Knudsen, P., Kenyon, S., Factor, J.K. & Holmes, S. 2013: *The DTU13 Global marine gravity field – first evaluation*. Ocean Surface Topography Science Team (OSTST) Meeting, Boulder, USA.

Andersen, T.B. 1993: The Role of Extensional Tectonics in the Caledonides of South Norway - Discussion. *Journal of Structural Geology 15*, 1379-1380.

Andersen, T.B. 1998: Extensional tectonics in the caledonides of southern Norway, an overview. *Tectonophysics 285,* 333-351.

Andersen, T.B., Jamtveit, B., Dewey, J.F. & Swensson, E. 1991: Subduction and Eduction of Continental-Crust - Major Mechanisms during Continent-Continent Collision and Orogenic Extensional Collapse, a Model Based on the South Norwegian Caledonides. *Terra Nova* 3, 303-310.

Artemieva, I.M. & Thybo, H. 2013: EUNAseis: A seismic model for Moho and crustal structure in Europe, Greenland, and the North Atlantic region. *Tectonophysics 609*, 97-153, doi 10.1016/j.tecto.2013.08.004.

Artemieva, I.M., Thybo, H. & Kaban, M.K. 2006: Deep Europe today: Geophysical synthesis of the upper mantle structure and lithospheric processes over 3.5 Ga. *Journal of The Geological Society of London, Memoirs 32*, 11–41.

Askvik, H., Rokoengen, K. 1985: Berggrunnskart Kristiansund, M 1:250000. Norges geologiske undersøkelse.

Audet, P. & Burgmann, R. 2011: Dominant role of tectonic inheritance in supercontinent cycles. *Nature Geoscience* 4, 184-187.

Augier, R., Turillot, B., Hallégouët, B., Van-Vliet-Lanoë, B., Thinon, I. & Menier, D. 2000: Vannes ST Gildas-de-Rhuys feuille 417, BRGM geological map., *BRGM*.

Balling, N., Breiner, N. & Waagstein, R. 2006: Thermal structure of the deep Lopra-1/1A borehole in the Faroe Islands. *Geological Survey of Denmark and Greenland Bulletin 9,* 91–107.

Bainbridge, G., Musselman, C., Whitehead, N. & McDonald, N. 2002: *Euler 3D Deconvolution (v5.1.5). Processing, analysis and visualization system for 3D inversion of potential field*. Tutorial and User guide. Geosoft Manual, 66 pp.

Baranwal V.C., Rodionov A., & Ofstad F. 2012: Helicopter-borne magnetic and radiometric geophysical survey in Kviteseid area, Telemark, Norway. *NGU Report 2012.043*, 25 pp.

Baranwal V. C., Ofstad F., Rønning J.S. & Watson R.J. 2011: Mapping of caesium fallout from the Chernobyl accident in the Jotunheimen area. *NGU Report 2011.062*, 27 pp.

Baranwal V.C., Rodionov A., Ofstad F., Koziel J. & Lynum R. 2013: Helicopter-borne magnetic, electromagnetic and radiometric geophysical surveys in the Kongsberg region: Krøderen, Sokna, Hønefoss, Kongsberg and Numedalen. *NGU Report 2013.029*, 53 pp.

Barnes, C.G., Frost, C.D., Yoshinobu, A., McArthur, K., Barnes, M., Allen, C.M., Nordgulen, Ø. & Prestvik, T. 2007: Timing of sedimentation, metamorphism and plutonism in the Helgeland Nappe Complex, north-central Norwegian Caledonides. *Geosphere 3*, 683-703.

Barnes, C.G., Reid, K., Frost, C.D., Barnes, M.A. , Allen, C.M., & Yosinobu, A. 2011: Ordovician and Silurian magmatism in the Upper Nappe, Uppermost Allochthon, Helgeland Nappe Complex, North-Central Norway. *Norwegian Journal of Geology 91*, 121-136.

Barnes, C.G., Frost, C.D., Nordgulen, Ø. & Prestvik, T. 2012: Magma hybridization in the middle crust: Possible consequences for deep-crustal mixing. *Geosphere 8*, 518-533.

Bassett, M.G. 1985: SIlurian stratigraphy and facies developement in Scandinavia. *In* Gee, D.G. & Sturt, B.A. (eds.). The Caledonian Orogen-Scandinavia and Related Areas. *Chichester, John Wiley and Sons*, 283-292.

Bates, R. & Jackson, J. 1987: *Glossary of Geology*, American Geological Institute. Alexandria, Virginia, 788.

Bartlein, P.J., Anderson, K.H., Anderson, P.M., Edwards, M.E., Mock, C.J., Thompson, R.S., Webb, R.S., Webb III T. & Whitlock, C. 1998: Palaeoclimate simulations for North America over the past 21,000 years: Features of the simulated climate and comparisons with palaeoenvironmental data. *Quaternary Science Reviews 17*, 549-585.

Beard, L.P. 1998: Data acquisition and processing - helicopter geophysical survey, Oppkuven and Gran, 1997. *NGU Report 98.079*, 20 pp.

Beard, L.P. 1999: Data acquistion and processing - helicopter geophysical survey, Larvik, 1998. *NGU Report 99.026*, 13 pp.

Beard, L.P. & Mogaard, J.O. 2001: Data acquisition and processing – helicopter geophysical survey, Hurdal 2000. *NGU Report 2001.018*, 16 pp.

Beard, L.P. & Rønning, S. 1997: Data aquisition and processing report – helicopter geophysical survey, Krokskogen. *NGU Report 97.134*, 9 pp.

Behn, M.D. & Lin, J. 2000: Segmentation in gravity and magnetic anomalies along the US East Coast passive margin: Implications for incipient structure of the oceanic lithosphere. *Journal of Geophysical Research-Solid Earth 105*, 25769-25790.

Bell, R.E., Jackson, C.A-L., Elliott, G.M., Gawthorpe, R.L., Sharp, I.R. & Michelsen, L. 2014: Insights into the development of major rift-related unconformities fromgeologically constrained subsidence modelling: HaltenTerrace, offshore mid Norway. *Basin Research 26*, 203–224, doi: 10.1111/bre.12049.

Bellahsen, N., Fournier, M., d'Acremont, E., Leroy, S.,& Daniel, J.M. 2006: Fault reactivation and rift localization: Northeastern Gulf of Aden margin. *Tectonics 25*.

Bellahsen, N., Leroy, S., Autin, J., Razin, P., d'Acremont, E., Sloan, H., Pik, R., Ahmed, A. & Khanbari, K. 2013: Pre-existing oblique transfer zones and transfer/transform relationships in continental margins: New insights from the southeastern Gulf of Aden, Socotra Island, Yemen. *Tectonophysics 607*, 32-50.

Ben Mansour, W., Moorkamp, M. & England, R.W. 2014: Joint inversion of seismological data and magnetotelluric data for the northern Scandinavian mountains. *AGU Fall Meeting, Abstract T23B-4668*, San Francisco, USA.

Berndt, C., Planke, S., Alvestad, E., Tsikalas, F. & Rasmussen, T. 2001: Seismic volcanostratigraphy of the Norwegian Margin: constraints on tectonomagmatic break-up processes. *Journal of the Geological Society 158*, 413-426.

Berndt, C., Skogly, O.P., Planke, S., Eldholm, O. & Mjelde, R. 2000: High velocity breakup-related sills in the Vøring Basin, off Norway. *Journal of Geophysical Research B, Solid Earth Planets 105*, 28443–28454.

Bingen, B. & Solli, A. 2009: Geochronology of magmatism in the Caledonian and Sveconorwegian belts of Baltica: Synopsis for detrital zircon provenance studies. *Norwegian Journal of Geology 89*, 267-290.

Bingen, B., Skar, O., Marker, M., Sigmond, E.M.O., Nordgulen, O., Ragnhildstveit, J., Mansfeld, J., Tucker, R.D. & Liegeois, J.P. 2005: Timing of continental building in the Sveconorwegian orogen, SW Scandinavia. *Norwegian Journal of Geology 85*, 87-116.

Birch, F. 1996: Compressibility, elastic constants. *In* Clark, S.P. (eds.). Handbook of physical constants. Volume 97, *Geological Sosciety of America, Memoir*, 97-174.

Bird, P.C., Cartwright, J.A. & Davies, T.L. 2015: Basement reactivation in the development of rift basins: an example of reactivated Caledonide structures in the West Orkney Basin. *Journal of the Geological Society 172*, 77-85.

Bjørkum, P.A., Oelkers, E.H., Nadeau, P.H., Walderhaug, O. & Murphy, W.M. 1998: Porosity prediction in quartzose sandstones as a function of time, temperature, depth, stylolite frequency, and hydrocarbon saturation. AAPG Bulletin – American Association of Petroleum Geologists 82, 637-648.

Bjørlykke, K., Elvsborg, A. & Høy, T. 1976: Late Precambrian sedimentation in the central sparagmite basin of south Norway. *Norsk Geologisk Tidsskrift 56*, 233-290.

Blaich, O.A., Faleide, J.I., Tsikalas, F., Franke, D. & Leon, E. 2009: Crustal-scale architecture and segmentation of the Argentine margin and its conjugate off South Africa. *Geophysical Journal International* 178, 85-105.

Blaich, O.A., Tsikalas, F. & Faleide, J.I. 2008: Northeastern Brazilian margin: Regional tectonic evolution based on integrated analysis of seismic reflection and potential field data and modelling. *Tectonophysics 458*, 51-67.

Blakely, R. 1995: *Potential theory in gravity and magnetic applications*. Cambridge University Press, 461 pp.

Blystad, P., Brekke, H., Faerseth, R.B., Larsen, R.B., Skogseid, J. & Torudbakken, B. 1995: Structural elements of the Norwegian continental shelf. Part II: The Norwegian Sea region. *Norwegian Petroleum Directorate Bulletin 8*, 45 p.

Boillot, G., Mougenot, D., Girardeau, J. & Winterer, E.L. 1989: Rifting Processes on the West Galician Margin, Spain. *In* Tankard, A.J. & Balkwill, H.R. (eds.). Extensional Tectonics and Stratigraphy of the North Atlantic Margins. Volume 46, *American Association of Petroleum Geologists, Memoir*, 363-377.

Bowling, J.C. & Harry, D.L. 2001: Geodynamic models of continental extension and the formation of non-volcanic rifted continental margins. *In* Wilson, R.C.L., Withmarch, R.B., Taylor, B. & Froitzheim, N. (eds.). Non-Volcanic Rifting of Continental Margins: A Comparison of Evidence from Land and Sea. *Geological Society of London, Special Publications 187*.

Braathen, A., Osmundsen, P.T., Nordgulen, Ø., Roberts, D. & Meyer, G. 2002: Orogen-parallel extension in the Caledonides in Central Norway: an overview. *Norwegian Journal of Geology 82*, 225-241.

Braathen, A., Nordgulen, Ø., Osmundsen, P.T., Andersen, T.B., Solli, A. & Roberts, D. 2000: Devonian, bi-directional, opposed extension in the Central Norwegian Caledonides. *Geology 28*, 615-618.

Brantley, S. L., White, T. S. & Ragnarsdottir, K. V. (eds.) 2007: The critical zone: Where rock meets life. *Elements 3.*

Breivik, A.J., Verhoe, J. & Faleide, J.I. 1999: Effect of thermal contrasts on gravity modelling at passive margins: results from the western Barents Sea, *Journal of Geophysical Research B*, *Solid Earth. 104*, 15 293–15 311.

Breivik, A.J., Faleide, J.I., Mjelde, R. & Flueh, R. 2009: Magma productivity and early seafloor spreading rate correlation on the northern Vøring Margin, Norway - Constraints on mantle melting. *Tectonophysics 468*, 206-223.

Breivik, A.J., Mjelde, R., Faleide, J.I. & Murai, Y. 2006: Rates of continental breakup magmatism and seafloor spreading in the Norway Basin – Iceland plume interaction. *Journal of Geophysical Research 111*, B07102, doi:10.1029/2005JB004004.

Breivik, A.J., Mjelde, R., Raum, T., Faleide, J.I., Murai, Y. & Flueh, E.R. 2011: Crustal structure beneath the Trøndelag Platform and adjacent areas of the mid-Norwegian margin, as derived from wide-angle seismic and potential field data. *Norwegian Journal of Geology 90*, 141–161.

Brekke, H. & Riis, F. 1987: Tectonics and basin evolution of the Norwegian shelf between 62°N and 72°N. *Norsk Geologisk Tissskrift* 67, 285-322.

Brekke, H. 2000: The tectonic evolution of the Norwegian Sea Contiental Margin with emphasis on the Vøring and Møre Basin. *In:* Nøttvedt, A., et al. (eds.) *Dynamics of the Norwegian Margin. Geological Society of London, Special Publication 167*, 327-378.

Brekke, H. 2000: The tectonic evolution of the Norwegian Sea continental margin with emphasis on the Vøring and Møre basins. *In:* Nøttvedt, A. et al. (eds.) *Dynamics of the Norwegian Margin*. *Geological Society of London, Special Publications 136*, 327-378.

Brigaud, F., Vasseur, G. & Caillet, G. 1992: Thermal state in the north Viking Graben (North Sea) determined from oil exploration well data. *Geophysics 18*, 69-88.

Brown, L.L. & McEnroe, S.A. 2004: Palaeomagnetism of the Egersund-Ogna anorthosite, Rogaland, Norway, and the position of Fennoscandia in the Late Proterozoic, *Geophysical Journal International 158*, 479–488.

Brönner, M., Olesen, O. & Nasuti, A. 2013: Onshore-offshore aeromagnetic interpretation. In: Olesen, O., Brönner, M., Ebbing, J., Elvebakk, H., Gellein, J., Koziel, J., Lauritsen, T., Lutro, O., Maystrenko, Y., Müller, C., Nauti, A., Osmundsen, P.T., Slagstad, T., & Storrø, G. (eds.) *Coop Phase I - Crustal Onshore-Offshore Project.* NGU Report 2013.002, pp. *112-134.*

Brönner, M., Dalsegg, E., Fabian, K., Rønning, J.S. & Tønnesen, J.F. 2012b: Geophysical methods. *In* Olesen, O., Bering, D., Brönner, M., Dalsegg, E., Fabian, K., Fredin, O., Gellein, J., Husteli, B., Magnus, C., Rønning, J.S., Solbakk, T., Tønnesen J.F. & Øverland, J.A. (eds.): *Tropical Weathering In Norway, TWIN Final Report.* NGU Report 2012.005, pp. *19–26.*

Brönner, A., Sauter, D., Manatschal, G., Peron-Pinvidic, G. & Munschy, M. 2011: Magmatic breakup as an explanation for magnetic anomalies at magma-poor rifted margins. *Nature Geoscience 4*, 549-553.

Brönner, M., Dalsegg, E., Fabian, K., Fredin, O., Gellein, J., Rønning, J.S., Solbakk, T. & Tønnesen, J.F. 2012a: Northern Norway. *In* Olesen, O., Bering, D., Brönner, M., Dalsegg, E., Fabian, K., Fredin, O., Gellein, J., Husteli, B., Magnus, C., Rønning, J.S., Solbakk, T., Tønnesen J.F. & Øverland, J.A. (eds.): *Tropical Weathering In Norway, TWIN Final Report.* NGU Report 2012.005, pp. *77–119.*

Brönner, M. et al. 2015: Ramså Basin integrated study, NGU project.

Brune, S., Heine, C., Pérez-Gussinyé, M. & Sobolev, S.V. 2014: Rift migration explains continental margin: asymmetry and crustal hyper-extension. *Nature Communications* DOI: 10.1038/ncomms5014, 1-9.

Buck, W.R., Einarsson, P. & Brandsdottir, B. 2006: Tectonic stress and magma chamber size as controls on dike propagation: Constraints from the 1975-1984 Krafla rifting episode. *Journal of Geophysical Research-Solid Earth 111*.

Bukovics, C., Cartier, E.G., Shaw, P.A. & Ziegler, P.A. 1984: Structure and development of the Mid-Norway continental margin. *In*: Society, N.P. (ed.), *Petroleum Geology of the North European Margin*. Graham & Trotman, London, pp. 407–423.

Bücker, C. & Rybach L. 1996: A simple method to determine heat production from gamma-ray logs. *Marine and Petroleum Geology 13*, 373-375.

Bystrøm S. 2006: Slutrapport. Produksjon av flygmagnetiska mätdata för prosjekt ROGAS-06. Report from SGU dated 2006.08.18, 90 pp.

Bøe, R. & Bjerkli, K., 1989: Mesozoic Sedimentary-Rocks in Edoyfjorden and Beitstadfjorden, Central Norway - Implications for the Structural History of the More-Trondelag Fault Zone. *Marine Geology* 87, 287-299.

Bøe, R. & Skilbrei, J.R. 1998: Structure and seismic stratigraphy of the Griptarane area, More Basin margin, mid-Norway continental shelf. *Marine Geology* 147, 85-107.

Bøe, R. 1991: Structure and Seismic Stratigraphy of the Innermost Mid-Norwegian Continental-Shelf - an Example from the Frohavet Area. *Marine and Petroleum Geology* 8, 140-151.

Bøe, R., Fossen, H. & Smelror, M. 2010: Mesozoic sediments and structures onshore Norway and in the coastal zone. *Norges geologiske undersøkelse Bulletin,* 450, 15-32.

Bøe, R., Mørk, M.B., Roberts, D. & Vigran, J.O. 2005: Possible Mesozoic sediments in fault and brecciation zone in Frøyfjorden, Mid Norway. *Norges geologiske undersøkelse Bulletin* 443, 25-35.

Calcagnile, G. 1982: The lithosphere-asthenosphere system in Fennoscandia, *Tectonophysics 90*, 19–35.

Callot, J.P., Grigné, C., Geoffroy, L. & Brun, J.P. 2001: Development of volcanic passive margins: Two-dimensional laboratory models. *Tectonics 20*, 148-159.

Čermak, V. & Rybach, L. 1982: Thermal properties: Thermal conductivity and specific heat of minerals and rocks, *In:* Angenheister, G. (ed.), Landolt-Börnstein, *New Series, Geophysics and space research*, Volume 1, subvolume A: Berlin, Springer, 305–343.

Chand, S., Rise, L., Knies, J., Haflidason, H., Hjelstuen, B.O. & Bøe, R. 2011: Stratigraphic development of the south Vøring margin (Mid-Norway) since early Cenozoic time and its influence on subsurface fluid flow. *Marine and Petroleum Geology 28*, 1350-1363. DOI: 10.1016/j.marpetgeo.2011.01.005.

Channell, J.E.T., Kanamatsu, T., Sato, T., Stein, R., Alvarez Zarikian, C.A., Malone, M.J., & the Expedition 303/306 Scientists 2006: Site U1315. Proceedings of the Integrated Ocean Drilling Program, Volume 303/306, doi:10.2204/iodp.proc.303306.114.2006.

Chen, Y.J. & Lin, L. 2004: High sensitivity of ocean ridge thermal structure to changes in magma supply: the Galapagos Spreading Center. *Earth and Planetary Science Letters 221*, 263-273.

Chenin, P., Manatschal, G., Lavier, L. & Erratt, D. 2015: Assessing the impact of orogenic inheritance on the architecture, timing and magmatic budget of the North Atlantic rift system: a mapping approach. *Journal of the Geological Society of India* doi:10.1144/jgs2014-139.

Christensen, N.I. & Mooney, W.D. 1995: Seismic velocity structure and composition of the continental crust: A global view. *Journal of Geophysical Research - Solid Earth 100*, 9761-9788.

Clark, D.A. 1997: Magnetic petrophysics and magnetic petrology: aids to geological interpretation of magnetic surveys. *AGSO Journal of Australian Geology and Geophysics 17*, 83-103.

Clauser, C. 2011: Thermal storage and transport properties of rocks, *In:* Gupta, H. (ed.), *Heat capacity and latent heat*, *Encyclopedia of Solid Earth´s Geophysics, 2nd ed.* Vol. 2, 1423-1431.

Clerc, C., Jolivet, L. & Ringenbach, J.C. 2015: Ductile extensional shear zones in the lower crust of a passive margin. *Earth and Planetary Science Letters 431*, 1-7.

Cochran, J.R. & Martinez, F. 1988: from the northern Red Sea on the transition from continental to oceanic rifting. *Tectonophysics 153*, 25-53.

Cochran, J.R. & Karner, G.D. 2007: Constraints on the deformation and rupturing of continental lithosphere of the Red Sea: the transition from rifting to drifting. *Geological Society of London, Special Publications 282*, 265-289.

Coleman, N. T. & Leroux, F. H. 1963: Biotite - Hydrobiotite - Vermiculite in Soils, *Nature, 198,* Issue 4878, 409-410.

Contrucci, I., Matias, L., Moulin, M., Geli, L., Klingelhofer, F., Nouze, H., Aslanian, D., Olivet, J.L., Rehault, J.P. & Sibuet, J.C. 2004: Deep structure of the West African continental margin (Congo, Zaire, Angola), between 5 degrees S and 8 degrees S, from reflection/refraction seismics and gravity data. *Geophysical Journal International 158*, 529-553.

Cooper, G.R.J. & Cowan, D.R. 2006: Enhancing potential field data using filters based on the local phase. *Computers & Geosciences 32 (10),* 1585–1591.

Corfield, S.M., Wheeler, W., Karpuz, R., Wilson, M. & Helland, R. 2004: Exploration 3D seismic over the Gjallar Ridge, Mid-Norway; visualization of structures on the Norwegian volcanic margin from Moho to seafloor. *In: 3D seismic technology; application to the exploration of sedimentary basins. R.J. Davies, J.A. Cartwright, S.A. Stewart, M. Lappin and J.R. Underhill (eds.).* Memoir - Geological Society of London 29, 185.

Corsini, M., Vauchez, A. & Caby, R. 1996: Ductile duplexing at a bend of a continental-scale strike-slip shear zone: Example from NE Brazil. *Journal of Structural Geology* 18, 385-394.

Cowie, L., Angelo, R.M., Kusznir, N., Manatschal, G. & Horn, B. 2015: The palaeo-bathymetry of base Aptian salt deposition on the northern Angolan rifted margin: constraints from flexural back-stripping and reverse post-break-up thermal subsidence modelling. *Petroleum Geoscience* doi:10.1144/petgeo2014-087, 1-12.

Davis, B.A.S., Brewer, S., Stevenson, A.C., Guiot, J. & Data Contributors 2003: The temperature of Europe during the Holocene reconstructed from pollen data. *Quaternary Science Reviews* 22, 1701-1716.

Deer, W.A., Howie, RA. & Zussman, J. 1966, An introduction to the rock-forming minerals, Longmans, Green & Co. Ltd., London.

Dietrich, W. E., Reiss, R., Hsu, M.-L. & Montgomery, D. R. 1995: A process-based model for colluvial soil depth and shallow landsliding using digital elevation data. *Hydrol. Proc. 9,* 383–400.

Dobinski, W. 2011: Permafrost. *Earth´s-Science Reviews 108*, 158–169.

Doré, A.G., Lundin, E.R., Fichler, C. & Olesen, O. 1997: Patterns of basement structure and reactivation along the NE Atlantic margin.; The role of basement reactivation in continental deformation. *Journal of the Geological Society of London 154*, 85-92.

Dowdeswell, J.A., Ottesen, D. & Rise, L. 2006: Flow-switching and large-scale deposition by ice streams draining former ice sheets: *Geology 34*, 313–316, doi: 10.1130/G22253.1.

Dowdeswell, J.A., Ottesen, D. & Rise, L. 2010: Rates of sediment delivery from the Fennoscandian Ice Sheet through an ice age. *Geology 38*, 3–6.

Ebbing, J. & Gellein, J. 2013: Gravity data-New measurements and compilation. *In* Olesen, O. (eds.). Coop Phase I-Crustal Onshore-Offshore Project. Report 2013.002. Trondheim, *Geological Survey of Norway (NGU)*, 359.

Ebbing, J. & Olesen, O. 2010: New compilation of to basement and basement thickness for the Norwegian continental shelf reveals the segmentation of the passive margin system. *In:* Vining, B.A. & Pickering, S.C. (eds.) Petroleum Geology: From mature basins to new frontiers. *Proceedings of the 7th Petroleum Geology Conference. Petroleum Geology Conference Series 7*, Geological Society of London, 885-897.

Ebbing, J., Lundin, E., Olesen, O. & Hansen, E.K. 2006: The mid-Norwegian margin: a discussion of crustal lineaments, mafic intrusions, and remnants of the Caledonian root by 3-D density modelling and structural interpretation, *Journal of the Geological Society 163,* 47–59.

Ebbing, J., England, R., Korja, T., Lauritsen, T., Olesen, O., Stratford, W. & Weidle, C. 2012: Structure of the Scandes lithosphere from surface to depth. *Tectonophysics* 536-537, doi:10.1016/j.tecto.2012.02.016.

Ebbing, O., Gernigon, L., Pascal, C., Olesen, O. & Osmundsen, P.T. 2009: A discussion of structural and thermal control of magnetic anomalies on the mid-Norwegian margin. *Geophysical Prospecting 57*, 665–681.

Ebinger, C.J. & Casey, M. 2001: Continental breakup in magmatic provinces: An Ethiopian example. *Geology* 29, 527-530.

Ehrlich, R. & Gabrielsen, R.H. 2004: The complexity of a ramp-flat-ramp fault and its effect on hanging-wall structuring: an example from the Njord oil field, offshore mid-Norway. *Petroleum Geoscience 10*, 305-317(13).

Eide, E.A., Haabesland, N.E., Osmundsen, P.T., Andersen, T.B., Roberts, D. & Kendrick, M.A. 2005: Modern techniques and Old Red problems - determining the age of continental sedimentary deposits with Ar-40/Ar-39 provenance analysis in west-central Norway. *Norwegian Journal of Geology 85*, 133-149.

Eide, E.A., Torsvik, T.H. & Andersen, T.B. 1997: Absolute dating of brittle fault movements: Late Permian and late Jurassic extensional fault breccias in western Norway. *Terra Nova* 9, 135-139.

Eidvin, T., Bugge, T. & Smelror, M. 2007: The Molo Formation, deposited by coastal progradation on the inner Mid-Norwegian continental shelf, coeval with the Kai Formation to the west and the Utsira Formation in the North Sea: *Norwegian Journal of Geology 87*, 35–102.

Eidvin, T., Riis, F. & Rasmussen, E.S. 2014: Oligocene to Lower Pliocene deposits of the Norwegian continental shelf, Norwegian Sea, Svalbard, Denmark and their relation to the uplift of Fennoscandia: A synthesis. *Marine and Petroleum Geology 56*, 184-221.

Eldevik, T., Risebrobakken, B., Bjune, A.E., Andersson, C., Birks, H.J.B., Dokken, T.M., Drange, H., Glessmer, M.S., Li, C., Nilsen, J.E.Ø., Otterå, O.H., Richter, K. & Skagseth, Ø. 2014: A brief history of climate – the northern seas from the Last Glacial Maximum to global warming. *Quaternary Science Reviews 106*, 225-246.

Eldholm, O. & Grue, K. 1994: North-Atlantic Volcanic Margins - Dimensions and Production-Rates. *Journal of Geophysical Research-Solid Earth* 99, 2955-2968.

Eldholm, O. & Mutter, J.C. 1986: Basin structure on the Norwegian margin from analysis of digitally recorded sonobuoys. *Journal of Geophysical Research 91*, 3763-3783.

Eldholm, O., Thiede, J., Taylor, E. et al. 1987: 6. SITE 644: Norwegian Sea. Proc, Init. Repts. (Pt. A), ODP, 104.

Elliott, G.M., Wilson, P., Jackson, C.A.L., Gawthorpe, R.L., Michelsen, L. & Sharp, I.R. 2012: The linkage between fault throw and footwall scarp erosion patterns: an example from the Bremstein Fault Complex, offshore Mid-Norway. *Basin Research* 24, 180-197.

Ellis, R.G., de Wet, B. & Macleod, I.N. 2012: Inversion of Magnetic Data from Remanent and Induced Sources. 22nd International Geophysical Conference and Exhibition. Brisbane, Australia.

England, R.W. & Ebbing, J. 2012: Crustal structure of central Norway and Sweden from integrated modelling of teleseismic receiver functions and the gravity anomaly. *Geophysical Journal International 191*, 1–11.

Evans, T.R. 1977: Thermal properties of North Sea rocks. *The Log Analyst* 8, 3-12.

Fediuk, F.& Siedlecki, S. 1977: Smøla. Beskrivelse til det berggrunnsgeologiske kart 1321 I - 1:50 000 (icl. colour-printed map). *NGU Skrifter 330; 23 pp.*

Fernandez, M., Ayala, C., Torne, M., Verges, J., Gomez, M. & Karpuz, R. 2005: Lithospheric structure of the mid-Norwegian margin; comparison between the More and Voring margins, *Journal of the Geological Society 162*, 1005–1012.

Fichler, C., Odinsen, T., Rueslåtten, H., Olesen, O., Vindstad, J.E. & Wienecke, S. 2011: Crustal inhomogeneities in the Northern North Sea from potential field modelling: Inherited structure and serpentinites? *Tectonophysics 510*, 172–185.

Fichler, C., Rundhovde, E., Olesen, O., Saether, B.M., Rueslatten, H., Lundin, E. & Dore, A.G. 1999: Regional tectonic interpretation of image enhanced gravity and magnetic data covering the mid-Norwegian shelf and adjacent mainland. *Tectonophysics 306*, 183-197.

Fossen, H. 1992: The Role of Extensional Tectonics in the Caledonides of South Norway. *Journal of Structural Geology 14*, 1033-1046.

Fossen, H. 2010: Extensional tectonics in the North Atlantic Caledonides:a regional view. *In* Law, R.D., Butler, R.W.H., Holdsworth, R.E., Krabbendam, M. & Strachan, R.A. (eds.). Continental tectonics and mountain building: the legacy of Peach and Horne. *Geological Society of London 335,* 767-793.

Foulger, G.R., Natland, J.H. & Anderson, D.L. 2005: A source for Icelandic magmas in remelted Iapetus crust. *Journal of Volcanology and Geothermal Research 141*, 23-44.

Franke, D. 2013: Rifting, lithosphere breakup and volcanism: Comparison of magma-poor and volcanic rifted margins. *Marine and Petroleum Geology 43*, 63-87.

Fredin, O., Zwingmann, H., Knies, J., Sorlie, R., Grandal, E.M., Lie, J.E., Müller, A. & Vogt, C. 2014: Saprolites on- and offshore Norway: New constraints on formation processes and age. Programme with Abstracts, 31st Nordic Geological Winter Meeting, 8–10 January, Lund, Sweden, p. 132.

Frizon de Lamotte, D., Fourdan, B., Leleu, S., Leparmentier, F.,& de Clarens, P. 2015: Style of rifting and the stages of Pangea breakup. *Tectonics 34*, 1009-1029.

Fugro Airborne Surveys 2003: Logistics report, fixed-wing borne magnetic, radiometric and VLF-EM survey in the Oslo region, southern Norway. *Report FCR 2241*, 124 pp.

Færseth, R.B. & Lien, T. 2002: Cretaceous evolution in the Norwegian Sea-a period characterized by tectonic quiescence. *Marine and Petroleum Geology 19*, 1005-1027(23).

Færseth, R.B. 2012: Structural development of the continental shelf offshore Lofoten-Vesteralen, northern Norway. *Norwegian Journal of Geology 92*, 19-40.

Færseth, R.B., Gabrielsen, R.H.,& Hurich, C.A. 1995: Influence of Basement in Structuring of the North-Sea Basin, Offshore Southwest Norway. *Norsk Geologisk Tidsskrift 75*, 105-119.

Gabrielsen, R.H. & Ramberg, I.B. 1979: Fracture patterns in Norway from LANDSAT imagery: results and potential use. Proceedings of the Norwegian Sea Symposium, NSS/20, Tromsø. *Norwegian Petroleum Society (NPF)*, 1–10.

Gabrielsen, R.H., Odinsen, T. & Grunnaleite, I. 1999: Structuring of the Northern Viking Graben and the Møre Basin; the influence of basement structural grain, and the particular role of the Møre–Trøndelag Fault Complex. *Marine and Petroleum Geology 16*, 443–465.

Gabrielsen, R.H., Braathen, A., Dehls, J. & Roberts, D. 2002: Tectonic lineaments of Norway. *Norwegian Journal of Geology 82*, 153-174.

Gac, S. & Geoffroy, L. 2009: 3D Thermo-mechanical modelling of a stretched continental lithosphere containing localized low-viscosity anomalies (the soft-point theory of plate break-up). *Tectonophysics 468*, 158-168.

Gardner, G.H.F., Gardner, L.W. & Gregory, A.R. 1984: Formation velocity and density -The diagnostic basics for stratigraphic traps. *Geophysics 39*, 770-780.

Gasser, D. 2014: The Caledonides of Greenland, Svalbard and other Arctic areas: status of research and open questions. *In* Corfu, F., Gasser, D. & Chew, D.M. (eds). New Perspectives on the Caledonides of Scandinavia and Related Areas. *Geological Society of London 390*.

Gautneb, H. & Roberts, D. 1989: Geology and petrochemistry of the Smola-Hitra Batholith, Central Norway. *Norges geologiske undersøkelse Bulletin* 416, 1-24.

Gee, D.G. & Stephenson, R.A. 2006: European Lithosphere Dynamics. *Geological Society of London, Memoir 32,* 662 pp.

Gee, D.G., Fossen, H., Henriksen, N. & Higgins, A.K. 2008: From the Early Palaeozoic platforms of Baltica and Laurentia to the Caledonide orogen of Scandinavia and Greenland. *Episodes 31*, 44-51.

Gee, D.G., Guezou, J.C., Roberts, D. & Wolff, F.C. 1985: The central-southern part of the Scandinavian Caledonides. In: Gee, D.G. & Sturt, B.A. (eds) The Caledonide Orogen-Scandinavian and related areas. *John Wiley & Sons Ltd, Chichester*, 109-133.

Gee, D.G., Janák, M., Majka, J., Robinson, P. & van Roermund, H. 2013: Subduction along and within the Baltoscandian margin during closing of the Iapetus Ocean and Baltica–Laurentia collision. *Lithosphere 5*, 169–178.

Geoffroy, L. 2005: Volcanic passive margins. *Comptes Rendus Geoscience* 337, 1395-1408.

Geosoft 2004: OASIS Montaj v 6.0 mapping and processing system, The core software platform for working with large volume spatial data. Quick start tutorials. 258 p.

Geosoft 2010a: Montaj MAGMAP filtering, 2-D frequency domain processing of potential field data, Extension for Oasis Montaj v7.1. Geosoft Incorporated, 79 pp.

Geosoft 2010b: OASIS Montaj v7.2 Mapping and processing system, The core software platform for working with large volume spatial data. Quick start tutorials. Geosoft Incorporated, 325 pp.

Gernigon, L., Blischke, A., Nasuti, A. & Sand, M. 2015: Conjugate volcanic rifted margins, seafloor spreading, and microcontinent: Insights from new high-resolution aeromagnetic surveys in the Norway Basin. *Tectonics 34*, 907–933.

Gernigon, L., Olesen, O., Koziel, J. & Lynum, R. 2008: Norway Basin Aeromagnetic Survey NB-07-Acquisition, Processing and Interpretation, *NGU Report 2008.052*, Trondheim, 216 pp.

Gernigon, L., Ringenbach, J.C., Planke, S., Le Gall, B. & Jonquet-Kolstø, H. 2003: Extension, crustal structure and magmatism at the outer Vøring Basin, Norwegian margin. *Journal of the Geological Society 160*, 197-208(12).

Gernigon, L., Olesen, O., Ebbing, J., Wienecke, S., Gaina, C., Mogaard, J.O., Sand, M. & Myklebust, R. 2009: Geophysical insights and early spreading history in the vicinity of the Jan Mayen Fracture Zone, Norwegian-Greenland Sea, *Tectonophysics 468*, 185–205.

Gilbert G. K. 1877: Report on the geology of the Henry Mountains. U.S. Geological and Geographical Survey.

Götze, H.J. 1978: Ein numerisches Verfahren zur Berechnung der gravimetrischen Feldgrößen drei-dimensionaler Modellkörper. *Arch. Met. Geoph. Biokl. Ser. A(25),* 195-215.

Götze, H.J. & Lahmeyer, B. 1988: Application of three-dimensional interactive modelling in gravity and magnetics. *Geophysics 53*, 1096-1108.

Götze H.J. & Schmidt, S. 2010: IGMAS+: A new 3D gravity, FTG and magnetic modelling software tool: *ASEG-PESA Airborne Gravity Workshop, Expanded Abstracts*, 91-96, ISBN 978-1-921781-17-9.

Grad, M., Tiira, T. & ESC Working Group 2009: The Moho depth map of the European Plate. *Geophysical Journal International* 176, 279-292, doi: 10.1111/j.1365-246X.2008.03919.x.

Gradmann, S. & Ebbing, J. 2015: Large-scale gravity anomaly in northern Norway: tectonic implications of shallow or deep source depth and a possible conjugate in northeast Greenland. *Geophysical Journal International 203*, 2070-2088.

Gradmann, S., Ebbing, J. & Fullea, J. 2013: Integrated geophysical modelling of boundary zone in lithospheric mantle under Norway and Sweden. *Geophysical Journal International 194,* 1358–1373.

Grenne, T. 2015: pers.com regarding greenstone composition.

Grenne, T., Grammeltvedt, G. & Vokes, F. 1980: Cyprus-type sulphide deposits in the western Trondheim District, central Norwegian Caledonides. Cyprus-type sulphide deposits in the western Trondheim District, central Norwegian Caledonides. *In*: Panayiotou, A. (ed.) *Proceedings of the International Ophiolite Symposium, Cyprus, 1979*. Cyprus Geological Survey, Nicosia, 727–743.

Grunnaleite, I. & Gabrielsen, R.H. 1995: Structure of the Møre Basin, mid-Norway Continental margin. *Tectonophysics 252*, 221-251.

Grønlie, A. & Roberts, D. 1989: Resurgent strike-slip duplex development along the Hitra-Snåsa and Verran Faults, Møre-Trøndelag Fault Zone, Central Norway. *Journal of Structural Geology 11*, 285-305.

Grønlie, A., Naeser, C. W., Naeser, N. D., Mitchell, J. G., Sturt, B. A. & Ineson, P.R. 1994: Fission-track and K-Ar dating of tectonic activity in a transect across the Møre-Trøndelag Fault Zone, central Norway. *Norsk Geologisk Tidsskrift 74,* 24-34.

Haase, C. & Ebbing, J. 2013: Complete Bouguer Correction – Statoil database Offshore Mid-Norway. *NGU Report 2013.038*, 19 pp.

Hansen, J., Jerram, D.A., McCaffrey, K. & Passey, S.R. 2009: The onset of the North Atlantic Igneous Province in a rifting perspective. *Geological Magazine* 146, 309-325.

Hardwick, A.J., Wittaker, J. & Woodburn, N. 2012: Combining Bandwidth Extension Techniques and Pre-stack Q Inversion for Enhanced Imaging of Intra-basalt Plays. 74th EAGE Conference & Exhibition incorporating SPE EUROPEC 2012. Copenhagen, Denmark.

Hartman, R.R., Tesky, D.J. & Friedberg, J.L. 1971: A system for rapid digital aeromagnetic interpretation. *Geophysics* 36, 891-918.

Hartz, E. & Andresen, A. 1995: Caledonian Sole Thrust of Central East Greenland - a Crustal-Scale Devonian Extensional Detachment. *Geology* 23, 637-640.

Henstra, G.A., Rotevatn, A., Gawthorpe, R.L. & Ravnas, R. 2015: Evolution of a major segmented normal fault during multiphase rifting: The origin of plan-view zigzag geometry. *Journal of Structural Geology* 74, 45-63.

Hofer, D., Raible, C.C., Dehnert, A. & Kuhlemann, J. 2012: The impact of different glacial boundary conditions on atmospheric dynamics and precipitation in the North Atlantic region. *Climate of the Past Discussions 8*, 935-949, DOI 10.5194/cp-8-935-2012.

Hofmeister, A.M. 1999: Mantle values of thermal conductivity and the geotherm from phonon lifetimes. *Science 283*, 1699-1706.

Hohl, V. 2005: Northern European long term climate archives. *Technical Report TR-05-01*, Swedish Nuclear Fuel and Waste Management Co (SKB), Stockholm, Sweden.

Hollocher, K., Robinson, P., Walsh, E. & Roberts, D. 2012: Geochemistry of Amphibolite-Facies Volcanics and Gabbros of the Storen Nappe in Extensions West and Southwest of Trondheim, Western Gneiss Region, Norway: A Key to Correlations and Paleotectonic Settings. *American Journal of Science* 312, 357-416.

Holtedahl, O. 1929: On the geology and physiography of some Antarctic and Sub-Antarctic islands. Scientific results of the Norwegian Antarctic expeditions 1927-28 and 1928-1929, instituted and financed by consul Lars Christensen. *Det Nor. Vid. Ak. Oslo 3.* 172 pp.

Holtedahl, H. 1959: Den norske strandflate. Med særlig henblikk på dens utvikling i kystområdene på Møre. *Norsk Geografisk Tidsskrift 16,* 285-385.

Holtedahl, H. 1998: The Norwegian strandflat – a geomorphological puzzle. *Norsk Geologisk Tidsskrift 78*, 47–66.

Hsu, S.-K. 2002: Imaging magnetic sources using Euler's equation. *Geophysical Prospecting 50*, 15-25.

Huismans, R.S. & Beaumont, C. 2014: Rifted continental margins: The case for depth-dependent extension. *Earth and Planetary Science Letters* 407, 148-162.

Hurich, C.A. 1996: Kinematic evolution of the lower plate during intracontinental subduction: an example from the Scandinavian Caledonides. *Tectonics* 15, 1248-1263.

Högdahl, K., Andersson, B. & Eklund, O. 2004: The Transscandinavian Igneous Belt (TIB) in Sweden: a review of its character and evoluation. Volume 37. *Geological Survey of Finland, Special Paper*.

Håbrekke H. 1980a: Magnetiske-, elektromagnetiske-, radiometriske- og VLF-målinger fra helikopter over et område ved Kvikne i Tynset. *NGU Report 1748*, 12 pp.

Håbrekke, H. 1980b: Magnetiske-, elektromagnetiske og radiometriske målinger fra helikopter over Nord-Gudbrandsdalen 1979. *NGU Report 1709/A* , 11 pp.

Håbrekke, H. 1982a: Magnetiske-, elektromagnetiske-, VLF- og radiometriske målinger fra helikopter over et område vest for Glomma mellom Alvdal sent. og Telneset. *NGU Report 1847*, 13pp.

Håbrekke, H. 1982b: Magnetiske-, elektromagnetiske-, VLF- og radiometriske målinger fra helikopter over et område vest for Tønsberg, Vestfold og Telemark fylker. *NGU Report 1835*, 13 pp.

Håbrekke, H. 1983: Geofysiske målinger fra helikopter over et område vest for Berkåk i Rennebu. *NGU Report 2089*, 16 pp.

IAEA 1991: Airborne Gamma Ray Spectrometer Surveying. *Technical Reports Series 323*, Vienna, Austria, 97 pp.

ICES 2012: Factors affecting the distribution of North Sea fish, http://www.google.no/url?sa=t&rct=j&q=&esrc=s&source=web&cd=1&cad=rja&ved=0CGIQFjAA&url=http%3A%2F%2Fwww.ices.dk%2Fmarineworld%2Ffishmap%2Fpdfs%2Ffactors.pdf&ei=5xwyUOPvJ5KN4gSl_YGwAQ&usg=AFQjCNFP7NOm.

IOC, IHO & BODC 2003: Centenary Edition of the GEBCO Digital Atlas, published on CD-ROM on behalf of the Intergovernmental Oceanographic Commission and the International Hydrographic Organization as part of the General Bathymetric Chart of the Oceans; British Oceanographic Data Centre, Liverpool, UK.

Jakobsson, M., Mayer, L., Coakley, B., Dowdeswell, J.A., Forbes, S., Fridman, B., Hodnesdal, H., Noormets, R., Pedersen, R., Rebesco, M., Schenke, H.W., Zarayskaya, Y., Accettella, D., Armstrong, A., Anderson, R.M., Bienhoff, P., Camerlenghi, A., Church, I., Edwards, M., Gardner, J.V., Hall, J.K., Hell, B., Hestvik, O., Kristoffersen, Y., Marcussen, C., Mohammad, R., Mosher, D., Nghiem, S.V., Pedrosa, M.T., Travaglini, P.G. & Weatherall, P. 2012: The International Bathymetric Chart of the Arctic Ocean (IBCAO) Version 3.0. *Geophysical Research Letters* 39.

Johannessen, K. C. 2012: Low-temperature thermochronological and structural study of the inner Hardangerfjord area, southern Norway. MSc thesis, University of Bergen.

Johnston, S.M., Hacker, B.R. & Andersen, T.B. 2007: Exhuming Norwegian ultrahigh-pressure rocks: Overprinting extensional structures and the role of the Nordfjord-Sogn Detachment zone. *Tectonics* 26.

Jones, N. 2012: Russians celebrate Vostok victory. Team finally drills into biggest Antarctic subglacial lake. Nature 482, 287, doi:10.1038/482287a.

Jongepier, K., Rui, J.C. & Grue, K. 1996: Triassic to Early Cretaceous stratigraphic and structural development of the northeastern Møre Basin margin, off Mid-Norway. *Norsk Geologisk Tidsskrift 76*, 200-216.

Karson, J.A. & Brooks, C.K. 1999: Structural and magmatic segmentation of the Tertiary East Greenland volcanic rifted margin. *In* Mac Niocaill, C. & Ryan, P.D. (eds.). Continental Tectonics. *Geological Society of London, Special Publications 164*, 313-338.

Kelly, A., England, R.W. & Maguire, P.K.H. 2007: A crustal seismic velocity model for the UK, Ireland and surrounding seas. *Geophysical Journal International 171*, 1172-1184, doi: 10.1111/j.1365-246X.2007.03569.x.

Kendrick, M.A., Eide, E.A., Roberts, D. & Osmundsen, P.T. 2004. The Mid–Late Devonian Høybakken Detachment, Central Norway: 40Ar/39Ar evidencefor prolonged late/post Scandian extension and uplift. *Geological Magazine 141*, 329–344.

Killeen, P.G. & Heier, K.S. 1975: Radioelement and heat production measurements in the Trysil granite, east Hedmark, Norway. *Norsk Geologisk Tidsskrift 55*, 179-184.

Kilty, .S & Dvorak Z. 1982: Dighem II Survey Løkken Area for Orkla Industrier NS. *Bergvesenet Report BV 4637*.

Klausen, M.B. & Larsen, H.C. 2002: East Greenland coast-parallel dike swarm and its role in continental breakup. *In* Menzies, M.A., Klemperer, S.L., Ebinger, C.J. & Baker, J. (eds.). Volcanic rifted margins. *Geological Society of America Special Paper 362*, Boulder Colorado, 133-158.

Klemsdal, T. 1982: Coastal classification and the coast of Norway. *Norsk Geografisk Tidsskift 36*, 117–146.

Koistinen, T., Stephens, M.B., Bogatchev, V., Nordgulen, Ø., Wennerström, M. & Korhonen, J. 2001: Geological map of the Fennoscandian shield, 1:2.000.000. *Geological surveys of Finland, Norway, Sweeden and the North-West Department of Natural Ressources of Russia*.

Korablev, A., Smirnov, A. & Baranova, O.K. 2014: Climatological Atlas of the Nordic Seas and Northern North Atlantic. *In:* D. Seidov, A. R. Parsons, (eds.) *NOAA Atlas NESDIS 77*, 122 pp., doi: 10.7289/V54B2Z78

Korja, A., Korja, T., Luosto, U. & Heikkinen, P. 1993: Seismic and Geoelectric Evidence for Collisional and Extensional Events in the Fennoscandian Shield - Implications for Precambrian Crustal Evolution. *Tectonophysics 219*, 129-152.

Krabbendam, M. & Bradwell, T. 2014: Quaternary evolution of glaciated gneiss terrains: pre-glacial weathering vs. glacial erosion. *Quaternary Science Reviews 95*, 20-42

Ksienzyk, A.K., Dunkl, I., Jacobs, J., Fossen, H. & Hohlmann, F. 2014: From orogen to passive margin: constraints from fission track and (U–Th)/He analyses on Mesozoic uplift and fault reactivation in SW Norway. *In:* Corfu, F., Gasser, D. & Chew, D. M. (eds) *New Perspectives on the Caledonides of Scandinavia and Related Areas.* Geological Society of London, Special Publications 390.

Ku, C.C. & Sharp, J.A. 1983: Werner deconvolution for automated magnetic interpretation and its refinement using Marquardt´s inverse modeling. *Geophysics 48,* 754-774.

Kvarven, T., Ebbing, J., Mjelde, R., Faleide, J.I., Libak, A., Thybo, H., Flueh, E.R. & Murai, Y. 2014: Crustal structure across the land-ocean transition off Møre, mid-Norway, from wide-angle seismic and gravity data. *Tectonophysics 626*, 21-40. http://dx.doi.org/10.1016/j.tecto.2014.03.021.

Lahtinen, R., Huhma, H., Kahkonen, Y. & Manttari, I. 2009: Paleoproterozoic sediment recycling during multiphase orogenic evolution in Fennoscandia, the Tampere and Pirkanmaa belts, Finland. *Precambrian Research 174*, 310-336.

Lahtinen, R., Huhma, H., Lahaye, Y., Kousa, J. & Luukas, J. 2015: Archean-Proterozoic collision boundary in central Fennoscandia: Revisited. *Precambrian Research* 261, 127-165. Bingen, B., Griffin, W.L., Torsvik, T.H. & Saeed, A. 2005: Timing of Late Neoproterozoic glaciation on Baltica constrained by detrital zircon geochronology in the Hedmark Group, south-east Norway. *Terra Nova 17*, 250-258.

Lake Vostok Drilling Project, 2014:
http://www.southpolestation.com/trivia/10s/lakevostok.html

Larsen, E. & Longva, O. 1979: Jordans kartlegging, glasialgeologi og kvartær stratigrafi på Stad og Vågsøy, ytre Nordfjord. Cand. real. thesis, Univ. of Bergen.

Lavier, L.L. & Manatschal, G. 2006: A mechanism to thin the continental lithosphere at magma-poor margins. *Nature 440*, 324-328.

Lidmar-Bergström, K. 1989: Exhumed Cretaceous landforms in south Sweden. Z. *Geomorphol., N.F., Suppl.-Bd. 72*, 21–40.

Lidmar-Bergström, K. 1999: Uplift histories revealed by landforms of the Scandinavian domes. *Geological Society of London, Special Publication 162*, 85 – 91.

Lidmar-Bergström, K., Ollier, C. D. & Sulebak, J.R. 2000: Landforms and uplift history of southern Norway. *Global and Planetary Change 24*, 211-231.

Lien, T. 2005: From rifting to drifting: effects on the development of deep-water hydrocarbon reservoirs in a passive margin setting, Norwegian Sea. *Norwegian Journal of Geology 85*, 319-332.

Lister, G.S., Etheridge, M.A. & Symonds, P.A. 1986: Detachment faulting and the evolution of passive continental margins. *Geology* 14, 246-250.

Lister, G.S., Etheridge, M.A. & Symonds, P.A. 1986: Detachment faulting and the evolution of passive continental margins. *Geology 14*, 246-250.

Longva, O. & Thorsnes, T. (eds.), 1997. Skagerrak in the past and at the present—an integrated study of geology, geochemistry, hydrography and microfossil ecology. *Norges Geologiske Undersøkelse Special Publication 8*, 100 pp.

Lundin, E.R. & Doré, A.G. 1997: A tectonic model for the Norwegian passive margin with implications for the NE Atlantic: Early Cretaceous to break-up. *Journal of the Geological Society 154*, 545-550.

Lundin, E.R. & Doré, A.G. 2011: Hyperextension, serpentinization, and weakening: A new paradigm for rifted margin compressional deformation. *Geology* 39, 347-350.

Lutro, O., Tveten, E. & Thorsnes, T. 1998: Berggrunnskart Ålesund, M 1:250 000. *Norges geologiske undersøkelse*, *Trondheim.*

Lutro,O., Solli, Heldal, T. 2015: Compilation of geological maps. *In:* Olesen, O., Baranwal, V., Brönner, M., Dalsegg, E., Dumais, M.A., Gellein, J., Heldal, T., Larsen, B.E., Lauritsen, T., Lutro, O., Maystrenko, Y., Nasuti, A., Roberts, D., Rueslåtten, H., Rønning, J.S., Solli, A. Slagstad, T. & Stampolidis, A. (eds.) *Coop Phase 2 - Crustal Onshore-Offshore Project.* NGU Report 2015.063, 51-158.

Malm, O. A., Christensen, O. B., Furnes, H., Løvlie, R., Rueslåtten, H. & Østby, K. L. 1984: The Lower Tertiary Balder Formation: an organogenic and tuffaceous deposit in the North Sea region. *In:* Spencer, A. M. et al. (eds.): *Petroleum Geology of the North European Margin*, 149-170. Graham and Trotman, London.

Manatschal, G., Lavier, L. & Chenin, P. 2015: The role of inheritance in structuring hyperextended rift systems: Some considerations based on observations and numerical modeling. *Gondwana Research 27*, 140-164.

Mann, M.E., Zhang, Z., Rutherford, S., Bradley, R.S., Hughes, M.K., Shindell, D., Ammann, C., Faluvegi, G. & Ni, F. 2009: Global signatures and dynamical originsof the Little Ice Age and Medieval Climate Anomaly. *Science 326*, 1256–1260, http://dx.doi.org/10.1126/science.1177303.

Marello, L., Ebbing, J. & Gernigon, L. 2013: Basement inhomogeneities and crustal setting in the Barents Sea from a combined 3D gravity and magnetic model. *Geophysical Journal International*, doi: 10.1093/gji/ggt018.

Martelat, J.E., Lardeaux, J.M., Nicollet, C. & Rakotondrazafy, R. 2000: Strain pattern and late Precambrian deformation history in southern Madagascar. *Precambrian Research 102,* 1-20.

Maupin, V., Agostini, A., Artemieva, I., Balling, N., Beekman, F., Ebbing, J., England, R.W., Frassetto, A., Gradmann, S., Jacobsen, B.H., Kohler, A., Kvarven, T., Medhus, A.B., Mjelde, R., Ritter, J., Sokoutis, D., Stratford, W., Thybo, H., Wawerzinek, B. & Weidle, C. 2013: The deep structure of the Scandes and its relation to tectonic history and present-day topography. *Tectonophysics 602,* 15-37.

Maystrenko, Y. 2013: 2D gravity, magnetic and thermal modelling near Bergen and Stavanger; a COOP Report. *NGU Report 2013.059*, 103 pp.

Maystrenko, Y. 2014: 3D gravity, magnetic and thermal modelling within the northern North Sea and adjacent areas; a Coop Report, *NGU Report 2014.026*, 114 pp.

Maystrenko, Y., Scheck-Wenderoth, M. 2009: Density contrasts in the upper mantle and lower crust across the continent–ocean transition: constraints from 3-D gravity modelling at the Norwegian margin. *Geophysical Journal International 179*, 536-548. doi: 10.1111/j.1365-246X.2009.04273.x.

Maystrenko, Y.P., Olesen, O. & Elvebakk, H.K. 2015: Indication of deep groundwater flow through the crystalline rocks of southern Norway. *Geology 43*, 327-330, doi: 10.1130/G36318.1.

Maystrenko, Y.P., Elvebakk, H.K., Ganerød, G.V., Lutro, O., Olesen, O. & Rønning, J.S. 2014. 2D structural and thermal models in southeastern Norway based on the recently drilled Årvollskogen borehole and 2D density, magnetic and thermal modelling. *Geothermal Energy 2*, doi: 10.1186/s40517-014-0015-z.

McArthur, K., Frost, C.F., Barnes, C.G., Prestvik, T. & Nordgulen, Ø. 2013: Tectonic reconstruction and sediment provenance of a far-traveled oceanic nappe, Helgeland Nappe Complex, west-central Norway. *In*: Corfu, F., Gasser, D., Chew, D. M. (eds)

New Perspectives on the Caledonides of Scandinavia and Related Areas. Geological Society of London, Special Publications 390, http://dx.doi.org/10.1144/SP390.3

McEnroe, S.A., Harrison, R.J., Jackson, M.J., Hirt, A.M., Robinson, P., Langenhorst, F., Heidelbach, F., Kasama, T., Putnis, A., Brown, L.L. & Golla-Schindler, U. 2005: Lamellar magnetism: Effects of interface versus exchange interactions of nanoscale exsolutions in the ilmenite-hematite system. *Journal of Physics: Conference Series 17* 154–167.

McDermott, K. & Reston, T. 2015: To see, or not to see? Rifted margin extension. *geology* doi:10.1130/G36982.1.

McKenna, T.E. & Sharp, J.M. 1998: Radiogenic heat production in sedimentary rocks. *AAPG Bulletin 82*, 484-496.

Meyer, R., Hertogen, J., Pedersen, R.B., Viereck-Gotte, L. & Abratis, M. 2009: Interaction of mantle derived melts with crust during the emplacement of the Vøring Plateau, NE Atlantic. *Marine Geology 261*, 3-16.

Meyer, R., van Wijk, J. & Gernigon, L. 2006: North Atlantic Igneous Province formation: An interdisciplinary geophysical and geochemical review. *In* (EGU), E.G.U. (eds.). European Geosciences Union (EGU) General Assembly 2006, Volume 8. Vienna, Austria, *Geophysical Research Abstracts.*

Midttømme, K. & Roaldset, E. 1999: Thermal conductivity of sedimentary rocks: uncertainties in measurement and modelling. *Geological Society of London, Special Publications 158*, 45-60.

Midttømme, K., Sættem, J., Roaldset, E. & Zielinski, G.W. 1995: Thermal conductivity of unconsolidated marine sediments from Vøring Basin, Norwegian Sea. SAGE 57th Conference and Technical Exhibition - Glasgow, Scotland.

Migon, P. & Lidmar-Bergström, K. 2002: Deep weathering through time in central and interpretation of geological record, *Catena 49*, 25-40

Miller, H.G. & Singh, V. 1994: Potential field tilt — a new concept for location of potential field sources. *Journal of Applied Geophysics 32*, 213–217.

Minshull, T.A. 2009: Geophysical characterisation of the ocean-continent transition at magma-poor rifted margins. *Comptes Rendus Geoscience* 341, 382-393.

Misra, A.A.,& Mukherjee, S. 2015: Tectonic Inheritance in Continental Rifts and Passive Margins. *Springer*, 88 p.

Mjelde, R., Kodaira, S. & Sellevoll, M.A. 1997: Crustal structure of the central part of the Voring Basin, mid-Norway margin, from ocean bottom seismographs, *Tectonophysics 277*, 235–257.

Mjelde, R., Raum, T., Kandilarov, A., Murai, Y. & Takanami, T. 2009: Crustal structure and evolution of the outer Møre Margin, NE Atlantic, *Tectonophysics 468*, 224–243.

Mjelde, R., Shimamura, H., Kanazawa, T.,Kodaira, S., Raum, T. & Shiobara, H. 2003: Crustal lineaments, distribution of lower-crustal intrusives and structural evolution of the Voring Margin, NE Atlantic; new insight from wide-angle seismic models, *Tectonophysics 369*, 199–218.

Mjelde, R., Raum, T.A.B., Shimamura, H., Murai, Y., Takanami, T. & Faleide, J.I. 2005: Crustal structure of the Vøring margin, NE Atlantic: a review of geological implications based on recent OBS-data. *In:* Doré, A.G. & Vining, B.A. (eds.). North-West European Petroleum Geology and Global Perspectives: Proceedings of the 6th Conference. *Geological Society of London*, 803-813.

Mjelde, R., Digranes, P., van Schaack, M., Shimamura, H., Shiobara, H., Kodaira, S. & Næss, O. 2001: Crustal structure of the outer Vøring Plateau, offshore Norway, from

ocean bottom seismic and gravity data, *Journal of Geophysical Research 106*, 6769–6791.

Mjelde, R., Kasahara, J., Shimamura, H., Kamimura, A., Kanazawa, T., Kodaira, S., Raum, T. & Shiobara, H. 2002: Lower-crustal seismic velocity-anomalies; magmatic underplating or serpentinized peridotite? Evidence from the Voring Margin, NE Atlantic, *Mar. Geophys. Res. 23*, 169–183.

Mjelde, R., Raum, T., Myhren, B., Shimamura, H., Murai, Y., Takanami, T., Karpuz, R. & Næss, U. 2005: Continent-ocean transition on the Voring Plateau, NE Atlantic, derived from densely sampled ocean bottom seismometer data, *Journal of Geophysical Research 110*, B05101, 1–19.

Mogaard, J.O. 1998: Geofysiske målinger fra helikopter ved Larvik, Vestfold. *NGU Report 98.021*, 11 pp.

Mogaard, J.O. 2001: Geofysiske målinger fra helikopter ved Sandefjord, Vestfold 2000. *NGU Report 2001.003*, 12 pp.

Mogaard, J.O. 2004: Data acquisition and processing - Helicopter geophysical survey, Kvikne, Hedemark county, Norway. *NGU Report 2004.042*, 12 pp.

Mogaard, J.O. 2006: Data acquisition and processing - Helicopter Geophysical Survey, Bamle, Ertlien and Sigdal 2005. *NGU Report 2006.021*, 11 pp.

Mogaard, J.O. & Beard, L.P. 2000: Geofyiske målinger fra helikopter ved Skien, Telemark 1999. *NGU Rapport 2000.031*, 12 pp.

Mogaard, J.O. & Blokkum, O. 1993: Geofysiske målinger fra helikopter over Meråkerfeltet, Nord-Trøndelag. *NGU Report 92.153*, 9 pp.

Mogaard, J.O., Rønning, S., Blokkum, O. & Khile, O. 1989: Helikoptermålinger kartblad Steinkjer, Nord-Trøndelag. NGU Report 89.142, 30 pp.

Mohriak, W.U. & Leroy, S. 2012: Architecture of rifted continental margins and break-up evolution: insights from the South Atlantic, North Atlantic and Red Sea–Gulf of Aden conjugate margins. *In* Mohriak, W.U., Danforth, A., Post, P.J., Brown, D.E., Tari, G.C., Nemcok, M. & Sinha, S.T. (eds.). Conjugate Divergent Margins. *Geological Society of London, Special Publications 369*.

Morley, C.K. 1999: How successful are analogue models in addressing the influence of pre-existing fabrics on rift structure. *Journal of Structural Geology* 21, 1267-1274.

Mosar, J., Osmundsen, P.T., Sommaruga, A., Torsvik, T.H. & Eide, E.A. 2002: Greenland-Norway separation: a geodynamic model for the North Atlantic. *Norwegian Journal of Geology 82*, 281–298.

Moulin, M., Aslanian, D. & Unternehr, P. 2010: A new starting point for the South and Equatorial Atlantic Ocean. *Earth-Science Reviews 98*, 1-37.

Möller, C. 1988: Geology and metamorphic evolution of the Roan area, Vestranden, Western Gneiss Region, Central Norwegian Caledonides. *Geological Survey of Norway, Bulletin 413*, 1-31.

Mørk, M.B.E. & Johnsen, S.O. 2005: Jurassic sandstone provenance and basement erosion in the Møre margin-Froan Basin area. *Norges geologiske undersøkelse Bulletin* 443, 5-18.

Mørk, M.B.E., McEnroe, S. & Olesen, O. 2002: Magnetic susceptibility of Mesozoic and Cenozoic sediments off Mid Norway and the role of siderite: implications for interpretation of high-resolution aeromagnetic anomalies. *Marine and Petroleum Geology 19*, 1115-1126.

Müller, R., Nystuen, J.P., Eide, F. & Lie, H. 2005: Late Permian to Triassic basin infill history and palaeogeography of the Mid-Norwegian shelf -- East Greenland region. *In* Wandås, B., Nystuen, J.P., Eide, E.A. & Gradstein, F.M. (eds.). Onshore-Offshore

Relationships on the North Atlantic Margin. *Norwegian Petroleum Society (NPF) 12*, 165-189.

Müller, R.D., Sdrolias, M., Gaina, C. & Roest, W.R. 2008: Age spreading rates and spreading asymmetry of the world's ocean crust. *Geochemistry, Geophysics, Geosystems 9*, Q04006, doi:10.1029/2007GC001743.

Nafe, J.E. & Drake, C. 1957: Variation in depth in shallow and deep water sediments of porosity, density and the velocities of compressional and shear waves. *Geophysics 22*, 523-552.

Nansen, F. 1922: The strandflat and isostasy. *Skrifter Videnskapsselskapet i Kristiania. Matematisk-Naturvitenskaplig klasse 2*, 1–313.

Nasuti, A., Pascal, C. & Ebbing, J. 2012: Onshore–offshore potential field analysis of the Møre–Trøndelag Fault Complex and adjacent structures of Mid Norway. *Tectonophysics 518*, 17–28.

Nasuti, A., Brönner, M., Lauritsen, T. & Olesen, O. 2013: 3D aeromagnetic processing and compilation of the Coop data. In: Olesen, O., Brönner, M., Ebbing, J., Elvebakk, H., Gellein, J., Koziel, J., Lauritsen, T., Lutro, O., Maystrenko, Y., Müller, C., Nasuti, A., Osmundsen, P.T., Slagstad, T. & Storrø G. (eds.) Coop Phase I - Crustal Onshore-Offshore Project, *NGU Report 2013.002*, 9-29.

Nasuti, A., Aarset, M., Brönner, M., Koziel, J., & Lauritsen, T. 2012: Central North Sea Aeromagnetic Survey 2010 (CNAS-10) data acquisition and processing . *NGU Report 2012.023*. 34 pp.

Nesje, A., Dahl, S.O., Thun, T. & Nordli, Ø. 2008: The 'Little Ice Age' glacial expansion inwestern Scandinavia: summer temperature or winter precipitation? *Clim. Dyn. 30,* 789–801, http://dx.doi.org/10.1007/s00382-007-0324-z.

Nicolas, A., Achauer, U. & Daignieres, M. 1994: Rift Initiation by Lithospheric Rupture. *Earth and Planetary Science Letters 123*, 281-298.

Nielsen, S. B., Gallagher, K. et al. . 2009. The evolution of western Scandinavian topography: a review of Neogene uplift versus the ICE (isostasy–climate– erosion) hypothesis. *Journal of Geodynamics 47,* 72–95.

Nirrengarten, M., Gernigon, L. & Manatschal, G. 2014: Lower-crustal bodies in the Møre volcanic rifted margin: Geophysical determination and geological implications. *Tectonophysics 636* 143–157.

Njone, I. 2014: Hydrothermal vent activities at the Gjallar Ridge in the Vøring Basin, mid-Norway, *Master's thesis*. The Arctic University of Norway, Tromsø, Norway.

Norden, B. & Förster, A. 2006: Thermal conductivity and radiogenic heat production of sedimentary and magmatic rocks in the Northeast German Basin. *AAPG Bulletin 90*, 939–962.

Nordgulen, Ø. & Solli, A. 1992: Froan. Berggrunnskart; Froan; 1423 II; 1:50 000. *Geological Survey of Norway (NGU)*.

Nordgulen, Ø., Solli, A. & Sundvoll, B. 1995: Caledonian granitoids in the Frøya-Froan area, central Norway. *Norges Geologiske Undersøkelse Bulletin 427*, 48-51.

Nordgulen, Ø., Braathen, A., Corfu, F., Osmundsen, P.T. & Husmo, T. 2002: Polyphase kinematics and geochronology of the Kollstraumen detachment, central Norway. *Norwegian Journal of Geology 82*, 299-316.

Northwest Geophysical Associates 2006: GM-SYS Gravity and Magnetic Modeling software. Users Guide v 4.10. 110 p.

Norton, M.G. 1987: The Nordfjord-Sogn Detachment, W. Norway. *Norsk Geologisk Tidsskrift 67*, 93-106.

Novatem 2012: Fixed-wing magnetic and radiometric survey of the Stad Region in Western Norway. C11089, Airborne survey for NGU - Stad project, Norway 2012. Novatem internal report.

Novatem 2014: Fixed-wing magnetic and radiometric survey of the Trøndelag Region in Norway. C12095, Airborne survey for NGU, TRAS-12 Norway 2011-2014 project. Novatem internal report.

Norwegian Petroleum Directorate (NPD) 2014: The NPD's fact pages; well data summary sheets: http://factpages.npd.no/FactPages/Default.aspx?nav1=wellbore&nav2=PageView|Exploration|All&nav3=6753 (September 2014).

Nystuen, J.P. 1987: Synthesis of the tectonic and sedimentological evolution of the late Proteroroic-early Cambrian Hedmark Basin, the Caledonian Thrust Belt, southem Norway. *Norsk Geologisk Tidsskrift 67*, 395-418.

Oberhardt, N. 2013: *Granite weathering, saprolitization and the formation of secondary clay particles, SW Bornholm*, Master Thesis, Univ. Oslo.

Ofstad, F. 2015: Helicopter-borne magnetic and radiometric geophysical survey in Kvinesdal and Sirdal, Vest-Agder. *NGU Report 2015.007*, 25 pp.

Oftedahl, C. 1975: Middle Jurassic graben tectonics in Mid Norway. *Proceedings Jurassic Northern North Sea Symposium 21*, 1–13.

Olafsson, I., Sundvor, E., Eldholm, O. & Grue, K. 1992: Møre Margin: Crustal Structure and Analysis of Expanded Spread Profiles. *Marine Geophysical Researches 14*, 137-163.

Olesen, O. 2014: Strand-flaten – ett skritt nærmere en løsning på gåten. *GEO Energi & Ressurser 17, 5,* 48-52.

Olesen, O. & Smethurst M.A. 1995: NAS-94 Interpretation Report, Part III: Combined interpretation of aeromagnetic and gravity data. *NGU Report 95.040*, 50 pp.

Olesen, O., Reitan, M. & Sæther, P.O. 1993: Petrofysisk Database PETBASE 3.0,Brukerbeskrivelse, *NGU Internrapport 93.023*, Trondheim, Norway.

Olesen, O., Lundin, E., Nordgulen, O., Osmundsen, P.T., Skilbrei, J.R., Smethurst, M.A., Solli, A., Bugge, T. & Fichler, C. 2002: Bridging the gap between the onshore and offshore geology in Nordland, northern Norway, *Norwegian Journal of Geology 82*, 243-262.

Olesen, O., Smethurst, M.A., Torsvik, T.H. & Bidstrup, T. 2004: Sveconorwegian igneous complexes beneath the Norwegian-Danish Basin. *Tectonophysics 387*, 105-130.

Olesen, O., Dehls, J.F., Ebbing, J., Henriksen, H., Kihle, O. & Lundin, E. 2007a: Aeromagnetic mapping of deep-weathered fracture zones in the Oslo Region – a new tool for improved planning of tunnels. *Norwegian Journal of Geology 87,* 253-267.

Olesen, O., Ebbing, J., Lundin, E., Mauring, E., Skilbrei, J.R., Torsvik, T.H., Hansen, E.K., Henningsen, T., Midbøe, P. & Sand, M. 2007b: An improved tectonic model for the Eocene opening of the Norwegian-Greenland Sea: Use of modern magnetic data, *Marine and Petroleum Geology 24*, 53-66.

Olesen, Brönner, M., Ebbing, J., Gellein, J., Gernigon, L., Koziel, J., Lauritsen, T., Mykelbust, R., Pascal, C., Sand, M., Solheim, A. & Usov, S. 2010: New aeromagnetic and gravity compilations from Norway and adjacent areas - methods and applications. *In:* Vining, B.A. & Pickering, S.C. (eds.). Petroleum Geology: From mature basins to new frontiers. Proceedings of the 7th Petroleum Geology Conference. *Geological Society of London* 559-586.

Olesen, O., Bering, D., Brönner, M., Dalsegg, E., Fabian, K., Fredin, O., Gellein, J., Husteli, B., Magnus, Ch., Rønning, J.S., Solbakk, T., Tønnesen J.F. & Øverland, J.A. 2012: Tropical Weathering In Norway, *TWIN Final Report. NGU Report 2012.005,* 188 pp.

Olesen, O. Kierulf, H.P., Brönner, M., Dalsegg, E. & Fredin, O. 2013a: Deep weathering, neotectonics and strandflat formation in Nordland, northern Norway. *Norwegian Journal of Geology 93,* 189-213.

Olesen, O., Brönner, M., Ebbing, J., Elvebakk, H., Gellein, J., Koziel, J., Lauritsen, T., Lutro, O., Maystrenko, Y., Müller, C., Nauti, A., Osmundsen, P.T., Slagstad, T., & Storrø, G. 2013b: Coop Phase I - Crustal Onshore-Offshore Project. *NGU Report 2013.002,* 361 pp.

Olsen, E., Gabrielsen, R.H., Braathen, A. & Redfield, T.F. 2007: Fault systems marginal to the More-Trondelag fault complex, Osen - Vikna area, central-Norway. *Norwegian Journal of Geology 87*, 59-73.

Olsen, L. 2006: Fennoscandia M-LWeichselian glacial variations - much more than just local ice-margin fluctuations. In: Peltonen, P., Pasanen, A. (Eds.), The 27th Nordic Geological Wintermeeting. *Bulletin of the Geological Society of Finland, Special Issue. Geological Society of Finland,* Oulu, Finland, p. 118.

Olsen, L., Sveian, H., Ottesen, D. & Rise, L. 2013: Quaternary glacial, interglacial and interstadial deposits of Norway and adjacent onshore and offshore areas. *In:* Olsen, L., Fredin, O. & Olesen, O. (eds.) *Quaternary Geology of Norway, Geological Survey of Norway Special Publication 13*, 79–144.

Olsson, S., Roberts, R.G. & Bödvarsson, R. 2008: Moho depth variation in the Baltic Shield from analysis of converted waves. *Geologiska Föreningen i Stockholm Förhandlingar* 130, 113-122. http://dx.doi.org/10.1080/11035890809453227.

Osmundsen, P.T. & Ebbing, J. 2008: Styles of extension offshore mid-Norway and implications for mechanisms of crustal thinning at passive margins. *Tectonics* doi:10.1029/2007TC002242, 1-25.

Osmundsen, P.T., Eide, E.A. & Haabesland, N.E., Roberts, D., Andersen, T.B., Kendrick, M, Bingen, B., Braathen, A. & Redfield, T.F. 2006. Kinematics of the Høybakken detachment zone and the Møre-Trøndelag Fault Complex, central Norway. *Journal of the Geological Society of London 163*, 303-318.

Osmundsen, P.T., Sommaruga, A., Skilbrei, J.R. & Olesen, O. 2002: Deep structure of the Mid Norway rifted margin. *Norwegian Journal of Geology* 82, 205-224.

Osmundsen, P.T., Braathen, A., Nordgulen, Ø., Roberts, D., Meyer, G.B. & Eide, E.A. 2003: The Nesna shear zone and adjacent gneiss-cored culminations, North-Central Norwegian Caledonides. *Journal of the Geological Society of London 160*, 1-14.

Ottemöller, L. & Midzi, V. 2003: The crustal structure of Norway from inversion of teleseismic receiver functions, *J. Seismol.* 7, 35–48.

Ottersen, G. 2009: A digital temperature archive for the Norwegian Sea. Institue of marine research, Bergen, Norway, 38 pp.

Ottesen, D., Dowdeswell, J.A., Rise, L. & Bugge, T. 2012: Large-scale development of the mid-Norwegian shelf over the last three million years and potential for hydrocarbon reservoirs in glacial sediments. *Geological Society of London, Special Publications 368*, doi: 10.1144/SP368.6

Ottesen, D., Rise, L., Andersen, E. S., Bugge, T. & Eidvin, T. 2009: Geological evolution of the Norwegian continental shelf between 61°N and 68°N during the last 3 million years. *Norwegian Journal of Geology 89*, 251–265.

Otto-Bliesner, B.L., Brady, E. Clauzet, G. Tomas, R., Levis, S. & Kothavala, Z. 2006: Last glacial maximum and Holocene climate in CCSM3. *J. Climate 19*, 2526-2544.

P'an, C.H. 1982: Petroleum in Basement Rocks. *American Association of Petroleum Geologists Bulletin 66,* 1597-1643.

Pascal, C. 2015: Heat flow of Norway and its continental shelf. *Marine and Petroleum Geology 66*, 956-969.

Pascal, C. & Midttømme, K. 2006. Impact of recent glacial erosion on subsurface temperatures: the Mid-Norwegian Margin. *NGU Report 2006.088*, 25 pp.

Pascal, C., Ebbing, J. & Skilbrei, M.R. 2007: Interplay between the Scandes and the Trans-Scandinavian Igneous Belt: integrated thermo-rheological and potential field modelling of the Central Scandes profile. *Norwegian Journal of Geology 87*, 3-12.

Pasquale, V. 2011: Curie Temperature. Encyclopedia of Solid Earth Geophysics, *Encyclopedia of Earth Sciences Series*, 89-90.

Pattyn, F. 2010: Antarctic subglacial conditions inferred from a hybrid ice sheet/ice stream model, *Earth´s Planet. Sci. Lett. 295*, 451-461.

Peron-Pinvidic, G., Manatschal, G. & Osmundsen, P.T. 2013: Structural comparison of archetypal Atlantic rifted margins: A review of observations and concepts. *Marine and Petroleum Geology 43*, 21-47.

Planke, S., Skogseid, J. & Eldholm, O. 1991: Crustal Structure Off Norway, 62-Degrees to 70-Degrees North. *Tectonophysics 189*, 91-107.

Planke, S., Symonds, P.A., Alvestad, E. & Skogseid, J. 2000: Seismic volcanostratigraphy of large-volume basaltic extrusive complexes on rifted margins. *Journal of Geophysical Research-Solid Earth 105*, 19335-19351.

Piper., J.D.A. & Poppelton, T.J. 1990: A palaeomagnetic study of the Basal Gneiss Region and Jotun Nappe Complex, central-southern Scandinavian Caledonides. *Geophysical Journal International 101*, 591-612

Price, P.B., Nagornov, O.V., Bay, R., Chirkin, D., He, Y., Miocinovic, P., Richards, A., Woschnagg, K., Koci, B. & Zagorodnov V. 2002: Temperature profile for glacial ice at the South Pole: implications for life in a nearby subglacial lake*. Proceedings National Academy of Sciences USA 99*, 7844-7847.

Raab, B. & Vedin, H. (Eds.) 1995: The National Atlas of Sweden: Climate, lakes, and rivers, Bokförlaget Bra Böcker, Höganäs, Sweden.

Ranero, C.R. & Perez-Gussinye, M. 2010: Sequential faulting explains the asymmetry and extension discrepancy of conjugate margins. *Nature 468*, 294-U180.

Raum, T. 2000: Crustal structure and evolution of the Faeroe, Møre and Vøring margins from wide-angle seismic and gravity data, *Dr. thesis*. *University of Bergen, Bergen, Norway*.

Raum, T., Mjelde, R., Digranes, P., Shimamura, H., Shiobara, K.S., Haatvedt, G., Sorenes, N. & Thorbjornsen, T. 2002: Crustal structure of the southern part of the Voring Basin, mid-Norway margin, from wide-angle seismic and gravity data, *Tectonophysics 355*, 99–126.

Raum, T., Mjelde, R., Shimamura, H., Murai, Y., Bråstein, E., Karpuz, R.M., Kravik, K. & Kolstø, H.J. 2006: Crustal structure and evolution of the southern Vøring Basin and Vøring Transform Margin, NE Atlantic, *Tectonophysics 415*, 167–202.

Redfield, T. F.& Osmundsen, P. T. 2013. The long-term topographic response of a continent adjacent to a hyperextended margin: a case study from Scandinavia. GSA Bulletin, 125, 184–200.

Redfield, T.F., Osmundsen, P.T. & Hendriks, B.W.H. 2005: The role of fault reactivation and growth in the uplift of western Fennoscandia. *Journal of the Geological Society 162*, 1013-1030.

Renssen, H. & Isarin, R.F.B. 1998: Surface temperature in NW Europe during the Younger Dryas: AGCM simulation compared with temperature reconstructions. *Climate Dynamics 14*, 33-44.

Reston, T.J., Krawczyk, C.M. & Klaeschen, D. 1996: The S reflector west of Galicia (Spain): Evidence from prestack depth migration for detachment faulting during continental breakup. *Journal of Geophysical Research-Solid Earth 101*, 8075-8091.

Reusch, H.H. 1894: Strandflaten, et nyt trek i Norges Geografi. *Norges geologiske undersøkelse 14*, 1–14.

Reynisson, R.F. 2010: *Deep structure and sub-basalt exploration of the mid-Norwegian margin with emphasis on the Møre margin*. Thesis for the degree of Philosophiae Doctor, Norwegian University of Science and Technology, 142 pp.

Reynisson, F., Ebbing, J., Lundin, E.R. & Osmundsen, P.T. 2010: Properties and sistribution of lower crustal bodies on the mid-Norwegian margin. *In* Vinning, B.A. & Pickering, S.C. (eds.). Petroleum Geology: From Mature Basins to New Frontiers-Proceedings of the 7th Petroleum Geology Conference. London, UK, *Geological Society of London*, 843-854.

Richardson, N.J., Underhill, J.R. & Lewis, G. 2005: The role of evaporite mobility in modifying subsidence patterns during normal fault growth and linkage, Halten Terrace, Mid-Norway. *Basin Research 17*, 203-223.

Riebe, C.S., Kirchner, J.W. & Finkel, R.C. 2003: Long-term rates of chemical weathering and physical erosion from cosmogenic nuclides and geochemical mass balance. *Geochim. Cosmochim. Acta 67,* 4411 –4427.

Rise, L., Ottesen, D., Berg, K. & Lundin, E. 2005: Large-scale development of the mid-Norwegian margin during the last 3 million years. *Marine and Petroleum Geology 22*, 33–44.

Rise, L., Chand, S., Hjelstuen, Haflidason, H. & Bøe, R. 2010: Late Cenozoic geological development of the south Vøring margin, mid-Norway. *Marine and Petroleum Geology 27*, 1789-1803.

Rise, L., Ottesen, D., Longva, O., Solheim, A., Andersen, E.S., & Ayers, S. 2006: The Sklinnadjupet slide and its relation to the Elsterian glaciation on the mid-Norwegian shelf: *Marine and Petroleum Geology 23*, 569–583, doi: 10.1016/j.marpetgeo.2006.05.005.

Ritter, U., Zielinski, G.W., Weiss, H.M., Zielinski, R.L.B. & Sættem, J. 2004: Heat flow in the Vøring Basin, Mid. Norwegian Shelf. *Petroleum Geoscience 10,* 353-365.

Ritzmann, O., Jokat, W., Mjelde, R. & Shimamura, H. 2002: Crustal structure between the Knipovich Ridge and the Van Mijenfjorden (Svalbard). *Mar. Geophys. Res. 23*, 379–401.

Roaldset, E., Pettersen, E., Longva, O. & Mangerud, J. 1982: Remnants of preglacial weathering in western Norway. *Norsk Geologisk Tidsskrift 62*, 169-178.

Roberts, D. 1986: A late- to post-Caledonian hydrothermal pebble breccia from the basal gneiss region of Nord-Trøndelag, Central Norway. *Norsk Geologisk Tidsskrift 66,* 235-241.

Roberts, D. 2003: The Scandinavian Caledonides: event chronology, palaeogeographic settings and likely, modern analogues. *Tectonophysics 365*, 283-299.

Roberts, D. & Gee, D.G. 1985: An introduction to the structure of the Scandinavian Caledonides. *In* Gee, D., &Sturt, B.A. (eds.). The Caledonide orogen - Scandinavia and related areas. *John Wiley & Sons, Chichester*, 55-68 pp.

Roberts, D. & Stephens, M. 2000: Caledonian Orogenic Belt. *In* Lundqvist, T. & Autio, S. (eds.). Description to the Bedrock Map of Central Fennoscandia (Mid-Norden). *Geological Survey of Finland Special Paper 28*, 79-104.

Roberts, D., Melezhik, V.M. & Heldal, T. 2002: Carbonate formations and early NW-directed thrusting in the highest allochthons of the Norwegian Caledonides: evidence of a Laurentian ancestry. *Journal of the Geological Society of London 159*, 117-120.

Roberts, D., Andersen, T.B., Olesen, O. & Mosar, J. 2005: Metamorphic core complexes and gneiss-cored culminations along the Mid-Norwegian margin: an overview and some current ideas. *In*: Wandås, B. et al.: *Onshore-offshore Relationships on the North Atlantic Margin*. NPF Special Publication 12, 29-41.

Roberts, D., Nordgulen, Ø. & Melezhik, V. 2007: The Uppermost Allochthon in the Scandinavian Caledonides: From a Laurentian ancestry through Taconian orogeny to Scandian crustal growth on Baltica. *In:* Hatcher, R.D., Jr., Carlson, M.P., McBride, J.H. Martinez Catalán, J.R. (eds.) *4-D Framework of Continental Crust: Geological Society of America Memoir.* Geological Society of America 357-377.

Roberts, D. 1997: Berggrunnskart Grong, M 1:250 000. Norges geologiske undersøkelse.

Robinson, P., Roberts, D., Gee, D.G. & Solli, A. 2014: A major synmetamorphic Early Devonian thrust and extensional fault system in the Mid Norway Caledonides: relevance to exhumation of HP and UHP rocks. *In* Corfu, F., Gasser, D. & Chew, D.M. (eds.). New Perspectives on the Caledonides of Scandinavia and Related Areas. *Geological Society of London, Special Publications 390*, 1-31.

Rodionov A., Ofstad F., Stampolidis A. & Tassis G. 2014: Helicopter-borne magnetic, electromagnetic and radiometric geophysical survey in the Hjartdal-Rjukan-Lyngdal area, Telemark County. *NGU Report 2014.052*, 29 pp.

Rueslåtten, H. 1985: A deep-weathered profile at Stora Silevatten, Southern Sweden, Proceedings Clay Minerals – Modern Society, Uppsala Symposium, 1985.

Rueslåtten, H.G. 2015: Chapter 8. Mineralogical and geochemical studies of deep basement weathering in Norway. *In:* Olesen, O., Baranwal, V., Brönner, M., Dalsegg, E., Dumais, M.A., Gellein, J., Heldal, T., Larsen, B.E., Lauritsen, T., Lutro, O., Maystrenko, Y., Nasuti, A., Roberts, D., Rueslåtten, H., Rønning, J.S., Solli, A. Slagstad, T. & Stampolidis, A. (eds.) *Coop Phase 2 - Crustal Onshore-Offshore Project.* NGU Report 2015.063, 107-166.

Rueslåtten, H.G. & Jørgensen, P. 1977: Mineralogical composition and changes due to weathering in tills from Southern Norway, Proceedings 2nd Int. Symp. On Water-Rock Interactions 1, 184-194.

Rupke, L.H., Schmid, D.W., Perez-Gussinye, M. & Hartz, E. 2013: Interrelation between rifting, faulting, sedimentation, and mantle serpentinization during continental margin formation-including examples from the Norwegian. *Geochemistry Geophysics Geosystems 14*, 4351-4369.

Rønning, J. S., Baranwal, V. & Ofstad, F. 2012: Magnetiske og radiometriske målinger fra helikopter i Nissedal, Telemark. *NGU Report 2012.075*, 9 pp.

Rønning, J.S., Ganerød, G.V., Dalsegg, E. & Reiser, F. 2013: Resistivity mapping as a tool for identification and characterization of weakness zones in bedrock - definition and testing of an interpretational model. *Bull. Eng. Geol. Environment 73,* 1225-1244.

Rønning, S. 1991: Helikoptermålinger over kartblad Andorsjøen 1823 I. *NGU Report 91.153*, 14 pp.

Rønning, S. 1992a: Helikoptermålinger over kartblad 1823 III, Snåsa. *NGU Report 92.144*, 13 pp.

Rønning, S. 1992b: Helikoptermålinger over kartblad 1723 I, Overhalla. *NGU Report 92.146*, 13 pp.

Rønning, S. 1992c: Helikoptermålinger over kartblad 1723 II, Snåsavatnet. *NGU Report 92.145*, 13 pp.

Rønning, S. 1995a: Helikoptermålinger over Grongfeltet, Nord-Trøndelag 1993 og 94. *NGU Report 95.057*, 14 pp.

Rønning, S. 1995b: Helikoptermålinger over kartblad 1722 IV, Stiklestad. *NGU Report 93.084*, 13 pp.

Rønning, S. 1995c: Helikoptermålinger over Fosenhalvøya, kartbladene 1622 I-IV og 1623 II og III. *NGU Report 95.064*, 19 pp.

Rønning, S. 1995d: Helikoptermålinger over kartblad 1311-IV Sokndal. *NGU Report 95.120*, 14 pp.

Rønning, S., Kihle, O., Blokkum, O. & Håbrekke, H. 1990: Helikoptermålinger kartblad GRONG og sydlige halvpart av kartblad HARRAN. *NGU Report 89.085*, 22 pp.

Rønning S. & Mogaard, J.O. 1995: Helicopter measurements over the Gjølanger area. *NGU Report 95.053*, 15 pp.

Sarkar, D. & Tsvankin, I. 2003: Analysis of image gathers in factorized VTI media: *Geophysics* 68, 2016–2025, doi: 10.1190/1.1635055.

Sass, J. H., Lachenbruch, A. H., Moses, T. H., Jr. & Morgan, T. 1992: Heat flow from a scientific research well at Cajon Pass, California. *Journal of Geophysical Research 97(B4)*, 5017–5030.

Scheck-Wenderoth, M. & Maystrenko, Y.P. 2013: Deep control on shallow heat in sedimentary basins. *Energy Procedia 40*, 266-275, doi.org/10.1016/j.egypro.2013.08.031.

Scheck-Wenderoth, M., Faleide, J.I., Raum, T., Mjelde, R. & Horsfield, B. 2007: The transition from the continent to the ocean—a deeper view on the Norwegian continental margin, *Journal of the Geological Society 164*, 855–868.

Scheck-Wenderoth, M. & Maystrenko, Y. 2008: How warm are passive continental margins? A 3D lithosphere-scale study from the Norwegian margin. *Geology 36*, 419-422, doi: 10.1130/G24545A.1.

Scheck-Wenderoth, M. & Maystrenko, Y. 2011: 3D lithospheric-scale structural model of the Norwegian continental margin (the Vøring and Møre basins). *Scientific Technical Report STR11/02* - Data, Helmholtz Centre Potsdam GFZ German Research Centre for Geosciences, Germany, 31 pp., doi: 10.2312/GFZ.b103-11027.

Schiffer, C., Stephenson, R.A., Petersen, K.D., Nilsen, S.B., Jacobsen, B.O., Balling, N. & Macdonald, D.I.M. 2015: A sub-crustal piercing point for North Atlantic reconstructions and tectonic implications. *Geology* doi: 10.1130/G37245.1, 1-5.

Schmidt, S. & Götze, H.-J. 1998. Interactive visualization and modification of 3-D models using GIS functions. *Phys. Chem. Earth´s 23*, 289-295, doi:10.1016/S0079-1946(98)00027-5.

Schmidt-Aursch, M.C. & Jokat, W. 2005: The crustal structure of central East Greenland – II: from the Precambrian shield to the recent mid-oceanic ridges. *Geophysical Journal International 160*, 753–760.

Schmittner, A., Urban, N.M., Shakun, J.D., Mahowald, N.M., Clark, P.U., Bartlein, P.J., Mix, A.C. & Rosell-Mele, A. 2011: Climate Sensitivity Estimated from Temperature Reconstructions of the Last Glacial Maximum. *Science 334*, 1385-1388, doi: http://dx.doi.org/10.1126/science.1203513

Schönharting, G. & Abrahamsen, N. 1989: Paleomagnetism of the volcanic sequence in Hole 642E, ODP Leg 104, Vøring Basin Plateau, and correlation with Early Tertiary basalts in the North Atlantic. *In* Eldholm, O., Thiede, J. & Taylor, E. (eds.). Proceedings of the Ocean Drilling Program, Scientific Results 104. Volume 104, 912-920.

Sclater, J., G. & Christie, P., A., F. 1980: Continental stretching: an explanation of the post-Mid-Cretaceous subsidence of the central North Sea basin. *Journal of Geophysical Research 85-B7*, 3711-3739.

Sejrup, H.P., King, E., Aarseth, I., Haflidason, H., Elverhøi, A., 1996. Quaternary Erosion and Depositional Processes: Western Norwegian Fjords, Norwegian Channel and North Sea Fan. In: De Batist, M., Jacobs, P. (eds.), *Geology of Siliciclastic Seas*. Geological Society of London, Special Publication 117, pp. 187–202.

Sejrup, H.P., Larsen, E., Haflidason, H., Berstad, I.M., Hjelstuen, B.O, Jonsdottir, H.E., King, E.L., Landvik, J., Longva, O., Nygåard, A., Ottesen, D., Raunholm, S., Rise, L. &

Seppä, H., Bjune, A.E., Telford, R.J., Birks, H.J.B. & Veski, S. 2009: Last nine-thousandyears of temperature variability in Northern Europe. *Clim. Past 5*, 523–535,http://dx.doi.org/10.5194/cp-5-523-2009.

Sequeira Braga, M.A., Paquet H. & Begonha, A. 2002: Weathering of granites in a temperate climate (NW Portugal): granitic saprolites and arenization. *Catena 49*, 41– 56.

Séranne, M. 1992: Late Palaeozoic Kinematics of the More-Trondelag Fault Zone and Adjacent Areas, Central Norway. *Norsk Geologisk Tidsskrift 72*, 141-158.

SGU 2009: Produktion av flyggeofysiska mätdata för projekt SPAS-09. Sveriges geologiska undersökning's slutrapport.

Sibuet, J.C. & Tucholke, B.E. 2012: The geodynamic province of transitional lithosphere adjacent to magma-poor continental margins. *In* Mohriak, W.U., Danforth, A., Post, P.J., Brown, D.E., Tari, G.C., Nemcok, M. & Sinha, S.T. (eds.). Conjugate Divergent Margins. *Geological Society of London 369*, http://dx.doi.org/10.1144/SP369.15.

Sibuet, J.C., Sirastava, S. & Manatschal, G. 2007: Exhumed mantle-forming transitional crust in the Newfoundland-Iberia rift and associated magnetic anomalies. *Journal of Geophysical Research 112*, doi:10.1029/2005JB003856.

Siegert, M.J., Dowdeswell, J.A., Hald, M. & Svendsen, J.I.. 2001: Modelling the Eurasian ice sheet through a full (Weichselian) glacial cycle. *Global and Planetary Change 31*, 367-385.

Sigmond, E.M.O. 2002: Geological Map, Land and Sea Areas of Northern Europe, Scale 1: 4 million, Geological Survey of Norway.

Silva, I.A.B.C. & Barbosa, V.C.F. 2003: 3D Euler deconvolution: Theoretical basis for automatically selecting good solutions. *Geophysics 68*, 1962-1968.

Skilbrei, J.R. 1990: Structure of the Jotun Nappe Complex, southern Norwegian Caledonides: ambiguity of gravity modelling and reinterpretation. *NGU Report 89.169,* 26 pp.

Skilbrei, J.R. 1993: Helikoptermålinger i Vuku-området, Steinkjer og Verdal kommuner, Nord-Trøndelag. *NGU Report 93.104*, 18 pp.

Skilbrei, J.R. 1994: Kartframstilling av helikoptermåledata fra Røyrvik, Nord-Trøndelag fylkesko. *NGU Report 94.040*, 6 pp.

Skilbrei, J. R., & O. Kihle 1995: Reprocessing and interpretation of the Hunting 1986 Aeromagnetic Data. *NGU Report 95.026*.

Skilbrei, J.R., Skyseth, T. & Olesen, O. 1991: Petrophysical data and opaque mineralogy of high grade and retrogressed lithologies: Implications for the interpretation of aeromagnetic anomalies in northern Vestranden, Western Gneiss Region, Central Norway. *Tectonophysics 192*, 21-31.

Skilbrei, J.R., Olesen, O., Osmundsen, P.T., Kihle, O., Aaro, S. & Fjellanger, E. 2002: A study of basement structures and onshore-offshore correlations in Central Norway. *Norwegian Journal of Geology 82*, 263-279.

Skogseid, J., Planke, S., Faleide, J.I., Pedersen, T., Eldholm, O. & Neverdal, F. 2000: NE Atlantic continental rifting and volcanic margin formation. *In* Nøttvedt, A. (eds). Dynamics of the Norwegian margin. *Geological Society of London, Special Publications 167*, 295-326.

Slagstad, T. 2008: Radiogenic heat production of Archean to Permian geological provinces in Norway. *Norwegian Journal of Geology 88*, 149-166.

Slagstad, T. & Lauritsen, T. 2013: Heat production calculations. In: Olesen, O., Brönner, M., Ebbing, J., Elvebakk, H., Gellein, J., Koziel, J., Lauritsen, T., Lutro, O., Maystrenko, Y., Müller, C., Nasuti, A., Osmundsen, P.T., Slagstad, T. & Storrø G. (eds.) Coop Phase I - Crustal Onshore-Offshore Project, *NGU Report 2013.002*, 74-111.

Slagstad, T., Davidsen, B. & Daly, J.S. 2011: Age and composition of crystalline basement rocks on the Norwegian continental margin: offshore extension and continuity of the Caledonian–Appalachian orogenic belt. *Journal of the Geological Society of London 168*, 1167–1185

Slagstad, T., Barrére, C., Davidsen, B. & Ramstad, R. K. 2008: Petrophysical and thermal properties of pre-Devonian basement rocks on the Norwegian continental margin. *Geological Survey of Norway Bulletin 448*, 1–6.

Slagstad, T., Pin, C. et al. 2013: Tectonomagmatic evolution of the Early Ordovician supra-subduction zone ophiolites of the Trondheim Region, Mid-Norwegian Caledonides. *In:* Corfu, F., Gasser, D. & Chew, D. M. (eds.) *New Perspectives on the Caledonides of Scandinavia and Related Areas*. Geological Society of London, Special Publications 390, 541-562.

Slagstad, T., Balling, N., Elvebakk, H., Midttømme, K., Olesen, O., Olsen, O. & Pascal, C. 2009: Heat-flow measurements in Late Palaeoproterozoic to Permian geological provinces in south and central Norway and a new heat-flow map of Fennoscandia and the Norwegian–Greenland Sea. *Tectonophysics 473*, 341–361.

Smethurst, M.A. 2000: Land-offshore tectonic links in western Norway and the northern North Sea. *Journal of the Geological Society of London 157*, 769-781.

Solli, A. 1995: Digitalt berggrunnskart over Nord-Trøndelag og Fosen. *Norges geologiske undersøkelse, Trondheim.*

Solli, A. & Nordgulen, Ø. 2006: Berggrunnskart over Norge og kaledonidene i Sverige og Finland- 1:2.000.000. *Norges geologiske undersøkelse (NGU)*.

Solli, A., Bugge, T. & Thorsnes, T. 1997: Geologisk kart over Norge, berggrunnskart NANSOS 1:250000. *Norges geologiske undersøkelse*.

Solli, A., Grenne, T., Slagstad, T. & Roberts, D. 2003: Berggrunnskart Trondheim 1621 IV, M 1:50.000, foreløpig utgave, Norges geologiske undersøkelse.

Sommaruga, A. & Bøe, R. 2002: Geometry and subcrop maps of shallow Jurassic basins along the Mid-Norway coast. *Marine and Petroleum Geology 19*, 1029-1042.

Stampolidis A. & Ofstad F. 2014: Helicopter-borne magnetic and radiometric geophysical survey at Drangedal, Telemark County. *NGU Report 2014.044*, 29 pp.

Stampolidis A. & Ofstad F. 2015: Helicopter-borne magnetic and radiometric geophysical survey at Kviteseid, Nissedal, Fyresdal and Dalen,Telemark county. *NGU Report 2015.040*, 29 pp.

Stampolidis A., Ofstad F. & Barnawal V. 2013: Helicopter-borne magnetic and radiometric geophysical at Kviteseid, Notodden, Ulefoss in Telemark county Nordland. *NGU Report 2013.049*, 28 pp.

Steel, R., Siedlecka, A. & Roberts, D. 1985: The Old Red Sandstone basins of Norway: a review. *In* Gee, D.G. & Sturt, B.A. (eds.). The Caledonide orogen-Scandinavia and related areas. *John Wiley & Sons, Chichester*, 293-315.

Stephens, M.B. & Gee, D. 1985: A tectonic model for the evolution of the eugeoclinal terranes in the central Scandinavian Caledonides. *In* Gee, D. & Sturt, B.A. (eds.). The Caledonide Orogen—Scandinavia and Related Areas. *Wiley, Chichester*, p. 953-970.

Storti, F., Holdsworth, R.E. & Salvini, F. 2003: Intraplate strike-slip deformation belts. *In* Storti, F., Holdsworth, R.E. & Salvini, F. (eds.). Intraplate strike-slip deformation belts. *Geological Society of London, Special Publications 210*, 1-14.

Storti, F., Salvini, F., Rossetti, F. & Morgan, J.P. 2007: Intraplate termination of transform faulting within the Antarctic continent. *Earth and Planetary Science Letters 260,* 115-126.

Stratford, W. & Thybo, H. 2011: Seismic structure and composition of the crust beneath the southern Scandes, Norway. *Tectonophysics 502*, 364-382.

Stratford, W., Thybo, H., Faleide, J.I., Olesen, O. & Tryggvason, A. 2009: New Moho map for onshore southern Norway. *Geophysical Journal International 178*, 1755-1765, doi: 10.1111/j.1365-246X.2009.04240.x.

Strömberg, A.G.B. 1976: A pattern of tectonic zones in the western part of the East European Platform. *Geologiska Föreningens i Stockholm Förhandlingar 98*, 227-243.

Sturt, B.A. & Braathen, A. 2001: Deformation and metamorphism of Devonian rocks in the outer Solund area, western Norway: implications for models of Devonian deformation. *International Journal of Earth Sciences 90*, 270-286.

Sturt, B.A., Dalland, A. & Mitchell, J.L. 1979: The age of the sub Mid-Jurassic tropical weathering profile of Andøya, northern Norway, and the implications for the Late Palaeozoic paleography in the North Atlantic region. *Geologische Rundschau 68*, 523–542.

Sulebak, J.R. 2007: Landformer og prosesser, en innføring i naturgeografiske tema. Fagbokforlaget, Bergen. 391 pp.

Sun, Z., Zhou, D., Wu, S.M., Zhong, Z.H., Myra, K., Jiang, J.Q. & Fan, H. 2009: Patterns and Dynamics of Rifting on Passive Continental Margin from Shelf to Slope of the Northern South China Sea: Evidence from 3D Analogue Modeling. *Journal of Earth Science 20*, 136-146.

Sutra, E. & Manatschal, G. 2012: How does the continental crust thin in a hyperextended rifted margin? Insights from the Iberia margin. *Geology 40*, 139-142.

Sæther, O. M., Xie, R., Aagaard, P., Endre, E., Løken, T., & Rudolph-Lund, K. 2009: Main and trace element content of shales from Ankerskogen (Hamar) and Øvre Slottsgt (Oslo), Norway, *NGU Report 2009.063.*

Sættem, J. & Mørk, M.B.E. 1996: Frøyatunnelen: Studie basert på vertikal-boringer og regional lineament-informasjon. *IKU Petroleumsforskning A.S report 96.018*, p. 35.

Takanashi, M. & Tsvankin, I. 2012: Migration velocity analysis for TI media in the presence of quadratic lateral velocity variation. *Geophysics 77*, u87–u96. 10.1190/geo2012-0032.1

Tesauro, M., Kaban, M.K. & Cloetingh, S.A.P.L. 2008: EuCRUST-07: A new reference model for the European crust. *Geophys. Res. Lett. 35*, L05313, doi:10.1029/2007GL032244.

Theunissen, K., Klerkx, J., Melnikov, A.,& Mruma, A. 1996: Mechanisms of inheritance of rift faulting in the western branch of the East African Rift, Tanzania. *Tectonics 15*, 776-790.

Tommasi, A., Vauchez, A. & Daudre, B. 1995: Initiation and Propagation of Shear Zones in a Heterogeneous Continental Lithosphere. *Journal of Geophysical Research-Solid Earth 100*, 22083-22101.

Torske, T. & Prestvik, T. 1991: Mesozoic detachment faulting between Greenland and Norway; inferences from Jan Mayen fracture zone system and associated alkalic volcanic rocks. *Geology 19*, 481–484.

Torsvik, T.H. & Cocks, L.R.M. 2005: Norway in space and time: A Centennial Cavalcade. *Norwegian Journal of Geology 85*, 73-86.

Trice, R. 2014: Basement exploration, West of Shetlands: progress in opening a new play on the UKCS. *In* Cannon, S.J.C. & Ellis, D. (eds). Hydrocarbon Exploration to Exploitation West of Shetlands. *Geological Society of London, Special Publications 397*, 81-105.

Tsikalas, F., Elderholm, O. & Faleide, J.I. 2005: Crustal structure of the Lofoten-Vesteralen continental margin, off Norway. *Tectonophysics 404*, 151–174.

Tsikalas, F., Faleide, J.I., Eldholm, O. & Blaich, O.A. 2012: The NE Atlantic conjugate margins. *In* Roberts, D.G. & Bally, A.W. (eds.). hanerozoic Passive Margins, Cratonic Basins and Global Tectonic Maps. 141-201.

Tucker, R. D., Robinson, P. Solli, A., Gee, D.G., Thorsnes, T., Krogh, T.E., Nordgulen, Ø. & Bickford, M.E. 2004: Thrusting and extension in the Scandian hinterland, Norway: new U–Pb ages and tectonostratigraphic evidence. *American Journal of Science 304*, 477–532.

Tullborg, E.-L. & Larson, S.Å. 2006: Porosity in crystalline rocks - A matter of scale. *Engineering Geology 84*, 75–83.

Turcotte, D.L. & Schubert, G. 2002: *Geodynamics* (2nd edition): Cambridge University Press, Cambridge, 456 p.

Tveito, O.E., Førland, E., Heino, R., Hanssen-Bauer, I., Alexandersson, H., Dahlström, B., Drebs, A., Kern-Hansen, C., Jónsson, T., Vaarby Laursen, E. & Westman, Y. 2000: Nordic temperature maps. *DNMI-Report 09/00 KLIMA*, 54 pp.

Tveten, E., Lutro, O. & Thorsnes, T. 1998: Berggrunnskart Ulsteinvik, M 1:250000. *Norges geologiske undersøkelse, Trondheim.*

Unternehr, P., Peron-Pinvidic, G., Manatschal, G. & Sutra, E. 2010: Hyper-extended crust in the South Atlantic: in search of a model. *Petroleum Geoscience 16*, 207-215.

van den Berg, A.P., Yuen, D.A. & Steinbach, V. 2001: The effects of variable thermal conductivity on mantle heat-transfer. *Geophys. Res. Lett. 28*, 875-878.

Vauchez, A., Barruol, G.,& Tommasi, A. 1997: Why do continents break-up parallel to ancient orogenic belts? *Terra Nova 9*, 62-66.

Vauchez, A., Neves, S., Caby, R., Corsini, M., Egydiosilva, M., Arthaud, M. & Amaro, V. 1995: The Borborema Shear Zone System, Ne Brazil. *Journal of South American Earth Sciences 8*, 247-266.

Verhoef, J., W. R. Roest, R. Macnab, J. Arkani-Hamed & Members of the ProjectTeam 1996: Magnetic anomalies of the Arctic and North Atlantic Oceans and adjacent land areas. *Report Geological Survey of Canada*, *Open File 3125.*

Vetel, W., Le Gall, B. & Walsh, J.J. 2005: Geometry and growth of an inner rift fault pattern: The Kino Sogo Fault Belt, Turkana Rift (North Kenya). *Journal of Structural Geology 27*, 2204-2222.

Vetti, V.V. & Fossen, H. 2012: Origin of contrasting Devonian supradetachment basin types in the Scandinavian Caledonides. *Geology 40*, 571-574.

Vially, R. & de Clarens, P. 1986: Rapport d´interprétation de la campagne Refranorge 2. Premiére partie : Mer de Norvége. *Institut Français du Pétrole 34*, 0-136.

Vilà, M., Fernández, M. & Jiménez-Munt, I. 2010: Radiogenic heat production variability of some common lithological groups and its significance to lithospheric thermal modeling. *Tectonophysics 490*, 152–164.

Vodyanitskii, Yu. N. 2012: Geochemical fractionation of lanthanides in soils and rocks: A review of publications, *Eurasian Soil Science 45*, 1, 56-67.

Vosteen, H.-D. & Schellschmidt, R. 2003: Influence of temperature on thermal conductivity, thermal capacity, and thermal diffusivity for different types of rock. *Physics and Chemistry of the Earth 28*, 499–509.

Wagner, W. & Kretzschmar, H.-J. 2008: *International steam tables – properties of water and steam based on the Industrial Formulation IAPWS-IF97*. Springer-Verlag, Berlin.

Watts, L.M., Holdsworth, R.E., Sleight, J.A., Strachan, R.A. & Smith, S.A.F. 2007: The movement history and fault rock evolution of a reactivated crustal-scale strike-slip fault: the Walls Boundary Fault Zone, Shetland. *Journal of the Geological Society of London 164*, 1037-1058.

Werner, S. 1955: Interpretation of magnetic anomalies at sheet-like bodies. *Sveriges Geologiska Undersökning, Ser. C.C. 43*.

White, R.S., Smith, L.K., Roberts, A.W., Christie, P.A.F., Kuznir, N.J. & iSIMM_team 2008: Lower-crustal intrusion on the North Atlantic continental margin. *Nature* 452, 460-464.

Whitmarsh, R.B., Manatschal, G. & Minshull, T.A. 2001: Evolution of magma-poor continental margins from rifting to seafloor spreading. *Nature 413*, 150-154.

Wilson, J.R., Pedersen, S., Berthelsen, C.R. & Jakobsen, B.M. 1977: New light on the Precambrian Holum granite, south Norway. *Norsk Geologisk Tidsskrift 57*, 347-360.

Withjack, M.O. & Callaway, S. 2000: Active normal faulting beneath a salt layer: An experimental study of deformation patterns in the cover sequence. *Aapg Bulletin-American Association of Petroleum Geologists 84*, 627-651.

Wolff, F.C. 1979: Beskrivelse til de berggrunnsgeologiske kartene Trondheim og Östersund 1:250 000. *Norges geologiske undersøkelse 353*, 77 pp.

Wollenberg, H.A. & Smith, A.R. 1987: Radiogenic heat production of crustal rocks: an assessment based on geochemical data. *Geophysical Research Letters 14*, 295-298.

Yamasaki, T. & Gernigon, L. 2009: Styles of lithospheric extension controlled by underplated mafic bodies. *Tectonophysics 468,* 169-184.

Yoshinobu, A.S., Barnes, C.G., Nordgulen, Ø., Prestvik, T., Fanning, M. & Pedersen, R.B. 2002: Ordovician magmatism, deformation and exhumation in the Caledonides of central Norway: An orphan of the Taconic orogeny? *Geology 30*, 883-886.

Zhang, Y.S. & Lay, T. 1996: Global surface wave phase velocity variations. *Journal of Geophysical Research - Solid Earth and Planets 101B*, 8415–8436, doi: 10.1029/96JB00167.

Ziegler, P.A. 1992: European rift system. *Tectonophysics 208,* 91-111.

Ziemen, F., Rodehacke, C. & Mikolajewicz, U. 2012: LGM ice sheets simulated with a complex fully coupled ice sheet - climate model. EGU General Assembly, memory stick: *Geophysical Research Abstracts 14*, EGU2012-6277, Vienna, Austria.

Åhäll, K.-I. & Larson, S.Å. 2000: Growth-related 1.85-1.55 Ga magmatism in the Baltic Shield; a review addressing the tectonic characteristics of Svecofennian, TIB 1-related and Gothian events. *Geologiska Föreningen i Stockholm Förhandlingar 122*, 193-206.

APPENDIX A. 2D-RESISTIVITY METHOD DESCRIPTION

Method outline, data acquisition and inversion

Bjørn Eskil Larsen

The 2D-resistivity method is carried out by injecting current into the ground with the use of two electrodes and by measuring the voltage between the two separate electrodes. The resistance and subsequently the apparent resistivity can then be calculated.

The Lund System (Dahlin 1993) was used with the measuring instrument ABEM Terrameter LS (ABEM 2012) to acquire the data. As seen in Figure A1 it uses 4 multielectrode cables and for the surveys presented in this report, a Multiple Gradient electrode configuration (Dahlin & Zhou 2006) was applied. 10 m electrode separation was used for all measurements except Profiles 1 & 2 from Estenstadmarka, where a 5 m electrode spacing was used.

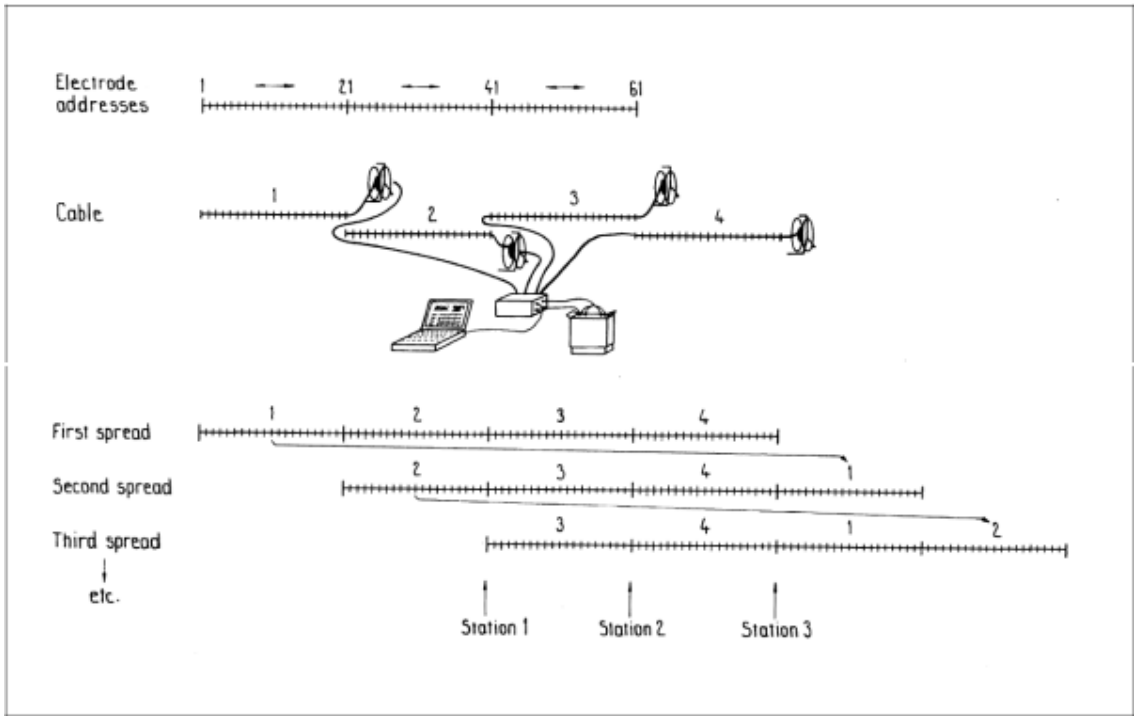

Figure A1. Diagram of measuring procedure that illustrates the set-up of the Lund System and the roll-along method for performing as many measurements as required (From Dahlin 1993).

As the measurements only give an apparent resistivity value that represents the average resistivity between the potential electrodes, inversion of the data is necessary to find the specific resistivity. The program RES2DINV was used with robust data constraint for the inversion procedure.

References

ABEM, 2012: *ABEM Terrameter LS. Instruction Manual*. ABEM 20120109, based on release 1.10. ABEM, Sweden.

Dahlin, T. 1993: *On the automation of 2D resistivity surveying for engineering and environmental applications*. PhD thesis, Department of Engineering Geology, Lund Institute of Technology, Lund University. 187 pp, ISBN 91-628-1032-4.

Dahlin, T. and Zhou, B. 2006: *Multiple-gradient array measurements for multichannel 2D resistivity imaging*. *Near Surface Geophysics 4,* 113 - 123.

GEOLOGICAL
SURVEY OF
NORWAY

· NGU ·

Geological Survey of Norway
PO Box 6315, Sluppen
N-7491 Trondheim, Norway

Visitor address
Leiv Eirikssons vei 39
7040 Trondheim

Tel (+ 47) 73 90 40 00
E-mail ngu@ngu.no
Web www.ngu.no/en-gb/